

FAULT BASED PROBABILISTIC SEISMIC HAZARD ASSESSMENT AT
DIFFERENT TECTONIC REGIMES AND DATA SAMPLING CONDITIONS:
EMPHASIS ON SENSITIVITY OF SEISMIC SOURCE CHARACTERIZATION

A THESIS SUBMITTED TO
THE GRADUATE SCHOOL OF NATURAL AND APPLIED SCIENCES
OF
MIDDLE EAST TECHNICAL UNIVERSITY

BY

SYED TANVIR SHAH

IN PARTIAL FULFILLMENT OF THE REQUIREMENTS
FOR
THE DEGREE OF DOCTOR OF PHILOSOPHY
IN
GEOLOGICAL ENGINEERING

OCTOBER 2019

Approval of the thesis:

**FAULT BASED PROBABILISTIC SEISMIC HAZARD ASSESSMENT AT
DIFFERENT TECTONIC REGIMES AND DATA SAMPLING
CONDITIONS: EMPHASIS ON SENSITIVITY OF SEISMIC SOURCE
CHARACTERIZATION**

submitted by **SYED TANVIR SHAH** in partial fulfillment of the requirements for
the degree of **Doctor of Philosophy in Geological Engineering Department,**
Middle East Technical University by,

Prof. Dr. Halil Kalıpçılar
Dean, Graduate School of **Natural and Applied Sciences**

Prof. Dr. Erdin Bozkurt
Head of Department, **Geological Engineering**

Assist. Prof. Dr. A. Arda Özacar
Supervisor, **Geological Engineering, METU**

Assoc. Prof. Dr. Zeynep Gülerce
Co-Supervisor, **Civil Engineering, METU**

Examining Committee Members:

Prof. Dr. Erdin Bozkurt
Geological Engineering, METU

Assist. Prof. Dr. A. Arda Özacar
Geological Engineering, METU

Prof. Dr. Ayşegül Askan Gündoğan
Civil Engineering, METU

Prof. Dr. Erhan Altunel
Geological Engineering, Eskişehir Osmangazi University

Assoc. Prof. Dr. M. Abdullah Sandıkkaya
Civil Engineering, Hacettepe University

Date: 31.10.2019

I hereby declare that all information in this document has been obtained and presented in accordance with academic rules and ethical conduct. I also declare that, as required by these rules and conduct, I have fully cited and referenced all material and results that are not original to this work.

Name, Surname: Syed Tanvir Shah

Signature:

ABSTRACT

FAULT BASED PROBABILISTIC SEISMIC HAZARD ASSESSMENT AT DIFFERENT TECTONIC REGIMES AND DATA SAMPLING CONDITIONS: EMPHASIS ON SENSITIVITY OF SEISMIC SOURCE CHARACTERIZATION

Shah, Syed Tanvir
Doctor of Philosophy, Geological Engineering
Supervisor: Assist. Prof. Dr. A. Arda Özacar
Co-Supervisor: Assoc. Prof. Dr. Zeynep Gülerce

October 2019, 327 pages

Seismogenic sources often display intrinsic complexities; hence they pose a challenge for accurate representation of source geometries and constraining source parameters in seismic hazard assessment. Subduction zone complexities involving megathrust interface, intraslab and accretionary prism faults leads to enhanced uncertainties in seismic source characterization (SSC). Similarly, extensional regimes are often characterized by multiple sets of inclined faults and paucity of individual slip rates; causing considerable ambiguity in activity rate estimation. Moreover, regions characterized by complex tectonics producing mixed earthquake mechanisms lead to challenges in SSC modelling. In this study, detailed seismic hazard analysis with sensitivity tests for various enigmatic parameters is carried out for subduction, extensional and mixed tectonic regimes. For subduction, sensitivity of the hazard outcomes to the alternative magnitude distribution models, dip amounts and interface depth extents is tested. Truncated exponential magnitude distribution model resulted in ~10% higher peak ground accelerations (PGA), when compared to the composite model that has a better match with the seismicity. Gentler and deeper-extending interface geometries resulted in higher PGA values towards the accretionary wedge.

For extensional regimes, alternative approaches utilizing geodetic and seismic data are employed to determine the activity rates which are later partitioned among fault systems using morphology and length. Later, a procedure that provides weighted, maximum and minimum PGA maps is established to evaluate and minimize bias on hazard estimates. Finally, polarity data is analyzed to constrain focal mechanism solutions in a regime characterized by mixed strike-slip and normal faulting to constrain the seismic source parameters. The updated planar SSC model that includes an additional areal seismic source to account for off-fault seismicity and complex tectonics, led up to 0.08g increase in hazard estimates.

Keywords: Makran Subduction Zone, Western Anatolia, Central Anatolia, Probabilistic Seismic Hazard Assessment

ÖZ

FARKLI TEKTONİK REJİMLERDE VE VERİ TOPLAMA DURUMLARINDA FAY KAYNAKLI OLASILIKSAL SİSMİK TEHLİKE ANALİZİ: SİSMİK KAYNAK KARAKTERİZASYONUNUN DUYARLILIĞINA VURGU

Shah, Syed Tanvir
Doktora, Jeoloji Mühendisliği
Tez Danışmanı: Dr. Öğr. Üyesi A. Arda Özacar
Ortak Tez Danışmanı: Doç. Dr. Zeynep Gülerce

Ekim 2019, 327 sayfa

Karmaşıklıklar içeren sismojenik kaynaklar doğru kaynak geometrisinin ve parametrelerinin belirlenmesini zorlaştırarak, bu kaynakların sismik tehlike analizi için modellenmesinde güçlüğe sebep olmaktadır. Dalma-batma zonlarındaki büyük bindirme yüzeyleri, dalan plaka içerisindeki ve yığışım prizmasındaki faylar sismik kaynak karakterizasyonunda (SKK) önemli belirsizliklere yol açmaktadır. Buna benzer şekilde, gerilmeli rejimlerde genellikle birçok eğimli fay seti bulunması ve bu fayların düşük kayma hızları göstermeleri de aktivite oranının karakterizasyonunda belirsizliğe neden olur. Ayrıca, karma deprem mekanizmaları üreten karmaşık tektonizma bölgeleri SKK için zorluklara yol açmaktadır. Bu çalışmada, dalma-batma, genişleme ve karışık tektonik rejimler için duyarlılık testleri uygulayarak detaylı sismik tehlike analizleri yapılmıştır. Dalma-batma için, farklı deprem büyüklüğü dağılım modelleri, eğim miktarları ve arayüzlerin derinliği-uzanımı değerleri test edilmiştir. Kesik üstel deprem büyüklüğü dağılım modeliyle en büyük yer ivmesi (PGA) ~10% oranında yüksek hesaplanmıştır ancak kompozit model deprenselliğe daha uygun sonuçlar vermiştir. Düşük eğimli ve derine giden dalma-batma yüzeylerinde yığışım prizmasına doğru daha yüksek PGA değerleri gözlenmiştir.

Genişlemeli rejimlerde jeodezik ve sismik verileri kullanan alternatif yöntemlerle aktivite oranları hesaplanmış ve fayların uzunlukları ve morfolojisine göre fay sistemlerine paylaştırılmıştır. Daha sonra, sismik tehlike tahminlerindeki belirsizlikleri modellemek için; en düşük, en yüksek ve ağırlıklandırılmış PGA haritalarının oluşturulduğu bir prosedür geliştirilmiştir. Son olarak, doğrultu atımlı ve normal faylanma içeren karma bir tektonik rejimde SKK parametrelerini belirlemek amacıyla odak mekanizması için kutuplanma verileri analiz edilmiştir. Fay dışı depremselliği ve karmaşık tektonizmayı hesaba katmak için alansal bir kaynağın eklendiği güncelleştirilmiş SKK modeli deprem tehlike tahminlerinde fay bazlı modelellere göre PGA değerinde yaklaşık 0.08g lik bir artışa neden olmuştur.

Anahtar Kelimeler: Makran Dalma-Batma Bölgesi, Batı Anadolu, İç Anadolu, Sismik Kaynak Karakterizasyonu, Olasılıksal Sismik Tehlike Analizi

Dedicated to Hoorain

ACKNOWLEDGEMENTS

First, I would like to express my heartfelt gratitude and sincere thanks to my Supervisors; Dr. A. Arda Özacar and Dr. Zeynep Gülerce. Their invaluable guidance, patience, immense knowledge, enthusiastic approach and useful critiques helped me throughout this research and writing of the thesis.

Besides, I would also like to extend my gratitude to the committee members of this thesis for their insightful comments and providing suggestions to improve my research work.

I would like to acknowledge the Higher Education Commission of Pakistan for providing the financial support for my postgraduate studies.

I am deeply grateful to all my friends and colleagues including; Ishfaq Bashir, Saeed Yousafzai, Rizwan Aziz, Bakht Zamir, Saad Arshad, Mohsin Ali, Abdul Qayyum and others for their continuous support and motivation. It would have been very hard to accomplish this study without them.

Last but not the least, I would like to thank my beloved family: especially my Parents, *Amraiza & Said Malik* and my elder brother Said Kashif Shah. Words cannot express how grateful I am to them. Their sacrifices and support for me in my studies and in life, is what sustained me thus far.

TABLE OF CONTENTS

ABSTRACT	v
ÖZ	vii
ACKNOWLEDGEMENTS	x
TABLE OF CONTENTS	xi
LIST OF TABLES	xv
LIST OF FIGURES	xvi
CHAPTERS	
1. INTRODUCTION	1
1.1. Background	1
1.2. Problem Statement	3
1.3. Purpose and Scope.....	6
1.4. Organization of Thesis	9
2. FAULT BASED PROBABILISTIC SEISMIC HAZARD ASSESSMENT OF THE MAKRAN SUBDUCTION ZONE AND THE CHAMAN FAULT SYSTEM IN PAKISTAN: EMPHASIS ON THE EFFECT OF SOURCE CHARACTERIZATION OF MEGATHRUST	11
2.1. Introduction	12
2.2. Seismic Source Characterization.....	15
2.2.1. Chaman Transform Fault Zone.....	15
2.2.2. Makran Subduction Zone.....	20
2.3. Magnitude Recurrence Relations	24

2.4. Sensitivity Analysis of the Hazard Results to Seismic Source Model Parameters	29
2.5. Relative Contribution of Different Tectonic Structures on the Final Hazard Map	36
2.6. Conclusions and Recommendations	39
3. PROCEDURE FOR FAULT BASED PSHA IN EXTENSIONAL TECTONIC REGIMES, CASE STUDY FROM WESTERN ANATOLIA: IMPLICATIONS OF ACTIVITY RATE CHARACTERIZATION.....	45
3.1. Introduction.....	46
3.2. Fault Based Seismic Source Characterization Models	50
3.2.1. Instrumental Seismicity	50
3.2.2. Focal Mechanism Solutions and the Stress Regime.....	53
3.2.3. Defining the Polygons and Slip Rate Characterization	54
3.2.4. Defining Fault Systems	58
3.2.5. Calculation and Distribution of Activity Rates	60
3.2.5.1. Approach 1: Activity Rates Based on Seismicity.....	61
3.2.5.2. Approach 2: Activity Rates Based on Moment rate	61
3.2.5.3. Approach 3: Activity Rates Based on Slip Rate	63
3.2.6. Ground Motion Models	63
3.3. Seismic Hazard Analysis	64
3.4. Results and Discussions	70
4. FOCAL MECHANISM ANALYSIS OF CENTRAL ANATOLIA AND PROBABILISTIC SEISMIC HAZARD ASSESSMENT FOR ADANA BASIN AND GULF OF ISKENDERUN REGION, TURKEY	79
4.1. Introduction.....	80

4.2. Tectonic Settings and Active Fault Structures	81
4.3. Focal Mechanism Analysis	85
4.3.1. Seismic Data and Methodology	86
4.3.2. Focal Mechanism Solutions.....	93
4.4. Present Day Stress Analysis	98
4.4.1. SH_{max} Orientations	98
4.4.2. Stress Tensor Inversion.....	100
4.4.2.1. Stress Mapping.....	102
4.5. Probabilistic Seismic Hazard Analysis of Adana Basin and Gulf of Iskenderun: Comparison with the New Turkish Seismic Hazard Map (2018)	116
4.5.1. Source Characterization for the New Areal Source Zone.....	118
4.5.2. Logic Tree for the Ground Motion Models	125
4.5.3. Probabilistic Seismic Hazard Assessment using Virtual Fault Concept.	126
4.5.4. PSHA Maps for the Study Area and Comparison with TSHM (2018) ..	129
5. CONCLUSIONS AND RECOMMENDATIONS	135
REFERENCES.....	145
APPENDICES	
A. Seismic source parameters used of all the fault systems used for Makran subduction zone and Chaman transform fault zone. The weights for each parameter in the SSC logic tree is provided in the brackets. Length and depth parameters are in km while Slip rates are in mm/yr.	165
B. Fault segments and the fault rupture systems included in the Seismic source model used in for western Anatolia case study. Slip rates assigned to fault systems using maturity and length ratio are shown. The seismicity rates and moment rates computed for seven polygons in the area are also presented. DOWNDIP WIDTHS (N =	

15.7Km; SS = 12.8km) are calculated from seismogenic depth (12km) and the dip amount of faults (N =50°; SS =70°). The observed Maximum magnitude earthquake (Mmax, observed) within each polygon is provided. The maximum magnitude earthquake that can occur on fault systems within each polygon (Mmax, computed) is calculated using Wells & Coppersmith (1994) relationships. N= Normal faults; SS = Strike-slip faults..... 169

C. Logic Tree for Ground Motion Models for Western Anatolia Case Study..... 171

D. List of focal mechanism solutions compiled from literature for Central Anatolian region, Turkey. References are (1: Jackson & McKenzie, 1984; 2: Salamon et al., 2003; 3: Canitez and Üçer, 1967; 4: Taymaz et al., 1991; 5: Yılmaztürk and Burton, 1999; 6: Dziewonski et al., 1987; Ekström et al., 2012 (CMT); 7: Ergin et al., 2004; 8: Pondrelli et al., 1999 (EMSC); 9: Pondrelli et al., 2002; 2004; 2006; 2007; 2011 (RCMT); 10: Örgülü et al., 2003; 11: Bernardi, et al., 2004, (SRMT); 12: Karasözen, 2014; 13: General Directorate of Disaster Affairs, Earthquake Research Department (AFAD), 14: National Earthquake Information Center of USGS (NEIC); 15: Kandilli Observatory and Earthquake Research Institute National Earthquake Monitoring Center (KOERI); 16: GEOFON Data Centre (GFZ)..... 173

E. List of stations. Station’s name starting with ‘AT’ were installed during the CAT project. The rest of the stations are from KOERI network..... 177

F. Graphical output files of the Focal Mechanism Solutions (FMS) computed in this study..... 181

G. Average Pressure (P) and Tension (T) axis azimuth (az.) and dip angles, maximum and minimum horizontal stress orientations (SHmax, SHmin) orientations and tectonic regimes obtained from all the focal mechanisms (FMS) for Central Anatolia (Chapter 4). 321

CURRICULUM VITAE..... 327

LIST OF TABLES

TABLES

Table 4.1. List of events analyzed in this study and their strike, dip, rake values. Events with * in their ID are discarded due to less amount of data or bad quality of solutions and not used for further analysis	88
Table 4.2. Comparison of stress tensor inversion results for the whole region and sub-regions; using Michael's method (1987) and Win-Tensor program (Delvaux and Sperner, 2003). The results obtained from both methods are presented in the upper and lower row respectively for each subset	112
Table 4.3. Comparison of ground motion characterization logic trees of this study and TSHM.....	126

LIST OF FIGURES

FIGURES

- Figure 1.1. Figure showing locations of selected regions for this thesis. Red bold lines represent plate boundaries (Bird, 2003). The shaded rectangles indicate the approximate limits of study regions selected in this study 8
- Figure 2.1. Seismotectonic map of Pakistan and its surrounding overlaid on topography. Grey dots represent earthquakes gathered from the International Seismological Centre (ISC) catalogue. Centroid Moment Tensor (CMT) solutions are mostly taken from global CMT Catalog (Dziewonski, et al 1981 and Ekström, et al., 2012); Penney et al., 2017 and references therein for Makran region. Bold black lines represent the faults included in our analysis. The green and purple shaded areas demarcate the approximate limits of Chaman transform zone and Makran subduction zone, respectively. Red arrows show the plate motion velocities with respect to a fixed Eurasian plate (DeMets et al., 2010). Inset map on the top shows the location with respect to global plate configuration..... 14
- Figure 2.2. Active fault map of the region compiled from literature data overlaid on the SRTM image. The fault systems identified in this study are outlined by white lines. Fault segments comprising the fault systems are shown by different colors (red and blue). Fault ruptures produced by instrumental and historical earthquakes are shown by yellow fill or dashed yellow lines with their associated year of occurrences. Except accretionary wedge faults, assigned slip rates of fault systems are given in parentheses. Surface projection of intra-slab zone and Quetta-Pishin areal source are shown by purple and grey rectangles, respectively 17
- Figure 2.3. (a) Sketch showing along-dip variation in seismogenic behavior of Makran subduction zone and its interaction with the transform Chaman fault zone (modified from Wang & Hu, 2006; Bilek & Lay, 2002) (b) Satellite image with identified fault segments and selected partitioning of Northward motion between megathrust interface

and accretionary wedge faults. The transition zone between transform faulting and thrusting is shown by black dashed rectangle. The green lines indicate the oblique faults that have both thrust and strike-slip components, while the yellow segments indicate the thrust faults. Red dashed line shows the rupture of 2013, Baluchistan earthquake (Avouac et al., 2014) (c) Kinematic block model constructed to compute the slip rates along the oblique faults in transition zone22

Figure 2.4. Magnitude distribution plots and computed a- and b-values using Maximum likelihood (MLE) and Weighted Least Square (WLS) regression methods for (a) the whole study area, (b) Chaman transform fault zone, (c) Makran subduction zone, (d) Makran intra-slab zone, and (e) Quetta-Pishin areal source, respectively..27

Figure 2.5. Activity rates of the rupture scenarios considered for Makran megathrust interface plane based on the (a) truncated exponential (TE) model, (b) composite magnitude distribution (YC) model and, (c) TE model with increased M_{max} . In each plot, cumulative rates of the associated seismicity with the Makran interface plane are presented by the brown points and the error bars are estimated by considering the catalogue completeness intervals as suggested by Weichert (1980). Activity rate for large magnitude events proposed by Byrne et al. (1992) is shown by blue line in each plot. The PGA maps for 475-year return period for the megathrust interface based on alternative magnitude distribution models are plotted to the right of (a), (b) and (c). (d) Comparison of the weighted average of the cumulative rate of events for (a), (b) and (c).....34

Figure 2.6 (a) North-South oriented cross section passing from 63.5° latitude across Makran subduction zone displaying surface topography, tested and published slab geometries along with focal mechanism solutions (FMS) recorded within 2° width on both sides of the profile. Compressive quadrants of FMS are color coded according to the type of faulting: black for thrust, green for strike-slip and red for normal events. Solid black line in the aseismic portion is the basement reflector observed by Kopp et al. (2000). Black curved line shows the geometry of slab proposed by Penney et al. (2017). Red, pink and blue lines represent the tested slab geometries (in this study) with different dip amounts (Red = 05°; Pink = 03; blue = 07°). Bold dashed black and

red lines represent steeper and buried geometry of Makran megathrust in the aseismic portion. Two thin dashed black lines indicate the alternative downdip depth extents used for megathrust interface. (b), (c) & (d) shows 475-year PGA maps based on Model 1a, 1b & 1c, respectively (e) Residual PGA map is constructed by subtracting the PGA values with 475-years return period calculated for the megathrust interface with shallower (30 km) downdip depth extent (Model 2) from deeper (40 km) extending one (Model 1c) (f) Residual PGA map is constructed by subtracting the PGA values with 475-years return period calculated for more steeply dipping (07°) megathrust interface (Model 4) from gentle dipping (03°) one (Model 3)..... 35

Figure 2.7. PGA map with 475-year return period constructed using only seismic sources associated with Chaman Transform fault zone. Inset map shows PGA values associated to Quetta-Pishin areal source zone 38

Figure 2.8. PGA maps with 475-year return period constructed for oblique fault segments (a) and thrust fault segments (b) of Makran accretionary wedge and for intra-slab areal zone (c) of Makran subduction..... 39

Figure 2.9. Final PSHA hazard map for western and southern margin of Pakistan showing peak ground acceleration (PGA) for return period of 475yr and V_{S30} of 760 m/s..... 41

Figure 3.1. Seismicity and focal mechanism solutions (FMS) overlaid over the topography and active fault map of the region compiled from Emre et al., 2016. Black dots show the seismicity from catalogue obtained from Kandilli Observatory and Earthquake Research Institute (KOERI) for the period of 1900-2016. Blue dots are the $M \geq 4.0$ events. The compressive quadrants of FMS are color coded according to size of the events: black for $M < 4.0$, blue for $4.0 \leq M < 5.8$ and yellow for $M \geq 5.8$. Important large magnitude events are shown by yellow stars. The Inset map presents the generalized tectonic map of Turkey and surrounding regions. The approximate limit of western Anatolian extensional province (WAEP) is shown with the dark shaded topography (Koçyigit & Özacar, 2003) and the rectangle bounds the study area. Bold arrows indicate the general plate motion directions. Other abbreviations are EAF: East Anatolian Fault, NAF: North Anatolian Fault 48

Figure 3.2. (a) Histogram of day vs night time events (b) Map showing the grids colored according to day/night event ratio (c) Graph showing correlation between different magnitude scales (d) Cumulative number of events verses Depth. (e) Magnitude of completeness (M_c) with time plot for the whole region52

Figure 3.3. Strike Direction and Dip angle rose diagrams of focal mechanism solutions (FMS) (a) for all the events (b) events greater than or equal to Magnitude 5.0 (c) for normal events (d) strikeslip events (e) Results of stress tensor inversion for the whole region.....54

Figure 3.4. (a) Figure showing the slip vectors obtained from Aktug et al. 2009 (Black arrows). The residual vectors obtained from slip vectors situated on both sides of the graben are shown as blue arrows. The geographic limits of the the seven (7) polygons are shown by dashed lines. Active faults are shown as lines marked by numbers that can be used for additional information provided in Appendix B and are colored according to the fault types (i-e Red = Normal faults; Green = Strike-slip faults) (b) Figure showing seismicity (Magnitude ≥ 4.0) overlaid on the fault systems. Orange and Pink lines show fault systems comprising multiple segments that can rupture together or individually; black lines shows the individual segments systems that will rupture independently. Stars shows the recent major events in the area which are mentioned in Section 3.1. The inset shows the amount of slip assigned to each fault system based on maturity and length ratio methods respectively56

Figure 3.5. Gutenberg Richter relationship for the whole region and for the seven Polygons shown in Figure 4. Maximum likelihood estimate (MLE) and weighted least square (WLS) methods are used for obtaining the best fit to the distribution62

Figure 3.6. PSHA Map obtained using seismicity based activity rates for 475-years return period PGA for VS30=760 m/s (a) activity rate distributed using maturity (b) activity rate distributed using length ratio. Dashed yellow lines shows the contours for PGA value of 0.4g (c) Residual obtained by subtracting PGA values in (a) from (b). For polygons and fault numbers, refer to Figure 3.5.....66

Figure 3.7. PSHA Map obtained using moment rate based activity rates for 475-years return period PGA for VS30=760 m/s (a) activity rate distributed using maturity (b)

activity rate distributed using length ratio. Dashed yellow shows the contours for PGA value of 0.4g. Red stars shows the location of recent major earthquakes in the region (c) Residual obtained by subtracting PGA values in (a) from (b). For polygons distribution and fault numbers, refer to Figure 3.5 67

Figure 3.8. PSHA Map obtained using slip based activity rates for 475-years return period PGA for VS30=760 m/s (a) activity rate distributed using maturity (b) activity rate distributed using length ratio. Dashed yellow lines shows the contours for PGA value of 0.4g (c) Residual map obtained by subtracting PGA values in (a) from (b)68

Figure 3.9. (a) PSHA Map obtained using weighted (slip 0.5, seismicity 0.25, moment 0.25) activity rates for 475-years return period PGA for VS30=760 m/s. (b) Maximum PGA value map for 475-years return period and VS30=760 m/s; obtained from all the methods i-e slip, seismicity, moment rate based activity rates (c) Minimum PGA value map from all the methods. Dashed Yellow and Blue lines show the contours for PGA value of 0.4 and 0.5g respectively. Red stars show the location of recent major earthquakes in the region 69

Figure 3.10. PSHA Map of Simav and Afyon-Akşehir region obtained from Turkish Seismic Hazard Map (Akkar et al., 2018) for 475-years return period PGA and VS₃₀=760 m/s..... 73

Figure 3.11. Figure showing residual maps obtained by subtracting hazard maps of Figure 3.9 ($M_{min} = 5.0$) from hazard maps computed using a small Minimum magnitude threshold ($M_{min} = 3.0$) (a) Residuals for Weighted map (b) Residual for Maximum PGA value map (c) Residual for Minimum PGA value map 74

Figure 3.12. Flow chart for PSHA analysis in Western Anatolia. The Chart shows various methodological steps involved in fault characterization for fault based PSHA analysis. The chart also shows the protocol for calculating and distributing activity rates among individual faults and subsequently their use in computing seismic hazard maps for the study region 78

Figure 4.1. Figure showing generalized tectonic map of the study area and surroundings. Black rectangle represents the CAT project region. Bold black arrows show the general directions of plate motions while blue arrows represent the GPS

velocity vectors obtained for the region from UNAVCO with respect to a fixed African plate. The focal mechanism solutions compiled for the study area from literature (Appendix D) and the seismicity of the region (black dots, $M \geq 4.0$) obtained from ISC is also shown. Abbreviations are: EAFZ: East Anatolian Fault Zone, NAFZ: North Anatolian Fault Zone81

Figure 4.2. Map showing the active fault map of the area compiled from MTA active fault map (Emre et., 2016). Inverted triangles show broad band stations locations in the region. CAT stations are shown in blue while KOERI stations are shown in magenta color. Red dots represent the events whose first motion data is analyzed in this study. Abbreviations for some of the major structures in the area are BZSZ: Bitlis Zagros Suture Zone, CAFZ: Central Anatolian Fault Zone, DSFZ: Dead Sea Fault Zone, EAFZ: East Anatolian Fault Zone, EF: Ecemiş Fault, KFZ: Karasu Fault Zone, MOFZ: Malatya-Ovacık Fault Zone, SFZ: Sürgü Fault Zone, SRF: Sarız Fault, TGFZ: Tuz Gölü Fault Zone84

Figure 4.3. (a) An output summary plot showing all the possible focal solution mechanisms and related information computed for an event in this study (b) An example file of the observed P-wave's first motion polarities for the given solution. Polarity directions are shown as upward or downward arrows.....92

Figure 4.4. Distribution of all the Focal Mechanism Solutions computed in this study. Black solutions are reliable and kept for further analysis while the Red solutions are discarded94

Figure 4.5. Comparison of Focal Mechanism Solutions computed in this study with solutions computed by Birsoy (2018) and literature (This study; Black; Birsoy, 2018 =Red; literature = Blue)95

Figure 4.6. Focal mechanism solutions categorized according to the stress regimes (a). (N = Normal, SS = strikeslip, T= Thrust and UF = unidentified solutions), distribution of only strike-slip (b) , only normal (c), only thrust (d) and only unidentified solutions (e)97

Figure 4.7. (a) Ternary plots (b) Pressure & Tension axis plots and (c) Pressure & Tension axis density plots for the whole study area98

Figure 4.8. Stress map showing maximum horizontal stress axes (SH_{max}) associated to each earthquake solution in the FMS catalogue. The resultant axes indicate the compression directions in the study area 99

Figure 4.9. (a) Results of stress tensor inversion of all available focal mechanism solutions in the study area using Michael’s method and (b) the resultant histogram of stress ratio (R) vs frequency 102

Figure 4.10. Figure showing focal mechanism solutions and geographical limits of sub-regions that are selected for analyzing stress patterns independently. Each sub-region is assigned an identification number (1-14) that will be used in further analysis 103

Figure 4.11. Ternary plots and P-T axis density plots for each sub-region..... 104

Figure 4.12. (a) Results of stress tensor inversion for each sub-region and (b) the resultant histogram of stress ratio (R) vs frequency. The numbers indicate the sub-region number assigned to each domain as shown in Figure 4.10 107

Figure 4.13. Summary of stress tensor inversion results for all the selected sub-regions in study area..... 115

Figure 4.14. Mapped faults in the study area (red lines, taken from Emre et al., 2016), geometry of the area source zone (black rectangle), and the distribution of the FMS. Insets show the spatial distribution of the strike-slip and normal events in the area source..... 118

Figure 4.15. (a) Active fault map of the study area adopted from Emre et al. (2016), (b) fault based planar seismic sources used in Gülerce et al. (2017). Shaded rectangle shows the new areal source zone and the yellow boxes represent the buffer zones defined in Gülerce et al. (2017). Black points show the de-clustered seismicity catalogue ($M \geq 4.0$)..... 120

Figure 4.16. Magnitude recurrence parameters for the area source zone estimated by (a) Maximum likelihood estimate (MLE) and (b) Weighted least square (WLS) methods..... 120

Figure 4.17. (a) Posterior distribution, (b) discretized logic tree weights for Maximum magnitude (M_{max})..... 121

Figure 4.18. (a) Ternary plot of the focal mechanism solutions (FMS) (b) Rose diagram of strike direction and dip angles obtained from FMS of strike-slip and normal events and (c) results of stress tensor inversion and the resultant histogram of stress ratio (R) vs frequency.....122

Figure 4.19. Comparison of the source geometry parameters between the proposed area source in this study and the zone with ID:TURAS009 (EAF Zone) of Şeşetyan et al. (2018) model124

Figure 4.20. Vertical projection of a rectangular areal source zone defined for hazard calculations. (a) Diagram that shows how the epicenter of the scenario earthquake is moved within the source geometry and calculation of the source-to-site-distance without point source correction, (b) application of virtual fault concept for point source correction.....127

Figure 4.21. (a) Map view of 20 grid points selected in the region to analyze the influence of style of faulting and point source correction on the estimated ground motions. PGA values obtained along the WE profile for (b) 475-year return period and (c) 2475-year return period. PGA values obtained along the SN profile for (d) 475-year return period and (e) 2475-year return period. In (b-e), PS=0: no point source correction, PS=1: with point source correction.....128

Figure 4.22. (a) 475-year PGA values estimated by combining the planar seismic sources of Gülerce et al. (2017) with the new additional source zone and with the new ground motion logic tree (proposed map), (b) 475-year PGA values estimated by combining only the planar seismic sources of Gülerce et al. (2017) with the new ground motion logic tree, (c) Residual PGA value map (a) – (b) showing the effect of adding the new area source zone (d) Percentage increase in PGA values from (b) to (a)131

Figure 4.23. (a) Residuals calculated from our proposed SSC model with our GMM logic tree minus (-) our proposed SSC model with TSHM GMM logic. (b) Residual PGA value map obtained by subtracting the PGA value map of TSHM from the PGA value map computed in this study. SSC model utilized for this study is Gülerce et al

2017 planar model + areal source and the logic tree for GMM is adopted from TSHM
..... 133

Figure 5.1. Flow chart showing the seismic source modelling complexities
investigated in this study 137

CHAPTER 1

INTRODUCTION

1.1. Background

Seismic hazard analysis (SHA) refers to the quantitative estimation of ground-shaking expected to occur at a selected site and the probabilities of occurrence of future earthquakes that cause them. SHA is used to describe only the level of ground motion at a site (Anderson and Trifunac, 1977, 1978), regardless of its consequences or damages that it will cause to the buildings and other engineering structures. Reliable seismic hazard assessments in earthquake prone regions are essential to minimize the loss of life, for hazard mitigation to avoid destruction of existing infrastructures, for earthquake-resistant design of new structures and for preventing social and economic disruptions. SHA can be conducted deterministically (scenario earthquake), as when particular earthquake scenario is assumed, or probabilistically (an ensemble of earthquakes), in which uncertainties in earthquake size, location and time of occurrence are considered (Kramer, 1996). The former is aimed at predicting ground motions for the maximum earthquake magnitude i.e. the one that will produce the highest ground motion at a site while the latter advocates that probabilities of occurrence should also be considered since the life of engineering structures are generally shorter than the return periods of maximum magnitude earthquakes. Deterministic seismic hazard analysis (DSHA) provides a straightforward framework for evaluation of the ‘worst-case’ earthquake scenario. However, it does not provide any information on the likelihood of occurrence of the controlling earthquake, its location or the ground motion uncertainties. On the contrary, Probabilistic seismic hazard analysis (PSHA) allows the quantification of uncertainties involved in the size, location, rate of recurrence, and ground shaking effects of earthquakes.

DSHA was first adopted for nuclear power plant applications but the history of its evolution is not well documented since the practical application might be quite different around the world. Typical DSHA can be described as a four-step process (Reiter, 1990). First, (1) seismic sources are identified within an area of interest (generally 200-300 km radius) and the maximum possible earthquake magnitude or critical earthquake scenario(s) are developed for each seismic source (2) source-to-site distance is calculated for each source, (3) appropriate attenuation relations are selected, and finally (4) the site-specific ground motions are estimated deterministically using the attenuation relation; given the magnitude, minimum possible source-to-site distances and site characteristic. Although DSHA does not provide any information on the frequency of occurrence or the return periods of scenario earthquake and ground motions, the practice is robust and still remains a useful approach for decision making. PSHA provides a framework in which the inherent random uncertainties in the size, location, rate of earthquakes and the variation of ground motion can be explicitly considered for the evaluation of seismic hazard. The practice involves integrating the probabilities of experiencing a particular level of ground motion that can be caused by seismicity expected to occur in the area during a specified life period (Cornell, 1968; Anderson and Trifunac, 1977, 1978). The results are generally presented in the form of PGA maps, seismic hazard curve or a uniform hazard spectrum. PSHA analysis were first conceived in the 1960s and have become the basis for majority of seismic designs for engineering facilities since then. The practice can be described in a typical five steps procedure. It starts with (1) identification of earthquake sources and (2) the characterization of distribution of source-to-site distances associated with potential earthquakes. Then (3) the earthquake magnitude distribution and recurrences are constrained for the area of interest based on the available datasets. Using empirical relations, (4) ground motion produced at a site by earthquakes of any possible size at any location on a seismic source is calculated. Finally (5), the probability that the ground motion parameter will be exceeded during a particular time period is computed.

During the early stages of PSHA development; due to lack of fault specific parameters, the practice was based on areal sources in which seismic sources were modeled as single or a set of seismo-tectonic zones with homogeneous seismicity. With the availability of extensive datasets and sophisticated fault parameterization techniques, the trend has shifted towards fault-based PSHA analysis (e.g. Fujiwara et al., 2009; Wang et al., 2016; Valentini et al., 2017; Walker et al., 2010). Fault based PSHA techniques have been evolving rapidly and finding its way in the hazard community throughout Europe, USA, Japan, New Zealand and Turkey. Efforts are directed towards the inclusion of physically sound models and providing logical constraints for minimizing the epistemic uncertainties involved in hazard computations. Nevertheless, a large degree of uncertainty still exists in the estimation of ground motions due to model parameter assumptions and complexities involved in seismotectonic environments. In this respect, the evaluation of these uncertainties is crucial for reliable SHA, especially in regions that are characterized by sparse geological, seismological and geodetic datasets. So far, attempts have been made on constructing state-of-the-art fault-based SSC models for tectonic regimes characterized by dense datasets and comparatively simple planar nature (e.g. strikeslip fault zones). The notable studies include the PSHA practices in US (UCERF2, UCERF3), Europe (SHARE-Woessner et al. 2015) and in Turkey (Gulerce et al., 2017; Demircioğlu et al., 2017). The availability of state-of-the-art fault based PSHA studies are very limited in extensional, compressional and mixed tectonic regimes due to their dipping geometry and complex tectonic nature. Only recently, researchers have started using sophisticated models for inclined tectonic regimes; except a few notable studies (Pace et al., 2006; Walker et al., 2010; Chartier et al., 2017a, 2017b).

1.2. Problem Statement

Fault-based PSHA involves considerable amount of uncertainties. A large degree of these uncertainties is induced by the simplifications required to build the seismic source characterization (SSC) models with limited model parameters. Lack of detailed datasets and proper source characterization techniques and/or the oversimplification

of seismic source complexities enhances these uncertainties which in turn translates to the uncertainties in the ground motions estimates. Furthermore, tectonic regimes which are characterized by inclined fault geometries (i.e. thrust & normal regimes) adds to the challenges associated with the accurate representation of seismogenic sources and constraining source parameters. Therefore, the motivation of this study is to perform fault-based PSHA in complex tectonic regimes and to investigate problems associated with the SSC modelling and ultimately provide constraints on these ambiguities through sensitivity tests. Each complex tectonic regime is characterized by unique SSC problem(s) which is influenced by the nature of seismic sources and data conditions in the region. For instance, lack of detailed datasets enhances the enigma involved in geometric parameters of subduction megathrusts which are often characterized by gently dipping, large scale regional thrust faults. Similarly, extensional regimes are often characterized by multiple sets of faults and paucity of fault specific slip rates; thereon, causing considerable ambiguity in calculation and distribution of activity rates. Moreover, some tectonic regimes are characterized by simultaneous active faults that can generate mixture of earthquake mechanisms. Correlating seismicity to individual faults and assigning fault mechanisms to seismic sources in such regions involves significant uncertainties. For these reasons: geometric properties of subduction megathrusts, activity rate characterization in normal faults and seismic characterization of mixed tectonic regimes are the prime research problems that will be investigated in this thesis.

Subduction zones are generally characterized by shallow dip angles with hundreds of kilometers along-strike length and large seismogenic depths which makes the procedures for SSC modelling very intricate as compared to rather simple shallow crustal sources. Lack of well documented historical, geodetic and seismological datasets increases the ambiguities related to source geometry, depth extent of interface and intra-slab events, maximum magnitude potential and activity rate characterization in subduction zones. Among the SSC model parameters, source geometry of the subducting plate is the most controversial parameter. Due to megathrust nature and

shallow dipping angles, a couple of degree changes in the dip angle of subducting plate will lead to 100s of km changes in the rupture widths, maximum magnitude and source-to-site distances etc. Changes in maximum magnitudes will in turn lead to changes in the frequency-magnitude distribution of earthquakes that will change the recurrence or activity rates of controlling earthquakes for short return periods. Change in the seismogenic depth will have a similar effect on the other SSC model parameters. The sparsity of seismic and geodetic datasets in relatively quiescent subduction zones augments the complications involved in activity rate characterization and magnitude distribution models. Additionally, the aseismic portions associated with oceanic-oceanic or oceanic-continental subduction zones requires systematic characterization due to its considerable influence on near trench ground motions. Adding further complexity to the SSC in subduction megathrusts is the incorporation of associated accretionary prism faults and its interaction with other fault zones. The aforementioned problems will be investigated in this study by selecting a case study region, which is characterized by subduction zone complexities and sparse data conditions. Extensional provinces (e.g. graben systems) are often characterized by oppositely dipping, closely spaced fault structures. Such regimes are often characterized by lack and/or paucity of fault specific activity rates which is essential for fault-based PSHA analysis. Standard PSHA practices utilizes seismicity and geodetic data to characterize the activity rates of seismic sources, depending on its availability and density. Seismicity data in such closely spaced fault regimes is generally diffused and the epicenters are not well-located, which makes the association of events with individual faults an erroneous practice. A large degree of ambiguity is involved in associating events located in central parts of graben structures due to the fact that the graben-bounding faults are dipping towards each other which leads to overlap of surface projection of fault planes. On the other hand, geodetic data also has certain limitations for use in seismic hazard analysis in such regions. For instance, geodetic data does not provide sufficient resolution for structurally complex areas, akin closely spaced oppositely dipping graben fault systems. The resolution and the large error margin of the GPS data in these region does not allow us to discretize the slip rate among

individual faults. The uncertainties of individual fault slip rates in such regions trade-off with one another, although the net slip across the grabens may be constrained up to some confidence level. Additionally, the data usually covers small time spans and sometimes may include transient strains or aseismic strains, which are difficult to identify and eliminate (Hearn et al., 2013; Chuang and Johnson, 2011). Therefore, calculating and distributing activity rate is one of the most ambiguous and crucial parameter associated with SSC modelling of closely spaced oppositely dipping normal faults and needs thorough investigation.

Moreover, regions characterized by simultaneous active fault structures that can produce mixed earthquake mechanisms (e.g. combination of normal, strikeslip, thrust) are frequently oversimplified in SSC practices. Such regions are commonly associated with trans-tensional and trans-compressional tectonic regimes and are characterized by diffused seismicity patterns and mixed earthquake solutions. Despite the complexities involved, the off-fault seismicity and the mixed faulting mechanisms ought to be integrated to the SSC models in order to reduce uncertainties caused by complex tectonism. In standard SSC practice, the buffer zone approach or background areal sources are utilized to account for the diffused seismicity. For these cases, the fault-based source-to-site-distance metrics are hard to calculate with the point source approach; therefore, virtual faults within the source zone boundaries should be employed to estimate the distance metrics properly for areal sources. Unfortunately, the virtual-fault approach is typically ignored in current applications (e.g. Sesetyan et al., 2017), leading to increased uncertainties in hazard estimates.

1.3. Purpose and Scope

The scope of this thesis covers three regions characterized by different tectonic regimes and data availability: and in each region a unique problem associated with SSC modelling practice is investigated. By analyzing publicly available data resources; considerable amount of seismic, geodetic and geological datasets that can be used for designing planar seismic source models are compiled for each region. Makran megathrust and Chaman transform fault region of Pakistan is selected as a

representative example for compressional tectonic environments. The scope of this case study includes; carrying out fault-based PSHA on a continental scale megathrust fault domain and addressing issues involved in characterizing the SSC parameters. The scope of this particular case study also covers the accretionary prism faults associated with the subduction zone and the Chaman fault system (Figure 1.1). Another reason for selecting this region is the lack of a detailed fault-based SSC model and state-of-the-art ground motion estimates in this part of the globe, despite the high hazard level associated with the active faults in the region. For closely spaced extensional regimes and associated problem of activity rate characterization, northern part of western Anatolian extensional province (WAEP) is selected as the representative study area. The scope of this particular case study covers the normal faults of Simav and Afyon-Akşehir graben systems of WAEP (Figure 1.1). The study will minimize the uncertainties associated to hazard estimates for the region and will mechanize a protocol that can be extended and applied to other active seismic sources in the surrounding regions. Finally, focal mechanism solutions (FMS), which can be decisive tool on constraining the faulting type of a seismic source are computed for earthquake events in Central Anatolian region of Turkey (Figure 1.1). The region is characterized by an active trans-tensional seismic source (mixture of normal and strike-slip faulting) near the Adana Basin and Gulf of Iskenderun (Figure 1.1). The FMS database for central Anatolian region is updated by carrying out FMS computations from P- and S- waves first motion arrivals and amplitude ratio (SH/P) data technique. The FMS solutions are combined with the previously published data to investigate active stress patterns. By utilizing the findings of FMS computations and stress tensor inversion results, the seismic source parameters for the Adana Basin and Gulf of Iskenderun seismic source are updated and implemented in PSHA analysis. The updated SSC model is incorporated to the previously published planar fault model (Gülerce et al., 2017) to update the hazard map of the region.

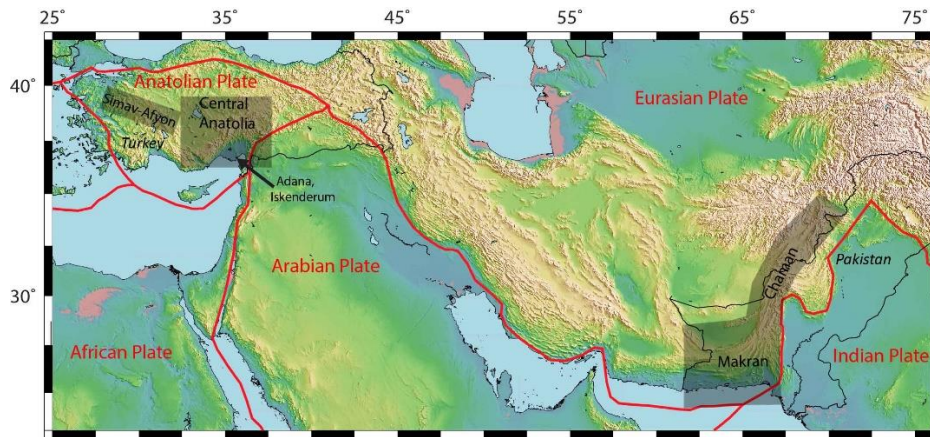


Figure 1.1. Figure showing locations of selected regions for this thesis. Red bold lines represent plate boundaries (Bird, 2003). The shaded rectangles indicate the approximate limits of study regions selected in this study

In summary, the aim of this thesis is to develop SSC models for selected complex tectonic regimes in parts of Pakistan and Turkey and ultimately provide reliable seismic hazard maps which would be an important step towards the seismic safety improvement of existing infrastructure and seismic risk management of critical facilities in the region. The main objectives of the thesis can be summarized as under:

- Compilation of geological, seismological and geodetic datasets for the study regions and incorporating them to SSC models to characterize the active fault systems in terms of parameters required for performing fault-based PSHA. These parameters include the geometry and dimensions of the active sources, fault segmentation models, tectonic regimes, activity rates, annual slip rates and recurrence intervals of characteristic earthquakes and magnitude distribution models.
- Identifying various ambiguous parameters associated with the SSC modelling in PSHA, analyzing their impacts on hazard estimates and providing constraints to control their influence and in the process minimizing the uncertainties induced by these parameters.
- Developing updated and state-of-the-art the seismic hazard maps of the selected regions by implementing the developed SSC models and selected ground motion models in suitable seismic hazard assessment software.

We have adopted the traditional Cornell-McGuire PSHA methodology (Cornell, 1968; McGuire, 2004) for computing the seismic hazard for the regions. The numerical integration of the hazard integral is performed by using the computer code, HAZ45 (Hale et al., 2018). The processing of seismic catalogues and computation of seismicity parameters is performed in the ZMAP software package (Wiemer, 2001). Seismic Analysis Code (SAC) (Goldstein et al., 2003) is utilized to process the waveform data, while focal mechanism solutions are computed using the FOCMEC (Snoke, 2003) software package.

1.4. Organization of Thesis

This thesis includes 5 chapters. Chapter 1 provides introductory remarks in addition to the problem statement and purpose of the thesis. Chapters 2, 3 and 4 includes different case studies for fault-based PSHA analysis and are organized in suitable format for stand-alone articles. Chapters 2 and 3 discusses the case studies of Makran megathrust region of Pakistan and WAEP (Simav and Afyon-Akşehir) of Turkey, respectively. Both chapters start with an introduction followed by the seismic source characterization and identification of problems associated with SSC models. At the end, sensitivity analysis and hazard maps along with results and discussions are provided. Chapter 4 is focused on reducing uncertainties in the PSHA caused by complex tectonism in the Central Anatolian region, thus includes focal mechanism solution (FMS) computation of earthquakes with $M (M_I) > 3.0$ and integrated stress tensor inversion that will reveal the source characteristics of off-fault seismicity and ambiguous active tectonic structures. Later, PSHA is carried out across the Adana Basin and Gulf of Iskenderun region, using planar fault models along with the virtual fault approach and results are compared with previous studies. In the final chapter (Chapter 5) of the thesis, the results obtained by these different case studies are discussed and main conclusions including future recommendations are summarized.

CHAPTER 2

FAULT BASED PROBABILISTIC SEISMIC HAZARD ASSESSMENT OF THE MAKRAN SUBDUCTION ZONE AND THE CHAMAN FAULT SYSTEM IN PAKISTAN: EMPHASIS ON THE EFFECT OF SOURCE CHARACTERIZATION OF MEGATHRUST

Seismic source characterization (SSC) for probabilistic seismic hazard assessment (PSHA) in regions characterized by subduction megathrusts involves a considerable degree of ambiguity. The lack of detailed geologic, seismic and geodetic data increases the uncertainties involved in constraining the SSC model. The enigma is further enhanced in the regions where thin-skinned accretionary wedge faults are part of active deformation. In this study, a planar SSC model for seismically active eastern Makran subduction zone, its associated accretionary prism faults and Chaman transform fault is proposed. Sensitivity tests for various ambiguous parameters associated with the SSC model are performed and presented in the form of peak ground acceleration (PGA) maps with 475-year return period. Especially in gently dipping subduction zones such as Makran, the estimated ground motions and their spatial distribution are highly sensitive (changing up to 0.3g) to the selected depth extent and dip amount of the megathrust interface which defines the maximum rupture width. For short return periods (475 years), gentler and deeper extending interfaces resulted in slightly lower PGA values towards trench and significantly higher PGA values towards inland, along the accretionary wedge. Moreover, testing the alternative magnitude distribution models which influence the activity rates for Makran subduction zone showed that the truncated exponential model resulted in ~10% higher PGA values than the composite recurrence model. Using the selected SSC model, the highest 475-year PGA values computed for the region are around 0.6-0.7g in the vicinity of Makran megathrust and Ornach-Nal fault.

2.1. Introduction

Geodynamic processes related to subduction plates have generated some of the most energetic and damaging earthquakes around the globe, e.g. 2004 Sumatra ($M_w=9.1$), 2010 Chile ($M_w=8.8$) and 2011 Tohoku ($M_w=9.1$) earthquakes caused significant damage on engineering structures. On the other hand, due to large seismogenic depths and complex nature of subduction zones, the SSC practice for these tectonic structures in PSHA is not straight-forward or similar to that of shallow crustal and active tectonic sources. SSC models for megathrust zones require thorough procedures and expert judgment to constrain the ambiguities involved in the subduction plate geometry and for modeling the magnitude recurrence relations for earthquakes originating within the interface and intra-slab zones. Incorporation of the accretionary prism faults associated with the subduction zones and their interaction with the other fault zones adds further complexity to the problem. The number of up-to-date SSC models encompassing subduction zones are limited to regions characterized by diverse geodetic and seismological datasets: e.g. the 2014 United States Geological Survey-National Seismic Hazard Model for Cascadia subduction zone (Petersen et al., 2015; Frankel et al., 2015); SHARE SSC model for subduction zones in the Mediterranean (Woessner et al., 2015) and the 2010 update of the New Zealand National Seismic Hazard Model (Stirling et al., 2012). On the other hand, quiescent subduction zones having poorly known seismic histories like Makran megathrust are particularly vulnerable and often ill-prepared in terms of SSC models. Due to the lack of well documented historical, geodetic and seismological datasets; the source geometries, the depth extent of megathrust interface, maximum magnitude potential and activity rates of such subduction zones remain enigmatic and the state-of-art models for fault based PSHA practice is currently lacking.

The primary concern of this study is to propose novel SSC models for the subduction and transform faults in the southern and western margins of Pakistan. The study area coincides with the western margin of the Indian plate, defined by the Chaman fault zone and the southern margin of Afghan block of Eurasian plate delineated with the

Makran subduction zone (Figure 2.1). The region is considered appropriate for discussing the interaction between the subduction zones (Makran) and the strike-slip faults (Chaman) and it offers a challenge in kinematic block modeling for strain partitioning (slip distribution) among these systems. The scope of this study is restricted to the eastern part of Makran subduction zone (in Pakistan territory), associated actively deforming accretionary prism faults and the Chaman transform fault zone. Western counterpart of Makran subduction zone in Iran separated by Sistan shear zone (Byrne et al., 1992) is not included. Previously published seismic source models for the study area and surroundings includes: the SSC model for Global Seismic Hazard Assessment Program (GSHAP) hazard map (Giardini et al., 1999), the SSC model proposed by Norwegian Seismic Array (NORSAR) and Pakistan Meteorological Department (PMD) (NORSAR & PMD, 2006); the NESPAK model (NESPAK, 2006); the hazard estimates given in Boyd et al. (2007), Monalisa et al. (2007), Bhatti et al. (2010), Rafi et al. (2012), Zaman et al. (2012), Waseem et al. (2018) and the recently proposed SSC model for 2014 Earthquake Model for Middle East Project (EMME, Danciu et al., 2017). Most of the abovementioned studies modeled the Makran and Chaman fault zones as areal source zones with homogeneous seismicity distribution. Planar fault models were defined for region by Boyd et al. (2007), Zaman et al. (2012) and Danciu et al. (2017); however, the source model parameters such as the annual slip rate and fault dip angle were not well-constrained. Thus, the seismic source modeling practice presented here is a significant step-forward when compared to the previous PSHA studies for Pakistan.

The secondary objective of the study is to underline the important seismic source model parameters for subduction zones by evaluating the effect of these parameters (e.g. downdip depth extent and dip amount of megathrust interface and magnitude distribution model) on the PSHA results. A series of PSHA maps are provided to analyze the spatial distribution of these effects. In this respect, findings of this study will also be useful for identifying the parameters of the megathrust zones and transform fault boundaries that have a significant impact on the hazard output, which

will lead the way for future efforts to better constrain the fault model parameters and reduce the uncertainty in the hazard estimates on regional and global scale.

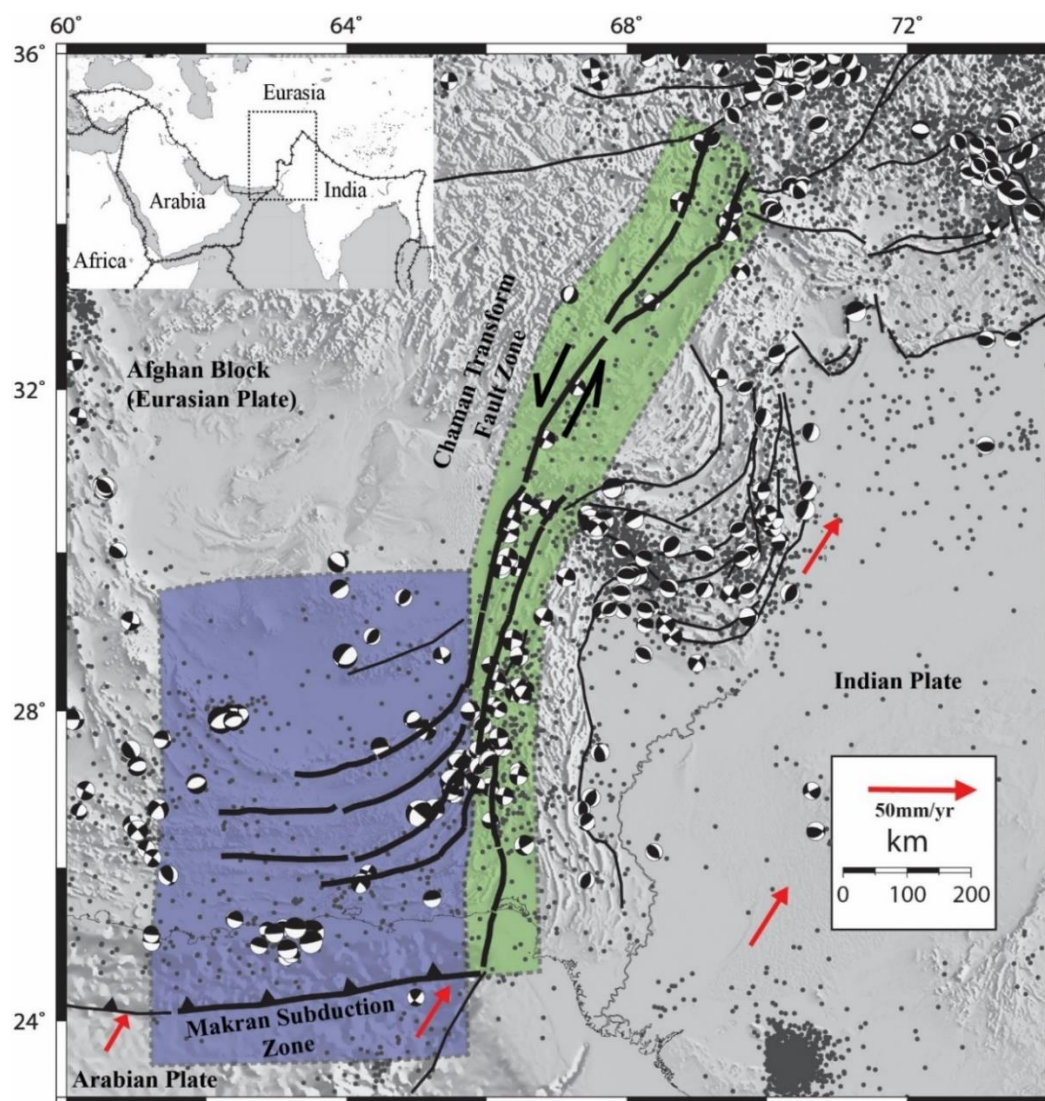


Figure 2.1. Seismotectonic map of Pakistan and its surrounding overlaid on topography. Grey dots represent earthquakes gathered from the International Seismological Centre (ISC) catalogue. Centroid Moment Tensor (CMT) solutions are mostly taken from global CMT Catalog (Dziewonski, et al 1981 and Ekström, et al., 2012); Penney et al., 2017 and references therein for Makran region. Bold black lines represent the faults included in our analysis. The green and purple shaded areas demarcate the approximate limits of Chaman transform zone and Makran subduction zone, respectively. Red arrows show the plate motion velocities with respect to a fixed Eurasian plate (DeMets et al., 2010). Inset map on the top shows the location with respect to global plate configuration

2.2. Seismic Source Characterization

Unlike previous efforts, planar and fault-based source models are built by using published active fault maps and annual slip rates along with kinematic block models. Fault systems and their segments with representative planar geometries are identified based on the structural heterogeneities; e.g. restraining bends, fault gaps, changes in fault orientations and seismic data; e.g. seismicity, focal mechanism solutions (FMS) and rupture dimensions of previous large earthquakes. Figure 2.2 shows the fault systems and their segments with their associated slip rates utilized in the seismic hazard analysis. The details about SSC and fault systems are provided in the following sections.

2.2.1. Chaman Transform Fault Zone

The Chaman fault zone is a major continental left lateral transform, acting as a boundary between Indian and Eurasian plates. Kinematic and block models for Indian plate's western margin indicate that pure strike-slip motion is required along the transform zone while the compression is being accommodated in the Sulaimon Fold and Thrust Belt and Kirthar Ranges located on east of the transform fault (Haq and Davis, 1997; Bernard et al., 2000). Geological slip rates suggest average slip rate of 19-24 mm/yr over the last 20-25 My (Lawrence et al., 1992); while, the geodetic estimates of modern plate motions propose the slip rate of 24-30 mm/yr (Altamimi et al., 2012) along the Chaman transform fault zone. The state of high strain conditions in the region has been frequently confirmed by the occurrence of large magnitude earthquakes. Chaman fault zone produced four strike-slip earthquakes ($M > 6$) that have been recorded historically: the 1505 event at the west of Kabul (Oldham, 1883; Lawrence et al., 1992; Ambraseys and Bilham, 2003); 1892 $M_w=6.5$ event near Chaman (Ambraseys and Bilham, 2003); 1975 $M_s=6.7$ event on the south of Chaman (Lawrence and Yeats, 1979; Engdahl and Villasenor, 2002) and 1978 $M_w=6.1$ earthquake on the north of Naushki (Yeats et al., 1979; Engdahl and Villasenor, 2002) (Figure 2.2).

Chaman transform fault zone comprises of three left stepping left-lateral faults known as the *Chaman*, *Ghazaband* and *Ornach-Nal* faults (Figure 2.2). Among these, Chaman fault is the longest, extending for almost 800 km starting from 28.2°N, continuing near the northernmost end of Makran fold and thrust belt (up to 32.6°N) where it branches into two faults located to the west and east of Kabul, and terminates around 35.1°N. The fault is connected to the Makran megathrust in the south and to the currently inactive right-lateral Herat Fault in northern Afghanistan. We have divided the Chaman fault into three separate fault systems (*S1*, *S2*, *S3* shown in Figure 2.2) with multiple fault segments based on the distribution of seismicity, occurrence of large magnitude earthquake ruptures, fault bends, changes in the orientation of fault (restraining bends), bifurcation of the system and available slip rates from literature. Starting from the north, around 32.7°N, the Chaman fault bifurcates into two almost-parallel systems: the western branch situated on the west of Kabul (also known as Paghman fault) is referred as the *Chaman Fault System #1* (hereafter *S1*); while the eastern branch continuing to north is known as the *Gardez Fault System* (Lawrence et al., 1992). Both these systems are divided into two fault segments around 34°N due to present fault gaps where strike directions change slightly. Szeliga et al. (2012) observed 16.8 ± 0.51 m/yr left lateral motion along the strike-slip faults in this region (*S1* and *Gardez*) based on geodetic data. Mohadjer et al. (2010) proposed that the upper bound of left lateral shear across the *Gardez Fault* is 5.4 ± 2 mm/yr and 18.1 ± 1 mm/yr along the northern end of the Chaman fault system (*S1* and *Gardez* combined). Similarly, Boyd et al. (2007) assigned a slip rate of 10 mm/yr to *S1*. Based on these findings, 10 mm/yr annual slip rate is assigned to *S1* and 5.4 mm/yr to the *Gardez Fault Systems* in our analysis (Figure 2.2).

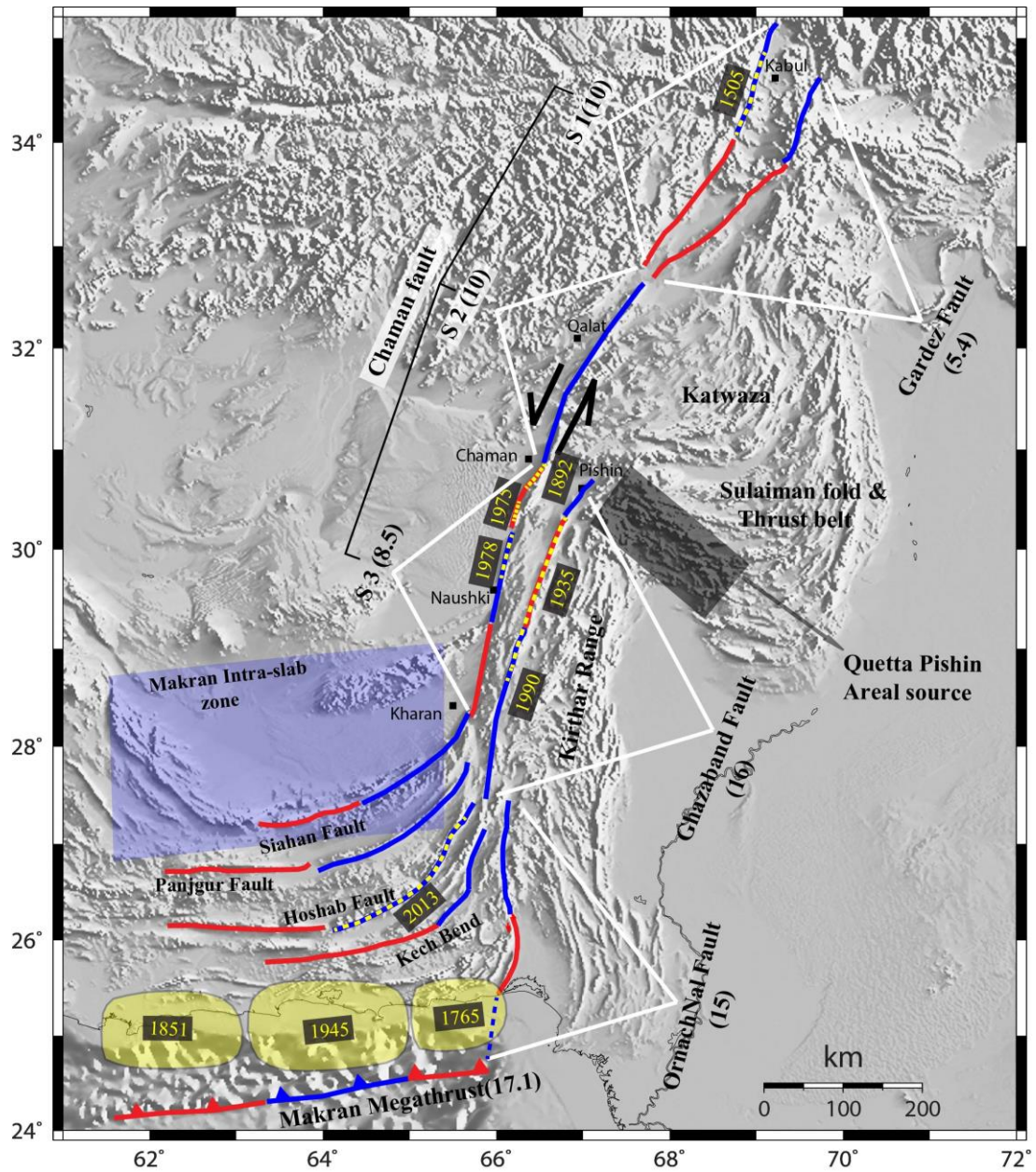


Figure 2.2. Active fault map of the region compiled from literature data overlaid on the SRTM image. The fault systems identified in this study are outlined by white lines. Fault segments comprising the fault systems are shown by different colors (red and blue). Fault ruptures produced by instrumental and historical earthquakes are shown by yellow fill or dashed yellow lines with their associated year of occurrences. Except accretionary wedge faults, assigned slip rates of fault systems are given in parentheses. Surface projection of intra-slab zone and Quetta-Pishin areal source are shown by purple and grey rectangles, respectively

Chaman Fault System #2 (hereafter *S2*) constitutes the central portion of the Chaman fault: it starts at the bifurcation point of *S1* and *Gardez Fault Systems* and continues in the south until the town of Chaman (around 30.9°N). The southern limit of this single-segment system is selected on the basis of a small restraining bend. The motive for separating this system from *S1* is the absence of any reported rupture zones for previous moderate-to-large magnitude earthquakes on this part of the transform fault zone. Some of the previous studies regarded this section as a seismic gap (Szeliga, 2010; Bernard et al., 2000; Ambraseys and Bilham, 2003); while, InSAR studies suggest a creep motion along this system (Crupa et al., 2017; Szeliga, et al., 2006). The most reliable long term slip rate estimates for this section were given in Szeliga et al. (2012). The authors suggested an inter-seismic deformation across this system consistent with 16.8 ± 2.7 mm/yr of slip rate based on their observations near Qalat, Afghanistan. On the other hand, Furaya and Satyabal (2008) and Crupa et al. (2017) computed a slip rate of 8 to 10 mm/yr based on InSAR analysis along this portion of the fault. Previous seismicity along the fold belt (Figure 2.1) and the relatively high strike-slip shear estimates ($\approx 6-8$ mm) along the Quetta-Pishin shear zone (Khan et al., 2008) indicate that a substantial amount of deformation along this portion of Indian plate boundary (16 mm/yr given by Szeliga et al., 2012) is either dissipated in the form of creep and/or accommodated along the Sulaiman Fold and Thrust Belt. Therefore, we have assigned a slip rate of 10mm/yr to *S2 Fault System* (Figure 2.2).

Chaman Fault System #3 (*S3*) is the southernmost portion of Chaman fault. The system is divided into three segments based on fault bends, previous rupture zones and topographic breaks. Szeliga et al. (2012) assigned a slip rate of 8.5 mm/yr to this part of the fault zone, suggesting that most of the plate boundary motion (≈ 22 mm/yr) in this region is accommodated by the faults on the Indian Plate, i.e. *Ghazaband Fault*, which is the most probable candidate for accommodating this deformation. Similarly, the GPS data analysis by Cruppa et al. (2017) yielded ≈ 8.8 mm/yr displacement rate along this section of Chaman fault. *Ghazaband Fault System* runs parallel to Chaman fault and disappears into the seismically quiet Katawaz Block on the north (Haq and

Davis, 1997). *Ghazaband Fault System* is also divided into three segments based on the rupture zones of previous earthquakes and changes in the fault geometry. Recently relocated epicenters published by Engdahl and Villasenor (2002) suggest that *Ghazaband Fault System* is likely to have hosted the 1935 Quetta earthquake ($M_w=7.7$). There are no direct reliable estimates regarding the slip rate of *Ghazaband Fault System* from geodetic data. The measurements of Szeliga *et al.* (2012) are unfavorably disposed to quantify the slip rate on this system: the low rate assigned to *S3* system leaves the total of ≈ 22 mm/yr strike-slip motion along the plate boundary unaccounted for. Recently, InSAR data of Fattahi *et al.* (2016) estimated the long-term slip rates of 16 ± 2.3 mm/yr and 8 ± 3 mm/yr for *Ghazaband* and *S3* fault systems, which are adopted in this study (Figure 2.2).

Ornach-Nal Fault System is the southernmost on-land portion of Chaman transform fault zone (Zaigham, 1991; Lawrence *et al.*, 1992). The system is nearly 230km-long, upon which no major earthquake is known to have occurred in the instrumental and historical period. We have extended this system to the offshore, reaching to the Makran megathrust with a total length of 295 km. Szeliga *et al.* (2012) proposed the slip rate of 15 mm/yr across the Ornach-Nal fault which is adopted in this study (Figure 2.2). In the west, Makran accretionary prism faults display arcuate nature with strikes bending towards North, indicating the influence of the left lateral shear along the *OrnachNal* fault. At its northern end, deformation likely steps westward onto the *Ghazaband* fault. Between 27°N and 31°N , strike-slip deformation is increasingly accommodated by the *Ghazaband* fault.

In addition, there is a remarkable cluster of seismicity around the Sulaiman fold and thrust belt (Figure 2.1). The cumulative seismic moment release from earthquakes that have occurred within about 100 km of this zone in the past century (1892-2009) is equivalent a $M_w=8.0$ earthquake (Ambraseys and Bilham, 2003) and this activity may influence the hazard estimates around central portion of Chaman fault system. Even though the zone is beyond the scope of this study, we have included this active zone

as an areal source zone (Quetta-Pishin Zone) in the analysis to prevent the underestimation of the hazard (Figure 2.2).

2.2.2. Makran Subduction Zone

Subduction zones are typically characterized by a megathrust fault formed by the subduction of high density subducting plate beneath the low density overriding plate. The subducting plate is further subdivided into two parts: a gently dipping, highly coupled seismic interface at shallow depths that hosts the subduction megathrust earthquakes and a steeply dipping deep intra-slab earthquake zone characterized by extensional or compressional events due to the flexural bending of the subducting plate (Figure 2.3a). These zones are generally characterized by distinct type of earthquakes; the interface earthquakes are associated to thrusting with shallow dip-angle and the intra-slab events are related to high-angled normal or reverse faulting. Apart from interface and intra-slab zones; series of shallow crustal faults develop along the accretionary prism on the overriding plate. These faults are formed by the squeezing of soft sediments and it is believed that a fraction of inter-seismic deformation attributed to coupling of megathrust is shared by the deformation within the accretionary wedge (Figure 2.3b). Thus, separate seismic sources are modeled for each of these different elements: megathrust interface, intra-slab zone and accretionary prism faults.

Frohling and Szeliga (2016) showed that the Makran subduction zone is partially locked and accumulating strain at a rate of 17.1 mm/year. This annual slip rate is employed to define the activity rate of the megathrust interface in this study. Along-strike segmentation pattern of the subduction interface plane was formulated by considering the ruptures produced by previous large magnitude earthquakes. As shown in Figure 2.2, three along-strike segments of the megathrust are defined based on the extent of rupture zones of 1765, 1851 and 1945 earthquakes (Byrne et al., 1992). The down-dip characterization of the subduction plane geometry is more complicated than defining the along-strike segmentation pattern. Sections of the megathrust that can accumulate moment energy and slip in a seismic fashion are mutually exclusive

from those sections that are creeping in the post-seismic period (Hsu et al., 2006; Baba et al., 2006). Shallow up-dip portions of the subduction plate are conventionally believed to slip in a velocity-strengthening manner (Byrne et al., 1988; Hyndman et al., 1997; Wang and Hu, 2006). Although large magnitude earthquakes do not originate at shallow aseismic portions, these ruptures may propagate to shallow depths or to the surface (Wang and Hu, 2006). For Makran megathrust, we adopted a similar model in which the shallower up-dip part of the subducting Arabian plate is aseismic (Figure 2.3a); i.e. the shallower part of the megathrust interface is not able to store or accumulate moment energy in agreement with the lack of seismicity near the trench at the surface (Figure 2.1). However, it should be underlined that the ruptures initiated in the interface plane are assumed to propagate to the aseismic part and to the surface in the rupture forecast for PSHA.

Although changing megathrust interface dip amount by only few degrees or assigning different downdip depth extent results in remarkable changes on the maximum rupture width for shallow dipping subduction zones; defining these parameters for megathrust interface are not straight forward, especially for Makran subduction zone with limited amount of associated seismicity and earthquake focal mechanism solutions. Thus, a range of dip amounts and downdip depth extents are tested in this study to map out the resultant uncertainties associated to the megathrust interface width and geometry on the PSHA results which are later mentioned in the text.

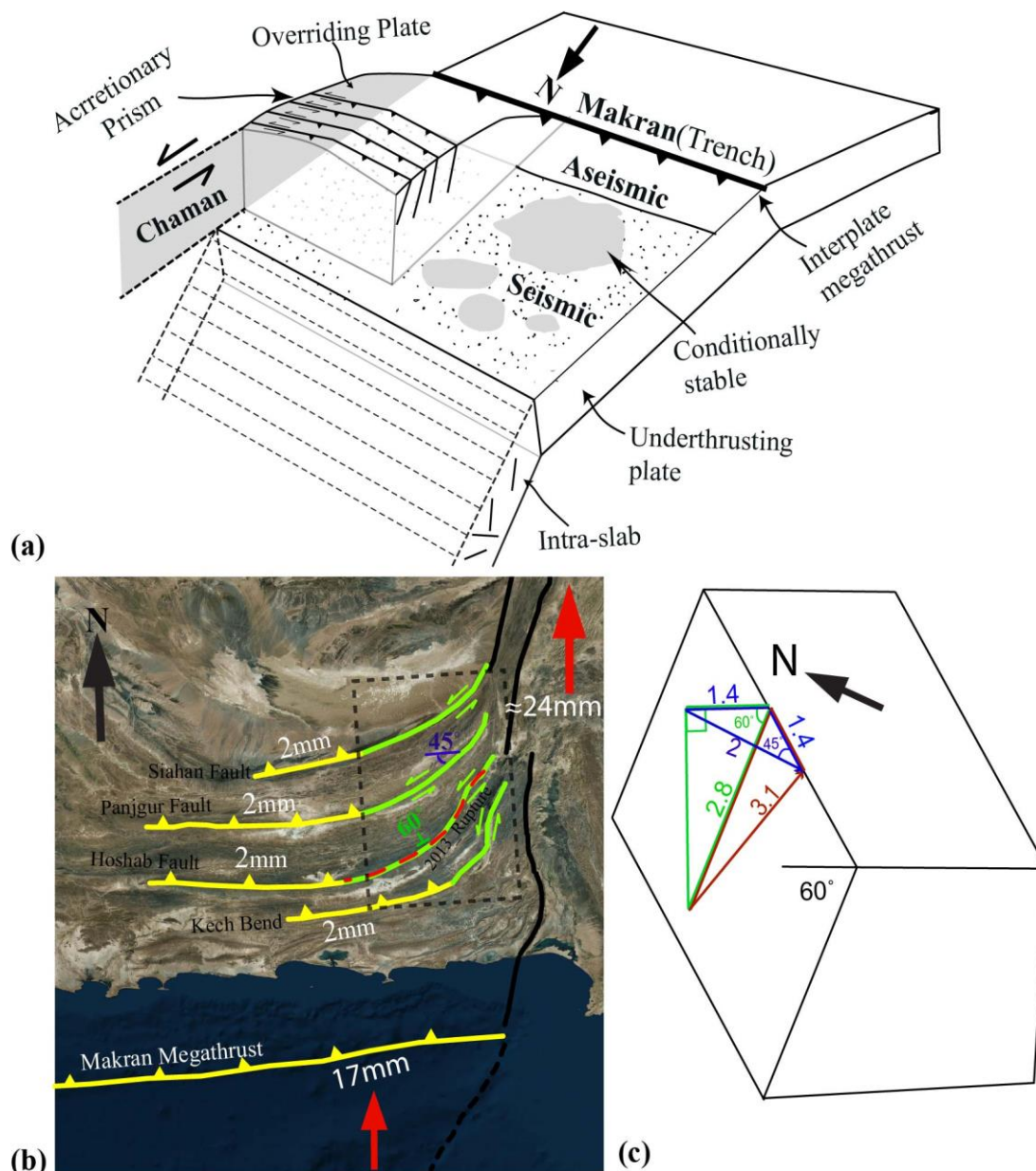


Figure 2.3. (a) Sketch showing along-dip variation in seismogenic behavior of Makran subduction zone and its interaction with the transform Chaman fault zone (modified from Wang & Hu, 2006; Bilek & Lay, 2002) (b) Satellite image with identified fault segments and selected partitioning of Northward motion between megathrust interface and accretionary wedge faults. The transition zone between transform faulting and thrusting is shown by black dashed rectangle. The green lines indicate the oblique faults that have both thrust and strike-slip components, while the yellow segments indicate the thrust faults. Red dashed line shows the rupture of 2013, Baluchistan earthquake (Avoauc et al., 2014) (c) Kinematic block model constructed to compute the slip rates along the oblique faults in transition zone

One of the common approaches for modeling in-slab seismicity sources is the use of uniform area sources placed at different depths to be able to incorporate the effect of the slab volume (examples are provided by Weatherill et al., 2017). Because the dip angle of the slab is very shallow, the intra-slab earthquakes are modeled to occur within the slab forming a single areal source representing the deeper seismicity. In order to avoid any underestimation, the upper boundary of the intra-slab areal source closest to the surface that starts at the downdip end of the megathrust interface (i.e. 40km) and extends up to 80km depth is selected during PSHA. The surface projection of the intra-slab zone is shown in Figure 2.2. Unlike megathrust interface, the intra-slab zone displays neither planar nature nor uniform slip and therefore its activity rate is defined using the rate of associated seismicity that is very limited (Figure 2.1).

The accretionary wedge faults overlying the subducting zone are also undergoing active deformation as recently manifested by the occurrence of 2013 $M_w=7.7$, Baluchistan earthquake (Jolivet et al., 2014). Mapped faults on Makran accretionary prism include; Siahan, Panjgur, Hoshab and Kech bend (Nai-Rud) faults (Figure 2.3b). The 2013 earthquake nucleated close to the Chaman Fault and propagated southwestward along the Hoshab Fault at the front of the Kechbend (Figure 2.3b). Barnhart et al. (2015) proposed that the northeastern section of the fault striking NNE-SSW has a strike-slip mechanism which changes into thrust as the orientation of the fault becomes directed more towards E-W. Although the 2013 mainshock was characterized mainly as a strike-slip event, the mechanisms of the aftershocks also revealed active thrusting in the southwestern section fault (Avouac et al., 2014). In this respect, there is a transition zone between the accretionary wedge and the Chaman transform fault zone where E-W striking accretionary wedge thrust faults bend towards North, forming oblique faults striking subparallel to the transform fault zone. The arch type model was proposed by Lawrence et al. (1981) for this type of interaction. Based on this deformation model, the eastern ~NE-SW oriented segments (green segments in Figure 2.3b) are assumed to rupture in oblique manner as they are more likely to be influenced by the Chaman fault. A dip amount of 60° was assigned

to these faults based on dip histogram constructed from the available focal mechanism solutions and the tectono-morphic study carried out by Zhou et al. (2016). On the other hand, the western segments (yellow lines in Figure 2.3b), which are striking almost in E-W direction, are more likely to be influenced by the N-S compression driving the active subduction. The dominant motion vector in the area (DeMets et al., 2010) which is nearly perpendicular to the fault planes suggests close to pure thrust mechanism for these ruptures. In the absence of any geologic and geophysical data, the dip of these faults is assumed as 30° which is typical for pure thrust faulting. Cruppa et al. (2017) computed a slip rate of ~2 mm/yr along the northern end of Siahhan fault near Kharan area using InSAR data. A similar study carried out by Huang et al. (2016) close to the Kharan region also shows a slip rate of 2 mm/yr. In accordance with these recent studies, a compressional motion of 2mm/yr which balances the motions in the region is assumed to be accommodated by each fault in the accretionary wedge (Figure 2.3b). Unlike vertical faults, identified horizontal motions should be projected on the inclined fault plane in the direction of displacement vector to compute the active slip rate on each individual fault segment. Assuming pure thrusting along faults with 30° dip amount, slip rate along the dipping plane was estimated as 2.3 mm/yr for the western fault segments of the accretionary wedge. However, for oblique faults, slip vector is oblique (~45°) to the orientation of faults and requires the computation of resultant slip along the dipping plane (60°) as depicted in Figure 2.3(c). The resultant slip rate computed for eastern fault segments of the accretionary wedge is 3.1mm/yr.

2.3. Magnitude Recurrence Relations

Two alternative magnitude distribution models (f_M) are utilized for developing the magnitude recurrence relation of seismic sources: the truncated exponential model (f_m^{TE} , Cosentino et al., 1977) given in Eq. (2.1) and the composite model (f_m^{YC}) proposed by Youngs and Coppersmith (1985) shown in Eq. (2.2):

$$f_m^{TE}(M) = \frac{\beta \exp(-\beta(M-M_{min}))}{1-\exp(-\beta(M_{max}-M_{min}))} \quad (2.1)$$

$$f_m^{YC}(M) = \begin{cases} \frac{1}{1+c_2} \times \frac{\beta \exp(-\beta(\bar{M}_{char}-M_{min}-1.25))}{1-\exp(-\beta(\bar{M}_{char}-M_{min}-0.25))} & \text{for } \bar{M}_{char}-0.25 < M \leq \bar{M}_{char}+0.25 \\ \frac{1}{1+c_2} \times \frac{\beta \exp(-\beta(M-M_{min}))}{1-\exp(-\beta(\bar{M}_{char}-M_{min}-0.25))} & \text{for } M_{min} < M \leq \bar{M}_{char}-0.25 \end{cases} \quad (2.2a)$$

$$c_2 = \frac{\beta \exp(-\beta(\bar{M}_{char}-M_{min}-\Delta m_2-\Delta m_3))}{1-\exp(-\beta(M_{char}-M_{min}-\Delta m_3))} \Delta m_1 \quad (2.2b)$$

In both equations, β is equal to $\ln(10)$ times the b-value, a.k.a. the relative rates of the small, moderate, and large magnitude events. The b-values are estimated by the maximum likelihood (MLE) and weighted least square (WLS) regression methods in ZMAP software package (Wiemer, 2001) for the whole study area, Chaman transform fault zone, Makran subduction zone, the intra-slab zone and Quetta-Pishin areal source zone as shown in Figure 2.4, using the compiled earthquake catalogue. Estimated b-values lie within the expected range and the influence of the regression method on the estimated values is small for the whole study area (Figure 2.4a) and for the Chaman transform fault zone (Figure 2.4b) with relatively high rate of earthquakes. However, for other zones with limited seismicity, the change in the b-value is approximately 20% when different regression methods are utilized. Considering other factors that affect the b-value estimates for low seismicity regions, this variation is represented in the SSC logic tree. For this purpose, both the region-specific (Figure 2.4a) and zone-specific b-values are adopted for shallow crustal sources and only zone-specific MLE and WLS estimations are adopted for Makran interface with equal weights in the SSC logic tree (Appendix A).

M_{min} given in Eq. (2.1) and (2.2) is the minimum magnitude value, which is set to $M_w=5.0$ for all rupture sources. The mean characteristic magnitude (M_{char}) in Eq. (2.2) is calculated using the magnitude-rupture area relations proposed by Wells and Coppersmith (1994, hereafter WC94) for Chaman transform fault zone; requiring that the fault width (or the seismogenic depth) of this fault system is estimated. Depth histograms of the seismicity for Chaman transform fault zone involve data in rather large seismogenic depth ranges, which are probably poorly constrained due to sparse network coverage. On the other hand, the depth histogram obtained from compiled

FMS, showing predominantly 20km depth, is considered to be better-constrained. This predominant value is consistent with the seismogenic depths of other major transform faults, e.g. San Andreas and North Anatolian fault zones; therefore, seismogenic depth of 20km is adopted in the calculations for Chaman transform fault zone. For the shallow crustal faults located on the accretionary wedge, the WC94 magnitude-rupture length relations for strike slip and thrust mechanisms are utilized to avoid abrupt changes in M_{char} values among the neighboring thrust and strike slip segments due to shallow dip angles leading to large along-dip widths. The epistemic uncertainty in the M_{char} value is modelled by utilizing two additional alternative magnitude-rupture area relations (Strasser et al., 2010 and Allen & Hayes, 2017 for subduction interface) for the single or multi-segment rupture sources of Makran interface plane.

$\Delta m1 - \Delta m3$ in Eq. (2.2) are the parameters of the composite magnitude distribution model that adjusts the distribution of the seismic moment release between the characteristic magnitude “box” and the exponential magnitude “tail”. The width of the characteristic box is usually taken as 0.5 magnitude units (represented by $\Delta m1$); while $\Delta m3$ is typically the half of it (0.25). The maximum magnitude (M_{max}) for each shallow crustal rupture source is defined as $M_{char} \pm 1SD$ ($M_{max} = M_{char} \pm 1$ standard deviation) based on WC94 relations; while for Makran interface, the M_{char} value obtained from each alternative relation (i.e. Strasser et al., 2010, WC94, Allen & Hayes, 2017) are equally weighed in the logic tree for M_{max} (Appendix A). Moreover, using the magnitude-rupture area correlations to calculate the M_{char} value for the intra-slab plane of Makran subduction zone will provide unrealistically high estimates for the maximum magnitude potential of the intra-slab zones. Therefore, the maximum magnitude potential of world-wide intra-slab zones and previous large magnitude intra-slab events are used to constrain the logic tree branches (Appendix A) of M_{max} for Makran intra-slab areal source zone (Moschetti et al., 2015).

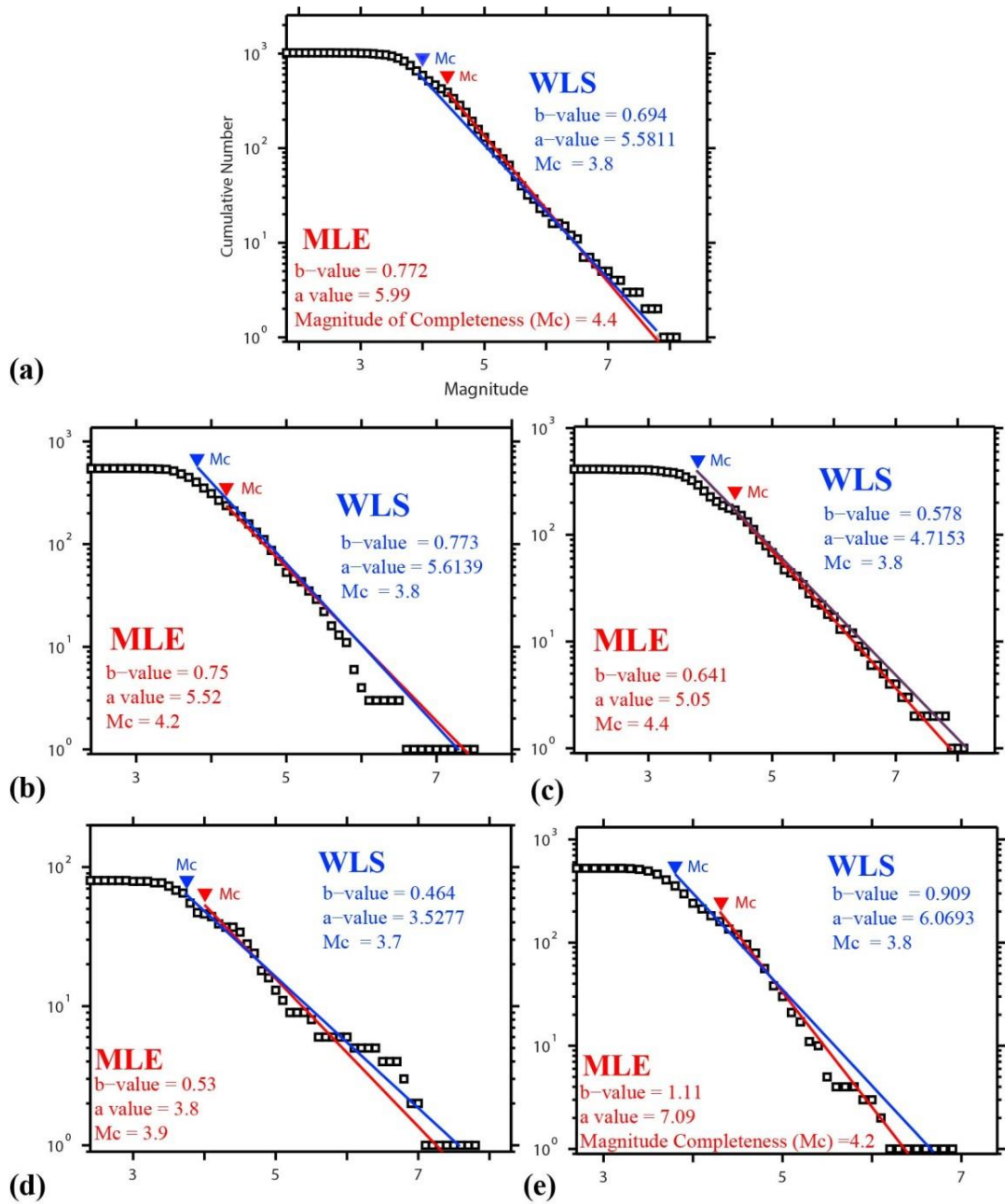


Figure 2.4. Magnitude distribution plots and computed a - and b -values using Maximum likelihood (MLE) and Weighted Least Square (WLS) regression methods for (a) the whole study area, (b) Chaman transform fault zone, (c) Makran subduction zone, (d) Makran intra-slab zone, and (e) Quetta-Pishin areal source, respectively

The proportion of the seismic moment release among the characteristic box and the truncated exponential tail is controlled by the value of Δm_2 . When Δm_2 is set to 1.0 (as in most of the applications), 94% of the seismic moment energy is released by the characteristic earthquakes. The composite magnitude distribution model with $\Delta m_2=1.0$ is utilized for the shallow crustal (Chaman and accretionary prism) faults and the activity rates for these seismic sources are calculated by balancing the accumulated and released seismic moments as shown in Eq. (2.3). The nominator of Eq. (3) shows the accumulating seismic moment (S is the annual slip rate in cm/years, A is the area of the fault in cm^2 and μ is the shear modulus of the crust in dyne/cm^2); while the denominator represents the moment release for each earthquake multiplied by the relative rate of earthquakes.

$$N(M_{\min}) = \frac{\mu AS}{\int_{M_{\min}}^{M_{\max}} f_m(M_w) 10^{1.5M_w + 16.05} dM} \quad (2.3)$$

Figure 2.5(a-c) presents the cumulative rate of events for Makran interface calculated by using Eq. (2.3) for three alternative magnitude distribution models. In each plot, 4 alternative full-rupture scenarios are defined, considering the single and multiple segments along the strike. The weighted average of the cumulative rate of events calculated for each full-rupture scenario is given by the red lines in each figure. In Figure 2.5(a), f_m^{TE} is utilized in Eq. (2.3) in combination with the M_{char} value calculated by the WC94 magnitude-rupture area relation for each rupture source; in other words, the fault dimensions are used to constrain the maximum magnitude potential. This option (Option#1) leads to a much higher rate of small and moderate magnitude earthquakes than has been observed for this seismic source; in agreement with the previous observations for many shallow crustal faults (Hecker et al., 2013). To resolve this discrepancy, two alternatives are considered. In Option#2, f_m^{YC} is utilized and the proportion of the seismic moment released by the exponential tail is increased by decreasing the value of Δm_2 to 0.37. Figure 2.5(b) shows that the weighted average of cumulative rate of earthquakes (red line) in this alternative is in good agreement with the cumulative rate of events associated with the Makran interface (brown dots).

In Option 3, f_m^{TE} is utilized in Eq. (2.3); however, the M_{max} value is increased by 0.5 magnitude units to lower the rate of small magnitude events (Figure 2.5c). This modification results in a better fit with the rate of small-to-moderate magnitude events; however, the rate of large magnitude events (e.g. $M_w=8.1$) is underestimated. Blue line in Figure 2.5 represents the cumulative rate of large magnitude earthquake for Makran interface as proposed by Byrne et al. (1992). Byrne et al. (1992) suggested a return period of 175 to ~300 years for $M=8.1$ earthquake, in agreement with the cumulative rates suggested in this study. Figure 2.5(d) compares the weighted average lines for all three options (2.5a-c) and shows that Options #1 and #2 have a good match with the cumulative rate of large magnitude events associated with the Makran interface; while Option #2 and Option #3 has a better match with the cumulative rate of small-to-moderate magnitude events.

For the Makran intra-slab zone and the Quetta-Pishin areal source zone, the activity rates ($N(M_{min})$) are calculated using the de-clustered earthquake catalogue by assigning equal weights to MLE and WLS estimates shown in Figure 2.4(d) and 2.4(e) and truncated exponential magnitude distribution model is preferred.

2.4. Sensitivity Analysis of the Hazard Results to Seismic Source Model Parameters

To evaluate the sensitivity of the seismic hazard results to the SSC model parameters, PGA maps for 475-year return period are developed using the traditional Cornell-McGuire PSHA approach (Cornell, 1968; McGuire, 2004). The numerical integration of the hazard integral is performed using the HAZ45 software (Hale et al, 2018). The Monte Carlo sampling of the full SSC logic tree is used to combine the epistemic uncertainty for each seismic source. Two different types of ground motion models (GMMs) are utilized: for shallow crustal active seismic sources (Chaman Fault Systems, Quetta-Pishin areal source zone and accretionary prism faults); recently developed NGA-West2 models proposed by Abrahamson et al. (2014), Boore et al. (2014), Campbell and Bozorgnia (2014) and Chiou and Youngs (2014) are selected while the BC Hydro GMM (Abrahamson et al., 2016) is combined with the Makran

interface and intra-slab planes. Equal weights are assigned to the GMMs of each type in the ground motion characterization logic tree. A full logic tree for the ground motion characterization of subduction zone could not be utilized because the GMMs in the context of NGA-Subduction project are still under development. In order to prepare the 475-year PGA maps, 1295 grid points are selected across the study area and the density of the grid points is increased within the close vicinity of the faults for accuracy. The PGA values are estimated for $V_{S30}=760$ m/s, representing the rock site conditions (soil type B/C boundary in NEHRP site classification system).

The first set of sensitivity analyses is conducted to evaluate the effect of magnitude distribution model on the distribution of ground motion estimates for Makran megathrust interface. For this purpose, the fault geometry of Makran interface is defined by a plane with dip angle of 5° , reaching up to 40 km depth. Maps of 475-year PGA values obtained by using Options 1-3 are provided in Figure 2.5(a-c). When Option#1 (f_m^{TE} model) is utilized, the hazard estimates are larger than 0.4g for sites located within ~ 200 km north of the fault's strike. PGA values estimated by using Option#1 (f_m^{TE} model) are approximately 10% higher than values estimated by using Option#2 (f_m^{YC} model). The PSHA outputs (e.g. deaggregation results) show that the dominating scenario of each site for this hazard level is within the magnitude range of 7.7-8.2, depending on the distance of the site from the fault. Therefore; Option#3 (f_m^{TE} model with increased M_{max}) results in the lowest hazard estimates due to the low rates of large magnitude events as shown in Figure 2.5(c-d). Although truncated exponential magnitude distribution model was preferred in modelling the magnitude distribution of other gently dipping subduction zones (e.g. Cascadia subduction zone, Rong et al., 2014); cumulative rates of associated seismicity favor the f_m^{YC} model (Option#2) in the case of Makran interface plane. Therefore, Option#2 is adopted in the PSHA for the further sensitivity analyses and for the final hazard map. Considering that the earthquake catalogue for the region is incomplete and the actual rates of seismicity might be considerably higher than the one given in Figure 2.5, Option#1 may also be considered in the future PSHA studies. It should be underlined that the

variances in the PGA values for higher hazard levels (e.g. 5000-year return period) might be quite different than the results presented for this case.

The second set of sensitivity analysis is related to the aseismic section of the Makran megathrust interface, with the objective of evaluating the impact of this section on the ground motion estimates. Figure 2.6(a) shows the alternative fault geometry models developed for Makran interface plane. For Models 1a, 1b & 1c, the bottom boundary of the interface plane is placed at 40km depth, based on the distribution of FMS: beyond 40km seismogenic depth, mostly normal FMS are observed (Figure 2.6a). The dip angle of this plane is calculated from the cross section as $\sim 5^\circ$. In Model 1a, a steep plane shown by the bold black dashed line in Figure 2.6(a) is selected to represent the aseismic section. The aseismic portion is excluded in Model 1b (only the red line is included); while a buried interface (dashed red line in Fig. 2.6a) that is extended until the trench position is defined to represent the aseismic portion in Model 1c. It should be noted that the width of the interface plane is different in each model; therefore, the M_{char} values are re-estimated for each model using the rupture area of the interface plane. The inclusion or exclusion of the aseismic portion in the seismic source model or its geometry has a minor influence on the calculated M_{char} values; but it has a significant effect on the source-to-site distances for near trench sites. The 475-year PGA maps based on Models 1a-c are presented in Figures 2.6(b-d), respectively. Spatial distribution of the ground motion estimates is quite similar in the mainland (accretionary wedge region); however, the influence of the aseismic portion on the estimates is significant in the near trench sites ($\sim 50\text{km}$). Model 1b represents the lower bound of the estimates; the 475-year PGA values in the near fault are significantly smaller for this model when compared to the other alternatives. In the close vicinity of the trench (off-shore), Model 1a results in systematically larger PGA values than Models 1b & 1c. This difference is related to the short-distance scaling of the BC Hydro GMM. Unfortunately, the short-distance scaling of the BC Hydro GMM suffer from the lack of data: there is no recording in the model's dataset with rupture distances (R_{RUP}) less than 10km and the data is very sparse for $R_{\text{RUP}} < 30\text{km}$

(Abrahamson et al., 2016). Because the distance scaling of the GMM for $R_{RUP} < 30\text{km}$ is not well-constrained, Model 1c is preferred for further sensitivity analysis and for the final hazard map.

Finally, sensitivity analysis for the depth extent and the dip angle of interface plane is conducted. Model 2 is created as an alternative to Model 1c to account for the uncertainty in the bottom boundary of interface plane: an alternative depth of 30km is selected based on the analysis of receiver functions (Penney et al., 2017). Alternative values for dip angle (03° and 07°) of Model 1c are also considered (Model 3 and Model 4). To get a clear picture of the spatial distribution of the difference, these alternative models are incorporated into the PSHA analysis and their residual maps are presented in Figure 2.6(e-f). The map in Figure 2.6(e) shows the difference in 475-years PGA values (or the residual PGA values) based on Model 1c and Model 2 with the same dip angles but different lower boundaries for the interface plane. The residual PGA values are noteworthy; varying from -0.05 to 0.17g, because a couple different inputs of the PSHA integral interact with each other to create that difference. The extent of the interface plane for Model 2 is shallower than that of Model 1c, which reduces the hazard estimates on the northern side of the interface plane as expected. Shallower bottom boundary for interface plane reduces the along-dip width dimension (294 km vs. 208km for Model 1c and 2 respectively), which leads to a significant decrease in the M_{char} value (8.93 vs. 8.8 for Model 1c and 2). The reduction in the M_{char} value in Eq. (2.3) leads to higher rates for small-to-moderate magnitude earthquakes and smaller rates for large magnitude events (for an example of this reduction, please refer to Figures 2.5a and 2.5c). The increase in the rate of small-to-moderate magnitude events results in a general increase in the ground motions for relatively short return periods (i.e. 475 years). The negative residual PGA values are restricted to near-field (off-shore region), indicating that the smaller interface plane with the same activity rate utilized in Model 2 resulted in a higher concentration of ruptures assigned to the shallower part of the plane and consequent decrease in the source to site distances leads to slightly higher near-field ground motion estimates. The residuals are positive

(up to 0.17g) in the onshore accretionary wedge regions with higher PGA values for Model 1c in the respective region.

Figure 2.6(f) shows the spatial distribution of the residual PGA values when the ground motions estimates based on Model 3 and Model 4 are compared. It should be noted that these models have the same depth extent for the interface plane, but the dip angles are different (7° for Model 4 and 3° for Model 3). Gentler dip angle (3°) creates a larger plane (Figure 2.6a) which increases the M_{char} value (and consequently reduces the 475-years PGA values) and extends the surface projection of the interface plane towards north. This extension results in the positive residual PGA values (up to 0.3g) in the north of the Makran megathrust. However, smaller interface plane with steeper dip angle (07°) and smaller M_{char} value with the same activity rate leads to higher near-field ground motion estimates, similar to the case given in Figure 2.6(e).

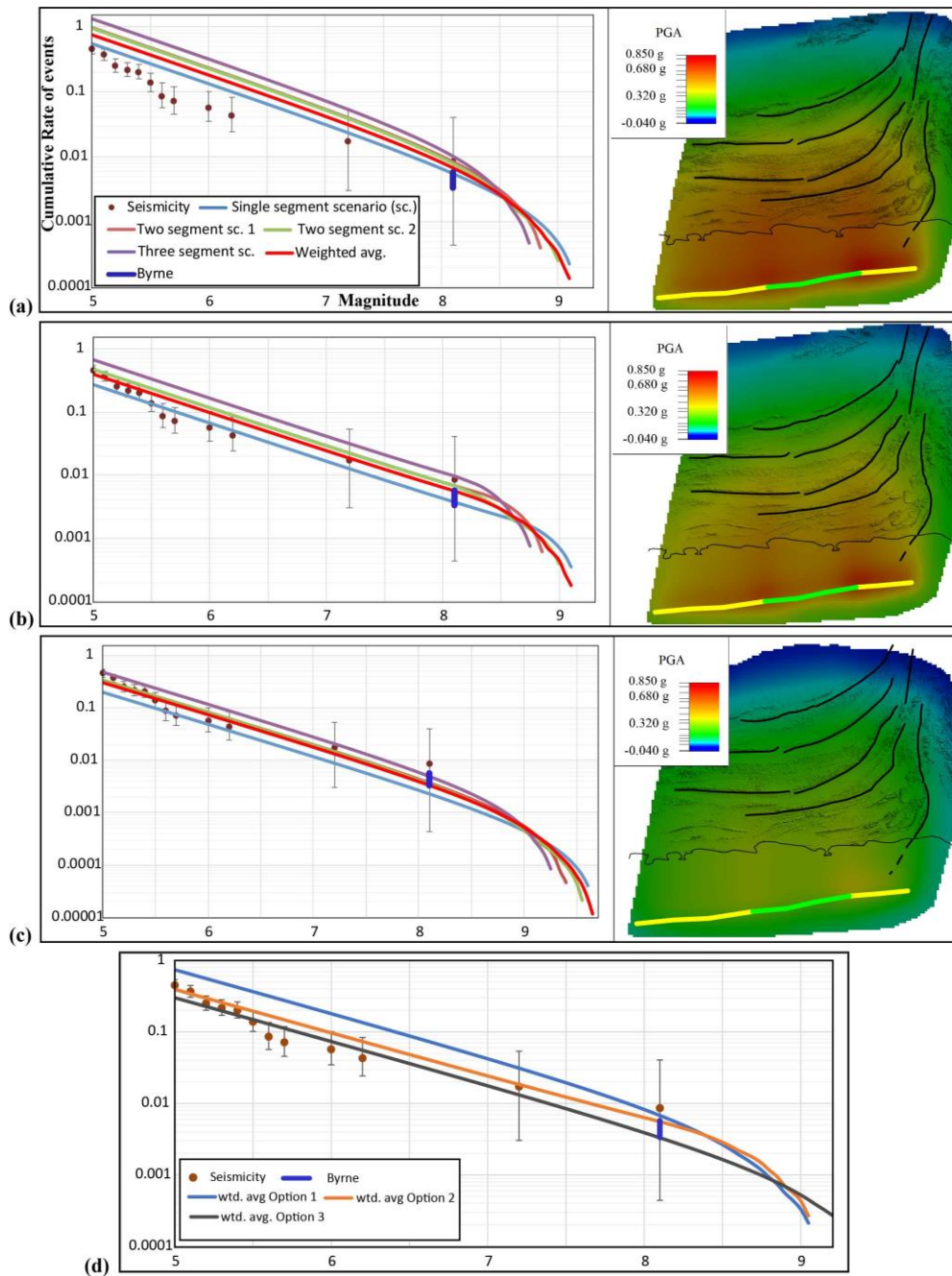


Figure 2.5. Activity rates of the rupture scenarios considered for Makran megathrust interface plane based on the (a) truncated exponential (TE) model, (b) composite magnitude distribution (YC) model and, (c) TE model with increased M_{max} . In each plot, cumulative rates of the associated seismicity with the Makran interface plane are presented by the brown points and the error bars are estimated by considering the catalogue completeness intervals as suggested by Weichert (1980). Activity rate for large magnitude events proposed by Byrne et al. (1992) is shown by blue line in each plot. The PGA maps for 475-year return period for the megathrust interface based on alternative magnitude distribution models are plotted to the right of (a), (b) and (c). (d) Comparison of the weighted average of the cumulative rate of events for (a), (b) and (c)

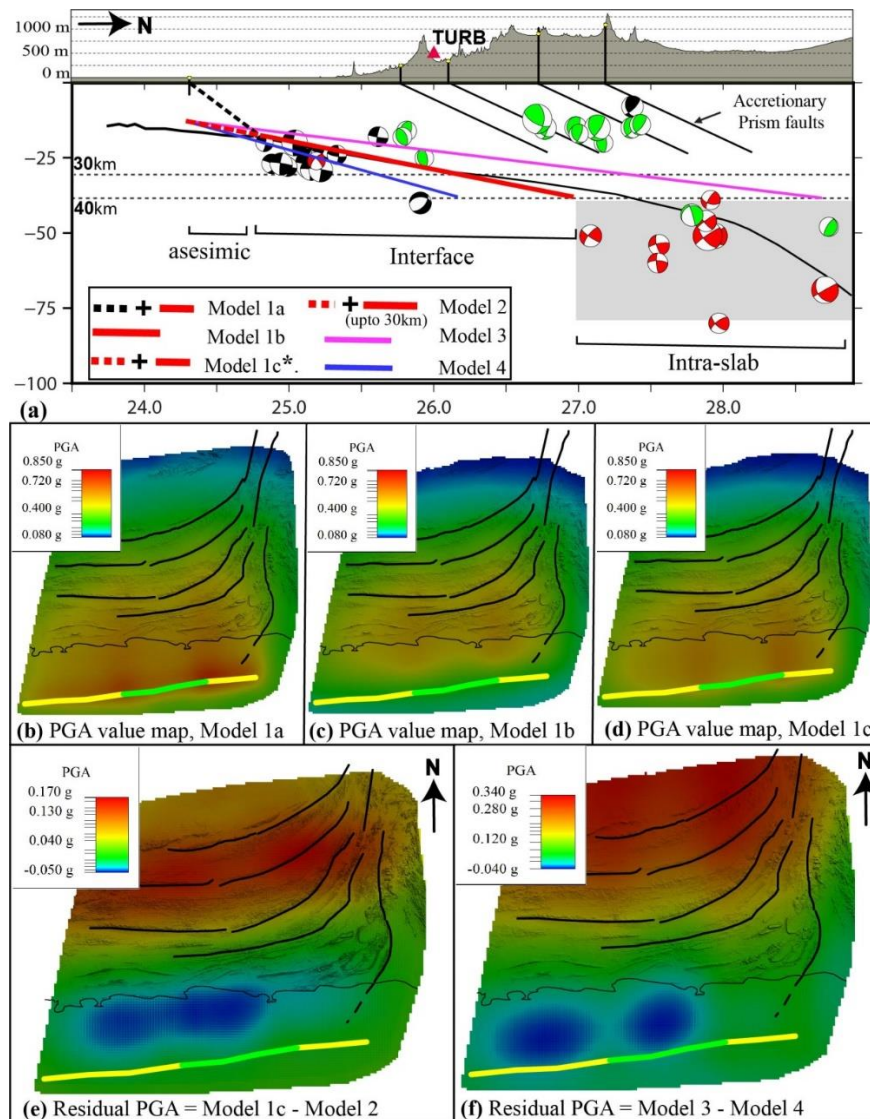


Figure 2.6 (a) North-South oriented cross section passing from 63.5° latitude across Makran subduction zone displaying surface topography, tested and published slab geometries along with focal mechanism solutions (FMS) recorded within 2° width on both sides of the profile. Compressive quadrants of FMS are color coded according to the type of faulting: black for thrust, green for strike-slip and red for normal events. Solid black line in the aseismic portion is the basement reflector observed by Kopp et al. (2000). Black curved line shows the geometry of slab proposed by Penney et al. (2017). Red, pink and blue lines represent the tested slab geometries (in this study) with different dip amounts (Red = 05° ; Pink = 03° ; blue = 07°). Bold dashed black and red lines represent steeper and buried geometry of Makran megathrust in the aseismic portion. Two thin dashed black lines indicate the alternative downdip depth extents used for megathrust interface. (b), (c) & (d) shows 475-year PGA maps based on Model 1a, 1b & 1c, respectively (e) Residual PGA map is constructed by subtracting the PGA values with 475-years return period calculated for the megathrust interface with shallower (30 km) downdip depth extent (Model 2) from deeper (40 km) extending one (Model 1c) (f) Residual PGA map is constructed by subtracting the PGA values with 475-years return period calculated for more steeply dipping (07°) megathrust interface (Model 4) from gentle dipping (03°) one (Model 3)

2.5. Relative Contribution of Different Tectonic Structures on the Final Hazard Map

One of the concerns of this study is to quantify the relative contribution of megathrust earthquakes within the subduction interface to the ground motion estimates in a zone that also includes a major transform fault. Hazard potential of the subduction megathrust earthquakes that occur in the subduction interface are quite significant and the large PGA zone extend along the dip direction of the slab as shown in Figures 2.5 & Figure 2.6. The seismic zones representing the shallow crustal earthquakes (Chaman fault system and accretionary prism faults) and the subduction intra-slab plane are incorporated into the hazard calculations one-by-one and the resulting PGA maps with 475-year return period are presented in Figures 2.7 and 2.8, respectively. In Figure 2.7, the ground motion estimates have a symmetrical distribution along the Chaman fault due to the fault's vertical strike-slip nature. Highest 475-year PGA values are observed around Ornach-Nal and Ghazaband Rupture Systems (up to 0.7g) because these segments of the Chaman fault are associated with higher slip rates (15-16mm/yr) when compared to the others. Reduction in the slip rate due to the creeping behavior of Chaman fault system S2 reduced the ground motion estimates significantly in this area. Chaman Fault System S3 lies closely parallel to the Ghazaband Rupture System; therefore, the combined slip rate associated with these parallel branches created a large high-PGA band ($PGA > 0.4g$) in the middle of the study area. Quetta-Pishin areal source zone is included in this study for the sole reason of not underestimating the ground motions on the east of Chaman fault: inset Figure 2.7 shows that the 475-years PGA values inside the zone boundaries reach up to 0.3g but its influence is almost negligible in the west of Chaman fault. It should be noted that the activity rate for the Quetta-Pishin areal source zone is calculated based on the catalogue seismicity; therefore, the estimated ground motions within the zone might be larger when other methods based on the seismic moment or slip rate are utilized for calculating the activity rates (Shah et al., 2018).

The 475-year PGA maps provided in Figure 2.8(a) and 2.8(b) are developed based on the accretionary prism faults with thrust and strike-slip/oblique mechanism, respectively. The ground motion estimates are quite low when compared to the Chaman Fault (Figure 2.7), mainly due to the dimensions, maximum magnitude potential, and slip rates associated with these faults. The thrust faults on the west have a slightly higher hazard potential, especially on the hanging wall side when compared to the strike-slip/oblique faults in the east because the shallow dip angles of the thrust faults results in shorter source-to-site distances for points located away from the fault as compared to steeply dipping or vertical faults. In both maps, the PGA values with 475-year return period reach up to 0.25-0.3g in a limited area around the fault line; eventually creating a moderate-hazard zone since the fault lines are close to each other and their zones of influence overlap. Figure 2.8(c) is prepared to evaluate the contribution of the intra-slab areal zone to the ground motion estimates. Petersen et al. (2002) mentioned that modeling the deep intra-slab earthquakes as homogeneous seismic source along the subduction zone increases the PGA values by about 20% in some regions. Our observations are similar; only by incorporating the seismic source representing the deep intra-slab events of the Makran subduction zone with a homogenous seismicity distribution in PSHA, PGA values up to 0.25g are estimated as shown in Figure 2.8(c). The influence of intra-slab zone on the 475-year PGA values is homogeneous throughout the zone as expected. The intra-slab zone can be modeled as planar source in the presence of a detailed dataset that can characterize its rupture dimensions and dip angle. The planar approach will lead to higher hazard estimates as compared to the areal approach, but the latter is favored in this study due to its consistency with the available intra-slab GMMs (Hale et al., 2018) and sparse dataset for the region. Moreover, it should be noted that the M_{\max} value assigned to the intra-slab zone has a significant impact on the hazard potential; therefore, a different logic tree implemented for this parameter might change the ground motion estimates.

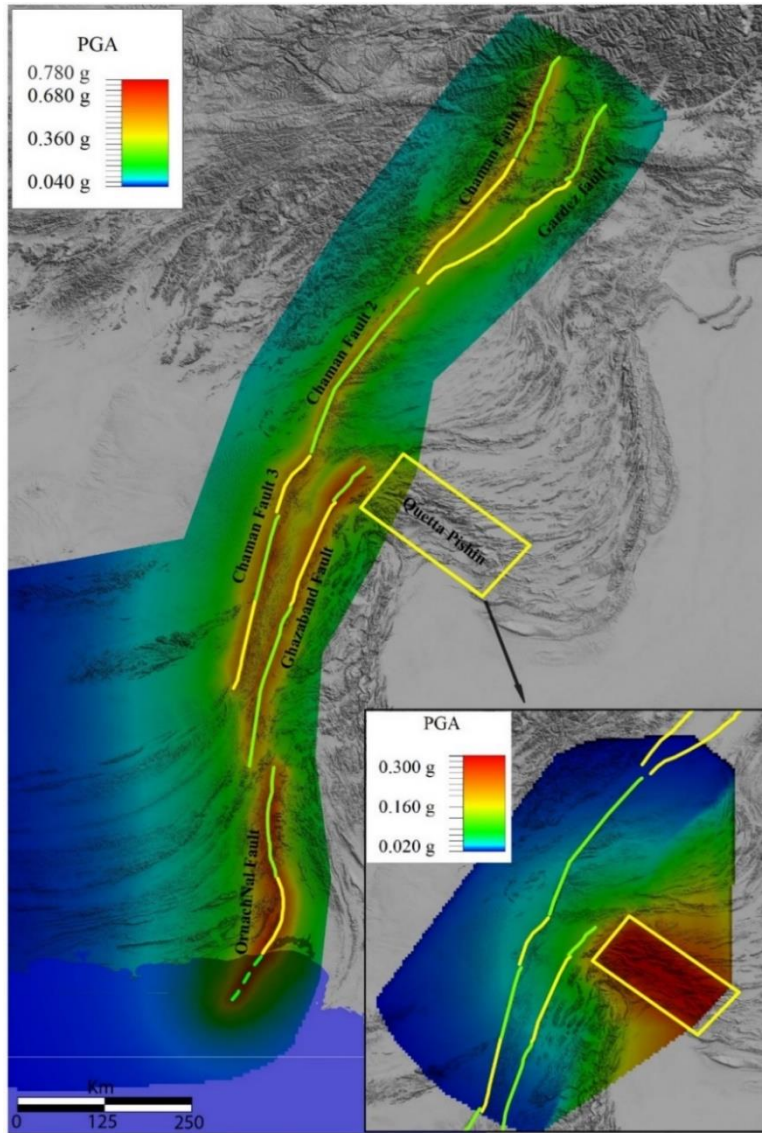


Figure 2.7. PGA map with 475-year return period constructed using only seismic sources associated with Chaman Transform fault zone. Inset map shows PGA values associated to Quetta-Pishin areal source zone

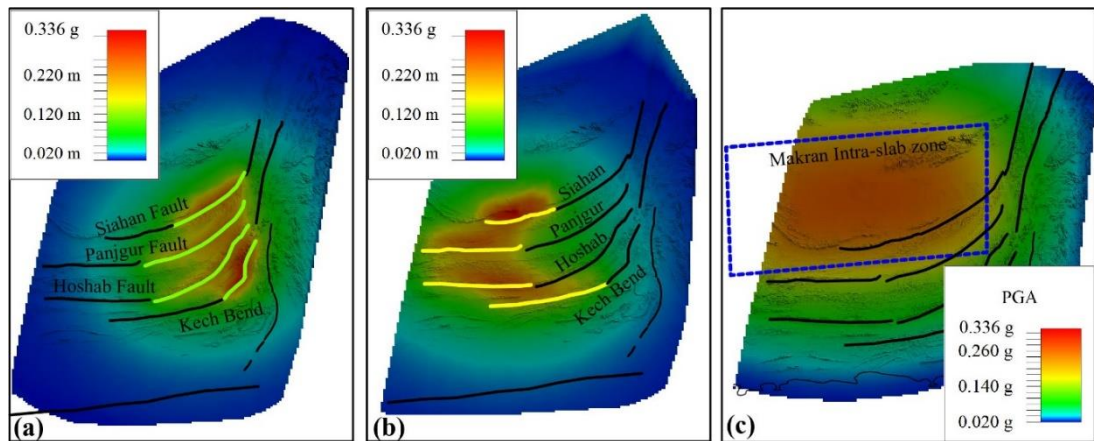


Figure 2.8. PGA maps with 475-year return period constructed for oblique fault segments (a) and thrust fault segments (b) of Makran accretionary wedge and for intra-slab areal zone (c) of Makran subduction

2.6. Conclusions and Recommendations

Makran is a relatively slow-moving subduction zone with shallow dipping angle, which is located on a tectonically complex area with a large accretionary wedge connected to major Chaman transform fault. The interaction among these tectonic structures combined with lack of detailed geologic, seismic, and geodetic dataset created a challenging environment for developing the SSC model for Makran region. The primary objective of this study was to build state-of-the-art SSC models for Makran subduction zone to be used in PSHA and to develop an up-to-date reference hazard map of the region. During these efforts, several issues were faced for parametrizing the SSC model, especially in modeling the geometry of interface plane and intra-slab zone, developing the magnitude recurrence relation and estimating the maximum magnitude potential. Therefore, the conclusions of this study can be clustered into two main headings: the discussions related to the 475-year return period PGA map of the region and the results of the sensitivity analysis for the impact of SSC model parameters on the hazard map.

The 475-year return period PGA map, considering all seismic sources in the region, is presented in Figure 2.9. This map underlines that the megathrust events in the Makran

subduction zone results in significant ground motion estimates; the high hazard zone ($PGA > 0.4g$) extends for almost 250km along the dipping plane. The seismic source representing the megathrust earthquakes is the main contributor of the ground motions estimated in the first 150km of the overriding plane; however, the role of the accretionary prism faults, especially in the close vicinity of the fault lines should not be underestimated. As the distance to the strike of the subduction zone increases, the contribution of the deep intra-slab events also becomes more critical, almost equal to the contribution of accretionary prism faults. Figure 2.9 shows that the PGA values with 475-year return period around the Chaman Fault is also considerably high ($>0.4g$), especially in a thin band located in the close vicinity of the fault plane ($\pm 20km$ around the fault). In this study, the activity rates for the seismic sources (except for the Makran intra-slab zone and Quetta-Pishin areal source zone) are calculated using the seismic moment balancing approach based on the annual slip rate. Therefore, the shape of the high-hazard band around the Chaman Fault is not uniform; it changes with the annual slip rate assigned to each particular fault segment. This difference is especially striking for the Chaman Fault System S2 because a proportion of the annual slip rate is accommodated in form of fault creep, which reduces the amount of slip rate used for calculating the activity rates and eventually the ground motion estimates. Because the annual slip rate along the dipping plane is an important parameter for calculating the activity rate, a block model is proposed for computing the slip rates along the oblique shallow crustal faults in the Makran accretionary wedge (Figure 2.3c). This model and the slip rates associated with each fault segment can be directly implemented in future PSHA efforts in the regional and global scale until geodetic data with sufficient resolution provides more accurate results.

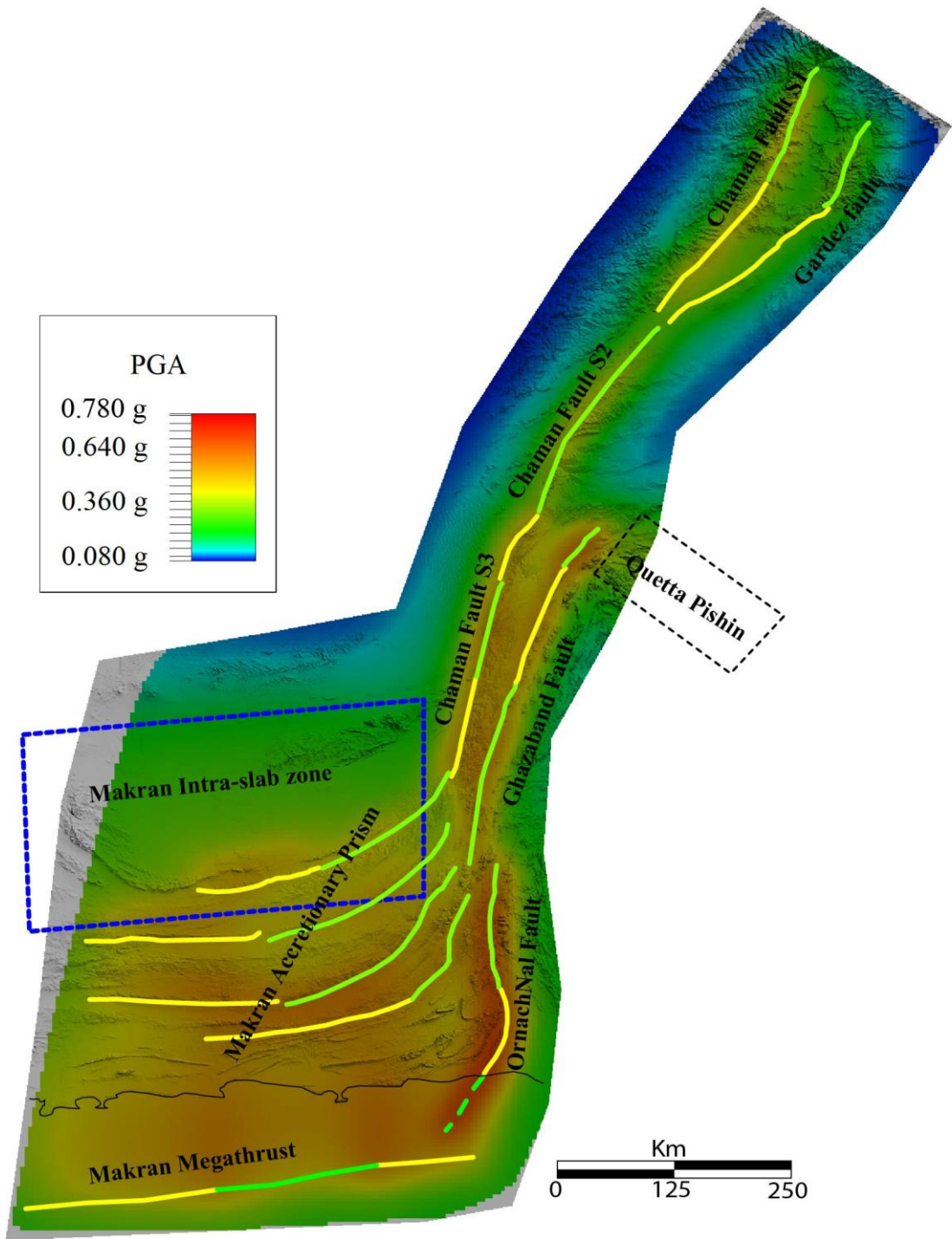


Figure 2.9. Final PSHA hazard map for western and southern margin of Pakistan showing peak ground acceleration (PGA) for return period of 475yr and V_{s30} of 760 m/s

Four different fault geometry models were developed for the megathrust earthquakes by changing the dip angle and the bottom boundary of the interface plane to account for the uncertainties in these parameters. It should be noted that changing the fault plane geometry results in three significant changes: (i) rupture plane dimensions directly modify the maximum magnitude values and magnitude recurrence distribution, (ii) source-to-site distance changes according to the dip angle, and (iii) changing rupture plane dimensions result in different activity rates in moment-balancing approach. Therefore, effect of fault geometry on the ground motion estimates and their spatial distribution must be discussed by implementing each alternative in PSHA and creating individual PGA maps. In gently dipping subduction zones such as Makran, the estimated ground motions and their spatial distribution are highly sensitive (changing by approximately 0.2-0.3g) to the selected depth extent and dip amount of the megathrust interface which defines the maximum rupture width. Gentler and deeper extending interface geometries resulted in slightly lower PGA values towards the trench and significantly higher PGA values towards inland along accretionary wedge due to their influence on the rupture dimensions and source-to-site distances. Additionally, the influence of aseismic section of megathrust on hazard estimates in near trench sites was analyzed. Results showed that the influence of aseismic portion is restricted to only near trench sites (~50km) and its influence on inland accretionary wedge region is insignificant. Moreover, alternative magnitude distribution models which influence the activity rates of controlling earthquake scenarios are tested for Makran subduction zone and truncated exponential model resulted in ~10 % higher PGA values than composite models for short return periods, but the later correlates well with the seismicity distribution of the region. Based on these observations, it is clear that these parameters (i.e. dip angle, interface depth, recurrence models) play a vital role in controlling the level and spatial distribution of hazard and should be scrutinized in detail before implementation. Among the alternative models suggested in this study for Makran interface plane; Model 1c is preferred due to its well constrained dip angle with FMS distribution, its higher hazard estimates for hazard studies aimed to compute the ground motions in the mainland

accretionary wedge regions (Figure 2.6), similarity to previously proposed interface geometry (Penny et al., 2017), correlation with recorded cumulative seismicity rates, comparable M_{char} and rupture width estimates with literature (Herrendörfer et al., 2015; Schellart & Rawlinson, 2013; Smith et al., 2013) and its moderate hazard estimates.

It should be underlined that the hazard estimates obtained in this practice does not account for the additional faults in the vicinity of our study area and may be underestimated in this regard. Seismicity catalogue for the region might be incomplete and marked by inhomogeneities in space and time. They require further improvement that can be achieved by increasing the density of seismic network in the region in the future. More data and observations from seismological records and physics based mechanical models will further improve the SSC model for the region. A planar fault model (3-D) which includes information regarding the down-dip geometry of interface plane, interface depth, intra-slab zone and accretionary wedge faults (if there are any) must be adopted for regions characterized by megathrusts such as Makran, in order to reduce uncertainties induced by areal and oversimplified discrete models.

CHAPTER 3

PROCEDURE FOR FAULT BASED PSHA IN EXTENSIONAL TECTONIC REGIMES, CASE STUDY FROM WESTERN ANATOLIA: IMPLICATIONS OF ACTIVITY RATE CHARACTERIZATION

Both extensional and compressional tectonic regimes display rather complex fault geometries including multiple sets of inclined active faults and pose a challenge for accurate representation of seismogenic sources for fault-based probabilistic seismic hazard assessment (PSHA). In the absence of individual fault slip rates and presence of only sparse seismic and geodetic data, calculation and distribution of activity rate in these regimes also includes a considerable amount of uncertainty. In this study, a detailed PSHA with sensitivity analyses of activity rate has been carried out for the northern margin of Western Anatolian Extensional Province. First, fault segments and systems are defined using connections between available active fault traces and first order geological complexities. The down-dip extent and dip of faults are determined using available earthquake depths and focal mechanism solutions respectively. Next, three alternative approaches based on slip rate, seismicity rate and moment rate are employed to determine the activity rates for each sub-region. Later, calculated activity rates are partitioned among fault systems using two different approaches based on the fault morphology and the length of fault trace. Finally, proposed seismic source characterizations are incorporated into the hazard integral and peak ground acceleration (PGA) maps for 475-year return period are provided for each alternative. Results of the analysis showed that the slip rate based activity rates translate into high hazard estimates and more uniform distribution of PGA values, while seismicity and moment rate based hazard maps are more sensitive to the occurrence of large magnitude earthquakes in the region. Also, the effect of the approach utilized to partition activity rate is only noticeable at areas where strong asymmetric fault activity

is inferred from morphology. As a result, a fault-based PSHA procedure that provides weighted, maximum and minimum PGA value maps incorporating activity rates from all the methods is established to evaluate and minimize the bias on hazard estimates of complex tectonic regimes in the current practice.

3.1. Introduction

Fault-based seismic source characterization (SSC) models that consider the geological and geodetic constraints, uncertainty in the fault geometry, the seismicity rate associated with the fault system and the recurrence rates for the characteristic earthquakes have been developed for the major and well-defined strike-slip fault systems around the world (e.g. the fault source and background model for Europe-Woessner et al., 2015 and Uniform California Earthquake Rupture Forecast Version 3- UCERF3, Field et al., 2014). In the recently published UCERF3 model, the segmentation models that link the adjacent fault segments and build the Fault-to-Fault (FtF) ruptures were proposed. On the other hand, developing fault-based SSC models in extensional regimes (e.g. Northern California, Italy, Western Turkey and Greece) are more challenging than modelling strike-slip faults for several reasons, especially because of the issues related to fault geometry. Typically, extensional fault systems include shorter fault segments (10-60 km); therefore, the SSC model developer needs to integrate these single fault segments into combined seismic sources in order to simplify the fault geometry. When the fault segments are combined, a single dip value has to be used for the entire fault plane for simplification; therefore, the down-dip and along-the-strike changes cannot be properly reflected in the SSC model. Dimensions of the combined fault segments and the connection between the geological fault traces should be considered in developing the segmentation and magnitude recurrence models. In UCERF2 (Field et al., 2009) and UCERF3 (Field et al., 2014), the seismic moment “budgets” based on the observed seismicity, rupture dimensions and annual slip rate over the fault are used to test the proposed recurrence rates in the SSC model. It is quite challenging to perform this budgeting in extensional systems since the surface projections of the fault planes overlap to a great extent and it is not always

possible to match the seismicity with the fault source. In addition, slip rate participation over the closely spaced graben-bounding structures includes a considerable amount of uncertainty (e.g. Boncio et al., 2004; Chartier et al., 2017). Based on these considerations, traditional seismotectonic zoning that is based primarily on the earthquake catalogues may be preferred by the SSC model developer for extensional systems and this preference may lead to the underestimation of the hazard (Peruzza et al., 2006; Hecker et al., 2013; Gülerce and Vakilinezhad, 2015).

This paper summarizes one of the first attempts in building fault-based SSC models for the northern margin of the Western Anatolia graben system in southwest Turkey (Figure 3.1 inset), which is mainly characterized by normal faults bounding the Simav and Afyon-Akşehir graben systems (Figure 3.1). The region is currently undergoing a continental lithospheric extension in the ~NS direction (e.g. McKenzie, 1972; Angelier, 1978; McKenzie, 1978; Le Pichon and Angelier, 1981; Şengör et al., 1985) although there are different views on the driving mechanism of this extension process (McKenzie, 1978; Le Pichon and Angelier, 1981; Dewey and Şengör, 1979; Taymaz et al., 1991). Focal mechanism solutions gathered from several different sources indicate ~WNW-ESE normal faulting with nodal plane dip angles in the range of 30-60° for Simav fault zone (Eyidoğan and Jackson 1985; Kiratzi and Louvari, 2003; Karasozen et al., 2016). Afyon-Akşehir graben system is an active low-angle normal fault bordered by the Sultandagi rise in the west and Afyon-Akşehir Graben (AAG) in the east.

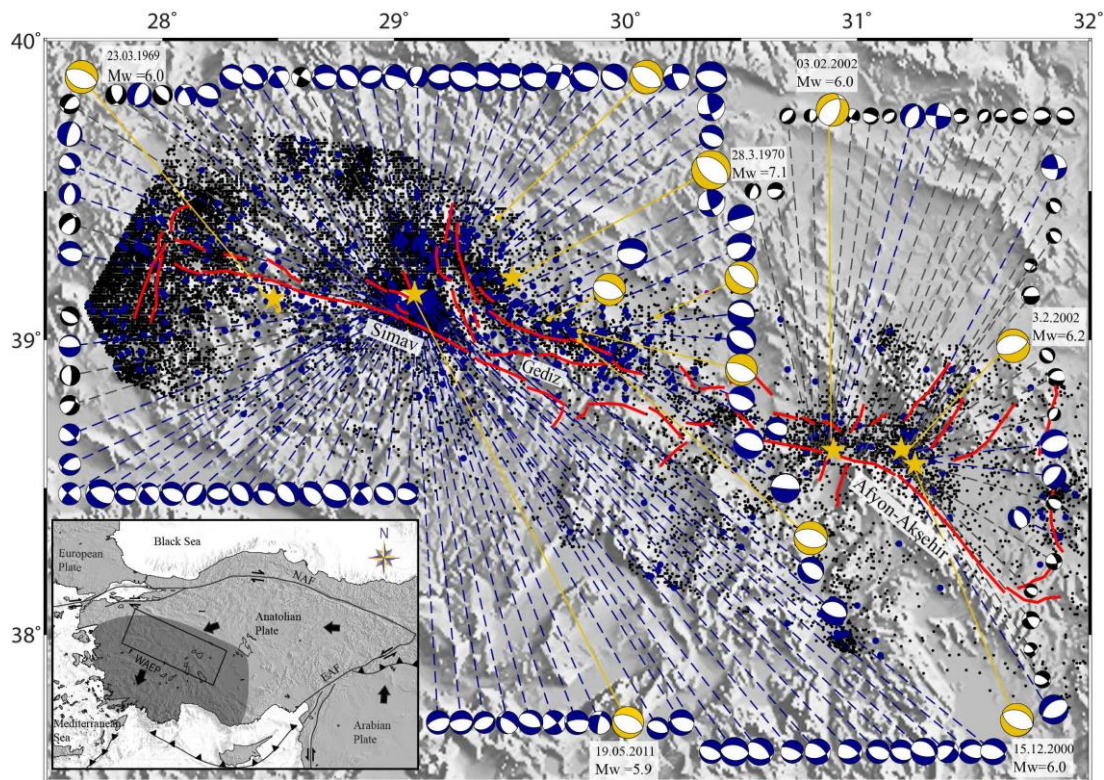


Figure 3.1. Seismicity and focal mechanism solutions (FMS) overlaid over the topography and active fault map of the region compiled from Emre et al., 2016. Black dots show the seismicity from catalogue obtained from Kandilli Observatory and Earthquake Research Institute (KOERI) for the period of 1900-2016. Blue dots are the $M \geq 4.0$ events. The compressive quadrants of FMS are color coded according to size of the events: black for $M < 4.0$, blue for $4.0 \leq M < 5.8$ and yellow for $M \geq 5.8$. Important large magnitude events are shown by yellow stars. The Inset map presents the generalized tectonic map of Turkey and surrounding regions. The approximate limit of western Anatolian extensional province (WAEP) is shown with the dark shaded topography (Koçyigit & Özacar, 2003) and the rectangle bounds the study area. Bold arrows indicate the general plate motion directions. Other abbreviations are EAF: East Anatolian Fault, NAF: North Anatolian Fault

The region has been struck by many moderate to large magnitude earthquakes in the instrumental period. The pattern of the seismicity distribution (Figure 3.1) shows that the earthquakes are clustered along the graben bounding structures and in the graben basins. In Simav graben, majority of the seismicity is located in the central part of the graben. Despite the lack of any record for large historical earthquakes in the Simav area, some important earthquakes were observed during the instrumental period (McKenzie, 1972 & 1978; Jackson and McKenzie, 1988; Taymaz et al., 1991; Kiratzi, 2002; Tan et al., 2008). The most prominent earthquakes in the instrumental period

were the 1969 Demirci ($M_w=6.0$) and 1970 Gediz ($M_w=7.1$) earthquakes denoted by yellow stars in Figure 3.1 (Eyidođan and Jackson 1985, Seyitođlu 1997). The most recent moderate-to-large magnitude event on the Simav fault occurred on 2011 ($M_w=5.9$ Simav earthquake) and followed by the aftershock sequence for several months. A number of moderate-to-large events have occurred along the Afyon-Akşehir graben system during the last century (Şarođlu et al., 1987). The seismicity in Afyon- Akşehir graben is more concentrated in its western part, mostly related to the 2002 Sultandagi ($M_w=6.2$, $M_w=6.0$ KOERI) earthquake sequence. The focal mechanisms based on seismological solutions in this sequence also indicated that all three earthquakes had normal faulting mechanisms (Ergin et al., 2009).

Primary objective of this study is to develop SSC models for the Simav and Afyon-Akşehir graben systems using the active fault maps of Turkey compiled from Emre et al. (2016), available geodetic measurements of the slip rates over the region, the instrumental earthquake catalogue published by Kandilli Observatory and Earthquake Research Institute (KOERI) and the compiled database of focal mechanism solutions (FMS). Details and the limitations of compiled seismotectonic database, fault segments, assigned slip rates, catalogue completeness and declustering issues, etc. are provided in the next section. The seismic sources are modelled using fault-based planar structures. On the other hand, three alternative approaches that are frequently used in the practice are employed to calculate the activity rates for each source; based on the slip rate over the fault plane, based on the moment rates and based on seismicity rates from the earthquake catalogue. Calculated activity rates are distributed among the parallel graben bounding structures using two alternative approaches depending on the length and maturity of the fault segments. Proposed planar SSC models are incorporated into the hazard integral and the PSHA maps for 475-year return period PGA are provided for each alternative.

The effects of the method of calculating the activity rates on the hazard outcome are quantified by comparing the 475-year return period PGA maps for each alternative. Nevertheless, differences in the maps provided in this study clearly shows that the

limitations of the seismotectonic database and the choices of the SSC model developer on calculating and distributing the activity rates over the faults also have a significant impact on the hazard even if fault-based source models are employed. Considering these differences, a protocol for compiling the seismotectonic database and calculating the activity rates for closely spaced normal faults in extensional environments is created and presented at the end of this Chapter. Proposed protocol will help the earthquake engineering community to evaluate the limitations in the previously developed SSC models and to improve the understanding of uncertainty in the current practice.

3.2. Fault Based Seismic Source Characterization Models

A multi-dimensional approach including the active fault maps of the region (Emre et al., 2016), instrumental catalogue, focal mechanism solutions, stress regimes and geodetic data is utilized to characterize the active faults, define their segmentation patterns, determine the down-dip extent of seismogenic faults, fault types and planar fault geometries. This step-by-step procedure is explained from different perspectives in this section.

3.2.1. Instrumental Seismicity

The earthquake catalogue used in this study is gathered from KOERI for the period of 1900-2016 (13553 events) (<http://www.koeri.boun.edu.tr/>, last accessed, 31 July, 2016). Processing of the catalogue and majority of the analysis on the seismicity data were carried out in ZMAP software package (Wiemer, 2001). First step in processing the catalogue involves the elimination of the quarry blast events and aftershocks. The hour histogram (Figure 3.2a) and day vs. night events ratio map (Figure 3.2b) do not show any evidence for the presence of quarry blast events; therefore, the catalogue is not processed for the removal of quarry events. The area has been struck by major events in the past that are followed by aftershock sequences. These aftershocks should be eliminated from the catalogue in order to obtain the independent seismicity rate. For removing the aftershock events; Reasenber (1984) algorithm which uses a time

and space window approach to identify the aftershocks associated with a major event is utilized. The algorithm has identified around 30% of the events in the catalogue as aftershocks which are eliminated from the mainshock catalogue. Later, the magnitude scales in the catalogue are evaluated: in the initial catalogue, 64.16% of the events have duration magnitude (Md), 24.18% have local magnitude (MI) and 11.65% events have body-wave magnitude (Mb). The comparison of MI, Mb and Md scales based on the events that have multiple assigned magnitude scales in Figure 3.2(c) shows that these scales can be used interchangeably without any conversion at this stage.

Thickness of the seismogenic crust defines the depth extent of the ruptures that releases seismic energy. Recently, the seismogenic depth is estimated from D90 or D95 which are defined as the depth above which 90 or 95% of the events are located, respectively (EPRI, 2012; PNNL, 2014). The rationale for using these methods is the physical considerations that suggest that the base of seismogenic zone occurs near the base of observed focal depths (Sibson, 1982 & 1986; Scholz, 1998; Tanaka 2004). Depth histograms for different parts of the study area indicate that the distribution does not change significantly along the Simav and Afyon-Akşehir graben systems. Analysis of the unprocessed catalogue revealed that out of 21631 events, 18874 events falls within 12 km depth range which translates to around 87% of the total events (Figure 3.2d). Therefore, the seismogenic depth for all the faults is selected as 12 km.

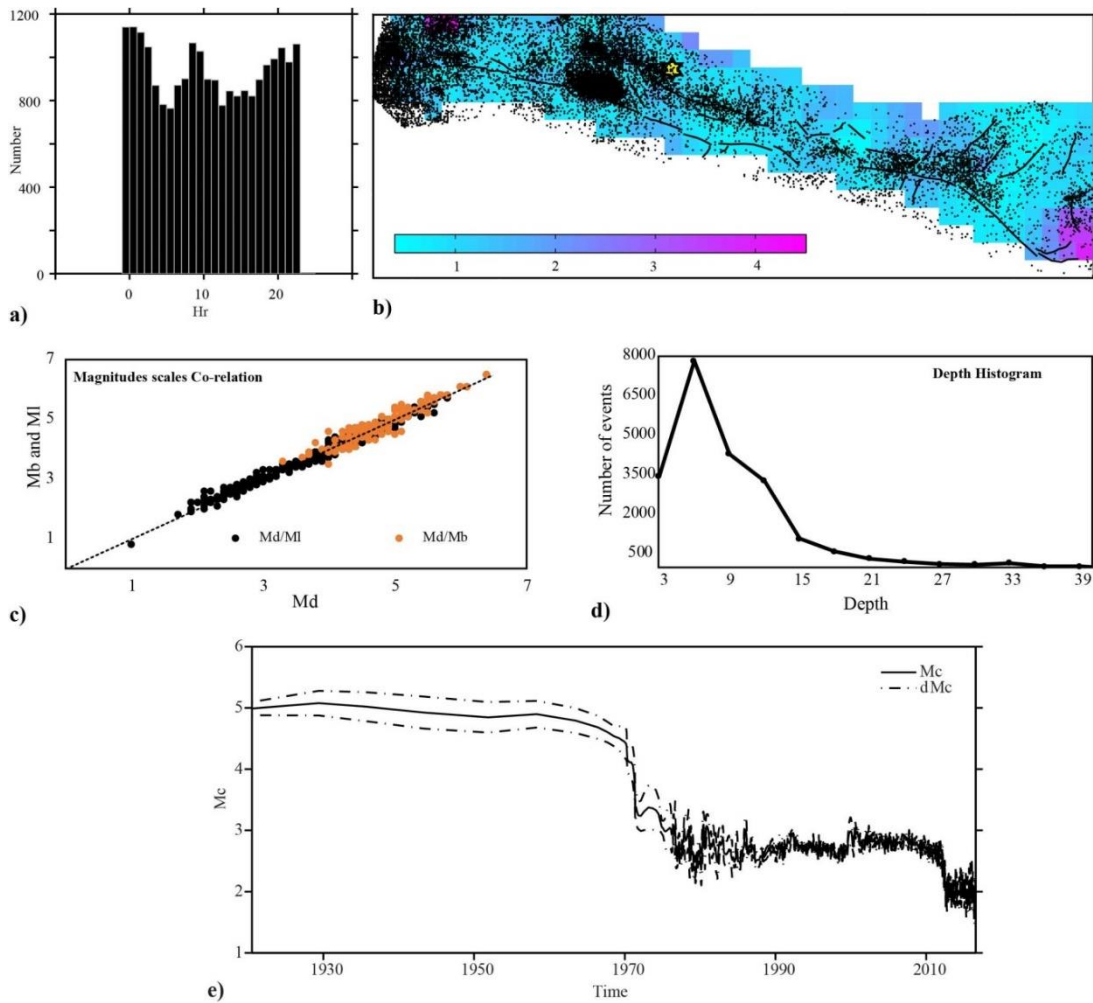


Figure 3.2. (a) Histogram of day vs night time events (b) Map showing the grids colored according to day/night event ratio (c) Graph showing correlation between different magnitude scales (d) Cumulative number of events versus Depth. (e) Magnitude of completeness (M_c) with time plot for the whole region

The catalogue for the whole region was analyzed for completeness. The completeness magnitude (M_c) vs. time plot (Figure 3.2e) shows that the $M \geq 5.0$ catalogue for the whole region is complete until ≈ 1920 s. The completeness time for $M \geq 5.0$ events are extended to 1900 in our analysis due to the fact that there are $M \geq 5.0$ events in early 1900s in the catalogue. The plot shows the completeness until ≈ 1920 s, because the minimum number of events for this plot was set up to 15. Completeness of the

catalogue and M_c is taken into account for defining the minimum magnitude (M_{min}) in hazard calculations.

3.2.2. Focal Mechanism Solutions and the Stress Regime

The FMS catalogue for the region was compiled from various national and international agencies and recently published literature (Mckenzie 1972; McKenzie, 1978; EMMA-Vannucci and Gasperini, 2004; Eyidoğan and Jackson, 1985; Zanchi and Angelier, 1993; Taymaz and Price, 1992; Papazachos et al., 1991; Yılmaztürk and Burton, 1999; Taymaz et al., 1991; Harvard CMT- Dziewonski et al., 1987a & b; RCMT-Pondrelli et al., 2002, 2004, 2007; Ergin et al., 2009; AFAD-www.deprem.gov.tr; Gorgun, 2014; GFZ-<http://geofon.gfz-potsdam.de> and Karasözen et al., 2016). The pattern of the collected FMS is mostly concentrated along the Simav graben in the west and Afyon-Akşehir graben in the east (Figure 3.1). The FMS catalogue is predominantly characterized by normal solutions (some of them having minor oblique-slip components) and includes only a few pure strike-slip (SS) solutions. Analysis of dip angles of the FMS nodal planes shows that the dip angle varies between 50 to 70° (Figure 3.3a). Dip directions of the faults are constrained based on depression directions i.e. faults are dipping towards the depression or graben basins. The steep nodal planes are associated with the SS solutions in the region (Figure 3.3d). Most of these SS solutions are small-magnitude aftershocks related to the major earthquakes (Figure 3.3b). Therefore, average dip angles of 50° and 70° were assigned to normal and strike-slip faults in the region, respectively. The stress tensor inversion from these solutions shows that the area is characterized by almost N-S extension which is in accordance with majority of the structures in the region (Figure 3.3e). The inversion shows that σ_1 is oriented vertically in the region with σ_3 being sub-horizontal trending in NNE-SSE. The orientation of fault structures with respect to the stress orientations suggests normal fault mechanism for majority of the faults in the area except few faults oriented mostly in ~N-S direction.

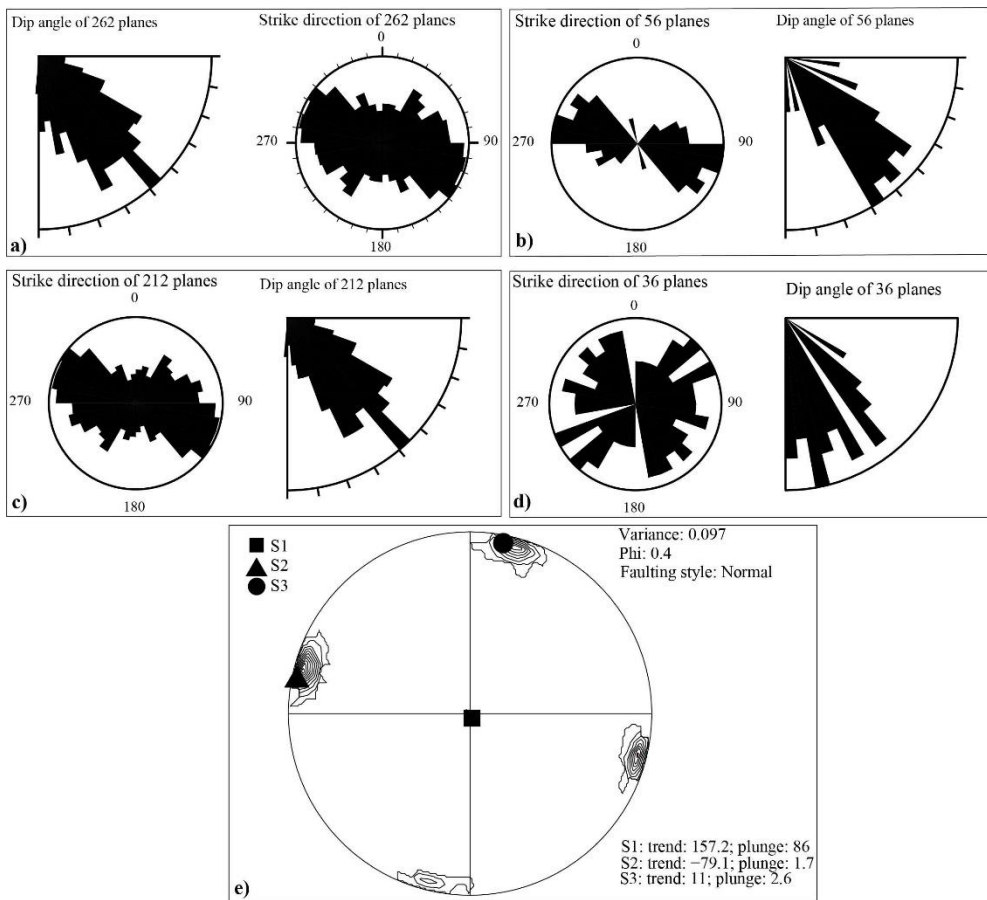


Figure 3.3. Strike Direction and Dip angle rose diagrams of focal mechanism solutions (FMS) (a) for all the events (b) events greater than or equal to Magnitude 5.0 (c) for normal events (d) strikeslip events (e) Results of stress tensor inversion for the whole region

3.2.3. Defining the Polygons and Slip Rate Characterization

Geodetic data may not provide enough resolution for structurally complex areas characterized by closely spaced faults (e.g. graben bounding structures), because the uncertainties of the slip rates along individual faults trade-off with one another. However, the net slip rate in slightly larger zones covering the graben systems may be constrained up to a certain confidence level. Recently, Aktug et al. (2009) found that the strain rate in western Turkey varies between 50-180 nstrain/yr; reaches up to 140 nstrain/yr in the Buyuk Menderes graben, 85 nstrain/yr in the Gediz graben and around 60 nstrain/yr around Simav graben. If taken up on the grabens alone, these strain rates

are equivalent to an opening rate of 6mm/yr for the Buyuk Menderes graben and 4mm/yr for the Gediz graben. Aktuğ et al. (2009) defined a boundary for western Anatolia following the Simav fault zone in the west up to the Afyon-Akşehir fault in the east and assigned an extensional rate varying between 1-2 mm/year and a right lateral component of up to 3 mm/year to this boundary. The resolution and the large error margin of the GPS data do not allow us to directly estimate the slip rate among the individual faults. Moreover, seismicity data is not dense enough and the epicenters are not well-located to associate each event with individual faults. A lot of ambiguity is involved in associating events located in central parts of graben to individual faults since all the graben-bounding faults are dipping towards each other which lead to the overlap of surface projection of fault planes in closely spaced faults.

The slip rate vectors given by Aktug et al. (2009) is used for estimating the average extensional slip rates across the graben systems from the residual slip vectors across the grabens. In order to discretize the slip rates to individual faults; the area is subdivided into seven polygons as shown in Figure 3.4(a). The subdivision is carried-out by considering the changes in orientations of the faults, variations in the pattern of seismicity distribution, moderate-to-large magnitude events in the catalogue, variations in FMS, and slip vector orientations with respect to the fault structures. The average slip rate over each polygon is calculated and distributed over the faults within the polygon using two alternative methods: (i) based on the length of the fault segments or the length ratio and (ii) based on the maturity ratio that considers the maturity of the fault segment. Same methods are applied later for calculating and distributing the seismicity and moment rates among fault systems within each polygon.

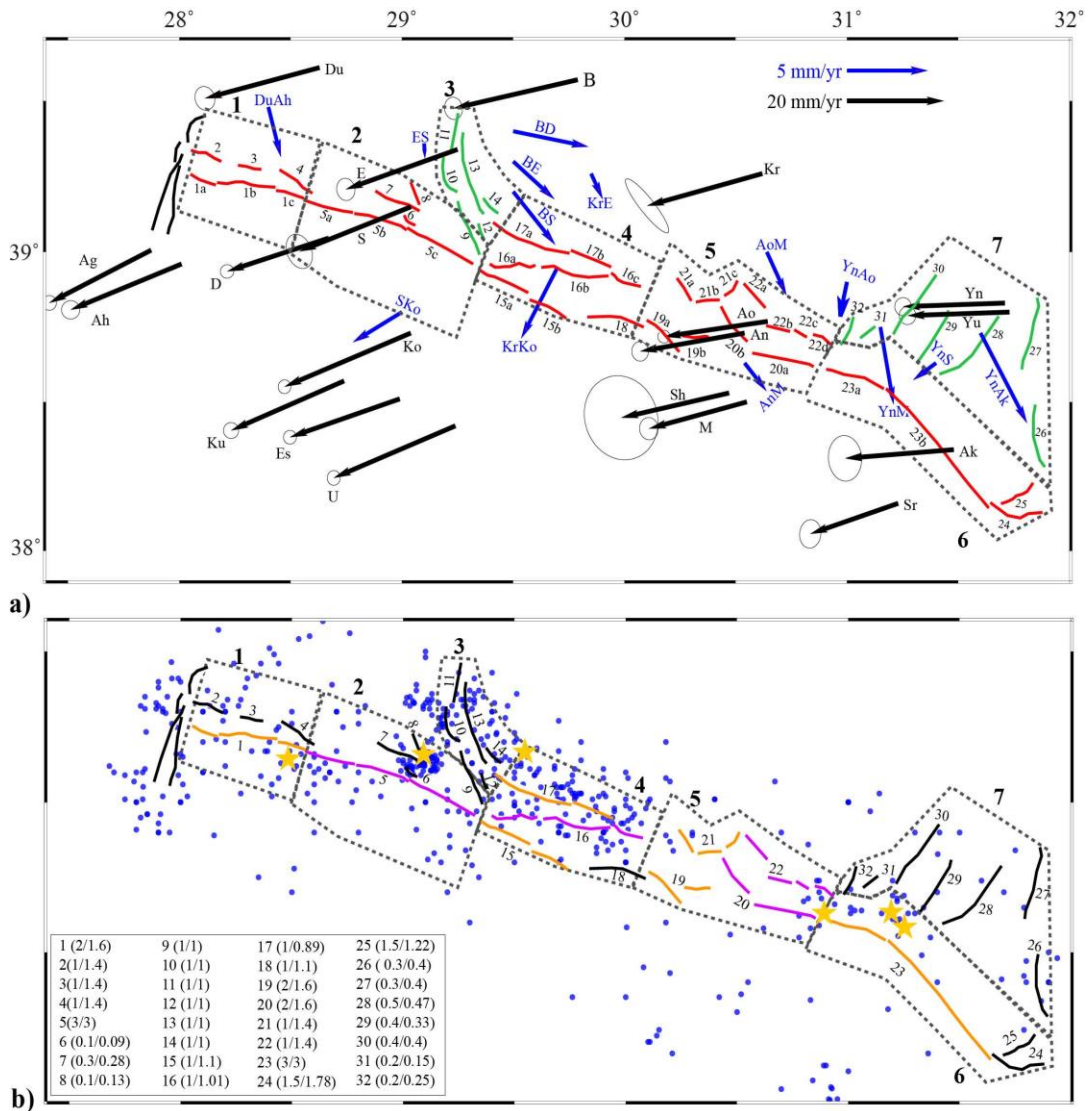


Figure 3.4. (a) Figure showing the slip vectors obtained from Aktug et al. 2009 (Black arrows). The residual vectors obtained from slip vectors situated on both sides of the graben are shown as blue arrows. The geographic limits of the the seven (7) polygons are shown by dashed lines. Active faults are shown as lines marked by numbers that can be used for additional information provided in Appendix B and are colored according to the fault types (i-e Red = Normal faults; Green = Strike-slip faults) (b) Figure showing seismicity (Magnitude ≥ 4.0) overlaid on the fault systems. Orange and Pink lines show fault systems comprising multiple segments that can rupture together or individually; black lines shows the individual segments systems that will rupture independently. Stars shows the recent major events in the area which are mentioned in Section 3.1. The inset shows the amount of slip assigned to each fault system based on maturity and length ratio methods respectively

Polygon 1 covers a graben with oppositely dipping normal faults and consists of six fault segments (Fault system#1: 1a-1b-1c and Faults 2, 3 and 4, Figure 3.4a). The residual slip vector (arrow DuAh in Figure 3.4a) obtained from stations Du and Ah situated on both sides of the graben system gives an average slip rate of 3mm/yr for the entire polygon. There are no other mapped faults in this region; therefore, this slip rate can be distributed among the parallel faults located in the polygon based on maturity and length ratio methods. For instance; 2 mm/yr slip rate is assigned to Fault system#1 (1a-1b-1c) and 1 mm/yr to Faults 2, 3, and 4 based on maturity ratio, while in the length-based method they are assigned with the slip rates of 1.6 mm/yr and 1.4 mm/yr, respectively. Same procedure is applied in each polygon and the slip rates assigned to each fault system using alternative methods are given in the legend of Figure 3.4(b) and listed in Appendix B.

Polygon 2 comprises the active Simav fault (5a-5b-5c) on the south and few small segments on the northern side of the graben. The average slip rate over the polygon is allocated from the resultant slip rates of stations S and Ko (arrow SKo in Figure 3.4a). The residual slip rate obtained from these stations is 3.5 mm/yr, out of which 3 mm/yr is assigned to Simav fault (5a-5b-5c) and the rest is distributed among the small fault segments (6, 7, and 8).

Polygon 3 encompasses 6 faults (Fault# 9, 10, 11, 12, 13, and 14). The resultant slip vector orientations (BD, BE and BS) around this polygon and the FMS are complex and suggests heterogeneous stress conditions. The resultant slip vector ES suggests a slip rate of ≈ 1 mm/yr for the western margin faults (9, 10, 11). For the segments on the eastern margin (12, 13, 14); the resultant slip vector calculated from stations Kr and E (KrE) is approximately 1.7 mm/yr. Considering that there are other faults between these stations and the standard deviation of the slip vector from station Kr is high, the faults on the eastern side is assigned with the same slip rate (1 mm/yr) as the western side.

Polygon 4 comprises long, linear, and connected faults with comparatively simple geometries. The resultant slip vector obtained from station Kr and Ko (KrKo) is 4.7

mm/yr. However, we assigned an average slip rate of 3 mm/yr to this polygon to be consistent with the slip rate associated with the neighboring polygons since assigning a higher slip rate to this polygon is not justifiable.

Polygon 5 is comprised of shorter segments that are spaced apart at small distances and the orientations of the faults are not consistent. The average slip assigned to this polygon is taken as 3mm/yr based on residuals obtained from stations Ao, M and An.

Polygon 6 includes Fault# 23a, 23b, 24 and 25. The Afyon-Akşehir Fault (23a-23b) is assigned with the slip rate of 3mm/yr on the basis of residual velocities from stations Yn and M. The total amount of residual slip among these stations is 4.6 mm/yr, out of which, 3mm/yr is assigned to Polygon #6. Further west, this fault system bifurcates into two branches (24, 25).

Faults in Polygon 7 (26, 27, 28, 29, 30, 31, 32) are almost parallel to each other and are assigned to strike-slip mechanism based on orientations of resultant slip vectors YnM, YnAo and YnS. Residuals from and YnM suggests a slip rate of 1.6 mm/yr for the polygon (please note that the total average slip rate is 4.6mm/yr, shared by 3mm/yr and 1.6 mm/yr among Polygon 6 and Polygon 7).

3.2.4. Defining Fault Systems

The fault segmentation model is developed using the information gathered to form the polygons and considering the evidences of structural and/or geometrical complexities. Study area is generally characterized by two sets of oppositely dipping NW-SE trending normal faults that bound the graben structures (Figure 3.4b). The seismogenic master faults in the area are generally separated from each other by first-order structural or geometrical complexities; e.g. complexities in kilometeric dimension. These complexities consist of considerable amount of (4-5 km) fault gaps among aligned structures, sharp bends or intersections, etc. Starting from the west, there are two sets of active faults located adjacent to the Simav graben (Polygon 1 in Figure 3.4b). The north dipping normal faults on the southern side (Faults 1a-1b-1c) are structurally more mature and are well connected as compared to the south dipping

normal faults on the northern side (Faults 2, 3, and 4). The faults on the northern side are spaced up to 10 km apart and shorter in length. Therefore, all the three segments on the southern side are considered as a fault system such that the segments of the system (1a-1b-1c) can rupture together or separately, while the segments on the north side are considered as individual fault segments (each fault are independent and multiple-segment ruptures are not considered). The residual slip vector (DuAh) is oriented in an approximately orthogonal position to the fault system, favoring normal fault mechanism for the faults in the polygon (Figure 3.4a). Further west, there are N-S trending strike-slip faults of Soma region, which are taken as western limit of the study area and are not included in the analysis. Polygon 2 includes the Simav fault zone, which is the most prominent tectonic structure in the area. Simav fault consists of three segments (5a-5b-5c) that are separated by not more than hundreds of meters of distance. Therefore, Simav fault is defined as a three-segment normal fault system. Although SS component is associated with Simav fault in geologic studies; the FMS solutions in the area indicates the normal fault character for the Simav fault (Figure 3.1). The northern part of the graben does not have any documented or mapped faults except for small and parallel fault segments (Faults 6, 7, and 8) in the central portion of the graben. On the north of Simav graben, faults whose orientations are almost N-S, bound a small graben system. The considerable distance (up to 5 km) among faults on the western side of this graben (Faults 9, 10, and 11) and the curvilinear morphology of the middle segment (Fault 10) suggests that these segments are unlikely to rupture together. Therefore, these faults are modelled as individual fault segments. The analysis of slip vectors in accordance to the orientation of the faults suggests a strike-slip mechanism for this polygon. Same is the case with the faults (faults 12, 13, and 14) on the eastern side of this NS trending graben system. Further east, the faults on the southern (15a-15b) and northern sides (17a-17b) of the graben are well defined. There is an additional fault system in the central portion of the graben (16a-16b-16c), which is regarded as the rupture area for 1970 Gediz earthquake. The general trend of slip vectors is almost orthogonal to majority of the faults favoring an overall normal fault mechanism for the Polygon #4. The faults to the west of Afyon

graben system are marked by complex orientations and small segment lengths. On the south side of Polygon 5; Faults 19a-19b and 20a-20b are considered as two separate systems because of the spacing and the variance in the orientations of the faults. Similarly, two separate systems for Faults 21a-21b-21c and 22a-22b-22c-22d are defined. The eastern limit of our study area is the Afyon-Akşehir graben system located in Polygon 6. The area is marked by the well-developed Afyon-Akşehir Fault System (Faults 23a-23b) and two individual segments (24 and 25) on the south. On the other hand, the north side of the graben does not have any mapped EW bounding faults. Normal fault mechanism is assigned to Afyon-Akşehir fault system as suggested by geological records, FMS and literature. The faults north of the graben system (Faults 26, 27, 28, 29, 30, 31, and 32) are NE-SW oriented and are considered as individual segments in the rupture forecast. The slip vectors are almost parallel to the faults in this region and that favors a strike-slip mechanism.

3.2.5. Calculation and Distribution of Activity Rates

The activity rates in each polygon are modelled using the Truncated Exponential magnitude distribution function (MDF) (Cosentino et al., 1977) as given in Eq. (3.1):

$$N(M_{min}) \times f_m^{TE}(M) = N(M_{min}) \times \frac{\beta \exp(-\beta(M-M_{min}))}{1-\exp(-\beta(M_{max}-M_{min}))} \quad (3.1)$$

where $N(M_{min})$ is the rate of earthquakes bigger than the minimum magnitude, $\beta = \ln(10) \times b - value$, M_{min} is the minimum magnitude, and M_{max} is the maximum magnitude. M_{min} is set to $M_w=5.0$ for all polygons considering the completeness magnitude. The mean characteristic magnitudes (M_{char}) for each single segment or multi-segment rupture sources are calculated using the relationships proposed by Wells and Coppersmith (1994).

$$M_{char} = 1.02 * \log(length * downdip\ width) + 3.93; \text{ for Normal faults (3.2)}$$

$$M_{char} = 1.02 * \log(length * downdip\ width) + 3.98; \text{ for SS faults (3.3)}$$

M_{max} is defined as $M_{char} \pm 1SD$ ($SD = 0.25$ for eq. 3.2 and 0.23 for Eq. 3.3) for each rupture source. Truncated exponential MFD is preferred to the characteristic MFD

(Wesnousky, 1994) because the faults in the area suggest short irregular arrangement of asperities for majority of the faults. This will in turn lead to release of seismic energy in the form of small to moderate magnitude earthquakes, consistent with the general exponential distribution pattern. Three alternative approaches that are frequently used in the practice are employed to calculate $N(M_{min})$ for each polygon: Approach 1 uses the seismicity rates in the earthquake catalogue, Approach 2 depends on the moment rate calculation and Approach 3 is based on seismic moment accumulation by the slip rate over the fault plane. For Approach 1 and 2, calculated activity rates are distributed among the tectonic structures within the polygon assuming that the earthquakes are likely to be produced from every fault segment within that polygon. However, the likelihood for the occurrence of earthquake is proportional to the continuity (maturity or length) of the fault. The longer the fault; the more moment energy it will release and the more earthquakes it will produce. Similarly, in Approach 3: the longer and/or mature the fault is, larger the proportion of slip it will accommodate. Therefore, the activity rates can be distributed among the faults based on their maturity and length ratios.

3.2.5.1. Approach 1: Activity Rates Based on Seismicity

In this approach, the parameters a and b are estimated using the de-clustered instrumental catalogue for the whole region and for each polygon by maximum likelihood and (MLE) and weighted least square (WLS) methods as shown in Figure 3.5. $N(M_{min}=5)$ is calculated from the slope of the lines and equal weights are given to MLE and WLS estimates. The activity rates obtained for each polygon are listed in Appendix B.

3.2.5.2. Approach 2: Activity Rates Based on Moment rate

In this approach, the rate of released seismic moment in specific time interval is calculated for each polygon using Eq. (3.4 & 3.5). For this purpose, the clustered (unprocessed) catalogue is used and the magnitudes in the original catalogue are

converted to moment magnitude using the magnitude conversion equations proposed by Akkar et al. (2010). The moment rate catalogue for each polygon was analyzed to mark the time interval, from where onwards there is almost constant release of moment energy. These time intervals lie around 1970 (≈ 46 years) for all the polygons. The moment rates for each polygon are shown in Appendix B.

$$\text{Moment Rate } (M_o) = \sum M_o(\text{All EQs in Polygon}) / \text{Time} \quad (3.4)$$

$$M_o = 10^{1.5M_w + 16.05} \quad (3.5)$$

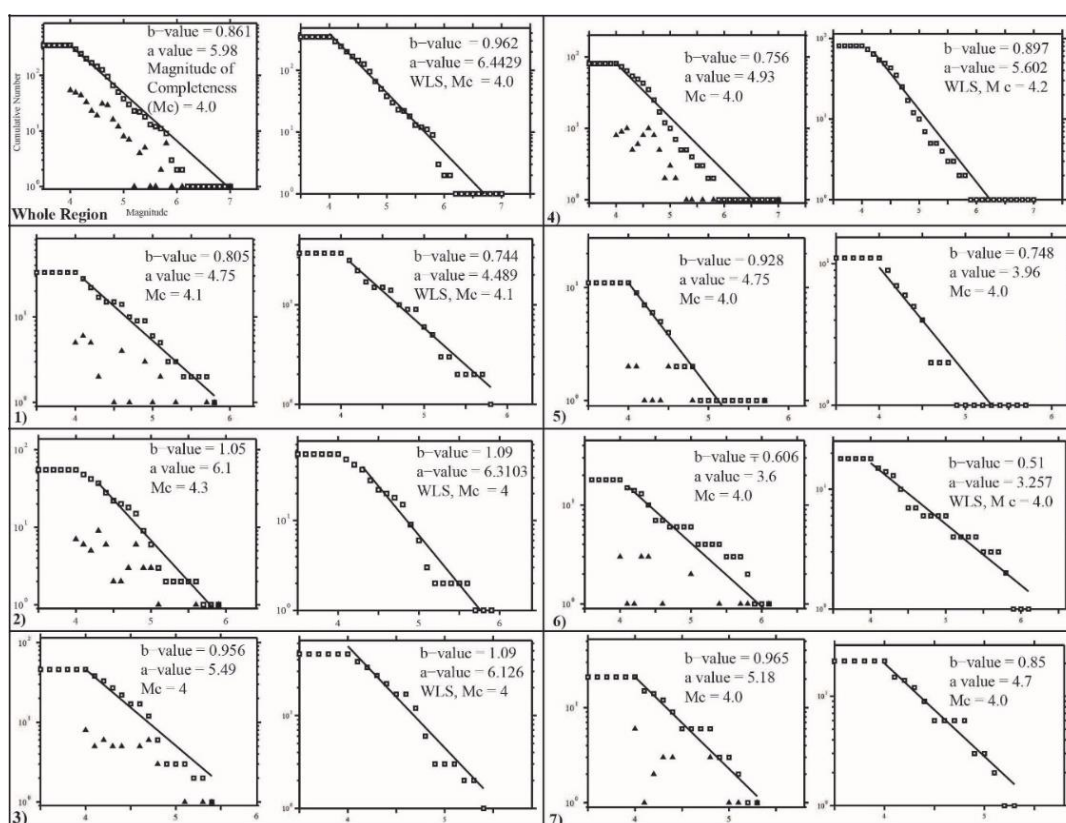


Figure 3.5. Gutenberg Richter relationship for the whole region and for the seven Polygons shown in Figure 4. Maximum likelihood estimate (MLE) and weighted least square (WLS) methods are used for obtaining the best fit to the distribution

3.2.5.3. Approach 3: Activity Rates Based on Slip Rate

In this approach, the activity rates for each rupture source (single or multi segment source) in each polygon is calculated as shown by Eq. (3.6) using the balance between the accumulated and released seismic moments. The accumulated seismic moment is a function of the annual slip rate (s) in cm/year, area of the fault (in cm^2) and the shear modulus of the crust (μ in dyne/cm^2).

$$N(M_{min}) = \frac{\mu AS}{\int_{M_{min}}^{M_{max}} f_m(M_w) 10^{1.5M_w+16.05} dm} \quad (3.6)$$

3.2.6. Ground Motion Models

Ground motion models (GMMs) are used to estimate the ground motion parameters based on the earthquake scenarios from each seismic source; therefore, they are the vital components of PSHA and have a significant effect on the hazard results. Recently, very detailed discussions on selection of GMMs for PSHA studies to be performed in Turkey were provided by Gülerce et al. (2016) and Kale (2017). In both of these recent works, candidate GMMs were selected among global (NGA-West1, Power et al., 2008 – NGA-West2, Bozorgnia et al., 2014) and local (e.g. Akkar and Çağnan, 2010, Kale et al., 2015) alternatives. Gülerce et al. (2016) tested the competency of the NGA-West1 GMMs with the Turkish ground motion dataset (Akkar et al., 2010) in terms of magnitude, distance, and site amplification scaling, and “adjusted” these models (TR-adjusted NGA-West1 models) for Turkey. Whereas, Kale (2017) used an updated version of the Akkar et al. (2010) dataset to rank the prediction performance of candidate models using log-likelihood and Euclidian distance ranking methods.

Because the focus of this study is on the seismic source characterization rather than the GMM selection, the GMM logic tree used by Gülerce et al. (2017) is directly adopted: 50% weight is given to global NGA-West2 models (Abrahamson et al., 2014 (ASK14), Boore et al., 2014 (BSSA14), Campbell and Bozorgnia, 2014 (CB14), and Chiou and Youngs, 2014 (CY14)) and 50% weight is assigned to TR-adjusted versions

of NGA-West1 models (Abrahamson and Silva, 2008 (TR-AS08), Boore and Atkinson, 2008 (TR-BA08), Campbell and Bozorgnia, 2008 (TR-CB08), and Chiou and Youngs, 2008 (TR-CY08)). However, the ranking results presented in Kale (2017) are used to modify the distribution of the logic tree weights among the global and local GMM sets. Kale (2017) found that the prediction performance of TR-BA08, TR-CB08 and CY14 models are superior when compared to the others, therefore, weights assigned to these GMMs are increased as shown in Appendix C.

3.3. Seismic Hazard Analysis

We used the traditional Cornell-McGuire PSHA methodology (Cornell, 1968; McGuire, 2004) for computing the seismic hazard for the region. The numerical integration of the hazard integral is performed by using the computer code HAZ45 (Hale et al., 2018) which treats the epistemic uncertainties in the seismic source models and the GMMs by using the logic tree approach. For estimating the total hazard on a site, Monte Carlo sampling of source characterization uncertainty is used to combine the epistemic uncertainty for each seismic source. In order to prepare the seismic hazard maps, 462 grid points are defined around the graben system and the density of the grid points are increased within the close vicinity of the fault plane for accuracy. Moreover, we have defined the rock site conditions with $V_{S30}=760$ m/s; being the B/C boundary in NEHRP site classification system. Based on the PSHA results, seismic hazard maps for PGA corresponding to the return periods of 475 years (10% chance of exceedance at 50 years) are computed in terms of PGA maps. A total of 6 PGA maps are constructed using three different methods for computing the activity rates (seismicity, moment, slip rate) and two alternative methods (i.e. maturity, length) for activity rate partitioning among individual faults. Results of partitioning methods are presented separately for each activity rate calculation method and the differences are compared by using residual maps between the two partitioning methods to outline the effect of selected partitioning methods on seismic hazard estimates (Figures 3.6, 3.7, 3.8). At the end, a weighted hazard map (Figure 3.9a) is

computed by combining activity rates of all utilized methods and the maximum and minimum PGA values obtained at each grid point for proper assessment of uncertainties (Figure 3.9b, 3.9c).

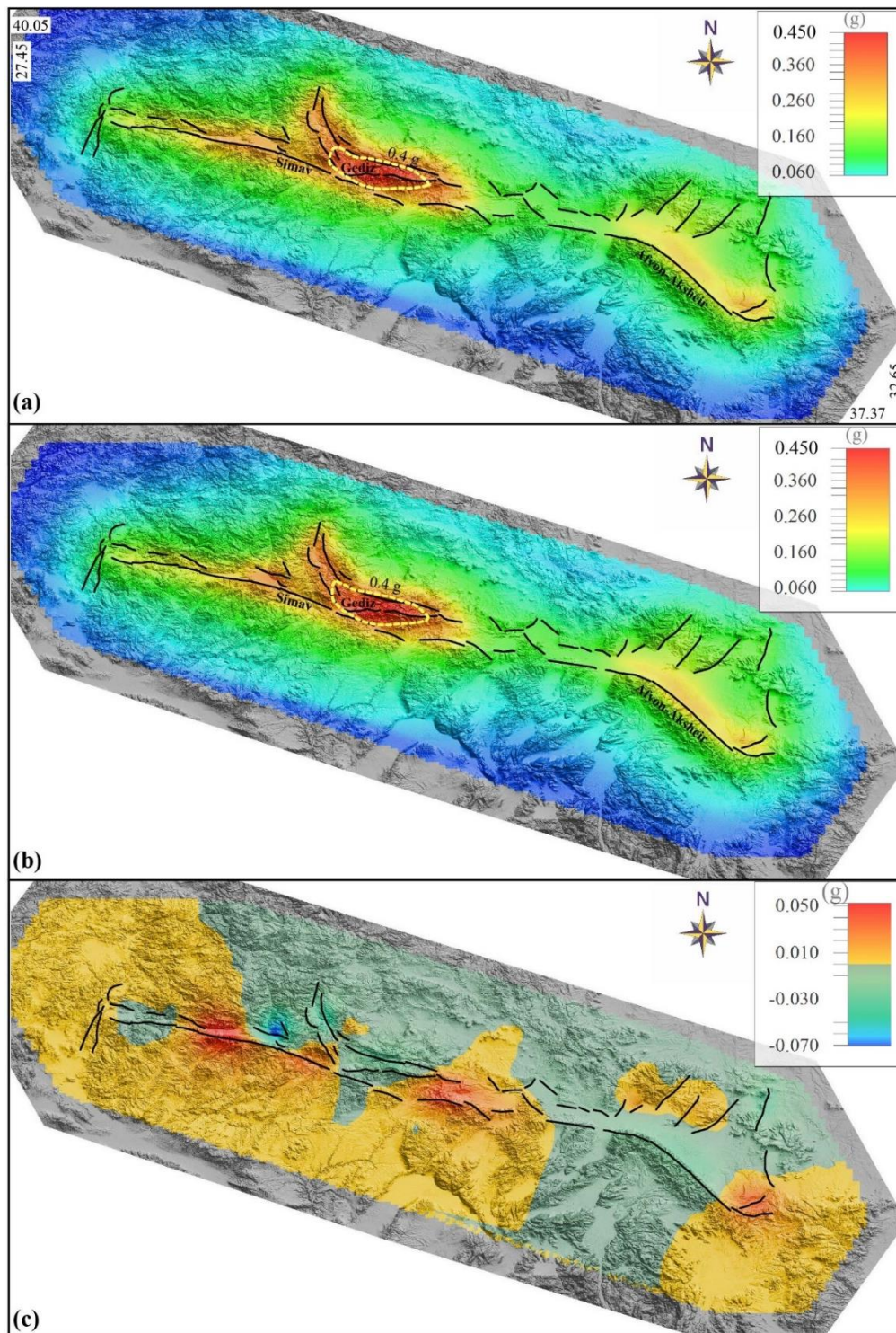


Figure 3.6. PSHA Map obtained using seismicity based activity rates for 475-years return period PGA for $V_{S30}=760$ m/s (a) activity rate distributed using maturity (b) activity rate distributed using length ratio. Dashed yellow lines shows the contours for PGA value of 0.4g (c) Residual obtained by subtracting PGA values in (a) from (b). For polygons and fault numbers, refer to Figure 3.5

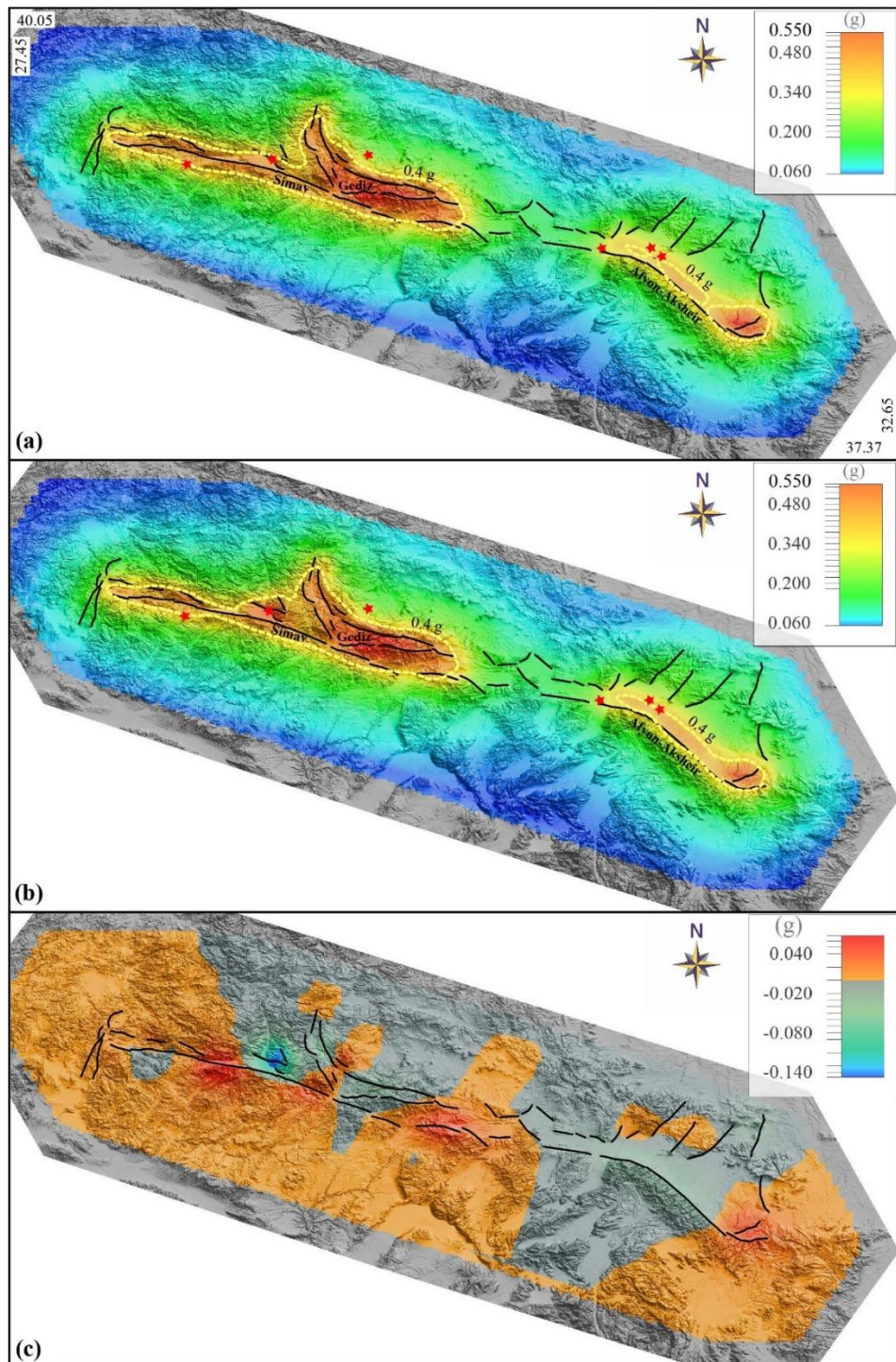


Figure 3.7. PSHA Map obtained using moment rate based activity rates for 475-years return period PGA for $V_{S30}=760$ m/s (a) activity rate distributed using maturity (b) activity rate distributed using length ratio. Dashed yellow shows the contours for PGA value of 0.4g. Red stars shows the location of recent major earthquakes in the region (c) Residual obtained by subtracting PGA values in (a) from (b). For polygons distribution and fault numbers, refer to Figure 3.5

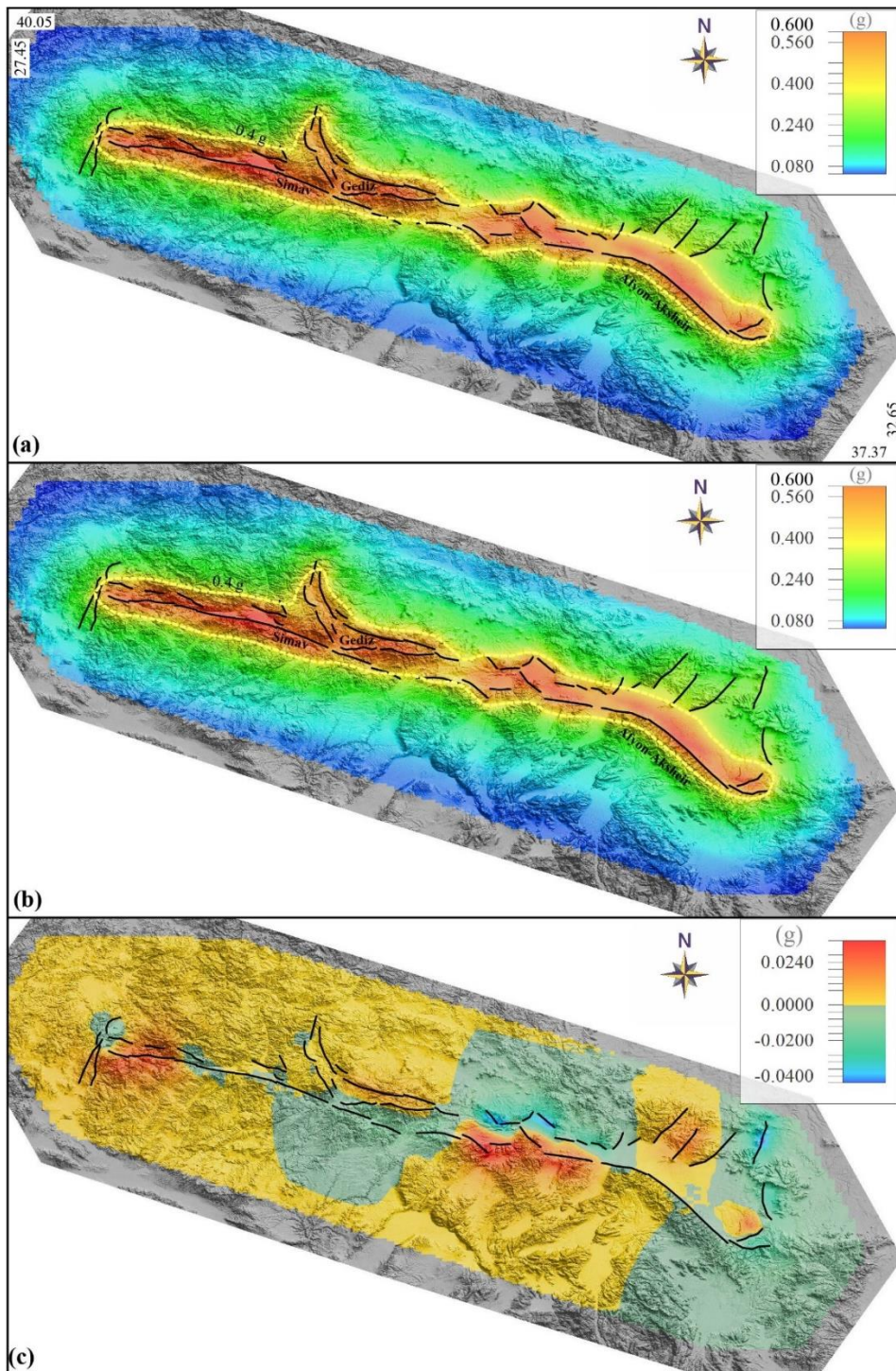


Figure 3.8. PSHA Map obtained using slip based activity rates for 475-years return period PGA for $V_{S30}=760$ m/s (a) activity rate distributed using maturity (b) activity rate distributed using length ratio. Dashed yellow lines shows the contours for PGA value of 0.4g (c) Residual map obtained by subtracting PGA values in (a) from (b)

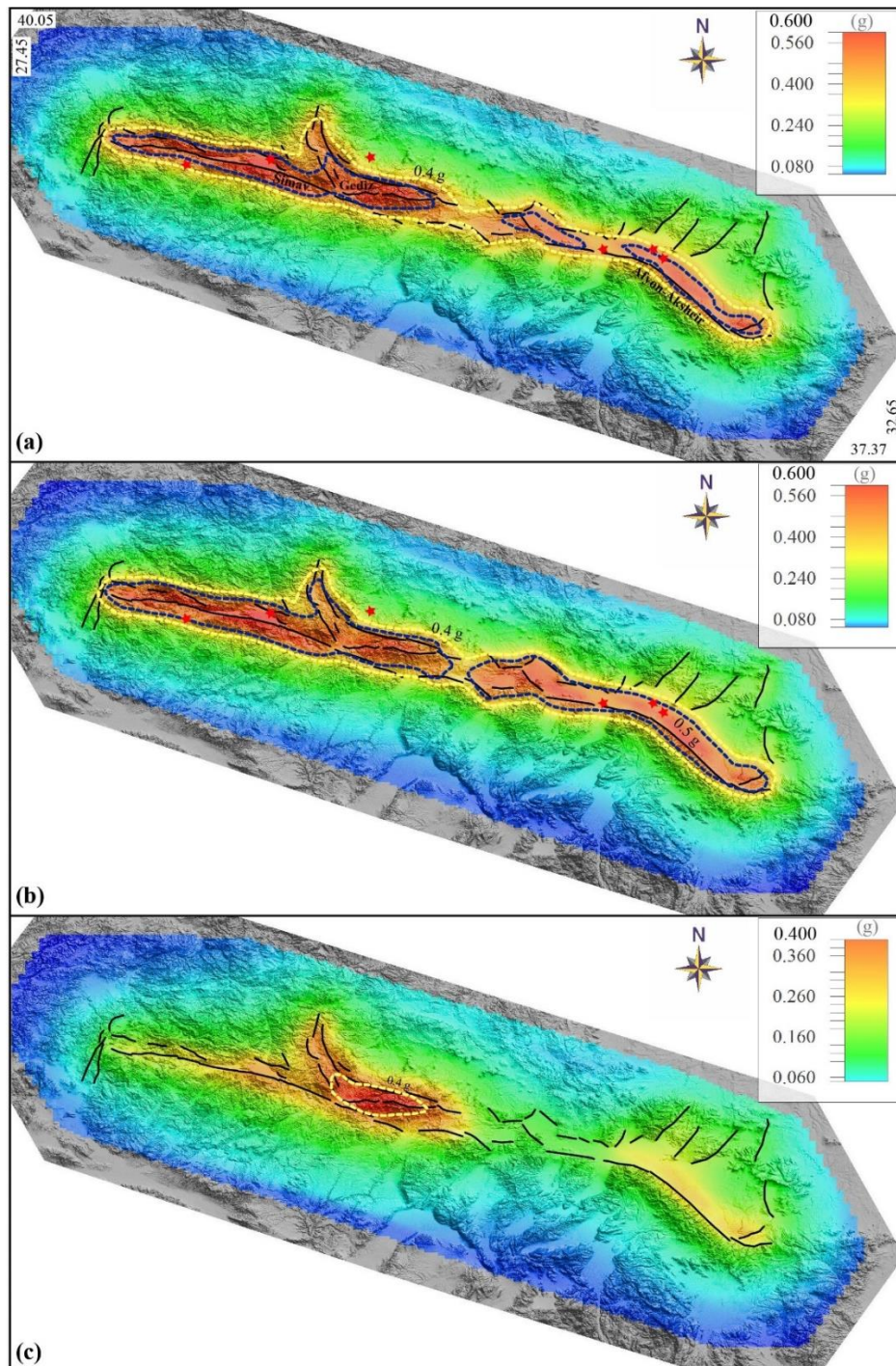


Figure 3.9. (a) PSHA Map obtained using weighted (slip 0.5, seismicity 0.25, moment 0.25) activity rates for 475-years return period PGA for VS30=760 m/s. (b) Maximum PGA value map for 475-years return period and VS30=760 m/s; obtained from all the methods i-e slip, seismicity, moment rate based activity rates (c) Minimum PGA value map from all the methods. Dashed Yellow and Blue lines show the contours for PGA value of 0.4 and 0.5g respectively. Red stars show the location of recent major earthquakes in the region

3.4. Results and Discussions

The 475-year PGA map based on the activity rates calculated by using the seismicity rates (Approach 1) (Figure 3.6a, 3.6b) show that the fault systems in Gediz region (Polygon 4) produce the highest ground motion estimates ($\approx 0.4g$) due to the high density of seismicity within this polygon. The high density of seismicity results in higher activity rates (Figure 3.4b), which in turn translates into higher ground motion estimates for this hazard level. On the contrary, the fault systems on the east of Gediz region (Polygon 5) result in the lowest ground motion estimates due to the lack of earthquakes within the polygon. The residual PGA map is computed (Figure 3.6c) in order to analyze the influence of activity rate partitioning methods (i.e. length based & maturity) on the spatial distribution of hazard estimates. The residual map showed that alternative partitioning methods lead to a maximum difference of $0.05g$, which is insignificant considering the high ground shaking levels observed in the region. The moment rate based maps (Approach 2, Figure 3.7a, 3.7b) are not very different than the seismicity-based maps (Approach 1). Figure 3.7 also show that the fault systems around Gediz (Polygon 4) results in the highest ground motion estimates and the lowest hazard estimates (around $0.2g$) are observed in the region to the east of Polygon 4 (Polygon 5). The low hazard estimates obtained for most of the polygons by Approach 1 and 2 might be to the fact that the earthquake catalogue does not sample the return period of the characteristic earthquake in these areas; which leads to the underestimation of activity rates. In the slip-rate based hazard maps (Approach 3, Figure 3.8a-b), the Simav Fault yields the highest ground motion estimates due to the higher slip rate ($3mm/yr$ horizontal slip rate) associated with the individual segments. Other faults share the $3mm/yr$ annual slip rate among the oppositely dipping faults. Similarly, the Afyon-Akşehir Fault System produces relatively high hazard estimates due to the high slip rate associated with the segments ($3mm/yr$). The lowest ground motion estimates are related to the fault systems in NE corner of the study area (Polygon 7) due to quite low slip rates assigned to these faults. There is an abrupt drop in the PGA values at the central portion of study area (between Polygons 4 and 5) due

to the discontinuity and spacing among mapped faults in the region (Figure 3.8a, Figure 3.8b). Contrary to Approach 1 and 2, Approach 3 might overestimate the activity rates (hence overestimate the hazard); if a portion of the total slip is accommodated in the form of aseismic creep. Comparison of the hazard maps (Figures 3.6, 3.7 & 3.8) obtained from three different approaches indicates that the hazard estimates obtained by Approach 3 are more uniform as compared to the seismicity and moment rate based methods, because the overall slip rate is almost constant (~3mm) across the region, but the density of seismicity is uneven. Figures 3.6, 3.7 & 3.8 also underline that the activity rates based on annual slip rate translate into the highest ground motion estimates, while the ground motion estimates based on Approach 1 and 2 are systematically lower.

In order to evaluate and provide constraints on the spatial extent of the differences among proposed approaches: weighted, maximum and minimum 475-year PGA maps for the region are computed. For the weighted 475-year PGA map, equal weights are assigned to geodetic (slip rate = 0.5) and seismicity-based (seismicity rate = 0.25 and moment rate = 0.25) activity rates. The weighted 475-year PGA map (Figure 3.9a) shows that combining three approaches has considerably reduced the effect of type and density of data on the hazard estimates. In Figure 3.9(a), highest ground motions are associated with the polygons that are characterized by both high slip rates and high rate of seismicity (Figure 3.4b). The maximum PGA values observed in Figure 3.9(a) (around 0.5g) are located around the Simav Fault System, in Gediz Region and around Afyon-Akşehir Fault System. Nevertheless, the maximum width of the $PGA \geq 0.5g$ contour in Figure 3.9(a) is approximately 20 km and the 475-year PGA values are quite low for the rest of the study area. The $PGA \geq 0.5g$ contour closely follows the graben system boundaries as expected, and as the distance from the graben system increases, the ground motion values decrease significantly. The break in the contours in the central portion of the study area demonstrates the effect of fault discontinuity and complex orientation of faults on the ground motion estimates. The width and extent of 0.5g contour is increased considerably in the maximum PGA value map

(Figure 3.9b), which is constructed by selecting the maximum PGA values for each grid point from all the methods to evaluate highest possible ground motions. The minimum PGA value map (Figure 3.9c), which outlines the data sensitivity results in the highest values for Gediz region, indicating the abundance of data in this section with respect to other polygons.

The ground motions computed in this study are comparatively higher than the previously proposed hazard maps for the region (e.g. Erdik et al., 1999; SHARE maps proposed by Woessner et al., 2015). The 475-year PGA map proposed by the most recent effort; the Turkish Seismic Hazard Map (TSHM, Akkar et al., 2018) is presented in Figure 3.10 for comparison. In order to quantitatively compare the hazard estimates of TSHM with Figure 3.9(a), the PGA contour that shows the regions with $PGA \geq 0.4g$ are delineated by dashed yellow lines in both maps. In TSHM, the estimated PGA values are around 0.4g in Simav and Gediz regions, while the 475-year PGA values are below 0.4g in the vicinity of Afyon-Akşehir graben system. On the other hand, PGA values can reach beyond 0.5g as shown by the contours of 0.5g (blue dashed line) in the weighted hazard map computed in this study (Figure 3.9a). The reason for comparatively higher estimates of PGA values is predominantly attributed to the fact that a pure planar (fault-based) source model is utilized in this study, while Akkar et al. (2018) adopted a mix model that combines both areal and planar source models with equal weights. It is also worth noting that the 0.4g contour in TSHM is restricted only to Simav and Gediz regions. The reduction in the PGA values in Afyon-Akşehir region to the east can be explained by the low activity rate (slip rate of planar fault sources) of the region in the TSHM fault model (details in Demircioğlu et al., 2017 and Emre et al., 2016). On the contrary, 0.4g contour in Figure 3.9(a) is continuous across the study area due to a constant extensional slip rate ($\sim 3\text{mm/yr}$) across the graben structure. Additionally, TSHM has comparatively higher hazard estimates for regions that are situated outside the graben system due to the large regional influence of areal sources utilized in their SSC model.

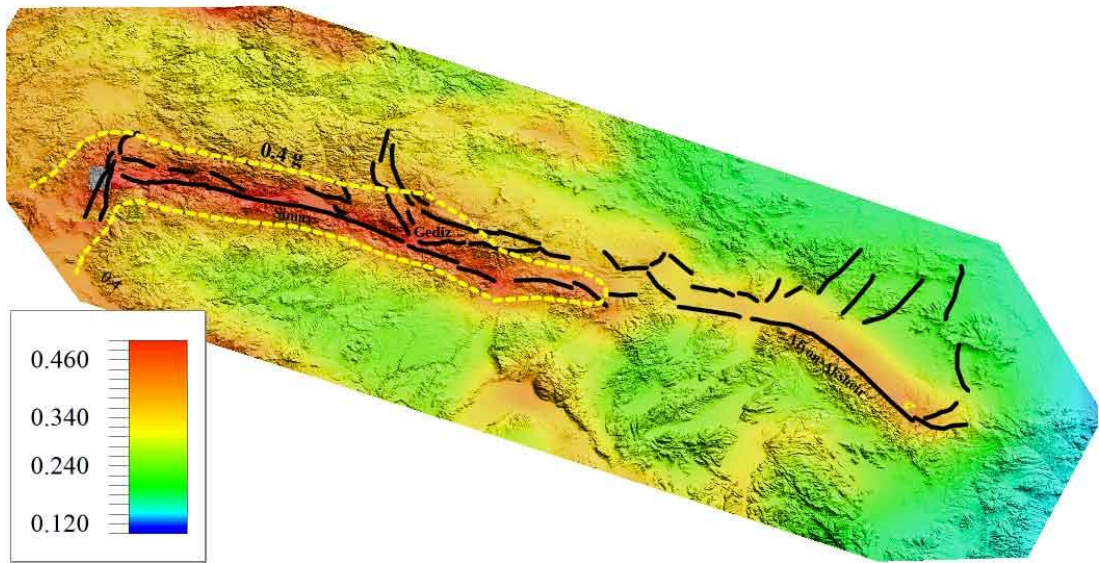


Figure 3.10. PSHA Map of Simav and Afyon-Akşehir region obtained from Turkish Seismic Hazard Map (Akkar et al., 2018) for 475-years return period PGA and $V_{S30}=760$ m/s.

The minimum magnitude threshold for the seismic sources defined in this study is selected as 5.0. In order to analyze the contribution of smaller magnitude events to the total hazard, a background areal source zone for each polygon is added to the planar SSC model. The results showed that selecting a lower minimum magnitude ($M_{\text{Min}}=3.0$) does not have a significant effect on hazard estimates (residuals are in the range of 0.01-0.02g) as shown in Figure 3.11.

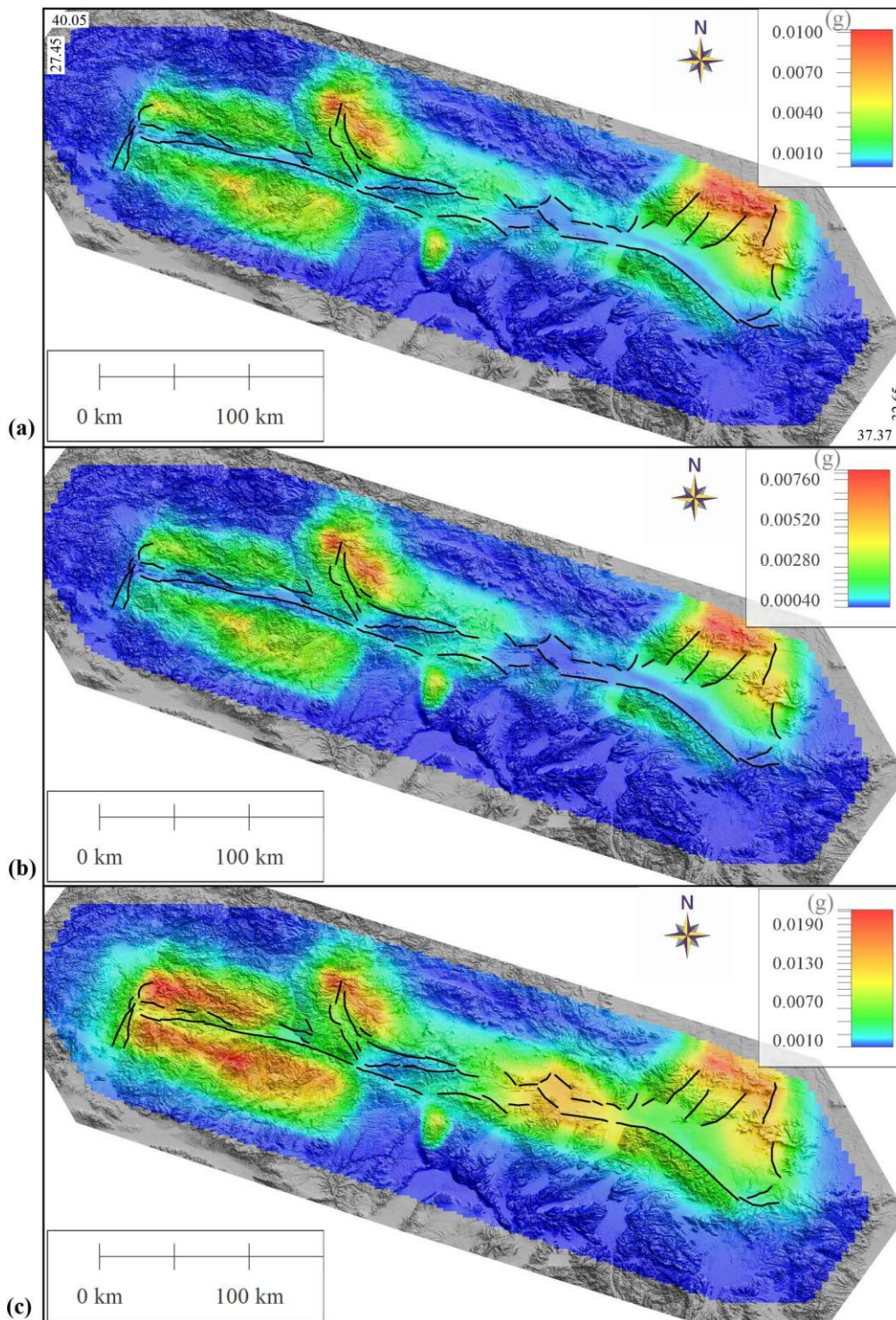


Figure 3.11. Figure showing residual maps obtained by subtracting hazard maps of Figure 3.9 ($M_{min} = 5.0$) from hazard maps computed using a small Minimum magnitude threshold ($M_{min} = 3.0$) (a) Residuals for Weighted map (b) Residual for Maximum PGA value map (c) Residual for Minimum PGA value map

A flow chart of the analysis carried out in this study that summarizes the compilation of the seismotectonic database, data analysis techniques, activity rate calculation and partitioning is presented in Figure 3.12. The protocol summarized in this flow chart can be extended to other parts of the world that are characterized by similar complex tectonic regimes and sparse data conditions. According to the flow chart:

- 1) A seismotectonic database that includes the tectonic structures from the active fault maps, the seismicity data from the instrumental earthquake catalogues, available literature on geodetic data, and focal mechanism solutions is compiled.
- 2) Mapped faults are modelled into planar seismic sources by integrating the surface geomorphologic and geologic data with instrumental seismicity and geodetic data. The fault segmentation model is developed based on several indicators such as fault orientations and discontinuities, structural gaps, etc. On the other hand, the down-dip extent of the fault segments is constrained by using dip amounts revealed by focal mechanism solutions and seismogenic depth interpreted from the seismic catalog.
- 3) The geodetic data does not provide sufficient resolution for the complex and closely spaced planar sources. Instead of trying to constrain the geodetic data over each individual fault segment, the study area is divided into several polygons by taking the fault segmentation model into account. The annual extensional slip rate for each polygon is computed from the available geodetic data by the residual slip vector analysis.
- 4) The total annual slip rate for each polygon is partitioned among the individual fault segments within the polygon using two alternative approaches: based on fault length (length ratio) and fault maturity which reflects on the surface topography.
- 5) During activity rate calculation, three different methodology are utilized. The seismicity rate (Approach 1) and moment rate (Approach 2) are first computed within each polygon using the instrumental earthquake catalogue and later

distributed among fault segments following the approaches used to partition the slip rates. Considering the non-uniform nature of available seismic data, the activity rate is also defined by the associated slip rate (Approach 3) of each fault segment. In essence; this step of the recommended protocol combines the past practice of estimating the activity rates for areal sources with the current practice that collapse the activity rate on planar seismic sources.

- 6) Hazard calculations are performed by implementing each alternative in the PSHA framework individually and by the logic tree approach. The results are analyzed by creating the weighted, maximum and minimum PGA value maps.
- 7) The weighted 475-year PGA map that follows the protocol given above has considerably reduced the effect of type and density of the available seismic and geodetic data on the hazard estimates. In this respect, maximum PGA value map that plots the highest value computed by alternative methods for each grid point, is particularly useful to spatially evaluate the worst ground motion scenarios. On the other hand, minimum PGA value map provides a proxy to assess data and method sensitivity. It is worth to note that in cases where the level of confidence in the geodetic and seismic data differs, weighted seismic hazard map can be computed by a set of weights different than used in this study.

Even if the protocol proposed in this study can be implemented in other regions with similar characteristics, attention should be paid on following critical issues that remain unresolved. The segmentation model proposed in this study provides a systematic way to include the fault to fault ruptures within each polygon, but it does not allow the multi-segment ruptures to “jump” across the polygon boundaries. Therefore, the polygons should be carefully designed by considering the fault gaps, structural complexities, and the rupture zones of previous large magnitude events. More data and observations from paleoseismological records and physics based mechanical models will further improve uncertainty in polygon boundaries and allow the user to create more realistic rupture forecasts. Moreover, motion along each fault segment is

defined as vertical or lateral using the fault types identified from the focal mechanisms, thus no effect of oblique motions across the graben are considered by the proposed protocol. In the current form, the slip rates and activity rates across the individual fault segments are partitioned using both subjective (maturity) and quantitative (length) approaches. Both of these approaches ignore the unidentified faults within these polygons; therefore, spatial distribution of the hazard estimates has a strong dependence on available fault maps.

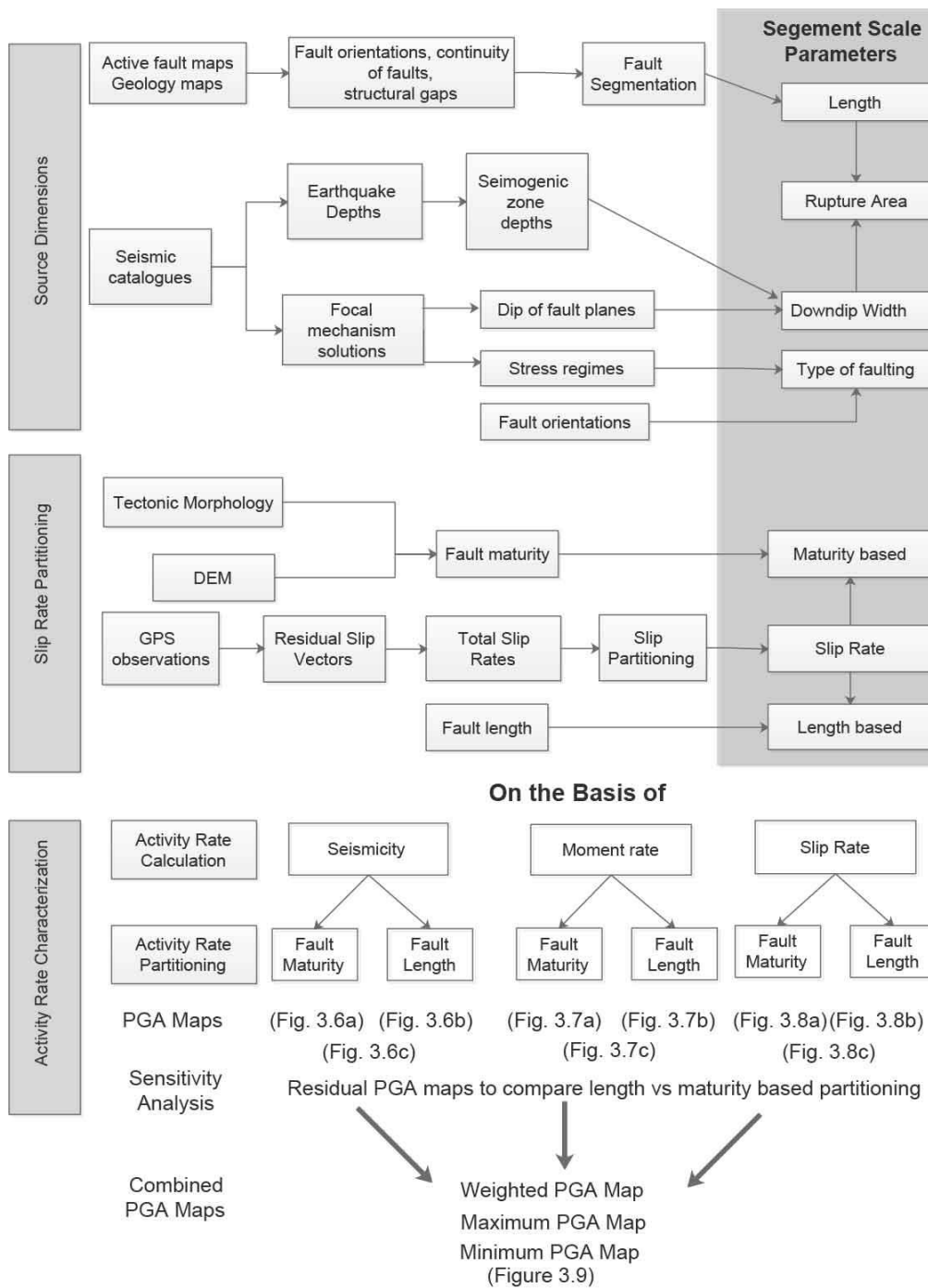


Figure 3.12. Flow chart for PSHA analysis in Western Anatolia. The Chart shows various methodological steps involved in fault characterization for fault based PSHA analysis. The chart also shows the protocol for calculating and distributing activity rates among individual faults and subsequently their use in computing seismic hazard maps for the study region

CHAPTER 4

FOCAL MECHANISM ANALYSIS OF CENTRAL ANATOLIA AND PROBABILISTIC SEISMIC HAZARD ASSESSMENT FOR ADANA BASIN AND GULF OF ISKENDERUN REGION, TURKEY

We analyzed waveform data of 141 events with magnitude (M_l) ≥ 3 , recorded in the period of 2013-2015 by a broad-band seismic station network deployed during the Central Anatolian Tectonics (CAT) project and KOERI network around the Central Anatolian region. First motion arrivals of P- and S- waves and amplitude ratio (SH/P) data is analyzed to constrain the focal mechanism solutions (FMS) using a grid-search algorithm in an iterative scheme. Our analysis showed that the region is characterized by strike-slip events along with considerable amount of normal events. Tension axis is horizontal and Pressure axis is sub-horizontal while maximum horizontal stress directions (SH_{max}) are oriented predominantly in N-S direction which is consistent with the activity of NE-SW and NW-SE trending strike-slip and N-S trending normal faults. Later, computed focal mechanisms are utilized to carry out stress tensor inversions and investigate the active stress patterns in the region. The stress tensor inversion results of 14 sub-regions revealed that the majority of the sub-regions are characterized by horizontal maximum (σ_1) and minimum (σ_3) principal stresses and vertically oriented intermediate principle stress (σ_2), consistent with the strikeslip faulting except for the Adana Basin and Gulf of Iskenderun region which is characterized by trans-tensional regime resulting in a mixture of strikeslip and normal FMS. In order to minimize uncertainties associated to unassociated off-fault seismicity and tectonic complexity, the seismic source model (SSC) of the Adana Basin and Gulf of Iskenderun region is updated by using an additional area source with point source correction based on virtual faults concept that is compatible with our FMS and stress tensor inversion results. The updated peak ground acceleration

(PGA) map has slightly increased hazard estimates (up to 0.08g) at sites situated away from the planar fault structures of Gulerce et al., 2017 and revealed considerably high hazard estimates (up to 0.2g) as compared to the Turkish seismic hazard map along some of planar fault structures.

4.1. Introduction

The study area investigated in this part of thesis covers the Central Anatolian region of Turkey. The region, generally referred to as the Central Anatolian ‘Ova’ Province (Sengor et al. 1985), is a wedge-shaped structure confined between North Anatolian Fault zone (NAFZ) and East Anatolian Fault zone (EAFZ) (Figure 4.1). Central Anatolian Plateau is comprised of an amalgamation of continental fragments that coalesced during the closure of the Neo-Tethy between Africa-Arabia and Eurasia (Sengor & Yilmaz, 1981). The compression related to the Arabia and Eurasia continental collision governs the development of tectonic structures to the east while regional extension related to the rollback of the African slab dominates the deformation to the west of Central Anatolia plateau (Sengor et al. 1985; Bozkurt 2001). These processes in combination lead to the development of Anatolian Plate, which has been extruding westwards since the Miocene (Sengor et al. 1985; Dewey, et al., 1986; Bozkurt, 2001). The region has been studied extensively in terms of its geodynamic evolution based on geological and geodetic data. Despite this, the active crustal deformation and associated seismicity around central Anatolia region is relatively less known as compared to other parts of Turkey. In order to investigate the geodynamic evolution of the Anatolian plateau crustal structures and its relationship with mantle, a wide range of multidisciplinary seismotectonic studies have been carried out under the scope of Central Anatolian Tectonics (CAT) project (2013-2015). The scope of our study includes computation of focal mechanism solutions (FMS) from seismic data that was recorded during the scope of the CAT project. Although the region has been the subject of various focal mechanism solutions studies (Figure 4.1 & Appendix D), the additional FMS will help improve the FMS catalogue that will in turn lead to better understanding the active stress patterns of the region.

Moreover, the FMS and stress tensor inversion results can provide valuable information on the seismic source characterization of active faults which is crucial for seismic hazard assessment and risk studies of the surrounding regions.

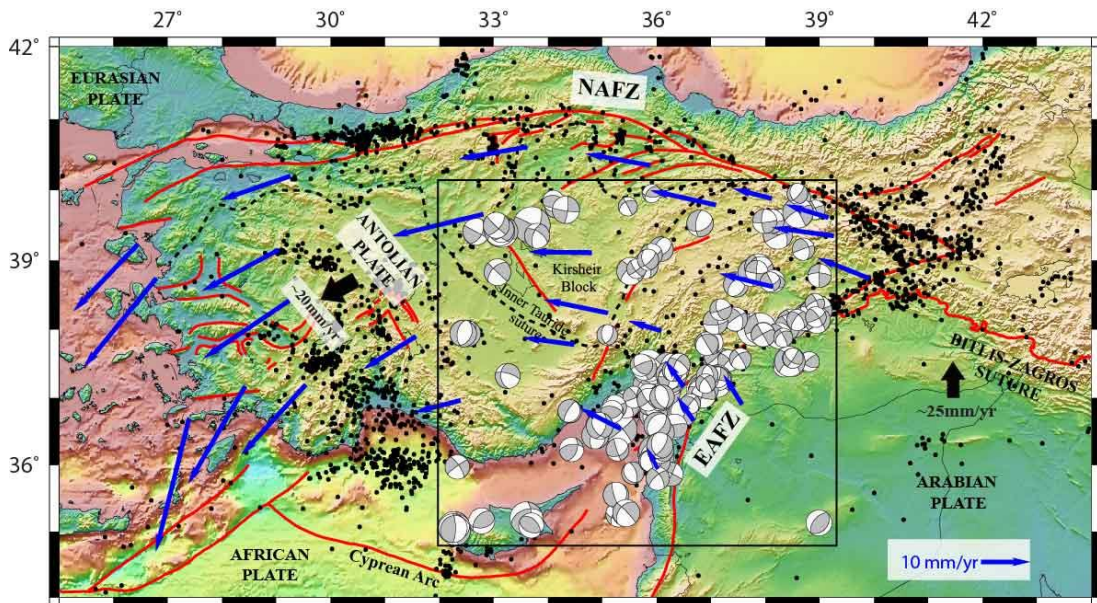


Figure 4.1. Figure showing generalized tectonic map of the study area and surroundings. Black rectangle represents the CAT project region. Bold black arrows show the general directions of plate motions while blue arrows represent the GPS velocity vectors obtained for the region from UNAVCO with respect to a fixed African plate. The focal mechanism solutions compiled for the study area from literature (Appendix D) and the seismicity of the region (black dots, $M \geq 4.0$) obtained from ISC is also shown. Abbreviations are: EAFZ: East Anatolian Fault Zone, NAFZ: North Anatolian Fault Zone

4.2. Tectonic Settings and Active Fault Structures

We have compiled an active fault map for the region from recently published active fault map of Turkey (Emre et al., 2016) by the General Directorate of Mineral Research and Exploration (MTA) (Figure 4.2). Central Anatolia is bounded to the north and east by NAF and EAF zones respectively and Eskisehir fault & Tuzgolu fault zone to the west. Apart from few individual fault segments trending in NW direction, the region is predominantly characterized by NE-SW trending strike-slip faults which are bifurcating from the NAF system (Sengor et al. 1985). There are many small to large scale active faults in the region, some of which have been ruptured by

earthquakes in the historical and instrumental period. Among the major faults; Central Anatolian Fault Zone (CAFZ) is the largest intraplate left lateral transform fault zone which is believed to have originated by the N-NE propagation of paleotectonic block “Ecemiş Corridor” in the Plio-Quaternary times due to convergence of the Arabian and Eurasian plates (Koçyiğit and Beyhan, 1998). According to the MTA map, the fault is comprised of three active segments running sub parallel to EAFZ i-e Ecemiş, Erciyes and Deliler faults (Emre et al., 2016). These faults are predominantly strikeslip in nature but some of them also have measurable normal components along the pull-apart basins. The fault is a seismically active structure and has produced some moderate size earthquakes in the historical (i-e 1717 and 1835 Ecemiş earthquakes) and instrumental period (e.g May 1914 Gemerek (M=5.6); 1938 Kırşehir (M=6.8); 14 August 1996 Mecitözü-Çorum (M=5.6)). Other prominent structures involved in active deformation includes Tuz Gölü Fault Zone (TGFZ), Malatya-Ovacık Fault Zone (MOFZ) and Sarız Fault (SRF). The NW-SE trending TGFZ is predominantly dextral in nature with a significant normal component (Koçyiğit and Beyhan, 1998; Koçyiğit and Erol, 2001; Bozkurt, 2001; Dirik and Göncüoğlu, 1996). MOFZ is a NE-striking left-lateral strike slip fault zone consisting of two fault segments: namely the northern Ovacık Fault segment and the Malatya segment. There have been debates about the activity of the fault but a recent paleoseismic study showed that there have been four earthquakes along the MF during the last 10 ka (Sançar et al., 2019). Sarız Fault is a left lateral strikeslip part located between the CAFZ and EAFZ and accommodating a part of the internal deformation of Central Taurus Mountains (Kaymakçı et al., 2010). Although majority of the active fault zones associated with CAFZ deformation are predominantly sinistral strikeslip in nature, they have a considerable normal component of slip. Regional studies suggest a ~ 4-5 mm/yr sinistral strike-slip and pure extension on the structures in the region (Reilinger et al., 2006; Aktug et al. 2009, 2013).

Apart from the Central Anatolian tectonics, the deformation in our study area is controlled by East Anatolian Fault Zone (EAFZ) to the east. The fault is a sinistral

strikeslip intracontinental fault that translates the Anatolian Plate towards the west (Şengör et al., 1985; Dewey et al., 1986; Hempton, 1987; Westaway, 1994). The NE-SW trending EAFZ zone runs between Karlıova in the north to Antakya in the south comprising seven fault segments, namely: Karlıova, Ilica, Palu, Puturge, Erkenek, Pazarcık and Amanos segments (Emre et al., 2016). The fault zone develops two triple junction points: Karlıova triple junction with the NAFZ in the northeast and Kahramanmaraş triple junction with the Dead Sea fault zone (DSFZ) in the southwest (Arpat et al., 1972; McKenzie, 1972; Hempton et al., 1981; Şengör et al., 1985; Westaway & Arger, 1996; Bozkurt, 2001). While the fault zone exhibits a narrow deformation zone in the north-east, it is separated into northern (Surgu) and southern fault strands (Erkenek-Pazarcık- Amanos) to the west where the deformation zone extends to a wider area. Contrary to the general trend, Sürgü Fault Zone (SFZ) is unusually trending the E-W direction. The primary deformations along the EAFZ is sinistral strikeslip motion, but the jog structures related to local restraining bends can lead to localized compression structures in the eastern part of the fault (Duman et al., 2016). Similarly, normal and reverse faulting deformations has also been observed in the broad deformation zone of the EAF to the west (Duman et al., 2016). Regional geodetic studies suggest a slip rate of ~10 mm/yr slip across the EAFZ (McClusky et al. 2000; Reilinger et al., 2006). The strain energy has been often manifested in the form of large magnitude earthquakes. The prominent earthquakes in the historical and instrumental period along EAFZ includes: the 1866 ($M_s=7.2$), 1874 ($M_s=7.1$), 1893 ($M_s=7.1$) and 1971 earthquakes ($M_s=6.8$) generated by the Karlıova, Palu, Erkenek and Ilica segments, respectively. Furthermore, the 1905 earthquake ($M_s=6.8$) (Ambraseys & Jackson, 1998) and the 2010 ($M_w=6.1, 6.0$) earthquake (Tan et al. 2011) occurred on the Yarpuzlu and Gokdere restraining bends, respectively.

The southeastern corner of our study area coincides with the northern part of Dead Sea Fault Zone (DSFZ). DSFZ is a major N-S trending, left-lateral strikeslip fault that accommodates the motion between Arabian and African plates (Courtilot et al. 1987; Hempton, 1987; LePichon & Gaulier, 1988; Salamon et al. 1996). The fault

zone consists of a series of en-echelon faults with extensional jogs and releasing bends such as Dead sea pull apart basin (Klinger et al ., 2000). DSFZ is regarded as the most significant tectonic structure of the Middle East region that has generated large magnitude recurrent earthquake in the historical times (Ambraseys and Barazangi, 1989; Ambraseys et al. 1994; Klinger et al., 2000). The details about the historical earthquake activity along the northern part of DSFZ in southern Turkey can be found in Akyuz et al., 2006 and the references therein.

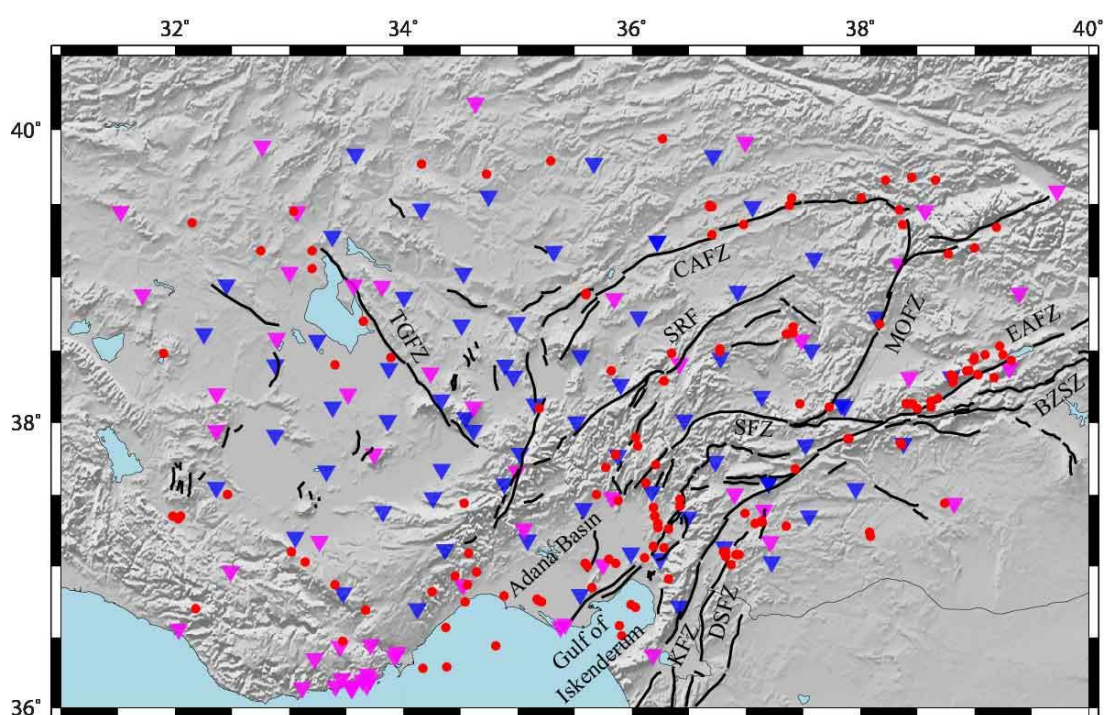


Figure 4.2. Map showing the active fault map of the area compiled from MTA active fault map (Emre et., 2016). Inverted triangles show broad band stations locations in the region. CAT stations are shown in blue while KOERI stations are shown in magenta color. Red dots represent the events whose first motion data is analyzed in this study. Abbreviations for some of the major structures in the area are BZSZ: Bitlis Zagros Suture Zone, CAFZ: Central Anatolian Fault Zone, DSFZ: Dead Sea Fault Zone, EAFZ: East Anatolian Fault Zone, EF: Ecemiş Fault, KFZ: Karasu Fault Zone, MOFZ: Malatya-Ovacık Fault Zone, SFZ: Sürgü Fault Zone, SRF: Sarız Fault, TGFZ: Tuz Gölü Fault Zone

4.3. Focal Mechanism Analysis

Focal mechanism solution (FMS) defines the geometry and mechanism of the faulting during an earthquake. FMS can be constructed from waveforms produced by an earthquake, recorded by several seismograms at a range of distances and azimuths. FMS construction relies on the fact that the pattern of radiated seismic waves is dependent on the fault geometry (Stein and Wysession, 2003). In this study we used the classical approach of determining FMS from polarities of P- wave's first motions. P-waves are the first waves that are recorded from an earthquake source due their fast velocity. P-wave's polarities represent the direction of the motion recorded at the seismometer. The direction of these first motions can be used to define four quadrants (two compressional, two dilatational) surrounding the source: "Upward" motion defines compressional quadrants, where earth moves "toward" the station while "Downward" motions define dilatational quadrants, where the movement of earth is "away from" the station. The quadrants are divided by two nodal planes; a fault plane and an auxiliary plane perpendicular to fault plane. The two nodal planes define the fault geometry, but the fault plane cannot be determined with first motion data only. In order to determine, which nodal plane is the fault plane, additional geologic or geodetic information is required (Stein and Wysession, 2003). FMS are determined by plotting the first motion polarities of P-waves on lower hemisphere projection stereonet. The polarities are then partitioned into four quadrants by great arcs orientated 90° from each other (Stein and Wysession, 2003) resulting in a "beachball" diagram. The great arc circles represent the nodal planes while dark and light-colored quadrants correspond to the compressional and dilatational first motions respectively (Stein and Wysession, 2003).

According to the radiation patterns, P-wave amplitude diminishes near the nodal planes while S-wave amplitude are maximum near the nodal planes. Therefore, the ratio (SH/P) of their amplitudes can be used to determine if the point is located near to the plane or away from the plane (Stein and Wysession, 2003). Large SH/P ratios can be related to a point near the nodal plane and vice versa. Therefore, in addition to

P-waves polarities, S-wave polarization and SH/P amplitude ratios can also be used to obtain more unique solutions. It should be noted that S-wave polarities are generally hard to pick due to noise and attenuates quickly as the wave propagates (Walsh et al., 2008 and references therein). Once FMS determination is complete, P- and T-axes for a solution can be determined by bisecting the dilatational and compressional quadrants with a great circle connecting the poles for the nodal planes and finding halfway between them. T-axis lies at the center of compressional quadrant, whereas P-axis lies at the center of dilatational quadrant (Stein and Wysession, 2003).

4.3.1. Seismic Data and Methodology

Waveform data of 141 earthquake events with magnitudes greater than 3 ($M_l \geq 3.0$) for the period of 2013-2015 is analyzed in this study (Table 4.1). The data for this study is mainly acquired from the passive broadband seismic network, comprising of 72 stations; that was temporarily deployed under the scope of Continental Dynamics/Central Anatolian Tectonics: Surface to mantle dynamics during collision to escape (CAT) project (Figure 4.2). In addition, the waveform data from KOERI stations located in the vicinity was also acquired, in order to improve the azimuthal coverage of events that are located on the margins of study area. The station locations and events analyzed in this study are shown in Figure 4.2 and are documented in Appendix E & Table 4.1 respectively. The synchronized 3-component broadband waveforms with the motion directions of up-down (BHZ), north-south (BHE) and east-west (BHN) direction are utilized for picking first arrivals of P- and S- waves. P- and S- arrivals are hand-picked using the Seismic Analysis Code (SAC) program (Goldstein et al., 2003). The shear wave velocity model of Delph et al., 2017 is used as a base model to constrain the P- and S- wave, 1-D velocities for the region. TauP raytracing program (Crotwell et al., 1999) along with the 1-D velocity model (Delph et al., 2017) is used to calculate the angle of incidence of rays at each recorded station. After defining the 1-D crustal velocity model and locations, FMS determination is carried out using FOCMEC program (Snoke, 2003). The FOCMEC program uses an inversion scheme that searches for all the acceptable FMS using first motion polarity

and amplitude ratio (SH/P) data. The possible solutions are determined by a grid search approach, with minimum polarity and/or amplitude errors (Anderson et al., 2007). Users can interactively define the necessary criteria i.e the grid search parameters and maximum allowed polarity and amplitude ratio errors for FMS determination. For amplitude ratio, corresponding amplitude ratio error is calculated according to the maximum allowed log₁₀ ratio (Anderson et al., 2007). The program allows the difference between the theoretical amplitude ratio and related observed ratio up to the limit (selected as 0.6 in this study); and values greater than the limit are assigned as amplitude error. For calculating the amplitude ratio (SH/P), a moving time window of 0.5 second is used while the grid search increment is selected as 5°. The minimum number of data points selected for computing a FMS is selected as four. FOCMEC is constructed in a way that it allows increasing number of data errors until it finds a solution. In cases where the number of solutions produced by FOCMEC for an event are more than one; Fisher statistics, which give the mean direction from observed directional data (Tauxe et al., 1991) is adopted to calculate the mean value of P- T-axis axes. The quality or precision of the results depends on the value of precision parameter, κ . High values of κ (> 20) represent less scattered data and vice versa (Anderson et al., 2007). An automated code to run the FOCMEC program is utilized in this study. Once the run is completed and the program finds solution within the selected criteria, all the possible solutions along with their information are plotted in one-page summary plot. The output files for each event analyzed in this study are presented in Appendix F.

Table 4.1. List of events analyzed in this study and their strike, dip, rake values. Events with * in their ID are discarded due to less amount of data or bad quality of solutions and not used for further analysis

ID	D/M/Yr	Hr:Min	Long	Lat	Depth	ML	Strike	Dip	Rake
1*	11.10.2013	16:39	38.81	38.28	5	3.0	190	40	-6
2*	22.11.2013	11:05	38.22	39.66	5	3.5	19	81	-70
3	10.12.2013	09:30	36.05	37.84	1	3.0	66	48	63
4	21.12.2013	10:17	36.42	37.42	4	3.3	184	47	-69
5	28.12.2013	17:05	36.35	38.48	3	3.0	222	87	-10
6	30.12.2013	00:02	38.36	37.85	3	3.7	81	73	-25
7	1.06.2013	19:41	39.03	38.33	1	3.0	64	78	-22
8*	4.06.2013	04:12	37.41	38.66	1	4.1	235	61	-42
9	4.06.2013	04:12	37.41	38.62	5	4.1	235	61	-73
10	4.06.2013	23:55	37.36	38.61	1	3.3	82	88	20
11	7.06.2013	00:33	32.03	37.33	4	3.3	305	45	-83
12	7.06.2013	19:57	32.05	37.35	5	3.2	334	31	-71
13	7.06.2013	19:56	31.98	37.35	5	3.2	334	30	-80
14*	25.06.2013	06:06	33.47	36.47	15	3.0	180	0	-100
15	28.06.2013	19:30	32.75	39.18	1	3.0	338	54	-59
16	4.07.2013	19:01	32.15	39.37	5	3.5	25	36	14
17*	13.07.2013	12:57	39.22	38.53	5	3.1	12	65	-84
18	24.07.2013	03:41	35.86	37.78	6	3.0	225	25	-90
19	27.07.2013	20:13	35.61	37	19	3.6	62	84	35
20	4.08.2013	19:59	36.12	37.58	1	3.5	197	44	-60
21	10.08.2013	11:56	33.4	38.4	3	3.0	50	90	30
22*	23.08.2013	10:35	37.4	39.54	5	3.1	325	65	-90
23	28.08.2013	06:26	38.95	38.36	4	4.1	65	85	-2
24	29.08.2013	23:20	38.93	38.36	2	3.1	67	83	29
25	30.08.2013	07:54	36.98	39.36	3	3.1	221	62	-22
26*	17.09.2013	10:37	35.65	36.85	29	3.4	120	15	90
27	18.09.2013	21:10	36.2	37.35	4	3.9	225	50	-57
28	20.09.2013	02:02	36.99	37.37	5	3.0	223	55	3
29	7.01.2014	21:17	38.35	37.86	2	3.1	53	85	9
30	21.02.2014	00:54	37.43	37.68	3	3.2	62	86	-15
31	22.02.2014	15:42	36.42	37.42	5	4.5	211	55	-30
32	2.03.2014	04:25	35.21	36.75	3	4.3	204	36	-73
33	13.03.2014	14:28	38.09	37.21	5	3.2	230	88	10
34	15.03.2014	09:39	36.28	37.13	5	3.3	58	70	52
35	6.04.2014	22:06	34.56	36.87	2	3.2	183	48	-63
36	8.04.2014	03:54	35.86	37.02	12	3.0	229	86	55
37	13.04.2014	08:00	33.67	36.69	2	3.4	37	80	23
38	9.05.2014	13:14	35.59	37.02	12	3.1	76	53	16
39	9.06.2014	03:38	36.03	36.71	4	4.9	184	73	-42
40	26.06.2014	07:29	37.08	37.3	1	3.0	227	55	84
41	2.07.2014	14:22	35.8	37.05	9	3.0	252	35	0
42	2.08.2014	07:38	32.46	37.5	1	3.0	253	31	-71
43	28.08.2014	10:22	36.91	37.08	2	4.0	241	51	-8
44	29.08.2014	00:19	34.37	36.57	2	3.2	213	75	-48
45	26.09.2014	21:24	37.47	38.13	3	3.4	265	84	8

46	5.01.2015	06:46	38.82	38.32	4	3.9	82	48	-63
47	9.01.2015	21:54	36.19	37.41	5	3.5	200	65	-79
48*	8.03.2015	22:06	34.81	36.44	15	3.5	75	85	-85
49	31.03.2015	04:16	36.87	37.01	6	3.4	221	27	-67
50	10.10.2013	09:48	33.4	36.87	3	3.1	279	38	-36
51	21.10.2013	04:09	34.16	39.77	0	3.4	37	48	-48
52	23.10.2013	12:24	34.38	36.29	0	4.7	200	42	-51
53	1.11.2013	01:27	35.19	38.1	0	3.6	215	74	20
54	3.11.2013	22:42	36.19	37.14	0	3.0	234	48	-48
55	7.11.2013	06:39	36.2	37.35	0	4.1	214	56	-53
56	8.11.2013	05:55	36.77	38.51	0	3.6	80	88	-5
57	18.11.2013	06:18	36.03	37.9	0	3.4	215	48	-63
58*	9.12.2013	04:34	33.04	39.45	3	3.1	24	58	-26
59*	9.12.2013	05:12	34.25	36.82	0	3.1	205	50	-90
60*	10.12.2013	08:00	38.34	39.46	0	3.5	264	90	25
61*	25.12.2013	07:23	38.66	39.66	0	3.5	91	59	-16
62	27.12.2013	05:44	37.14	37.31	0	3.4	196	59	-60
63	5.10.2013	21:31	33.14	37.03	1	3.3	219	77	-38
64*	7.01.2014	02:46	39.19	39.34	0	3.1	221	70	4
65	10.01.2014	13:20	36.23	37.27	0	4.2	216	54	-59
66	20.10.2014	15:45	38.68	38.17	0	3.9	248	80	-28
67	2.11.2014	04:58	39.25	38.47	0	3.7	265	60	55
68	3.11.2014	21:39	36.28	38.29	0	3.2	41	46	76
69	7.11.2014	17:20	34.64	36.96	3	3.5	253	61	-9
70	7.02.2014	04:48	36.23	37.3	0	3.8	194	48	-63
71	8.02.2014	17:48	37.35	38.61	0	3.3	244	76	21
72	14.02.2014	00:33	35.99	36.73	6	4.7	226	56	-53
73	20.11.2014	20:12	34.73	39.7	0	3.0	34	69	-13
74	23.11.2014	08:54	36.28	38.29	0	3.4	41	44	60
75	23.11.2014	12:07	39.17	38.31	0	3.0	103	48	-39
76	2.03.2014	04:29	35.18	36.76	0	3.5	249	45	5
77	2.03.2014	05:33	35.17	36.77	0	3.0	240	81	-5
78	7.12.2014	08:49	34.54	36.75	0	3.6	185	89	15
79	6.03.2014	13:40	35.86	37.78	0	3.0	265	36	73
80	11.03.2014	10:23	31.9	38.48	0	3.7	258	76	-43
81	11.03.2014	13:56	38.08	37.24	0	3.1	30	66	33
82	17.12.2014	14:24	37.35	37.28	5	3.0	87	76	-27
83	18.03.2014	17:01	37.14	37.32	3	3.2	220	88	5
84	25.12.2014	06:52	35.77	37.69	2	3.2	233	77	-16
85*	25.12.2014	12:12	33.2	39.18	2	3.1	15	36	-54
86	26.03.2014	14:00	38.62	38.11	0	4.3	100	70	-15
87*	28.03.2014	19:25	32.18	36.7	22	3.0	92	70	-85
88*	2.04.2014	00:21	38.41	38.13	2	3.2	NA	NA	NA
89	9.04.2014	00:37	38.4	38.13	0	3.0	228	38	20
90	9.04.2014	12:27	36.77	38.49	1	3.0	80	86	15
91	26.03.2015	02:14	35.6	38.88	0	3.7	75	85	-1
92	27.03.2015	12:19	38.37	39.36	0	3.0	233	81	34
93	28.03.2015	05:04	35.6	38.89	0	3.9	56	71	-24
94	28.03.2015	10:08	36.42	37.47	0	4.2	227	51	-43
95	30.03.2015	03:16	37.73	38.11	0	3.2	253	76	5
96*	5.04.2015	03:57	38.74	37.44	3	3.2	195	46	-27

97	6.04.2015	00:27	36.82	37.1	2	3.0	188	54	-59
98	6.04.2015	04:35	34.57	37.09	1	3.0	265	88	-5
99	11.04.2015	15:23	33.65	38.7	1	3.0	253	36	-54
100	19.04.2015	02:17	39	38.45	0	3.1	175	46	-27
101	24.04.2015	22:18	35.29	39.79	0	3.3	352	59	-60
102	25.04.2015	21:57	38.62	38.15	1	3.0	74	82	-18
103	5.05.2015	19:37	33.2	39.06	3	3.1	342	73	-18
104	20.04.2014	12:28	36.21	37.71	1	3.6	142	57	-33
105	1.05.2014	07:36	37.38	39.49	1	4.4	40	56	-53
106	10.05.2014	22:45	38.17	38.68	3	3.0	227	74	20
107	21.05.2014	23:26	36.32	37.26	3	3.2	250	44	-60
108	29.05.2014	21:22	34.17	36.28	2	3.2	159	46	-76
109*	17.06.2014	17:47	38.45	39.68	4	3.0	162	45	45
110	19.06.2014	05:21	35.69	37.5	3	3.1	235	79	10
111*	23.06.2014	21:07	35.88	37.46	19	3.0	NA	NA	NA
112	30.06.2014	14:40	38.99	38.43	0	3.2	52	81	-34
113	9.07.2014	07:27	38.01	39.54	0	3.4	129	50	0
114	12.07.2014	21:58	35.89	36.58	7	3.9	196	62	-49
115	14.07.2014	14:08	36.11	37.06	6	3.2	182	66	-74
116	15.07.2014	11:45	36.68	39.49	3	3.0	295	36	73
117	8.08.2014	15:01	37.9	37.89	1	3.1	58	83	-7
118	11.08.2014	04:10	36.7	39.48	2	3.3	56	48	-63
119	11.08.2014	04:22	36.68	39.48	2	3.9	194	41	75
120	18.08.2014	22:54	39	39.2	3	3.2	63	40	-58
121	19.08.2014	04:19	36.94	37.08	3	3.0	228	63	14
122	29.08.2014	23:03	38.79	38.33	1	3.1	222	90	10
123	3.09.2014	03:15	35.91	36.51	2	3.5	197	88	-25
124	6.09.2014	22:25	35.82	38.36	5	3.3	1	61	-78
125	19.09.2014	19:17	39.09	38.47	3	3.5	20	45	-83
126	20.09.2014	02:52	38.77	39.16	4	4.4	78	58	-48
127	20.09.2014	03:09	39.32	38.43	3	3.5	220	45	45
128	22.09.2014	21:33	36.27	39.94	5	3.0	212	73	31
129*	3.01.2015	14:23	33.02	37.1	2	3.2	259	75	-48
130	3.01.2015	23:24	37.89	37.89	3	3.5	99	85	-9
131	6.01.2015	22:16	34.45	36.93	1	4.0	163	58	-48
132	8.01.2015	18:44	36.8	37.1	2	4.7	177	54	-59
133	18.01.2015	16:01	38.81	38.32	2	3.7	264	90	25
134	20.01.2015	13:27	33.89	38.45	2	3.0	348	61	-28
135	25.01.2015	22:21	36.32	36.91	4	3.5	227	51	-43
136	28.01.2015	14:25	38.5	38.1	2	3.6	265	40	58
137	12.02.2015	18:52	38.46	38.13	3	3.8	255	52	71
138*	18.02.2015	12:39	34.88	36.79	16	3.7	109	80	85
139	22.02.2015	10:06	36.7	39.29	3	3.0	56	76	-21
140	28.02.2015	22:03	34.53	37.44	3	3.0	247	65	-5
141	1.03.2015	02:16	36.82	37.07	5	3.5	206	71	-7

An example of the output plot for a FMS computed in this study is given in Figure 4.3. The plot shows the location of the event shown as star in map view along with additional information related to the event (e.g. Date, location, time, magnitude, depth). Moreover, number of solutions, search increment, polarity errors and the P- and T-axes for each solution and their mean orientations are also shown in the plot. The possible solutions are plotted in two boxes. Solutions to the right are calculated by utilizing the polarity data only while solution in the left box is obtained from both polarity & amplitude data. In this example (Figure 4.3), two potential solutions are calculated from polarity data and as expected, the addition of amplitude ratio data limited the number of solutions to one and resulted in well constrained solution. The P-waves polarities plotted over the radiation pattern for the given example are also shown in Figure 4.3(b).

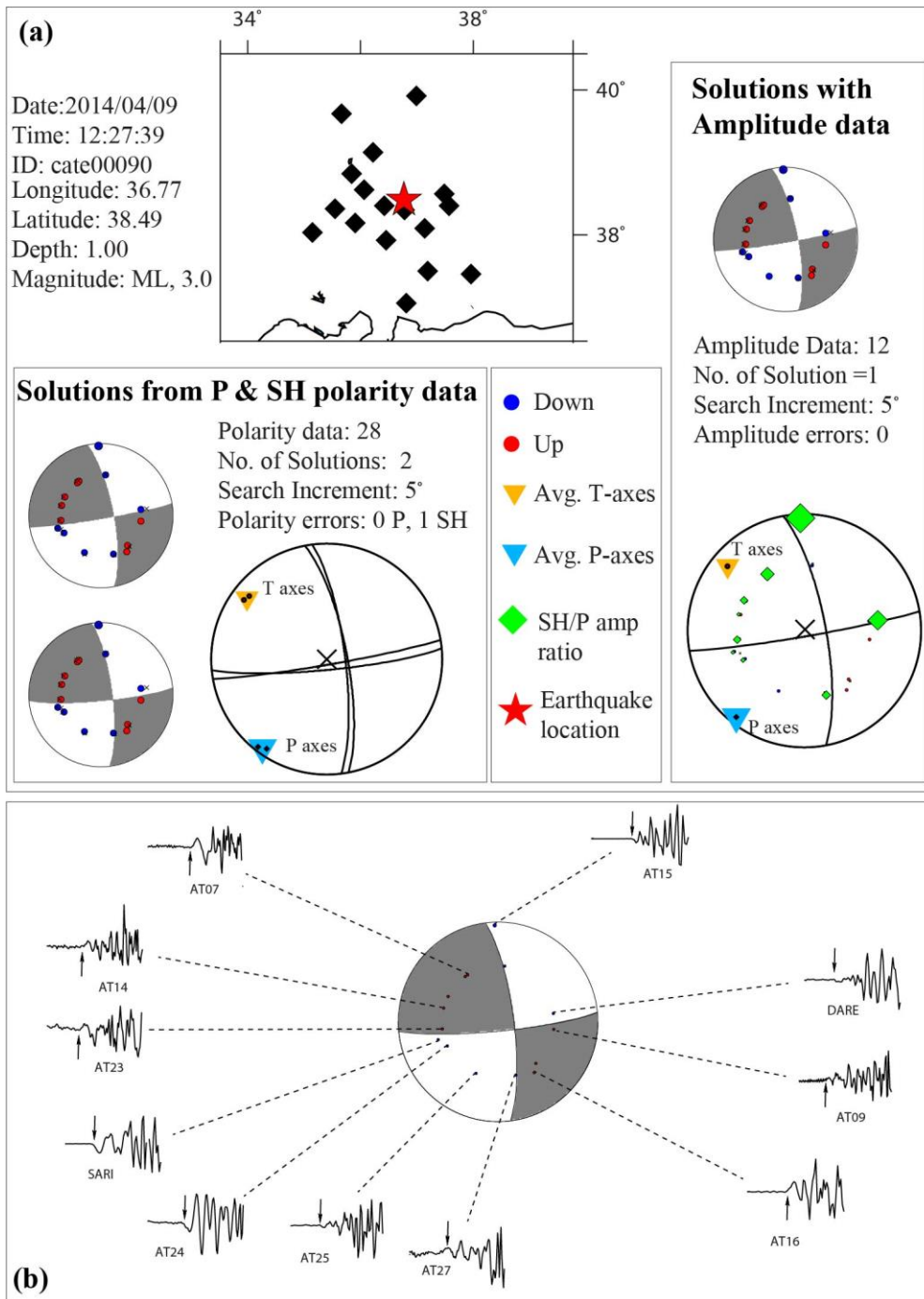


Figure 4.3. (a) An output summary plot showing all the possible focal solution mechanisms and related information computed for an event in this study (b) An example file of the observed P-wave's first motion polarities for the given solution. Polarity directions are shown as upward or downward arrows

4.3.2. Focal Mechanism Solutions

Once the potential solutions for the analyzed events are computed, the solutions with lowest polarity and amplitude ratio errors and RMS misfits are selected as best-fitting focal mechanisms. 2 events were eliminated due to lack of data and 19 solutions were eliminated due to bad quality and errors; which led to a total of 120 well constrained solutions for the region that were utilized for further analysis (Figure 4.4, Table 4.1). The distribution of focal mechanism solutions shows that majority of them are confined to the EAFZ, Adana basin and Gulf of Iskenderun region (Figure 4.4), along with considerable number of solutions associated with CAFZ and Tuz Golu fault zone. Majority of the solutions along the EAFZ have strike-slip mechanisms which is consistent with the left lateral sense of slip along the fault. There are few small magnitude thrust solutions in the vicinity of EAFZ, which can be associated with the intersection zone of EAFZ and Bitlis-Zagros suture zone (BZSZ). The solutions in Adana Basin and Gulf of Iskenderun region consists of a mixture of strikeslip and normal fault mechanisms. The mechanism of solutions along the CAFZ, MOFZ and Sariz fault are pre-dominantly strikeslip with associated normal components but there are few pure normal solutions as well. The NW corner of the study area that coincides mainly with Tuz Golu fault is dominated by normal mechanisms with strikeslip components. The SW corner of the region is characterized by normal fault solutions that cannot be associated with the mapped active faults.

Birsoy (2018) determined focal mechanism solutions for 29 earthquakes ($M_l \geq 3.5$) by applying regional moment tensor inversion technique, utilizing data recorded by the CAT network (2013-2015). Besides, there are regional networks that provide FMS for events in the region. In order to assess the quality of FMS computed in this study, we have compared the solutions computed in this study to Birsoy (2018) and published solutions for the region (Figure 4.5). A total of 23 solutions could be found for comparison. The analysis shows that majority of the solutions computed in this study are in agreement with the previously published solutions with minor difference in the

orientation of nodal planes. We prefer the solutions computed in this study over the published solutions due to large amount of data utilized for this analysis.

Later, the solutions computed in this study are combined with the FMS available from literature studies and regional networks and a composite FMS catalogue for the period of 1900 to present, comprising of 280 solutions has been compiled for the region. The combined catalogue has considerably improved resolution in space and time.

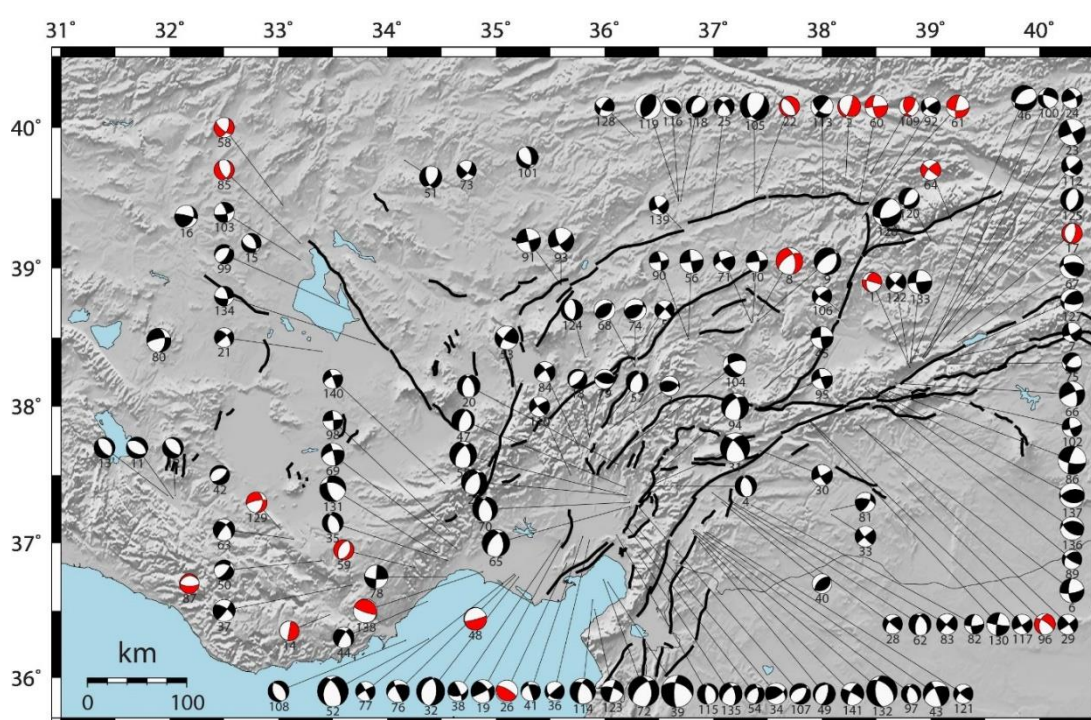


Figure 4.4. Distribution of all the Focal Mechanism Solutions computed in this study. Black solutions are reliable and kept for further analysis while the Red solutions are discarded

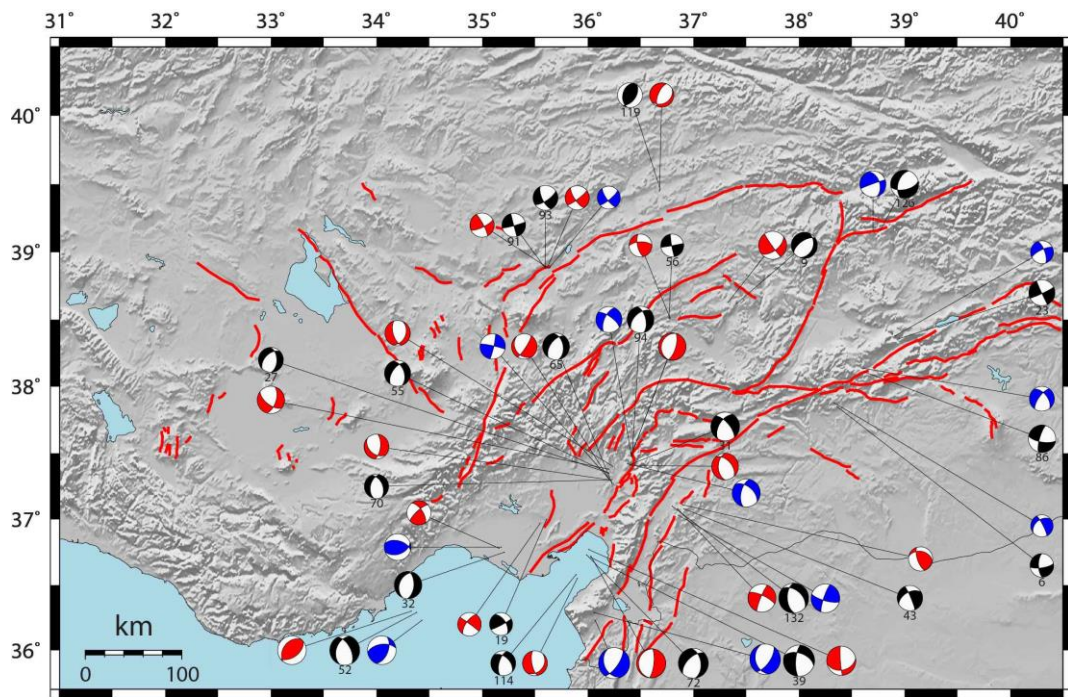


Figure 4.5. Comparison of Focal Mechanism Solutions computed in this study with solutions computed by Birsoy (2018) and literature (This study; Black; Birsoy, 2018 =Red; literature = Blue)

All the solutions in the combined FMS catalogue are categorized according to their faulting styles in Win-Tensor software (Delvaux & Sperner, 2003) and plotted in Figure 4.6. The information about the faulting styles is provided in Appendix G. It can be noted that the eastern and central portions of the study area is dominated by strikeslip solutions (Figure 4.6b) but there are considerable number of normal fault solutions as well, especially in the Adana Basin and Gulf of Iskenderun regions (Figure 4.6c). There are few small-magnitude thrust solutions in the region, which are mainly confined to the vicinity of BZSZ and Sürgü fault (Figure 4.6d). The central part of study area is characterized by a mixture of strikeslip, normal and strikeslip-normal faulting style. The Win-Tensor software could not categorize some solutions as can be seen in Figure 4.6(e).

Rake-based Ternary diagram of the resultant FMS (Figure 4.7a) shows that the region is dominated by strikeslip and normal faulting which corresponds well with the active

fault structures in the region. Apart from strikeslip and normal events, there are few thrust events which can be associated to BZSZ, Sürgü fault and trans-pressional structures along the restraining bends in the region. Out of 280 FMS compiled for the region: 45% of the solution are strikeslip, ~32% are normal and normal-strikeslip, ~10% are thrust and ~11% of earthquakes cannot be categorized. Calculated Pressure (P-) and Tension (T-) axes orientations obtained from the FMS catalogue are shown in Figure 4.7(b). The resultant P- T- axis plot shows that the whole region is experiencing horizontal ~EW directed dilatation and sub-vertical ~NS directed compression. These orientations are consistent with the tectonic characteristics of the region (i.e. strikeslip-normal). The P- T- axis density plot shows that the P- axis is oriented in sub-vertical position while tension axis is horizontal in the region (Figure 4.7c).

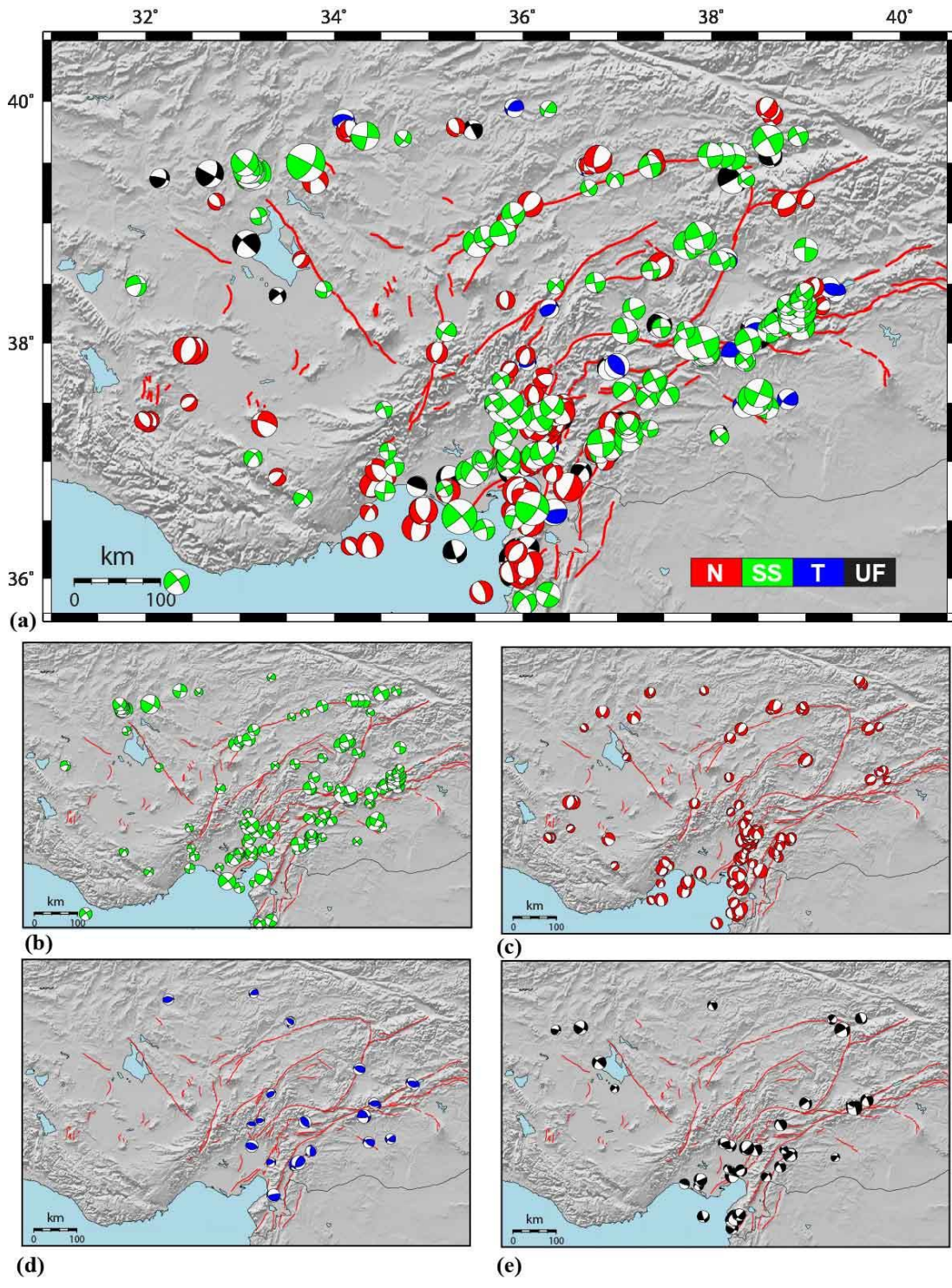


Figure 4.6. Focal mechanism solutions categorized according to the stress regimes (a). (N = Normal, SS = strikeslip, T= Thrust and UF = unidentified solutions), distribution of only strike-slip (b) , only normal (c), only thrust (d) and only unidentified solutions (e)

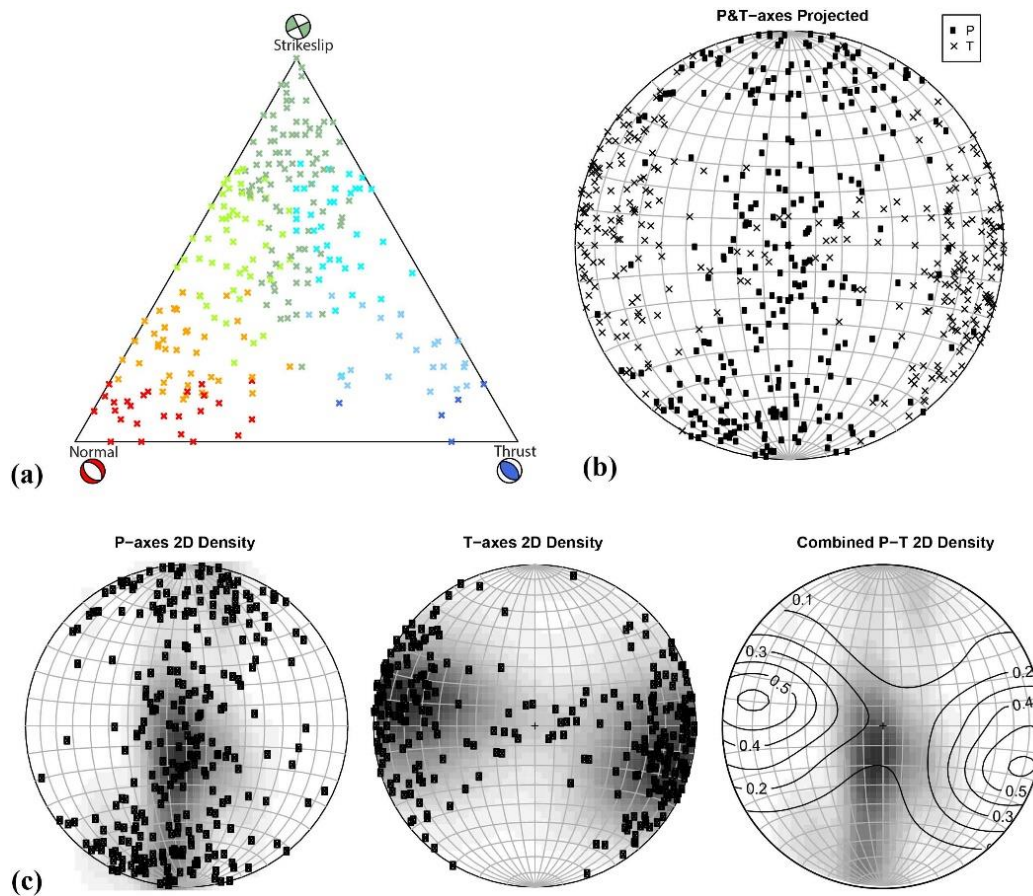


Figure 4.7. (a) Ternary plots (b) Pressure & Tension axis plots and (c) Pressure & Tension axis density plots for the whole study area

4.4. Present Day Stress Analysis

The focal mechanism solution catalogue is later utilized to investigate the present day stress patterns throughout the region. The FMS catalogue is used to compute the maximum horizontal stress orientation (SH_{max}) and the principal stress orientations ($\sigma_1, \sigma_2, \sigma_3$).

4.4.1. SH_{max} Orientations

Figure 4.8 shows the maximum horizontal stress orientation (SH_{max}) computed from the FMS catalogue. The SH_{max} orientations are calculated using Lund and Townend (2007) methodology within Win-Tensor program. The SH_{max} orientation along with

the faulting type are plotted over topography using world stress map (WSM) web-based program. The map shows that in eastern and central portion of the study area, where majority of the FMS are located, SH_{max} bars are oriented in ~NS or NE-SW direction. These orientations are parallel or sub-parallel to the mapped fault structures and corresponds well with the strikeslip and normal slip character of faults in the region. On the contrary, the SH_{max} in NW corner of the study area are marked by a counterclockwise shift in NW-SE direction. The NW-SE trend of faults in this region (e.g. TGFZ) suggests, strikeslip or strikeslip-normal deformation in the region which is consistent with our results. SH_{max} orientations in the SW corner of the region are marked by abrupt changes.

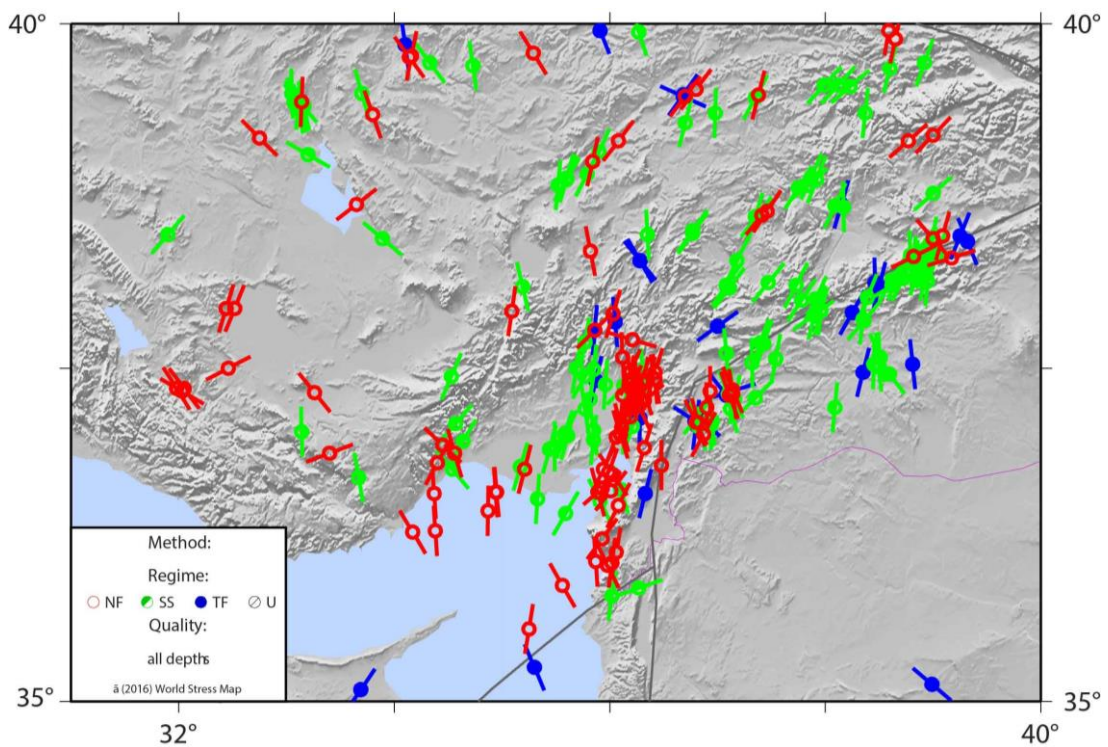


Figure 4.8. Stress map showing maximum horizontal stress axes (SH_{max}) associated to each earthquake solution in the FMS catalogue. The resultant axes indicate the compression directions in the study area

4.4.2. Stress Tensor Inversion

Stress tensor inversion refers to the determination of stress field orientations from fault plane and or focal mechanism solution data. There are various methods devised for stress tensor inversion from focal mechanism solutions; but in this study we adopted the techniques proposed by Michael (1984) and Delvaux & Sperner (2003). The objective of these techniques is to determine the stress which minimizes the misfit between the resolved shear stress direction and the slip direction obtained from the dataset. The inversion algorithms solve for the orientations of principle stress axes and the relative magnitudes of the stress axes or stress ratio $R = (\sigma_2 - \sigma_3) / (\sigma_1 - \sigma_3)$. σ_1 , σ_2 , σ_3 indicates maximum, intermediate and minimum principal compressive stresses respectively and 'R' describes the relative magnitude of the principal stresses and hence constrains the shape of deviatoric stress ellipsoid. All stress tensor inversion techniques assume that the stress is uniform and invariant in space and time and earthquake slip occurs along the direction of maximum shear stress. The difference between the methods is the technique they use to handle the fault plane ambiguity. Michael's (1984) approach applies a bootstrap routine that randomly picks fault planes from the original data. It determines the orientation of principle stress axes and stress magnitude ratio using the statistical method of bootstrap resampling. Heterogeneity of a stress field can be quantified with variance which is defined as the squared and summed solution misfit and it represents the angle between individual FMS and assumed tensor. For a spatially uniform stress field determined from FMS data, variance should be less than 0.2. High variance indicates poor fitting stress orientation and hence stress field remains heterogeneous within the analyzed volume (Wiemer et al., 2002). We used the linearized stress inversion technique of Michael (1987) in the ZMAP software package (Wiemer 2001). For Delvaux & Sperner (2003) method, we have used Win-Tensor program which utilizes an interactive process for data separation and stress tensor inversion in order to obtain good quality tensor solutions. In the software, interactive graphical "Right Dihedron method" tool is used for determining the possible range of stress orientations. These results are used as a

starting point for iterative grid-search “Rotational Optimization” technique. The misfit function in “Rotational Optimization” allows minimizing the angular deviation between the observed and theoretical slip directions and maximizes the shear stress magnitude on the focal planes (Delvaux & Sperner, 2003). The results of stress tensor inversion using Michael’s method (Michael, 1984, 1987) and Win-Tensor program (Delvaux and Sperner, 2003) are compared in Table 4.2. The results obtained from both these methods are similar with minor differences.

Figure 4.9 shows the stress tensor inversion result obtained for the whole region using Michael’s (1987) methods. Inversion of the entire FMS catalogue indicates predominantly strikeslip deformation in the region. Both maximum (σ_1) and minimum principal stresses (σ_3) are horizontal, trending in \sim NS and \sim EW directions respectively, whereas the intermediate principle stress (σ_2) is vertical. Variance of the region is 0.17, which is rather low considering the amount of data, suggesting relatively coherent stress conditions across the region. The resultant stress shape ratio (R) or Phi value; which characterizes the style of faulting is 0.77 and suggests that the magnitude of σ_2 is close to σ_1 that will result in strikeslip-normal (trans-tensional) tectonic deformation in the region.

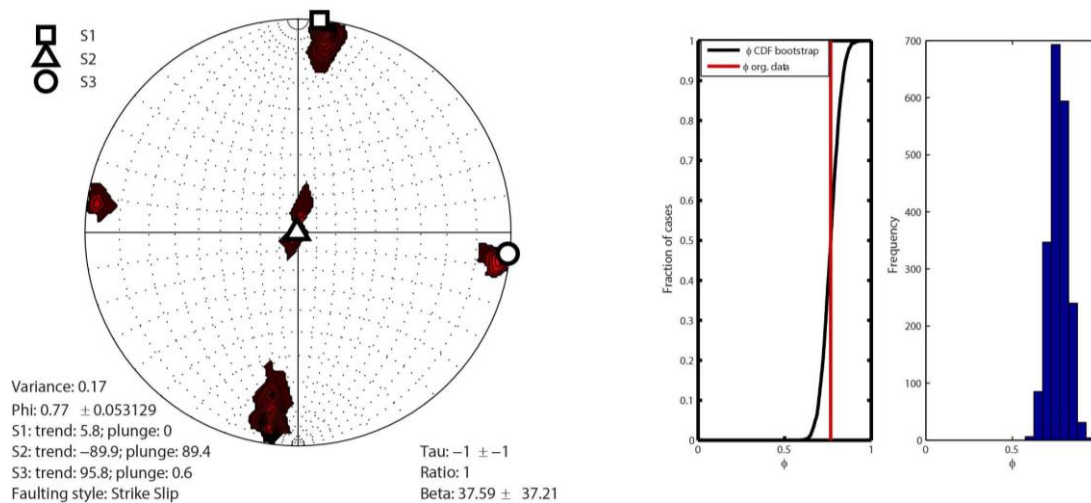


Figure 4.9. (a) Results of stress tensor inversion of all available focal mechanism solutions in the study area using Michael's method and (b) the resultant histogram of stress ratio (R) vs frequency

4.4.2.1. Stress Mapping

The stress tensor inversion for the whole region gave us a general sense of principal stresses in the region. But it can be noted, that the region is characterized by different types of FMS and complex fault structures. Therefore, the stress patterns in the region may vary spatially and a single stress inversion and the respective stress orientations will lead to oversimplification of stress conditions in the region. Considering the distribution and density of earthquake solutions across the region, it is obvious that FMS catalogue has enough resolution to detect inherit changes in stress patterns across the study area. In order to analyze these stress changes, we have subdivided the region into 14 sub-regions (Figure 4.10) based on variation in FMS, fault orientations, tectonic complexities, variations in SH_{max} orientations, clustering of events etc.

Ternary plots and Pressure and Tension axes (P-T axes) density diagrams are constructed for each sub-region and presented in Figure 4.11. The ternary plots of sub-regions 2, 3, 4, 5, 6, 7 and 13 are dominated by strikeslip events, indicating pure strikeslip deformation in these sub-regions. Sub-regions 8, 9, 10, 11 & 12 are dominated by a mixture of strike-slip and normal events, implying a trans-tensional

characteristic for the Adana basin and Gulf of Iskenderun region. The P-T axes plots for sub-regions shows that T- axis is horizontal, trending in EW to NW-SE direction (except for sub-region 1 & 2) with minor differences in orientations. P- axis is trending in ~NS (NNE-SSW) direction in majority of the sub-regions; but in sub-regions 9, 10, 11 & 12 the orientations are more vertical due to mixture of strikeslip and normal earthquake mechanisms.

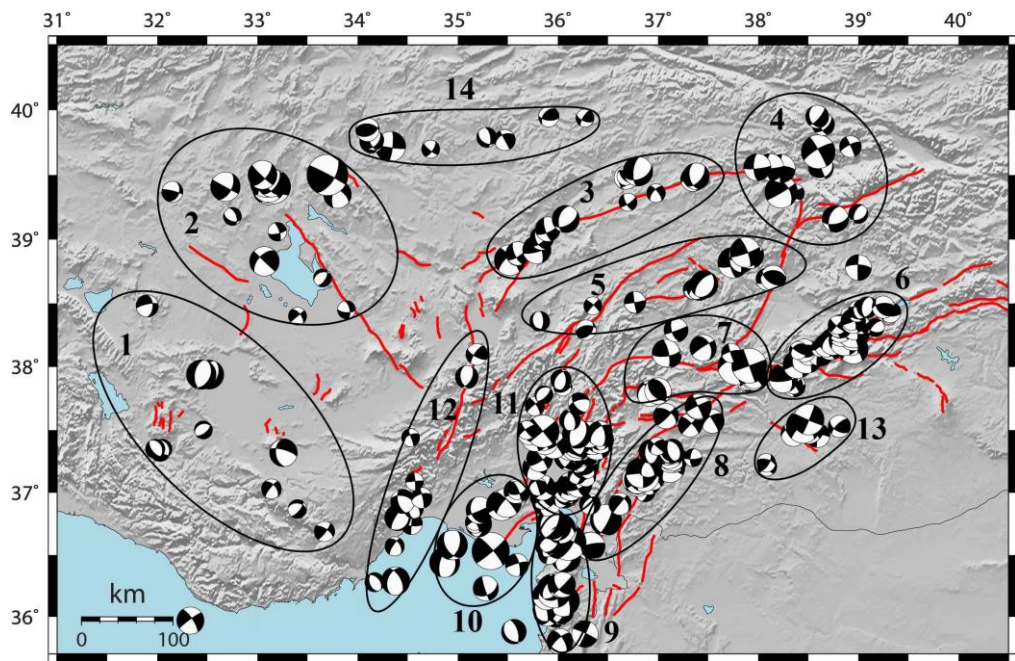


Figure 4.10. Figure showing focal mechanism solutions and geographical limits of sub-regions that are selected for analyzing stress patterns independently. Each sub-region is assigned an identification number (1-14) that will be used in further analysis

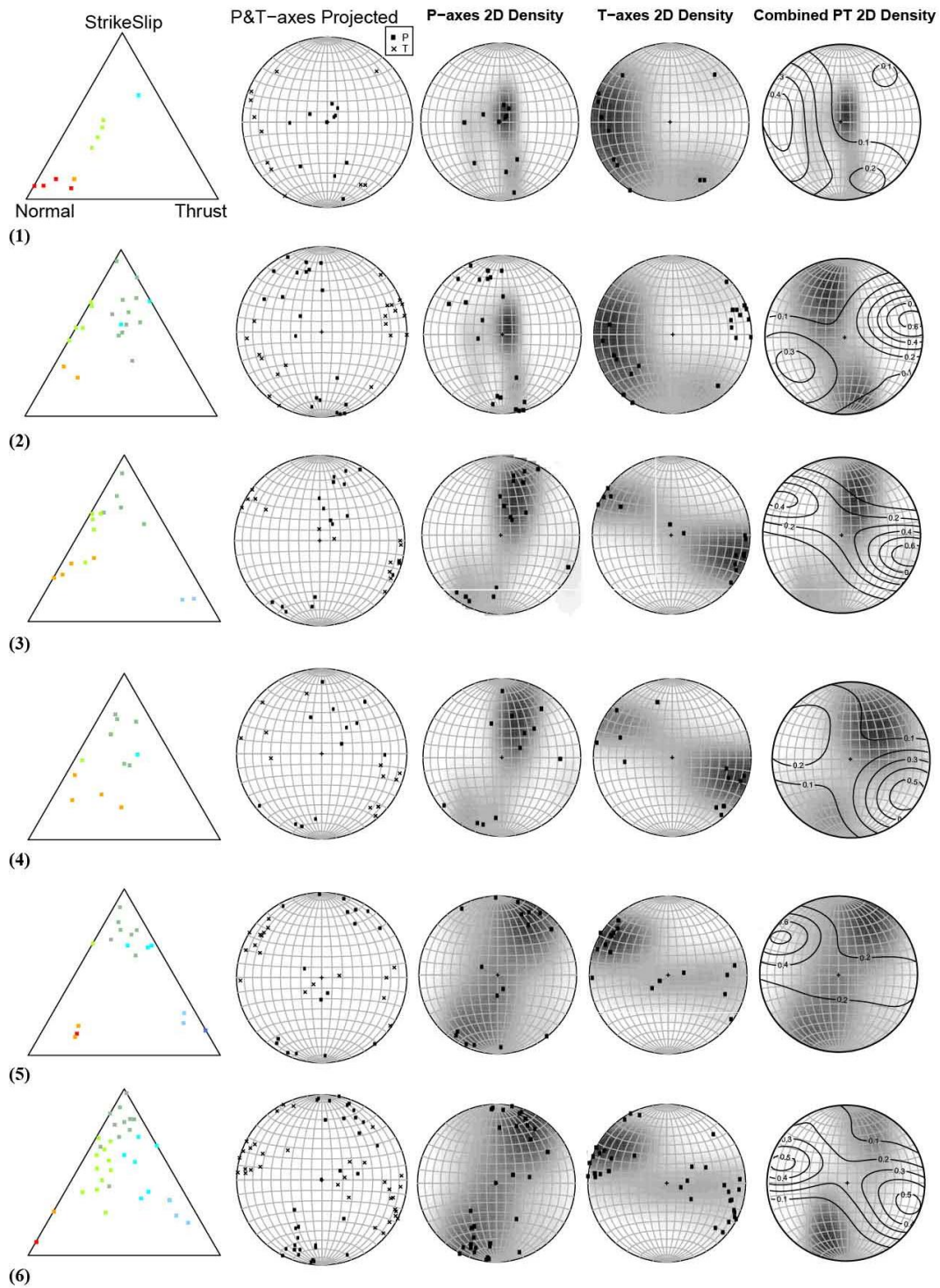


Figure 4.11. Ternary plots and P-T axis density plots for each sub-region

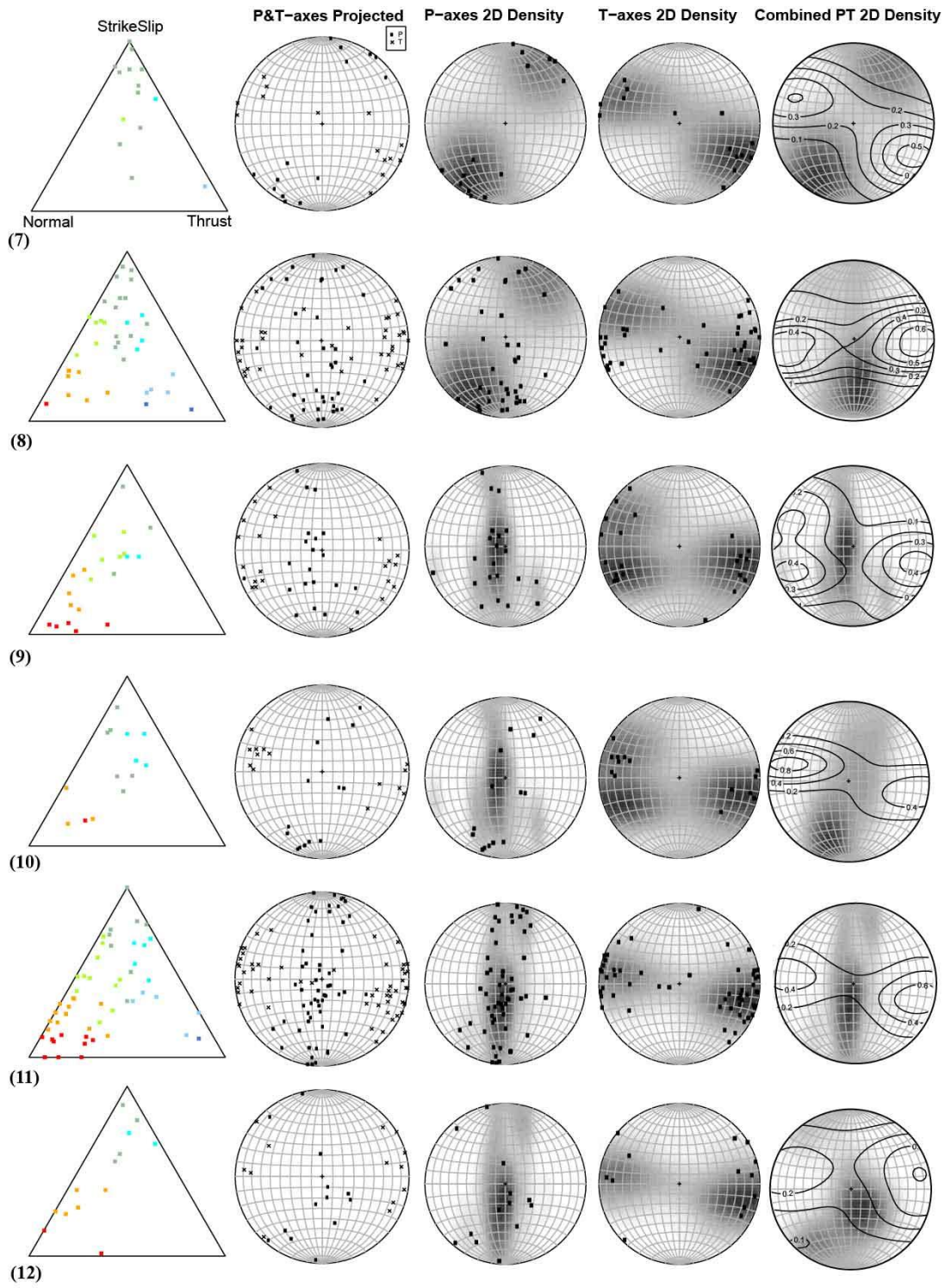


Figure 4.11. (continued)

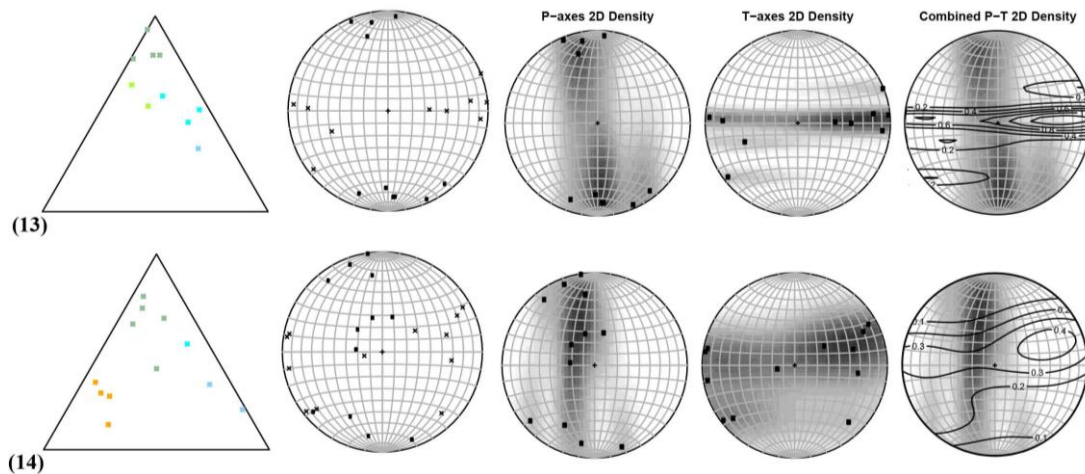


Figure 4.11. (continued)

In order to investigate the variations in stress patterns, stress tensors for each sub-region are inverted independently by utilizing the FMS that falls within their vicinity. The comparison of results obtained from Michael's method and Win-Tensor program shows that both methods produces similar results with minor differences (Table 4.2). The results show that the area is pre-dominantly characterized by strikeslip faulting sub-regimes with σ_2 oriented in vertical position, σ_3 oriented in sub-horizontal position and trending in ~EW direction and σ_1 trending in almost ~N-S directions (Figure 4.12 & Table 4.2). Apart from the strikeslip domains, sub-regions 1 and 9 are characterized by normal faulting, while sub-regime 11 and 12 are characterized by mixed (strikeslip-normal) tectonic regime. Sub-region 13 is characterized by thrust faulting in Michael's method and strikeslip faulting in Win-Tensor method. The variance and β values are within the permissible range ($\Phi < 0.2$ and $\beta < 33^\circ$), indicating coherent stress conditions within the sub-regions.

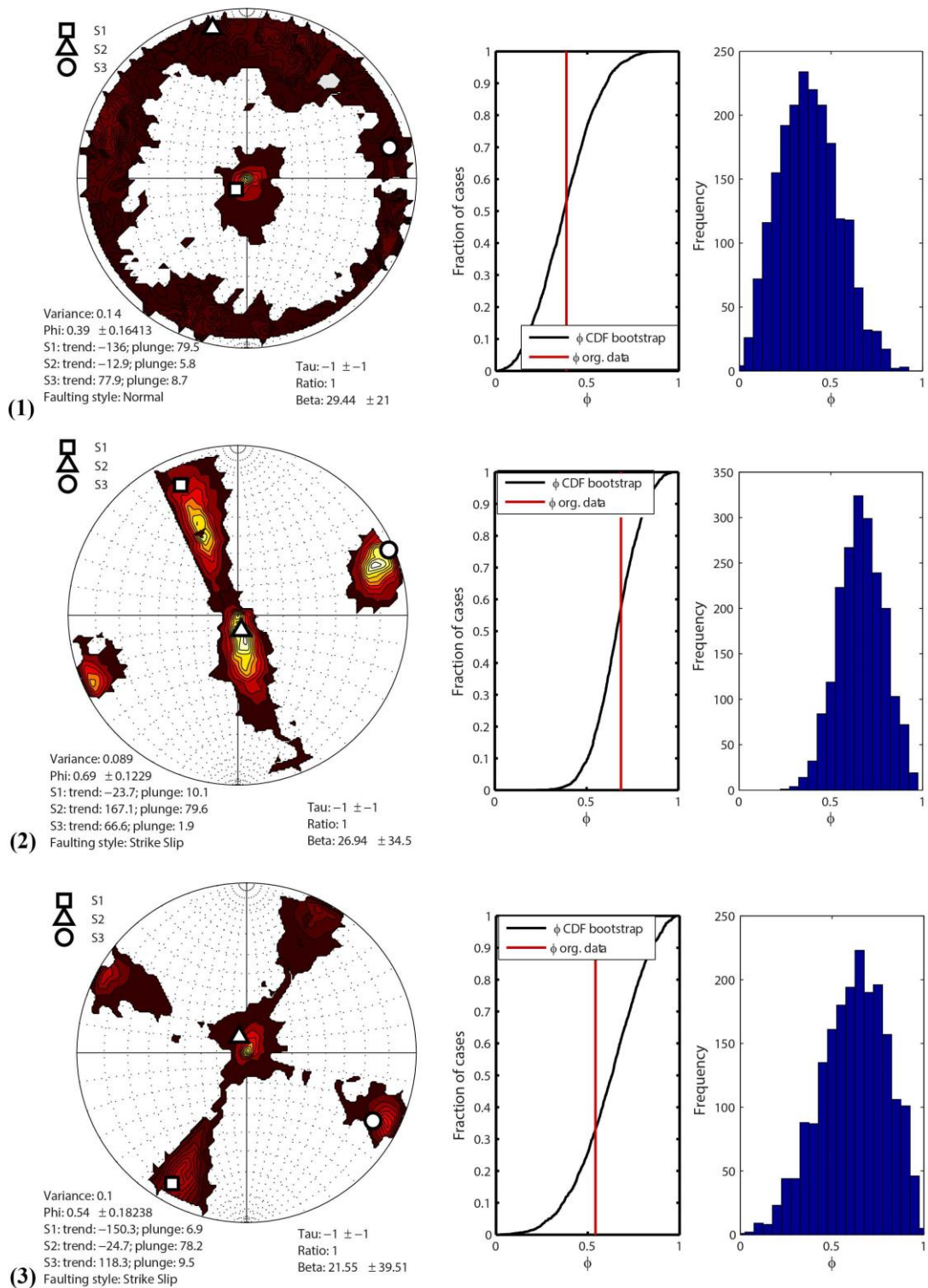


Figure 4.12. (a) Results of stress tensor inversion for each sub-region and (b) the resultant histogram of stress ratio (R) vs frequency. The numbers indicate the sub-region number assigned to each domain as shown in Figure 4.10

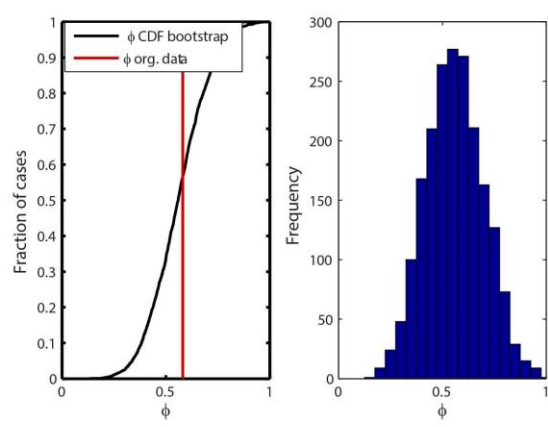
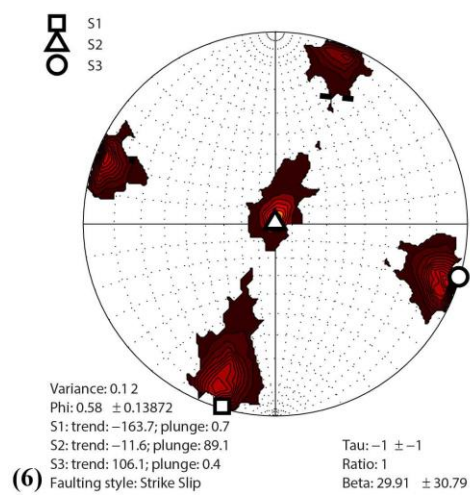
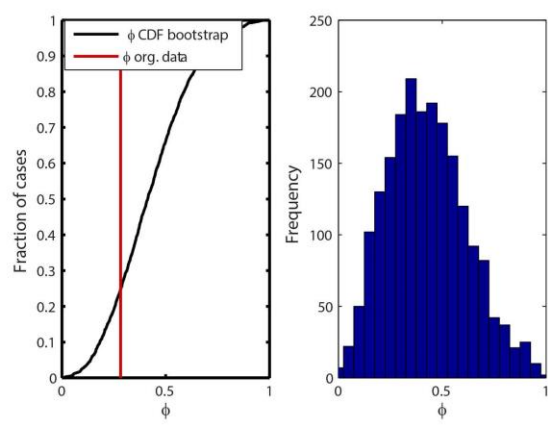
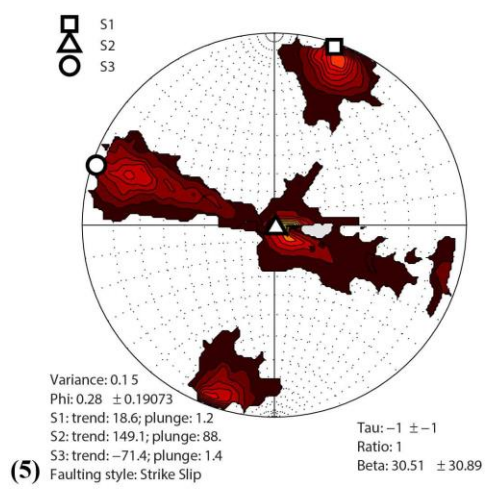
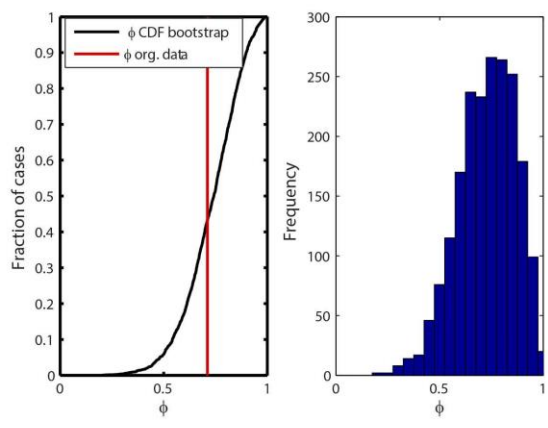
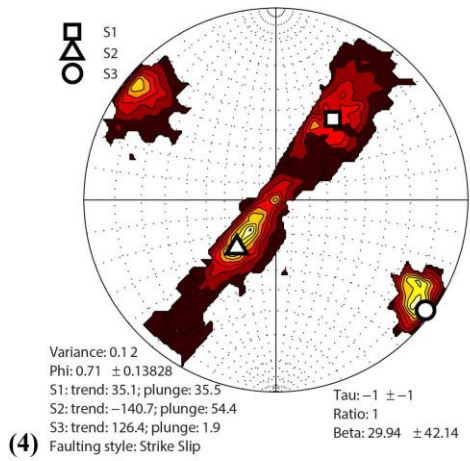


Figure 4.12. (continued)

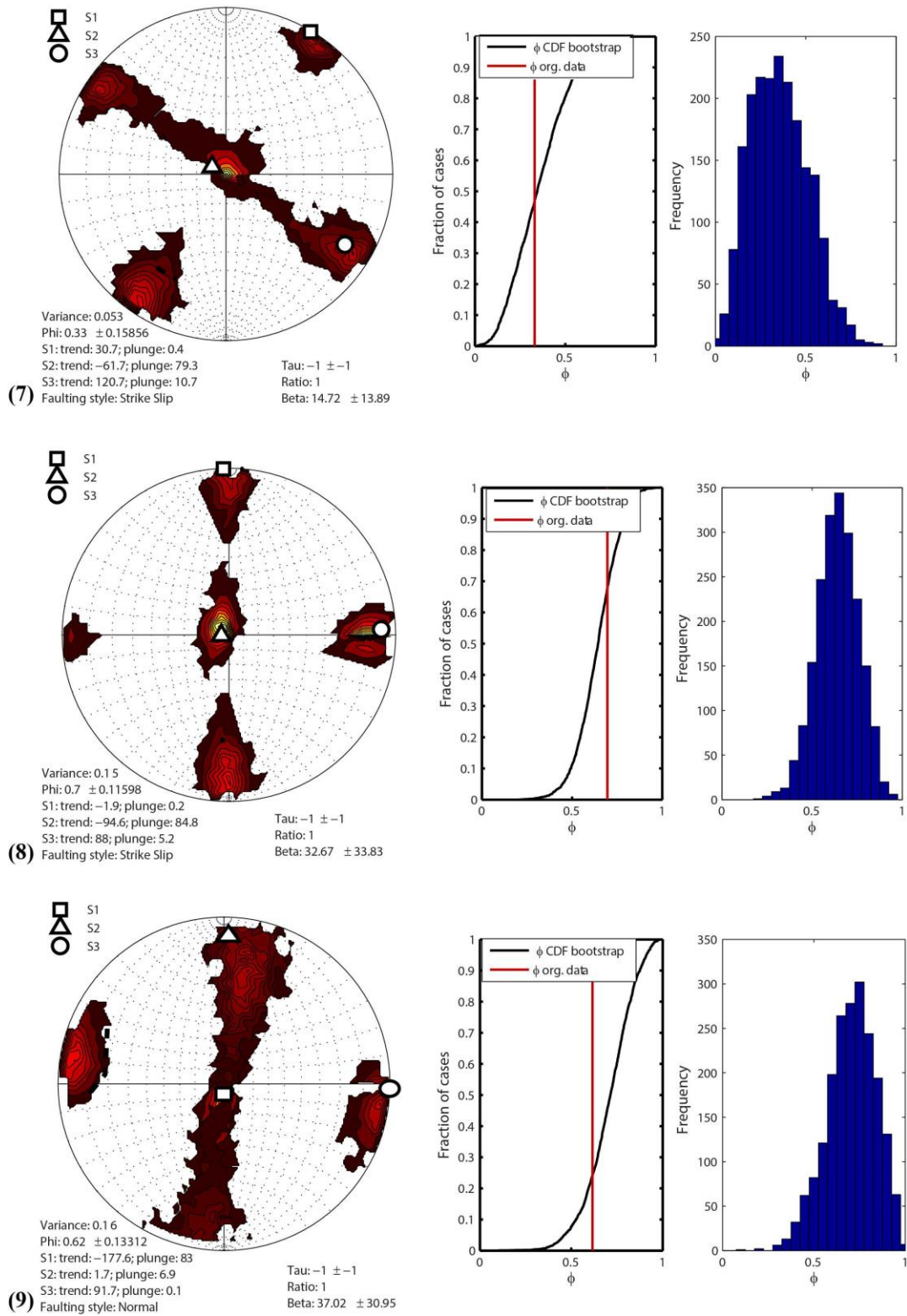


Figure 4.12. (continued)

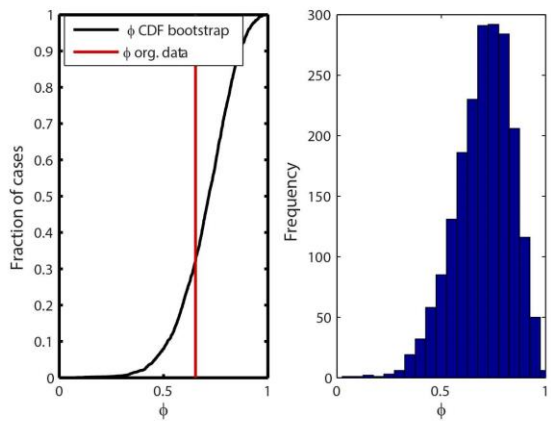
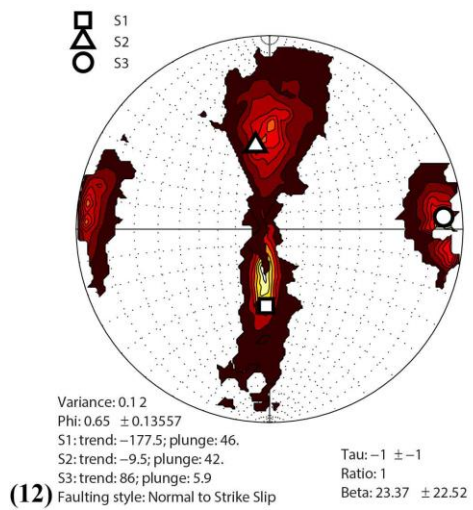
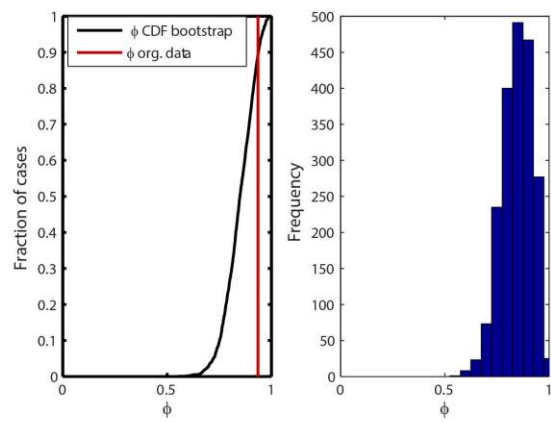
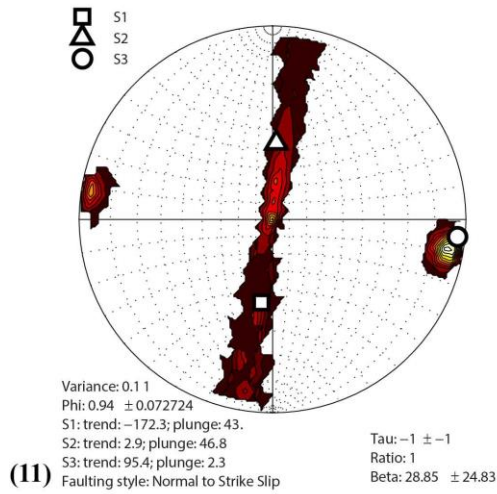
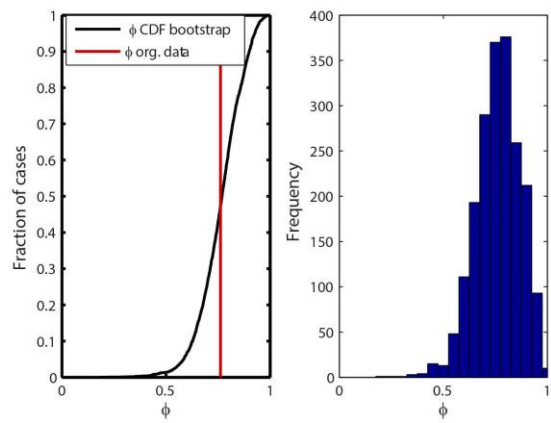
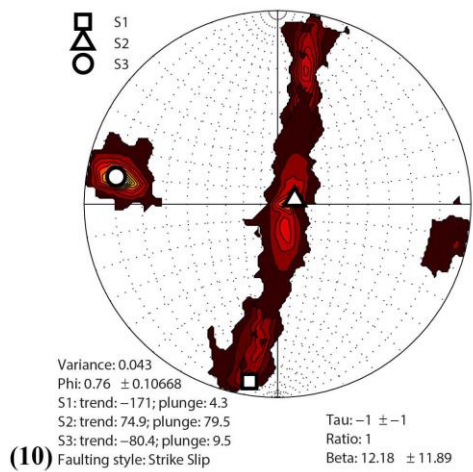


Figure 4.12. (continued)

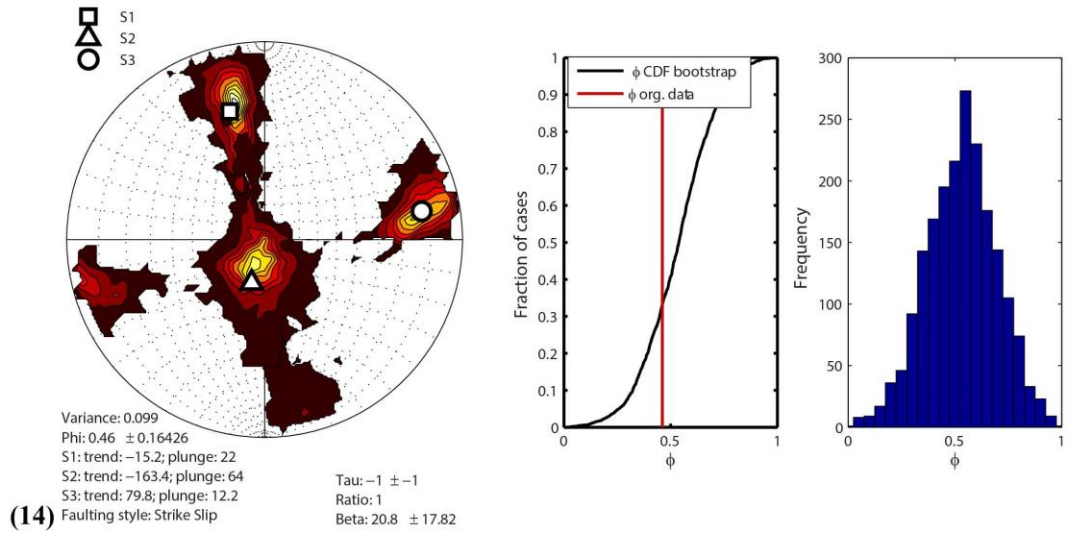
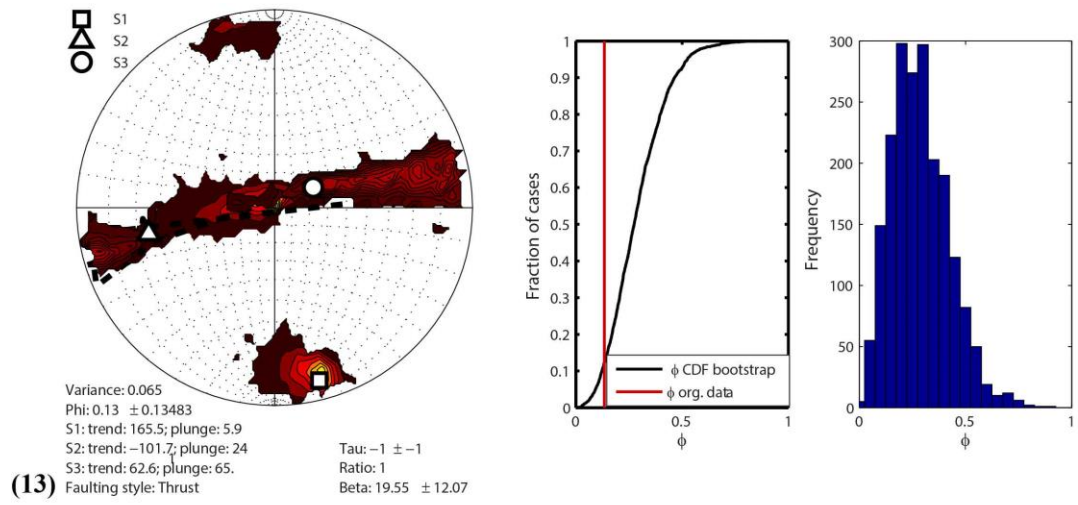


Figure 4.12. (continued)

Table 4.2. Comparison of stress tensor inversion results for the whole region and sub-regions; using Michael's method (1987) and Win-Tensor program (Delvaux and Sperner, 2003). The results obtained from both methods are presented in the upper and lower row respectively for each subset

Subset	S1(tr)	S1(pl)	S2(tr)	S2(pl)	S3(tr)	S3(pl)	Phi (R)	Variance	Faulting	Beta
Whole	6	0	270	89	96	1	0.77±0.05	0.17	SS	38±37
	5	13	189	77	95	1	0.85		SS	28±30
1	224	80	347	6	78	9	0.39±0.16	0.14	N	29±21
	32	74	195	16	286	5	0.45		N	26±19
2	336	10	167	80	67	2	0.69±0.12	0.089	SS	27±35
	342	37	164	53	72	1	0.63		SS	26±18
3	210	7	335	78	118	10	0.54±0.18	0.1	SS	22±40
	204	36	49	51	303	12	0.62		SS	27±36
4	35	36	219	54	126	2	0.71±0.13	0.12	SS	30±42
	39	26	216	64	308	1	0.9		SS	18±12
5	19	1	149	88	289	1	0.28±0.19	0.15	SS	31±31
	197	4	301	72	106	17	0.13		SS	27±25
6	196	1	348	89	106	0	0.58±0.14	0.12	SS	30±31
	193	21	14	69	283	0	0.7		SS	26±26
7	31	0	298	79	121	11	0.33±0.16	0.05	SS	15±14
	212	2	110	81	303	9	0.44		SS	13±12
8	358	0	265	85	88	5	0.7±0.11	0.15	SS	33±34
	358	15	192	74	89	4	0.61		SS	26±33
9	182	83	2	7	92	0	0.62±0.13	0.16	N	37±31
	113	77	9	3	278	12	0.94		N	30±29
10	189	4	75	80	280	10	0.76±0.1	0.04	SS	12±12
	193	0	100	81	283	9	0.56		SS	11±05
11	188	43	3	47	95	2	0.94±0.07	0.11	N-SS	29±25
	6	15	172	74	275	4	0.79		SS	22±21
12	182	46	350	42	86	6	0.65±0.14	0.12	N to SS	24±23
	186	64	3	26	94	1	0.86		N	18±10
13	166	6	258	24	63	65	0.13±0.14	0.06	T	20±12
	1	3	164	87	271	1	0.63		SS	06±04
14	345	22	197	64	80	12	0.46±0.16	0.09	SS	21±18
	2	11	184	79	92	0	0.83		SS	17±18

Figure 4.13 shows summary of the stress tensor inversion results obtained from Michael and Win-Tensor methods in a map view. The orientations of σ_1 , σ_2 and σ_3 obtained from Michael's method are plotted as black square, triangle and circles respectively. The sub-regions are color coded according to their faulting style obtained from Michael's method (i.e. Green = strikeslip, Red = Normal; Brown = Normal to Strikeslip and Blue = Thrust). Black arrows indicate horizontal projection of relative principle stresses obtained from Win-Tensor program. Outward and inward arrows represent orientations of extensional (σ_3) and compressional stresses (σ_1 & σ_2) respectively. The detailed analysis of results shows that the stress patterns in the area are marked by small scale variations in the directions of principle stress orientations. Extensional stress axis are oriented in NE-SW direction in sub-region 2; display a predominant ~E-W orientation in sub-regions 6, 8, 9, 10, 11, 12, 14 and NW-SE (~N65°W) directed extension in sub-regions 1, 3, 4, 5 and 7. The trend of compressive stresses varies between NS and N30°E for most of the sub-regions. Majority of the sub-regions are dominated by strikeslip tectonic regimes (green) with sub-horizontal maximum (σ_1) and minimum (σ_3) principal stress orientations. Among strikeslip regimes; sub-regions 3, 4, 5, 6, 7, 8 & 10 are characterized by almost similar stress patterns: with up to 25° clockwise shifts in σ_1 orientations with respect to the stress field of entire area (i.e. N6°E). On the other hand, sub-regions 2 and 14 are marked by a counterclockwise shift in σ_1 orientation (N25°W & N15°W respectively). In the northern part of study area; trans-tensional characteristic is observed for sub-regions 4 & 14 that are characterized by sub-vertical σ_1 and σ_3 orientations and high stress ratio (R) values. Sub-region 2 is also characterized by high R value (0.69) but σ_1 orientation is horizontal in the area, suggesting a predominant strikeslip along with normal faulting character for the Tuz Golu fault zone. In the central part; sub-regions 5, 6 & 7 have low R values (0.28, 0.58 & 0.33) pointing to a trans-compressional characteristics of faults in the region, which is consistent with the interaction of EAFZ with BZSZ and the trans-compressional characteristic of Surgu fault zone. It is also worth noting that in the southern part, Adana Basin and Gulf of Iskenderun regions (sub-regions 8, 9, 10, 11 & 12) are characterized by high R values (> 0.6), implying closer magnitudes

of σ_1 and σ_2 that will lead to a trans-tensional characteristic of faults in the region (strikeslip-normal). The mapped fault in the region includes: Amanos segment of EAFZ, Karasu fault and DSFZ to the east; Karatas-Turkoglu and Ceyhan-Kozan fault systems in the Adana basin region; and southward extension of CAFZ to the west. To the east, the region is characterized by en-echlon faults with extensional jogs, releasing bends and pull apart basins. The normal faulting regime with high R (0.62), variance ($\Phi=0.16$) and β (37°) values computed for sub-region 9 correlates well with the complex fault characteristics and heterogeneous stress conditions in the region. Sub-region 8 is characterized by almost similar stress ratios (0.7) and variance ($\Phi=0.15$, $\beta=33^\circ$), except that the region is dominated by a strikeslip regime. Karatas-Turkoglu and Ceyhan-Kozan fault systems, approximately coinciding with sub-region 11 in our analysis, are assigned strikeslip mechanism in literature. The inversion results showed sub-vertical σ_1 and σ_2 stress patterns and high stress ratios in the region, pointing to their trans-tensional nature. The strikeslip-normal nature of CAFZ obtained from literature is in agreement with our inversion results. The orientations of σ_3 in sub-region 1 shows 28° shift among Michael's and Win-Tensor method. Moreover, the resultant stress tensor has relatively higher β values (29°), considering the sample size of FMS (10 solutions), indicating complex faulting or heterogeneous stress conditions in the sub-region.

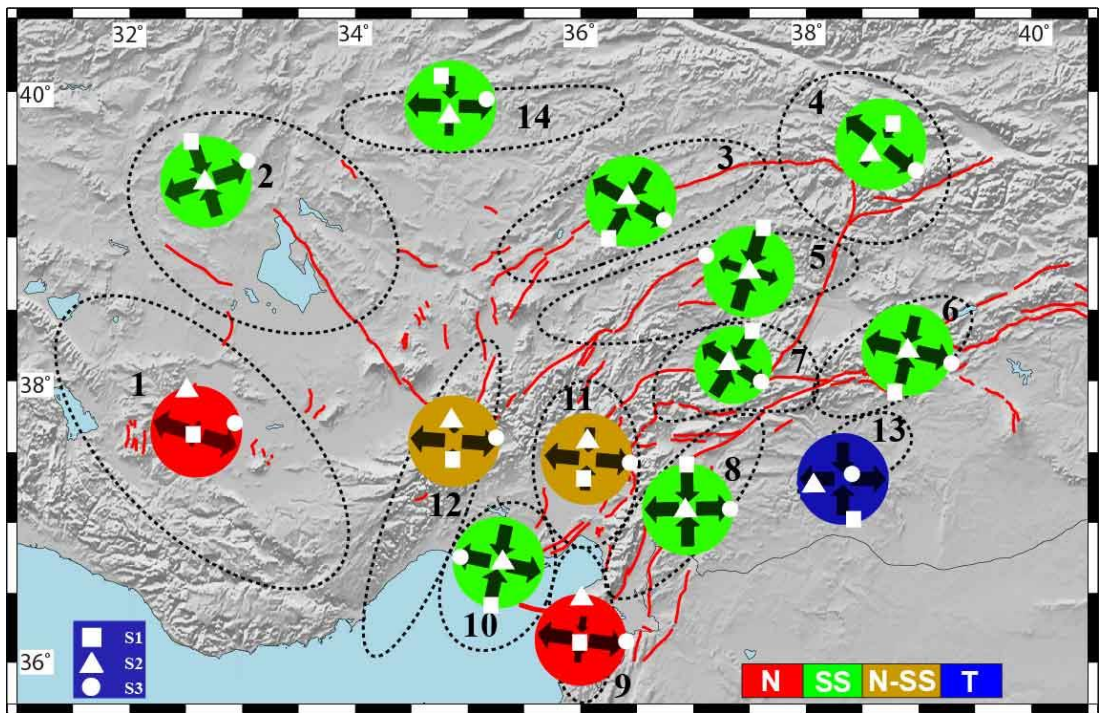


Figure 4.13. Summary of stress tensor inversion results for all the selected sub-regions in study area

4.5. Probabilistic Seismic Hazard Analysis of Adana Basin and Gulf of Iskenderun: Comparison with the New Turkish Seismic Hazard Map (2018)

The Turkish Seismic Hazard Map (TSHM) was updated in 2018 (Akkar et al., 2018) and it is being enforced by the updated Turkish Earthquake Building Code (TEBC, 2018) for developing the design spectrum of regular buildings for the last 10 months. The ground motions in the updated map were computed by utilizing the area source model (details in Şeşetyan et al., 2018) and the fault + smoothed seismicity model (details in Demircioğlu et al., 2017 and the fault parameters are provided in Emre et al., 2016) with equal weights assigned in the source characterization logic tree. Previous experience showed that smaller-scaled (or regional) Probabilistic Seismic Hazard Assessment (PSHA) maps could be quite different than the national hazard maps, depending on the tectonic complexity of the region. In this respect, Adana Basin and Gulf of Iskenderun region which is characterized by young basin fill deposits at the surface, displays a dense seismic cluster that cannot be explained solely by the mapped faults and represents a good example of tectonic diversity since it is characterized by a mixture of strike-slip and normal earthquake mechanisms indicating simultaneous activity of both strike-slip and normal faults (Figure 4.14).

Recently, Gülerce et al. (2017) proposed PSHA maps for the East Anatolian Fault Zone (EAFZ) and the spatial coverage of the proposed maps reach up to our study area at the south. The ground motions in the study area might be underestimated by Gülerce et al. (2017) because the utilized seismic source model was composed of planar seismic sources with pure strike-slip character and no floating seismic sources were included to model the earthquakes that may occur outside the buffer zones around the fault planes. A possible way of improving the ground motion estimates given in Gülerce et al. (2017) is to add a carefully designed area source zone by considering the buffer zones around the fault planes to avoid double-counting of the activity rates. The dense dataset of focal mechanism solutions (FMS) compiled in this study provided valuable information on the active tectonic stress patterns, which is utilized for estimating the parameters of the area source zone developed in this study.

Still, the underestimation of the ground motions for the sites that are not located in the close vicinity of the fault planes is possible, mainly because the activity rate is assumed to be homogeneous within the area source zone and determined by using the earthquake catalogue (please see Chapter 3 for other ways of calculating the activity rates). To reduce the possibility of underestimation and to make the hazard calculations more compatible with the source-to-site-distance metrics used by the ground motion models, the point-source correction based on virtual fault concept is also implemented.

Therefore, the primary objective of this study is to update the ground motion estimates given in Gülerce et al. (2017) using an additional area source that is compatible with the previously developed fault-based seismic sources and FMS database compiled in this study, with point source correction based on virtual faults concept. Sensitivity of the hazard results to the implementation of point-source correction is also thoroughly discussed, because the studies that quantify the differences in hazard based on point-source and finite-fault representation are very limited in global sense (e.g. Campbell and Gupta, 2019 and the references provided therein) and missing for Turkey. Because the source and ground motion characterization logic trees implemented in this study are quite different than the new Turkish Seismic Hazard Map, significant differences in the ground motion estimates are expected. Consequently, the secondary objective of this study is to compare the hazard estimates proposed in this study with the ground motions provided in the Turkish Seismic Hazard Map. Further discussions on the underlying reasons for these differences will contribute significantly to the current PSHA practice in Turkey and the next possible update of the national hazard map.

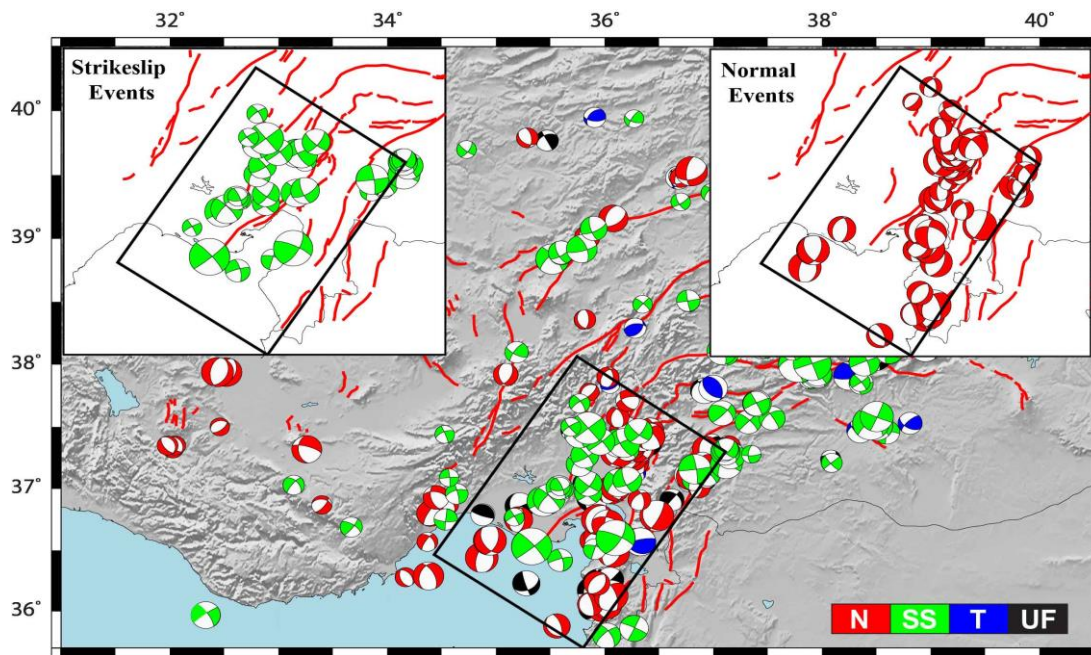


Figure 4.14. Mapped faults in the study area (red lines, taken from Emre et al., 2016), geometry of the area source zone (black rectangle), and the distribution of the FMS. Insets show the spatial distribution of the strike-slip and normal events in the area source

4.5.1. Source Characterization for the New Areal Source Zone

Geometry of the new area source zone is defined cautiously for the consistency with the distribution of the FMS and the fault-based seismic sources utilized in the previous attempt (Gülerce et al., 2017). We defined several sub-domains in Central Anatolia (Figure 4.10) based on the variation in FMS, fault orientations, tectonic complexities, orientation-clustering of events etc. Initial geometry of the area source zone is selected to cover the sub-domains that are characterized by a mixture of strike-slip and normal events (Figure 4.13 and 4.15a, blue circles). For the fault sources defined by Gülerce et al. (2017), source-to-epicenter matching was performed by creating 10 km wide (5 km in each side of the fault) buffer zones around the rupture systems. The buffer zones are only used to “associate” the earthquakes with the fault zones and collapse the earthquakes to the vertical fault planes. Therefore, the boundaries of the area source are slightly modified, considering the overlap between the buffer zones associated

with the fault sources as shown in Figure 4.15(b). Figure 4.15 also compares the active faults given in Emre et al. (2016) which were implemented in the TSHM and the fault sources utilized in Gülerce et al. (2017). The main objective of Gülerce et al. (2017) was to implement the fault model of Emre et al. (2016) in PSHA by modifying only the necessary aspects related to the modelling simplifications in PSHA. Implemented changes were thoroughly discussed in the original reference; however, the changes in the study area can be summarized as: (1) addition of Türkoğlu segment, (2) addition of Ceyhan segment, and (3) extension of the segments that were limited on land (Kyrenia) or by the country border (Dead Sea Fault).

The magnitude recurrence parameters and the seismogenic depth of the new area source are estimated using the de-clustered instrumental catalogue of Kandilli Observatory and Earthquake Research Institute (KOERI) that includes the events recorded from 1900 to 2019 using the maximum likelihood (MLE) and weighted least square (WLS) methods in ZMAP software package (Wiemer, 2001). The aftershocks and mainshocks are de-clustered based on the method proposed by Reasenberg (1985) with minimum and maximum look ahead times of 1 and 10 days, and event crack radius of 10km. To prevent the double counting of the activity rates, the epicenters located within the buffer zones of Figure 4.15(b) are removed from the de-clustered catalogue. Figure 4.16(a-b) shows that the completeness magnitude (M_c) and the magnitude recurrence parameters estimated by MLE and WLS methods are in good agreement; therefore, both sets of a- and b-values are included in the logic tree with equal weights to cover the epistemic uncertainty. Thickness of the seismogenic crust or the down-dip width of the seismic sources is typically defined by calculating D90 or D95 (the depth in which 90 or 95% of the events in the area are located). ~83% of the events in the catalogue lie within 0-15 km depth from the surface, while 91% of the events are located within the first 20km; therefore, the seismogenic depth is selected as 20 km for the area source.

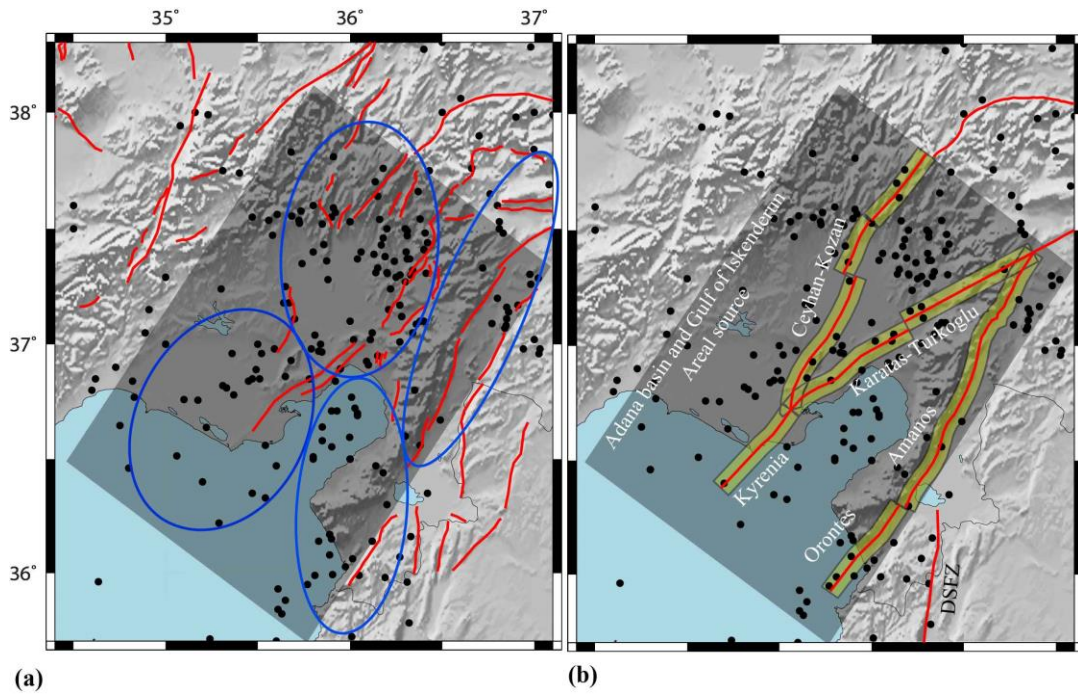


Figure 4.15. (a) Active fault map of the study area adopted from Emre et al. (2016), (b) fault based planar seismic sources used in Gülerce et al. (2017). Shaded rectangle shows the new areal source zone and the yellow boxes represent the buffer zones defined in Gülerce et al. (2017). Black points show the de-clustered seismicity catalogue ($M \geq 4.0$)

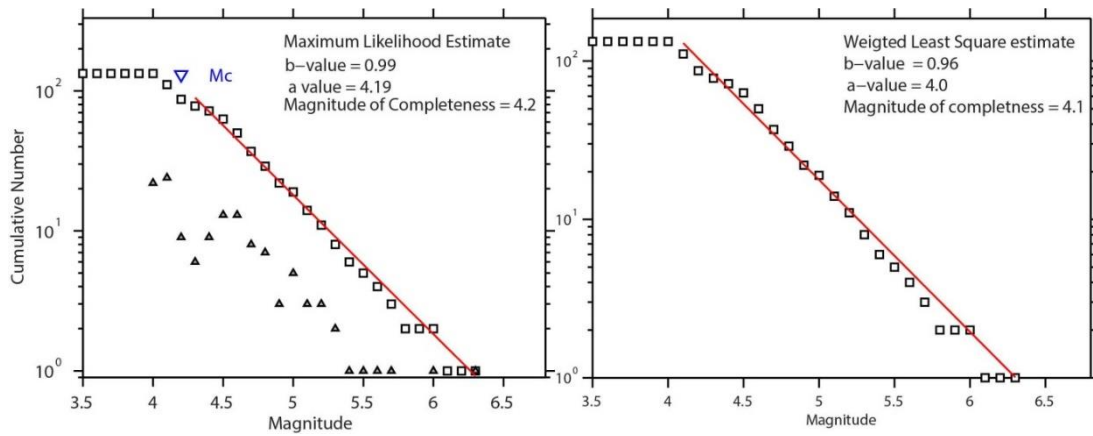


Figure 4.16. Magnitude recurrence parameters for the area source zone estimated by (a) Maximum likelihood estimate (MLE) and (b) Weighted least square (WLS) methods

The truncated exponential magnitude distribution (Cosentino et al., 1977) is selected to represent the relative frequency of the different magnitude events for this source. Minimum magnitude threshold is defined as $M_w=4.0$ based on M_c and considering the magnitude limit below which the earthquake has no impact on the structure. The maximum magnitude (M_{max}) distribution of the area source is developed by using the EPRI-Bayesian approach (Johnston et al. 1994) that combines the earthquake catalogue of the source zone with the prior distribution developed for the worldwide database of large shallow crustal earthquakes. In this study, the prior distribution for the extended crust (a normal distribution with a mean of $M_{max}=6.4$ and a standard deviation of 0.84) is utilized. The resulting posterior distribution for the proposed area source (Figure 4.17a) is discretized for 0.25 magnitude units and the corresponding logic tree weights are shown in Figure 4.17(b).

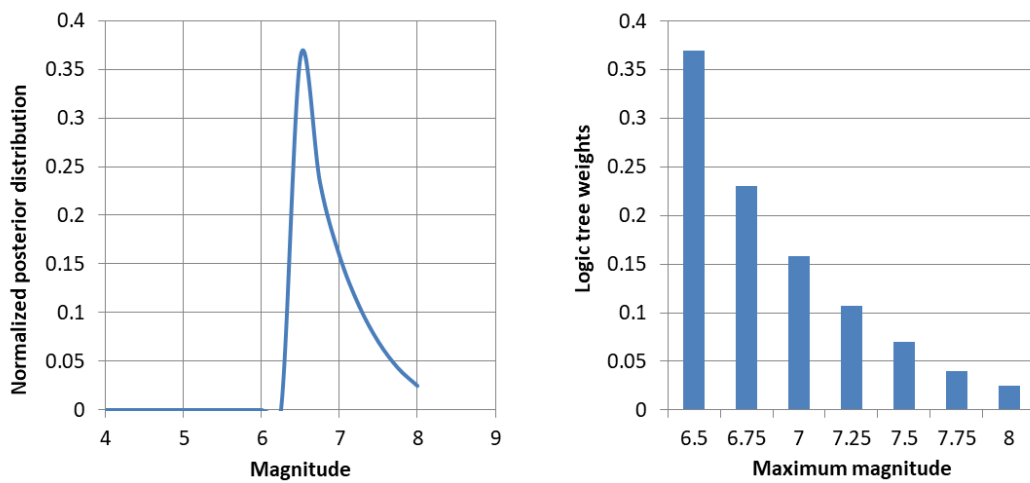


Figure 4.17. (a) Posterior distribution, (b) discretized logic tree weights for Maximum magnitude (M_{max})

The fault mechanism logic tree assigned to the area source should reflect the tectonic style of the region. The ternary plot of the events located in the area source boundaries obtained from the FMS catalogue shows that the region is characterized by large

number of strike-slip and normal FMS (Figure 4.18a). Analysis of normal and strike-slip solutions separately revealed NE-SW and NW-SE trending strike-slip faulting with dips ranging between 70-90° and ~NS trending normal faulting with dip amounts ranging between 45-60° in the region (Figure 4.18b). The stress tensor inversion results also showed that both σ_1 and σ_2 are oriented in sub-vertical position consistent with trans-tensional tectonic regime (Figure 4.18c). Based on the number of strike-slip and normal mechanisms, a weighted combination of strike-slip (SS, 60%), and normal (NM, 40%) motion is assigned to this source. Additionally, the uncertainty in the dip direction of the source is taken into consideration by assigning 3 alternative dip angles (90°, 80°, 70°) for strikeslip and 2 alternatives for normal faults (60°, 45°) with 20% weights in the logic tree.

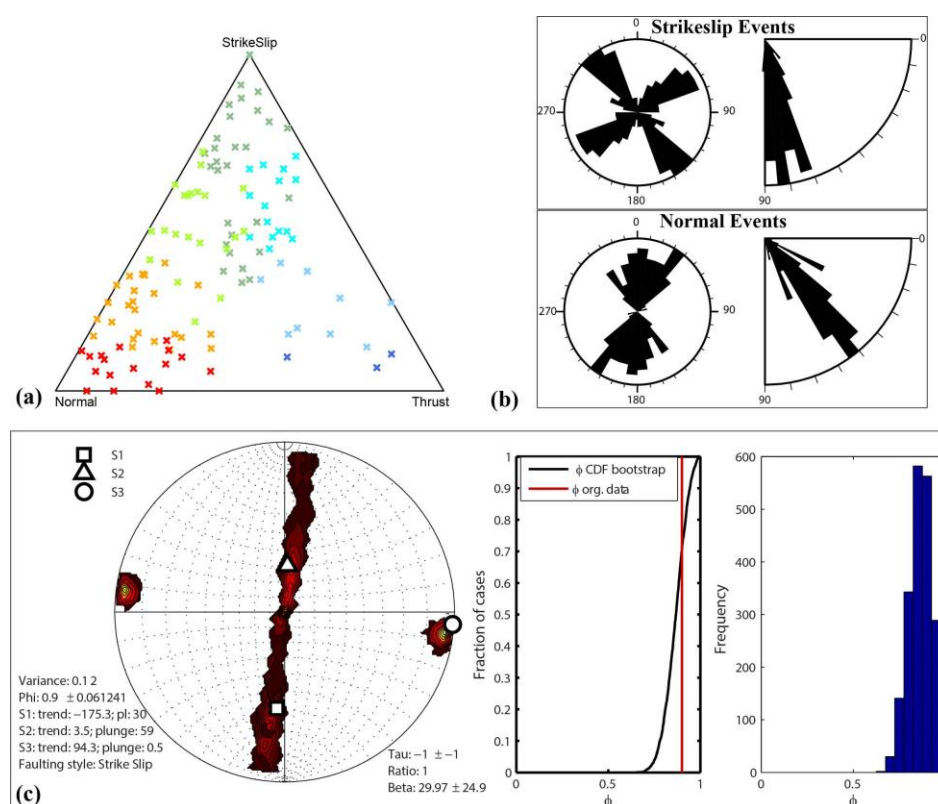


Figure 4.18. (a) Ternary plot of the focal mechanism solutions (FMS) (b) Rose diagram of strike direction and dip angles obtained from FMS of strike-slip and normal events and (c) results of stress tensor inversion and the resultant histogram of stress ratio (R) vs frequency

Geometry and the source characterization logic tree of the proposed area source are compared to the area source model implemented by Şeşetyan et al. (2018) in Figure 4.19. Spatial coverage of the source zone with ID:TURAS009 (EAF Zone) of Şeşetyan et al. (2018) model coincides (approximately) with the source model proposed here; however, TURAS009 was extended further down towards southwest, reaching up to east of Cyprus Arc. Therefore, the percentage of the reverse motion associated with TURAS009 zone and the seismogenic depth of the zone are higher than the values used in this study. A direct comparison between the activity rates (a-value) and maximum magnitude potential is not very descriptive due to the differences in the source geometry. On the other hand, the b-values defined in this study and Şeşetyan et al. (2018) are very similar, even if the compiled catalogues are different.

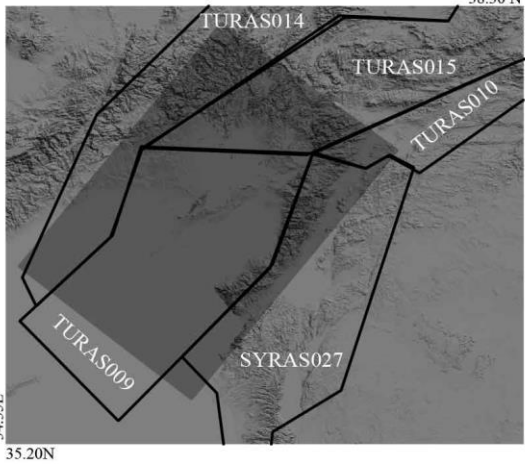
Logic Tree for TURAS009 of Şeşetyan et al. (2018)			Logic Tree for proposed zone		
Mechanism	Value	Weight (%)	Mechanism	Value	Weight (%)
	SS	60		SS	60
	NM	20		NM	40
	RV	20		RV	0
Seismogenic depth	35	100	Seismogenic depth	20	100
Dip angle	70	100	Dip angle	90	20
				80	20
				70	20
				60	20
				45	20
			6.5	37	
Mmax	7	25	Mmax	6.75	23
	7.3	50		7	15.8
	7.6	25		7.25	10.7
Magnitude Recurrence			Magnitude Recurrence		
a-value	3.97	100	a-value	4.19	50
				4.0	50
b-value	0.97	100	b-value	0.96	50
				0.99	50

Figure 4.19. Comparison of the source geometry parameters between the proposed area source in this study and the zone with ID: TURAS009 (EAF Zone) of Şeşetyan et al. (2018) model

4.5.2. Logic Tree for the Ground Motion Models

The ground motion model (GMM) logic tree used by Gülerce et al. (2017) is adopted in this study with small modifications: similar to the previous attempt, 50% weight is given to global NGA-West2 models (Abrahamson et al., 2014 (ASK14), Boore et al., 2014 (BSSA14), Campbell and Bozorgnia, 2014 (CB14), and Chiou and Youngs, 2014 (CY14)) and 50% weight is assigned to the TR-adjusted versions of NGA-West1 models (Abrahamson and Silva, 2008 (TR-AS08), Boore and Atkinson, 2008 (TR-BA08), Campbell and Bozorgnia, 2008 (TR-CB08), and Chiou and Youngs, 2008 (TR-CY08)). However, the ranking results presented in Kale (2017) are used to modify the distribution of the logic tree weights among the global and local GMM sets. Kale (2017) found that the prediction performance of TR-BA08, TR-CB08 and CY14 models are superior when compared to the others; therefore, weights assigned to these models are increased. The ground motion characterization logic tree of the TSHM (Akkar et al., 2018) was quite different than the logic tree used in this study. Four GMMs proposed by Akkar et al. (2014, Pan-European), Chiou and Youngs (2008, Global/NGA-West 1), Akkar and Çağnan (2010, local) and Zhao et al. (2006, Global/Japan) were included with different weighing. The differences in the logic trees implemented in this study and in the Turkish Seismic Hazard Map are summarized in Table 4.3.

Table 4.3. Comparison of ground motion characterization logic trees of this study and TSHM

	GMM Name	Weight in Gulerce et al. (2017)	Weight in this study	GMM Name	Weight in TSHM
Global	ASK (2014)	0.125	0.10	Akkar et al. (2014)	0.30
	BSSA (2014)	0.125	0.10	Chiou and Youngs (2008)	0.30
	CB (2014)	0.125	0.10	Zhao et al. (2006)	0.10
	CY (2014)	0.125	0.20	-	-
Regionalized or Local	TR-Adjusted AS08	0.125	0.10	Akkar and Çağnan (2010)	0.30
	TR-Adjusted BA08	0.125	0.15	-	-
	TR-Adjusted CB08	0.125	0.15	-	-
	TR-Adjusted CY08	0.125	0.10	-	-

4.5.3. Probabilistic Seismic Hazard Assessment using Virtual Fault Concept

Traditional Cornell-McGuire PSHA methodology (Cornell, 1968; McGuire, 2004) is utilized for computing the seismic hazard integral and the numerical integration is performed by using the computer code HAZ45 (Hale et al., 2018) which treats the epistemic uncertainties in the seismic source models and GMMs using the logic tree approach. When an area source zone is defined, HAZ45 software (like other hazard codes) moves the possible epicenter of the scenario earthquake on the vertical projection of the fault plane as shown in Figure 4.20, assuming that the earthquake is originating from a point source (Figure 4.20a). This definition requires a set of corrections to calculate the source-to-site distance metrics employed by GMMs, specifically the rupture and Joyner-Boore distances that depends on the fault plane geometry (Bommer and Akkar, 2012). HAZ45 (and some other hazard codes) provides the user another option with point source correction, by defining a fault plane with random strike, centered at the hypocenter as illustrated in Figure 4.20(b). In that case, the finite-fault source-to-site distances are measured depending on the geometry of the assumed fault plane; while the length of the fault plane is back-calculated from the magnitude-rupture length relations for each scenario earthquake. The strike of the

fault plane is rotated over 180° , assuming that the orientation of the plane has uniform probability for each strike orientation.

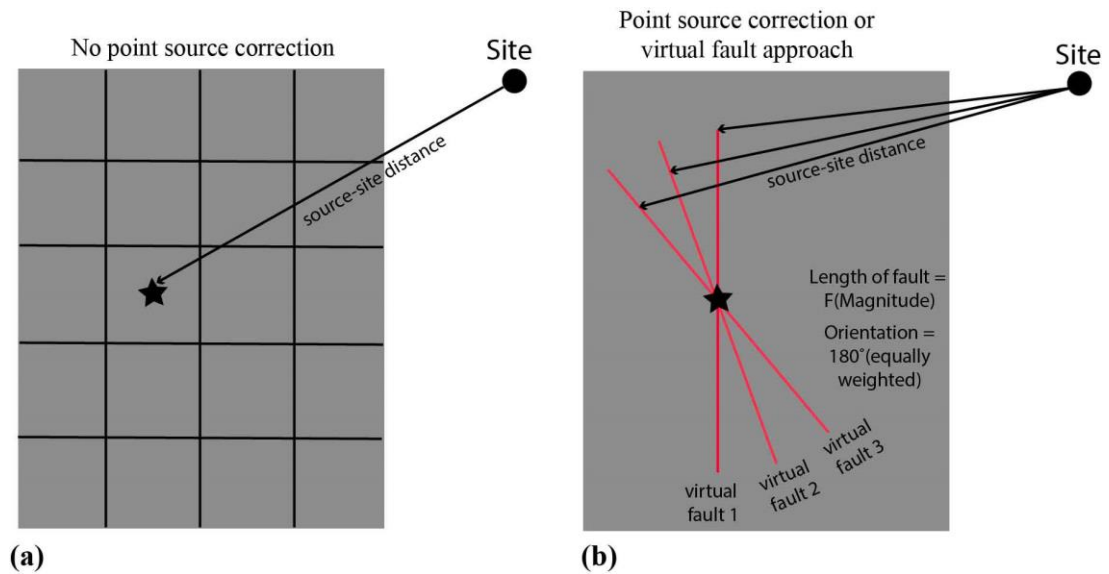


Figure 4.20. Vertical projection of a rectangular areal source zone defined for hazard calculations. (a) Diagram that shows how the epicenter of the scenario earthquake is moved within the source geometry and calculation of the source-to-site distance without point source correction, (b) application of virtual fault concept for point source correction

A set of preliminary analysis is conducted to evaluate the sensitivity of the hazard outcome to the style of faulting and application of the point source correction. In these sensitivity runs; rock site conditions are assumed with $V_{S30}=760$ m/s and only the area source zone is utilized in the hazard calculations. Because the activity rate is assumed to be homogenous within the source zone boundaries, instead of a regional map, the peak ground accelerations (PGA) at 20 representative points shown in Figure 4.21(a) are calculated. Figures 4.21(b) and 4.21(d) present the PGA values with 475-year return period for Points 1-10 (distributed in NW to SE direction) and Points 11-20 (distributed in SW to NE direction), respectively. Similarly, Figures 4.21(c) and 4.21(e) shows the PGA values with 2475-year return period for the same points.

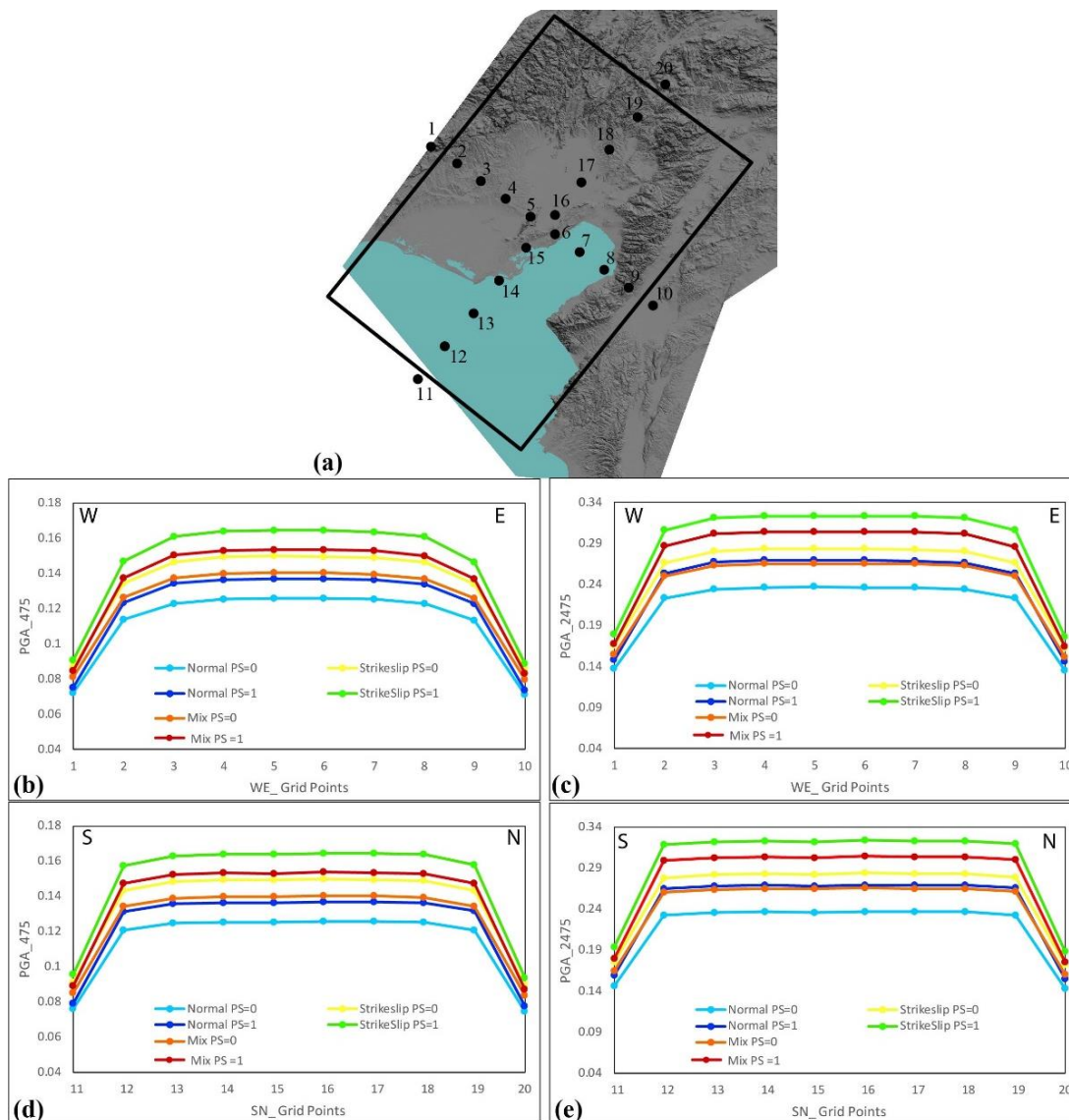


Figure 4.21. (a) Map view of 20 grid points selected in the region to analyze the influence of style of faulting and point source correction on the estimated ground motions. PGA values obtained along the WE profile for (b) 475-year return period and (c) 2475-year return period. PGA values obtained along the SN profile for (d) 475-year return period and (e) 2475-year return period. In (b-e), PS=0: no point source correction, PS=1: with point source correction

It should be noted that the PGA values for both return periods show almost no spatial variation along the EW and NS profiles, except for the points that are close to the edge; therefore, the ground motion estimates are approximately constant within source zone as expected. About 50% decrease in the PGA values is observed at the points that are located outside the area source boundaries (Points 1 & 10 in WE profile and Points 11 & 20 in SN profile). The influence of the style of faulting and dip angle assigned to the source is noticeable: when all the earthquakes generated by the area source are assumed to be normal events, estimated 475-year PGA values are equal to 0.12g (blue lines). If the mechanism of the area source zone is assumed to be 100% strike-slip, then the 475-year PGA values increase to 0.148g (yellow lines in Figure 4.21). Orange lines (Figure 4.21) show the ground motion estimates when the style-of-faulting implied by the FMS (Figure 4.14) is implemented in the logic tree with weights given in Figure 4.19, without the point source correction (PS=0). When the point source correction is applied (PS=1) (red line in Figure 4.21), approximately 10% increase in the hazard estimates is observed, independent of the style-of-faulting logic tree. Increase in the ground motion estimates is consistent with the previous literature (e.g. Gupta, 2013); therefore, the logic tree given in Figure 4.19 is combined with the point source correction for further PSHA analysis of the proposed area source zone.

4.5.4. PSHA Maps for the Study Area and Comparison with TSHM (2018)

In order to create the PSHA maps shown in Figure 4.22, two sets of hazard calculations are performed for 760 grid points in the study area, assuming rock site conditions ($V_{S30}=760$ m/s). For the ground motion estimates given in Figure 4.22(b), the planar (fault-based) seismic sources defined by Gülerce et al. (2017) are combined with the ground motion logic tree used in this study (Table 4.3). The 475-years PGA values shown in Figure 4.22(a) are calculated by adding the new area source zone to the planar seismic sources and using the same ground motion logic tree. For better visualization of the spatial distribution of the difference, residual and percent increase maps are given in Figures 4.22(c) and 4.22(d), respectively. Figure 4.22 shows that the ground motions in the Adana Basin and Gulf of Iskenderun are dominated by the

planar fault sources (Ceyhan-Kozan, Karatas-Turkoglu, Orontes, Amanos and Kyrneia fault systems). According to Figure 4.22(c), integration of the new area source zone results in 0.02g-0.08g increase in 475-year PGA values, for the locations within the area source zone boundaries. The influence of the new area source zone is negligible in the vicinity of planar structures with relatively higher slip rates (e.g. Kyrenia, Karataş-Türkoğlu); nevertheless, its influence increases in the vicinity of Orontes and Amanos fault systems due to the low slip rates assigned to these structures compared to other planar fault systems. As the distance between the site and the fault plane increases, the effect of area source on the hazard estimates increase gradually; estimated ground motions in the westernmost part of the study area is entirely dominated by the area source zone (Figure 4.22d).

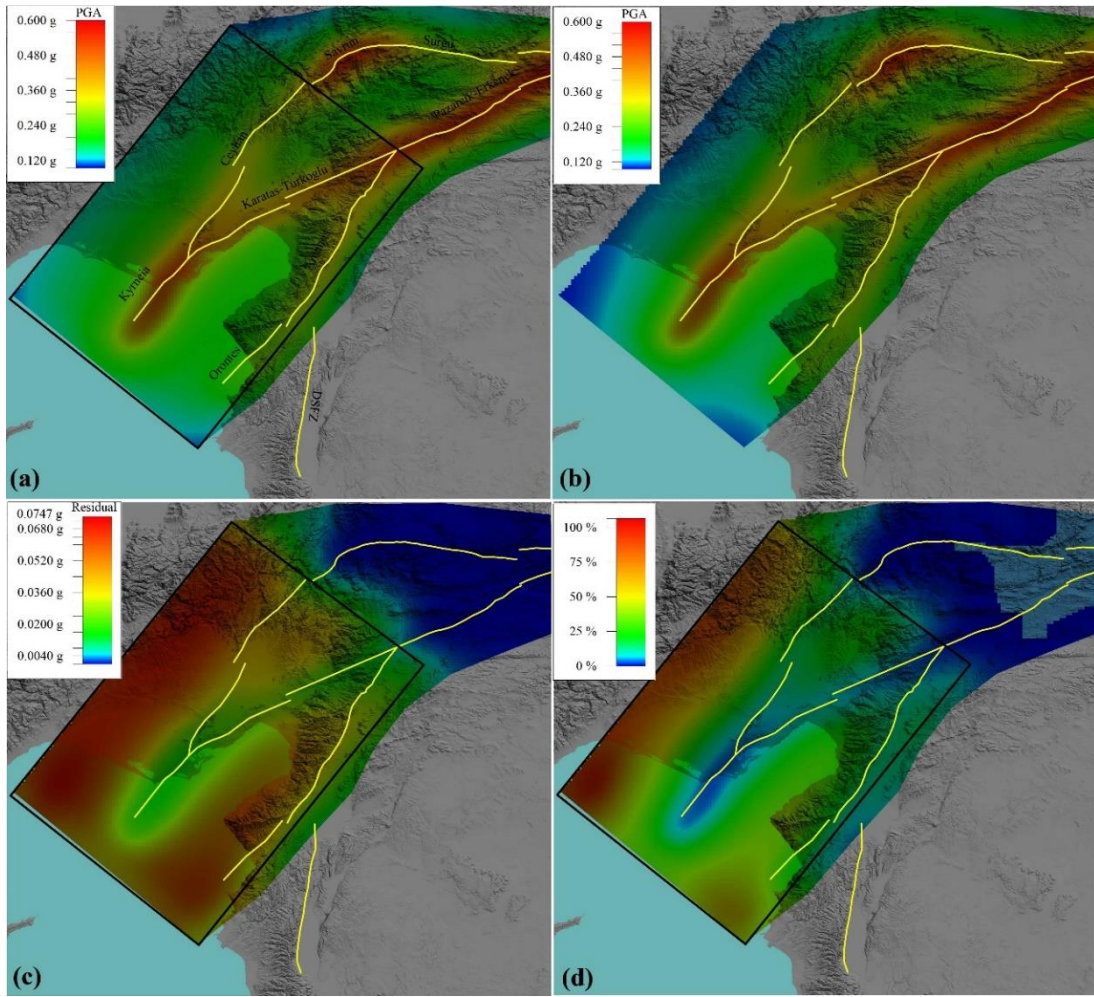


Figure 4.22. (a) 475-year PGA values estimated by combining the planar seismic sources of Gülerce et al. (2017) with the new additional source zone and with the new ground motion logic tree (proposed map), (b) 475-year PGA values estimated by combining only the planar seismic sources of Gülerce et al. (2017) with the new ground motion logic tree, (c) Residual PGA value map (a) – (b) showing the effect of adding the new area source zone (d) Percentage increase in PGA values from (b) to (a)

Figure 4.23 compares the PSHA map proposed in this study (Figure 4.22a) with TSHM for 475-year PGA at rock site conditions ($V_{S30}=760\text{m/sec}$) in terms of residual PGA maps. Residual PGA values in the first map (Figure 4.23a) is obtained by using the seismic source model (fault and area) proposed in this study; however, the ground motion logic tree proposed in this study is used in the first alternative and the GMM logic tree employed of TSMH is utilized in the second alternative. Hence, residuals in Figure 4.23(a) only quantifies the effect of the logic tree for ground motion models when the seismic source model proposed in this study is utilized in calculations. Residuals are varying from 0.02g to 0.04g, reaching up to 0.05g (negative). TSHM GMM are giving 0.02-0.04g higher estimates. Figure 4.23(b) quantifies the effect of SSC model on PGA estimates. Subtracting the PGA values in TSHM from the PGA values computed in this study (Figure 4.23b) shows that this study has significantly higher ground motion estimates (up to 0.2g) in the vicinity of Kyrneia, Turkoglu and Ceyhan-Kozan fault systems. The reason is that these planar fault systems are either missing in the planar SSC model of TSHM or they are assigned a lower activity rate. On the contrary, PGA values in the vicinity of Orontes (1.5mm slip) and Amanos systems (3.5mm slip rate) are slightly underestimated (up to 0.05g) due to the fact that TSHM utilized a single strand for EAFZ system in the SSC model while Gulerce et al., 2017 distributed the cumulative slip rate (~10mm) among the fault systems in the region. Kyrneia is accommodating majority of the slip rate (6.5mm), hence producing higher hazard estimates (up to 0.25g higher than TSHM). Apart from the planar fault sources, the areal source zone has produced slightly lower (~0.05g) PGA estimates in its western vicinity as compared to the TSHM.

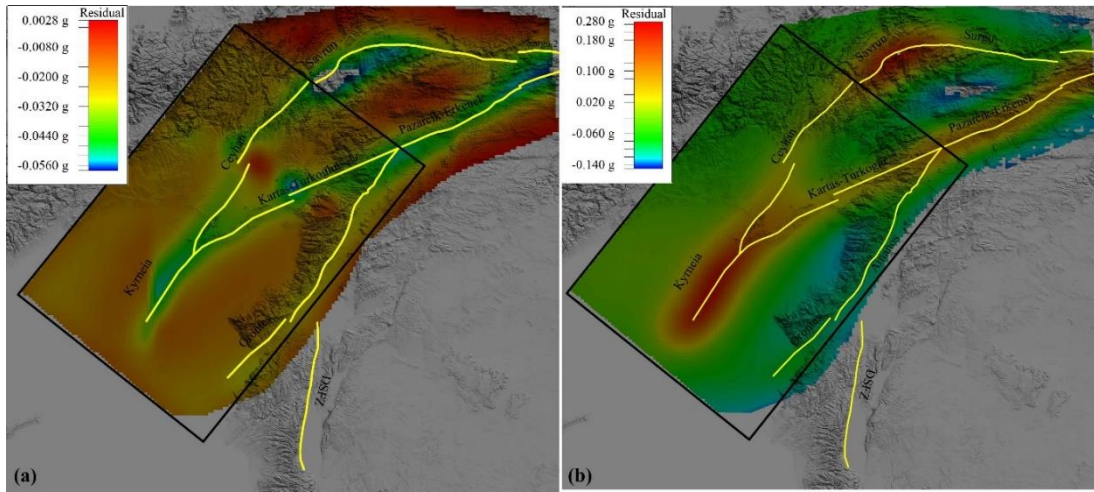


Figure 4.23. (a) Residuals calculated from our proposed SSC model with our GMM logic tree minus (-) our proposed SSC model with TSHM GMM logic. (b) Residual PGA value map obtained by subtracting the PGA value map of TSHM from the PGA value map computed in this study. SSC model utilized for this study is Gulerce et al 2017 planar model + areal source and the logic tree for GMM is adopted from TSHM

CHAPTER 5

CONCLUSIONS AND RECOMMENDATIONS

The primary objective of this study was to establish protocols for parameterization of seismic source models in fault-based probabilistic seismic hazard assessment (PSHA) for regions characterized by complex tectonic environments and sparse dataset conditions. For this purpose, state-of-the-art fault-based seismic source characterization (SSC) models for three representative cases of compressional, extensional and mixed tectonic environments are developed. For each case, a comprehensive seismotectonic database that includes geological, seismic and geodetic data is compiled and integrated into the SSC models in order to envisage the planar fault geometries and minimize the uncertainties induced by the simplifications in the source parameters due to the constraints of current PSHA practices. Along the course of this study, distinct issues in SSC modelling were faced for each tectonic environment; therefore, unique sets of sensitivity analysis are performed for each case to evaluate the effect of these issues on the hazard estimates.

For the first case study, the Makran subduction zone (Chapter 2), most of the critical issues that were faced during the SSC modelling are related to the geometry of the subducting plate; such as the seismogenic depth and dip angle of the interface and characterization of the aseismic portion of the megathrust. Effect of the selected magnitude distribution model on the spatial distribution of the ground motion estimates was also found to be significant due to the large magnitude potential of the interface zone. Based on the evaluation of various sensitivity test results; a planar SSC model for Makran subduction zone, its associated accretionary prism faults and the adjoining Chaman transform fault zone is developed and implemented in PSHA for updating the hazard map of the region. The case study given in Chapter 3 is related to extensional regimes that are often characterized by multiple sets of closely spaced

faults. Because the fault geometry in such regions does not allow the hazard modeler to estimate accurate activity rates for individual fault segment, a protocol to calculate and discretize the segment-specific activity rates using multiple dataset is established for the northern part of Western Anatolian Extensional province. Later, weighted, maximum and minimum 475-year PGA maps of the region are computed to provide constraints on the uncertainties induced by the type and density of data used for activity rate characterization. The last case study given in Chapter 4 was selected to assess the contribution of areal source zones that are created to model the seismicity that cannot be associated to known faults in a region. For this purpose, polarity and amplitude ratio data of 141 events is analyzed to compute the focal mechanism solutions (FMS) in the Central Anatolian region of Turkey. The updated FMS catalogue is utilized for investigating the active stress patterns and its association with the active fault structures in the region. The FMS and stress tensor inversion results are later extended to parameterize an areal source zone in this complex active tectonic setting. The SSC model for the region is updated by integrating the findings of this study with the previously published planar fault model and ultimately the seismic hazard map for the region is updated. A brief summary of the considered SSC modelling complexities and performed sensitivity analysis for each case study is provided in Figure 5.1.

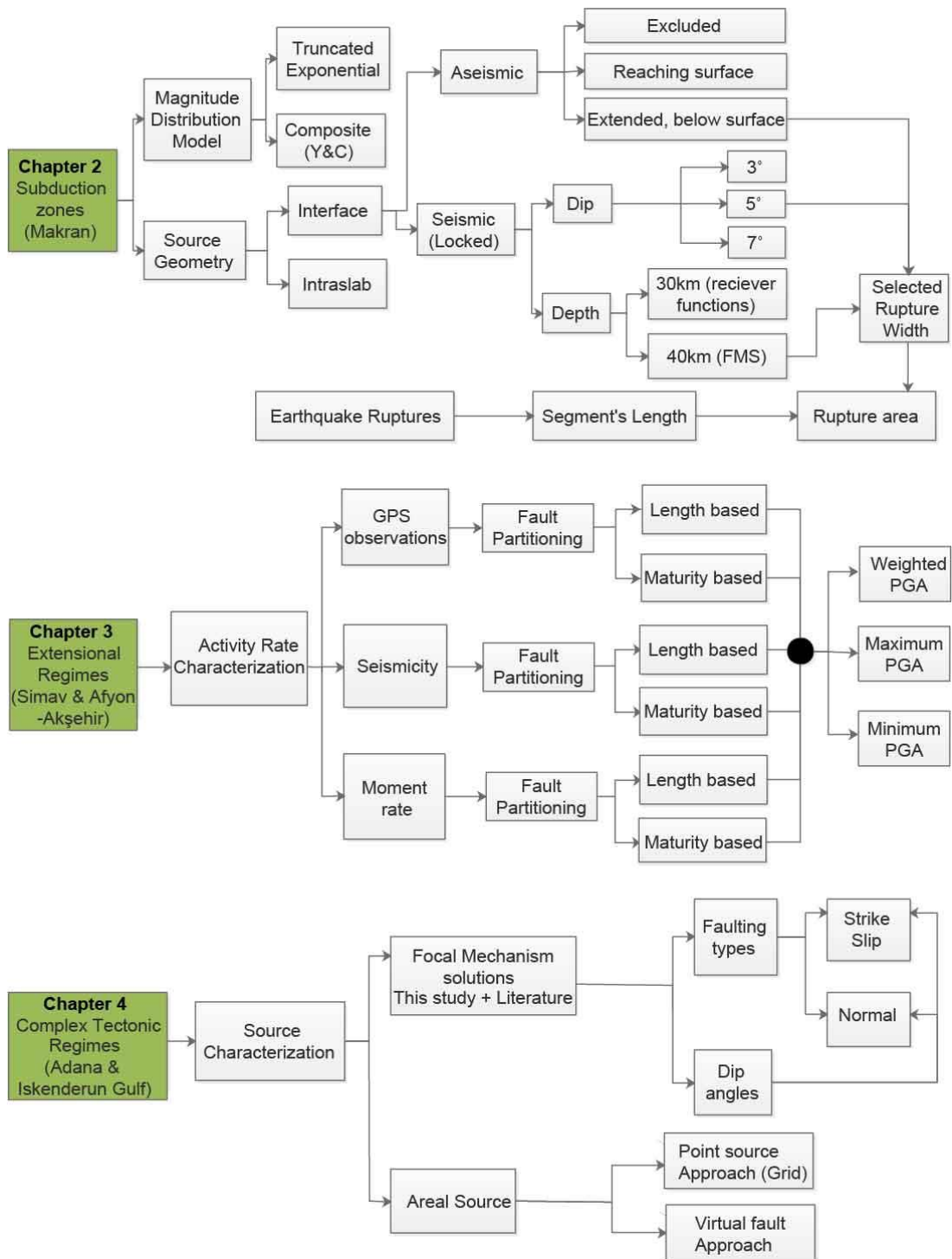


Figure 5.1. Flow chart showing the seismic source modelling complexities investigated in this study

Important findings and conclusions of this study can be summarized as follows:

- The fault-based PSHA conducted for the Makran subduction zone and Chaman transform fault zone in Pakistan (Chapter 2) has updated the seismic hazard map of the transitional region where active subduction is partly translated to large lateral motions by a major transform fault zone. Updated seismic hazard map for the region is one of the most significant contributions of this study (Figure 2.9).
- The ground motion estimates along the Chaman transform fault zone are equally distributed on both sides of transform fault zone due to its strike-slip nature. Among the transform fault systems, Ornach-Nal and Ghazaband fault systems result in the highest hazard estimates due to high slip rate; while, Gardez fault system results in the lowest PGA estimates due to the low slip rate assigned to this structure. Chaman Fault System S2 resulted in low ground motion estimates, because a part of the annual slip might be accommodated in the form of fault creep or by other faults in the vicinity.
- In regions that are governed by the interaction of subduction and transform deformation, the effects of transition deformation should be considered while characterizing the accretionary prism faults (Figure 2.3). These faults are generally governed by subduction deformation, but their nature can change along-strike to oblique, if transform deformation comes into play as shown by the Makran case study. In this study, two sets of faults with different mechanisms (thrust & oblique) were identified. Among these two sets, the set of thrust faults produced slightly higher ground motions when compared to the oblique counterpart faults (Figure 2.8).
- Makran intra-slab zone produced comparatively low 475-year PGA values due to its large seismogenic depth (i-e 40km).
- The combined hazard map (Figure 2.9) showed that the ground motions originating from the Makran megathrust are quite close to the ground motions originating from the Chaman transform fault zone. On the other hand, the high hazard zone associated with Makran extends for almost 250 km from the location

of trench, in contrast to the narrow (~20km on both sides of fault) high hazard zone of the Chaman fault system.

- A small change in the depth and dip angle of Makran interface plane leads to significant changes in the rupture dimensions. The sensitivity analysis showed that the estimated ground motions and their spatial distribution in the vicinity of Makran are sensitive to the selected depth extent and dip amount of the megathrust interface. Gentler and deeper extending interface geometries resulted in lower PGA values towards the trench and higher PGA values towards inland along accretionary wedge region. On the contrary, the effect of source geometry of the aseismic portion of Makran on ground motion estimates is restricted to only near trench offshore regions.
- The earthquake distribution models and their associated parameters also have considerable influence on the activity rates of controlling earthquake scenarios. Magnitude recurrence models for subduction zones that lack a detailed seismic history should be carefully chosen and the predicted recurrence rates should be compared to the recorded seismicity in order to avoid overestimation or underestimation of recurrence rates of controlling earthquakes.
- Fault-based PSHA analysis carried out across the Simav and Afyon-Akşehir graben systems in Western Anatolia (Chapter 3) addressed the problem of activity rate characterization in closely spaced faults in extensional regimes.
- PGA maps (Figures 3.6, 3.7, 3.8, 3.9) showed that among fault systems, the highest ground motion estimates are associated with the Simav fault and the central part of the study area (Gediz region), due to the high density of seismicity and geodetic data in these regions.
- Hazard maps also indicate that the activity rates and their effect on the ground shaking levels are influenced by the type and density of data available for the region. Comparison of hazard results obtained from all the methods showed that the slip rate based activity rates translate into the highest hazard estimates; while

moment and seismicity based activity rates translates to comparatively lower ground motion values.

- Spatial distribution of ground motion values is also dependent on type and density of the available data. For instance, in seismicity and moment rate based approaches: the regions that were struck by large magnitude earthquakes in the instrumental period have higher ground motion estimates and vice versa. On the contrary, slip rate based activity rates translates into more uniform spatial distribution of PGA values.
- The discretization or partitioning methodologies do not show considerable influence on the level and spatial distribution of estimated ground motions.
- Systematically low hazard estimates were obtained from the seismicity and moment rate based activity rate calculation methods. The underlying reason for this possible underestimation is that the utilized earthquake catalogue might not sample the return period of characteristic earthquake events in the concerned region. On the contrary, slip rate based calculation method might overestimate the activity rates (hence overestimate the hazard); if a part of the total slip is accommodated in the form of aseismic creep.
- Comparison of hazard estimates with the recently published Turkish Seismic Hazard Map (TSHM) showed that planar SSC models lead to higher PGA values in regions that are situated in the graben basins due to the oppositely dipping nature of faults. On the contrary, the mix model that includes both areal and planar source zones (e.g. TSHM) produced high hazard values for sites that are situated outside the graben due to homogeneous seismicity distribution of the areal sources.
- In order to evaluate uncertainties in PSHA associated with the off-fault seismicity in complex tectonic settings, focal mechanisms analysis followed by stress tensor inversions were conducted for the Central Anatolia (Chapter 4), where diffuse seismicity and mixed earthquake mechanisms are reported. Later, the PSHA analysis is updated for Adana Basin and Gulf of Iskenderun region using a revised SSC model utilizing virtual fault approach.

- FMS analysis showed that majority of the solutions computed are of strike-slip nature, followed by a considerable number of normal fault solutions. The mechanism of solutions correlated well with the active tectonic structures of the region. For instance, the solutions in eastern part of the study area are mostly strike-slip in nature that can be associated to EAFZ. The central part of the study area is dominated by mixture of strike-slip and normal solutions that can be associated with the strike-slip and normal structures in the region i.e. CAFZ, Tuz Gölü fault zone, Adana Basin and Gulf of Iskenderun regions etc.
- SH_{max} orientations in the area are pre-dominantly oriented in NS or NE-SW orientations favoring strike-slip or normal faulting along the major fault structures in the region.
- The results of stress tensor inversion showed that majority of sub-regions are characterized by strikeslip tectonic regimes with ~NS oriented maximum principal stress axes (σ_1) and ~EW oriented minimum principal stress (σ_3) axes.
- Adana Basin and Gulf of Iskenderun region is characterized by mixture of FMS solutions where the maximum (σ_1) and intermediate (σ_2) stress axis are oriented in sub-vertical position indicating a mixed tectonic regime that can facilitate both normal (σ_1 is vertical) and strikeslip (σ_2 is vertical) earthquake ruptures. The analysis showed that the strikeslip events are rupturing along a conjugate set of fault structures (oriented in NE-SW & NW-SE) while normal earthquakes are rupturing along ~NS oriented fault structures.
- An areal source zone characterized by utilizing the findings of this study was added to the previously published SSC model of the region (Gulerce et al. 2017) to account for off-fault seismicity and complex tectonics involved in the region.
- Sensitivity analysis showed that the virtual fault approach resulted in ~10% higher ground motions as opposed to the point source approach which is typically utilized for areal source zones. Although the hazard in the vicinity of areal source is dominated by the planar seismic sources due to their high slip rates; the additional

areal source increased the PGA estimates by up to 0.08g in locations that are situated at distance from the planar structures (Figure 4.22).

- The comparison with the recently published Turkish seismic hazard map showed that; due to differences in the SSC model and their parameters, the residual PGA values reaches up to ~0.2g (Figure 4.23).

There are still many issues related to the seismic source characterization for PSHA that remains unresolved due to lack of detailed datasets. A summary of recommendations to further improve the SSC models is given below:

- The planar (or fault-based) SSC models for all the regions selected as case studies in this thesis require more data and observations from geological field works and seismological records to further improve the models.
- The earthquake catalogues available for relatively quiescent and less explored regions such as Makran are incomplete and generally characterized by heterogeneities in space and time. They require further improvements that can be achieved by the addition of historical earthquake records from paleo-seismologic studies and by improving the density of seismic network in the future.
- The aseismic portions associated to the megathrust interfaces are generally overlooked in SSC models of subduction zones, even though they have significant influence on the near-trench ground motion estimates. The geometry and dimensions of aseismic sections in subduction zones needs systematic characterization, which may be achieved by seismic imaging studies.
- In shallow dipping subduction zones, the dip angle and the depth of megathrust interface play a vital role in controlling the rupture areas, source-to-site distances and the spatial distribution of hazard estimates. Therefore, these parameters should be examined in detail and should be constrained with available seismic data (e.g. FMS and receiver function studies etc.).
- The intra-slab zone of subduction zone had to be modelled as an areal source zone in this study due to the lack of seismologic and geologic data. More precise planar

SSC models should be developed for modelling the rather complex ruptures originating within the intra-slab zones.

- In closely spaced fault structures (e.g. graben systems); slip rate is often utilized for calculating the activity rate of seismic sources, provided that the resolution of geodetic data is sufficient to estimate the total slip that is accommodated across graben structures. But it is worth mentioning that graben structures may be asymmetric in nature, implying variable slip being accommodated on both sides of the graben. Similarly, the slip rates may also vary along the strike of graben structures. This issue of non-uniform slip rate needs further investigation that can be achieved by dense geodetic networks and supplementing the geodetic data with geologic/paleoseismic studies.
- The modeled slip rate was distributed among the individual faults using maturity and length ratio of faults in this study. Other geomorphic indices (e.g. mountain front sinuosity curves, drainage pattern asymmetry factors, valley floor to width ratio etc.) that indicates the relative tectonic activity of fault structures can be utilized in the future for slip rate partitioning.
- In order to account for off-fault seismicity and complex tectonics, areal source with virtual fault approach is utilized in this study. Although the approach has improved the ground motion estimates, it still has limitations. The approach assumes the virtual faults to be randomly oriented (180°) in the vicinity of areal source, hence not providing any control on the strike direction of faults which can influence the fault-to-site distances. The strike directions of such complex fault structures can be constrained to some degree (e.g. rose diagrams from FMS), but the hazard codes available at the moment cannot integrate strike directions of virtual faults into hazard computations and needs further improvement in this regard.
- The segmentation models proposed in this study are based on qualitative criteria such as fault gaps, structural complexities and earthquake ruptures etc. and needs further improvement based on paleoseismological earthquake records and physics

based mechanical models to improve and reduce the epistemic uncertainties related to segmentation models.

REFERENCES

- Abrahamson N. A., Silva W. J., Kamai R., 2014. Summary of the ASK14 ground motion relation for active crustal regions, *Earthquake Spectra*, 30, 1025-1055.
- Abrahamson, N. A., and Silva, W. J., 2008. Summary of the Abrahamson & Silva NGA ground motion relations, *Earthquake Spectra*, 24, 67-97.
- Abrahamson, N., Gregor, N., & Addo, K., 2016. BC hydro ground motion prediction equations for subduction earthquakes. *Earthquake Spectra*, 32(1), 23–44.
- Afet ve Acil Durum Yönetimi Başkanlığı, Turkey (AFAD). <http://www.deprem.gov.tr/>. Last accessed, July 2016.
- Akkar, S., Azak, T., Çan, T., Çeken, U., Demircioğlu-Tümsa, M. B., Duman, T. Y., & Zülfikar, Ö., 2018. Evolution of seismic hazard maps in Turkey. *Bulletin Earthquake Engineering*. <https://doi.org/10.1007/s10518-018-0349-1>
- Akkar, S., and Cagnan, Z., 2010. A Local Ground-motion Predictive Model for Turkey and its Comparison with Other Regional and Global Ground-motion Models. *Bulletin of the Seismological Society of America*, 100, 2978-2995.
- Akkar, S., Cagnan, Z., Yenier, E., Erdogan, E., Sandikkaya, M. A., and Gulkan, P., 2010. The Recently Compiled Turkish Strong Motion Database: Preliminary Investigation for Seismological Parameters, *Journal of Seismology*, 14, 457-479
- Akkar S, Sandikkaya, M. A., Bommer, J. J., 2014. Empirical ground-motion models for point- and extended- source crustal earthquake scenarios in Europe and the Middle East, *Bull. Earthq. Eng.* 12, 359–387
- Aktug, B., Nocquet, J. M., Cingöz, A., Parsons, B., Erkan, Y., England, P., Lenk, O., Gürdal, M.A., Kilicoglu, A., Akdeniz, H., and Tekgüll, A., 2009. Deformation of western Turkey from a combination of permanent and campaign GPS data, *Journal of Geophysical Research*, 114: B10404.
- Aktuğ, B., Parmaksız, E., Kurt, M., Lenk, O., Kılıçoğlu, A., Gürdal, M. A., and Özdemir, S., 2013. Deformation of Central Anatolia: GPS implications. *Journal of Geodynamics*, 67, 78-96.

- Akyuz, H. S., Altunel, E., Karabacak, V., and Yalciner, C. C., 2006. Historical earthquake activity of the northern part of the Dead Sea Fault Zone, southern Turkey, *Tectonophysics*, 426, 281-293.
- Altamimi, Z., Métivier, L., & Collilieux, X., 2012. ITRF2008 plate motion model. *Journal of Geophysical Research: Solid Earth*, 117(7), 1–14.
- Ambraseys N. N., Jackson, J. A., 1998. Faulting associated with historical and recent earthquakes in the Eastern Mediterranean region. *Geophys J. Int.*, 133, 390–406
- Ambraseys, N. N., and Barazangi, M., 1989. The 1759 earthquake in the Bekaa valley: Implications for earthquake hazard assessment in the Eastern Mediterranean region. *J. of Geophys. Res.*, 94, 4007–4013.
- Ambraseys, N. N., Melville, C. P., and Adams, R. D., 1994. The Seismicity of Egypt, Arabia and the Red Sea. King Abdulaziz City for Science & Technology. Cambridge University Press.
- Ambraseys, N., & Bilham, R., 2003. Earthquakes and associated deformation in Northern Baluchistan 1892-2001. *Bulletin of the Seismological Society of America*, 93(4), 1573–1605.
- Anderson, J.G. and Trifunac, M. D., 1978. Uniform Risk Functionals for Characterization of Strong Earthquake Ground Motion, *Bull. Seism. Soc. Am.*, 68, 205-218.
- Anderson, M., Alvarado, P., Zandt, G. and Beck, S., 2007. Geometry and brittle deformation of the subducting Nazca Plate, Central Chile and Argentina. *Geophysical Journal International*, 171(1), 419-434.
- Arpat, E., and Şaroğlu, F., 1972. The East Anatolian Fault System: thoughts on its development, *Min. Res. Expl. Inst. Turkey Bull.*, 78, 33-39.
- Avouac, J. P., Ayoub, F., Wei, S., Ampuero, J. P., Meng, L., Leprince, S., ... Helmberger, D., 2014. The 2013, Mw 7.7 Balochistan earthquake, energetic strike-slip reactivation of a thrust fault. *Earth and Planetary Science Letters*, 391, 128-134.
- Baba, T., Hirata, K., Hori, T., & Sakaguchi, H., 2006. Offshore geodetic data conducive to the estimation of the afterslip distribution following the 2003 Tokachi-oki earthquake. *Earth and Planetary Science Letters*, 241(1–2), 281–292.
- Barnhart, W., R. Briggs, N. Reitman, R. Gold, & G. Hayes, 2015. Evidence for slip partitioning and bimodal slip behavior on a single fault: Surface slip characteristics of

the 2013 Mw 7.7 Balochistan, Pakistan earthquake, *Earth Planet. Sci. Lett.*, 420, 1-11.

Bernard, M., B. Shen-Tu, W. Holt, and D. M. Davis, 2000. Kinematics of active deformation in the Sulaiman Lobe and Range, Pakistan, *J. Geophys. Res.*, 105(B6), 253–13, 279.

Bernardi, F., Braunmiller, J., Kradolfer, U., and Giardini, D., 2004. Automatic regional moment tensor inversion in the European-Mediterranean region, *Geophys. J. Int.*, 156, 1–14.

Bhatti, A. Q., Hassan, Z. S., Rafi, Z., Khatoon, Z., & Ali, Q., 2011. Probabilistic seismic hazard analysis of Islamabad, Pakistan. *Journal of Asian Earth Sciences*, 42, 468-478.

Bilek, S. L., & Lay, T., 2002. Tsunami earthquakes possibly widespread manifestations of frictional conditional stability, 29(14), 1–4.

Bird, P., 2003. An updated digital model of plate boundaries, *Geochem. Geophys. Geosyst.*, 4, 1027, doi:10.1029/2001GC000252.

Birsoy, S., 2018. Earthquake Focal Mechanism Analysis of Central Anatolia. *M.Sc. Thesis*, Middle East Technical University.

Bommer, J. J., & Akkar, S., 2012. Consistent source-to-site distance metrics in ground-motion prediction equations and seismic source models for PSHA, *Earthquake Spectra*, 28(1), 1-15.

Boore D. M., Stewart J. P., Seyhan E., Atkinson G. M., 2014. NGA-West2 equations for predicting PGA, PGV, and 5% damped PSA for shallow crustal earthquakes, *Earthquake Spectra*, 30, 1057-1085.

Boore, D. M., and Atkinson, G. M., 2008. Ground-motion prediction equations for the average horizontal component of PGA, PGV, and 5%-damped PSA at spectral periods between 0.0 1s and 10.0s, *Earthquake Spectra*, 24, 99-139.

Boore, D. M., Stewart, J. P., Seyhan, E., & Atkinson, G. M., 2014. NGA-West2 equations for predicting vertical-component PGA, PGV, and 5%-damped PSA from shallow crustal earthquakes. *Earthquake Spectra*, 32(2), 1005-1031.

Boyd, O. S., Mueller, C. S., & Rukstales, K. S., 2007. Preliminary probabilistic seismic hazard map for Afghanistan: U.S. Geological Survey. *Open-File Report*, 2007-1137.

- Bozkurt, E., 2001. Neotectonics of Turkey-a synthesis. *Geodinamica Acta*, 14, 3-30.
- Bozorgnia, Y., Abrahamson, N. A., Al Atik, L., Ancheta, T. D., Atkinson, G. M., Baker, J. W., ... Youngs, R., 2014. NGA-West2 research project. *Earthquake Spectra*, 30(3), 973-987.
- Byrne, D. E., Sykes, L. R., & Davis, D. M., 1992. Great Thrust Earthquakes and Aseismic Slip Along the Plate Boundary of the Makran subduction zone. *Journal of Geophysical Research*, 97(B1), 449-478.
- Byrne, D. E., D. M. Davis, & Sykes, L. R., 1988. Loci and maximum size of thrust earthquakes and the mechanics of the shallow region of subduction zones, *Tectonics*, 7(4), 833-857.
- Campbell, K. W., and Bozorgnia, Y., 2014. NGA-West2 ground motion model for the average horizontal components of PGA, PGV, and 5%-damped linear acceleration response spectra, *Earthquake Spectra*, 30, 1087-1115.
- Campbell, K. W., and Bozorgnia, Y., 2008. NGA ground motion model for the geometric meanhorizontal component of PGA, PGV, PGD and 5% damped linear elastic response spectra for periods ranging from 0.01 to 10s, *Earthquake Spectra*, 24, 139-173.
- Campbell, K. W., & Gupta, N., 2018. Modeling diffuse seismicity in probabilistic seismic hazard analysis: Treatment of virtual faults, *Earthquake Spectra*, 34(3), 1135-1154.
- Canitez, N., and Üçer, S. B., 1967. A Catalogue of Focal Mechanism Diagrams for Turkey and Adjoining Areas, *İTÜ Maden Fak., Arz Fizigi Enst.*, 25, 111.
- Chartier, T., Scotti, O., Clément, C., Jomard, H. and Baize, S., 2017a. Transposing an active fault database into a fault-based seismic hazard assessment for nuclear facilities-Part 2: Impact of fault parameter uncertainties on a site-specific PSHA exercise in the Upper Rhine Graben, eastern France, *Natural Hazards and Earth System Sciences*, 17(9), 1585-1593.
- Chartier, T., Scotti, O., Lyon-Caen, H., & Boiselet, A., 2017b. Methodology for earthquake rupture rate estimates of fault networks: Example for the western Corinth rift, Greece, *Nat. Hazards Earth Syst. Sci.*, 17(10), 1857-1869.
- Chiou, B. S. J. and Youngs, R. R., 2008. An NGA Model for the Average Horizontal Component of Peak Ground Motion and Response Spectra, *Earthquake Spectra*, 24, 173-215.

- Chiou, B. S. J. and Youngs, R. R., 2014. Update of the Chiou and Youngs NGA model for the average horizontal component of peak ground motion and response spectra, *Earthquake Spectra*, 30, 1117-1153.
- Chuang, R. Y., and K. M. Johnson, 2011. Reconciling geologic and geodetic model fault slip-rate discrepancies in Southern California: Consideration of nonsteady mantle flow and lower crustal fault creep, *Geology*, 39(7), 627-630, doi: 10.1130/G32120.1.
- Cornell, C. A., 1968. Engineering Seismic Risk Analysis, *Bull. Seism. Soc. Am.*, 58, 1583-1606.
- Cosentino, P., Ficara, V., and Luzio, D., 1977. Truncated Exponential Frequency-magnitude Relationship in the Earthquake Statistics, *Bull. Seismol. Am.*, 67, 1615–1623.
- Courtillot, V., R. Armijo, and P. Tapponier, 1987. The Sinai triple junction revisited, *Tectonophysics*, 141, 181-190.
- Crotwell, H. P., Owens, T. J. and Ritsema, J., 1999. The TauP Toolkit: Flexible seismic travel-time and ray-path utilities, *Seismological Research Letters*, 70, 154–160.
- Crupa, W. E., Khan, S. D., Huang, J., Khan, A. S., & Kasi, A., 2017. Active tectonic deformation of the western Indian plate boundary: A case study from the Chaman Fault System. *Journal of Asian Earth Sciences*, 147, 452–468.
- Danciu, L., Şeşetyan, K., Demircioglu, M., Gülen, L., Zare, M., Basili, R., ... Giardini, D., 2017. The 2014 Earthquake Model of the Middle East: seismogenic sources. *Bulletin of Earthquake Engineering*, 1–32.
- Delph, J.R., Abgarmi, B., Ward, K.M., Beck, S.L., Özacar, A.A., Zandt, G., Sandvol, E., Türkelli, N., and Kalafat, D., 2017, The effects of subduction termination on the continental lithosphere: Linking volcanism, deformation, surface uplift, and slab tearing in central Anatolia, *Geosphere*, 13(6), 1788–1805.
- Delvaux, D., and Sperner, B., 2003. Stress tensor inversion from fault kinematic indicators and focal mechanism data: the TENSOR program. In: Nieuwland, D. (Ed.), *New Insights into Structural Interpretation and Modelling*, *Geol. Soc. Lond. Spec. Publ.*, 212, 75–100.
- DeMets, C., Gordon, R. G., & Argus, D. F., 2010. Geologically current plate motions. *Geophysical Journal International*, 181(1), 1-80.

Demircioğlu M. B., Şeşetyan, K., Duman, T. Y., Çan, T., Tekin, S., Ergintav, S., 2017. A probabilistic seismic hazard assessment for the Turkish territory: part II-fault source and background seismicity model. *Bull. Earthq. Eng.* <https://doi.org/10.1007/s10518-017-0130-x>

Deutsches GeoForschungsZentrum (GFZ). <http://geofon.gfz-potsdam.de>. Last accessed July 2016.

Dewey, J. F., Hempton, M. R., Kidd, W.S.F., Şaroğlu, F., and Şengör, A. M. C., 1986. Shortening of continental lithosphere: the neotectonics of eastern Anatolia-a young collision zone, in: Coward M.O., Ries A.C. (Eds.), Collisional Tectonics. *Geological Society Special Publication*, 19, 3-36.

Dewey, J. F., Şengör, A. M. C., 1979. Aegean and surrounding regions: complex multiplate and continuum tectonics in a convergent zone, *Geol. Soc. Am. Bull.*, 90, 84

Duman, T. Y., Çan, T., Emre, Ö., Kadirioglu, F. T., Başarır, B. N., Kılıc, T., Arslan, S., Özalp, S., Kartal, R. F., Kalafat, D., Karakaya, F., Eroğlu, A. T., Özel, N. M., Ergintav, S., Akkar, S., Altınok, Y., Tekin, S., Cingöz, A., Kurt, A. İ., 2016. Seismotectonic database of Turkey. *Bull. Earthq. Eng.*, doi:10.1007/s10518-016-9965-9

Dziewonski, A. M., Chou, T. A. & Woodhouse, J. H., 1987. Determination of earthquake source parameters from waveform data for studies of global and regional seismicity. *J. Geophys. Res.*, 86, 2825-2852.

Dziewonski, A., Ekström, G., Franzen, J., and Woodhouse, J., 1987a. Global seismicity of 1977: centroid-moment tensor solutions for 471 earthquakes, *Physics of the Earth and Planetary Interiors*, 45 (1), 11–36.

Dziewonski, A., Ekström, G., Franzen, J., and Woodhouse, J., 1987b. Global seismicity of 1978: centroid-moment tensor solutions for 512 earthquakes, *Physics of the Earth and Planetary Interiors*, 46, (4), 316-342.

Ekström, G., M. Nettles, & Dziewonski, A. M., 2012. The global CMT project 2004-2010: Centroid-moment tensors for 13,017 earthquakes. *Phys. Earth Planet. Inter.*, 200-201, 1-9.

Electric Power Research Institute (EPRI), 2012. Technical Report: Central and Eastern United States (CEUS) Seismic Source Characterization for Nuclear Facilities. EPRI, Palo Alto, CA, U.S. DOE, and U.S. NRC: 2012.

Emre, Ö., T. Y. Duman, S. Özalp, F. Şaroğlu, Ş. Olgun, H. Elmacı, and T. Çan, 2016. Active fault database of Turkey, *Bull. Earthq. Eng.*, 1-47, doi: 10.1007/s10518-016-0041-2.

Engdahl, E. R., & Villaseñor, A., 2002. 41 Global seismicity: 1900-1999. *International Geophysics*, 81(PART A), 0–12. [https://doi.org/10.1016/S0074-6142\(02\)80244-3](https://doi.org/10.1016/S0074-6142(02)80244-3)

Erdik, M., Alpay, B. Y., Onur, T., Sesetyan, K. and Birgoren, G., 1999. Assessment of Earthquake Hazard in Turkey and Neighbouring Regions, *Ann. Di Geofisica*, 42, 1125-1138.

Erdik, M., K. Sesetian, M.B. Demircioglu, C. Tuzun, D. Giardini, L. Gulen, S. Akkar, M. Zare, 2012. Assessment of Seismic Hazard in the Middle East and Caucasus: *EMME (Earthquake Model of Middle East) Project, Proceedings*, 15th WCEE, Lisboa

Ergin, M., Aktar, M., and Eyidoğan, H., 2004. Present-day seismicity and seismotectonics of the Cilician Basin: eastern Mediterranean region of Turkey, *Bulletin of the Seism. Soc. of America*, 94(3), 930-939.

Ergin, M., Aktar, M., Özalaybey, S., Tapirdamaz, M.C., Selvi, O., Tarancıoğlu, A., 2009. A high-resolution aftershock seismicity image of the 2002 Sultandagi-Çay earthquake (Mw=6.2), Turkey, *Journal of Seismology*, 13, 633-646.

Eyidoğan, H., and Jackson, J. A., 1985. A seismological study of normal faulting in the Demirci, Alaşehir and Gediz earthquake of 1960-1970 in western Turkey: implications for the nature and geometry of deformation in the continental crust, *Geophysical Journal of Royal Astronomy Society*, 81, 569–607.

Fattahi, H., & Amelung, F., 2016. InSAR observations of strain accumulation and fault creep along the Chaman Fault system, Pakistan and Afghanistan. *Geophysical Research Letters*, 43(16), 8399–8406.

Frankel, A., 1995. Mapping seismic hazard in the Central and Eastern United States, *Seismological Research Letters*, 66, 8-21.

Frankel, A., Chen, R., Petersen, M., Moschetti, M., and Sherrod, B., 2015. 2014 Update of the Pacific Northwest Portion of the U.S. National Seismic Hazard Maps, 2015, *Earthquake Spectra*, 31(1), 131–148

Frohling, E., & Szeliga, W., 2016. GPS constraints on interplate locking within the Makran subduction zone. *Geophysical journal International*, 205(1), 67–76.

Fujiwara, H., Kawai, S., Aoi, S., Morikawa, N., Senna, S., Kudo, N., Ooi, M., Hao, K. X., Wakamatsu, K., Ishikawa, Y., Okumura, T., Ishii, T., Matsushima, S., Hayakawa, Y., Toyama, N., and Narita, A., 2009. Technical reports on national seismic hazard maps for Japan, National Res. Inst. for Earth Science and Disaster Prevention, *Technical Note*, 336, 52.

Furuya, M., & Satyabala, S. P., 2008. Slow earthquake in Afghanistan detected by InSAR. *Geophysical Research Letters*, 35(6), 4–7.

GEOFON Data Centre. GEOFON Seismic Network. Deutsches Geo Forschungs Zentrum (GFZ). <http://geofon.gfz-potsdam.de>.

Giardini, D., Gruenthal, G., Shedlock, K., & Zhang, P., 1999. The Global Seismic Hazard Map. *Annali Di Geofisica*. [https://doi.org/10.1016/S0074-6142\(03\)80188-2](https://doi.org/10.1016/S0074-6142(03)80188-2)

Goldstein, P., Dodge, D., Firpo, M., and Minner, L., 2003. SAC2000: signal processing and analysis tools for seismologists and engineers, in *The IASPEI International Handbook of Earthquake and Engineering Seismology*, edited by W. H. K. Lee et al., London: Academic Press.

Görgün, E., 2014. Source characteristics and Coulomb stress change of the 19May 2011Mw6.0 Simav-Kütahya earthquake, Turkey, *J. Asian Earth. Sci.*, 87, 79-88.

Grünthal, G., Bosse, C., Sellami, S., Mayer-Rosa, D., Giardini, D., 1999. Compilation of the GSHAP regional seismic hazard for Europe, Africa and the Middle East, *Annali di Geofisica*, 42, 1215-1223.

Gülerce, Z., Kargioğlu, B., and Abrahamson, N. A., 2016. Turkey-Adjusted NGA-West1 Horizontal Ground Motion Prediction Models, *Earthquake Spectra*, 32, 75-100.

Gülerce, Z., Shah, S. T., Menekşe, A., Özacar, A. A., Kaymakci, N. and Çetin, K. O., 2017. Probabilistic Seismic-Hazard Assessment for East Anatolian Fault Zone Using Planar Fault Source Models, *Bulletin of the Seismological Society of America*, 107(5), 2353–2366.

Gupta, I. D., 2013. Source-to-site distance distributions for area type of seismic sources used in PSHA applications. *Natural hazards*, 66(2), 485-499.

Habermann, R.E., 1987. Man-made changes of seismicity rates. *Bull. Seism. Soc. Am.*, 77(1), 141-159.

Haq, S. S. B., & Davis, D. M., 1997. Oblique convergence and the lobate mountain belts of western Pakistan. *Geology*, 25(1), 23–26.

- Hashash, Y. M. A., Kim, B., Olson, S. M., & Ahmad, I., 2012. Seismic Hazard Analysis Using Discrete Faults in Northwestern Pakistan: Part II – Results of Seismic Hazard Analysis. *Journal of Earthquake Engineering*, 16(8), 1161–1183.
- Hearn E. H., F. F. Pollitz, W. R. Thatcher, and C. T. Onishi, 2013. How do “ghost transients” from past earthquakes affect GPS slip rate estimates on southern California faults?, *Geochem. Geophys. Geosyst.*, 14, 828–838.
- Hecker, S., Abrahamson, N. A., & Wooddell, K. E., 2013. Variability of displacement at a point: Implications for earthquake-size distribution and rupture hazard on faults. *Bull. Seismol. Soc. Am.*, 103, 651–674.
- Hempton, M., 1987. Constraints on Arabian plate motion and extensional history of the Red Sea. *Tectonics*, 6(6), 687-705.
- Hempton, M. R., J. F. Dewey, and F. Şaroğlu, 1981. The East Anatolian Transform Fault: Along strike variations in geometry and behavior, *Eos Trans. AGU*, 62, 393
- Herrendörfer, R., Van Dinther, Y., Gerya, T., & Dalguer, L. A., 2015. Earthquake supercycle in subduction zones controlled by the width of the seismogenic zone. *Nature Geoscience*, 8(6), 471–474.
- Hsu, Y.-J., Rosenzweig, C., Livermore, M., Jones, J. W., Curry, R. B., Boote, K. J., ... Fischer, G., 2006. Frictional afterslip following the 2005 Nias-Simeulue earthquake, Sumatra. *Science*, 312, 1921–1926
- Hyndman, R. D., Yamano, M., & Oleskevich, D. A., 1997. The seismogenic zone of subduction thrust faults. *Island Arc*, 6(3), 244–260.
- International Seismological Centre (ISC). *On-line Bulletin*, <http://www.isc.ac.uk>, Internatl. Seismol. Cent., Thatcham, United Kingdom. Last accessed July, 2015. <http://doi.org/10.31905/D808B830>
- Jackson, J. A., and McKenzie, D. P., 1988. The relationship between plate motions and seismic moment tensors and rates of active deformation in the Mediterranean and Middle East, *Geophysical Journal*, 93, 45-73.
- Jackson, J., and McKenzie, D., 1984. Active tectonics of the Alpine-Himalayan Belt between western Turkey and Pakistan, *Geophysical Journal of Royal Astronomical Society*, 77, 185-264.
- Johnston, A. C., K. J. Coppersmith, L. R. Kanter, and C. A. Cornell, 1994. The Earthquakes of Stable Continental Regions, *Volume 1: Assessment of Large*

Earthquake Potential, Electric Power Research Institute (EPRI), Palo Alto, California, TR-102261s-V1.

Jolivet, R., et al., 2014. The 2013 Mw 7.7 Balochistan earthquake: Seismic potential of an accretionary wedge. *Bull. Seismol. Soc. Am.*, 104(2), 1020–1030.

Kale, Ö., 2017. Some discussions on data-driven testing of Ground Motion Prediction Equations under the Turkish ground-motion database, *Journal of Earthquake Engineering*, doi:10.1080/13632469.2017.1323047

Kalkan, E, and Gülkan, P., 2004. Site-dependent spectra derived from ground motion records in Turkey, *Earthquake Spectra*, 20, 1111-1138.

Kandilli Observatory and earthquake Research Institute (KOERI). <http://www.koeri.boun.edu.tr/>, Last accessed, 31 July 2016.

Karasözen, E., E., Nissen, E. A., Bergman, K. L., Johnson, and R. J. Walters, 2016. Normal faulting in the Simav graben of western Turkey reassessed with calibrated earthquake relocations, *J. Geophys. Res. Solid Earth*, 121, doi:10.1002/2016JB012828.

Karasözen, E., Özacar, A. A, Biryol, C. B., and Beck, S. L., 2014. Seismicity, focal mechanisms and active stress field around the central segment of the North Anatolian Fault in Turkey, *Geophys. J. Int.*, 196, 405-421.

Kayabalı, K., 2002. Modeling of seismic hazard for Turkey using the recent neotectonic data, *Eng. Geol.*, 63, 221-232.

Kaymakçı, N., Özmutlu, Ş., van Dijk, M., and Özçelik, Y., 2010. Surface and Subsurface Characteristics of the Çankırı Basin (Central Anatolia, Turkey): Integration of Remote Sensing, Seismic Interpretation and Gravity, *Turkish J. Earth Sci.*, 19, 79-100.

Khan, M. A., Bendick, R., Bhat, M. I., Bilham, R., Kakar, D. M., Khan, S. F., ... Wahab, A., 2008. Preliminary geodetic constraints on plate boundary deformation on the western edge of the Indian plate from TriGGnet (Tri-University GPS Geodesy Network). *Journal of Himalayan Earth Sciences*, 41, 71–87.

Kiratzi, A., 2002. Stress tensor inversions along the westernmost north and central Aegean Sea, *Geophys. J. Int.*, 106, 433-490.

Kiratzi, A., Louvari, E., 2003. Focal mechanisms of shallow earthquakes in the Aegean Sea and the surrounding lands determined by waveform modelling: a new database, *J. Geodyn.*, 36, 251-274.

Kishida, T., Bozorgnia, Y., Abrahamson, N., ... Youngs, R., 2017. Development of the NGA-Subduction Database. *16th World Conference on Earthquake Engineering, 16WCEE, Chile*, 3452.

Klinger, Y., Avouac, J. P., Abou-Karaki, N., Dorbath, L., Bourles, D., Reyss, J. L., 2000. Slip rate on the Dead Sea transform fault in northern Araba Valley (Jordan), *Geophysical Journal International*, 142, 755–768.

Koçyiğit, A. and Özacar, A., 2003. Extensional Neotectonic Regime through the NE Edge of the Outer Isparta Angle, Sw Turkey: New Field and Seismic Data. *Turkish Journal of Earth Sciences*, 12, 67–90.

Koçyiğit, A., and Beyhan, A., 1998. A new intracontinental transcurrent structure: the Central Fault Zone, Turkey, *Tectonophysics*, 284, 317-336.

Koçyiğit, A., and Erol, O., 2001. A tectonic escape structure: Erciyes pull-apart basin, Kayseri, Central Anatolia, Turkey, *Geodinamica Acta*, 14, 133-145.

Kopp, C., Fruehn, J., Flueh, E. R., Reichert, C., Kukowski, N., Bialas, J., & Klaeschen, D., 2000. Structure of the makran subduction zone from wide-angle and reflection seismic data. *Tectonophysics*, 329(1–4), 171–191.

Kramer, S. L., 1996. *Geotechnical Earthquake Engineering*. Published by Pearson Education Pte. Ltd.

Kreemer, C., Klein, E., Shen, Z.-K., Wang, M., Estey, L., Wier, S., & Boler, F., 2014. A geodetic platemotion and Global Strain Rate Model. *Geochemistry, Geophysics, Geosystems*, 130.

Lawrence, R. D., & Yeats, R. S., 1979. Geological reconnaissance of the Chaman Fault in Pakistan, in *Geodynamics of Pakistan*, edited by A. Farah and K. A. DeJong, Geological Survey of Pakistan, Quetta.

Lawrence, R. D., S. H. Khan, & Nakata, T., 1992. Chaman Fault, Pakistan-Afghanistan. *Annales Tectonicae*, 6, 196–223.

Lawrence, R. D., Yeats, R. S., Khan, S. H., Farah, A., & DeJong, K. A., 1981. Thrust and strike slip fault interaction along the Chaman transform zone, Pakistan. *Geological Society, London, Special Publications*, 9(1), 363–370.

Le Pichon, X. Angelier, J., 1981. The Aegean Sea, *Phil. Trans. R. Soc. Lond.*, 300, 357-372.

- Le Pichon, X., and J. M. Gaulier, 1988. The rotation of Arabia and the Levant fault system, *Tectonophysics*, 153, 271-274.
- Lund, B., and Townend, J., 2007. Calculating horizontal stress orientations with full or partial knowledge of the tectonic stress tensor, *Geophys. J. Int.*, 1328-1335.
- McClusky, S., Balassanian, S., Barka, A.A., Demir, C., Ergintav, S., Georgiev, I., Gürkan, O., Hamburger, M., Hurst, K., Kahle, H.G., Kastens, K., Kekelidze, G., King, R., Kotzev, V., Lenk, O., Mahmoud, S., Mishin, A., Nadariya, M., Ouzounis, A., Paradissis, D., Peter, Y., Prilepin, M., Reilinger, R.E., Sanlı İ., Seeger, H., Tealeb, A., Toksöz, M.N., and Veis, G., 2000. Global Positioning System constraints on plate kinematics and dynamics in the Eastern Mediterranean and Caucasus, *Journal of Geophysical Research*, 105, 5695–5720.
- McGuire, R. K., 2004. Seismic Hazard and Risk Analysis, Earthquake Engineering Research Institute, *MNO-10*.
- McKenzie, D. P., 1972. Active Tectonics of the Mediterranean Region, *Geophys. J. R. Astr. Soc.*, 30, 109-185.
- McKenzie, D. P., 1978. Active Tectonics of the Alpine-Himalayan Belt: the Aegean Sea and Surrounding Regions, *Geophys. J. R. Astr. Soc.*, 55, 217-254.
- Mohadjer, S., Bendick, R., Ischuk, A., Kuzikov, S., Kostuk, A., Saydullaev, U., ... Zubovich, A. V., 2010. Partitioning of India-Eurasia convergence in the Pamir-Hindu Kush from GPS measurements. *Geophysical Research Letters*, 37(4), 1–6.
- Monalisa, Khwaja, A. A., & Jan, M. Q., 2007. Seismic hazard assessment of the NW Himalayan fold-and-thrust belt, Pakistan, using probabilistic approach. *Journal of Earthquake Engineering*, 11(2), 257–301.
- National Engineering Services Pakistan (NESPAK), 2006. Revision/updating of building code of Pakistan, stage 1, Recommendations for preliminary seismic design parameters and criteria for seismic resistant design of buildings in Islamabad-Rawalpindi area. Ministry of Housing and Works, Government of Pakistan
- Norwegian Seismic Array (NORSAR) and Pakistan Meteorological Department (PMD), 2006. Seismic Hazard Analysis for the Cities of Islamabad and Rawalpindi. *Building Code of Pakistan: Seismic Provisions (2007)*, Ministry of Housing, Govt. of Pakistan
- Oldham, T., 1883. A catalogue of Indian earthquakes from the earliest time to the end of A.D. 1869. *Memoirs of the Geological Survey of India*, 29, 163–215.

Örgülü, G., Aktar, M., Türkelli, N., Sandvol, E., and Barazangi, M., 2003. Contribution to the seismotectonics of Eastern Turkey from moderate and small size events, *Geophysical Research Letters*, 30, 8040.

Orhan, A., Seyrek E., Tosun, H., 2007. A probabilistic approach for earthquake hazard assessment of the Province of Eskisehir, Turkey, *Nat. Hazards Earth Syst. Sci.*, 7, 607-614.

Özbey, C., Sari, A., Manuel, L., Erdik, M., Fahjan, Y., 2004. An empirical attenuation relationship for northwestern Turkey ground motion using a random effects approach, *Soil Dynamamics and Earthquake Engineering*, 24,115-125.

Pace, B., Peruzza, L., Lavecchia, G., and Boncio, P., 2006. Layered seismogenic source model and probabilistic seismic-hazard analyses in central Italy. *Bulletin of the Seismological Society of America*, 96(1), 107-132.

Pacific Northwest National Laboratory (PNNL), 2014. Hanford *Sitewide Probabilistic seismic Hazard Analysis*, Report PNNL-23361, prepared for the U.S. Department of Energy, under Contract DE-AC06076RL01830.

Papazachos, B., Kiratzi, A., Papadimitriou, E., 1991. Regional Focal Mechanism for Earthquakes in the Aegean area, *Pure Appl. Geophys.*, 136, 407-420.

Penney, C., Tavakoli, F., Saadat, A., Nankali, H. R., Sedighi, M., Khorrami, F., ... Priestley, K., 2017. Megathrust and accretionary wedge properties and behaviour in the Makran subduction zone, *Geophysical Journal International*, 209, 1800-1830.

Petersen, M. D., Harmsen, S. C., Jaiswal, K. S., Rukstales, K. S., Luco, N., Haller, K. M., ... Shumway, A. M., 2018. Seismic hazard, risk, and design for south america. *Bulletin of the Seismological Society of America*, 108(2), 781–800.

Petersen, M. D., Moschetti, M. P., Powers, P. M., Mueller, C. S., Haller, K. M., Frankel, A. D., ... Olsen, A. H., 2015. Documentation for the 2014 Update of the United States National Seismic Hazard Maps. *U.S. Geological Survey Open-File Report*, 243.

Pondrelli, S., A. Morelli, G. Ekström, S. Mazza, E. Boschi, and A. M. Dziewonski, 2002. European-Mediterranean regional centroid-moment tensors: 1997-2000, *Physics of the Earth and Planetary Interiors*, 130, 71-101.

Pondrelli, S., Ekström, G., Morelli, A., and Primerano, S., 1999. Study of source geometry for tsunamigenic events of the Euro-Mediterranean area, in *International Conference on Tsunamis*, 297-307.

- Pondrelli, S., Morelli, A. and Ekström, G., 2004. European-Mediterranean regional centroid-moment tensor catalog: solutions for years 2001 and 2002, *Physics of the Earth and Planetary Interiors*, 145, 127-147.
- Pondrelli, S., Salimbeni, S., Morelli, A., Ekström, G., and Boschi, E., 2007. European-Mediterranean Regional Centroid Moment Tensor catalog: Solutions for years 2003 and 2004, *Physics of the Earth and Planetary Interiors*, 164, 90-112.
- Pondrelli, S., Salimbeni, S., Morelli, A., Ekström, G., Postpischl, L., Vannucci, G., and Boschi, E., 2011. European-Mediterranean Regional Centroid Moment Tensor Catalog: solutions for 2005-2008, *Phys. Earth Planet. Int.*, 185, 74-81.
- Rafi, Z., Lindholm, C., Bungum, H., Laghari, A., & Ahmed, N., 2012. Probabilistic seismic hazard map of Pakistan, Azad Jammu and Kashmir. *Natural Hazards*, 61(03), 1317–1354
- Reasenberg, P., 1984. Second-order Moment of Central California Seismicity, 1969-82, *J. Geophys. Res.*, 90, 5479-5495.
- Reilinger, R., McClusky, S., Vernant, P., Lawrence, S., Ergintav, S., Cakmak, R., ... Karam, G., 2006. GPS constraints on continental deformation in the Africa-Arabia-Eurasia continental collision zone and implications for the dynamics of plate interactions. *Journal of Geophysical Research: Solid Earth*, 111(5), 1–26.
- Reiter, L., 1990. Earthquake Hazard Analysis: Issues and Insights, Columbia University Press, New York.
- Rong, Y., Jackson, D. D., Magistrale, H., & Goldfinger, C., 2014. Magnitude limits of subduction zone Earthquakes. *Bulletin of the Seismological Society of America*, 104(5), 2359–2377.
- Rydelek, P.A., and I.S. Sacks, 1992. Comment on “Seismicity and detection/location threshold in the southern Great Basin seismic network” by Joan Gomberg, *J. Geophys. Res.*, 97, 15361-15362.
- Salamon, A., A. Hofstetter, Z. Garfunkel, and H. Ron, 1996. Seismicity of the eastern Mediterranean region: Perspective from the Sinai subplate, *Tectonophysics*, 263, 293-305.
- Salamon, A., Hofstetter, A., Garfunkel, Z., and Ron, H., 2003. Seismotectonics of the Sinai subplate-the eastern Mediterranean region, *Geophys. J. Int.*, 155, 149-173.
- Sançar, T., Zabcı, C., Karabacak, V., Yazıcı, M., & Akyüz, H. S., 2019. Geometry and Paleoseismology of the Malatya Fault (Malatya-Ovacık Fault Zone), Eastern Turkey:

Implications for intraplate deformation of the Anatolian Scholle, *Journal of Seismology*, 23(2), 319-340.

Şaroğlu, F., Emre, Ö. and Kuşcu, İ., 1992. Active fault map of Turkey, MTA, Ankara.

Schellart, W. P., & Rawlinson, N., 2013. Global correlations between maximum magnitudes of subduction zone interface thrust earthquakes and physical parameters of subduction zones. *Physics of the Earth and Planetary Interiors*, 225, 41–67.

Scholz, C. H., 1998. Earthquakes and friction laws, *Nature*, 391, 37-42.

Şengör, A. M. C., Görür, N., and Şaroğlu, F., 1985. Strike slip faulting and related basin formation in zones of tectonic escape: Turkey as a case study, In K. Biddle, N. Christie-Blick, eds., *Strike Slip Deformation, Basin Formation and Sedimentation: SEPM Special Publication*, 37, 227-264.

Şeşetyan, K., Demircioğlu, M. B., Duman, T., Çan, T., Tekin, S, Eroğlu, T., Zulfikar, F. Ö., 2018. A probabilistic seismic hazard assessment for the Turkish territory-part I: the area source model, *Bull. Earthq. Eng.*, <https://doi.org/10.1007/s10518-016-0005-6>.

Seyitoğlu, G., 1997. Late Cenozoic tectono-sedimentary development of the Selendi and Uşak-Güre basins: a contribution to the discussion on the development of east-west and north trending basins in western Anatolia, *Geological Magazine*, 134, 163-175.

Shah, S. T., Özacar, A. A., & Gulerce, Z., 2018. Procedure for fault-based PSHA in complex tectonic regimes (e.g. Western Anatolia): Implications of activity rate characterization, *Geophysical Research Abstracts*, 20, EGU2018-7182

Sibson, R. H., 1982. Fault zone models, heat flow, and the depth distribution of earthquakes in the continental crust of the United States, *Bulletin of the Seismological Society of America*, 72, 151-163.

Sibson, R. H., 1986. Earthquakes and rock deformation in crustal fault zone, *Annual Review of Earth and Planetary Sciences*, 14, 149-175.

Smith, G. L., McNeill, L. C., Wang, K., He, J., & Henstock, T. J., 2013. Thermal structure and megathrust seismogenic potential of the Makran subduction zone. *Geophysical Research Letters*, 40(8), 1528–1533.

Snoke, J.A., 2003. FOCMEC: FOCal MECHANism Determinations in *International Handbook of Earthquake and Engineering Seismology*, edited by W. H. K. Lee et al., chap. 8512, Academic, San Diego, Calif.

Stein, S., and Wysession, M., 2003. An introduction to seismology, earthquakes, and earth structure, Blackwell Publishing, UK.

Stirling, M., D. Rhoades, and K. Berryman, 2002. Comparison of earthquake scaling relations derived from data of the instrumental and pre-instrumental era, *Bull. Seism. Soc. Am.*, 92, 812-830.

Stirling, M., McVerry, G., Gerstenberger, M., Litchfield, N., Van Dissen, R., Berryman, K., ... Jacobs, K., 2012. National seismic hazard model for New Zealand: 2010 update. *Bulletin of the Seismological Society of America*, 102(4), 1514–1542.

Szeliga, W. M., 2010. Historical and Modern Seismotectonics of the Indian Plate with an Emphasis on its Western Boundary with the Eurasian Plate. *PhD thesis*, University of Colorado.

Szeliga, W., Bilham, R., Kakar, D. M., & Lodi, S. H., 2012. Interseismic strain accumulation along the western boundary of the Indian subcontinent. *Journal of Geophysical Research: Solid Earth*, 117(8), 1–14.

Szeliga, W., Furuya, M., Satyabala, S., & Bilham, R., 2006. Surface Creep along the Chaman Fault on the Pakistan-Afghanistan Border imaged by SAR interferometry *Eos Trans. AGU*, 85(52).

Tan O, Pabuc, cu Z et. Al., 2011. Aftershock study and seismotectonic implications of the 8 March 2010 Kovancilar (Elazığ, Turkey) earthquake ($M_w = 6.1$), *Geophys. Res. Lett.*, 38, L11304. doi:10.1029/ 2011GL047702

Tan, O., Tapırdamaz, M. C., Yoruk, A., 2008. The earthquake catalogues for Turkey, *Turk. J. Earth Sci.*, 17, 405-418.

Tanaka, A., 2004. Geothermal gradient and heat flow data in and around Japan (II): crustal thermal structure and its relationship to seismogenic layer, *Earth Planets Space*, 56, 1195-1199.

Tauxe, L., Kylstra, N. and Constable, C., 1991. Bootstrap statistics for paleomagnetic data, *Journal of Geophysical Research*, 96(B7): 11,723-11,740.

Taymaz, T., Jackson, J., McKenzie, D., 1991. Active tectonics of the north and central Aegean Sea, *Geophys. J. Int.*, 106, 433-490.

Taymaz, T., Price, S. P., 1992. The 12.05.1971 Burdur earthquake sequence: a synthesis of seismological and geological observations, *Geophys. J. Int.*, 108, 589-603.

Tichelaar, B. W., & Ruff, L. J., 1993. Depth of seismic coupling along subduction zones. *Journal of Geophysical Research*, 98(B2), 2017–2037.

Turkey Earthquake Building Code (TEBC-2018), 2018. Afet ve Acil Durum Yönetimi Başkanlığı, Ankara, Turkey

Valentini, A., Visini, F., & Pace, B., 2017. Integrating faults and past earthquakes into a probabilistic seismic hazard model for peninsular Italy, *Natural Hazards and Earth System Sciences*, 17(11), 2017-2039.

Vannucci, G., and Gasperini, P., 2004. The new release of the database of Earthquake Mechanisms of the Mediterranean Area (EMMA Version 2), *Annals of Geophysics*, 47, 307-334.

Walker, J. P. F., Visini, F., Roberts, G., Galasso, C., McCaffrey, K. and Mildon, Z., 2018. Variable fault geometry suggests detailed fault slip-rate profiles and geometries are needed for fault-based probabilistic seismic hazard assessment (PSHA), *Bull. Seismol. Soc. Am.*, 109, 110-123.

Walsh, D., Arnold, R. and Townend, J., 2008. A Bayesian approach to determining and parameterising earthquake focal mechanisms, *Geophysical Journal International*, 176(1): 235-255.

Wang, K., & Hu, Y., 2006. Accretionary prisms in subduction earthquake cycles : The theory of dynamic Coulomb wedge, *J. Geophys. Res.*, 111, 1-16.

Wang, Y. J., Chan, C. H., Lee, Y. T., Ma, K. F., Shyu, J. H., Rau, R. J. and Cheng, C. T., 2016. Probabilistic seismic hazard assessments for Taiwan, *Terr. Atmos. Ocean. Sci.*, 27, 325-340.

Wang, Y. J., Chan, C. H., Lee, Y. T., Rau, R. J., & Cheng, C. T., 2016. Probabilistic Seismic Hazard Assessment for Taiwan. *Terrestrial, Atmospheric and Oceanic Sciences*, 27(3), 325–340.

Waseem, M., Giovanni, C., & Enrico, L., 2018. Seismic hazard assessment of northern Pakistan. *Natural Hazards*, 90(2), 563–600.

Weatherill, G. A., M. Pagani, J. Garcia, 2017. Modelling In-slab Subduction Earthquakes in PSHA: Current Practice and Challenges for the Future, *In Proceedings of the 16th World Conference on Earthquake Engineering*, Santiago, Chile.

Wells, D. L., 1994. New Empirical Relationships among Magnitude , Rupture Length, Rupture Width , Rupture Area , and Surface Displacement. *Bull. Seism. Soc. Am.*,

84(4), 974–1002.

Wesnowsky, S. G., 1994: The Gutenberg-Richter or characteristic earthquake distribution, which is it? *Bull. Seismol. Soc. Am.*, 84, 1940-1959

Westaway, R., 1994. Present-day kinematics of the Middle East and eastern Mediterranean, *J. of Geophys. Res.*, 99(6), 12071-12090.

Westaway, R., and Arger, J., 1996. The Gölbaşı basin, southeastern Turkey: A complex discontinuity in a major strike-slip fault zone, *J. Geol. Soc.*, 153, 729-743.

Wiemer, S., 2001. A software package to analyze seismicity: ZMAP, *Seismological Research Letters*, 72, 373-382.

Wiemer, S., and Wyss, M., 1997. Mapping the frequency-magnitude distribution in asperities: an improved technique to calculate recurrence times, *Journal of Geophysical Research*, 102(B7), 15115-15128.

Wiemer, S., and Wyss, M., 2000. Minimum magnitude of completeness in earthquake catalogs: Examples from Alaska, the Western United States, and Japan, *Bulletin of the Seismological Society of America*, 90, 859-869.

Woessner, J., Laurentiu, D., Giardini, D., Crowley, H., Cotton, F., Grünthal, G., et al., 2015. The 2013 European seismic hazard model: Key components and results, *Bulletin of Earthquake Engineering*, 13(12), 3553-3596.

Working Group on California Earthquake Probabilities, 1995. Seismic hazards in southern California: probable earthquakes, 1994-2024, *Bull. Seismol. Soc. Am.*, 85, 379-439.

Working Group on California Earthquake Probabilities, 2003. Earthquake probabilities in the 792 San Francisco Bay Region: 2002–2031, *U.S. Geol. Soc., Open-File Rept.*, 03-214.

Yarar, R., Ergunay, O., Erdick, M. and Gulkan, P., 1980. A preliminary probabilistic assessment of the seismic hazard in Turkey, *Proc. 7th World Conf. Earthquake Eng., Istanbul*, 309-316.

Yeats, R. S., R. D. Lawrence, S. Jamil-ud din, and S. H. Khan, 1979. Surface effects of the 16 March 1978 earthquake, Pakistan-Afghanistan border, in *Geodynamics of Pakistan*, edited by A. Farah and K. A. DeJong, Geological Survey of Pakistan, Quetta.

Yılmaztürk, A., Burton, P. W., 1999. Earthquake source parameters as inferred from body waveform modeling, southern Turkey, *J. Geodynamics*, 27, 469-499.

Youngs, R. R., & Coppersmith, K. J., 1985. Implications of fault slip rates and earthquake recurrence models to probabilistic seismic hazard estimates. *Bulletin of the Seismological Society of America*, 75(4), 939–964.

Zaigham, N. A., 1991. Bela ophiolites and associated mineralization in southern part of axial-belt of Pakistan, *Ph.D. thesis*, University of Karachi.

Zaman, S., Ornthammarath, T., & Warnitchai, P., 2012. Probabilistic Seismic Hazard Maps for Pakistan. In Proceedings of the *15th World Conference on Earthquake Engineering WCEE*, 1–10.

Zanchi, A., Angelier, J., 1993. Seismotectonics of western Anatolia: regional stress orientation from geophysical and geological data, *Tectonophysics*, 222, 259-274.

Zhao, J. X., Zhang, J., Asano, A., Ohno, Y., Oouchi, T., Takahashi, T., Ogawa, H., Irikura, K., Thio, H. K., Somerville, P. G., Fukushima, Y., 2006. Attenuation relations of strong ground motion in Japan using site classifications based on predominant period, *Bull. Seismol. Soc. Am.*, 96, 898–913

Zhou, Y., R. T. Walker, J. R. Elliott, & Parsons, B., 2016. Mapping 3D fault geometry in earthquakes using high-resolution topography: Examples from the 2010 El Mayor-Cucapah (Mexico) and 2013 Balochistan (Pakistan) earthquakes. *Geophys. Res. Lett.*, 43, 3134–3142.

APPENDICES

A. Seismic source parameters used of all the fault systems used for Makran subduction zone and Chaman transform fault zone. The weights for each parameter in the SSC logic tree is provided in the brackets. Length and depth parameters are in km while Slip rates are in mm/yr.

Fault Information							b-value		Mmax		
Fault System	Rupture scenarios	Type	Dip	Slip Rate	Length	Max depth	Region specific (0.5)	Zone specific (0.5)	Mchar-1SD (0.25)	Mchar (0.5)	Mchar+1SD (0.25)
Gardez system	Gardez f1	Strike-slip	90	5.4	191	20	0.73	0.76	7.40	7.63	7.86
	Gardez f2	Strike-slip	90	5.4	99	20	0.73	0.76	7.11	7.34	7.57
	Gardez f1-f2	Strike-slip	90	5.4	290	20	0.73	0.76	7.59	7.82	8.05
Chaman System 1	Chaman S1 f1	Strike-slip	90	10	167	20	0.73	0.76	7.34	7.57	7.80
	Chaman S1 f2	Strike-slip	90	10	127	20	0.73	0.76	7.22	7.45	7.68
	Chaman S1 f1-f2	Strike-slip	90	10	294	20	0.73	0.76	7.59	7.82	8.05

Chaman System 2	Chaman S2	Strike-slip	90	10	227	20	0.73	0.76	7.48	7.71	7.94
Chaman System 3	Chaman S3 f1	Strike-slip	90	8.5	77	20	0.73	0.76	7.00	7.23	7.46
	Chaman S3 f2	Strike-slip	90	8.5	103	20	0.73	0.76	7.13	7.36	7.59
	Chaman S3 f3	Strike-slip	90	8.5	107	20	0.73	0.76	7.15	7.38	7.61
	Chaman S3 f1-f2	Strike-slip	90	8.5	179	20	0.73	0.76	7.38	7.61	7.84
	Chaman S3 f2-f3	Strike-slip	90	8.5	210	20	0.73	0.76	7.45	7.68	7.91
	Chaman S3 f1-f2-f3	Strike-slip	90	8.5	287	20	0.73	0.76	7.58	7.81	8.04
Ghazaband System	Ghazaband f1	Strike-slip	90	16	200	20	0.73	0.76	7.42	7.65	7.88
	Ghazaband f2	Strike-slip	90	16	131	20	0.73	0.76	7.24	7.47	7.70
	Ghazaband f3	Strike-slip	90	16	51	20	0.73	0.76	6.82	7.05	7.28
	Ghazaband f1-f2	Strike-slip	90	16	331	20	0.73	0.76	7.65	7.88	8.11
	Ghazaband f2-f3	Strike-slip	90	16	182	20	0.73	0.76	7.38	7.61	7.84
	Ghazaband f1-f2-f3	Strike-slip	90	16	383	20	0.73	0.76	7.71	7.94	8.17
	OrnachNal f1	Strike-slip	90	15	132	20	0.73	0.76	7.24	7.47	7.70

OrnachNal fault System	OrnachNal f2	Strike-slip	90	15	96	20	0.73	0.76	7.10	7.33	7.56
	OrnachNal f3	Strike-slip	90	15	67	20	0.73	0.76	6.94	7.17	7.40
	OrnachNal f1-f2	Strike-slip	90	15	228	20	0.73	0.76	7.48	7.71	7.94
	OrnachNal f2-f3	Strike-slip	90	15	163	20	0.73	0.76	7.33	7.56	7.79
	OrnachNal f1-f2-f3	Strike-slip	90	15	295	20	0.73	0.76	7.60	7.83	8.06
Siahan System 1	Siahan f1	Oblique	60	2	162	20	0.73	0.61	7.35	7.63	7.91
Siahan System 2	Siahan f2	Thrust	30	2	120	20	0.73	0.61	7.26	7.54	7.82
Panjgur System 1	Panjgur f1	Oblique	60	2	220	20	0.73	0.61	7.50	7.78	8.06
Panjgur System 2	Panjgur f2	Thrust	30	2	169	20	0.73	0.61	7.44	7.72	8.00
Hoshab System 1	Hoshab f1	Oblique	60	2	229	20	0.73	0.61	7.52	7.80	8.08
Hoshab System 2	Hoshab f2	Thrust	30	2	182	20	0.73	0.61	7.48	7.76	8.04
Kech Bend System 1	Kech Bend f1	Oblique	60	2	127	20	0.73	0.61	7.24	7.52	7.80
Kech Bend System 2	Kech Bend f2	Thrust	30	2	206	20	0.73	0.61	7.54	7.82	8.10
Quetta-Pishin System	Quetta-Pashin	Strike-slip		0.314*		20		1.004	7.26	7.49	7.72

							MLE (0.5)	WLS (0.5)	Strasser 2010 (0.25)	WC94 (0.5)	Allen & Hayes 2017 (0.25)
Makran Interface System	Megathrust f1	Thrust	10	17.1	95	40	0.64	0.57	8.20	8.33	8.41
	Megathrust f2	Thrust	10	17.1	159	40	0.64	0.57	8.39	8.53	8.64
	Megathrust f3	Thrust	10	17.1	189	40	0.64	0.57	8.45	8.60	8.72
	Megathrust f1-f2	Thrust	10	17.1	253	40	0.64	0.57	8.56	8.71	8.85
	Megathrust f2-f3	Thrust	10	17.1	348	40	0.64	0.57	8.67	8.83	8.99
	Megathrust f1-f2-f3	Thrust	10	17.1	443	40	0.64	0.57	8.76	8.93	9.10
Makran Intraslab	Intraslab zone	N/R		0.139*				0.497	7.50*	7.80*	8.00*

* in column 5 indicates seismicity-based activity rates

* in column 10,11 and 12 indicates that the M_{max} are not derived from magnitude-rupture area relations. For details refer to the discussion in text

B. Fault segments and the fault rupture systems included in the Seismic source model used in for western Anatolia case study. Slip rates assigned to fault systems using maturity and length ratio are shown. The seismicity rates and moment rates computed for seven polygons in the area are also presented. Downdip widths (N = 15.7Km; SS = 12.8km) are calculated from seismogenic depth (12km) and the dip amount of faults (N =50°; SS =70°). The observed Maximum magnitude earthquake (Mmax, observed) within each polygon is provided. The maximum magnitude earthquake that can occur on fault systems within each polygon (Mmax, computed) is calculated using Wells & Coppersmith (1994) relationships. N= Normal faults; SS = Strike-slip faults

Polygon Number	Fault System Name	Fault Segment Number	Length (km)	Fault type	Mmax (observed, Mw) in each polygon	Mmax (computed, Mw) in each Polygon	Slip Rate (Maturity based) mm/yr	Slip Rate (length based) mm/yr	Seismicity based Activity rate of Polygons (For M=5)	Moment rates of Polygons
1	1	1a	10.73	N	6.0	7.08	2.0	1.6	0.02207	5E+23
		1b	22.93	N						
		1c	11.20	N						
	2	2	12.68	N			1.0	1.4		
	3	3	9.17	N			1.0	1.4		
4	4	15.49	N	1.0	1.4					
2	5	5a	19.65	N	5.9	7.28	3.0	3.0	0.06156	8E+23
		5b	21.42	N						
		5c	29.00	N						
	6	6	6.02	N			0.1	0.1		
	7	7	18.38	N			0.3	0.3		
	8	8	8.99	N			0.1	0.1		
3	9	9	21.62	SS	5.9	6.87	1.0		0.04288	3E+23
	10	10	15.42	SS			1.0			
	11	11	14.97	SS			1.0			
	12	12	6.34	SS			1.0			
	13	13	31.80	SS			1.0			
	14	14	8.14	SS			1.0			

4	15	15a	21.09	N	7.1	7.17	1.0	1.1	0.11825	2E+24
		15b	15.96	N			1.0	1.0		
	16	16a	18.61	N						
		16b	21.38	N						
		16c	14.48	N						
	17	17a	32.28	N			1.0	0.9		
		17b	15.85	N						
18	18	22.77	N	1.0	1.1					
5	19	19a	17.46	N	5.9	7.05	2.0	1.6	0.01282	6E+22
		19b	10.64	N			2.0	1.6		
	20	20a	24.61	N						
		20b	16.82	N						
	21	21a	10.14	N			1.0	1.4		
		21b	9.37	N						
		21c	7.95	N						
	22	22a	12.37	N			1.0	1.4		
		22b	9.56	N						
		22c	5.60	N						
22d		8.33	N							
6	23	23a	23.97	N	6.2	7.36	3.0	3.0	0.03783	1E+24
		23b	60.11	N			1.5	1.8		
	24	24	22.56	N						
25	25	15.36	N	1.5	1.2					
7	26	26	24.29	SS	5.5	6.88	0.3	0.4	0.02197	9E+22
	27	27	27.64	SS			0.3	0.4		
	28	28	32.58	SS			0.5	0.5		
	29	29	22.91	SS			0.4	0.3		
	30	30	27.82	SS			0.4	0.4		
	31	31	7.31	SS			0.2	0.15		
	32	32	11.68	SS			0.2	0.25		

C. Logic Tree for Ground Motion Models for Western Anatolia Case Study

	GMPE Name	Weight in Gulerce et al., 2017	Weight in this study
Global GMPEs	ASK (2014)	0.125	0.10
	BSSA (2014)	0.125	0.10
	CB (2014)	0.125	0.10
	CY (2014)	0.125	0.20
Regionalized GMPEs	TR-Adjusted AS08	0.125	0.10
	TR-Adjusted BA08	0.125	0.15
	TR-Adjusted CB08	0.125	0.15
	TR-Adjusted CY08	0.125	0.10

D. List of focal mechanism solutions compiled from literature for Central Anatolian region, Turkey. References are (1: Jackson & McKenzie, 1984; 2: Salamon et al., 2003; 3: Cantez and Üçer, 1967; 4: Taymaz et al., 1991; 5: Yılmaztürk and Burton, 1999; 6: Dziewonski et al., 1987; Ekström et al., 2012 (CMT); 7: Ergin et al., 2004; 8: Pondrelli et al., 1999 (EMSC); 9: Pondrelli et al., 2002; 2004; 2006; 2007; 2011 (RCMT); 10: Örgülü et al., 2003; 11: Bernardi, et al., 2004, (SRMT); 12: Karasözen, 2014; 13: General Directorate of Disaster Affairs, Earthquake Research Department (AFAD), 14: National Earthquake Information Center of USGS (NEIC); 15: Kandilli Observatory and Earthquake Research Institute National Earthquake Monitoring Center (KOERI); 16: GEOFON Data Centre (GFZ)

No	Date	Time	Long.	Lat.	Depth	Mag.	Strike	Dip	Rake	Ref.
1	19.04.1938	10:59	33.70	39.50	10	6.8	30	60	4	1
2	8.04.1951	21:38	36.10	36.60	15	6	30	68	15	3
3	14.06.1964	12:15	38.48	38.08	10.5	5.5	227	29	-28	4
4	7.04.1967	17:07	36.13	37.37	38	4.8	266	70	-10	2
5	7.04.1967	18:33	36.18	37.37	32	4.9	245	80	20	2
6	4.07.1967	18:33	36.20	37.40	39	5.1	156	30	-159	1
7	29.06.1971	09:08	36.86	37.13	35.2	5	70	40	130	2
8	11.07.1971	20:12	36.83	37.16	18.7	5	82	88	8	5
9	17.08.1971	04:29	36.79	37.11	35.3	4.9	50	78	99	2
10	1.01.1975	00:30	36.48	36.78	35.4	5.2	26	77	-74	2
11	9.02.1978	21:10	36.80	37.08	42.3	4.5	80	30	60	2
12	28.12.1979	03:09	35.85	37.49	47.1	5.4	141	90	180	6
13	2.01.1980	12:52	36.33	36.57	31.9	4.7	258	77	74	2
14	30.06.1981	07:59	35.89	36.17	63.3	4.7	76	82	40	2
15	24.11.1983	00:14	36.13	37.05	37.4	4.7	226	70	-10	2
16	5.05.1986	03:35	37.78	38.00	4.4	6	260	54	9	6
17	6.06.1986	10:39	37.91	38.01	10.6	5.8	160	90	180	6
18	24.06.1989	03:09	35.94	36.75	46.4	5.1	203	28	-93	6
19	10.04.1991	01:08	36.12	37.30	33	5.3	160	27	-136	6
20	10.02.1994	06:15	35.89	36.93	32	4.9	285	85	-140	7
21	21.01.1995	03:48	36.25	37.37	15	4.5	350	40	-100	7
22	13.04.1995	20:23	36.20	37.42	14	4.9	170	40	-90	7
23	22.01.1997	17:57	35.96	36.21	45.4	5.7	243	39	-15	6
24	22.01.1997	18:22	36.03	36.26	13	4.3	50	90	40	7
25	22.01.1997	18:24	36.06	36.13	4	5.2	219	41	-39	7
26	23.01.1997	14:53	36.05	36.26	4.8	4.2	45	85	-40	7
27	3.01.1998	21:15	35.77	37.20	15.8	4.1	125	85	150	7
28	28.03.1998	00:30	38.75	38.20	6.1	4.5	235	46	-15	9
29	9.05.1998	15:38	38.95	38.25	26.5	5.1	251	83	-7	6
30	27.06.1998	13:55	35.33	36.53	32	6.2	50	85	10	7
31	28.06.1998	03:59	35.49	36.92	10	4.9	223	71	-12	9
32	4.07.1998	02:15	35.44	36.90	37.6	5.1	60	90	20	7
33	4.12.1998	04:59	35.58	37.01	22.8	4	65	80	20	7

34	14.12.1998	13:06	35.79	38.92	15	4.7	339	64	166	9
35	15.01.1999	02:04	35.85	37.04	23.5	4.2	35	75	-10	7
36	6.04.1999	00:08	38.23	39.37	30.7	5.4	326	49	175	6
37	10.06.1999	23:25	35.96	37.38	19.5	4.5	50	85	10	7
38	11.06.1999	05:25	36.80	39.53	6.2	4.9	67	45	-39	9
39	24.08.1999	17:33	32.68	39.41	10	4.9	27	53	-2	9
40	2.01.2000	20:28	38.96	38.30	13.1	3.7	345	72	-147	10
41	2.04.2000	11:41	37.08	37.61	12.8	4.2	44	80	38	10
42	2.04.2000	17:26	37.32	37.54	10	4	224	89	-15	10
43	7.05.2000	09:08	38.83	38.26	22.7	4.2	53	82	16	10
44	7.05.2000	23:10	38.91	38.27	22.3	4.4	320	87	167	10
45	12.05.2000	03:01	36.06	36.99	32.7	4.7	10	45	-106	9
46	27.05.2000	07:49	35.28	36.23	6.9	4.2	65	45	-10	7
47	17.01.2001	12:09	36.21	37.07	9.6	4.4	60	65	-20	7
48	25.06.2001	13:28	36.27	37.22	7.9	4.6	320	50	-110	7
49	25.09.2001	11:53	32.33	35.97	40.3	4.5	326	75	-173	9
50	18.10.2001	15:50	35.22	36.86	10	4.5	161	34	-175	9
51	31.10.2001	12:33	36.25	37.26	6.7	4.9	35	35	-90	7
52	23.05.2002	01:08	36.35	37.41	10.3	4.4	231	58	-37	9
53	19.11.2002	01:25	38.39	38.02	10	4.7	338	74	-177	9
54	14.12.2002	01:02	36.19	37.47	29.2	4.8	30	41	-79	9
55	26.02.2003	03:08	36.27	35.86	10	4.4	295	84	-2	9
56	13.07.2003	01:48	38.95	38.28	12.9	5.5	72	89	1	6
57	24.09.2003	08:13	38.23	39.55	0.9	4.7	275	74	7	9
58	26.02.2004	04:13	38.25	37.91	5	4.8	334	44	155	9
59	18.08.2004	05:57	34.40	36.80	13.6	4.3	26	15	-95	9
60	4.07.2005	21:33	36.08	39.16	3.4	4.5	58	52	-61	11
61	30.07.2005	21:45	33.11	39.39	15.7	5.2	214	87	-2	6
62	31.07.2005	23:41	33.10	39.44	11.5	4.8	205	73	1	9
63	31.07.2005	00:45	33.13	39.43	2	4.3	8	62	14	11
64	31.07.2005	15:18	33.08	39.42	11.7	4.6	20	73	-20	11
65	1.08.2005	00:45	33.07	39.44	19.3	4.7	119	82	172	9
66	6.08.2005	09:09	33.10	39.39	6	4.7	111	74	171	9
67	18.10.2005	07:17	39.00	38.78	10	4.3	273	71	4	9
68	26.11.2005	15:56	38.86	38.21	10	5.1	237	51	-20	6
69	9.10.2006	05:01	35.56	35.88	18.3	4.1	137	28	-113	9
70	14.02.2007	11:59	34.14	39.76	18.8	3.9	349	38	-47	12
71	18.05.2007	23:27	33.26	37.32	8.3	4.6	176	43	-26	9
72	24.08.2007	02:53	37.45	38.15	1.2	4.4	334	43	-170	9
73	15.09.2007	05:26	37.00	37.81	8.5	4.4	334	43	105	9
74	15.09.2007	23:28	36.92	37.79	10.8	4.3	244	19	5	9
75	24.09.2007	23:21	35.47	39.77	6.8	3.5	242	45	0	12
76	13.12.2007	18:06	33.07	38.83	7.9	4.9	224	55	1	6
77	20.12.2007	09:48	33.16	39.41	11.3	5.7	214	73	17	6
78	26.12.2007	23:47	33.11	39.42	10.8	5.6	231	67	5	6
79	27.12.2007	13:48	33.14	39.44	3.8	4.7	150	57	-140	9
80	15.03.2008	10:15	33.05	39.50	12.5	4.8	41	66	-6	9
81	14.04.2008	15:16	35.91	39.95	9.7	3.4	220	45	45	12
82	3.09.2008	02:22	38.50	37.51	5.7	5	219	79	-10	6
83	12.11.2008	14:03	35.52	38.84	10	5.1	227	70	-13	6
84	17.06.2009	04:29	36.02	36.05	10.4	4.6	174	32	-113	9

85	10.09.2009	18:29	32.52	37.94	2	4.8	28	42	-82	6
86	11.09.2009	01:58	32.44	37.94	5	4.9	26	39	-76	6
87	1.02.2010	04:01	38.12	39.56	21.5	4.5	85	82	-22	9
88	1.02.2010	04:01	37.99	39.56	6	4.5	178	68	-171	9
89	23.03.2010	19:33	38.65	39.89	11	3.7	48	57	-33	13
90	16.08.2010	06:41	38.92	39.72	13	3.6	335	86	-165	13
91	17.09.2010	10:17	38.95	38.14	10	4.9	322	74	-165	9
92	14.11.2010	23:08	36.08	36.48	12	4.9	24	53	-94	6
93	14.11.2010	23:08	36.01	36.59	2.5	4.9	212	33	-99	9
94	16.11.2010	10:50	36.32	37.33	7.6	4.7	5	17	-48	9
95	29.06.2011	19:48	35.87	37.41	20.6	4.4	95	40	78	9
96	16.08.2011	07:53	35.90	39.08	5	4.1	65	70	-20	14
97	22.09.2011	03:22	38.60	39.68	16.1	5.6	239	77	-5	6
98	16.02.2012	11:01	37.46	38.65	15.3	4.6	22	31	-107	9
99	25.05.2012	11:22	38.72	38.16	14.8	4.4	70	85	-11	9
100	22.07.2012	09:26	36.23	37.34	19.2	4.8	38	53	-78	6
101	16.09.2012	07:54	35.77	37.44	21	4.6	163	86	161	9
102	19.09.2012	09:17	37.12	37.28	21.4	5	210	48	-11	6
103	5.10.2012	10:25	33.80	39.35	17.7	4.6	198	62	-32	9
104	16.10.2012	01:16	37.11	37.30	14.7	4.5	211	71	-27	9
105	16.10.2012	10:25	37.16	37.27	25	4.5	146	90	153	9
106	13.11.2012	23:55	37.12	37.20	24.9	4.9	119	90	153	9
107	14.11.2012	00:02	37.14	37.28	10	4.4	46	83	44	9
108	18.11.2012	19:18	37.13	37.33	28	3.9	187	74	108	13
109	1.12.2012	03:51	38.35	37.47	17.9	4.1	133	65	124	13
110	25.12.2012	15:35	34.10	39.85	17.1	3.9	276	48	110	13
111	30.12.2012	09:11	35.72	37.48	8	4.1	247	79	49	15
112	8.01.2013	06:05	37.96	37.93	13.8	4.3	51	88	1	9
113	8.01.2013	06:15	37.96	37.92	21.1	4.4	150	90	172	9
114	12.02.2013	20:20	36.95	37.11	13	3.7	314	74	-154	13
115	4.04.2013	06:34	37.12	37.32	9	3.7	140	68	-156	13
116	14.04.2013	18:25	36.21	37.31	20	3.5	59	51	19	13
117	1.05.2013	06:47	37.10	37.31	7.9	3.7	290	81	157	13
118	1.05.2013	06:50	37.11	37.30	13.3	3.9	0	44	-58	13
119	6.05.2013	18:33	37.13	37.30	12.4	3.8	109	74	-167	13
120	16.06.2013	20:31	37.08	38.11	13.1	4.6	347	75	160	13
121	26.07.2013	00:22	35.87	36.06	25.8	4	345	78	-95	13
122	28.08.2013	06:26	38.91	38.38	18.2	3.6	340	70	-162	13
123	23.10.2013	12:24	34.43	36.23	10.1	4.5	22	54	45	9
124	30.12.2013	00:02	38.33	37.88	19.9	3.5	333	81	-131	13
125	10.01.2014	13:20	36.23	37.28	6	4	282	85	173	15
126	14.02.2014	00:33	36.07	36.23	18	4.9	35	70	-59	6
127	22.02.2014	15:42	36.38	37.42	20	4.4	193	60	-45	9
128	2.03.2014	04:25	35.18	36.79	10	4.2	69	45	63	9
129	26.03.2014	14:00	38.59	38.14	4	3.9	216	69	-38	15
130	9.06.2014	03:38	36.06	36.29	20.9	4.8	164	36	-135	6
131	20.09.2014	02:52	38.70	39.16	10	4.1	250	87	-43	9
132	8.01.2015	18:44	36.86	37.03	21.6	4.5	106	75	170	9
133	22.01.2015	19:27	36.30	37.40	6	3.9	3	69	-99	15
134	10.02.2015	04:01	36.02	35.80	10	4.3	228	70	-27	9
135	28.03.2015	10:08	36.41	37.49	22	4.1	306	70	-150	15

136	28.03.2015	05:04	35.63	38.88	7	3.6	144	73	-167	15
137	17.04.2015	11:49	38.81	37.53	10.9	3.7	226	71	40	13
138	29.07.2015	22:01	34.94	36.58	23.7	4.9	193	68	-75	9
139	29.07.2015	22:01	34.87	36.44	33.4	5	195	64	-76	6
140	29.07.2015	00:56	34.95	36.58	34	4.9	149	50	-128	14
141	26.08.2015	23:01	36.93	37.33	7	4	353	43	-100	15
142	3.10.2015	21:08	38.93	38.18	9.8	3.8	324	71	160	15
143	29.11.2015	00:28	37.75	38.82	20.2	5.1	74	72	-19	6
144	29.11.2015	00:28	37.87	38.90	17	5	339	77	173	16
145	9.12.2015	09:03	37.92	38.88	22.8	4.5	65	73	-8	9
146	10.01.2016	17:40	34.33	39.72	21.2	5	7	79	-6	6
147	2.02.2016	14:21	37.84	38.84	10.2	4.1	184	88	-167	13
148	18.02.2016	07:56	35.84	39.01	5.4	3.9	46	69	-49	13
149	31.03.2016	21:33	35.85	36.97	14	4.2	142	77	-171	15
150	7.04.2016	11:11	35.09	37.92	12.9	3.8	27	53	-65	13
151	23.04.2016	19:51	36.62	36.91	5.8	3.7	312	39	-176	13
152	17.08.2016	01:07	38.15	38.70	11.2	4.2	271	40	66	13
153	16.09.2016	05:12	36.90	37.21	7.8	3.6	216	53	-26	13
154	20.11.2016	22:52	38.59	39.95	6.4	3.8	41	74	-62	13
155	3.02.2017	06:33	38.09	38.69	17.9	3.7	71	65	8	13
156	25.02.2017	21:06	36.10	37.01	3.8	4.5	351	45	-79	13
157	2.03.2017	11:07	38.45	37.53	17.2	5.6	225	78	-21	6
158	2.03.2017	17:03	38.50	37.58	7.7	3.7	45	86	26	13
159	10.03.2017	22:23	38.51	37.58	9.3	3.7	33	86	-31	13
160	28.03.2017	21:53	37.18	38.29	12	4	70	86	-31	13
161	18.08.2017	04:30	37.54	37.57	9	4	233	55	-9	13
162	20.02.2019	05:35	35.93	36.23	27.69	4	220	50	-85	13
163	2.02.2019	12:20	35.82	37.27	33.05	4.3	322	77	163	13
164	27.12.2018	14:36	38.63	39.56	11.18	4.1	158	88	-109	13
165	10.10.2018	09:08	35.85	37.43	7.02	4.1	65	55	3	13
166	2.10.2018	15:29	37.40	37.69	10.27	4.4	337	83	-175	13
167	19.08.2018	15:22	36.39	37.38	10.53	4.8	332	82	-136	13
168	4.08.2018	07:09	36.31	37.46	15.29	4.3	132	76	-161	13
169	31.07.2018	14:36	36.08	37.02	10	4.1	248	72	-57	13
170	3.07.2018	13:16	37.40	37.69	10.63	4.1	334	88	-176	13
171	21.05.2018	01:09	38.60	37.46	9.67	4	277	80	-179	13
172	24.04.2018	00:34	38.50	37.58	9.79	5.1	113	87	-177	13
173	19.01.2018	13:53	38.82	38.29	9.17	4.1	230	81	3	13

E. List of stations. Station's name starting with 'AT' were installed during the CAT project. The rest of the stations are from KOERI network

Name	Longitude	Latitude	Elevation (m)
AT01	36.711	39.824	1340
AT02	37.057	39.481	1524
AT03	37.596	39.13	1700
AT04	38.139	38.728	931
AT05	38.794	38.317	1162
AT06	35.667	39.773	1287
AT07	36.222	39.245	1448
AT08	36.927	38.904	1905
AT09	37.57	38.502	1650
AT10	37.861	38.112	1415
AT11	38.376	37.858	660
AT12	34.745	39.552	1026
AT13	35.315	39.177	1213
AT14	36.06	38.728	1464
AT15	36.776	38.448	1608
AT16	37.136	38.184	1265
AT17	37.52	37.847	1037
AT18	37.959	37.543	579
AT19	33.581	39.835	1017
AT20	34.157	39.464	1206
AT21	34.525	39.027	1190
AT22	34.99	38.691	1385
AT23	35.55	38.463	1429
AT24	35.902	38.265	1704
AT25	36.459	38.018	1718
AT26	36.731	37.73	595
AT27	37.196	37.584	835
AT28	37.55	37.353	761
AT29	33.378	39.279	918
AT30	34.005	38.864	1283
AT31	34.508	38.673	1266
AT32	34.889	38.397	1454
AT33	35.15	38.129	1784
AT34	35.515	38.005	1503
AT35	35.877	37.773	776
AT37	36.492	37.344	671
AT38	36.808	37.136	693
AT39	37.223	37.032	843
AT40	32.451	38.949	1118
AT41	33.245	38.568	939
AT42	33.873	38.375	968
AT43	34.331	38.158	1607
AT44	34.612	37.947	1188
AT45	35.02	37.788	1740
AT46	35.576	37.403	173
AT47	35.991	37.092	93

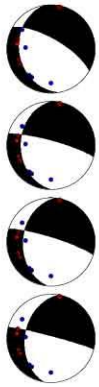
AT48	36.414	36.719	257
AT49	32.253	38.614	993
AT50	32.878	38.4	1013
AT51	33.38	38.108	1047
AT52	33.863	38.015	1090
AT53	34.334	37.677	1305
AT54	34.882	37.576	1356
AT55	35.087	37.184	123
AT56	35.547	36.802	4
AT57	32.877	37.914	1001
AT58	33.325	37.665	1009
AT59	33.82	37.383	1433
AT60	34.364	37.116	1473
AT61	32.362	37.55	1135
AT62	33.053	37.203	1284
AT63	33.472	36.813	770
AT64	34.121	36.701	774
AT65	34.963	38.321	1377
AT66	36.175	37.521	259
AT67	36.248	37.052	375
AT68	37.834	38.125	1427
AT69	37.197	37.584	837
AT70	34.543	38.034	1209
AT71	34.259	37.478	1963
AFSR	33.0707	39.4468	1055
AKK1	33.5405	36.1438	4
AKK2	33.5487	36.1371	2
AKKU	33.5508	36.1588	144
ALAN	32.0327	36.557	215
ARPR	38.3356	39.0929	1522
BERE	33.2228	36.3476	1383
BNN	35.8472	38.8522	1380
BOZY	26.0528	39.8417	202
CEYT	35.7478	37.0107	100
CHBY	32.8902	38.5823	1086
CMRD	34.9902	37.6623	1234
CORM	34.6302	40.1785	1292
DARE	37.4832	38.5712	1080
ERZN	39.722	39.5867	1317
GAZ	37.2113	37.1722	864
GULA	34.236	38.3444	1126
HDMB	32.486	36.964	1946
IKL	33.6852	36.2387	120
ILIC	38.5675	39.4518	1295
KARA	35.0547	37.2607	366
KARG	33.7087	36.203	275
KEBE	33.713	36.447	776
KHMN	37.1574	37.3916	640
KIZT	31.7163	38.8808	1222
KMRS	36.9	37.5053	590
KONT	32.3605	37.9453	1100

KOZT	35.8268	37.4805	381
KRMN	33.2636	37.174	1068
KRTD	35.4157	36.5934	47
KRTS	35.375	36.573	53
KULU	33.0023	39.0343	1120
LADK	32.3648	38.2	1168
LOD	32.764	39.8893	902
MALT	38.4273	38.3134	1112
MERS	34.522	36.8678	750
NIG	34.6142	38.108	2270
OREN	33.4587	36.2078	61
PTK	39.3923	38.8923	1835
SARI	36.4182	38.4072	1673
SERE	33.564	38.9463	1216
SILI	33.9239	36.3672	126
SLFK	33.9465	36.3926	54
SULT	33.5157	38.1988	982
SVRH	31.523	39.447	1000
SVRC	39.306	38.3775	1680
SVSK	36.9925	39.9175	1630
TAHT	36.1855	36.3755	278
TEKE	33.1142	36.1426	173
TEVE	33.4432	36.4357	848
TISA	33.6788	36.162	94
URFA	38.8213	37.441	938
YAYX	33.8115	38.9387	1142
YESI	33.6424	36.1955	24
YESY	33.7432	37.7825	1206
YORU	33.4057	36.1542	423

F. Graphical output files of the Focal Mechanism Solutions (FMS) computed in this study.

The events are labelled as 'cate00xxx' where 'xxx' denotes the ID of each event as given in Table 4.1. FMS for cate00088 & cate00111 are not shown here; because the solutions were not attempted due to lack of data.

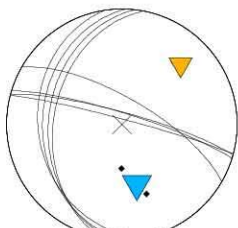
Pol Only



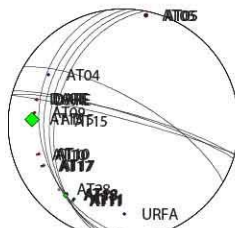
Pol + Ampl



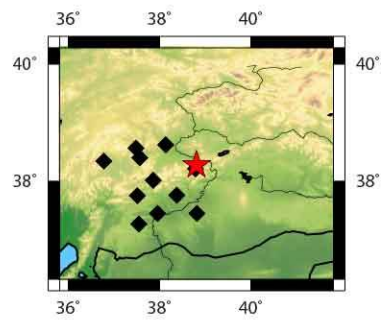
sta SH/P	Pqual	Squal	sta Pqual	Squal
AT05	4.27 g/l	g/E	AT04	o/E
AT10	0.60 g/l	o/E	AT05	g/l g/E
AT11	5.87 o/E	g/E	AT09	g/l
AT15	46.67 o/E	g/E	AT10	g/l o/E
AT17	5.77 o/E	g/E	AT11	o/E g/E
AT18	15.13 o/E	g/E	AT15	o/E g/E
DARE	1.00 g/l	g/E	AT17	o/E g/E
			AT18	o/E g/E
			DARE	g/l g/E
			URFA	g/l



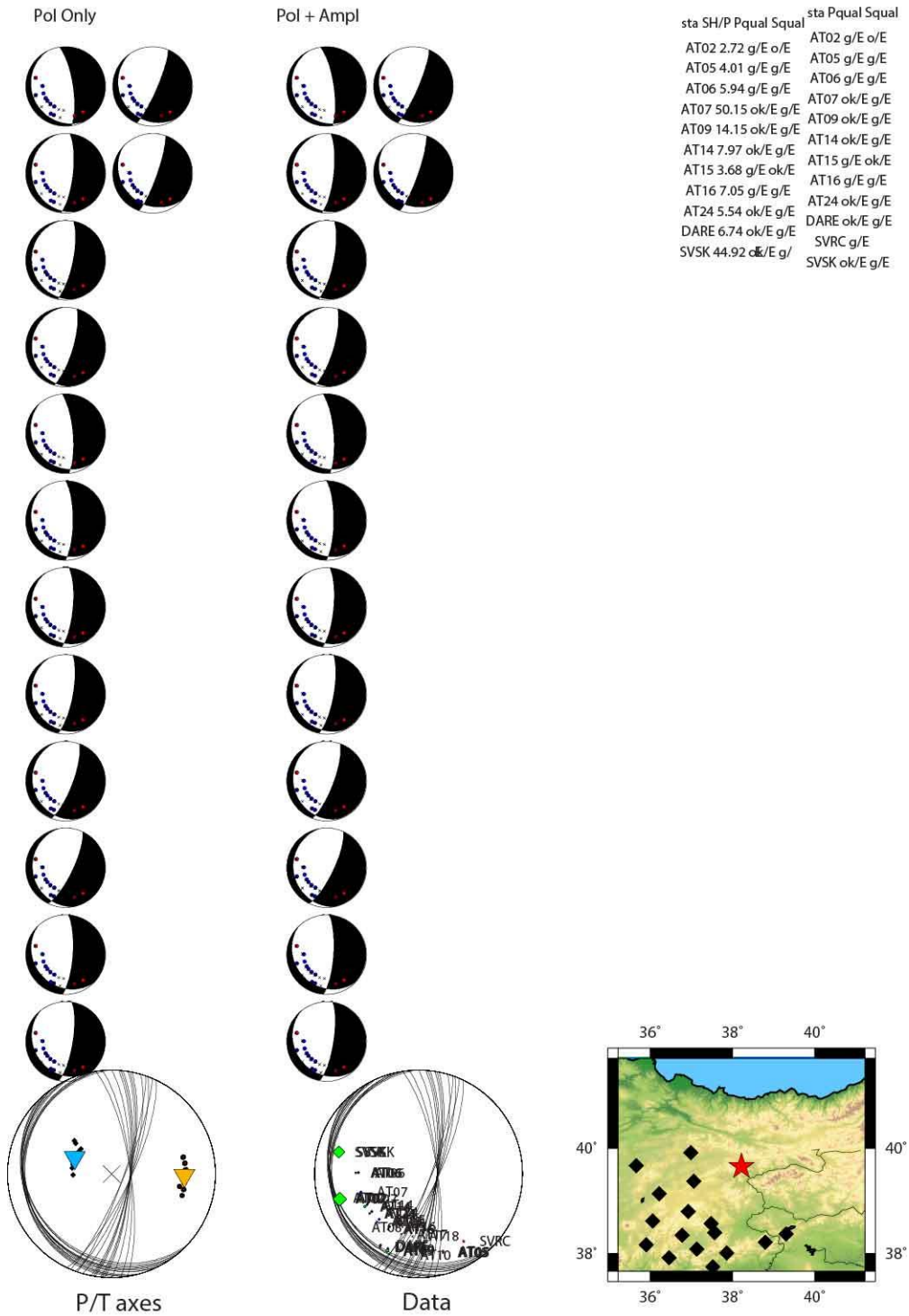
P/T axes



Data



P K: 53.4 95%: 12.7 T K: 401.8 95%: 4.6 Lon: 38.81 Lat: 38.28 Dep: 5.00 Mag: ML, 3.0
 cate00001 Data pts: 18 Solns: 4 Pol errs: 1 Nodal Wt: 0.8 Solns shown: 4 Search Inc: 5
 Ampl errs: 0 Ampl Data: 7 Solns: 3 Pol errs: 1 Nodal Wt: 0.8 Soln shown: 3 Search Inc: 5



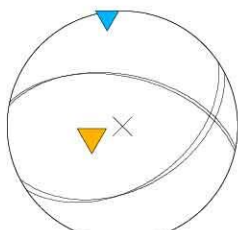
Pol Only



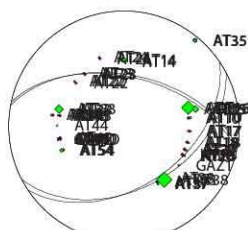
Pol + Ampl



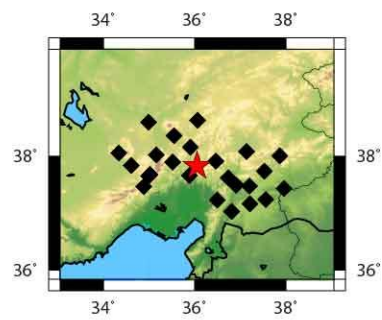
sta	SH/P	Pqual	Squal	sta	Pqual	Squal
AT10	9.59	ok/E	g/E	AT10	ok/E	g/E
AT14	11.55	ok/E	ok/E	AT14	ok/E	ok/E
AT16	44.34	g/E	g/E	AT16	g/E	g/E
AT17	4.25	g/E	ok/E	AT17	g/E	ok/E
AT18	4.58	g/E	g/E	AT18	g/E	g/E
AT22	1.84	g/E	g/E	AT22	g/l	g/E
AT23	1.17	g/l	ok/E	AT23	g/l	ok/E
AT24	1.25	g/E	g/E	AT24	g/E	g/E
AT25	21.01	g/E	e/l	AT25	g/E	e/l
AT27	3.20	g/E	g/E	AT26	g/l	
AT28	6.42	g/E	g/E	AT27	g/E	g/E
AT33	27.35	g/E	ok/E	AT28	g/E	g/E
AT34	2.57	g/l	ok/E	AT33	g/E	ok/E
AT35	9.62	g/E	g/E	AT34	g/l	ok/E
AT37	7.33	ok/E	ok/E	AT35	g/E	g/E
AT38	51.70	ok/E	g/E	AT37	ok/E	ok/E
AT43	4.24	ok/E	ok/E	AT38	ok/E	g/E
AT45	4.59	g/E	g/E	AT43	ok/E	ok/E
AT54	12.69	g/E	ok/E	AT45	g/E	g/E
CMRD	2.74	g/E	g/	AT54	g/E	ok/E
				CMRD	g/E	g/E
				KMRS	g/E	



P/T axes



Data



P K: 3186.0 95%: 4.4 T K: 550.1 95%: 10. 7 Lon: 36.05 Lat: 37.84 Dep: 1.00 Mag: ML 3.0
 cate00003 Data pts: 44 Solns: 2 Pol errs: 1 Nodal Wt: 0.3 Solns shown: 2 Search Inc: 5
 Ampl errs: 0 Ampl Data: 20 Solns: 1 Pol errs: 1 Nodal Wt: 0.2 Soln shown: 1 Search Inc: 5

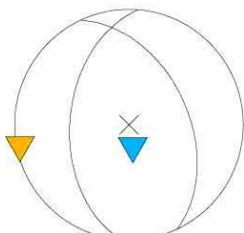
Pol Only



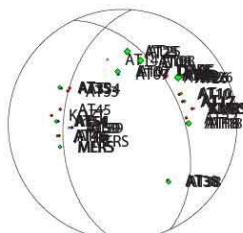
Pol + Ampl



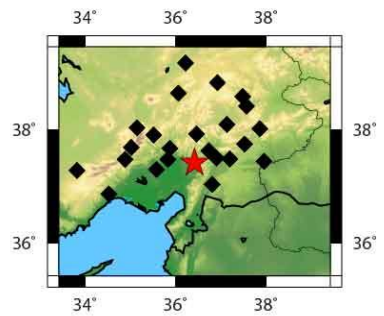
sta SH/P Pqual Squal	sta Pqual Squal
AT07 19.36 ok/E g/E	AT07 ok/E g/E
AT08 21.50 ok/E g/E	AT08 ok/E g/E
AT09 1.38 ok/E g/E	AT09 ok/E g/E
AT10 10.66 g/E ok/E	AT10 g/E ok/E
AT17 8.56 g/E ok/E	AT16 g/E
AT18 20.49 g/E ok/E	AT17 g/E ok/E
AT25 20.88 g/E g/E	AT18 g/E ok/E
AT26 23.84 g/E ok/E	AT25 g/E g/E
AT35 12.47 g/E g/E	AT26 g/E ok/E
AT38 16.25 ok/E g/E	AT27 g/E
AT46 6.33 g/E ok/E	AT33 ok/E
AT54 12.53 g/E o/E	AT34 g/E
AT59 4.47 ok/E o/E	AT35 g/E g/E
DARE 2.98 g/E ok/E	AT38 ok/E g/E
KMRS 0.08 g/E g/	AT45 ok/E
MERS 13.67 ok/E g/E	AT46 g/E ok/E
	AT54 g/E o/E
	AT59 ok/E o/E
	DARE g/E ok/E
	KMRS g/E g/E
	KOZT g/E
	MERS ok/E g/E



P/T axes



Data



P K: NaN 95%: NaN T K: NaN 95%: NaN Lon: 36.42 Lat: 37.42 Dep: 4.00 Mag: ML, 3.3
 cate00004 Data pts: 39 Solns: 1 Pol errs: 1 Nodal Wt: 0.2 Solns shown: 1 Search Inc: 5
 Ampl errs: 0 Ampl Data: 16 Solns: 1 Pol errs: 1 Nodal Wt: 0.2 Soln shown: 1 Search Inc: 5

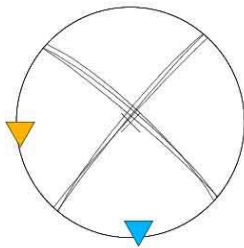
Pol Only



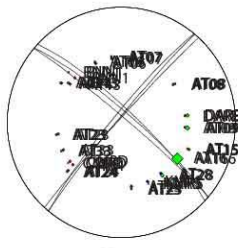
Pol + Ampl



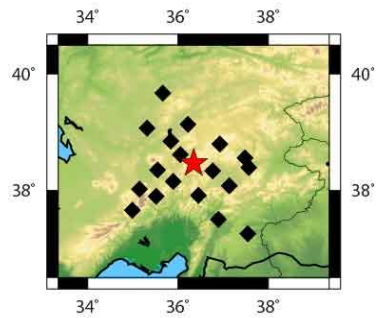
sta	SH/P	Pqual	Squal	sta	Pqual	Squal
AT06	2.24	ok/E	g/E	AT06	ok/E	g/E
AT07	5.24	g/E	g/E	AT07	g/E	g/E
AT08	6.53	ok/E	ok/E	AT08	ok/E	ok/E
AT09	15.08	g/E	g/E	AT09	g/E	g/E
AT13	5.67	ok/E	ok/E	AT13	ok/E	ok/E
AT14	1.78	e/l	g/	AT14	e/l	g/
AT15	5.45	g/E	e/l	AT15	g/E	e/l
AT16	37.35	g/E	g/E	AT16	g/E	g/E
AT23	4.96	g/E	ok/E	AT23	g/E	ok/E
AT24	5.01	g/l	g/E	AT24	g/l	g/E
AT25	5.69	ok/E	g/E	AT25	ok/E	g/E
AT28	11.26	ok/E	g/E	AT28	ok/E	g/E
AT33	6.10	ok/E	g/E	AT33	ok/E	g/E
BNN1	2.30	g/l	g/E	AT34	g/E	
CMRD	1.22	ok/E	ok/	BNN1	g/l	g/E
DARE	11.80	g/E	g/E	CMRD	ok/E	ok/E
KMRS	0.82	g/E	ok/	DARE	g/E	g/E
				KMRS	g/E	ok/E



P/T axes



Data



P K: 774.0 95%: 4.4 T K: 705.2 95%: 4.6 Lon: 36.35 Lat: 38.48 Dep: 3.00 Mag: ML, 3.0
 cate00005 Data pts: 35 Solns: 3 Pol errs: 0 Nodal Wt: 0.9 Solns shown: 3 Search Inc: 5
 Ampl errs: 0 Ampl Data: 17 Solns: 2 Pol errs: 0 Nodal Wt: 0.9 Solns shown: 2 Search Inc: 5

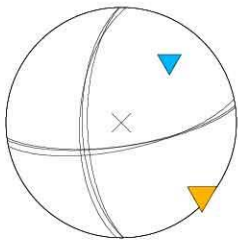
Pol Only



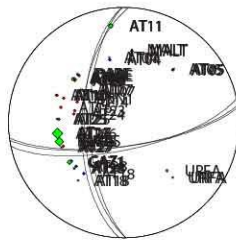
Pol + Ampl



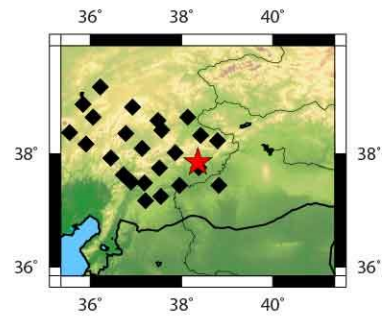
sta SH/P Pqual Squal	sta Pqual Squal
AT04 1.32 E/l g/	AT04 eE g/
AT05 1.88 E/E g/	AT05 e/E g/E
AT07 1.84 g/E ok/E	AT07 g/E ok/E
AT08 9.58 ok/E g/E	AT08 ok/E g/E
AT09 2.73 E/l g/	AT09 eE g/
AT10 0.96 g/E g/E	AT10 g/E g/E
AT11 12.1 l e/l e/	AT11 e/l e/
AT18 2.31 g/l ok/E	AT14 ok/E
AT25 4.72 g/E g/E	AT15 g/E
AT26 35.81 g/E ok/E	AT16 g/E
AT27 4.59 g/E ok/E	AT17 g/E
AT28 6.33 g/E g/E	AT18 g/l ok/E
DARE 5.24 g/E ok/E	AT23 ok/E
GAZ1 15.45 ok/E g/E	AT24 ok/E
KMRS 29.58 E/E g/	AT25 g/E g/E
MALT 1.36 e/l e/	AT26 g/E ok/E
URFA 3.13 g/l g/E	AT27 g/E ok/E
	AT28 g/E g/E
	BNN1 g/E
	DARE g/E ok/E
	GAZ1 ok/E g/
	KMRS g/E g/E
	MALT eE e/
	URFA g/l g/E



P/T axes



Data



P K: 769.4 95%: 4.4 TK: 717.3 95%: 4.6 Lon: 38.36 Lat: 37.85 Dep: 3.00 Mag: ML, 3.7
 cate00006 Data pts: 41 Solns: 3 Pol errs: 1 Nodal Wt: 0.5 Solns shown: 3 Search Inc: 5
 Ampl errs: 0 Ampl Data: 17 Solns: 3 Pol errs: 1 Nodal Wt: 0.5 Solns shown: 3 Search Inc: 5

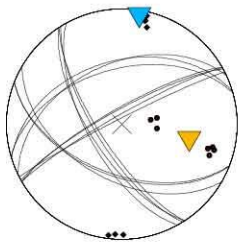
Pol Only



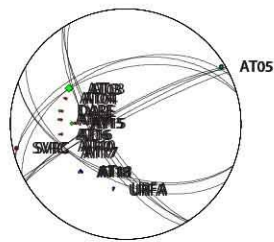
Pol + Ampl



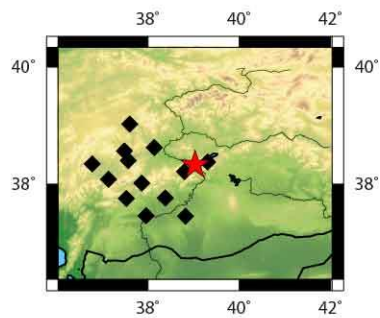
sta	SH/P	Pqual	Squal	sta	Pqual	Squal
AT03	26.78	ok/E	g/E	AT03	ok/E	g/E
AT04	1.35	g/l	ok/E	AT04	g/l	ok/E
AT05	8.38	g/E	g/E	AT05	g/E	g/E
AT09	5.01	g/l	g/E	AT09	g/l	g/E
AT10	1.84	g/E	g/E	AT10	g/E	g/E
AT15	13.64	ok/E	g/E	AT15	g/E	
AT16	4.25	ok/E	ok/E	AT15	ok/E	g/E
AT17	0.58	g/E	g/E	AT16	ok/E	ok/E
AT18	7.88	ok/E	ok/E	AT17	g/E	g/E
DARE	8.91	ok/E	g/E	AT18	ok/E	ok/E
SVRC	1.93	E/l	g/	DARE	ok/E	g/E
URFA	2.05	g/E	g/	SVRC	e/l	g/E
				URFA	g/E	g/E



P/T axes



Data



P K: 79.2 95%: 6.8 T K: 10.0 95%: 20. 1 Lon: 39.03 Lat: 38.33 Dep: 1.00 Mag: ML, 3.0
 cate00007 Data pts: 25 Solns: 7 Pol errs: 1 Nodal Wt: 0.8 Solns shown: 7 Search Inc: 5
 Ampl errs: 0 Ampl Data: 12 Solns: 2 Pol errs: 1 Nodal Wt: 0.5 Soln shown: 2 Search Inc: 5

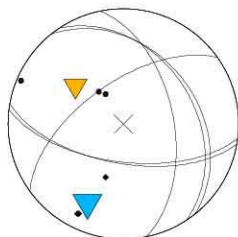
Pol Only



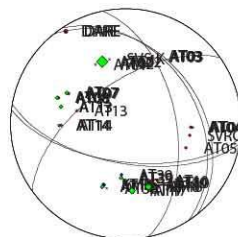
Pol + Ampl



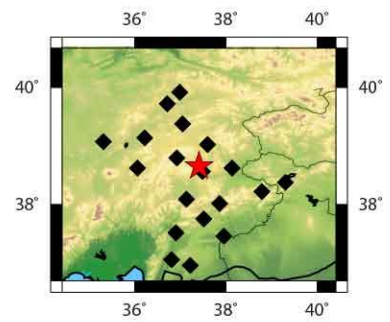
sta SH/P Pqual Squal	sta Pqual Squal
AT02 39.38 g/E g/E	AT02 g/E g/E
AT03 3.96 g/E g/E	AT03 g/E g/E
AT04 5.31 e/l g/	AT04 e/l g/
AT07 12.15 g/E g/E	AT05 e/l
AT08 12.91 g/E g/E	AT07 g/E g/E
AT10 2.34 g/E g/E	AT08 g/E g/E
AT13 11.53 g/E e/l	AT10 g/E g/E
AT14 8.57 g/E g/E	AT13 g/E e/l
AT16 11.79 g/E g/E	AT14 g/E g/E
AT17 23.69 g/E g/E	AT16 g/E g/E
AT18 20.98 g/E e/l	AT17 g/E g/E
AT39 13.93 g/E g/E	AT18 g/E e/l
DARE 3.48 e/l e/	AT39 g/E g/E
	DARE e/l e/l
	KMRS g/E
	SVRC g/E



P/T axes



Data



P K: 14.9 95%: 33.1 T K: 5.0 95%: 62. 6 Lon: 37.41 Lat: 38.66 Dep: 1.00 Mag: ML, 4.1
 cate00008 Data pts: 32 Solns: 3 Pol errs: 2 Nodal Wt: 0.4 Solns shown: 3 Search Inc: 5
 Ampl errs: 0 Ampl Data: 13 Solns: 3 Pol errs: 2 Nodal Wt: 0.4 Soln shown: 3 Search Inc: 5

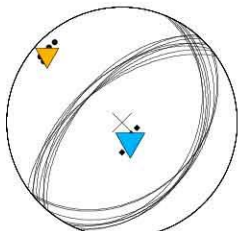
Pol Only



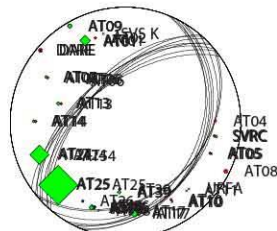
Pol + Ampl



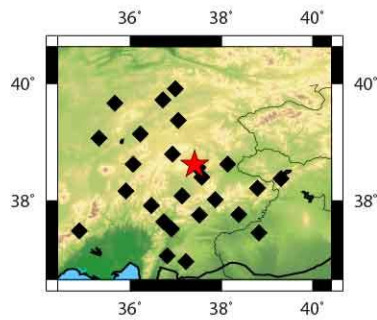
sta	SH/P	Pqual	Squal	sta	Pqual	Squal
AT01	33.77	o/E	g/E	AT01	o/E	g/E
AT05	3.44	e/l	g/	AT02	g/E	
AT06	3.33	g/E	g/E	AT04	e/l	
AT07	8.08	g/E	g/E	AT05	e/l	g/
AT09	11.72	e/l	g/	AT06	g/E	g/E
AT10	3.70	g/E	g/E	AT07	g/E	g/E
AT13	12.46	g/E	g/l	AT08	g/E	
AT14	8.67	g/l	g/E	AT09	e/l	g/
AT16	15.12	e/l	g/	AT10	g/E	g/E
AT17	23.77	g/E	g/E	AT13	g/E	g/l
AT24	63.03	g/E	g/E	AT14	g/l	g/E
AT25	130.38	g/E	g/E	AT16	e/l	g/l
AT39	13.42	g/E	g/E	AT17	g/E	g/E
DARE	3.10	g/l	g/l	AT24	g/E	g/E
KMRS	3.02	g/E	g/	AT25	g/E	g/E
SVRC	8.25	g/E	g/E	AT26	o/E	
				AT39	g/E	g/E
				DARE	g/l	g/l
				KMRS	g/E	g/E
				SVRC	g/E	g/



P/T axes



Data



P K: 130.4 95%: 4.9 T K: 285.6 95%: 3.3 Lon: 37.41 Lat: 38.62 Dep: 5.00 Mag: ML, 4.1
 cate00009 Data pts: 41 Solns: 8 Pol errs: 1 Nodal Wt: 0.2 Solns shown: 8 Search Inc: 5
 Ampl errs: 0 Ampl Data: 16 Solns: 8 Pol errs: 1 Nodal Wt: 0.2 Soln shown: 8 Search Inc: 5

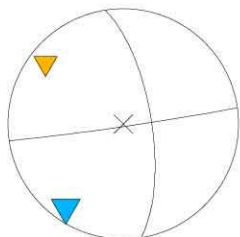
Pol Only



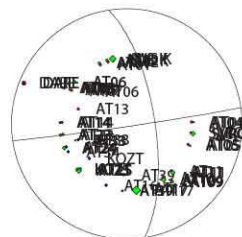
Pol + Ampl



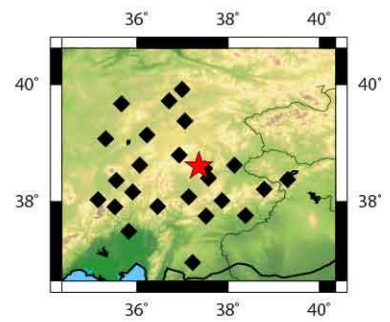
sta SH/P Pqual Squal	sta Pqual Squal
AT01 8.45 g/E g/E	AT01 g/E g/E
AT02 9.70 g/E ok/E	AT02 g/E ok/E
AT04 3.52 g/l ok/E	AT04 g/l ok/E
AT05 2.71 g/l g/E	AT05 g/l g/E
AT06 9.91 g/E o/E	AT06 g/E o/E
AT07 2.72 g/l g/E	AT07 g/l g/E
AT08 5.63 g/E g/E	AT08 g/E g/E
AT09 8.34 g/E g/E	AT09 g/E g/E
AT10 14.51 g/E g/E	AT10 g/E g/E
AT11 16.41 ok/E g/E	AT11 ok/E g/E
AT14 6.87 g/l g/E	AT13 g/E
AT17 29.82 ok/E g/E	AT14 g/l g/E
AT23 8.55 g/E ok/E	AT16 g/E
AT24 11.83 g/E g/E	AT17 ok/E g/E
AT25 20.24 ok/E g/E	AT23 g/E ok/E
AT33 4.05 ok/E g/E	AT24 g/E g/E
AT39 7.69 g/E g/E	AT25 ok/E g/E
DARE 1.69 g/E g/E	AT33 ok/E g/E
KOZT 8.86 g/E g/	AT34 g/E
SVRC 16.44 g/E g/E	AT39 g/E g/E
SVSK 22.68 g/E g/	DARE g/E g/E
	KOZT g/E g/E
	SVRC g/E g/
	SVSK g/E g/E



P/T axes



Data



P K: NaN 95%: NaN T K: NaN 95%: NaN Lon: 37.36 Lat: 38.61 Dep: 1.00 Mag: ML, 3.3
 cate00010 Data pts: 45 Solns: 1 Pol errs: 1 Nodal Wt: 0.8 Solns shown: 1 Search Inc: 5
 Ampl errs: 0 Ampl Data: 21 Solns: 1 Pol errs: 1 Nodal Wt: 0.8 Soln shown: 1 Search Inc: 5

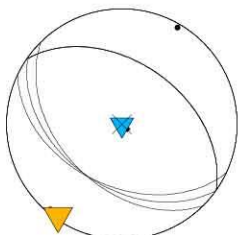
Pol Only



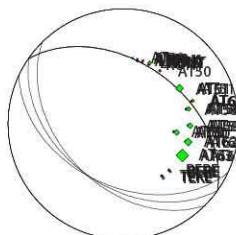
Pol + Ampl



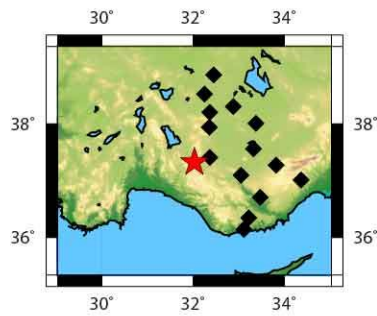
sta SH/P Pqual Squal	sta Pqual Squal
AT40 3.33 ok/E g/E	AT40 ok/E g/E
AT51 24.43 g/E g/E	AT50 g/E
AT58 16.32 ok/E g/E	AT51 g/E g/E
AT59 18.92 g/E g/E	AT58 ok/E g/E
AT60 18.23 ok/E g/E	AT59 g/E g/E
AT61 9.81 E/l g/	AT60 ok/E g/E
AT62 26.25 ok/E g/E	AT61 eB g/
AT63 41.20 ok/E g/E	AT62 ok/E g/E
BERE 6.17 g/E g/	AT63 ok/E g/E
KONT 13.89 ok/E g/	BERE g/E g/E
LADK 3.09 ok/E g/	KONT ok/E g/
TEKE 10.94 ok/E g/E	LADK ok/E g/
	TEKE ok/E g/E



P/T axes



Data



P K: 264.1 95%: 7.6 T K: 262.8 95%: 7.6 Lon: 32.03 Lat: 37.33 Dep: 4.00 Mag: ML, 3.3
 cate00011 Data pts: 26 Solns: 3 Pol errs: 1 Nodal Wt: 0.5 Solns shown: 3 Search Inc: 5
 Ampl errs: 0 Ampl Data: 12 Solns: 3 Pol errs: 1 Nodal Wt: 0.5 Soln shown: 3 Search Inc: 5

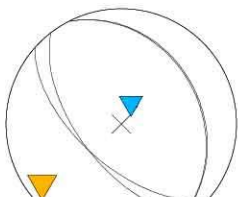
Pol Only



Pol + Ampl



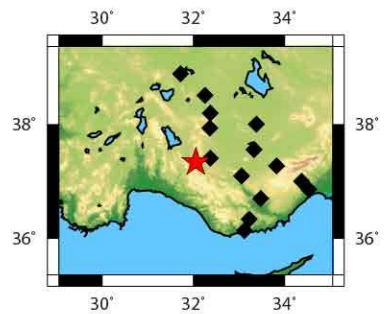
sta SH/P Pqual Squal	sta Pqual Squal
AT51 4.89 ok/E g/E	AT51 ok/E g/E
AT58 5.68 g/E g/E	AT58 g/E g/E
AT59 2.09 ok/E g/E	AT59 ok/E g/E
AT60 6.74 ok/E g/E	AT60 ok/E g/E
AT61 11.58 g/E g/E	AT61 g/E g/E
AT62 5.50 g/E ok/E	AT62 g/E ok/E
AT63 39.85 g/E g/E	AT63 g/E g/E
BERE 5.61 g/E g/E	BERE g/E g/E
KIZT 8.25 g/E g/E	KIZT g/E g/E
KONT 8.43 ok/E g/E	KONT ok/E g/E
MERS 3.49 ok/E g/E	MERS ok/E g/E
TEKE 7.63 ok/E g/E	TEKE ok/E g/E



P/T axes

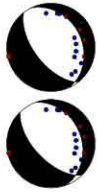


Data



P K: 270.1 95%: 15.3 T K: 306.6 95%: 14. 3 Lon: 32.05 Lat: 37.35 Dep: 5.00 Mag: ML, 3.2
 cate00012 Data pts: 26 Solns: 2 Pol errs: 1 Nodal Wt: 0.5 Solns shown: 2 Search Inc: 5
 Ampl errs: 0 Ampl Data: 12 Solns: 2 Pol errs: 1 Nodal Wt: 0.5 Soln shown: 2 Search Inc: 5

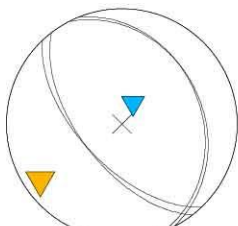
Pol Only



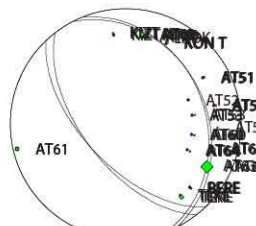
Pol + Ampl



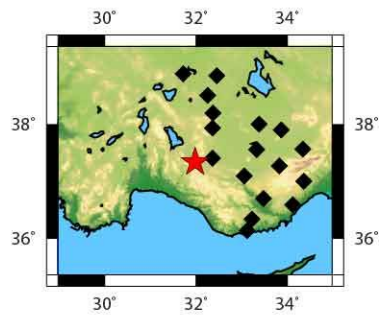
sta	SH/P	Pqual	Squal	sta	Pqual	Squal
AT40	2.35	ok/E	g/E	AT40	ok/E	g/E
AT49	16.73	ok/E	g/E	AT49	ok/E	g/E
AT51	4.93	ok/E	g/E	AT51	ok/E	g/E
AT53	0.50	ok/E	g/E	AT52	g/E	
AT58	5.70	ok/E	g/E	AT53	ok/E	g/E
AT60	3.65	o/E	g/E	AT58	ok/E	g/E
AT61	11.28	g/l	e/	AT60	o/E	g/E
AT62	9.38	g/E	ok/E	AT61	g/E	e/
AT63	40.48	g/E	g/E	AT62	g/E	ok/E
AT64	4.74	o/E	g/E	AT63	g/E	g/E
BERE	5.59	g/E	g/	AT64	o/E	g/E
KIZT	6.35	g/E	g/	BERE	g/E	g/E
KONT	10.62	ok/E	g/	KIZT	g/E	g/E
TEKE	17.35	ok/E	g/E	KONT	ok/E	g/
				TEKE	ok/E	g/



P/T axes



Data



P K: 416.3 95%: 12.3 T K: 4810.0 95%: 3.6 Lon: 31.98 Lat: 37.35 Dep: 5.00 Mag: ML, 3.2
 cate00013 Data pts: 31 Solns: 2 Pol errs: 1 Nodal Wt: 0.8 Solns shown: 2 Search Inc: 5
 Ampl errs: 0 Ampl Data: 14 Solns: 2 Pol errs: 1 Nodal Wt: 0.8 Soln shown: 2 Search Inc: 5

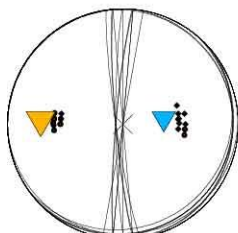
Pol Only



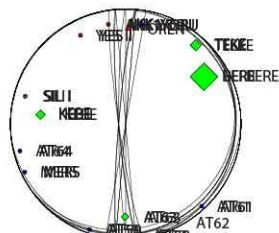
Pol + Ampl



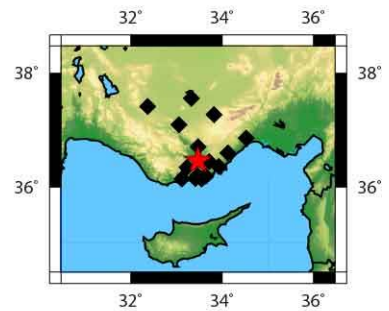
sta	SH/P	Pqual	Squal	sta	Pqual	Squal
AKK1	5.85	o/E/E	g/	AKK1	ok/E/g/	
AT58	2.02	ok/E	o/E	AT58	ok/E/o/E	
AT59	2.69	ok/E	ok/E	AT59	ok/E/ok/E	
AT61	0.73	g/E	o/E	AT61	g/E/o/E	
AT63	20.49	g/E	g/E	AT63	g/E/g/E	
AT64	1.82	e/l	ok/	AT64	e/l ok/E	
BERE	73.99	g/E	g/	BERE	g/E/g/E	
KEBE	25.48	g/E	o/E	KEBE	g/E/o/E	
MERS	2.36	ok/E	g/E	MERS	ok/E/g/E	
SILI	7.08	ok/E	g/E	OREN	o/E	
TEKE	29.77	g/E	g/E	SILI	ok/E/g/E	
YESI	1.61	g/E	o/E	TEKE	g/E/g/E	
YORU	1.00	o/E	ok/E	YESI	g/E/o/E	
				YORU	o/E ok/E	



P/T axes

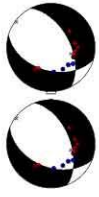


Data

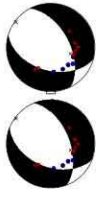


P K: 5.9 95%: 20.5 T K: 5.9 95%: 20. 5 Lon: 33.47 Lat: 36.47 Dep: 15.00 Mag: ML, 3.0
 cate00014 Data pts: 28 Solns: 11 Pol errs: 2 Nodal Wt: 0.1 Solns shown: 11 Search Inc: 5
 Ampl errs: 0 Ampl Data: 13 Solns: 1 Pol errs: 2 Nodal Wt: 0.1 Soln shown: 1 Search Inc: 5

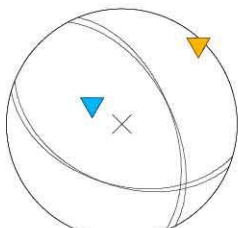
Pol Only



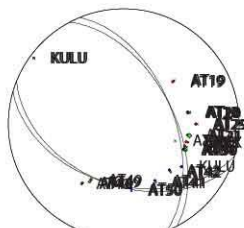
Pol + Ampl



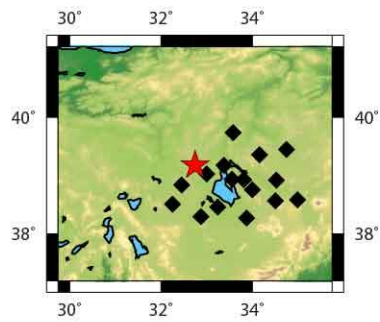
sta SH/P	Pqual	Squal	sta	Pqual	Squal
AT12	1.59 ok/E	ok/E	AT12	ok/E	ok/E
AT19	3.80 g/E	e/l	AT19	g/E	e/l
AT20	5.90 g/E	g/E	AT20	g/E	g/E
AT21	14.50 ok/E	ok/E	AT21	ok/E	ok/E
AT29	1.14 g/E	g/E	AT29	g/E	g/E
AT30	13.17 g/E	g/E	AT30	g/E	g/E
AT31	4.43 g/E	ok/E	AT31	g/E	ok/E
AT40	0.82 g/E	g/E	AT40	g/E	g/E
AT41	0.55 g/E	ok/E	AT41	g/E	ok/E
AT42	1.65 ok/E	g/E	AT42	ok/E	g/E
AT49	9.20 g/l	g/E	AT49	g/l	g/E
AT50	4.55 ok/E	ok/E	AT50	ok/E	ok/E
KULU	4.39 e/l	g/E	KULU	e/l	g/
SERE	2.45 g/E	g/	SERE	g/E	g/E
YAYX	2.44 g/l	g/	YAYX	g/l	g/E



P/T axes

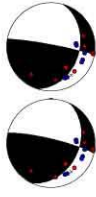


Data

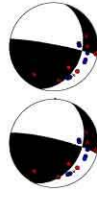


P K: 2316.7 95%: 5.2 T K: 432.2 95%: 12. 0 Lon: 32.75 Lat: 39.18 Dep: 1.00 Mag: ML, 3.0
 cate00015 Data pts: 31 Solns: 2 Pol errs: 1 Nodal Wt: 0.1 Solns shown: 2 Search Inc: 5
 Ampl errs: 0 Ampl Data: 15 Solns: 2 Pol errs: 1 Nodal Wt: 0.1 Soln shown: 2 Search Inc: 5

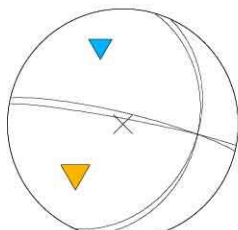
Pol Only



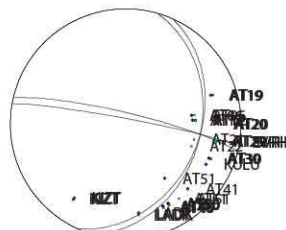
Pol + Ampl



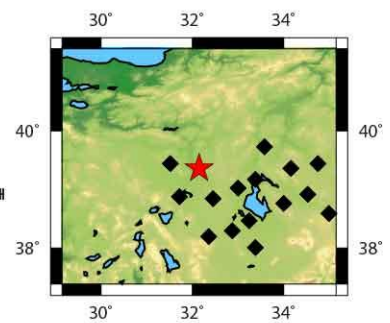
sta SH/P Pqual Squal	sta Pqual Squal
AT06 1.04 ok/E g/E	AT06 ok/E g/E
AT12 8.93 ok/E g/E	AT12 ok/E g/E
AT19 6.02 g/E g/E	AT19 g/E g/E
AT20 3.74 ok/E g/E	AT20 ok/E g/E
AT29 12.88 g/E ok/E	AT29 g/E ok/E
AT30 5.47 g/E ok/E	AT30 g/E ok/E
AT40 4.29 g/E g/E	AT40 g/E g/E
AT50 8.49 g/E g/E	AT50 g/E g/E
AT51 1.42 g/E ok/E	AT51 g/E ok/E
KIZT 5.16 g/E e/	KIZT g/E e/
LADK 2.89 ok/E g/	LADK ok/E g/
SVRH 3.41 g/E ok/	SVRH g/E ok/E



P/T axes



Data



PK: 524.9 95%: 10.9 TK: 524.9 95%: 10.9 Lon: 32.15 Lat: 39.37 Dep: 5.00 Mag: ML, 3.5
 cate00016 Data pts: 28 Solns: 2 Pol errs: 1 Nodal Wt: 0.2 Solns shown: 2 Search Inc: 5
 Ampl errs: 0 Ampl Data: 12 Solns: 2 Pol errs: 1 Nodal Wt: 0.2 Soln shown: 2 Search Inc: 5

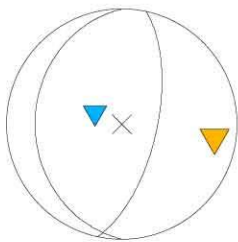
Pol Only



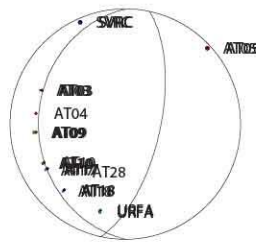
Pol + Ampl



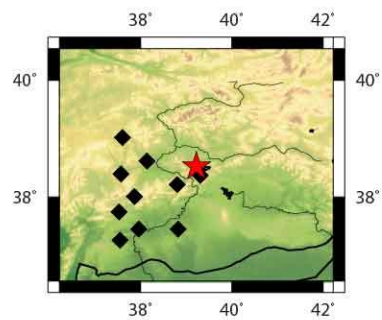
sta	SH/P	Pqual	Squal	sta	Pqual	Squal
AT03	3.63	g/E	ok/E	AT03	g/E	ok/E
AT05	3.50	g/E	g/E	AT04	g/E	
AT09	8.04	ok/E	g/E	AT05	g/E	
AT10	4.81	ok/E	g/E	AT09	ok/E	g/E
AT17	1.65	ok/E	ok/E	AT10	ok/E	g/E
AT18	1.77	g/E	ok/E	AT17	ok/E	ok/E
SVRC	4.28	g/E	g/E	AT18	g/E	ok/E
URFA	10.56	g/E	g/	SVRC	g/E	g/
				URFA	g/E	g/E



P/T axes



Data



P K: NaN 95%: NaN T K: NaN 95%: NaN Lon: 39.22 Lat: 38.53 Dep: 5.00 Mag: ML, 3.1
 cate00017 Data pts: 18 Solns: 1 Pol errs: 1 Nodal Wt: 0.3 Solns shown: 1 Search Inc: 5
 Ampl errs: 0 Ampl Data: 8 Solns: 1 Pol errs: 1 Nodal Wt: 0.3 Soln shown: 1 Search Inc: 5

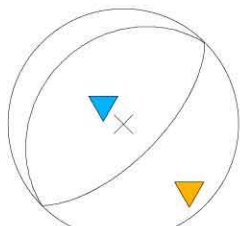
Pol Only



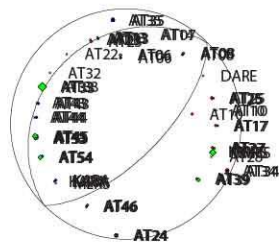
Pol + Ampl



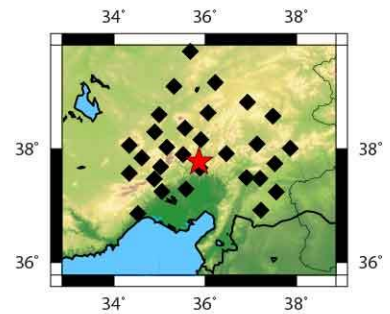
sta SH/P	Pqual	Squal	sta Pqual	Squal
AT06	9.13 ok/E	g/E	AT06	ok/E g/E
AT08	7.65 ok/E	g/E	AT08	ok/E g/E
AT10	1.13 g/E	ok/E	AT10	g/E ok/E
AT13	1.77 g/E	ok/E	AT13	g/E ok/E
AT17	5.06 g/E	g/E	AT17	g/E g/E
AT23	4.34 g/E	g/E	AT23	g/E g/E
AT24	6.19 g/E	g/E	AT24	g/E g/E
AT25	1.95 E/l	g/	AT25	eE g/
AT27	7.15 ok/E	g/E	AT27	ok/E g/E
AT33	28.48 g/E	ok/E	AT33	g/E ok/E
AT34	2.08 g/l	g/E	AT34	g/l g/E
AT35	2.84 g/E	g/E	AT35	g/E g/E
AT39	13.33 g/E	g/E	AT39	g/E g/E
AT43	1.84 ok/E	ok/E	AT43	ok/E ok/E
AT44	3.51 ok/E	g/E	AT44	ok/E g/E
AT45	18.89 g/E	g/E	AT45	g/E g/E
AT46	5.27 g/E	g/E	AT46	g/E g/E
AT53	10.40 ok/E	g/E	AT53	ok/E g/E
AT54	16.21 ok/E	g/E	AT54	ok/E g/E
KARA	0.74 g/E	g/E	KARA	g/E g/E
KMRS	20.65 g/E	ok/	KMRS	g/E ok/E



P/T axes

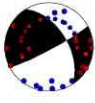


Data



P K: NaN 95%: NaN T K: 0.0 95%: NaN Lon: 35.86 Lat: 37.78 Dep: 6.00 Mag: ML, 3.0
 cate00018 Data pts: 50 Solns: 1 Pol errs: 1 Nodal Wt: 0.3 Solns shown: 1 Search Inc: 5
 Ampl errs: 0 Ampl Data: 21 Solns: 1 Pol errs: 1 Nodal Wt: 0.3 Soln shown: 1 Search Inc: 5

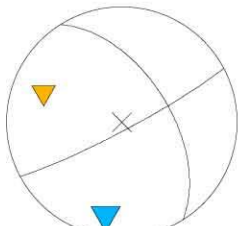
Pol Only



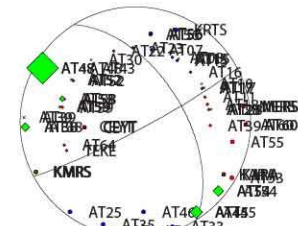
Pol + Ampl



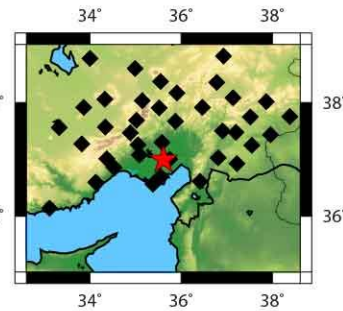
sta SH/P	Pqual	Squal	sta Pqual	Squal
AT07	g/E		AT07	g/E
AT15	3.62 g/E	E	AT08	g/E
AT17	2.32 ok/E	g/E	AT11	g/E
AT28	0.97 g/l	g/E	AT15	g/E
AT38	23.96 ok/E	g/E	AT16	g/E
AT39	1.20 g/l	g/E	AT17	ok/E
AT45	31.82 ok/E	g/E	AT18	g/E
AT48	84.81 ok/E	ok/E	AT22	g/E
AT52	5.27 g/E	g/E	AT23	g/E
AT54	27.77 g/E	g/E	AT24	g/E
AT56	1.69 E/l	g/	AT25	g/l
AT58	20.19 g/E	g/E	AT28	g/l
AT59	6.49 g/E	ok/E	AT33	g/E
AT60	1.30 g/l	g/E	AT34	g/l
CEYT	1.29 g/E	g/E	AT35	g/E
KARA	3.92 E/l	g/	AT38	ok/E
KMRS	7.56 ok/E	g/	AT39	g/l
MERS	2.88 g/E	g/E	AT43	g/E
			AT45	ok/E
			AT46	e/l
			AT48	ok/E
			AT52	g/E
			AT53	g/E
			AT54	g/E
			AT55	e/l
			AT56	e/l
			AT58	g/E
			AT59	g/E
			AT60	g/l
			AT64	g/E
			CEYT	g/E
			KARA	e/l
			KMRS	ok/E
			KRTS	g/E
			MERS	g/E
			TEKE	ok/E



P/T axes

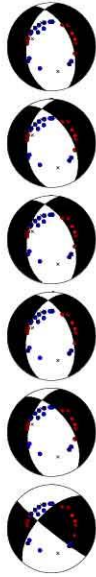


Data



P K: NaN 95%: NaN T K: NaN 95%: NaN Lon: 35.61 Lat: 37 Dep: 19.00 Mag: ML, 3.6
 cate00019 Data pts: 55 Solns: 1 Pol errs: 1 Nodal Wt: 0.3 Solns shown: 1 Search Inc: 5
 Ampl errs: 1 Ampl Data: 17 Solns: 1 Pol errs: 1 Nodal Wt: 0.3 Soln shown: 1 Search Inc: 5

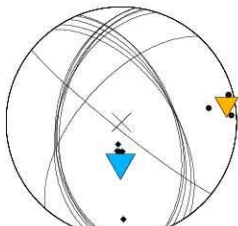
Pol Only



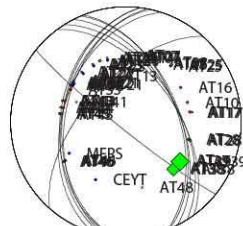
Pol + Ampl



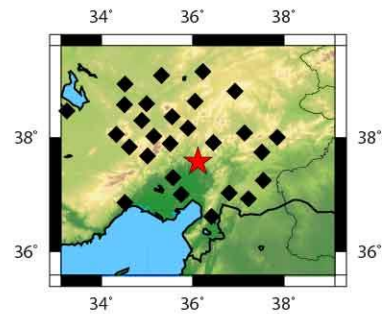
sta SH/P Pqual Squal	sta Pqual Squal
AT07 5.39 g/E g/E	AT07 g/E g/E
AT08 9.61 ok/E g/E	AT08 ok/E g/E
AT13 9.53 g/E ok/E	AT10 g/E
AT17 1.83 g/E g/E	AT13 g/E ok/E
AT21 3.84 g/E g/E	AT14 g/E
AT22 2.60 g/E g/E	AT16 g/E
AT23 3.61 g/E ok/E	AT17 g/E g/E
AT24 1.05 g/l ok/E	AT21 g/E g/E
AT25 10.52 g/l g/E	AT22 g/E g/E
AT28 10.53 ok/E g/E	AT23 g/E ok/E
AT32 1.31 g/E e/	AT24 g/l ok/E
AT34 3.34 g/E ok/E	AT25 g/l g/E
AT38 44.22 g/E g/E	AT28 ok/E g/E
AT39 60.70 g/E g/E	AT32 g/E e/E
AT43 7.75 g/E g/E	AT33 g/E
AT44 2.84 ok/E g/E	AT34 g/E ok/E
AT45 6.13 g/E ok/E	AT38 g/E g/E
AT46 5.44 g/E g/E	AT39 g/E g/E
	AT43 g/E g/E
	AT44 ok/E g/E
	AT45 g/E ok/E
	AT46 g/E g/E
	CEYT ok/E
	MERS ok/E



P/T axes



Data



P K: 14.3 95%: 18.3 T K: 83.0 95%: 7. 4 Lon: 36.12 Lat: 37.58 Dep: 1.00 Mag: ML, 3.5
 cate00020 Data pts: 45 Solns: 6 Pol errs: 1 Nodal Wt: 0.1 Solns shown: 6 Search Inc: 5
 Ampl errs: 0 Ampl Data: 18 Solns: 6 Pol errs: 1 Nodal Wt: 0.1 Soln shown: 6 Search Inc: 5

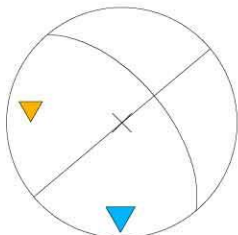
Pol Only



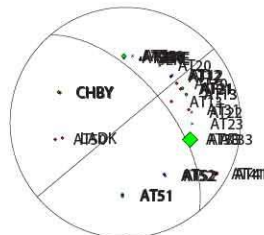
Pol + Ampl



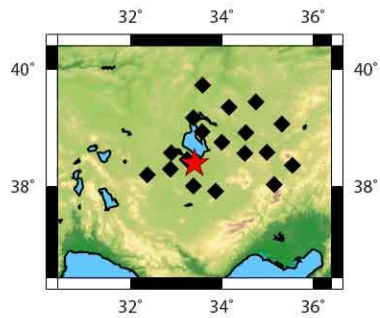
sta	SH/P	Pqual	Squal	sta	Pqual	Squal
AT12	1.92	ok/E	ok/E	AT12	ok/E	ok/E
AT13	10.38	ok/E	g/E	AT13	ok/E	g/E
AT21	8.38	ok/E	g/E	AT21	ok/E	g/E
AT29	17.35	g/E	ok/E	AT29	g/E	ok/E
AT33	49.89	ok/E	g/E	AT30	g/E	
AT41	1.29	e/l	g/	AT31	ok/E	
AT51	8.74	ok/E	g/E	AT33	ok/E	g/E
AT52	0.79	g/l	g/E	AT41	e/l	g/
CHBY	9.88	g/E	g/E	AT50	g/l	
SERE	3.82	ok/E	ok/	AT51	ok/E	g/E
				AT52	g/l	g/E
				CHBY	g/E	g/E
				LADK	g/E	
				SERE	ok/E	ok/E



P/T axes



Data



P K: NaN 95%: NaN T K: NaN 95%: NaN Lon: 33.4 Lat: 38.4 Dep: 3.00 Mag: ML, 3.0
 cate00021 Data pts: 28 Solns: 1 Pol errs: 1 Nodal Wt: 0.5 Solns shown: 1 Search Inc: 5
 Ampl errs: 0 Ampl Data: 10 Solns: 1 Pol errs: 1 Nodal Wt: 0.5 Soln shown: 1 Search Inc: 5

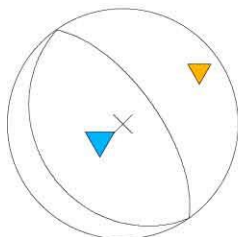
Pol Only



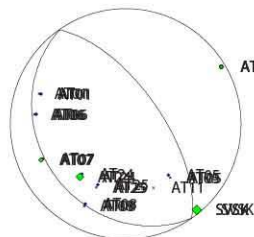
Pol + Ampl



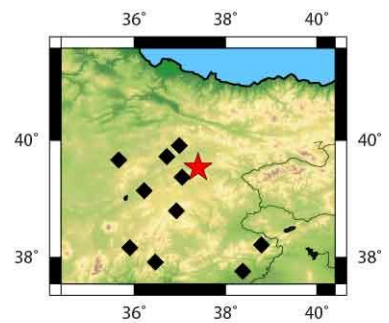
sta SH/P Pqual Squal	sta Pqual Squal
AT01 1.68 ok/E g/E	AT01 ok/E g/E
AT02 11.25 g/E g/E	AT02 g/E g/E
AT05 3.53 ok/E g/E	AT05 ok/E g/E
AT06 3.90 ok/E ok/E	AT06 ok/E ok/E
AT07 16.31 ok/E ok/E	AT07 ok/E ok/E
AT08 2.14 E/E g/	AT08 e/E g/E
AT24 24.27 ok/E g/E	AT24 ok/E g/E
AT25 4.45 ok/E g/E	AT25 ok/E g/E
SVSK 24.93 E/l g/	SVSK g/l g/E



P/T axes



Data



P K: NaN 95%: NaN T K: NaN 95%: NaN Lon: 37.4 Lat: 39.54 Dep: 5.00 Mag: ML, 3.1
 cate00022 Data pts: 19 Solns: 1 Pol errs: 1 Nodal Wt: 0.8 Solns shown: 1 Search Inc: 5
 Ampl errs: 0 Ampl Data: 9 Solns: 1 Pol errs: 1 Nodal Wt: 0.8 Soln shown: 1 Search Inc: 5

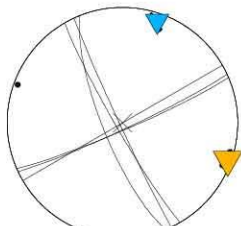
Pol Only



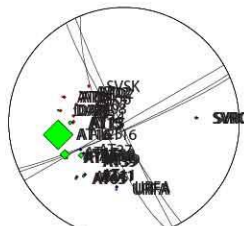
Pol + Ampl



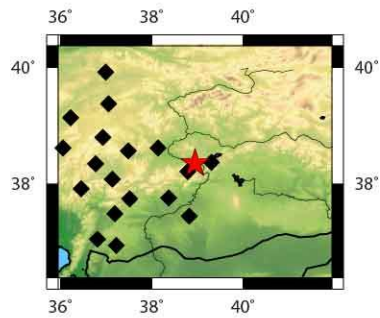
sta SH/P Pqual Squal	sta Pqual Squal
AT02 2.61 g/l g/E	AT02 g/l g/E
AT04 1.23 g/E ok/E	AT04 g/E ok/E
AT05 4.90 E/l g/	AT05 e/l g/
AT11 8.78 g/E g/E	AT06 g/E
AT15 13.58 ok/E g/E	AT07 g/l
AT16 99.42 g/E g/E	AT08 g/E
AT17 31.76 g/E g/E	AT11 g/E g/E
AT27 5.67 g/E g/E	AT14 o/E
AT38 18.83 g/E g/E	AT15 ok/E g/E
AT39 4.71 E/l ok/	AT16 g/E g/E
DARE 2.55 g/l g/E	AT17 g/E g/E
SVRC 2.00 E/l g/	AT23 g/E
URFA 3.01 E/E g/	AT27 g/E g/E
	AT38 g/E g/E
	AT39 e/l ok/E
	DARE g/l g/E
	SVRC e/l g/E
	SVSK g/l
	URFA g/E g/E



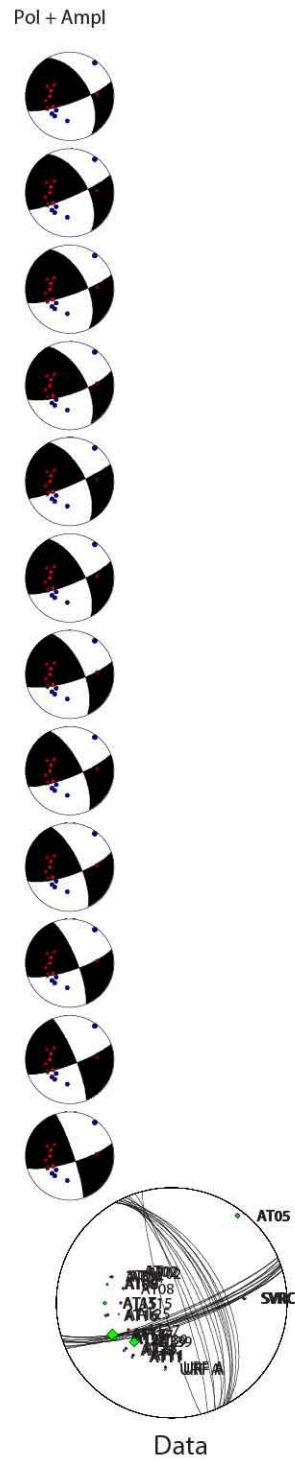
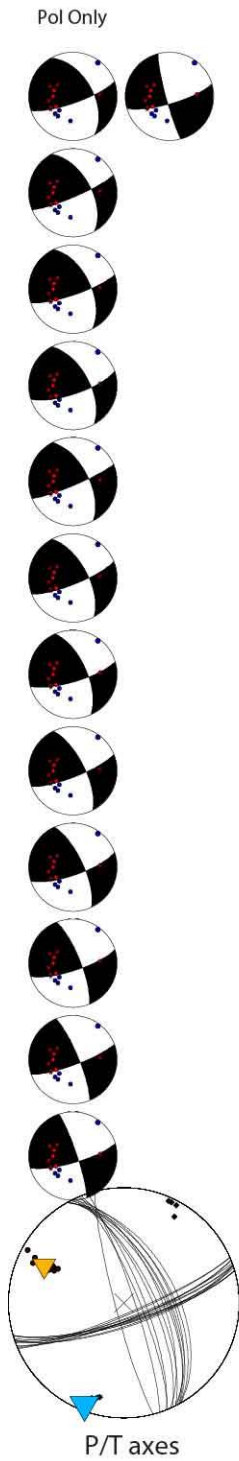
P/T axes



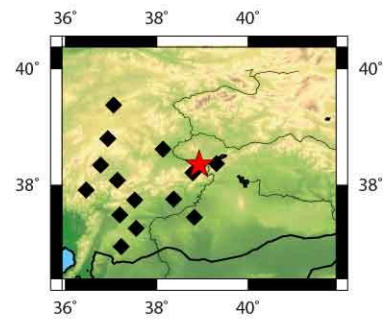
Data



P K: 155.4 95%: 9.9 T K: 201.1 95%: 8.7 Lon: 38.95 Lat: 38.36 Dep: 4.00 Mag: ML, 4.1
 cate00023 Data pts: 33 Solns: 3 Pol errs: 1 Nodal Wt: 0.5 Solns shown: 3 Search Inc: 5
 Ampl errs: 0 Ampl Data: 13 Solns: 3 Pol errs: 1 Nodal Wt: 0.5 Solns shown: 3 Search Inc: 5



sta SH/P	Pqual	Squal	sta Pqual	Squal
AT02	2.65 ok/E	g/E	AT02	ok/E g/E
AT04	1.39 g/E	ok/E	AT04	g/E ok/E
AT05	13.52 g/l	g/E	AT05	g/l g/E
AT08	5.46 ok/E	g/E	AT08	ok/E g/E
AT11	6.48 ok/E	g/E	AT11	ok/E g/E
AT15	13.65 g/E	ok/E	AT15	g/E ok/E
AT16	10.57 g/E	g/E	AT16	g/E g/E
AT17	39.48 ok/E	ok/E	AT17	ok/E ok/E
AT27	13.85 ok/E	g/E	AT27	ok/E g/E
AT28	4.80 ok/E	g/E	AT28	ok/E g/E
AT39	31.39 ok/E	g/E	AT39	ok/E g/E
SVRC	1.78 e/l	ok/E	SVRC	e/l ok/E
URFA	0.86 e/l	ok/E	URFA	e/l ok/E



P K: 64.4 95%: 5.2 T K: 83.6 95%: 4.6 Lon: 38.93 Lat: 38.36 Dep: 2.00 Mag: ML, 3.1
 cate00024 Data pts: 27 Solns: 13 Pol errs: 0 Nodal Wt: 0.9 Solns shown: 13 Search Inc: 5
 Ampl errs: 0 Ampl Data: 13 Solns: 12 Pol errs: 0 Nodal Wt: 0.9 Soln shown: 12 Search Inc: 5

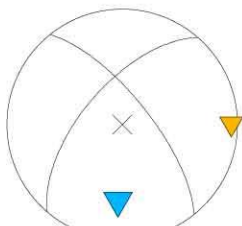
Pol Only



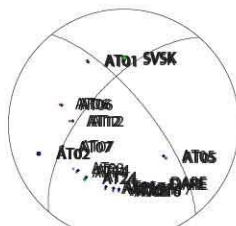
Pol + Ampl



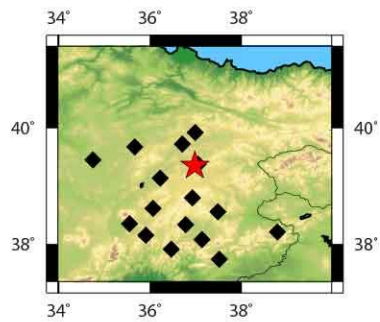
sta	SH/P	Pqual	Squal	sta	Pqual	Squal
AT01	6.74	g/E	e/E	AT01	g/E	e/E
AT02	5.99	g/E	g/E	AT02	g/E	g/E
AT05	5.68	g/E	ok/E	AT05	g/E	ok/E
AT06	1.01	g/E	g/E	AT06	g/E	g/E
AT07	7.94	g/E	g/E	AT07	g/E	g/E
AT08	2.81	E/l	g/	AT08	e/l	g/
AT12	3.95	ok/E	ok/E	AT12	ok/E	ok/E
AT14	2.01	g/E	ok/E	AT14	g/E	ok/E
AT15	3.65	g/E	g/E	AT15	g/E	g/E
AT16	7.64	g/E	g/E	AT16	g/E	g/E
AT24	8.36	ok/E	ok/E	AT24	ok/E	ok/E
AT25	3.52	g/E	g/E	AT25	g/E	g/E
DARE	2.88	ok/E	g/E	DARE	ok/E	g/E
SVSK	15.53	g/E	g/	SVSK	g/E	g/E



P/T axes



Data



P K: NaN 95%: NaN T K: NaN 95%: NaN Lon: 36.98 Lat: 39.36 Dep: 3.00 Mag: ML, 3.1
 cate00025 Data pts: 30 Solns: 1 Pol errs: 1 Nodal Wt: 0.8 Solns shown: 1 Search Inc: 5
 Ampl errs: 0 Ampl Data: 14 Solns: 1 Pol errs: 1 Nodal Wt: 0.8 Soln shown: 1 Search Inc: 5

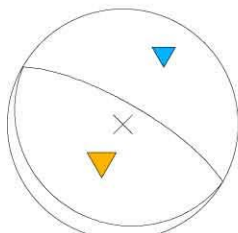
Pol Only



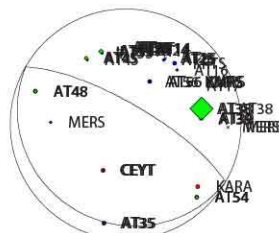
Pol + Ampl



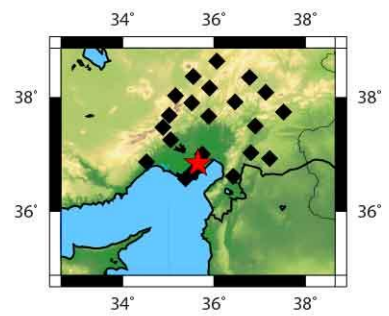
sta SH/P	Pqual	Squal	sta Pqual	Squal
AT14	4.46 ok/E	g/E	AT14	ok/E g/E
AT23	3.78 g/E	ok/E	AT15	g/E
AT25	2.90 ok/E	g/E	AT16	g/E
AT33	15.73 ok/E	g/E	AT17	g/E
AT34	2.44 g/E	ok/E	AT23	g/E ok/E
AT35	5.05 g/E	ok/E	AT24	g/E
AT38	76.63 g/E	g/E	AT25	ok/E g/E
AT39	4.27 ok/E	g/E	AT33	ok/E g/E
AT45	13.13 ok/E	ok/E	AT34	g/E ok/E
AT48	10.13 ok/E	g/E	AT35	g/E ok/E
AT54	9.36 ok/E	ok/E	AT38	g/E g/E
AT56	0.95 g/l	ok/E	AT39	ok/E g/E
CEYT	6.12 g/E	g/E	AT45	ok/E ok/E
KMRS	1.63 ok/E	g/	AT48	ok/E g/E
MERS	0.78 ok/E	e/	AT54	ok/E ok/E
			AT56	g/l ok/E
			CEYT	g/E g/E
			KARA	g/E
			KMRS	ok/E g/E
			KRTS	g/E
			MERS	ok/E e/E



P/T axes

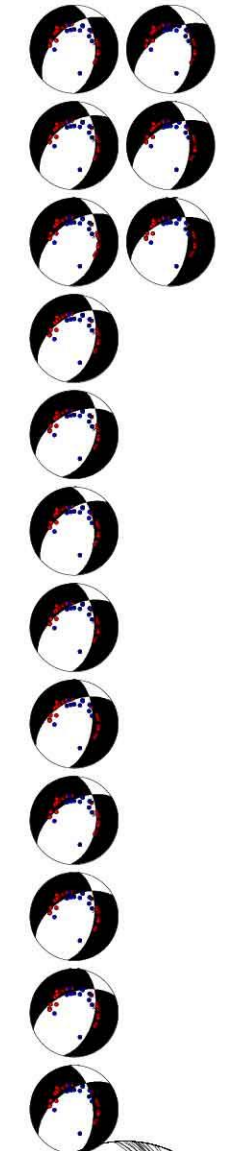


Data

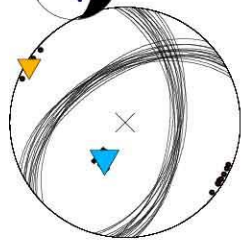
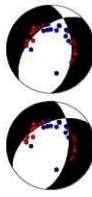


P K: NaN 95%: NaN T K: NaN 95%: NaN Lon: 35.65 Lat: 36.85 Dep: 29.00 Mag: ML, 3.4
 cate00026 Data pts: 36 Solns: 1 Pol errs: 1 Nodal Wt: 0.5 Solns shown: 1 Search Inc: 5
 Ampl errs: 0 Ampl Data: 15 Solns: 1 Pol errs: 1 Nodal Wt: 0.5 Soln shown: 1 Search Inc: 5

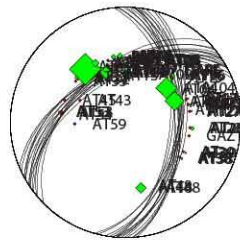
Pol Only



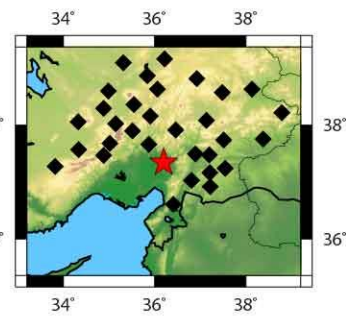
Pol + Ampl



P/T axes



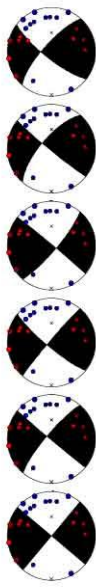
Data



sta SH/P Pqual Squal	sta Pqual Squal
AT04 68.52 ok/E g/E	AT02 ok/E
AT05 64.36 ok/E g/E	AT04 ok/E g/E
AT06 2.32 ok/E g/E	AT05 ok/E g/E
AT07 13.79 ok/E g/E	AT06 ok/E g/E
AT08 4.15 g/E ok/E	AT07 ok/E g/E
AT13 41.72 g/E g/E	AT08 g/E ok/E
AT14 18.44 ok/E g/E	AT13 g/E g/E
AT16 14.03 g/E ok/E	AT14 ok/E g/E
AT17 2.31 g/E g/E	AT16 g/E ok/E
AT22 103.58 ok/E ok/E	AT17 g/E g/E
AT23 24.03 g/E ok/E	AT22 ok/E ok/E
AT25 4.13 ok/E ok/E	AT23 g/E ok/E
AT27 2.32 g/E g/E	AT24 g/E
AT28 14.19 g/E g/E	AT25 ok/E ok/E
AT32 12.53 g/E ok/E	AT27 g/E g/E
AT38 7.05 g/E g/E	AT28 g/E g/E
AT39 2.38 g/E g/E	AT32 g/E ok/E
AT48 35.60 ok/E g/E	AT33 ok/E
AT53 6.77 g/E g/E	AT34 g/E
BNN1 16.87 ok/E ok/E	AT35 g/E
DARE 4.33 g/E g/E	AT38 g/E g/E
KMRS 1.06 g/l g/l	AT39 g/E g/E
	AT43 g/E
	AT45 g/E
	AT48 ok/E g/E
	AT53 g/E g/E
	AT54 g/E
	AT59 ok/E
	BNN1 ok/E ok/E
	DARE g/E g/E
	GAZ1 g/E
	KMRS g/l g/E

P K: 231.0 95%: 2.5 T K: 192.5 95%: 2.8 Lon: 36.2 Lat: 37.35 Dep: 4.00 Mag: ML, 3.9
 cate00027 Data pts: 55 Solns: 15 Pol errs: 2 Nodal Wt: 0.2 Solns shown: 15 Search Inc: 5
 Ampl errs: 0 Ampl Data: 22 Solns: 2 Pol errs: 2 Nodal Wt: 0.2 Soln shown: 2 Search Inc: 5

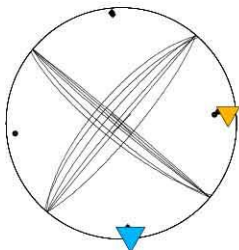
Pol Only



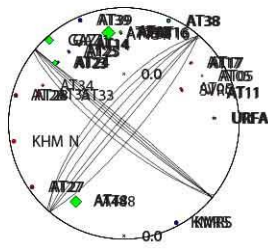
Pol + Ampl



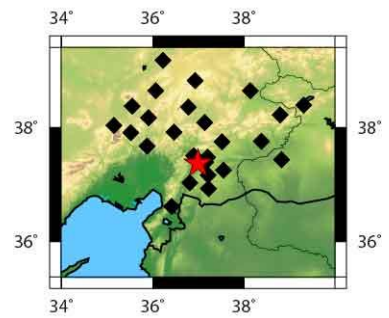
sta	SH/P	Pqual	Squal	sta	Pqual	Squal
AT05	2.60	g/E	ok/E	AT05	g/E	ok/E
AT08	7.95	ok/E	g/E	AT08	ok/E	g/E
AT11	7.30	g/l	g/E	AT11	g/l	g/E
AT14	7.29	g/E	g/E	AT14	g/E	g/E
AT15	42.99	g/E	g/E	AT15	g/E	g/E
AT16	3.20	g/E	g/E	AT16	g/E	g/E
AT17	0.51	e/l	g/	AT17	e/l	g/
AT23	18.45	g/E	g/E	AT23	g/E	g/E
AT25	2.46	g/E	g/E	AT24	ok/E	
AT27	3.43	e/l	g/	AT25	g/E	g/E
AT28	1.82	g/E	g/E	AT27	e/l	g/
AT38	6.56	g/E	g/E	AT28	g/E	g/E
AT39	3.77	g/E	g/E	AT33	ok/E	
AT48	39.42	ok/E	g/E	AT34	g/E	
GAZ1	22.99	e/	e/	AT35	g/E	
KMRS	1.59	e/l	e/E	AT38	g/E	g/E
URFA	7.49	ok/E	g/	AT39	g/E	g/E
				AT48	ok/E	g/E
				GAZ1	g/E	e/E
				KHM N	ok/E	
				KMRS	e/l	e/E
				SVRC	g/E	
				URFA	ok/E	g/E



P/T axes



Data

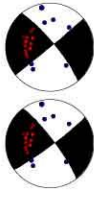


P K: 161.7 95%: 5.3 T K: 61.2 95%: 8. 6 Lon: 36.99 Lat: 37.37 Dep: 5.00 Mag: ML, 3.0
 cate00028 Data pts: 44 Solns: 39 Pol errs: 1 Nodal Wt: 0.8 Solns shown: 6 Search Inc: 10
 Ampl errs: 0 Ampl Data: 17 Solns: 4 Pol errs: 1 Nodal Wt: 0.8 Solns shown: 4 Search Inc: 5

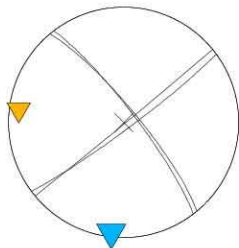
Pol Only



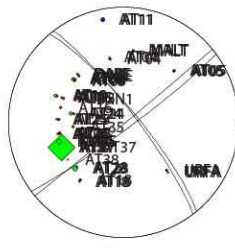
Pol + Ampl



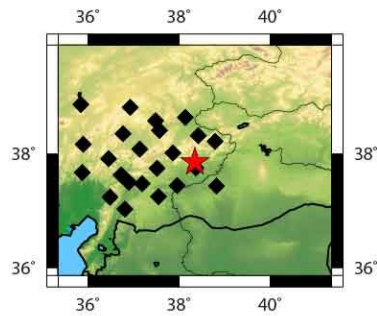
sta	SH/P	Pqual	Squal	sta	Pqual	Squal
AT04	0.77	g/l	ok/E	AT04	g/l	ok/E
AT05	1.52	E/l	g/	AT05	e/l	g/
AT08	8.80	ok/E	ok/E	AT08	ok/E	ok/E
AT09	6.30	E/E	g/	AT09	e/E	g/E
AT10	12.94	g/E	e/l	AT10	g/E	e/l
AT11	4.03	e/l	e/E	AT11	e/l	e/E
AT15	5.62	g/E	g/E	AT15	g/E	g/E
AT17	1.44	e/E	ok/	AT16	g/E	
AT18	4.21	g/E	g/E	AT17	e/E	ok/E
AT24	12.33	ok/E	ok/E	AT18	g/E	g/E
AT25	4.99	g/E	ok/E	AT24	ok/E	ok/E
AT26	3.14	ok/E	g/E	AT25	g/E	ok/E
AT27	10.61	g/E	g/E	AT26	ok/E	g/E
AT28	18.25	g/E	g/E	AT27	g/E	g/E
AT37	87.39	ok/E	g/E	AT28	g/E	g/E
DARE	4.83	g/E	g/E	AT35	ok/E	
KMRS	19.46	ok/E	g/	AT37	ok/E	g/E
MALT	1.83	e/l	e/E	BNN1	g/E	
URFA	2.80	g/E	g/	DARE	g/E	g/E
				KMRS	ok/E	g/E
				MALT	e/l	e/E
				URFA	g/E	g/E



P/T axes

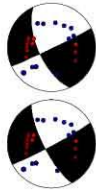


Data



P K: 569.0 95%: 10.5 T K: 1301.4 95%: 6.9 Lon: 38.35 Lat: 37.86 Dep: 2.00 Mag: ML, 3.1
 cate00029 Data pts: 42 Solns: 2 Pol errs: 0 Nodal Wt: 0.9 Solns shown: 2 Search Inc: 5
 Ampl errs: 0 Ampl Data: 19 Solns: 2 Pol errs: 0 Nodal Wt: 0.9 Solns shown: 2 Search Inc: 5

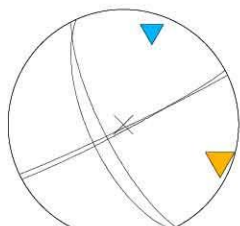
Pol Only



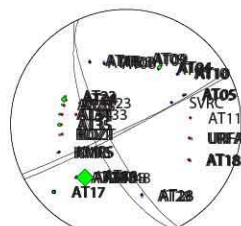
Pol + Ampl



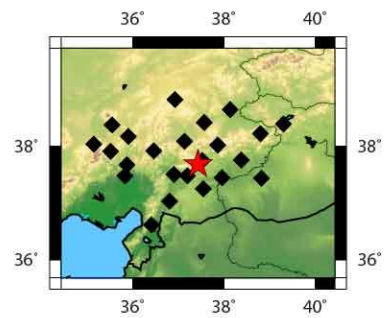
sta	SH/P	Pqual	Squal	sta	Pqual	Squal
AT04	15.39	g/E	ok/E	AT04	g/E	ok/E
AT05	7.81	g/E	g/E	AT05	g/E	g/E
AT08	1.95	ok/E	g/E	AT08	ok/E	g/E
AT09	2.68	g/l	g/E	AT09	g/l	g/E
AT10	1.50	g/l	g/E	AT10	g/l	g/E
AT16	3.74	g/E	g/E	AT11	g/l	
AT17	7.84	g/E	g/E	AT16	g/E	g/E
AT18	3.86	g/l	g/E	AT17	g/E	g/E
AT23	7.58	g/E	g/E	AT18	g/l	g/E
AT24	19.60	g/E	ok/E	AT23	g/E	g/E
AT25	1.28	g/l	g/E	AT24	g/E	ok/E
AT27	1.94	g/E	g/E	AT25	g/l	g/E
AT28	1.42	g/l	g/E	AT27	g/E	g/E
AT34	5.06	ok/E	g/E	AT28	g/l	g/E
AT35	11.45	g/E	g/E	AT33	ok/E	
AT38	43.70	ok/E	g/E	AT34	ok/E	g/E
AT48	57.13	ok/E	g/E	AT35	g/E	g/E
KMRS	3.22	g/E	g/	AT38	ok/E	g/E
KOZT	3.15	g/E	ok/	AT48	ok/E	g/E
URFA	2.76	g/E	g/	KMRS	g/E	g/E
				KOZT	g/E	ok/
				SVRC	g/E	
				URFA	g/E	g/E



P/T axes



Data



P K: 367.4 95%: 13.1 TK: 147.8 95%: 20. 7 Lon: 37.43 Lat: 37.68 Dep: 3.00 Mag: ML, 3.2
 cate00030 Data pts: 43 Solns: 2 Pol errs: 1 Nodal Wt: 0.2 Solns shown: 2 Search Inc: 5
 Ampl errs: 0 Ampl Data: 20 Solns: 1 Pol errs: 1 Nodal Wt: 0.2 Soln shown: 1 Search Inc: 5

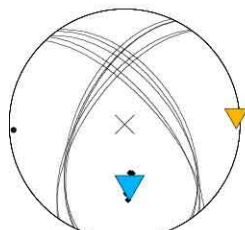
Pol Only



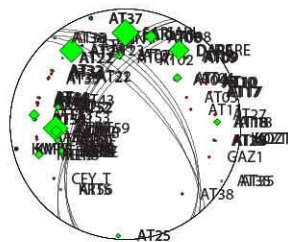
Pol + Ampl



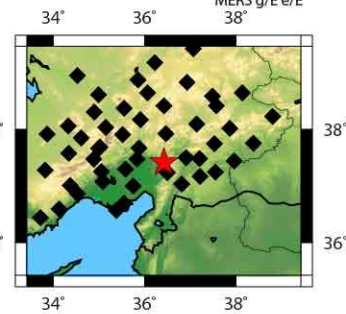
sta SH/P Pqual Squal	sta Pqual Squal
AT04 29.37 g/E o/E	AT02 g/E
AT07 28.91 o/E g/E	AT04 g/E o/E
AT08 39.90 g/E g/E	AT05 g/E
AT09 5.11 E/l g/	AT07 o/E g/E
AT10 0.75 E/l o/	AT08 g/E g/E
AT17 1.04 E/l o/	AT09 eB g/
AT18 22.44 g/E g/E	AT10 eB o/
AT22 7.34 g/E o/E	AT11 g/E
AT23 80.14 g/E o/E	AT14 o/E
AT25 11.50 E/l g/	AT16 o/E
AT28 3.41 g/l g/E	AT17 eB o/
AT32 8.22 g/E g/E	AT18 g/E g/E
AT35 2.43 E/l g/	AT21 g/E
AT37 7.99 E/l o/	AT22 g/E o/E
AT38 4.92 g/E g/E	AT23 g/E o/E
AT44 5.48 g/E g/E	AT24 g/E
AT45 6.72 g/E o/E	AT25 eB g/
AT52 21.19 g/E o/E	AT27 e/l
AT53 34.53 g/E g/E	AT28 g/l g/E
AT54 12.36 g/l g/E	AT32 g/E g/E
AT59 83.44 o/E g/E	AT33 g/E
AT60 23.35 o/E g/l	AT34 e/l
AT62 37.96 g/E g/E	AT35 eB g/
DARE 66.65 g/E o/E	AT37 eB o/
KEBE 29.78 o/E g/E	AT38 g/E g/E
KMRS 0.54 e/l g/E	AT43 g/E
KOZT 0.67 e/l g/E	AT44 g/E g/E
MERS 28.88 E/E e/	AT45 g/E o/E
SARI 88.21 E/E g/	AT46 g/E
	AT52 g/E o/E
	AT53 g/E g/E
	AT54 g/l g/E
	AT55 g/E
	AT59 o/E g/E
	AT60 o/E g/l
	AT62 g/E g/E
	AT64 g/E
	BERE o/E
	BNN1 o/E
	CEYT e/l
	CMRD g/E
	DARE g/E o/E
	GAZ1 g/E
	HDMB g/E
	KARA g/E
	KEBE o/E g/E
	KMRS e/l g/E
	KOZT eB g/
	MERS g/E e/E



P/T axes



Data



P K: 75.6 95%: 8.9 T K: 602.5 95%: 3. 1 Lon: 36.42 Lat: 37.42 Dep: 5.00 Mag: ML, 4.5
 cate00031 Data pts: 81 Solns: 5 Pol errs: 2 Nodal Wt: 0.2 Solns shown: 5 Search Inc: 5
 Ampl errs: 0 Ampl Data: 29 Solns: 2 Pol errs: 2 Nodal Wt: 0.1 Soln shown: 2 Search Inc: 5

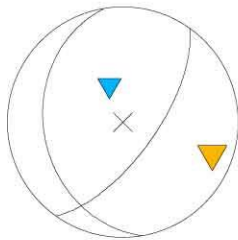
Pol Only



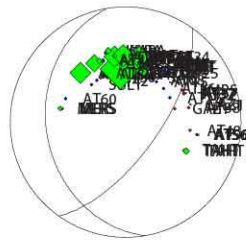
Pol + Ampl



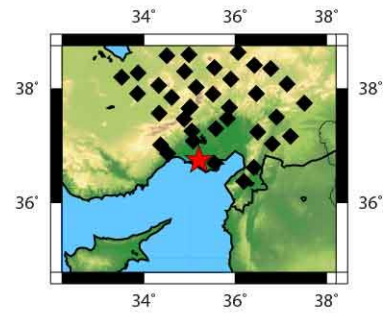
sta SH/P	Pqual	Squal	sta	Pqual	Squal
AT14	27.54 g/E ok/E		AT08	ok/E	
AT22	132.34 ok/E g/E		AT12	g/E	
AT23	12.27 g/E ok/E		AT14	g/E ok/E	
AT30	7.07 g/E g/E		AT15	g/l	
AT32	70.45 g/E g/E		AT16	ok/E	
AT33	73.59 ok/E g/E		AT17	ok/E	
AT34	73.04 g/E ok/E		AT20	g/E	
AT35	-3.85 g/l g/E		AT21	g/l	
AT37	3.17 ok/E g/E		AT22	ok/E g/E	
AT43	56.76 ok/E g/E		AT23	g/E ok/E	
AT44	19.77 g/E ok/E		AT24	ok/E	
AT45	12.23 g/E g/E		AT25	g/l	
AT46	5.06 g/l ok/E		AT30	g/E g/E	
AT52	68.85 g/E g/0		AT31	ok/E	
AT54	5.35 g/l g/E		AT32	g/E g/E	
AT56	2.85 g/E g/E		AT33	ok/E g/E	
GAZ1	2.70 g/E ok/E		AT34	g/E ok/E	
KARA	22.88 g/E g/E		AT35	g/l g/E	
KOZT	3.79 g/l ok/		AT37	ok/E g/E	
MERS	16.22 ok/E g/E		AT38	g/E	
TAHT	23.00 g/E g/		AT42	g/E	
			AT43	ok/E g/E	
			AT44	g/E ok/E	
			AT45	g/E g/E	
			AT46	g/l ok/E	
			AT48	ok/E	
			AT52	g/E g/0	
			AT53	g/E	
			AT54	g/l g/E	
			AT55	g/l	
			AT56	g/E g/E	
			AT60	g/E	
			CMRD	g/E	
			GAZ1	g/E ok/	
			KARA	g/E g/E	
			KMRS	ok/E	
			KOZT	g/l ok/E	
			MERS	ok/E g/E	
			SARI	ok/E	
			SULT	g/l	
			TAHT	g/E g/E	



P/T axes



Data



P K: NaN 95%: NaN T K: NaN 95%: NaN Lon: 35.21 Lat: 36.75 Dep: 3.00 Mag: ML, 4.3
 cate00032 Data pts: 62 Solns: 1 Pol errs: 1 Nodal Wt: 0.3 Solns shown: 1 Search Inc: 5
 Ampl errs: 1 Ampl Data: 21 Solns: 1 Pol errs: 1 Nodal Wt: 0.2 Soln shown: 1 Search Inc: 5

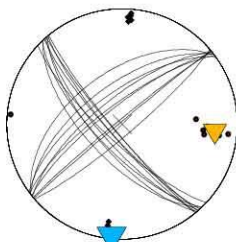
Pol Only



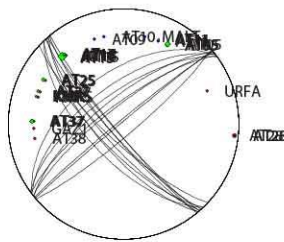
Pol + Ampl



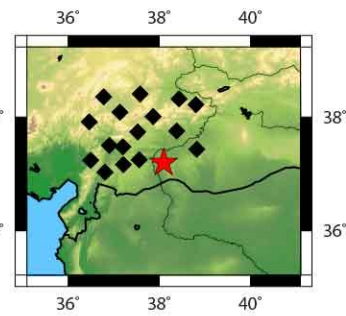
sta	SH/P	Pqual	Squal	sta	Pqual	Squal
AT05	19.25	ok/E	ok/E	AT05	ok/E	ok/E
AT11	4.78	g/l	g/E	AT09	g/E	
AT15	29.39	ok/E	g/E	AT10	g/l	
AT16	10.21	g/E	ok/E	AT11	g/l	g/E
AT17	9.30	g/E	g/E	AT15	ok/E	g/E
AT25	11.99	ok/E	g/E	AT16	g/E	ok/E
AT27	10.27	g/E	g/E	AT17	g/E	g/E
AT28	1.43	g/l	g/E	AT25	ok/E	g/E
AT37	15.70	ok/E	g/E	AT27	g/E	g/E
KMRS	5.68	ok/E	g/l	AT28	g/l	g/E
				AT37	ok/E	g/E
				AT38	g/E	
				GAZ1	g/l	
				KMRS	ok/E	g/E
				MALT	g/E	
				URFA	g/l	



P/T axes



Data



P K: 64.8 95%: 6.4 T K: 46.7 95%: 7.6 Lon: 38.09 Lat: 37.21 Dep: 5.00 Mag: ML, 3.2
 cate00033 Data pts: 26 Solns: 52 Pol errs: 1 Nodal Wt: 0.8 Solns shown: 9 Search Inc: 10
 Ampl errs: 0 Ampl Data: 10 Solns: 52 Pol errs: 1 Nodal Wt: 0.8 Soln shown: 9 Search Inc: 10

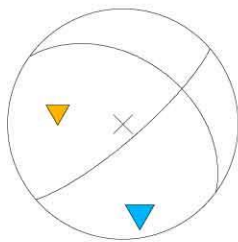
Pol Only



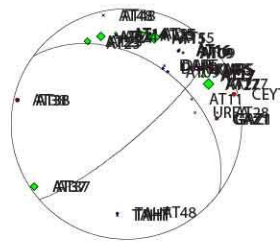
Pol + Ampl



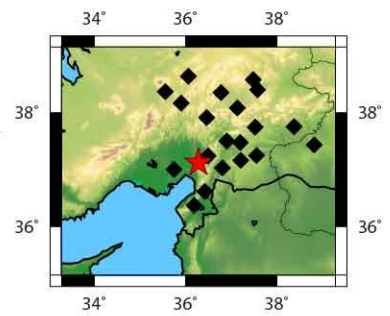
sta SH/P	Pqual	Squal	sta	Pqual	Squal
AT09	5.62 g/E	o/E	AT09	g/E	o/E
AT14	9.06 ok/E	o/E	AT14	ok/E	o/E
AT15	38.31 ok/E	o/E	AT15	ok/E	o/E
AT16	7.52 o/E	ok/E	AT16	o/E	ok/E
AT17	11.47 o/E	g/E	AT17	o/E	g/E
AT23	21.87 o/E	ok/E	AT23	o/E	ok/E
AT24	27.74 ok/E	o/E	AT24	ok/E	o/E
AT25	17.33 g/E	g/E	AT25	g/E	g/E
AT27	35.77 o/E	g/E	AT27	o/E	g/E
AT37	20.56 g/E	g/E	AT37	g/E	g/E
AT38	1.81 g/l	g/E	AT38	g/l	g/E
AT48	2.71 g/E	g/E	AT48	g/E	g/E
DARE	2.94 g/E	g/E	CEYT	o/E	
GAZ1	0.40 o/E	ok/E	DARE	g/E	g/E
KMRS	0.86 ok/E	g/	GAZ1	o/E	ok/E
TAHT	1.92 g/E	g/	KMRS	ok/E	g/E
			TAHT	g/E	g/E



P/T axes

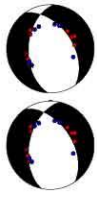


Data



P K: NaN 95%: NaN T K: NaN 95%: NaN Lon: 36.28 Lat: 37.13 Dep: 5.00 Mag: ML, 3.3
 cate00034 Data pts: 36 Solns: 1 Pol errs: 1 Nodal Wt: 0.3 Solns shown: 1 Search Inc: 5
 Ampl errs: 0 Ampl Data: 16 Solns: 1 Pol errs: 1 Nodal Wt: 0.1 Soln shown: 1 Search Inc: 5

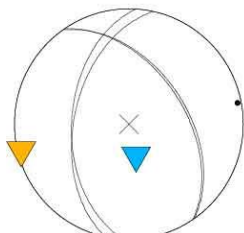
Pol Only



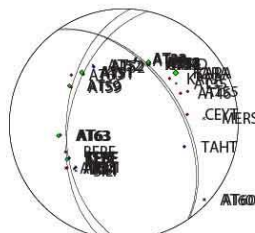
Pol + Ampl



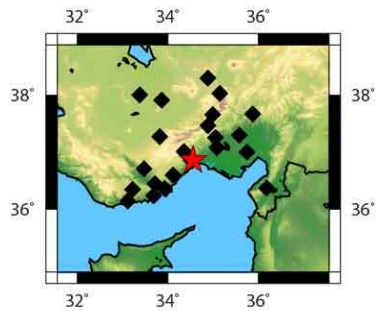
sta	SH/P	Pqual	Squal	sta	Pqual	Squal
AT32	7.28	ok/E	ok/E	AT32	ok/E	ok/E
AT33	16.07	g/E	ok/E	AT33	g/E	ok/E
AT51	16.27	ok/E	ok/E	AT46	g/E	
AT52	0.79	ok/E	g/E	AT51	ok/E	ok/E
AT54	4.67	g/E	g/E	AT52	ok/E	g/E
AT59	11.56	g/E	g/E	AT54	g/E	g/E
AT60	4.08	g/E	g/E	AT55	g/E	
AT63	14.13	g/E	g/E	AT59	g/E	g/E
AT64	0.75	g/E	ok/E	AT60	g/E	g/E
IKL1	3.11	ok/E	g/E	AT63	g/E	g/E
KARA	18.94	ok/E	g/E	AT64	g/E	ok/E
KEBE	12.80	g/E	g/E	BERE	g/E	
				CEYT	g/E	
				CMRD	g/E	
				IKL1	ok/E	g/E
				KARA	ok/E	g/E
				KEBE	g/E	g/E
				TAHT	ok/E	
				TEKE	g/E	



P/T axes



Data



P K: 463.6 95%: 11.6 T K: 570.0 95%: 10. 5 Lon: 34.56 Lat: 36.87 Dep: 2.00 Mag: ML, 3.2
 cate00035 Data pts: 34 Solns: 2 Pol errs: 1 Nodal Wt: 0.2 Solns shown: 2 Search Inc: 5
 Ampl errs: 0 Ampl Data: 12 Solns: 1 Pol errs: 1 Nodal Wt: 0.2 Solns shown: 1 Search Inc: 5

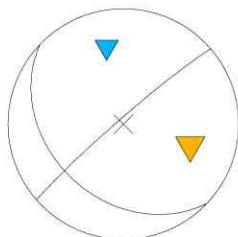
Pol Only



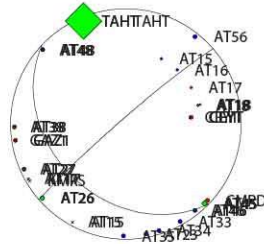
Pol + Ampl



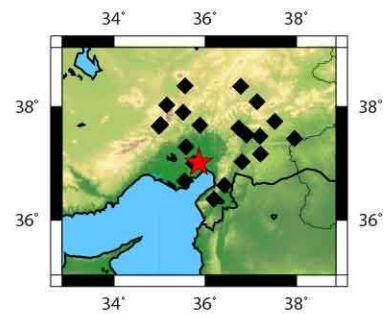
sta SH/P Pqual Squal	sta Pqual Squal
AT15 2.56 g/E ok/E	AT15 g/E ok/E
AT17 4.02 ok/E ok/E	AT16 g/E
AT18 5.15 g/E g/E	AT17 ok/E ok/E
AT26 11.62 ok/E ok/E	AT18 g/E g/E
AT27 4.64 ok/E g/E	AT23 g/E
AT38 4.58 g/E g/E	AT26 ok/E ok/E
AT45 14.46 ok/E ok/E	AT27 ok/E g/E
AT46 4.69 E/l g/	AT33 g/E
AT48 5.97 g/E ok/E	AT34 g/l
CEYT 1.01 g/l g/E	AT35 g/E
GAZ1 1.25 g/E g/E	AT38 g/E g/E
TAHT 95.44 dk/E g/	AT45 ok/E ok/E
	AT46 e# g/
	AT48 g/E ok/E
	AT56 g/l
	CEYT g/l g/E
	CMRD ok/E
	GAZ1 g/E g/E
	TAHT ok/E g/



P/T axes



Data

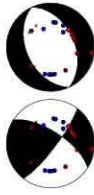


P K: NaN 95%: NaN T K: NaN 95%: NaN Lon: 35.86 Lat: 37.02 Dep: 12.00 Mag: ML, 3.0
 cate00036 Data pts: 32 Solns: 1 Pol errs: 1 Nodal Wt: 0.8 Solns shown: 1 Search Inc: 5
 Ampl errs: 0 Ampl Data: 12 Solns: 1 Pol errs: 1 Nodal Wt: 0.8 Soln shown: 1 Search Inc: 5

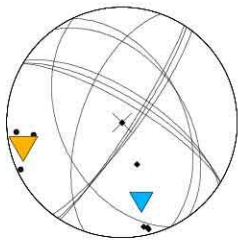
Pol Only



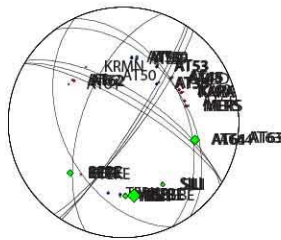
Pol + Ampl



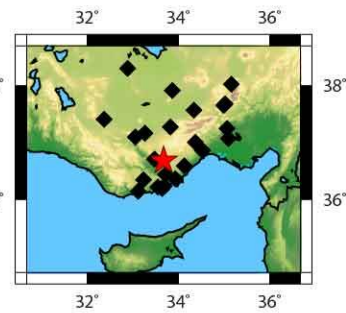
sta	SH/P	Pqual	Squal	sta	Pqual	Squal
AT33	3.97	ok/E	g/E	AT33	ok/E	g/E
AT45	3.79	g/E	ok/E	AT45	g/E	ok/E
AT52	1.19	ok/E	g/E	AT50	g/E	
AT53	6.22	ok/E	g/E	AT52	ok/E	g/E
AT59	10.08	g/E	ok/E	AT53	ok/E	g/E
AT62	0.64	E/E	o/	AT55	ok/E	
AT63	3.86	E/E	o/	AT59	g/E	ok/E
AT64	31.38	E/E	e/	AT60	g/E	
BERE	21.26	g/E	ok/	AT62	e/E	o/E
IKL1	17.88	g/E	ok/	AT63	e/E	o/E
KARA	1.01	g/E	g/E	AT64	g/E	e/E
KEBE	44.74	g/E	g/E	BERE	g/E	ok/E
MERS	1.98	g/E	g/E	CMRD	g/E	
SILI	16.59	g/E	o/E	IKL1	g/E	ok/E
YESI	4.43	ok/E	ok/E	KARA	g/E	g/E
				KEBE	g/E	g/E
				MERS	g/E	g/E
				SILI	g/E	o/E
				TEPK	ok/E	
				YESI	ok/E	ok/E



P/T axes



Data



P K: 4.6 95%: 40.0 T K: 47.5 95%: 11. 2 Lon: 33.67 Lat: 36.69 Dep: 2.00 Mag: ML, 3.4
 cate00037 Data pts: 38 Solns: 5 Pol errs: 2 Nodal Wt: 0.4 Solns shown: 5 Search Inc: 5
 Ampl errs: 0 Ampl Data: 15 Solns: 2 Pol errs: 2 Nodal Wt: 0.4 Soln shown: 2 Search Inc: 5

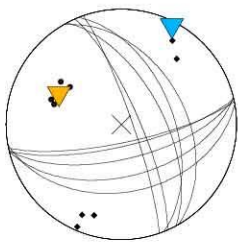
Pol Only



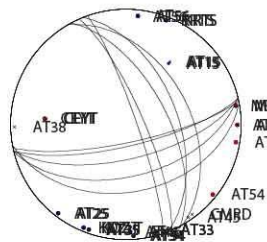
Pol + Ampl



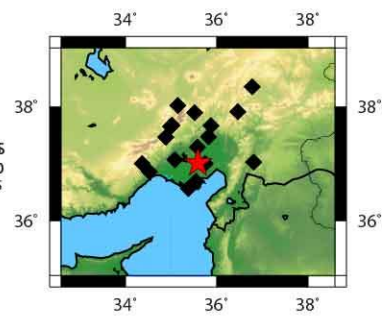
sta SH/P	Pqual	Squal	sta	Pqual	Squal
AT15	3.07 g/E	ok/E	AT15	g/E	ok/E
AT25	3.60 ok/E	ok/E	AT25	ok/E	ok/E
AT33	10.69 g/E	ok/E	AT33	g/E	ok/E
AT34	4.96 g/E	ok/E	AT34	g/E	ok/E
AT35	5.51 g/E	o/E	AT35	g/E	o/E
AT46	1.79 g/E	g/E	AT46	g/E	g/E
AT56	1.31 g/E	ok/E	AT54	g/E	
AT60	1.42 g/E	ok/E	AT55	g/E	
CEYT	2.33 g/E	g/E	AT56	g/E	ok/E
KOZT	1.14 g/E	ok/E	AT60	g/E	ok/E
KRTS	1.23 g/E	ok/E	CEYT	g/E	g/E
MERS	1.47 g/E	g/E	KOZT	g/E	ok/E
			KRTS	g/E	ok/E
			MERS	g/E	g/E



P/T axes

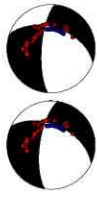


Data



P K: 14.5 95%: 20.8 T K: 112.7 95%: 7.2 Lon: 35.59 Lat: 37.02 Dep: 12.00 Mag: ML, 3.1
 cate00038 Data pts: 29 Solns: 51 Pol errs: 1 Nodal Wt: 0.8 Solns shown: 5 Search Inc: 10
 Ampl errs: 0 Ampl Data: 12 Solns: 30 Pol errs: 1 Nodal Wt: 0.8 Solns shown: 3 Search Inc: 10

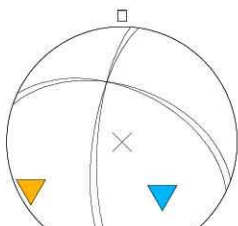
Pol Only



Pol + Ampl



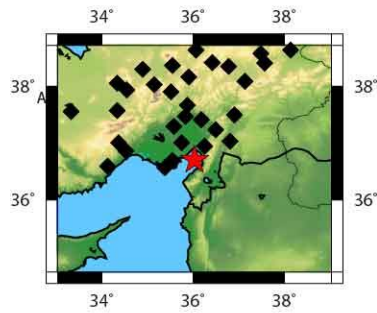
sta SH/P Pqual Squal	sta Pqual Squal
AT01 20.92 g/E g/l	AT01 g/E g/l
AT02 146.41 g/E g/l	AT02 g/E g/l
AT03 15.93 g/E g/E	AT03 g/E g/E
AT04 22.94 g/E g/l	AT04 g/E g/l
AT06 19.15 g/E g/E	AT06 g/E g/E
AT08 34.88 g/E g/E	AT07 g/E
AT09 21.39 g/E g/E	AT08 g/E g/E
AT14 61.59 g/E g/E	AT09 g/E g/E
AT15 10.63 g/E g/E	AT14 g/E g/E
AT23 16.18 g/E g/E	AT15 e/E o/E
AT24 16.27 g/E g/E	AT16 g/E
AT30 23.31 g/E o/E	AT23 g/E g/E
AT32 94.01 g/E g/E	AT24 g/E g/E
AT33 141.01 g/E g/E	AT30 g/E o/E
AT34 68.28 g/E g/E	AT32 g/E g/E
AT35 73.83 g/E g/l	AT33 g/E g/E
AT37 14.70 g/E g/l	AT34 g/E g/E
AT38 43.99 g/E e/l	AT35 e/E g/E
AT43 44.34 g/E g/E	AT37 e/E g/E
AT46 7.25 g/E l/g	AT38 e/E e/l
AT53 169.33 g/E g/E	AT43 g/E g/E
AT58 50.09 g/E g/E	AT46 e/l g/l
AT64 60.77 g/E g/E	AT53 g/E g/E
AT66 578.20 g/E e/l	AT56 e/l
AT67 20.14 g/E e/l	AT58 g/E g/E
AT70 7.66 g/E g/l	AT60 g/E
CEYT 12.12 g/E e/E	AT64 g/E g/E
DARE 36.10 g/E e/l	AT66 g/E e/E
KMRS 15.17 g/E g/l	AT67 g/E e/l
	AT70 e/E g/E
	CEYT g/E e/E
	DARE g/E e/E
	KMRS g/E g/E
	KOZT e/E
	KRTS e/l
	MERS g/E



P/T axes



Data

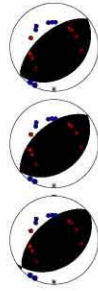


P K: 525.6 95%: 10.9 T K: 526.0 95%: 10.9 Lon: 36.03 Lat: 36.71 Dep: 4.00 Mag: ML, 4.9
 cate00039 Data pts: 66 Solns: 2 Pol errs: 1 Nodal Wt: 0.1 Solns shown: 2 Search Inc: 5
 Ampl errs: 1 Ampl Data: 29 Solns: 1 Pol errs: 1 Nodal Wt: 0.1 Soln shown: 1 Search Inc: 5

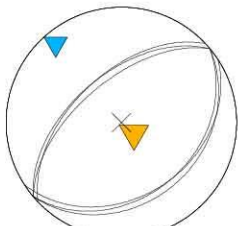
Pol Only



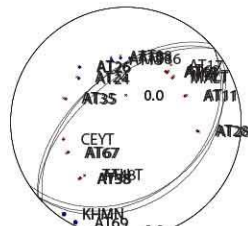
Pol + Ampl



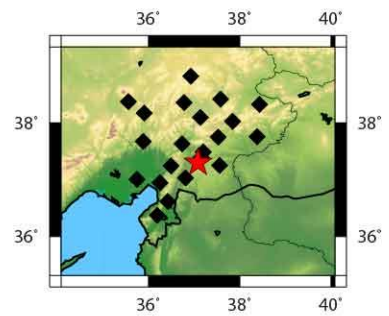
sta Pqual Squal
 AT08 ok/E g/E
 0.0 g/E ok/E
 AT11 g/E ok/E
 AT15 g/E ok/E
 AT16 g/E
 AT17 g/E g/E
 0.0 g/E ok/E
 AT24 ok/E g/E
 AT26 g/E ok/E
 AT28 g/l g/E
 AT35 g/E g/E
 0.0 g/E ok/E
 AT38 g/E e/E
 AT67 g/E ok/E
 AT68 g/E g/E
 AT69 g/E g/E
 CEYT g/E
 KHMN g/E ok/
 MALT g/E ok/E



P/T axes



Data



P K: 759.3 95%: 4.5 T K: 401.8 95%: 6.2 Lon: 37.08 Lat: 37.3 Dep: 1.00 Mag: ML, 3.0
 cate00040 Data pts: 38 Solns: 3 Pol errs: 1 Nodal Wt: 0.3 Solns shown: 3 Search Inc: 5
 Ampl errs: 1 Ampl Data: 17 Solns: 3 Pol errs: 1 Nodal Wt: 0.3 Soln shown: 3 Search Inc: 5

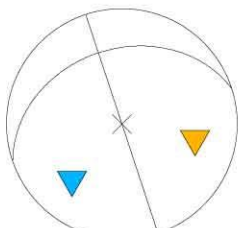
Pol Only



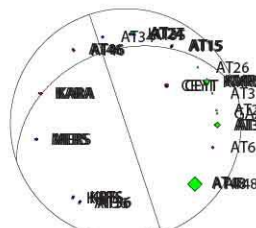
Pol + Ampl



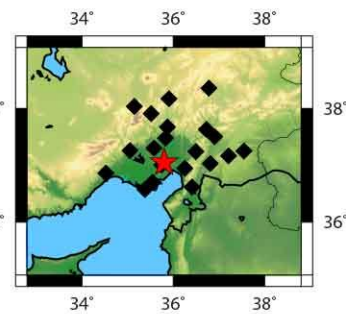
sta	SH/P	Pqual	Squal	sta	Pqual	Squal
AT15	2.37	ok/E	o/E	AT15	ok/E	o/E
AT24	8.14	o/E	ok/E	AT24	o/E	ok/E
AT38	18.32	o/E	g/E		0.0	g/E
AT46	3.39	g/l	o/E	AT34	ok/E	
AT48	48.84	ok/E	o/E	AT35	g/E	
AT56	0.61	E/l	o/	AT38	o/E	g/E
CEYT	2.37	g/E	g/E	AT46	g/l	o/E
KARA	4.09	g/E	g/E	AT48	ok/E	o/E
KMRS	17.54	ok/E	g/	AT56	e/l	o/
KRTS	0.40	o/E	ok/	AT67	g/E	
MERS	2.85	g/E	g/E	CEYT	g/E	g/E
				KARA	g/E	g/E
				KMRS	ok/E	g/E
				KOZT	e/l	
				KRTS	o/E	ok/E
				MERS	g/E	g/E



P/T axes



Data



P K: NaN 95%: NaN T K: NaN 95%: NaN Lon: 35.8 Lat: 37.05 Dep: 9.00 Mag: ML, 3.0
 cate00041 Data pts: 32 Solns: 1 Pol errs: 1 Nodal Wt: 0.4 Solns shown: 1 Search Inc: 5
 Ampl errs: 0 Ampl Data: 11 Solns: 1 Pol errs: 1 Nodal Wt: 0.4 Soln shown: 1 Search Inc: 5

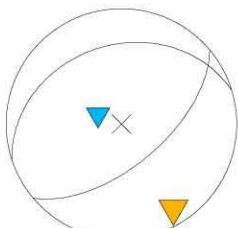
Pol Only



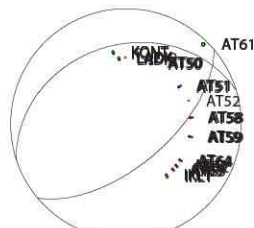
Pol + Ampl



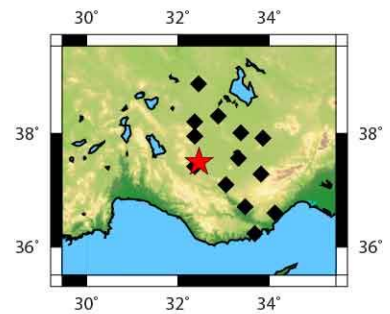
sta SH/P Pqual Squal	sta Pqual Squal
AT50 4.15 ok/E g/	AT50 ok/E g/
AT51 3.06 ok/E ok/	AT51 ok/E ok/
AT58 1.78 g/E g/	AT58 g/E g/
AT59 6.80 ok/E ok/	AT59 ok/E ok/
AT61 10.14 g/E g/	AT61 g/E g/
AT62 5.84 g/E ok/	AT62 g/E ok/
AT63 1.48 ok/E ok/	AT63 ok/E ok/
AT64 3.68 g/E g/	AT64 g/E g/
IKL1 9.84 g/E g/	IKL1 g/E g/
KONT 10.23 g/E ok/	KONT g/E ok/
LADK 8.39 g/E g/	LADK g/E g/



P/T axes



Data



P K: NaN 95%: NaN T K: NaN 95%: NaN Lon: 32.46 Lat: 37.5 Dep: 1.00 Mag: ML, 3.0
 cate00042 Data pts: 24 Solns: 1 Pol errs: 1 Nodal Wt: 0.3 Solns shown: 1 Search Inc: 5
 Ampl errs: 0 Ampl Data: 11 Solns: 1 Pol errs: 1 Nodal Wt: 0.3 Soln shown: 1 Search Inc: 5

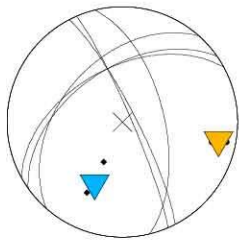
Pol Only



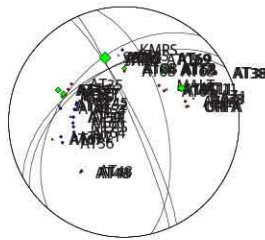
Pol + Ampl



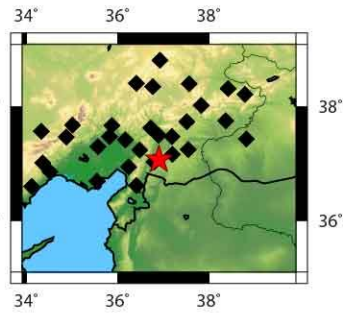
sta	SH/P	Pqual	Squal	sta	Pqual	Squal
AT05	4.19	g/l	g/E	AT05	g/l	g/E
AT08	16.04	g/E	o/E	AT08	g/E	o/E
AT11	25.58	g/l	g/E	AT11	g/l	g/E
AT17	10.85	g/E	o/E	AT17	g/E	o/E
AT26	15.29	g/E	g/E	AT26	g/E	g/E
AT28	4.75	g/E	g/E	AT28	g/E	g/E
AT37	19.48	g/E	e/l	AT35	g/E	
AT38	6.10	g/E	g/l	AT37	g/E	e/l
AT45	10.30	g/E	o/E	AT38	g/E	g/l
AT48	3.05	g/E	g/E	AT45	g/E	o/E
AT54	5.65	g/E	o/E	AT46	o/E	
AT59	7.23	g/E	g/E	AT48	g/E	g/E
AT67	6.25	g/E	g/l	AT52	o/l	
AT68	10.17	o/E	g/E	AT53	o/E	
AT69	8.08	o/E	g/E	AT54	g/E	o/E
KOZT	17.85	g/E	o/l	AT56	g/E	
SARI	38.74	g/E	g/l	AT59	g/E	g/E
URFA	2.88	g/l	o/E	AT60	o/l	
				AT64	o/E	
				AT66	o/E	
				AT67	g/E	g/l
				AT68	o/E	g/E
				AT69	o/E	g/E
				IKL1	g/l	
				KMRS	e/l	
				KOZT	g/E	o/E
				MALT	g/l	
				MERS	o/E	
				SARI	o/E	g/E
				URFA	g/l	o/E



P/T axes



Data



P K: 29.1 95%: 23.3 T K: 129.4 95%: 10. 9 Lon: 36.91 Lat: 37.08 Dep: 2.00 Mag: ML, 4.0
 cate00043 Data pts: 51 Solns: 3 Pol errs: 1 Nodal Wt: 0.2 Solns shown: 3 Search Inc: 5
 Ampl errs: 0 Ampl Data: 18 Solns: 3 Pol errs: 1 Nodal Wt: 0.2 Soln shown: 3 Search Inc: 5

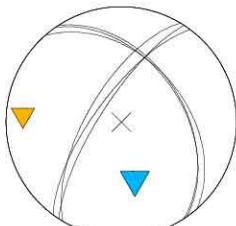
Pol Only



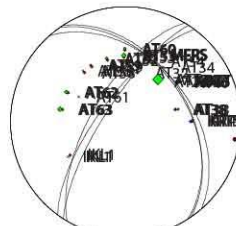
Pol + Ampl



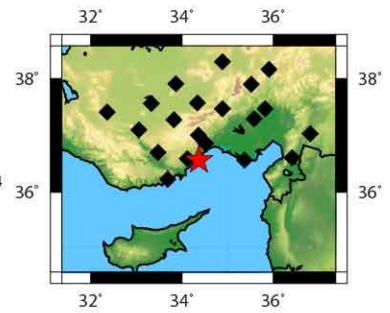
sta	SH/P	Pqual	Squal	sta	Pqual	Squal
AT24	35.42	ok/E	g/E	AT24	ok/E	g/E
AT38	5.66	ok/E	ok/E	AT32	ok/E	
AT46	2.61	ok/E	ok/E	AT38	ok/E	ok/E
AT52	10.96	ok/E	g/E	AT46	ok/E	ok/E
AT53	16.25	ok/E	g/E	AT52	ok/E	g/E
AT58	0.87	g/E	ok/E	AT53	ok/E	g/E
AT59	7.66	g/E	g/E	AT58	g/E	ok/E
AT60	7.94	g/E	ok/E	AT59	g/E	g/E
AT62	12.36	g/E	g/E	AT60	g/E	ok/E
AT63	15.09	g/E	g/E	AT62	g/E	g/E
AT64	1.25	E/I	g/	AT63	g/E	g/E
IKL1	0.63	g/E	g/	AT64	e/I	g/
KOZT	7.77	g/E	g/	IKL1	g/E	g/E
KRTS	0.84	ok/E	ok/	KOZT	g/E	g/E
MERS	6.29	g/E	g/E	KRTS	ok/E	ok/E
				MERS	g/E	g/E



P/T axes



Data



P K: 276.2 95%: 7.4 T K: 454.5 95%: 5.8 Lon: 34.37 Lat: 36.57 Dep: 2.00 Mag: ML, 3.2
 cate00044 Data pts: 35 Solns: 3 Pol errs: 1 Nodal Wt: 0.5 Solns shown: 3 Search Inc: 5
 Ampl errs: 0 Ampl Data: 15 Solns: 1 Pol errs: 1 Nodal Wt: 0.5 Soln shown: 1 Search Inc: 5

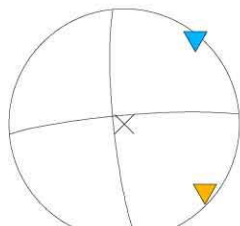
Pol Only



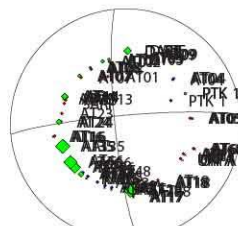
Pol + Ampl



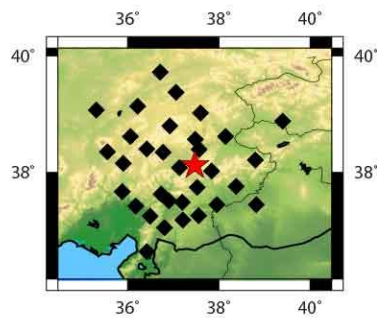
sta SH/P	Pqual	Squal	sta Pqual	Squal
AT01	12.91	ok/E g/E	AT01	ok/E g/E
AT02	9.20	ok/E g/E	AT02	ok/E g/E
AT03	5.88	g/E g/E	AT03	g/E g/E
AT04	3.52	g/E o/E	AT04	g/E o/E
AT05	6.84	g/E g/E	AT05	g/E g/E
AT07	12.40	g/E ok/E	AT07	g/E ok/E
AT08	4.87	g/E g/E	AT08	g/E g/E
AT09	2.03	g/l g/E	AT09	g/l g/E
AT11	0.62	g/l ok/	AT11	e/l ok/E
AT14	20.85	ok/E g/E	AT13	ok/E
AT15	0.90	E/l o/	AT14	ok/E g/E
AT16	3.76	g/l g/E	AT15	e/l o/
AT17	3.08	g/E g/E	AT16	g/l g/E
AT18	4.09	E/E o/	AT17	g/E g/E
AT24	20.04	g/E o/E	AT18	e/E o/E
AT26	39.60	g/E ok/E	AT23	g/E
AT28	40.02	g/E e/	AT24	g/E o/E
AT35	46.48	ok/E g/E	AT26	g/E ok/E
AT37	19.76	ok/E g/E	AT28	g/E e/E
AT66	44.09	ok/E g/E	AT35	ok/E g/E
AT68	0.78	E/l g/	AT37	ok/E g/E
AT69	2.64	g/E ok/E	AT38	ok/E
DARE	26.23	g/E e/l	AT66	ok/E g/E
GAZ1	2.45	g/E g/E	AT68	e/l g/
KMRS	2.27	g/E o/	AT69	g/E ok/E
PTK1	8.73	ok/E o/E	DARE	g/E e/
URFA	0.99	g/E o/	GAZ1	g/E g/E
			KMRS	g/E o/E
			PTK1	ok/E o/E
			SARI	g/E
			URFA	g/E o/E



P/T axes



Data



P K: NaN 95%: NaN T K: NaN 95%: NaN Lon: 37.47 Lat: 38.13 Dep: 3.00 Mag: ML, 3.4
 cate00045 Data pts: 59 Solns: 1 Pol errs: 2 Nodal Wt: 0.4 Solns shown: 1 Search Inc: 5
 Ampl errs: 0 Ampl Data: 27 Solns: 1 Pol errs: 2 Nodal Wt: 0.4 Solns shown: 1 Search Inc: 5

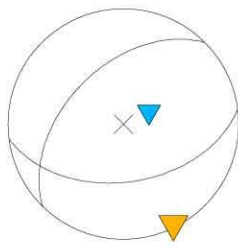
Pol Only



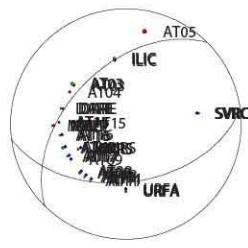
Pol + Ampl



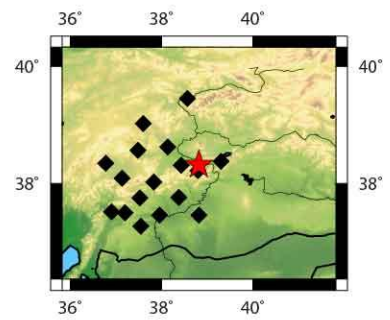
sta	SH/P	Pqual	Squal	sta	Pqual	Squal
AT03	12.13	ok/E	g/E	AT03	ok/E	g/E
AT11	1.46	g/l	ok/E	AT04	g/E	
AT15	6.89	g/E	g/E	AT05	g/E	
AT16	3.95	g/E	ok/E	AT11	g/l	ok/E
AT17	1.40	ok/E	g/E	AT15	g/E	g/E
AT18	4.25	g/E	ok/E	AT16	g/E	ok/E
AT28	10.90	g/E	ok/E	AT17	ok/E	g/E
AT68	8.55	g/E	g/E	AT18	g/E	ok/E
DARE	2.56	g/l	ok/E	AT28	g/E	ok/E
ILIC	9.77	ok/E	ok/E	AT68	g/E	g/E
KMRS	6.63	ok/E	ok/E	AT69	g/E	
MALT	2.19	g/l	g/E	DARE	g/E	ok/E
SVRC	3.33	g/l	g/E	ILIC	ok/E	ok/E
URFA	7.03	g/E	ok/E	KMRS	ok/E	ok/E
				MALT	g/l	g/E
				SVRC	g/l	g/E
				URFA	g/E	ok/E



P/T axes



Data



P K: 0.0 95%: NaN T K: NaN 95%: NaN Lon: 38.82 Lat: 38.32 Dep: 4.00 Mag: ML, 3.9
 cate00046 Data pts: 31 Solns: 1 Pol errs: 2 Nodal Wt: 0.4 Solns shown: 1 Search Inc: 5
 Ampl errs: 0 Ampl Data: 14 Solns: 1 Pol errs: 2 Nodal Wt: 0.4 Soln shown: 1 Search Inc: 5

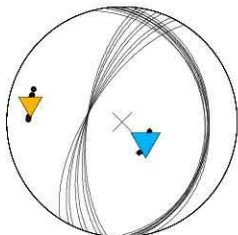
Pol Only



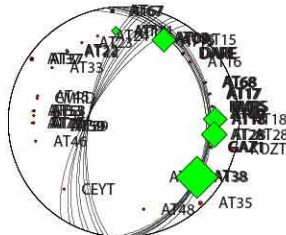
Pol + Ampl



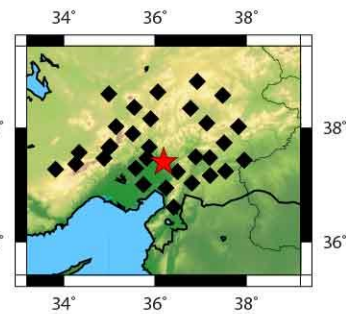
sta SH/P Pqual	Squal	sta	Pqual	Squal
AT08	2.46 g/E g/E	AT08	g/E g/E	
AT14	28.08 ok/E g/E	AT14	ok/E g/E	
AT15	80.77 g/E g/E	AT15	g/E g/E	
AT17	1.81 g/E g/E	AT16	g/E	
AT18	78.11 ok/E g/E	AT17	g/E g/E	
AT22	10.19 ok/E ok/E	AT18	ok/E g/E	
AT28	85.66 ok/E g/E	AT22	ok/E ok/E	
AT37	3.20 g/l g/E	AT23	g/E	
AT38	-138.41 g/E ok/E	AT24	g/E	
AT53	2.21 ok/E g/E	AT28	ok/E g/E	
AT59	5.90 ok/E g/E	AT33	g/E	
AT67	4.97 g/E ok/E	AT35	g/E	
AT68	4.61 g/E g/E	AT37	g/l g/E	
AT69	1.12 g/E g/E	AT38	g/E ok/E	
AT71	1.91 g/E ok/E	AT45	g/E	
DARE	2.00 g/E g/E	AT46	g/E	
GAZ1	8.37 g/E ok/E	AT48	ok/E	
KMRS	2.42 g/l g/	AT53	ok/E g/E	
		AT54	g/E	
		AT59	ok/E g/E	
		AT67	g/E ok/E	
		AT68	g/E g/E	
		AT69	g/E g/E	
		AT71	g/E ok/E	
		CEYT	g/E	
		CMRD	g/E	
		DARE	g/E g/E	
		GAZ1	g/E ok/	
		KMRS	g/l g/E	
		KOZT	e/l	



P/T axes



Data



P K: 176.8 95%: 4.2 T K: 171.8 95%: 4.2 Lon: 36.19 Lat: 37.41 Dep: 5.00 Mag: ML, 3.5
 cate00047 Data pts: 48 Solns: 8 Pol errs: 1 Nodal Wt: 0.1 Solns shown: 8 Search Inc: 5
 Ampl errs: 0 Ampl Data: 18 Solns: 6 Pol errs: 1 Nodal Wt: 0.1 Soln shown: 6 Search Inc: 5

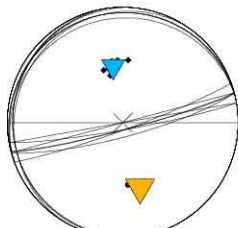
Pol Only



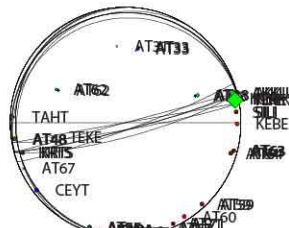
Pol + Ampl



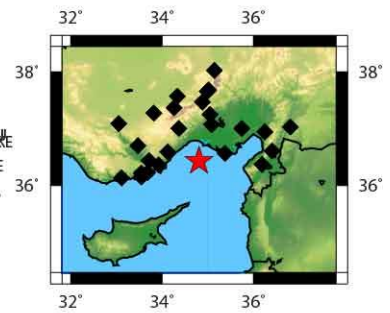
sta	SH/P	Pqual	Squal	sta	Pqual	Squal
AKKU	18.99	E/E	g/g	AKKU	g/E	g/E
AT33	7.92	g/E	g/E	AT33	g/E	g/E
AT38	11.45	g/E	g/E	AT38	g/E	g/E
AT45	4.72	ok/E	g/E	AT45	ok/E	g/E
AT48	7.62	ok/E	ok/E	AT48	ok/E	ok/E
AT53	4.33	g/E	g/E	AT53	g/E	g/E
AT54	5.20	g/E	g/E	AT54	g/E	g/E
AT55	7.98	g/E	ok/E	AT55	g/E	ok/E
AT59	1.69	g/E	ok/E	AT59	g/E	ok/E
AT62	9.55	ok/E	ok/E	AT62	g/E	g/E
AT63	6.18	g/E	g/E	AT63	ok/E	ok/E
AT64	1.81	E/E	g/g	AT64	g/E	g/E
AT71	2.68	g/E	g/E	AT71	g/E	g/E
CMRD	5.28	E/E	g/g	CMRD	g/E	g/E
IKL1	1.43	g/E	ok/E	IKL1	g/E	ok/E
KARA	5.73	g/E	g/E	KARA	g/E	g/E
KRTS	4.06	g/E	g/E	KRTS	g/E	g/E
SILI	4.38	g/E	g/E	SILI	g/E	g/E
TEKE	43.32	g/E	g/E	TEKE	g/E	g/E



P/T axes



Data



P K: 170.2 95%: 4.3 T K: 243.6 95%: 3.6 Lon: 34.81 Lat: 36.44 Dep: 15.00 Mag: ML, 3.5
 cate00048 Data pts: 45 Solns: 8 Pol errs: 2 Nodal Wt: 0.1 Solns shown: 8 Search Inc: 5
 Ampl errs: 0 Ampl Data: 19 Solns: 8 Pol errs: 2 Nodal Wt: 0.1 Solns shown: 8 Search Inc: 5

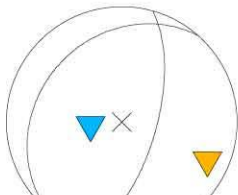
Pol Only



Pol + Ampl



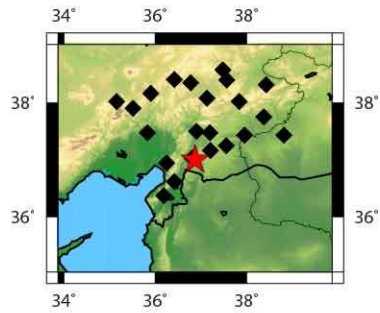
sta	SH/P	Pqual	Squal	sta	Pqual	Squal
AT09	7.18	ok/E	g/E	AT09	ok/E	g/E
AT11	7.00	ok/E	ok/E	AT11	ok/E	ok/E
AT15	0.71	g/E	ok/E	AT15	g/E	ok/E
AT16	141.96	ok/E	g/E	AT16	ok/E	g/E
AT18	17.31	g/E	g/E	AT18	g/E	g/E
AT24	25.72	ok/E	g/E	AT24	ok/E	g/E
AT28	1.93	g/E	ok/E	AT28	g/E	ok/E
AT38	6.41	g/E	g/E	AT33	g/E	
AT48	17.81	g/E	e/	AT34	ok/E	
AT59	3.79	ok/E	ok/E	AT38	g/E	g/E
AT69	5.37	ok/E	ok/E	AT48	g/E	e/E
GAZ1	10.79	ok/E	g/E	AT59	ok/E	ok/E
KMRS	3.32	g/E	o/	AT67	g/E	
KOZT	10.11	ok/E	o/	AT69	ok/E	ok/E
SARI	9.54	ok/E	ok/	GAZ1	ok/E	g/
				KMRS	g/E	o/E
				KOZT	ok/E	o/
				MALT	g/E	
				SARI	o/E	ok/E
				TAHT	g/E	
				URFA	g/E	



P/T axes



Data



P K: NaN 95%: NaN T K: NaN 95%: NaN Lon: 36.87 Lat: 37.01 Dep: 6.00 Mag: ML, 3.4
 cate00049 Data pts: 38 Solns: 1 Pol errs: 1 Nodal Wt: 0.5 Solns shown: 1 Search Inc: 5
 Ampl errs: 0 Ampl Data: 15 Solns: 1 Pol errs: 1 Nodal Wt: 0.5 Soln shown: 1 Search Inc: 5

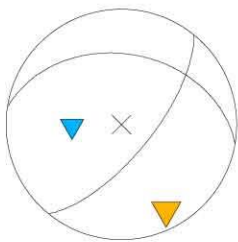
Pol Only



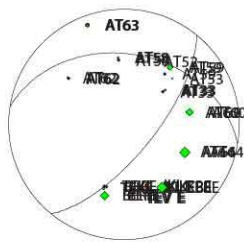
Pol + Ampl



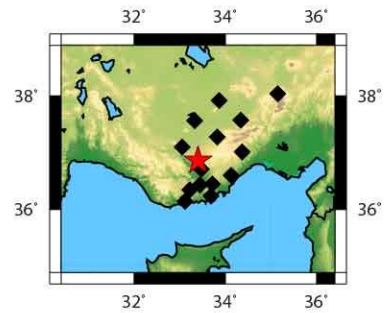
sta SH/P	Pqual	Squal	sta Pqual	Squal
AT33	6.01	ok/E g/E	AT33	ok/E g/E
AT58	6.23	ok/E ok/E	AT58	ok/E ok/E
AT59	18.95	ok/E g/E	AT59	ok/E g/E
AT60	26.50	g/E g/E	AT60	g/E g/E
AT62	2.09	g/E g/E	AT62	g/E g/E
AT63	7.28	E/E g/	AT63	e/E g/E
AT64	35.03	g/E g/E	AT64	g/E g/E
BERE	28.30	g/E g/	BERE	g/E g/E
IKL1	3.45	g/E ok/	IKL1	g/E ok/E
KEBE	34.61	g/E g/E	KEBE	g/E g/E
TEKE	8.78	g/E g/E	TEKE	g/E g/E
TEVE	3.97	g/E ok/E	TEVE	g/E ok/E



P/T axes



Data



P K: NaN 95%: NaN T K: NaN 95%: NaN Lon: 33.4 Lat: 36.87 Dep: 3.00 Mag: ML, 3.1
 cate00050 Data pts: 26 Solns: 1 Pol errs: 1 Nodal Wt: 0.8 Solns shown: 1 Search Inc: 5
 Ampl errs: 1 Ampl Data: 12 Solns: 1 Pol errs: 1 Nodal Wt: 0.8 Soln shown: 1 Search Inc: 5

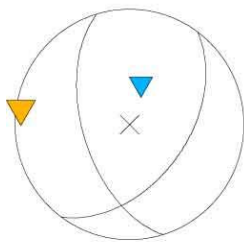
Pol Only



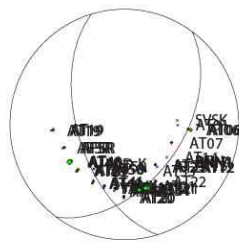
Pol + Ampl



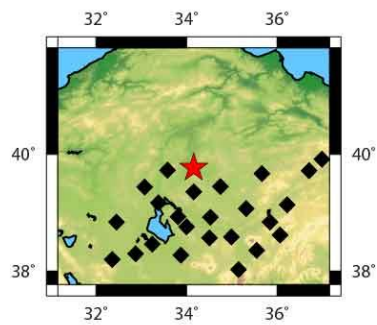
sta SH/P Pqual Squal	sta Pqual Squal
AFSR 0.92 g/l g/E	AFSR g/l g/E
AT06 11.31 g/E o/E	AT06 g/E o/E
AT12 6.06 g/l g/E	AT07 g/E
AT19 1.87 g/E g/E	AT12 g/l g/E
AT20 2.03 g/l o/E	AT19 g/E g/E
AT21 19.10 g/E o/E	AT20 g/l o/E
AT23 1.49 ok/E g/E	AT21 g/E o/E
AT29 8.45 g/E g/E	AT22 ok/E
AT31 15.86 ok/E g/E	AT23 ok/E g/E
AT40 17.85 ok/E g/E	AT29 g/E g/E
AT41 7.62 ok/E g/E	AT30 g/E
AT42 1.05 ok/E g/E	AT31 ok/E g/E
AT50 5.58 ok/E g/E	AT33 g/E
BNN1 6.34 ok/E g/E	AT40 ok/E g/E
YAYX 3.62 g/E o/	AT41 ok/E g/E
	AT42 ok/E g/E
	AT50 ok/E g/E
	BNN1 ok/E g/E
	YAYX g/E o/E



P/T axes



Data



P K: 0.0 95%: NaN T K: NaN 95%: NaN Lon: 34.16 Lat: 39.77 Dep: 0.00 Mag: ML, 3.4
 cate00051 Data pts: 39 Solns: 1 Pol errs: 1 Nodal Wt: 0.1 Solns shown: 1 Search Inc: 5
 Ampl errs: 0 Ampl Data: 15 Solns: 1 Pol errs: 1 Nodal Wt: 0.1 Solns shown: 1 Search Inc: 5

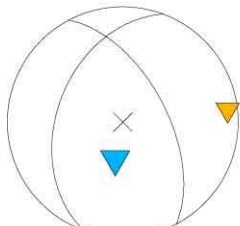
Pol Only



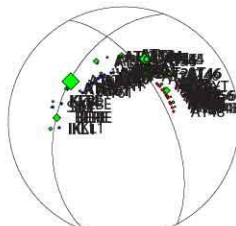
Pol + Ampl



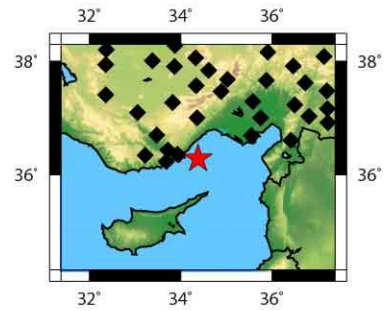
sta	SH/P	Pqual	Squal	sta	Pqual	Squal
AT16	2.03	g/E	o/E	AT10	g/E	
AT23	9.64	g/E	o/E	AT15	g/E	
AT25	8.26	g/E	g/E	AT16	g/E	o/E
AT26	20.95	g/E	o/E	AT17	g/E	
AT27	3.54	g/E	g/E	AT18	g/E	
AT30	5.38	g/E	o/E	AT23	g/E	o/E
AT31	7.41	o/E	g/E	AT24	g/E	
AT38	2.80	g/l	g/E	AT25	g/E	g/E
AT39	4.06	g/l	g/E	AT26	g/E	o/E
AT42	0.51	g/l	o/E	AT27	g/E	g/E
AT44	8.37	g/E	g/E	AT28	g/E	
AT45	30.42	g/E	o/E	AT30	g/E	o/E
AT46	14.10	g/l	o/E	AT31	o/E	g/E
AT48	0.75	g/l	g/E	AT35	g/E	
AT51	9.47	g/E	g/E	AT37	g/E	
AT52	6.74	o/E	g/E	AT38	g/l	g/E
AT53	18.92	g/E	o/E	AT39	g/l	g/E
AT54	35.12	o/E	g/E	AT40	g/l	
AT56	3.12	g/E	g/E	AT41	g/E	
AT59	20.37	g/E	g/E	AT42	g/l	o/E
AT61	5.53	g/E	g/E	AT43	g/E	
AT62	56.89	g/E	o/E	AT44	g/E	g/E
AT63	8.22	g/l	g/	AT45	g/E	o/E
BERE	26.05	g/E	g/	AT46	g/l	o/E
GAZ1	8.47	g/E	g/E	AT48	g/l	g/E
IKL1	13.75	g/E	g/	AT50	g/E	
KEBE	6.24	g/E	g/E	AT51	g/E	g/E
LADK	4.72	g/E	o/	AT52	o/E	g/E
SILI	1.98	g/E	g/E	AT53	g/E	o/E
				AT54	o/E	g/E
				AT56	g/E	g/E
				AT59	g/E	g/E
				AT60	g/E	
				AT61	g/E	g/E
				AT62	g/E	o/E
				AT63	g/l	g/
				BERE	g/E	g/E
				CEYT	g/l	
				CHBY	o/E	
				GAZ1	g/E	g/E
				IKL1	g/E	g/E
				KEBE	g/E	g/E
				KONT	g/l	
				LADK	g/E	o/E
				SILI	g/E	g/E



P/T axes



Data

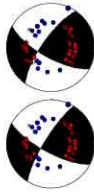


P K: NaN 95%: NaN T K: NaN 95%: NaN Lon: 34.38 Lat: 36.29 Dep: 0.00 Mag: ML, 4.7
 cate00052 Data pts: 74 Solns: 1 Pol errs: 2 Nodal Wt: 0.2 Solns shown: 1 Search Inc: 5
 Ampl errs: 0 Ampl Data: 29 Solns: 1 Pol errs: 2 Nodal Wt: 0.2 Soln shown: 1 Search Inc: 5

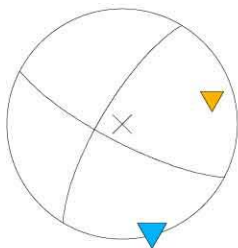
Pol Only



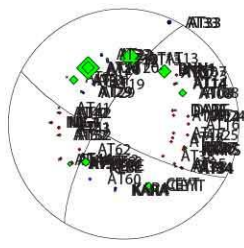
Pol + Ampl



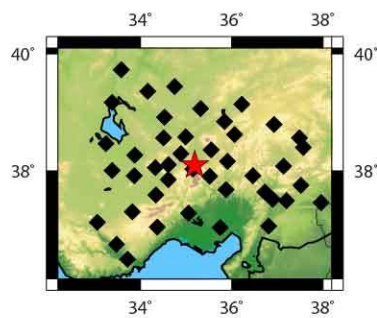
sta	SH/P	Pqual	Squal	sta	Pqual	Squal
AT07	45.34	ok/E	g/E	AT07	ok/E	g/E
AT08	25.18	g/E	g/E	AT08	g/E	g/E
AT12	9.22	ok/E	g/E	AT09		
AT13	66.59	g/E	g/E	AT12	ok/E	g/E
AT14	5.62	g/E	g/E	AT13	g/E	g/E
AT20	74.93	g/E	g/E	AT14	g/E	g/E
AT21	40.84	g/E	g/E	AT16	g/E	
AT22	2.76	g/E	ok/E	AT17	g/E	
AT24	1.97	ok/E	ok/E	AT18	g/E	
AT27	1.64	g/E	ok/E	AT19	g/E	
AT29	7.57	g/E	g/E	AT20	g/E	g/E
AT31	28.91	g/E	g/E	AT21	g/E	g/E
AT33	2.96	g/E	g/E	AT22	g/E	ok/E
AT34	6.15	g/E	g/E	AT23	e/l	
AT38	1.72	g/E	g/E	AT24	e/l	ok/E
AT42	3.02	g/E	g/E	AT25	e/E	
AT44	1.65	g/E	ok/E	AT26	g/E	
AT52	1.84	g/E	g/E	AT27	g/E	ok/E
AT59	16.23	g/E	g/E	AT29	g/E	g/E
AT63	29.14	g/E	g/E	AT31	g/E	g/E
BNN1	6.62	g/E	e/E	AT33	g/E	g/E
CEYT	25.32	ok/E	g/E	AT34	g/E	g/E
DARE	2.12	g/E	ok/E	AT35	g/E	
KARA	6.27	ok/E	g/E	AT38	g/E	g/E
KEBE	7.03	g/E	g/E	AT42	g/E	g/E
KMRS	10.74	g/E	g/E	AT43	e/l	
NIG1	4.97	g/E	ok/E	AT44	g/E	ok/E
				AT51	g/l	
				AT52	g/E	g/E
				AT53	g/l	
				AT59	g/E	g/E
				AT60	g/E	
				AT62	g/E	
				AT63	g/E	g/E
				BNN1	g/E	e/E
				CEYT	ok/E	g/E
				DARE	g/E	ok/E
				KARA	ok/E	g/E
				KEBE	g/E	g/E
				KMRS	g/E	g/E
				NIG1	g/E	ok/E



P/T axes



Data



P K: NaN 95%: NaN T K: NaN 95%: NaN Lon: 35.19 Lat: 38.1 Dep: 0.00 Mag: ML, 3.6
 cate00053 Data pts: 70 Solns: 1 Pol errs: 1 Nodal Wt: 0.8 Solns shown: 1 Search Inc: 5
 Ampl errs: 1 Ampl Data: 27 Solns: 2 Pol errs: 1 Nodal Wt: 0.1 Soln shown: 2 Search Inc: 5

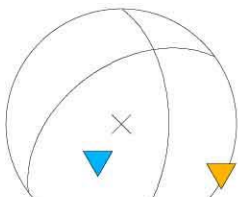
Pol Only



Pol + Ampl



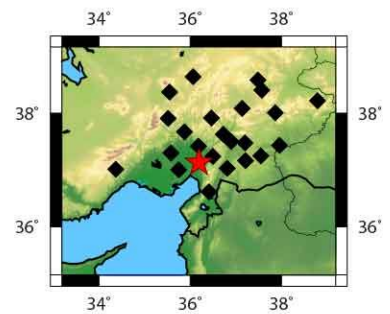
sta	SH/P	Pqual	Squal	sta	Pqual	Squal	
AT16	20.64	ok/E	ok/E	AT05	ok/E		
AT18	61.01	g/E	g/E		0.0	g/E	
AT23	14.38	g/E	g/E	AT16	ok/E	ok/E	
AT25	8.81	g/E	o/E	AT18	g/E	g/E	
AT26	25.90	g/E	g/E	AT23	g/E	g/E	
AT27	54.44	ok/E	g/E	AT25	g/E	o/E	
AT28	6.00	o/E	g/E	AT26	g/E	g/E	
AT37	3.34	g/E	g/E	AT27	ok/E	g/E	
AT38	1.43	g/l	g/E	AT28	o/E	g/E	
AT48	5.61	g/E	o/E		AT34	g/E	
AT66	2.77	g/E	o/E		AT35	g/E	
CEYT	4.35	g/E	ok/E	AT37	g/E	g/E	
GAZ1	3.21	g/E	ok/E	AT38	g/l	g/E	
					AT46	g/l	
					AT48	g/E	o/E
					AT60	g/E	
					AT66	g/E	o/E
					CEYT	g/E	ok/E
					GAZ1	g/E	ok/E



P/T axes

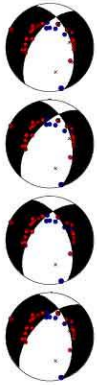


Data



P K: NaN 95%: NaN T K: NaN 95%: NaN Lon: 36.19 Lat: 37.14 Dep: 0.00 Mag: ML, 3.0
 cate00054 Data pts: 37 Solns: 1 Pol errs: 2 Nodal Wt: 0.4 Solns shown: 1 Search Inc: 5
 Ampl errs: 0 Ampl Data: 13 Solns: 1 Pol errs: 2 Nodal Wt: 0.4 Soln shown: 1 Search Inc: 5

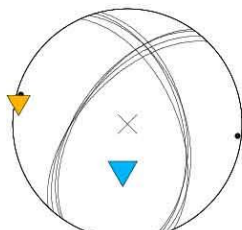
Pol Only



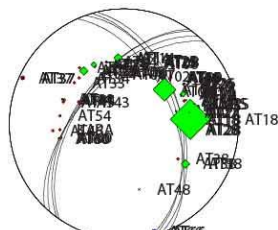
Pol + Ampl



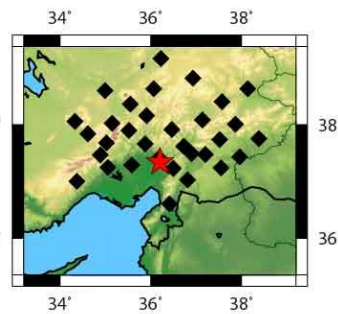
sta SH/P Pqual Squal	sta Pqual Squal
AT04 77.30 E/E g/	AT02 o/o
AT06 2.18 E/E o/	AT04 o/E g/
AT08 10.94 E/E o/	AT06 g/E o/
AT09 2.43 E/E g/	AT07 g/E
AT10 17.87 E/E o/	AT08 g/E o/
AT14 28.09 E/E g/	AT09 g/E g/
AT16 4.25 E/E g/	AT10 o/E o/
AT17 2.08 E/E g/	AT14 o/E g/
AT18 133.00 E/E g/	AT16 g/E g/
AT22 30.04 E/E o/	AT17 g/E g/
AT23 20.46 E/E g/	AT18 o/E g/
AT25 8.41 E/E g/	AT22 g/E o/
AT26 1.17 E/E o/	AT23 g/E g/
AT27 1.59 E/E g/	AT24 g/E
AT28 1.25 E/E g/	AT25 g/E g/
AT37 3.28 E/E g/	AT26 e/E o/
AT38 28.83 E/E g/	AT27 g/E g/
AT44 5.57 E/E g/	AT28 g/E g/
AT60 6.99 E/E g/	AT33 g/E
AT66 1.42 E/E g/	AT34 g/E
KMRS 2.61 E/E g/	AT35 g/E
	AT37 g/E g/
	AT38 g/E g/
	AT43 o/E
	AT44 o/E g/
	AT45 g/E
	AT46 e/E
	AT54 g/E
	AT60 g/E g/
	AT66 e/E g/
	KARA g/E
	KMRS e/E g/



P/T axes

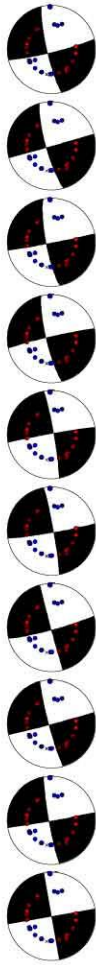


Data

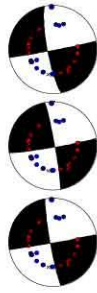


P K: 605.7 95%: 3.7 T K: 261.7 95%: 5.7 Lon: 36.2 Lat: 37.35 Dep: 0.00 Mag: ML, 4.1
 cate00055 Data pts: 55 Solns: 4 Pol errs: 2 Nodal Wt: 0.1 Solns shown: 4 Search Inc: 5
 Ampl errs: 0 Ampl Data: 21 Solns: 1 Pol errs: 2 Nodal Wt: 0.1 Solns shown: 1 Search Inc: 5

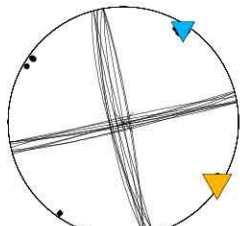
Pol Only



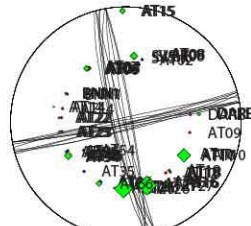
Pol + Ampl



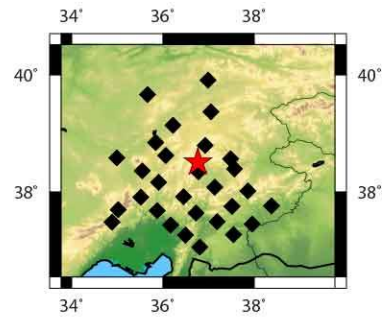
sta SH/P Pqual Squal	sta Pqual Squal
AT06 19.38 ok/E g/E	AT02 g/E
AT07 5.16 g/E g/E	AT06 ok/E g/E
AT08 6.67 E/l g/	AT07 g/E g/E
AT10 45.69 g/E g/E	AT08 eB g/
AT14 0.98 g/l g/E	AT09 g/E
AT15 15.47le/E e/	AT10 g/E g/E
AT16 14.42 g/E g/E	AT14 g/l g/E
AT18 4.80 g/E g/E	AT15 e/E e/l
AT22 4.97 g/E g/E	AT16 g/E g/E
AT23 5.31 g/E g/E	AT17 g/E
AT24 3.18 g/E g/E	AT18 g/E g/E
AT26 60.21 g/E g/E	AT22 g/E g/E
AT27 62.70 ok/E g/E	AT23 g/E g/E
AT34 7.57 g/E g/E	AT24 g/E g/E
AT45 24.59 ok/E ok/E	AT25 g/E
AT66 19.71 g/E g/E	AT26 g/E g/E
BNN1 6.92 g/E g/E	AT27 ok/E g/E
DARE 13.85 g/E g/E	AT34 g/E g/E
SVSK 23.83 d&E g/	AT35 g/E
	AT38 ok/E
	AT45 ok/E ok/E
	AT54 g/E
	AT66 g/E g/E
	BNN1 g/E g/E
	DARE g/E g/E
	SVSK ok/E g/E



P/T axes

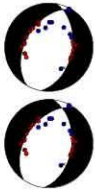


Data

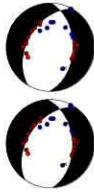


P K: 260.1 95%: 3.0 T K: 264.9 95%: 3.0 Lon: 36.77 Lat: 38.51 Dep: 0.00 Mag: ML, 3.6
 cate00056 Data pts: 48 Solns: 10 Pol errs: 2 Nodal Wt: 0.8 Solns shown: 10 Search Inc: 5
 Ampl errs: 0 Ampl Data: 19 Solns: 3 Pol errs: 2 Nodal Wt: 0.8 Soln shown: 3 Search Inc: 5

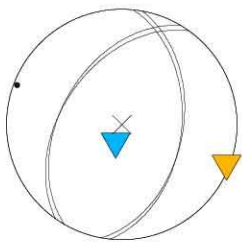
Pol Only



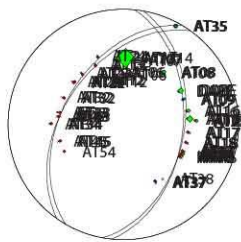
Pol + Ampl



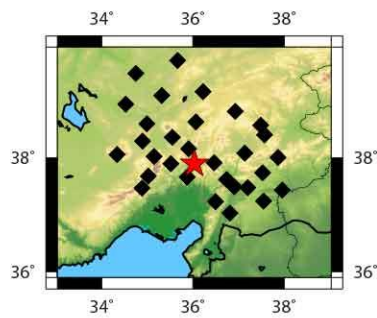
sta SH/P Pqual Squal	sta Pqual Squal
AT06 3.10 g/E o/E	AT06 g/E o/E
AT07 8.52 ok/E o/E	AT07 ok/E o/E
AT08 12.45 ok/E g/E	AT08 ok/E g/E
AT09 4.55 g/E g/E	AT09 g/E g/E
AT10 20.96 ok/E g/E	AT10 ok/E g/E
AT12 4.25 g/E g/E	AT12 g/E g/E
AT13 2.08 g/E g/E	AT13 g/E g/E
AT14 64.33 ok/E g/E	AT14 ok/E g/E
AT16 12.39 g/E g/E	AT16 g/E g/E
AT17 2.54 g/E ok/E	AT17 g/E ok/E
AT18 1.98 g/E ok/E	AT18 g/E ok/E
AT22 0.84 g/E g/E	AT21 ok/E
AT23 2.04 g/l o/E	AT22 g/E g/E
AT24 0.79 g/E g/E	AT23 g/l o/E
AT25 11.00 e/E e/	AT24 g/E g/E
AT26 9.57 g/E g/E	AT25 o/E e/E
AT27 2.35 g/E o/E	AT26 g/E g/E
AT28 2.71 g/E o/E	AT27 g/E o/E
AT32 0.53 g/E g/E	AT28 g/E o/E
AT33 2.47 g/E o/E	AT32 g/E g/E
AT34 1.39 g/l g/E	AT33 g/E o/E
AT35 7.35 g/E g/E	AT34 g/l g/E
AT37 3.42 g/E g/E	AT35 g/E g/E
AT43 0.83 g/E g/E	AT37 g/E g/E
AT45 0.76 g/E g/E	AT43 g/E g/E
DARE 18.75 ok/E g/E	AT45 g/E g/E
KMRS 2.59 ok/E g/	AT54 g/E
	DARE ok/E g/E
	KMRS ok/E g/E



P/T axes



Data



P K: 525.2 95%: 10.9 TK: ***** 95%: 0.6 Lon: 36.03 Lat: 37.9 Dep: 0.00 Mag: ML, 3.4
 cate00057 Data pts: 57 Solns: 2 Pol errs: 2 Nodal Wt: 0.3 Solns shown: 2 Search Inc: 5
 Ampl errs: 0 Ampl Data: 27 Solns: 2 Pol errs: 2 Nodal Wt: 0.2 Soln shown: 2 Search Inc: 5

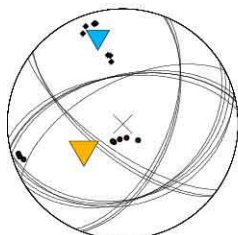
Pol Only



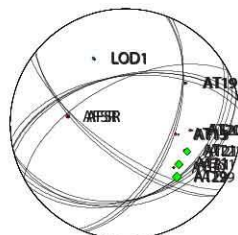
Pol + Ampl



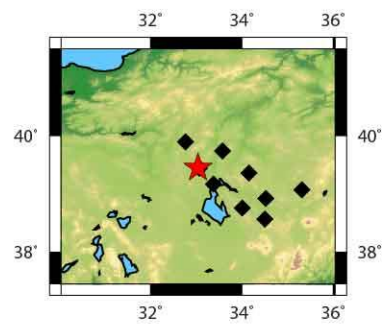
sta SH/P Pqual Squal	sta Pqual Squal
AFSR 0.18 ok/E g/E	AFSR ok/E g/E
AT13 3.93 g/E ok/E	AT13 g/E ok/E
AT19 6.71 g/E g/E	AT19 g/E g/E
AT20 0.70 g/E ok/E	AT20 g/E ok/E
AT21 25.19 g/E g/E	AT21 g/E g/E
AT29 31.80 ok/E e/l	AT29 ok/E e/
AT31 28.39 g/E g/E	AT31 g/E
LOD1 8.34 ok/E g/E	LOD1 g/E g/E
	LOD1 ok/E g/



P/T axes



Data



PK: 25.5 95%: 11.2 TK: 4.1 95%: 31. 3 Lon: 33.04 Lat: 39.45 Dep: 3.00 Mag: ML, 3.1
 cate00058 Data pts: 17 Solns: 8 Pol errs: 1 Nodal Wt: 0.8 Solns shown: 8 Search Inc: 5
 Ampl errs: 0 Ampl Data: 8 Solns: 1 Pol errs: 1 Nodal Wt: 0.8 Soln shown: 1 Search Inc: 5

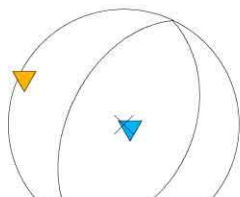
Pol Only



Pol + Ampl



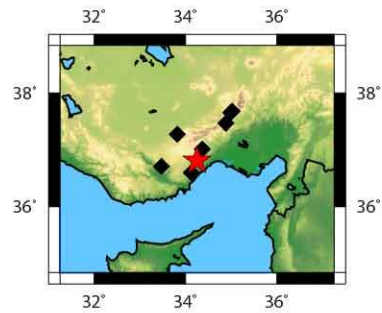
sta	SH/P	Pqual	Squal	sta	Pqual	Squal
AT54	29.47	ok/E	g/E	AT45	ok/E	
AT60	11.47	ok/E	g/E	AT54	ok/E	g/E
AT63	8.19	g/E	g/E	AT59	g/E	
AT64	9.20	g/E	g/E	AT60	ok/E	g/E
CMRD	8.94	o/E	ok/	AT63	g/E	g/E
				AT64	g/E	g/E
				CMRD	ok/E	ok/E



P/T axes

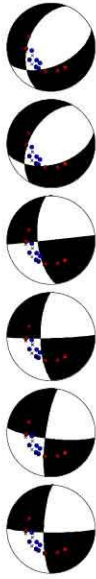


Data

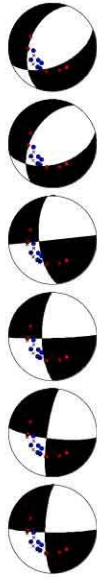


P K: NaN 95%: NaN T K: NaN 95%: NaN Lon: 34.25 Lat: 36.82 Dep: 0.00 Mag: ML, 3.1
 cate00059 Data pts: 12 Solns: 1 Pol errs: 0 Nodal Wt: 0.9 Solns shown: 1 Search Inc: 5
 Ampl errs: 0 Ampl Data: 5 Solns: 1 Pol errs: 0 Nodal Wt: 0.9 Soln shown: 1 Search Inc: 5

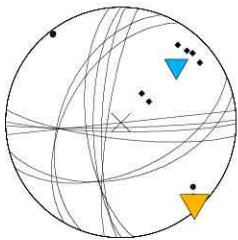
Pol Only



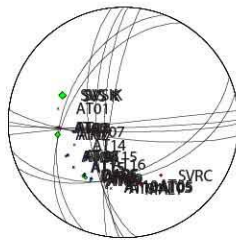
Pol + Ampl



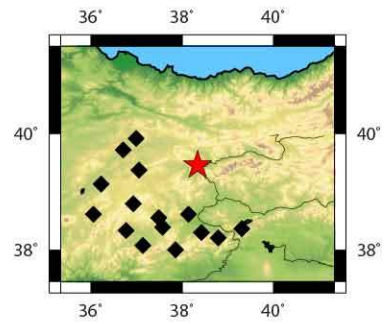
sta	SH/P	Pqual	Squal	sta	Pqual	Squal
AT02	7.47	g/E	g/E	AT02	g/E	g/E
AT05	4.76	g/E	g/E	AT05	g/E	g/E
AT07	20.37	ok/E	g/E	AT07	ok/E	g/E
AT08	3.01	ok/E	g/E	AT08	ok/E	g/E
AT09	3.88	g/E	g/E	AT09	g/E	g/E
AT10	9.65	g/E	g/E	AT10	g/E	g/E
AT15	7.84	g/E	g/E	AT15	g/E	g/E
AT16	12.05	ok/E	ok/E	AT16	ok/E	ok/E
DARE	10.13	g/E	ok/E	DARE	g/E	ok/E
SVSK	24.80	ok/E	g/	SVRC	ok/E	
				SVSK	ok/E	g/E



P/T axes

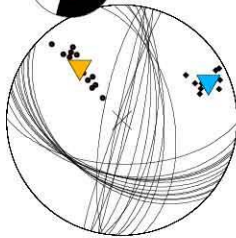
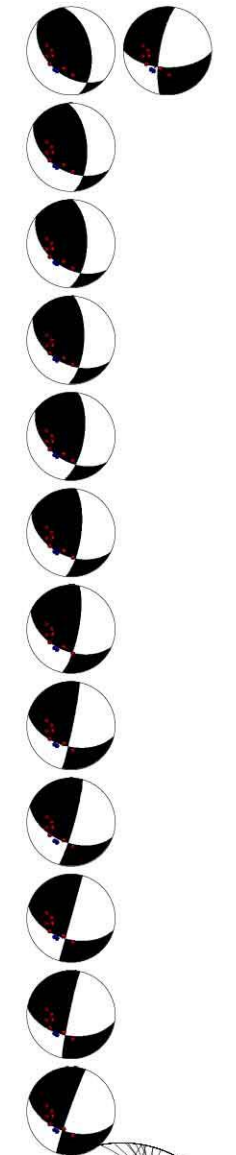


Data



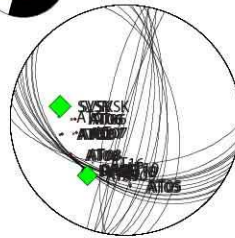
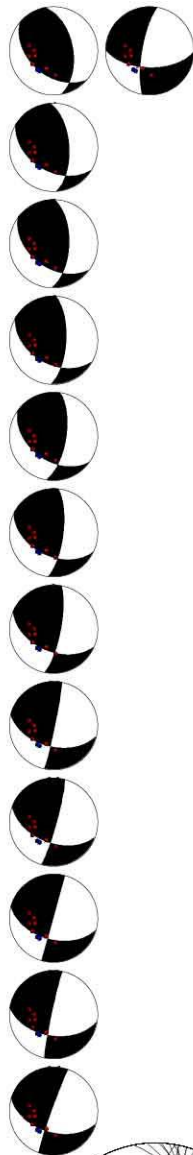
P K: 9.9 95%: 22.4 TK: 97.3 95%: 6.8 Lon: 38.34 Lat: 39.46 Dep: 0.00 Mag: ML, 3.5
 cate00060 Data pts: 25 Solns: 6 Pol errs: 0 Nodal Wt: 0.9 Solns shown: 6 Search Inc: 5
 Ampl errs: 0 Ampl Data: 10 Solns: 6 Pol errs: 0 Nodal Wt: 0.9 Soln shown: 6 Search Inc: 5

Pol Only



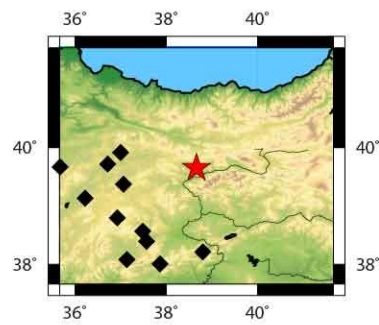
P/T axes

Pol + Ampl



Data

sta	SH/P	Pqual	Squal	sta	Pqual	Squal
AT02	6.01	g/E	g/E	AT02	g/E	g/E
AT05	2.76	g/E	ok/E	AT05	g/E	ok/E
AT06	6.05	ok/E	ok/E	AT06	ok/E	ok/E
AT07	3.59	g/E	g/E	AT07	g/E	g/E
AT08	5.41	ok/E	g/E	AT08	ok/E	g/E
AT09	65.98	ok/E	g/E	AT09	ok/E	g/E
AT10	5.32	ok/E	g/E	AT10	ok/E	g/E
DARE	5.89	g/E	ok/E	DARE	g/E	ok/E
SVSK	72.40	ok/E	g/E	SVSK	ok/E	g/E

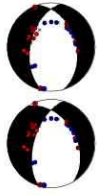


P K: 63.0 95%: 5.3 T K: 22.1 95%: 9.0 Lon: 38.66 Lat: 39.66 Dep: 0.00 Mag: ML, 3.5
 cate00061 Data pts: 20 Solns: 13 Pol errs: 1 Nodal Wt: 0.8 Solns shown: 13 Search Inc: 5
 Ampl errs: 0 Ampl Data: 9 Solns: 13 Pol errs: 1 Nodal Wt: 0.8 Soln shown: 13 Search Inc: 5

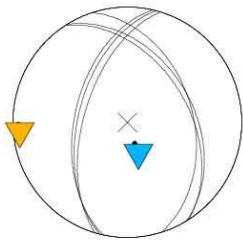
Pol Only



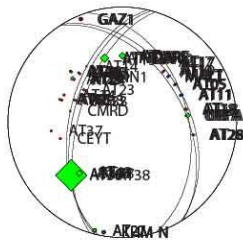
Pol + Ampl



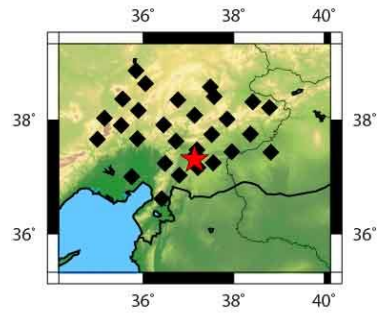
sta	SH/P	Pqual	Squal	sta	Pqual	Squal
AT05	4.86	g/E	ok/E	AT05	g/E	ok/E
AT10	2.35	g/l	o/E	AT10	g/l	o/E
AT11	5.52	g/E	g/E	AT11	g/E	g/E
AT15	27.31	g/E	g/E	AT15	g/E	g/E
AT16	21.60	g/E	ok/E	AT16	g/E	ok/E
AT17	1.36	g/E	o/E	AT17	g/E	o/E
AT18	1.12	g/l	g/E	AT18	g/l	g/E
AT23	1.92	g/E	ok/E	AT23	g/E	ok/E
AT24	13.29	g/E	g/E	AT24	g/E	g/E
AT25	2.28	g/E	g/E	AT25	g/E	g/E
AT26	6.78	o/E	ok/E	AT26	o/E	ok/E
AT27	10.93	g/E	g/E	AT27	g/E	g/E
AT28	1.18	g/E	g/E	AT28	g/E	g/E
AT33	6.20	g/E	ok/E	AT33	g/E	ok/E
AT35	7.21	g/E	ok/E	AT34	g/E	
AT38	103.39	g/E	g/E	AT35	g/E	ok/E
AT48	22.28	ok/E	o/E	AT37	g/l	
DARE	5.06	ok/E	o/E	AT38	g/E	g/E
GAZ1	5.39	ok/E	g/E	AT48	ok/E	o/E
KHMN	8.57	o/E	ok/E	CEYT	ok/E	
MALT	4.27	g/E	g/E	DARE	ok/E	o/E
URFA	16.34	g/E	g/E	GAZ1	ok/E	g/E
				KHMN	o/E	ok/E
				MALT	g/E	g/E
				URFA	g/E	g/E



P/T axes



Data



P K: 175.5 95%: 9.3 T K: 399.8 95%: 6.2 Lon: 37.14 Lat: 37.31 Dep: 0.00 Mag: ML, 3.4
 cate00062 Data pts: 51 Solns: 3 Pol errs: 1 Nodal Wt: 0.1 Solns shown: 3 Search Inc: 5
 Ampl errs: 0 Ampl Data: 22 Solns: 2 Pol errs: 1 Nodal Wt: 0.1 Solns shown: 2 Search Inc: 5

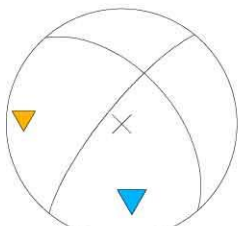
Pol Only



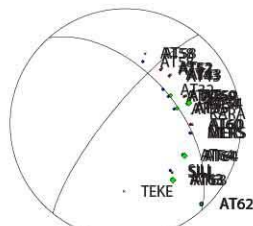
Pol + Ampl



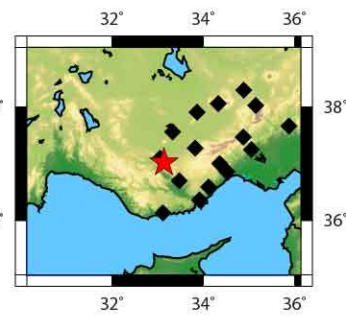
sta	SH/P	Pqual	Squal	sta	Pqual	Squal
AT33	11.46	g/E	ok/E	AT32	ok/E	
AT35	13.20	ok/E	ok/E	AT33	g/E	ok/E
AT43	1.04	g/E	g/E	AT35	ok/E	ok/E
AT52	4.52	g/E	g/E	AT43	g/E	g/E
AT54	18.47	g/E	g/E	AT52	g/E	g/E
AT58	2.02	ok/E	g/E	AT54	g/E	g/E
AT59	5.94	g/E	g/E	AT58	ok/E	g/E
AT60	4.82	g/E	ok/E	AT59	g/E	g/E
AT62	8.26	g/E	g/E	AT60	g/E	ok/E
AT63	19.86	ok/E	g/E	AT62	g/E	g/E
AT64	18.93	o/E	g/E	AT63	ok/E	g/E
MERS	4.75	ok/E	g/E	AT64	o/E	g/E
SILI	5.48	ok/E	g/E	MERS	ok/E	g/E
				SILI	ok/E	g/E



P/T axes



Data

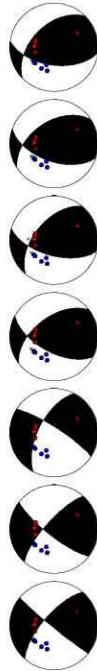


P K: NaN 95%: NaN T K: NaN 95%: NaN Lon: 33.14 Lat: 37.03 Dep: 1.00 Mag: ML, 3.3
 cate00063 Data pts: 29 Solns: 1 Pol errs: 0 Nodal Wt: 0.9 Solns shown: 1 Search Inc: 5
 Ampl errs: 0 Ampl Data: 13 Solns: 1 Pol errs: 0 Nodal Wt: 0.9 Soln shown: 1 Search Inc: 5

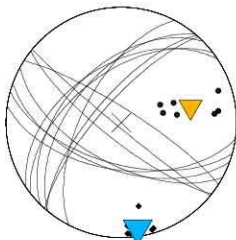
Pol Only



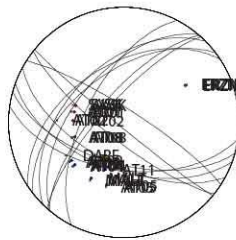
Pol + Ampl



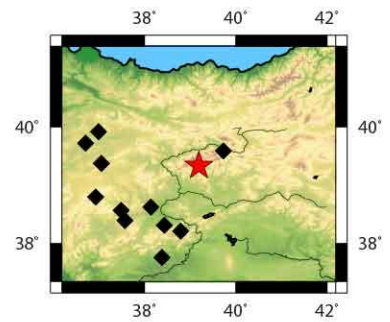
sta	SH/P	Pqual	Squal	sta	Pqual	Squal
AT01	4.26	g/E	ok/E	AT01	g/E	ok/E
AT02	2.31	g/E	ok/E	AT02	g/E	ok/E
AT04	7.55	g/E	g/E	AT04	g/E	g/E
AT05	1.36	g/E	g/E	AT05	g/E	g/E
AT08	5.63	g/E	g/E	AT08	g/E	g/E
AT09	4.60	ok/E	g/E	AT09	ok/E	g/E
ERZN	2.10	ok/E	g/E	AT11	ok/E	
MALT	2.47	g/E	ok/E	ERZN	ok/E	g/E
SVSK	1.25	g/E	ok/	MALT	g/E	ok/E
				SVSK	g/E	ok/E



P/T axes



Data



P K: 57.8 95%: 8.0 TK: 13.9 95%: 16. 8 Lon: 39.19 Lat: 39.34 Dep: 0.00 Mag: ML, 3.1
 cate00064 Data pts: 20 Solns: 40 Pol errs: 1 Nodal Wt: 0.8 Solns shown: 7 Search Inc: 10
 Ampl errs: 0 Ampl Data: 9 Solns: 40 Pol errs: 1 Nodal Wt: 0.8 Soln shown: 7 Search Inc: 10

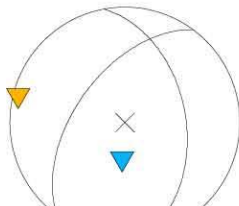
Pol Only



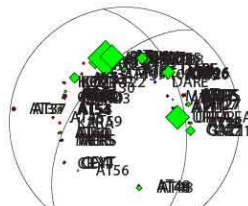
Pol + Ampl



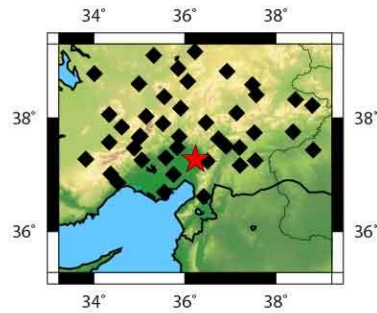
sta SH/P	Pqual	Squal	sta	Pqual	Squal
AT07	16.90	e/E g/	AT06	g/E	
AT08	29.58	e/E g/	AT07	e/E g/E	
AT09	8.96	e/E g/	AT08	e/E g/E	
AT11	4.27	ok/E g/E	AT09	e/E g/E	
AT14	3.73	g/E g/E	AT11	ok/E g/E	
AT16	43.25	g/E g/E	AT13	g/E	
AT17	4.54	g/E g/E	AT14	g/E g/E	
AT23	42.20	g/E g/E	AT16	g/E g/E	
AT24	118.67	g/E g/E	AT17	g/E g/E	
AT25	36.53	ok/E g/E	AT22	ok/E	
AT26	9.00	g/E e/	AT23	g/E g/E	
AT27	14.79	g/E g/E	AT24	g/E g/E	
AT28	8.94	g/E g/E	AT25	ok/E g/E	
AT33	34.10	e/E ok/	AT26	g/E e/E	
AT37	2.70	e/l g/	AT27	g/E g/E	
AT43	9.50	g/E ok/E	AT28	g/E g/E	
AT44	6.00	g/E e/l	AT33	e/E ok/E	
AT45	3.37	e/l g/	AT34	g/E	
AT48	19.29	g/E ok/E	AT35	e/E	
AT53	13.75	g/E g/E	AT37	e/l g/	
AT54	9.98	e/E g/	AT43	g/E ok/E	
AT60	5.46	g/E g/E	AT44	g/E e/l	
BNN1	78.53	ok/E g/E	AT45	e/l g/	
CEYT	1.10	g/E g/E	AT46	e/l	
CMRD	2.26	g/l g/	AT48	g/E ok/E	
DARE	6.68	g/E g/E	AT53	g/E g/E	
GAZ1	31.30	g/E g/E	AT54	e/E g/E	
KMRS	2.28	g/E e/	AT60	g/E g/E	
KOZT	1.02	e/l ok/E	BNN1	ok/E g/E	
MERS	3.43	e/E ok/	CEYT	g/E g/E	
URFA	79.35	e/E g/	CMRD	g/l g/E	
			DARE	g/E g/E	
			GAZ1	g/E g/E	
			KARA	g/E	
			KMRS	g/E e/l	
			KOZT	e/l ok/E	
			MALT	g/E	
			MERS	e/E ok/E	
			URFA	ok/E g/E	



P/T axes

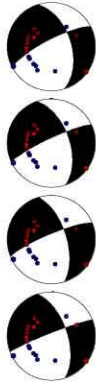


Data



P K: NaN 95%: NaN T K: 0.0 95%: NaN Lon: 36.23 Lat: 37.27 Dep: 0.00 Mag: ML, 4.2
 cate00065 Data pts: 74 Solns: 1 Pol errs: 2 Nodal Wt: 0.2 Solns shown: 1 Search Inc: 5
 Ampl errs: 0 Ampl Data: 31 Solns: 1 Pol errs: 2 Nodal Wt: 0.2 Solns shown: 1 Search Inc: 5

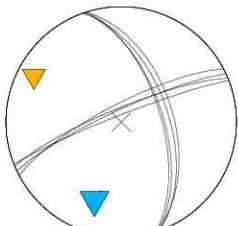
Pol Only



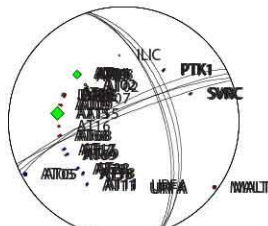
Pol + Ampl



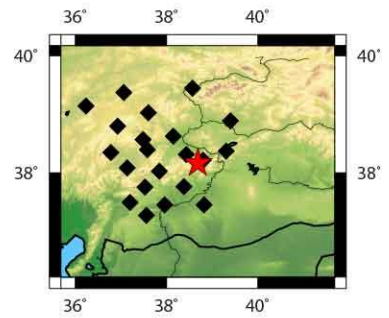
sta SH/P	Pqual	Squal	sta Pqual	Squal
AT02	8.27	ok/E g/E	AT02	ok/E g/E
AT03	28.66	E/E g/	AT03	e/E g/E
AT04	1.34	E/l g/	AT04	eE g/
AT05	1.45	g/E g/E	AT05	g/E g/E
AT08	7.49	g/E ok/E	AT07	g/E
AT09	2.47	g/E g/E	AT08	g/E ok/E
AT11	1.71	E/l g/	AT09	g/E g/E
AT15	44.89	g/E g/E	AT11	eE g/
AT17	1.29	g/E g/E	AT15	g/E g/E
AT18	6.78	g/E g/E	AT16	g/E
AT28	2.95	g/E g/E	AT17	g/E g/E
AT68	3.28	E/l g/	AT18	g/E g/E
AT69	5.33	g/E g/E	AT28	g/E g/E
DARE	0.74	g/l ok/E	AT68	eE g/
MALT	1.85	E/l g/	AT69	g/E g/E
PTK1	3.27	g/E g/E	DARE	g/Eok/
SVRC	1.60	g/E g/E	MALT	e/l g/E
URFA	1.91	g/l g/E	PTK1	g/E g/E
			SVRC	g/E g/
			URFA	g/l g/E



P/T axes



Data



P K: 217.4 95%: 6.2 T K: 1324.7 95%: 2.5 Lon: 38.68 Lat: 38.17 Dep: 0.00 Mag: ML, 3.9
 cate00066 Data pts: 39 Solns: 4 Pol errs: 1 Nodal Wt: 0.4 Solns shown: 4 Search Inc: 5
 Ampl errs: 0 Ampl Data: 18 Solns: 2 Pol errs: 1 Nodal Wt: 0.4 Soln shown: 2 Search Inc: 5

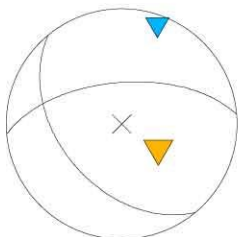
Pol Only



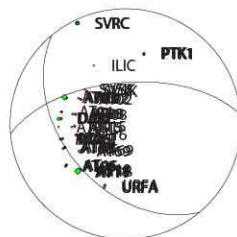
Pol + Ampl



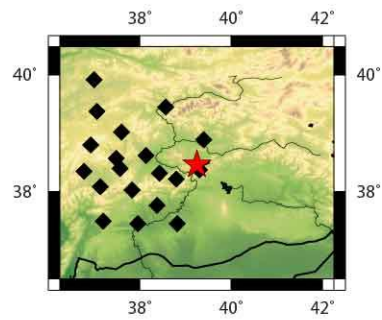
sta	SH/P	Pqual	Squal	sta	Pqual	Squal
AT02	2.99	g/E	g/E	AT02	g/E	g/E
AT03	19.18	ok/E	g/E	AT03	ok/E	g/E
AT05	7.50	g/E	g/E	AT04	g/E	
AT08	4.85	g/E	ok/E	AT05	g/E	g/E
AT11	5.90	g/E	g/E	AT08	g/E	ok/E
AT15	3.79	g/E	g/E	AT11	g/E	g/E
AT16	2.44	ok/E	g/E	AT15	g/E	g/E
AT18	20.71	g/E	e/E	AT16	ok/E	g/E
AT68	7.80	g/E	g/E	AT18	g/E	e/E
AT69	9.67	ok/E	g/E	AT68	g/E	g/E
DARE	14.15	g/E	g/E	AT69	ok/E	g/E
MALT	2.68	e/E	g/E	DARE	g/E	g/E
PTK1	3.79	e/E	g/E	MALT	e/E	g/E
SVRC	7.11	e/E	g/E	PTK1	e/E	g/E
SVSK	1.03	g/E	g/E	SVRC	e/E	g/E
URFA	8.28	g/E	g/E	SVSK	g/E	g/E
				URFA	g/E	g/E



P/T axes

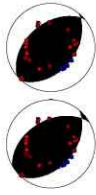


Data

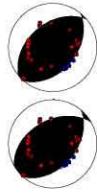


P K: NaN 95%: NaN T K: NaN 95%: NaN Lon: 39.25 Lat: 38.47 Dep: 0.00 Mag: ML, 3.7
 cate00067 Data pts: 35 Solns: 1 Pol errs: 1 Nodal Wt: 0.8 Solns shown: 1 Search Inc: 5
 Ampl errs: 0 Ampl Data: 16 Solns: 1 Pol errs: 1 Nodal Wt: 0.8 Soln shown: 1 Search Inc: 5

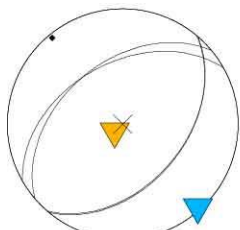
Pol Only



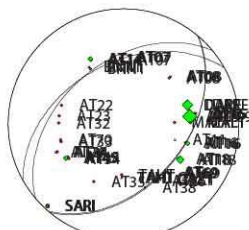
Pol + Ampl



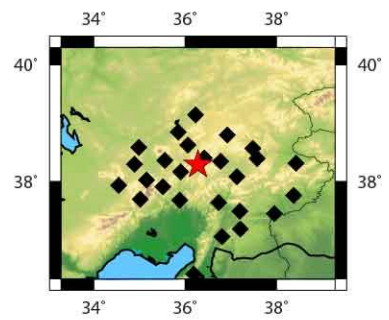
sta SH/P Pqual Squal	sta Pqual Squal
AT07 4.98 g/E g/E	AT07 g/E g/E
AT08 4.37 g/E ok/E	AT08 g/E ok/E
AT09 47.13 g/E g/E	AT09 g/E g/E
AT14 15.64 g/l g/E	AT14 g/l g/E
AT15 2.98 g/E g/E	AT15 g/E g/E
AT16 16.21 g/E e/	AT16 g/E e/E
AT18 25.17 g/E g/E	AT18 g/E g/E
AT24 1.18 g/E g/E	AT22 g/E
AT45 15.14 ok/E g/E	AT23 g/E
AT69 0.46 g/E ok/E	AT24 g/E g/E
BNN1 1.66 g/E g/E	AT26 ok/E
DARE 33.35 g/E g/E	AT32 g/E
GAZ1 2.59 g/E g/E	AT33 g/E
MALT 9.94 ok/E g/E	AT34 g/E
SARI 7.36 g/E g/	AT35 ok/E
TAHT 3.90 ok/E ok/	AT45 ok/E g/E
	AT69 g/E ok/E
	AT70 g/E
	BNN1 g/E g/E
	DARE g/E g/E
	GAZ1 g/E g/E
	MALT ok/E g/E
	SARI g/E g/E
	TAHT ok/E ok/



P/T axes

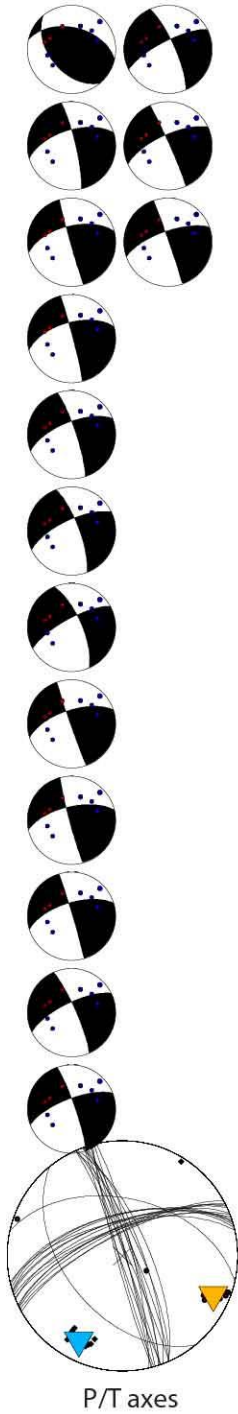


Data



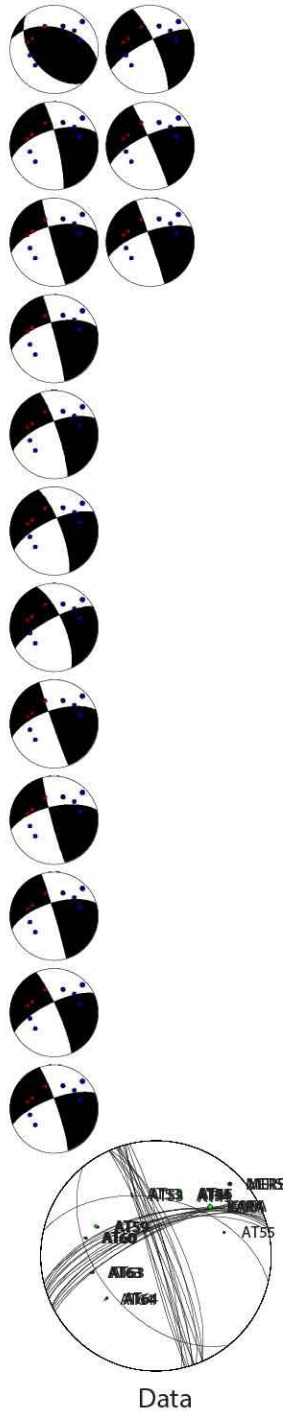
P K: 404.3 95%: 12.5 T K: 515.2 95%: 11.0 Lon: 36.28 Lat: 38.29 Dep: 0.00 Mag: ML, 3.2
 cate00068 Data pts: 42 Solns: 2 Pol errs: 1 Nodal Wt: 0.3 Solns shown: 2 Search Inc: 5
 Ampl errs: 0 Ampl Data: 16 Solns: 2 Pol errs: 1 Nodal Wt: 0.3 Soln shown: 2 Search Inc: 5

Pol Only



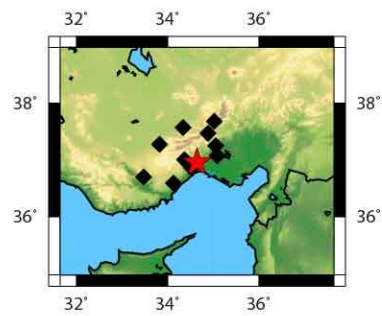
P/T axes

Pol + Ampl



Data

sta SH/P Pqual Squal	sta Pqual Squal
AT45 2.05 g/E ok/E	AT45 g/E ok/E
AT53 3.43 g/E g/E	AT53 g/E g/E
AT54 11.38 g/E ok/E	AT54 g/E ok/E
AT59 13.11 g/E ok/E	AT59 g/E
AT60 7.45 ok/E g/E	AT59 g/E ok/E
AT63 5.95 g/E g/E	AT60 ok/E g/E
AT64 1.31 g/E ok/E	AT63 g/E g/E
KARA 18.93 g/E g/E	AT64 g/E ok/E
MERS 4.57 g/E g/E	KARA g/E g/E
	MERS g/E g/E



P K: 99.8 95%: 3.8 T K: 24.2 95%: 7.9 Lon: 34.64 Lat: 36.96 Dep: 3.00 Mag: ML, 3.5
 cate00069 Data pts: 19 Solns: 15 Pol errs: 1 Nodal Wt: 0.8 Solns shown: 15 Search Inc: 5
 Ampl errs: 0 Ampl Data: 9 Solns: 15 Pol errs: 1 Nodal Wt: 0.8 Soln shown: 15 Search Inc: 5

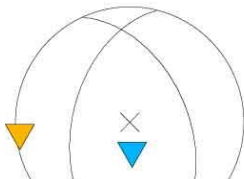
Pol Only



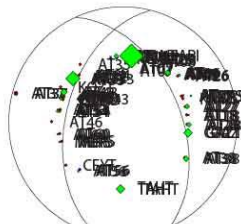
Pol + Ampl



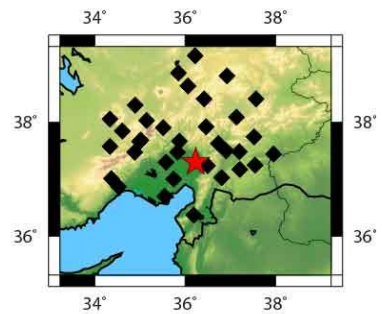
sta SH/P Pqual Squal	sta Pqual Squal
AT07 7.00 ok/E g/E	AT07 ok/E g/E
AT08 10.67 ok/E g/E	AT08 ok/E g/E
AT09 13.27 g/E g/E	AT09 g/E g/E
AT14 16.03 ok/E ok/E	AT14 ok/E ok/E
AT16 18.64 g/E g/E	AT16 g/E g/E
AT17 4.29 g/E g/E	AT17 g/E g/E
AT18 1.67 g/E g/E	AT18 g/E g/E
AT25 18.28 g/E g/E	AT25 g/E g/E
AT26 8.09 g/E g/E	AT26 g/E g/E
AT27 16.79 g/E ok/E	AT27 g/E ok/E
AT28 15.94 g/E g/E	AT28 g/E g/E
AT32 18.07 g/E g/E	AT32 g/E g/E
AT33 46.13 g/E ok/E	AT33 g/E ok/E
AT37 1.67 g/l g/E	AT34 g/E
AT38 19.43 g/E g/E	AT35 g/E
AT43 21.64 ok/E g/E	AT37 g/l g/E
AT44 8.18 g/E g/E	AT38 g/E g/E
AT45 7.40 g/E ok/E	AT43 ok/E g/E
AT53 2.66 ok/E g/E	AT44 g/E g/E
AT54 10.36 g/E ok/E	AT45 g/E ok/E
AT56 2.44 g/E ok/E	AT46 g/l
AT60 3.30 g/E g/E	AT53 ok/E g/E
BNN1 3.50 ok/E g/E	AT54 g/E ok/E
CMRD 9.14 g/l g/	AT56 g/E ok/E
GAZ1 28.30 g/E g/E	AT60 g/E g/E
KMRS 1.71 g/l g/	BNN1 ok/E g/E
MERS 2.24 g/E g/E	CEYT g/E
SARI 79.95 g/E g/	CMRD g/l g/E
TAHT 29.78 ok/E g/	GAZ1 g/E g/E
	KMRS g/l g/E
	KOZT e/l
	MERS g/E g/E
	SARI g/E g/E
	TAHT ok/E g/



P/T axes

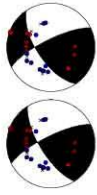


Data



P K: NaN 95%: NaN T K: NaN 95%: NaN Lon: 36.23 Lat: 37.3 Dep: 0.00 Mag: ML, 3.8
 cate00070 Data pts: 63 Solns: 1 Pol errs: 1 Nodal Wt: 0.1 Solns shown: 1 Search Inc: 5
 Ampl errs: 0 Ampl Data: 29 Solns: 1 Pol errs: 1 Nodal Wt: 0.1 Solns shown: 1 Search Inc: 5

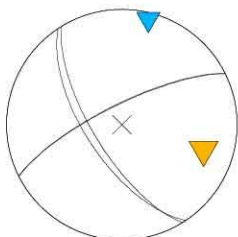
Pol Only



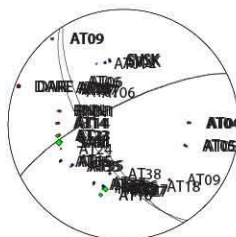
Pol + Ampl



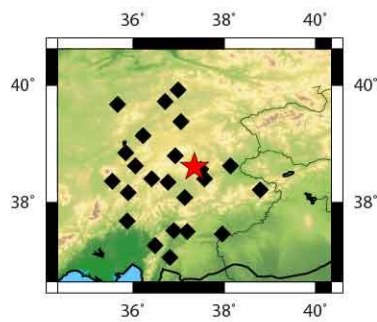
sta SH/PP	Q	S	Q	sta P	Q	S	Q
AT04	6.37	g/E	ok/E	AT02	g/E		
AT05	4.01	g/E	g/E	AT04	g/E	ok/E	
AT06	1.57	ok/E	g/E	AT05	g/E	g/E	
AT07	1.35	g/E	g/E	AT06	ok/E	g/E	
AT08	3.90	g/E	ok/E	AT07	g/E	g/E	
AT09	8.10	o/E	g/E	AT08	g/E	ok/E	
AT14	6.06	g/E	ok/E	AT09	o/E	g/E	
AT15	2.81	g/E	o/E	AT14	g/E	ok/E	
AT16	11.30	g/E	g/E	AT15	g/E	o/E	
AT23	12.49	g/E	ok/E	AT16	g/E	g/E	
AT27	3.89	g/E	g/E	AT23	g/E	ok/E	
AT35	2.88	ok/E	g/E	AT27	g/E	g/E	
AT37	3.94	g/E	ok/E	AT35	ok/E	g/E	
AT38	18.47	g/E	g/E	AT37	g/E	ok/E	
BNN1	2.90	g/E	g/E	AT38	g/E	g/E	
DARE	3.54	g/l	g/E	BNN1	g/E	g/E	
KMRS	1.23	g/E	ok/	DARE	g/l	g/E	
SARI	23.32	g/E	g/	KMRS	g/E	ok/E	
SVSK	6.67	o/E	g/E	SARI	g/E	g/E	
				SVSK	ok/E	g/E	



P/T axes



Data

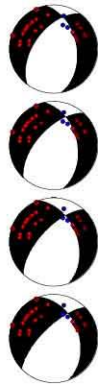


P K: 907.6 95%: 8.3 T K: 712.6 95%: 9.4 Lon: 37.35 Lat: 38.61 Dep: 0.00 Mag: ML, 3.3
 cate00071 Data pts: 42 Solns: 2 Pol errs: 2 Nodal Wt: 0.3 Solns shown: 2 Search Inc: 5
 Ampl errs: 0 Ampl Data: 19 Solns: 2 Pol errs: 2 Nodal Wt: 0.3 Soln shown: 2 Search Inc: 5

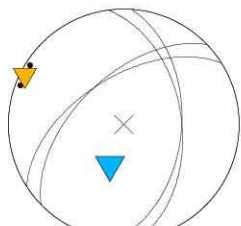
Pol Only



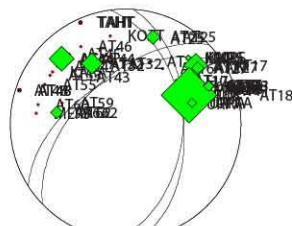
Pol + Ampl



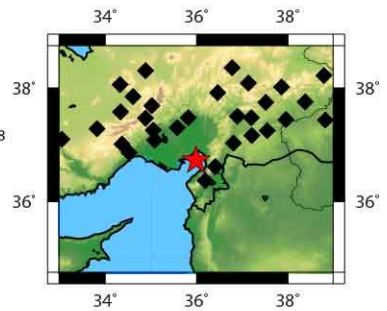
sta SH/P Pqual Squal	sta Pqual Squal
AT11 117.07 g/E o/E	AT05 o/E
AT17 78.17 o/E g/E	AT10 o/E
AT18 185.05 g/E g/E	AT11 g/E o/E
AT25 49.10 g/E g/E	AT15 g/E
AT27 40.11 g/E g/E	AT16 g/E
AT28 17.30 g/E g/E	AT17 o/E g/E
AT32 71.13 o/E g/E	AT18 g/E g/E
AT38 37.50 g/E g/E	AT25 g/E g/E
AT44 82.16 g/E g/E	AT27 g/E g/E
AT48 1.63 E/I g/	AT28 g/E g/E
AT62 40.33 g/E o/E	AT32 o/E g/E
GAZ1 33.50 g/E o/E	AT38 g/E g/E
KMRS 18.26 B/E o/	AT43 g/E
TAHT 6.23 g/E g/	AT44 g/E g/E
URFA 33.14 B/E g/	AT45 g/E
	AT46 g/E
	AT48 e/B g/
	AT53 g/E
	AT54 g/E
	AT55 g/E
	AT59 g/E
	AT60 g/E
	AT62 g/E o/E
	GAZ1 g/E o/E
	KARA g/E
	KMRS g/E o/E
	KOZT g/E
	MERS g/E
	TAHT g/E g/E
	URFA g/E g/E



P/T axes



Data



P K: 382.0 95%: 12.8 TK: 98.1 95%: 25. 5 Lon: 35.99 Lat: 36.73 Dep: 6.00 Mag: ML, 4.7
 cate00072 Data pts: 45 Solns: 27 Pol errs: 2 Nodal Wt: 0.2 Solns shown: 2 Search Inc: 10
 Ampl errs: 0 Ampl Data: 15 Solns: 4 Pol errs: 2 Nodal Wt: 0.2 Soln shown: 4 Search Inc: 5

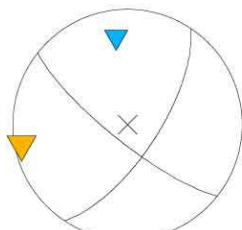
Pol Only



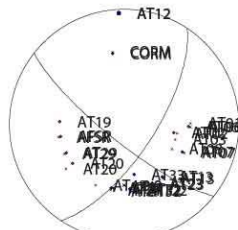
Pol + Ampl



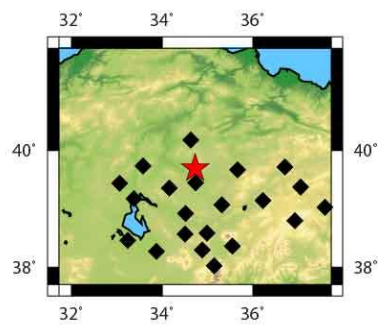
sta Pqual Squal
 AFSR ok/E g/E
 AT02 g/E g/E
 AT06 g/E g/E
 AT07 ok/E g/E
 AT12 eB e/
 AT13 g/E ok/E
 AT19 g/E
 AT20 g/E g/E
 AT21 ok/E g/E
 AT23 g/E ok/E
 AT29 ok/E ok/E
 AT31 g/E ok/E
 AT32 ok/E g/E
 AT33 g/E
 0.0 e/Ee/
 CORM g/l ok/E



P/T axes



Data



P K: NaN 95%: NaN T K: NaN 95%: NaN Lon: 34.73 Lat: 39.7 Dep: 0.00 Mag: ML, 3.0
 cate00073 Data pts: 35 Solns: 1 Pol errs: 1 Nodal Wt: 0.5 Solns shown: 1 Search Inc: 5
 Ampl errs: 0 Ampl Data: 14 Solns: 1 Pol errs: 1 Nodal Wt: 0.5 Solns shown: 1 Search Inc: 5

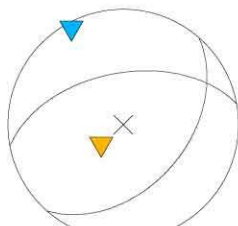
Pol Only



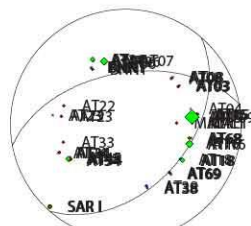
Pol + Ampl



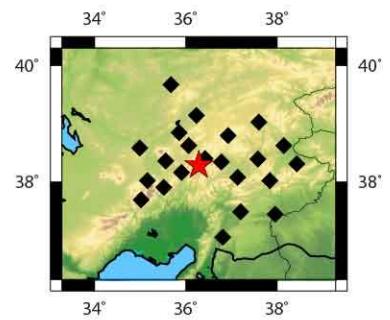
sta SH/P Pqual Squal	sta Pqual Squal
AT03 4.19 ok/E o/E	AT03 ok/E o/E
AT06 26.48 ok/E g/E	AT06 ok/E g/E
AT08 3.61 g/E ok/E	AT07 ok/E
AT09 46.82 ok/E o/E	AT08 g/E ok/E
AT14 16.64 E/E e/E	AT09 ok/E o/E
AT15 2.69 g/E g/E	AT14 o/E e/E
AT16 26.93 g/E o/E	AT15 g/E g/E
AT18 15.29 g/E g/E	AT16 g/E o/E
AT23 3.05 g/E g/E	AT18 g/E g/E
AT24 1.15 g/l o/E	AT22 ok/E
AT34 8.51 o/E g/E	AT23 g/E g/E
AT38 6.97 ok/E g/E	AT24 g/l o/E
AT45 15.32 ok/E g/E	AT33 g/E
AT68 6.05 g/E g/E	AT34 o/E g/E
AT69 6.01 ok/E g/E	AT38 ok/E g/E
BNN1 5.27 g/E g/E	AT45 ok/E g/E
MALT 3.36 g/E ok/E	AT68 g/E g/E
SARI 6.94 g/E g/E	AT69 ok/E g/E
	BNN1 g/E g/E
	MALT g/E ok/E
	SARI g/E g/E



P/T axes



Data



P K: NaN 95%: NaN T K: NaN 95%: NaN Lon: 36.28 Lat: 38.29 Dep: 0.00 Mag: ML, 3.4
 cate00074 Data pts: 40 Solns: 1 Pol errs: 1 Nodal Wt: 0.3 Solns shown: 1 Search Inc: 5
 Ampl errs: 0 Ampl Data: 18 Solns: 1 Pol errs: 1 Nodal Wt: 0.3 Solns shown: 1 Search Inc: 5

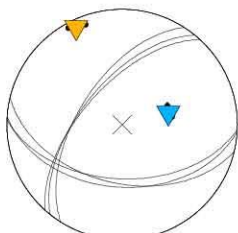
Pol Only



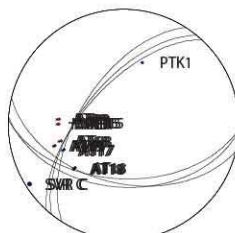
Pol + Ampl



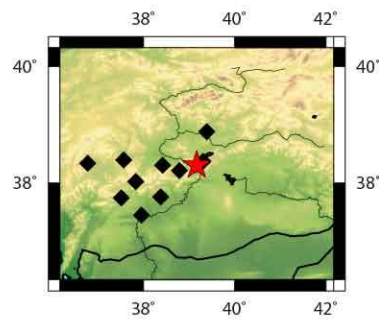
sta SH/P Pqual Squal	sta Pqual Squal
AT05 2.82 g/E g/E	AT05 g/E g/E
AT09 4.19 g/E ok/E	AT09 g/E ok/E
AT15 0.66 g/E ok/E	AT15 g/E ok/E
AT17 3.60 g/E g/E	AT17 g/E g/E
AT18 4.88 ok/E g/E	AT18 ok/E g/E
AT68 3.81 g/E g/E	AT68 g/E g/E
MALT 0.43 E/l g/	MALT e/l g/E
SVRC 3.17 g/E g/E	PTK1 ok/E
	SVRC g/E g/



P/T axes

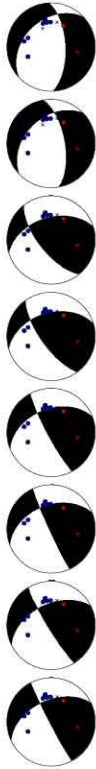


Data

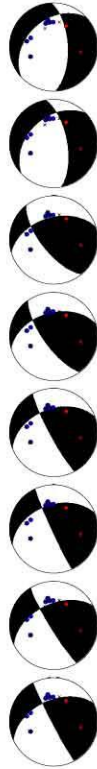


P K: 263.5 95%: 7.6 T K: 235.6 95%: 8.0 Lon: 39.17 Lat: 38.31 Dep: 0.00 Mag: ML, 3.0
 cate00075 Data pts: 18 Solns: 3 Pol errs: 0 Nodal Wt: 0.9 Solns shown: 3 Search Inc: 5
 Ampl errs: 1 Ampl Data: 8 Solns: 3 Pol errs: 0 Nodal Wt: 0.8 Soln shown: 3 Search Inc: 5

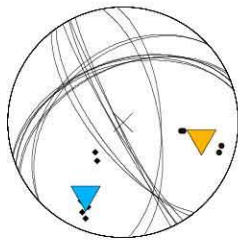
Pol Only



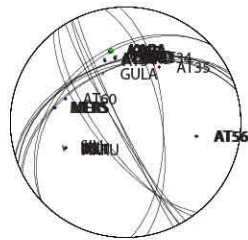
Pol + Ampl



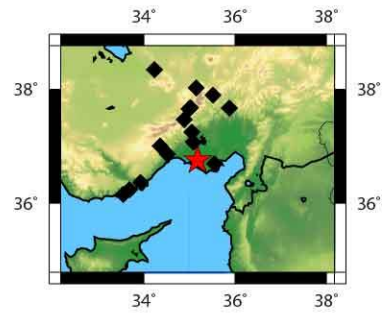
sta SH/P	Pqual	Squal	sta Pqual	Squal
AT54	6.85 g/E	g/E	AT33	ok/E
AT55	6.31 g/E	ok/E	AT35	ok/E
AT56	4.69 ok/E	g/E	AT54	g/E
CMRD	2.29 dk/E	g/	AT55	g/E
IKL1	6.69 ok/E	g/	AT56	ok/E
KARA	16.47 g/E	g/E	AT60	g/E
MERS	5.53 ok/E	ok/E	CMRD	ok/E
			IKL1	ok/E
			KARA	g/E
			MERS	ok/E



P/T axes



Data



PK: 18.0 95%: 13.4 TK: 38.1 95%: 9. 1 Lon: 35.18 Lat: 36.76 Dep: 0.00 Mag: ML, 3.5
 cate00076 Data pts: 22 Solns: 8 Pol errs: 0 Nodal Wt: 0.9 Solns shown: 8 Search Inc: 5
 Ampl errs: 0 Ampl Data: 7 Solns: 8 Pol errs: 0 Nodal Wt: 0.9 Soln shown: 8 Search Inc: 5

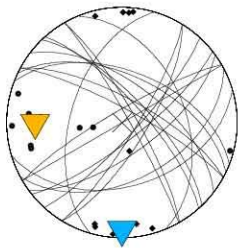
Pol Only



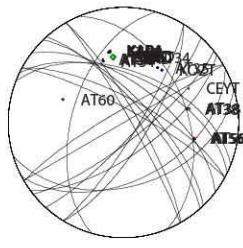
Pol + Ampl



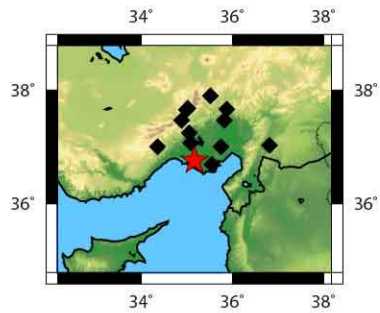
sta	SH/P	Pqual	Squal	sta	Pqual	Squal
AT38	10.69	ok/E	ok/E	AT35	g/E	
AT54	4.28	g/E	o/E	AT38	ok/E	ok/E
AT56	0.94	o/E	ok/E	AT54	g/E	o/E
CMRD	19.86	o/E	g/	AT55	g/E	
KARA	7.03	ok/E	g/E	AT56	o/E	ok/E
				AT60	ok/E	
				CMRD	o/E	g/E
				KARA	ok/E	g/E
				KOZT	g/E	



P/T axes



Data



P K: 11.5 95%: 14.9 T K: 10.7 95%: 15. 5 Lon: 35.17 Lat: 36.77 Dep: 0.00 Mag: ML, 3.0
 cate00077 Data pts: 17 Solns: 53 Pol errs: 1 Nodal Wt: 0.8 Solns shown: 10 Search Inc: 10
 Ampl errs: 0 Ampl Data: 5 Solns: 44 Pol errs: 1 Nodal Wt: 0.8 Soln shown: 8 Search Inc: 10

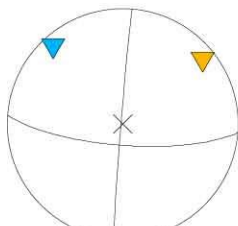
Pol Only



Pol + Ampl



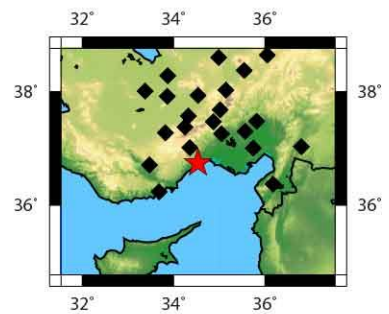
sta	SH/P	Pqual	Squal	sta	Pqual	Squal
AT22	17.53	ok/E	g/E	AT22	ok/E	g/E
AT23	35.27	ok/E	g/E	AT23	ok/E	g/E
AT33	128.48	g/E	ok/E	AT33	g/E	ok/E
AT38	2.68	g/E	g/E	AT38	g/E	g/E
AT45	16.03	g/E	g/E	AT42	g/E	
AT51	1.18	g/E	g/E	AT45	g/E	g/E
AT52	2.02	g/E	g/E	AT46	g/E	
AT53	1.40	g/l	g/E	AT51	g/E	g/E
AT54	13.60	g/E	e/	AT52	g/E	g/E
AT59	8.65	g/E	ok/E	AT53	g/l	g/E
AT60	12.30	g/E	g/E	AT54	g/E	e/E
AT63	25.43	ok/E	g/E	AT59	g/E	ok/E
CEYT	1.44	g/E	g/E	AT60	g/E	g/E
IKL1	6.45	g/E	g/E	AT63	ok/E	g/E
KARA	55.98	g/E	g/E	AT70	g/E	
KOZT	14.45	g/E	g/E	AT71	g/E	
TAHT	5.18	g/E	ok/	CEYT	g/E	g/E
				IKL1	g/E	g/E
				KARA	g/E	g/E
				KOZT	ok/E	g/
				TAHT	g/E	ok/



P/T axes

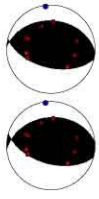


Data

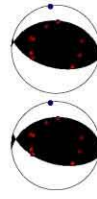


P K: 0.0 95%: NaN T K: NaN 95%: NaN Lon: 34.54 Lat: 36.75 Dep: 0.00 Mag: ML, 3.6
 cate00078 Data pts: 39 Solns: 1 Pol errs: 1 Nodal Wt: 0.4 Solns shown: 1 Search Inc: 5
 Ampl errs: 0 Ampl Data: 17 Solns: 1 Pol errs: 1 Nodal Wt: 0.4 Soln shown: 1 Search Inc: 5

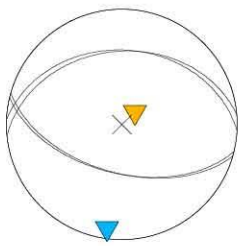
Pol Only



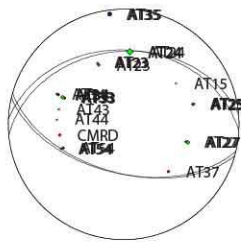
Pol + Ampl



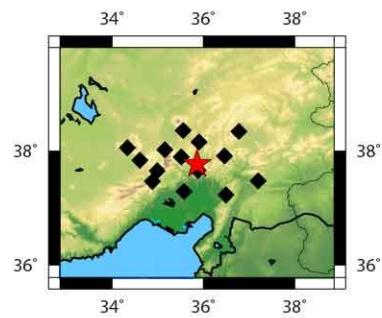
sta SH/P Pqual Squal	sta Pqual Squal
AT23 5.65 g/l g/	AT23 g/l g/
AT24 22.34 g/E g/	AT24 g/E g/
AT25 3.42 g/l g/	AT25 g/l g/
AT27 12.87 g/E g/	AT27 g/E g/
AT33 13.98 g/E g/	AT33 g/E g/
AT34 2.08 g/l g/	AT34 g/l g/
AT35 4.84 g/E g/	AT35 g/E g/
AT54 7.53 g/E ok/	AT37 g/E
	AT54 ok/E ok/
	CMRD ok/E



P/T axes

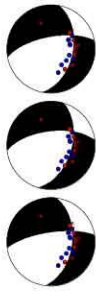


Data

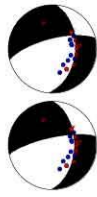


P K: 3371.6 95%: 4.3 T K: 586.0 95%: 10. 3 Lon: 35.86 Lat: 37.78 Dep: 0.00 Mag: ML, 3.0
 cate00079 Data pts: 21 Solns: 2 Pol errs: 1 Nodal Wt: 0.5 Solns shown: 2 Search Inc: 5
 Ampl errs: 0 Ampl Data: 8 Solns: 2 Pol errs: 1 Nodal Wt: 0.5 Soln shown: 2 Search Inc: 5

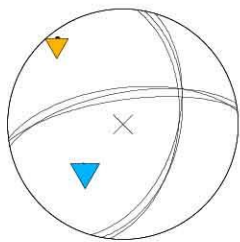
Pol Only



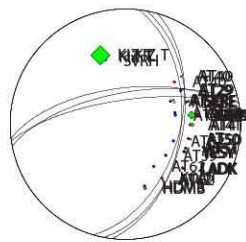
Pol + Ampl



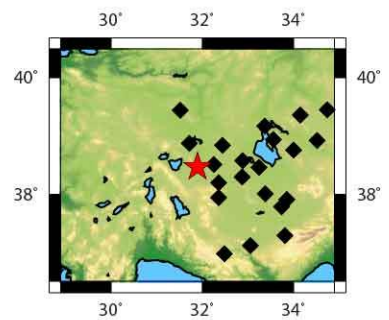
sta SH/P Pqual Squal	sta Pqual Squal
AT20 4.17 ok/E g/E	AT20 ok/E g/E
AT29 4.63 g/E g/E	AT21 ok/E
AT30 1.08 g/E g/E	AT29 g/E g/E
AT40 2.32 g/E g/E	AT30 g/E g/E
AT41 12.05 g/E g/E	AT40 g/E g/E
AT49 1.30 E/l g/	AT41 g/E g/E
AT50 4.27 E/l e/	AT49 eE g/
AT51 8.15 g/E g/E	AT50 eE e/
AT62 1.83 g/l g/E	AT51 g/E g/E
CHBY 26.71 E/E g/	AT52 ok/E
HDMB 10.62 ok/E g/E	AT59 g/E
KIZT 64.12 E/E g/	AT62 g/l g/E
LADK 3.37 E/l g/	CHBY g/E g/E
SERE 5.40 ok/E ok/	HDMB ok/E g/E
YESY 3.15 g/E ok/E	KIZT g/E g/E
	KONT g/E
	LADK g/l g/E
	SERE ok/E ok/E
	YESY g/E ok/E



P/T axes



Data



P K: 277.8 95%: 7.4 T K: 476.0 95%: 5.7 Lon: 31.9 Lat: 38.48 Dep: 0.00 Mag: ML, 3.7
 cate00080 Data pts: 36 Solns: 3 Pol errs: 1 Nodal Wt: 0.5 Solns shown: 3 Search Inc: 5
 Ampl errs: 0 Ampl Data: 15 Solns: 2 Pol errs: 1 Nodal Wt: 0.3 Soln shown: 2 Search Inc: 5

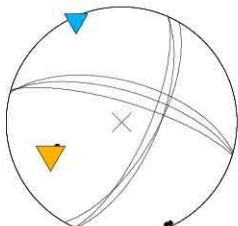
Pol Only



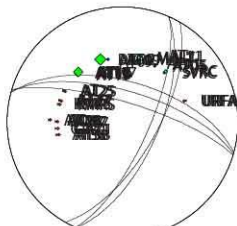
Pol + Ampl



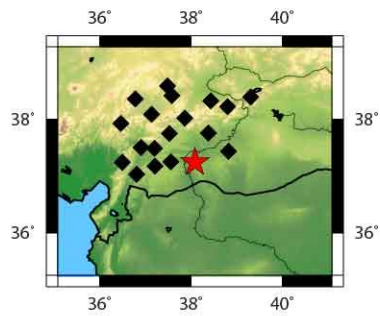
sta	SH/P	Pqual	Squal	sta	Pqual	Squal
AT05	6.24	ok/E	ok/E	AT05	ok/E	ok/E
AT09	38.27	ok/E	g/E	AT09	ok/E	g/E
AT11	2.76	g/l	e/	AT10	g/l	
AT15	17.85	ok/E	ok/E	AT11	gB	e/
AT16	18.71	ok/E	g/E	AT15	ok/E	ok/E
AT17	32.43	g/E	g/E	AT16	ok/E	g/E
AT25	7.12	ok/E	ok/E	AT17	g/E	g/E
AT27	7.26	g/E	g/E	AT25	ok/E	ok/E
AT28	1.37	g/l	ok/E	AT27	g/E	g/E
AT37	0.40	ok/E	ok/E	AT28	g/l	ok/E
AT38	2.40	g/E	g/E	AT37	ok/E	ok/E
GAZ1	1.04	g/l	ok/	AT38	g/E	g/E
KMRS	3.23	g/E	g/	GAZ1	g/l	ok/E
MALT	12.39	g/E	g/E	KMRS	g/E	g/E
SVRC	11.98	ok/E	g/E	MALT	g/E	g/E
URFA	0.70	e/l	ok/E	SVRC	ok/E	g/
				URFA	e/l	ok/E



P/T axes

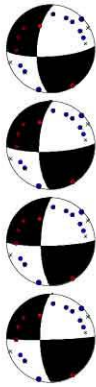


Data



PK: 175.9 95%: 9.3 TK: 151.2 95%: 10. 1 Lon: 38.08 Lat: 37.24 Dep: 0.00 Mag: ML, 3.1
 cate00081 Data pts: 34 Solns: 26 Pol errs: 1 Nodal Wt: 0.8 Solns shown: 3 Search Inc: 10
 Ampl errs: 0 Ampl Data: 16 Solns: 25 Pol errs: 1 Nodal Wt: 0.8 Soln shown: 2 Search Inc: 10

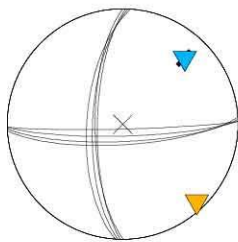
Pol Only



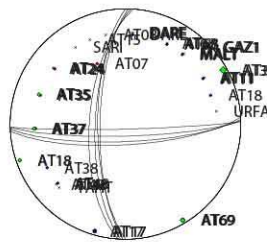
Pol + Ampl



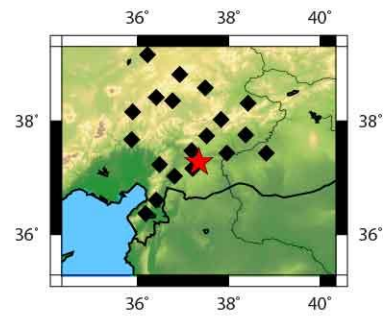
sta SH/P Pqual Squal	sta Pqual Squal
AT11 2.15 g/E ok/E	AT07 ok/E
AT17 2.55 g/E g/E	AT11 g/E ok/E
AT18 9.54 g/E ok/E	AT17 g/E g/E
AT24 5.34 g/E g/E	AT18 g/E ok/E
AT35 11.70 ok/E ok/E	AT24 g/E g/E
AT37 11.17 g/E g/E	AT35 ok/E ok/E
AT38 17.22 ok/E g/E	AT37 g/E g/E
AT48 0.88 ok/E g/E	AT38 ok/E g/E
AT68 1.23 e/E ok/	AT48 ok/E g/E
AT69 12.22 ok/E g/E	AT68 e/E ok/E
DARE 5.53 ok/E g/E	AT69 ok/E g/E
GAZ1 5.87 g/E g/E	DARE ok/E g/E
MALT 5.08 g/E g/E	GAZ1 g/E g/E
	MALT g/E g/E



P/T axes



Data



P K: 205.6 95%: 6.4 T K: 1188.1 95%: 2.7 Lon: 37.35 Lat: 37.28 Dep: 5.00 Mag: ML, 3.0
 cate00082 Data pts: 32 Solns: 4 Pol errs: 1 Nodal Wt: 0.8 Solns shown: 4 Search Inc: 5
 Ampl errs: 0 Ampl Data: 13 Solns: 4 Pol errs: 1 Nodal Wt: 0.8 Soln shown: 4 Search Inc: 5

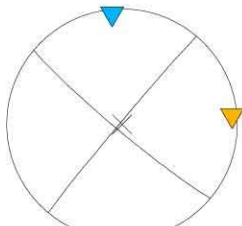
Pol Only



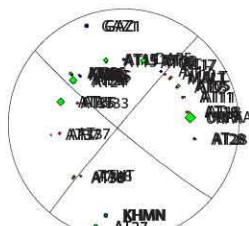
Pol + Ampl



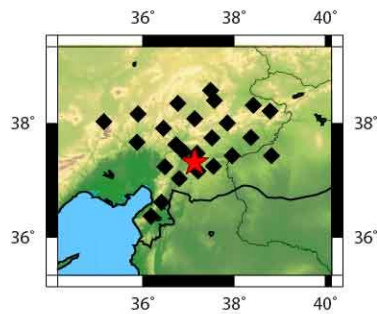
sta	SH/P	Pqual	Squal	sta	Pqual	Squal
AT05	14.28	g/E	g/E	AT05	g/E	g/E
AT09	18.47	ok/E	g/E	AT09	ok/E	g/E
AT11	2.04	g/E	ok/E	AT10	g/E	
AT15	16.74	g/E	g/E	AT11	g/E	ok/E
AT17	4.61	ok/E	g/E	AT15	g/E	g/E
AT18	1.54	ok/E	ok/E	AT16	g/E	
AT24	24.92	ok/E	g/E	AT17	ok/E	g/E
AT25	2.16	g/E	g/E	AT18	e/E	ok/E
AT26	6.61	g/E	g/E	AT24	ok/E	g/E
AT27	10.54	e/E	e/E	AT25	g/E	g/E
AT28	2.49	e/E	g/E	AT26	g/E	g/E
AT35	25.52	ok/E	ok/E	AT27	e/E	e/E
AT37	0.20	e/E	g/E	AT28	e/E	g/E
AT38	10.31	g/E	g/E	AT33	ok/E	
GAZ1	2.20	e/E	g/E	AT35	ok/E	ok/E
KHMN	6.65	g/E	ok/E	AT37	e/E	g/E
KMRS	10.73	g/E	e/E	AT38	g/E	g/E
MALT	10.47	g/E	g/E	GAZ1	e/E	g/E
URFA	36.23	ok/E	g/E	KHMN	g/E	ok/E
				KMRS	g/E	e/E
				MALT	g/E	g/E
				URFA	ok/E	g/E



P/T axes



Data



P K: NaN 95%: NaN T K: NaN 95%: NaN Lon: 37.14 Lat: 37.32 Dep: 3.00 Mag: ML, 3.2
 cate00083 Data pts: 44 Solns: 1 Pol errs: 0 Nodal Wt: 0.9 Solns shown: 1 Search Inc: 5
 Ampl errs: 0 Ampl Data: 19 Solns: 1 Pol errs: 0 Nodal Wt: 0.9 Solns shown: 1 Search Inc: 5

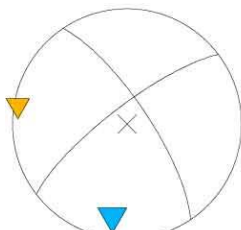
Pol Only



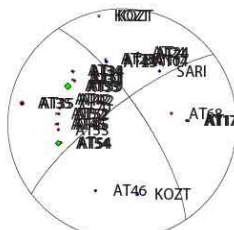
Pol + Ampl



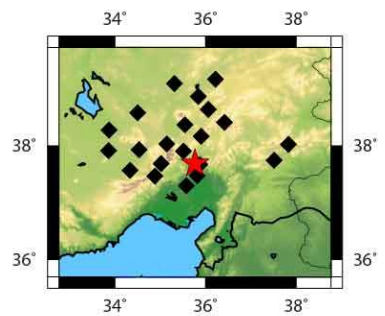
sta SH/P Pqual Squal	sta Pqual Squal
AT17 5.36 ok/E ok/E	AT07 ok/E
AT23 3.76 e/l g/E	AT13 ok/E
AT24 0.76 e/l ok/	AT14 g/E
AT31 4.16 ok/E g/E	AT17 ok/E ok/E
AT33 22.51 g/E ok/E	AT23 e/l g/E
AT34 3.90 g/E g/E	AT24 e/l ok/E
AT35 3.28 ok/E g/E	AT31 ok/E g/E
AT42 0.50 g/E g/E	AT33 g/E ok/E
AT45 2.79 g/E g/E	AT34 g/E g/E
AT52 1.05 g/E g/E	AT35 ok/E g/E
AT54 17.85 g/E g/E	AT42 g/E g/E
KOZT 1.61 g/E g/	AT45 g/E g/E
	AT46 g/E
	AT52 g/E g/E
	AT53 g/E
	AT54 g/E g/E
	AT68 g/E
	AT70 ok/E
	BNN1 ok/E
	KOZT g/E g/E
	SARI g/E



P/T axes



Data



P K: NaN 95%: NaN T K: NaN 95%: NaN Lon: 35.77 Lat: 37.69 Dep: 2.00 Mag: ML, 3.2
 cate00084 Data pts: 33 Solns: 1 Pol errs: 1 Nodal Wt: 0.5 Solns shown: 1 Search Inc: 5
 Ampl errs: 0 Ampl Data: 12 Solns: 1 Pol errs: 1 Nodal Wt: 0.5 Solns shown: 1 Search Inc: 5

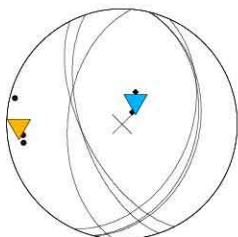
Pol Only



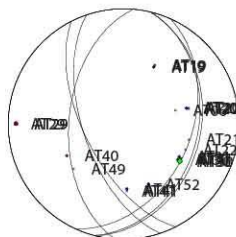
Pol + Ampl



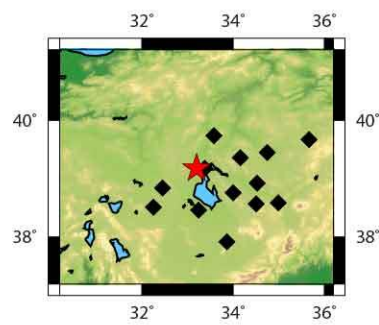
sta	SH/P	Pqual	Squal	sta	Pqual	Squal
AT19	6.89	ok/E	g/E	AT19	ok/E	g/E
AT20	1.07	ok/E	g/E	AT20	ok/E	g/E
AT29	1.22	g/l	g/E	AT29	g/l	g/E
AT30	18.29	g/E	g/E	AT30	g/E	g/E
AT31	4.02	ok/E	g/E	AT31	ok/E	g/E
AT41	1.08	g/E	g/E	AT40	g/l	
				AT41	g/E	g/E
				AT52	g/E	



P/T axes



Data



P K: 112.4 95%: 11.7 T K: 34.6 95%: 21. 3 Lon: 33.2 Lat: 39.18 Dep: 2.00 Mag: ML, 3.1
 cate00085 Data pts: 19 Solns: 3 Pol errs: 1 Nodal Wt: 0.3 Solns shown: 3 Search Inc: 5
 Ampl errs: 0 Ampl Data: 6 Solns: 3 Pol errs: 1 Nodal Wt: 0.3 Soln shown: 3 Search Inc: 5

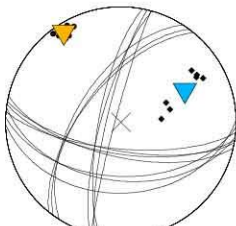
Pol Only



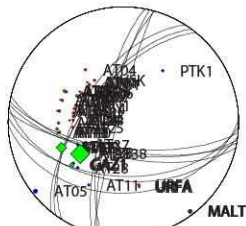
Pol + Ampl



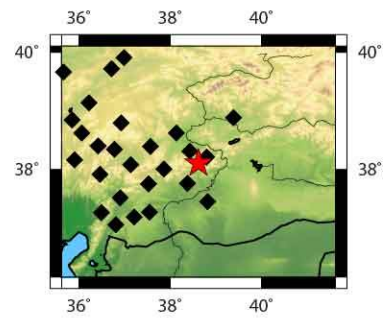
sta SH/P Pqual Squal	sta Pqual Squal
AT01 3.85 ok/E g/E	AT01 ok/E g/E
AT06 1.61 g/E ok/E	AT04 g/E
AT07 8.73 g/l ok/E	AT05 g/l
AT08 10.63 g/E g/E	AT06 g/E ok/E
AT09 0.63 e/l g/	AT07 g/l ok/E
AT10 2.17 g/E g/E	AT08 g/E g/E
AT15 3.83 g/E ok/E	AT09 e/l g/
AT17 33.97 g/E g/E	AT10 g/E g/E
AT24 1.68 ok/E ok/E	AT11 e/l
AT25 9.59 g/E ok/E	AT14 ok/E
AT38 62.96 g/E g/E	AT15 g/E ok/E
GAZ1 17.01 ok/E ok/E	AT16 g/E
MALT 7.45 e/l e/E	AT17 g/E g/E
URFA 4.31 ok/E g/	AT23 g/E
	AT24 ok/E ok/E
	AT25 g/E ok/E
	AT28 g/E
	AT37 ok/E
	AT38 g/E g/E
	BNN1 g/E
	GAZ1 ok/E ok/
	KMRS g/E
	MALT e/l e/
	PTK1 g/l
	SARI ok/E
	SVSK g/E
	URFA ok/E g/E



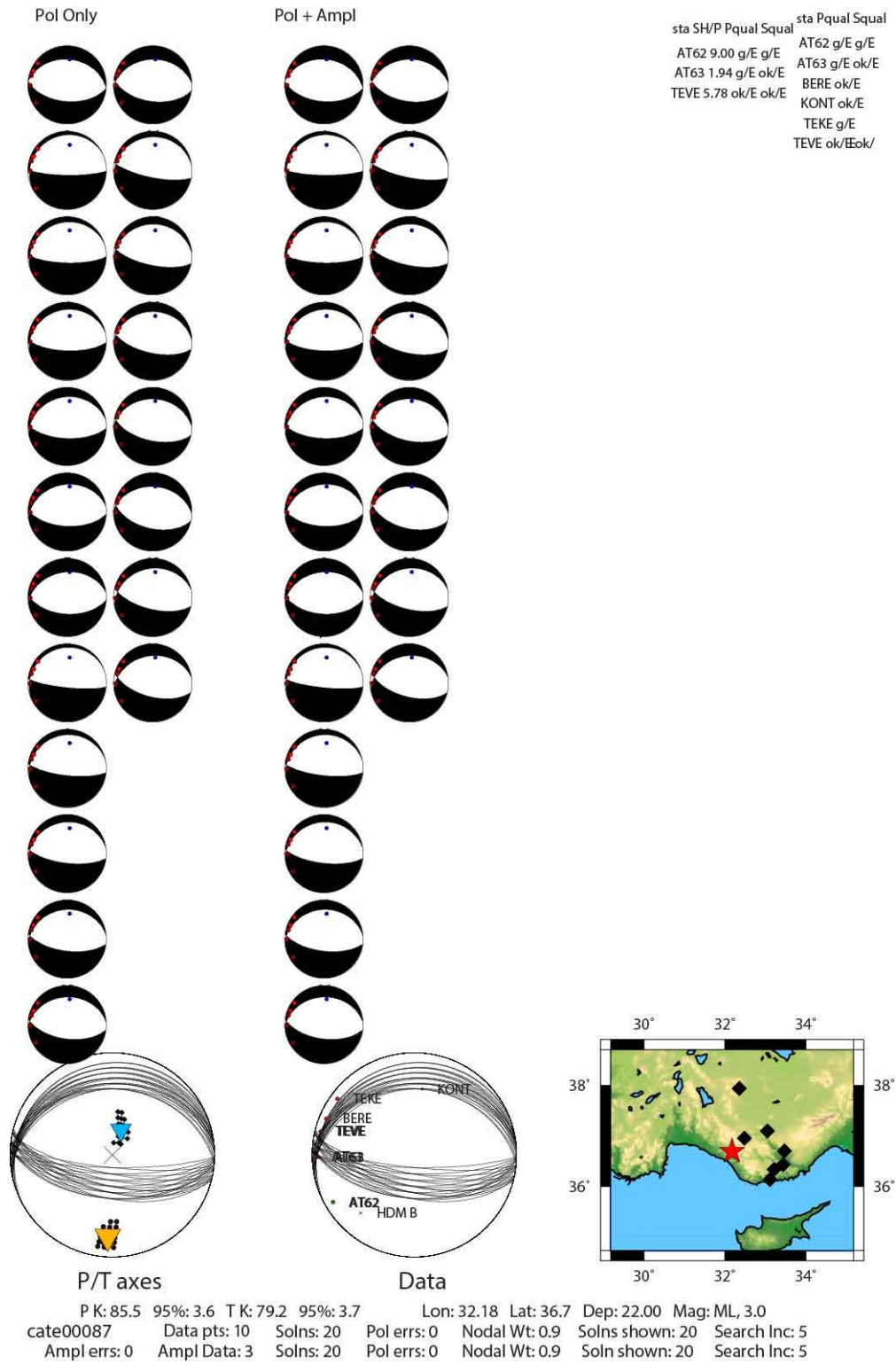
P/T axes

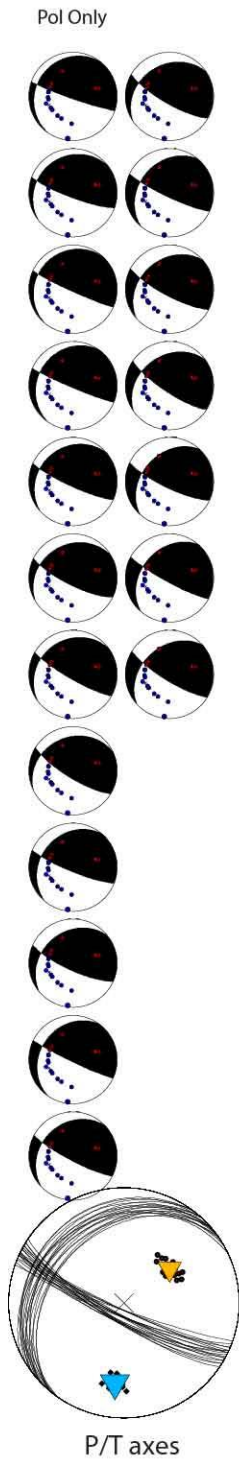


Data

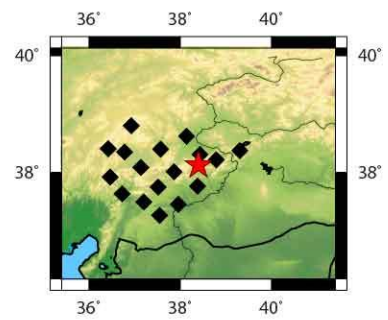


P K: 17.3 95%: 14.9 T K: 180.0 95%: 4.5 Lon: 38.62 Lat: 38.11 Dep: 0.00 Mag: ML, 4.3
 cate00086 Data pts: 41 Solns: 7 Pol errs: 1 Nodal Wt: 0.5 Solns shown: 7 Search Inc: 5
 Ampl errs: 0 Ampl Data: 14 Solns: 7 Pol errs: 1 Nodal Wt: 0.5 Soln shown: 7 Search Inc: 5



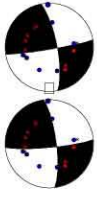


sta SH/P Pqual Squal	sta Pqual Squal
AT04 0.92 g/E ok/E	AT04 g/E ok/E
AT05 3.05 g/E g/E	AT05 g/E g/E
AT08 4.40 ok/E ok/E	AT08 ok/E ok/E
AT09 0.47 g/l g/E	AT09 g/l g/E
AT11 4.15 E/l g/	AT11 eB g/
AT15 23.46 ok/E g/E	AT15 ok/E g/E
AT16 3.51 g/E g/E	AT16 g/E g/E
AT17 5.90 g/E g/E	AT17 g/E g/E
AT18 9.12 g/E ok/E	AT18 g/E ok/E
AT25 5.75 ok/E ok/E	AT25 ok/E ok/E
AT27 15.15 ok/E ok/E	AT27 ok/E ok/E
AT28 0.79 g/E g/E	AT28 g/E g/E
MALT 2.11 E/l ok/	MALT e/l ok/E
SARI 7.34 ok/E ok/	SARI ok/E ok/E
SVRC 1.95 g/E ok/E	SVRC g/E ok/E



P K: 182.2 95%: 2.5 TK: 131.1 95%: 2.9 Lon: 38.4 Lat: 38.13 Dep: 0.00 Mag: ML, 3.0
 cate00089 Data pts: 32 Solns: 19 Pol errs: 1 Nodal Wt: 0.5 Solns shown: 19 Search Inc: 5
 Ampl errs: 0 Ampl Data: 15 Solns: 3 Pol errs: 1 Nodal Wt: 0.5 Soln shown: 3 Search Inc: 5

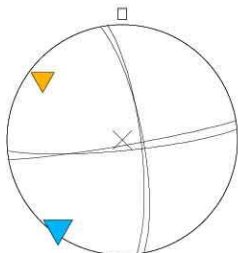
Pol Only



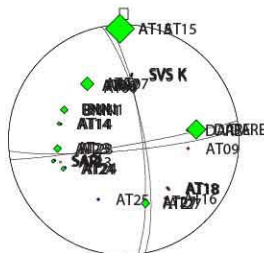
Pol + Ampl



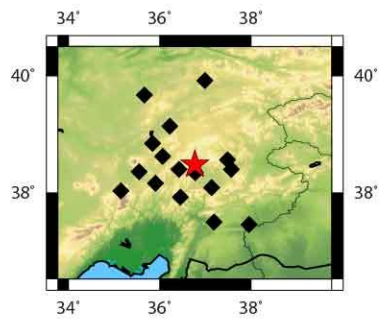
sta SH/P Pqual Squal	sta Pqual Squal
AT06 2.60 ok/E ok/E	AT06 ok/E ok/E
AT07 14.83 g/E g/E	AT07 g/E g/E
AT14 3.79 g/E o/E	AT09 g/E
AT15 25.50 g/E g/l	AT14 g/E o/E
AT18 2.35 g/E ok/E	AT15 g/E g/l
AT23 8.54 ok/E o/E	AT16 g/E
AT24 5.24 g/E g/E	AT18 g/E ok/E
AT27 9.20 g/E ok/E	AT23 ok/E o/E
BNN1 8.99 ok/E g/E	AT24 g/E g/E
DARE 20.81 g/E g/E	AT25 ok/E
SARI 4.32 g/E g/	AT27 g/E ok/E
SVSK 2.30 g/E ok/	BNN1 ok/E g/E
	DARE g/E g/E
	SARI g/E g/E
	SVSK g/E ok/E



P/T axes



Data

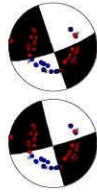


P K: 417.8 95%: 12.2 T K: 905.6 95%: 8.3 Lon: 36.77 Lat: 38.49 Dep: 1.00 Mag: ML, 3.0
 cate00090 Data pts: 28 Solns: 2 Pol errs: 1 Nodal Wt: 0.8 Solns shown: 2 Search Inc: 5
 Ampl errs: 0 Ampl Data: 12 Solns: 1 Pol errs: 1 Nodal Wt: 0.8 Soln shown: 1 Search Inc: 5

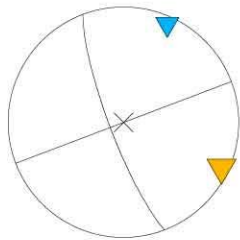
Pol Only



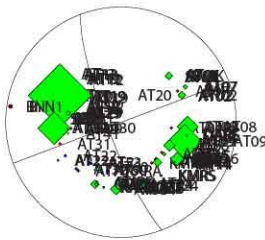
Pol + Ampl



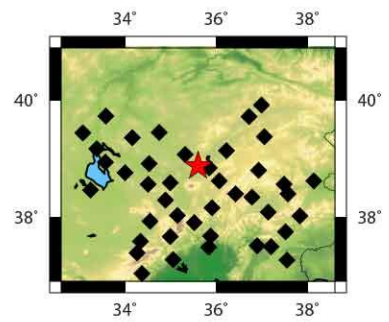
sta	SH/P	Pqual	Squal	sta	Pqual	Squal
AFSR	6.50	g/E	g/E	AFSR	g/E	g/E
AT01	9.08	ok/E	g/E	AT01	ok/E	g/E
AT02	24.64	ok/E	g/E	AT02	ok/E	g/E
AT04				AT04	g/E	
AT07	15.95	g/E	g/E	AT07	g/E	g/E
AT08	68.68	g/E	g/E	AT08	g/E	g/E
AT09	112.74	ok/E	g/E	AT09	ok/E	g/E
AT12	4.81	e/E	e/E	AT12	e/E	e/E
AT13	2.33	E/E	g/E	AT13	e/E	g/E
AT14	0.91	E/E	g/E	AT14	e/E	g/E
AT15	9.02	e/E	ok/E	AT15	e/E	ok/E
AT16	45.13	ok/E	g/E	AT16	ok/E	g/E
AT17	11.84	g/E	g/E	AT17	g/E	g/E
AT19	13.71	g/E	g/E	AT19	g/E	g/E
AT20	209.54	g/E	g/E	AT20	g/E	g/E
AT21	37.76	g/E	g/E	AT21	g/E	g/E
AT22	6.04	ok/E	ok/E	AT22	ok/E	ok/E
AT24	26.08	g/E	g/E	AT24	g/E	g/E
AT29	16.01	g/E	g/E	AT29	ok/E	
AT30	108.47	g/E	g/E	AT30	g/E	g/E
AT33	27.90	ok/E	g/E	AT33	ok/E	
AT34	36.82	ok/E	g/E	AT34	ok/E	
AT35	11.94	ok/E	g/E	AT35	ok/E	
AT49	7.14	ok/E	ok/E	AT49	ok/E	ok/E
AT60	10.17	ok/E	g/E	AT60	ok/E	g/E
AT68	38.45	g/E	g/E	AT68	g/E	g/E
AT69	28.41	ok/E	g/E	AT69	ok/E	g/E
BNN1	2.68	E/E	g/E	BNN1	e/E	g/E
CMRD	11.36	ok/E	g/E	CMRD	ok/E	g/E
DARE	6.44	g/E	ok/E	DARE	g/E	ok/E
KARA	5.32	g/E	g/E	KARA	g/E	g/E
KMRS	6.36	g/E	g/E	KMRS	g/E	g/E
KOZT	1.91	g/E	g/E	KOZT	g/E	g/E
SARI	3.68	e/E	g/E	SARI	e/E	g/E
SERE	4.47	g/E	g/E	SERE	g/E	g/E
SVSK	25.44	g/E	g/E	SVSK	g/E	g/E



P/T axes



Data



P K: 0.0 95%: NaN T K: NaN 95%: NaN Lon: 35.6 Lat: 38.88 Dep: 0.00 Mag: ML, 3.7
 cate00091 Data pts: 78 Solns: 1 Pol errs: 1 Nodal Wt: 0.8 Solns shown: 1 Search Inc: 5
 Ampl errs: 1 Ampl Data: 35 Solns: 2 Pol errs: 1 Nodal Wt: 0.3 Soln shown: 2 Search Inc: 5

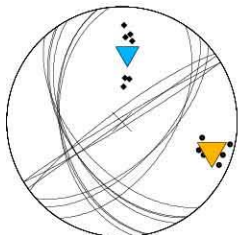
Pol Only



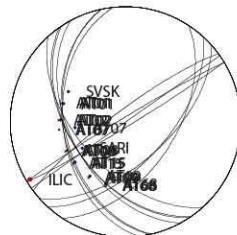
Pol + Ampl



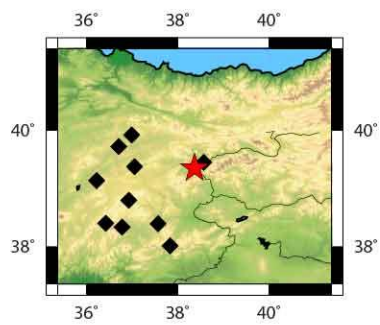
sta SH/P Pqual Squal	sta Pqual Squal
AT01 1.62 ok/E g/E	AT01 ok/E g/E
AT02 1.70 g/E ok/E	AT02 g/E ok/E
AT07 4.47 ok/E g/E	AT07 ok/E g/E
AT08 4.73 ok/E ok/E	AT08 ok/E ok/E
AT09 3.93 g/E g/E	AT09 g/E g/E
AT15 3.28 ok/E ok/E	AT15 ok/E ok/E
AT68 8.76 ok/E g/E	AT68 ok/E g/E
	ILIC e/l
	SARI g/E
	SVSK ok/E



P/T axes



Data



P K: 16.7 95%: 15.2 TK: 45.3 95%: 9. 1 Lon: 38.37 Lat: 39.36 Dep: 0.00 Mag: ML, 3.0
 cate00092 Data pts: 17 Solns: 7 Pol errs: 1 Nodal Wt: 0.8 Solns shown: 7 Search Inc: 5
 Ampl errs: 0 Ampl Data: 7 Solns: 7 Pol errs: 1 Nodal Wt: 0.8 Soln shown: 7 Search Inc: 5

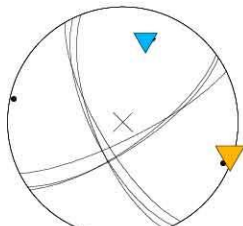
Pol Only



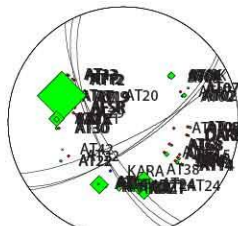
Pol + Ampl



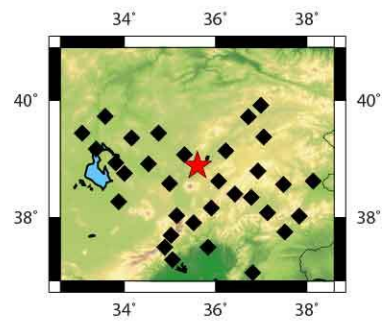
sta SH/P	Pqual	Squal	sta Pqual	Squal
AFSR	15.77	g/E g/E	AFSR	g/E g/
AT01	5.99	ok/E g/E	AT01	ok/E g/E
AT02	15.38	ok/E g/E	AT02	ok/E g/E
AT07	6.78	g/E ok/E	AT04	g/E
AT08	8.83	ok/E g/E	AT07	g/E ok/E
AT12	6.73	g/E g/E	AT08	ok/E g/E
AT13	6.22	E/E g/	AT12	g/E g/E
AT14	4.15	E/l g/	AT13	e/E g/E
AT16	9.12	ok/E g/E	AT14	eE g/
AT17	16.55	g/E g/E	AT15	g/E
AT19	16.64	ok/E g/E	AT16	ok/E g/E
AT20	160.75	ok/E g/E	AT17	g/E g/E
AT21	51.12	ok/E g/E	AT19	ok/E g/E
AT22	8.63	g/E g/E	AT20	ok/E g/E
AT24	93.44	g/E e/l	AT21	ok/E g/E
AT30	10.76	ok/E g/E	AT22	g/E g/E
AT33	19.19	g/E g/E	AT24	g/E e/l
AT34	15.93	ok/E g/E	AT29	g/E
AT45	61.88	ok/E ok/E	AT30	ok/E g/E
AT54	5.24	ok/E g/E	AT33	g/E g/E
AT68	6.13	g/E g/E	AT34	ok/E g/E
DARE	6.82	g/E ok/E	AT45	ok/E ok/E
KARA	3.59	ok/E g/E	AT54	ok/E g/E
KOZT	7.14	g/E g/	AT68	g/E g/E
SARI	13.93	E/l e/	DARE	g/E ok/E
SVSK	25.81	ok/E ok/	KARA	ok/E g/E
YAYX	19.30	ok/E g/	KOZT	g/E g/E
			SARI	e/E e/
			SVSK	ok/E ok/
			YAYX	ok/E g/



P/T axes



Data



P K: 300.6 95%: 7.1 T K: 175.7 95%: 9.3 Lon: 35.6 Lat: 38.89 Dep: 0.00 Mag: ML, 3.9
 cate00093 Data pts: 59 Solns: 3 Pol errs: 2 Nodal Wt: 0.2 Solns shown: 3 Search Inc: 5
 Ampl errs: 0 Ampl Data: 27 Solns: 1 Pol errs: 2 Nodal Wt: 0.2 Soln shown: 1 Search Inc: 5

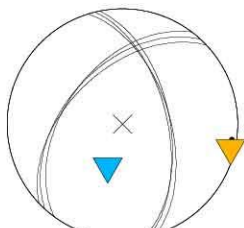
Pol Only



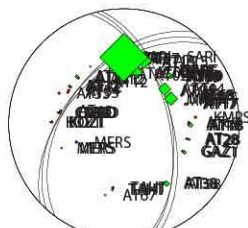
Pol + Ampl



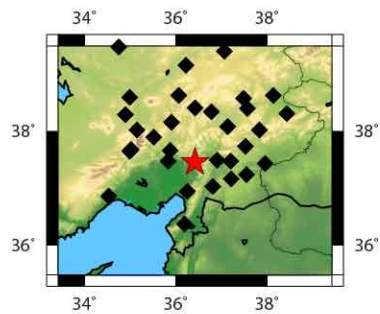
sta	SH/P	Pqual	Squal	sta	Pqual	Squal
AT02	33.59	ok/E	g/E	AT02	ok/E	g/E
AT04	41.09	ok/E	ok/E	AT04	ok/E	ok/E
AT07	44.23	g/E	g/l	AT07	g/E	g/l
AT09	14.61	g/E	e/l	AT09	g/E	e/l
AT12	1.51	ok/E	ok/E	AT12	ok/E	ok/E
AT15	51.36	g/E	e/l	AT15	g/E	e/l
AT16	14.87	g/E	g/E	AT16	g/E	g/E
AT17	2.76	e/l	g/	AT17	e/l	g/
AT18	14.98	ok/E	g/E	AT18	ok/E	g/E
AT22	13.55	g/E	g/E	AT22	g/E	g/E
AT28	5.44	g/l	g/E	AT28	g/l	g/E
AT32	5.01	g/E	g/E	AT32	g/E	g/E
AT38	20.54	e/E	g/	AT33	g/E	
AT68	3.92	g/E	g/E	AT34	e/l	
CMRD	6.98	g/E	ok/	AT35	e/l	
DARE	2.00	g/E	g/E	AT38	e/E	g/E
GAZ1	11.42	g/E	g/E	AT45	g/E	
KOZT	0.92	e/l	g/E	AT68	g/E	g/E
MALT	45.98	g/E	g/l	AT69	e/l	
MERS	2.84	g/E	g/E	CMRD	g/E	ok/E
SARI	160.22	g/E	g/	DARE	g/E	g/E
TAHT	4.82	g/E	g/	GAZ1	g/E	g/E
				KMRS	e/l	
				KOZT	e/l	g/
				MALT	g/E	g/l
				MERS	g/E	g/E
				SARI	g/E	g/E
				TAHT	g/E	g/E



P/T axes



Data



P K: 605.0 95%: 5.0 T K: 491.5 95%: 5.6 Lon: 36.42 Lat: 37.47 Dep: 0.00 Mag: ML, 4.2
 cate00094 Data pts: 53 Solns: 3 Pol errs: 2 Nodal Wt: 0.1 Solns shown: 3 Search Inc: 5
 Ampl errs: 0 Ampl Data: 22 Solns: 3 Pol errs: 2 Nodal Wt: 0.1 Solns shown: 3 Search Inc: 5

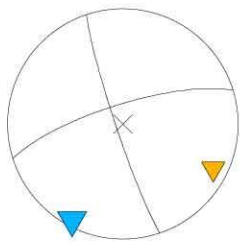
Pol Only



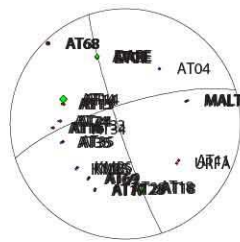
Pol + Ampl



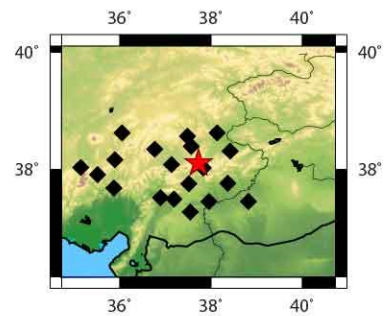
sta SH/P	Pqual	Squal	sta Pqual	Squal
AT09	4.91 g/E	E	AT04	ok/E
AT14	26.05 ok/E	g/E	AT09	g/E g/E
AT15	6.00 E/l	g/	AT11	g/l
AT16	4.06 E/l	g/	AT14	ok/E g/E
AT17	5.56 e/E	g/l	AT15	eE g/
AT18	17.04 g/E	g/E	AT16	eE g/
AT24	2.87 g/E	ok/E	AT17	e/E g/l
AT28	4.04 g/E	ok/E	AT18	g/E g/E
AT35	4.07 g/E	ok/E	AT24	g/E ok/E
AT68	5.74 e/l	E/E	AT28	g/E ok/E
AT69	5.51 g/E	ok/E	AT33	ok/E
DARE	15.43 E/E	e/	AT34	ok/E
KMRS	2.75 E/g/	g/	AT35	g/E ok/E
MALT	5.49 g/E	g/E	AT68	eE e/
			AT69	g/E ok/E
			DARE	g/E e/E
			KMRS	g/E g/E
			MALT	g/E g/E
			URFA	g/E



P/T axes



Data



P K: 0.0 95%: NaN T K: NaN 95%: NaN Lon: 37.73 Lat: 38.11 Dep: 0.00 Mag: ML, 3.2
 cate00095 Data pts: 33 Solns: 1 Pol errs: 0 Nodal Wt: 0.9 Solns shown: 1 Search Inc: 5
 Ampl errs: 0 Ampl Data: 14 Solns: 1 Pol errs: 0 Nodal Wt: 0.9 Soln shown: 1 Search Inc: 5

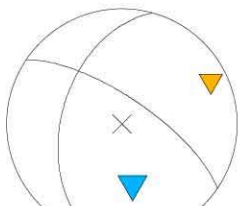
Pol Only



Pol + Ampl



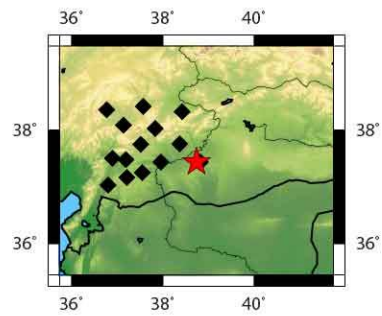
sta SH/P Pqual Squal	sta Pqual Squal
AT09 37.55 ok/E g/E	AT09 ok/E g/E
AT11 12.51 g/l g/E	AT11 g/l g/E
AT16 7.63 g/E g/E	AT16 g/E g/E
AT17 1.55 g/E ok/E	AT17 g/E ok/E
AT18 1.40 e/l ok/	AT18 e/l ok/E
AT28 9.42 g/E g/E	AT28 g/E g/E
AT38 24.20 ok/E g/E	AT38 ok/E g/E
AT68 2.93 e/l g/	AT68 e/l g/
GAZ1 6.58 ok/E g/E	GAZ1 ok/E g/
KMRS 1.02 g/E ok/	KMRS g/E ok/E
MALT 2.66 g/E g/E	MALT g/E g/E
URFA 0.24 g/E g/	URFA g/E g/E



P/T axes



Data



P K: NaN 95%: NaN T K: 0.0 95%: NaN Lon: 38.74 Lat: 37.44 Dep: 3.00 Mag: ML, 3.2
 cate00096 Data pts: 26 Solns: 1 Pol errs: 1 Nodal Wt: 0.5 Solns shown: 1 Search Inc: 5
 Ampl errs: 0 Ampl Data: 12 Solns: 1 Pol errs: 1 Nodal Wt: 0.5 Soln shown: 1 Search Inc: 5

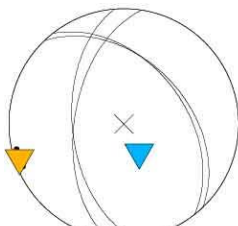
Pol Only



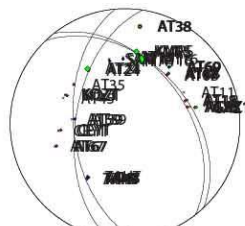
Pol + Ampl



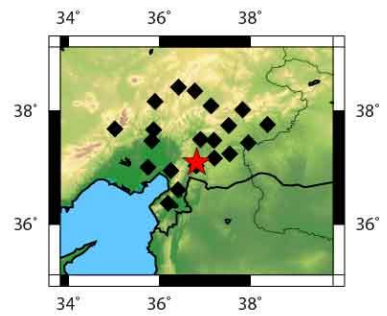
sta SH/P Pqual Squal	sta Pqual Squal
AT15 3.59 g/E ok/E	AT15 g/E ok/E
AT16 27.71 g/E g/E	AT16 g/E g/E
AT17 8.05 g/E g/E	AT17 g/E g/E
AT18 2.97 g/E g/E	AT18 g/E g/E
AT24 18.12 ok/E ok/E	AT24 ok/E ok/E
AT28 1.05 E/I o/	AT28 eB o/
AT38 7.88 g/E g/E	AT35 g/E
AT48 4.34 ok/E g/E	AT38 g/E g/E
AT59 1.22 o/E g/E	AT48 ok/E g/E
AT67 1.90 E/I g/	AT59 o/E g/E
AT68 4.88 g/E g/E	AT67 eB g/
AT69 5.96 g/E g/E	AT68 g/E g/E
CEYT 1.83 g/E ok/E	AT69 g/E g/E
GAZ1 8.00 g/E g/E	CEYT g/E ok/E
KMRS 17.50 g/E g/	GAZ1 g/E g/E
KOZT 4.69 ok/E e/	KMRS g/E g/E
SARI 3.62 o/E g/	KOZT ok/E e/E
TAHT 6.82 g/E ok/	SARI ok/E g/E
	TAHT g/E ok/



P/T axes



Data



P K: 272.1 95%: 15.2 T K: 140.5 95%: 21. 2 Lon: 36.82 Lat: 37.1 Dep: 2.00 Mag: ML, 3.0
 cate00097 Data pts: 39 Solns: 2 Pol errs: 1 Nodal Wt: 0.1 Solns shown: 2 Search Inc: 5
 Ampl errs: 0 Ampl Data: 18 Solns: 2 Pol errs: 1 Nodal Wt: 0.1 Soln shown: 2 Search Inc: 5

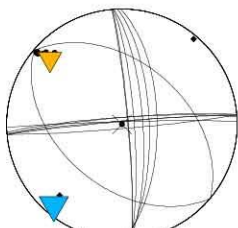
Pol Only



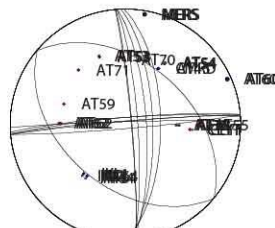
Pol + Ampl



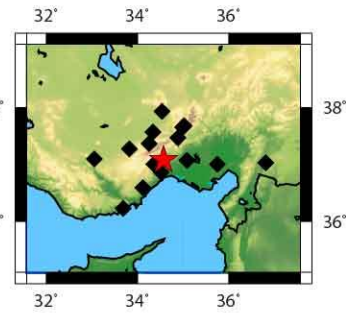
sta SH/P Pqual Squal	sta Pqual Squal
AT38 6.79 ok/E ok/E	AT38 ok/E ok/E
AT53 3.75 g/l g/E	AT45 g/E
AT54 8.94 g/E g/E	AT53 g/l g/E
AT60 4.05 ok/E ok/E	AT54 g/E g/E
AT62 1.43 g/E ok/E	AT55 g/E
AT64 2.29 g/E ok/E	AT59 g/E
CEYT 1.38 g/E ok/E	AT60 ok/E ok/E
IKL1 2.41 g/E ok/E	AT62 g/E ok/E
MERS 5.18 g/l g/	AT64 g/E ok/E
	AT70 g/E
	AT71 g/E
	CEYT g/E ok/E
	CMRD g/E
	IKL1 g/E ok/E
	MERS g/l g/E



P/T axes

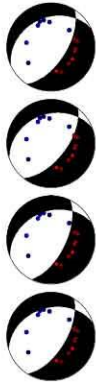


Data

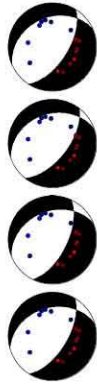


P K: 115.0 95%: 5.7 TK: 7.3 95%: 23. 9 Lon: 34.57 Lat: 37.09 Dep: 1.00 Mag: ML, 3.0
 cate00098 Data pts: 24 Solns: 7 Pol errs: 1 Nodal Wt: 0.8 Solns shown: 7 Search Inc: 5
 Ampl errs: 0 Ampl Data: 9 Solns: 3 Pol errs: 1 Nodal Wt: 0.8 Soln shown: 3 Search Inc: 5

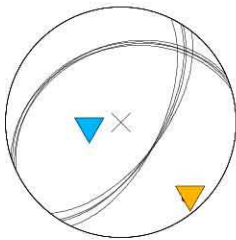
Pol Only



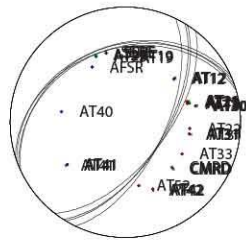
Pol + Ampl



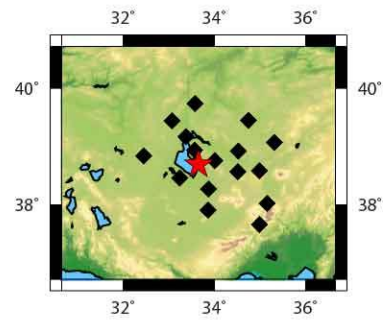
sta SH/P Pqual Squal	sta Pqual Squal
AT12 6.39 g/E ok/E	AFSR ok/E
AT13 7.09 g/E ok/E	AT12 g/E ok/E
AT19 10.22 g/E g/E	AT13 g/E ok/E
AT21 6.75 g/E g/E	AT19 g/E g/E
AT29 8.93 g/l g/E	AT21 g/E g/E
AT30 4.87 g/l g/l	AT22 g/l
AT31 0.44 g/E g/E	AT29 g/l g/E
AT41 1.20 g/l g/E	AT30 g/l g/l
AT42 2.47 g/l g/l	AT31 g/E g/E
CMRD 6.15 g/E ok/	AT33 ok/E
SERE 1.69 g/l ok/	AT40 g/E
	AT41 g/l g/E
	AT42 g/l g/l
	AT52 g/E
	CMRD g/E ok/E
	SERE g/l ok/E



P/T axes

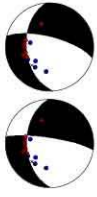


Data

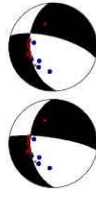


P K: 500.6 95%: 4.1 T K: 602.0 95%: 3.7 Lon: 33.65 Lat: 38.7 Dep: 1.00 Mag: ML, 3.0
 cate00099 Data pts: 27 Solns: 4 Pol errs: 1 Nodal Wt: 0.8 Solns shown: 4 Search Inc: 5
 Ampl errs: 0 Ampl Data: 11 Solns: 4 Pol errs: 1 Nodal Wt: 0.8 Soln shown: 4 Search Inc: 5

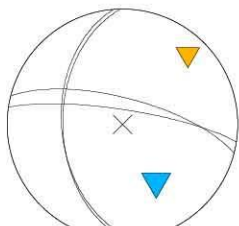
Pol Only



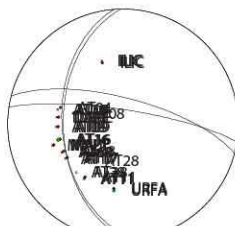
Pol + Ampl



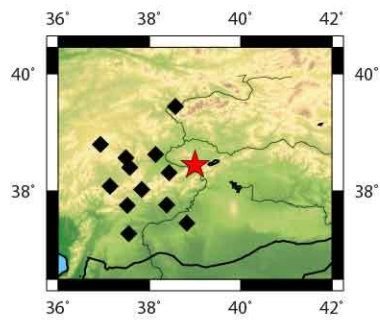
sta SH/P Pqual Squal	sta Pqual Squal
AT08 2.61 ok/E ok/E	AT04 e/l
AT09 3.78 g/E ok/E	AT08 ok/E ok/E
AT11 6.87 ok/E g/E	AT09 g/E ok/E
AT16 11.56 ok/E ok/E	AT11 ok/E g/E
AT17 2.01 g/E ok/E	AT16 ok/E ok/E
AT28 1.55 g/E ok/E	AT17 g/E ok/E
AT68 5.48 g/E g/E	AT28 g/E ok/E
DARE 2.94 g/E g/E	AT68 g/E g/E
ILIC 3.57 g/E g/E	DARE g/E g/E
MALT 0.57 g/E g/E	ILIC g/E g/E
URFA 9.61 g/E g/E	MALT g/E g/E
	URFA g/E g/E



P/T axes

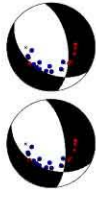


Data

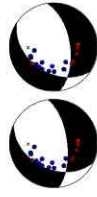


P K: 185.8 95%: 18.4 TK: 358.3 95%: 13. 2 Lon: 39 Lat: 38.45 Dep: 0.00 Mag: ML, 3.1
 cate00100 Data pts: 23 Solns: 2 Pol errs: 1 Nodal Wt: 0.3 Solns shown: 2 Search Inc: 5
 Ampl errs: 0 Ampl Data: 11 Solns: 2 Pol errs: 1 Nodal Wt: 0.3 Soln shown: 2 Search Inc: 5

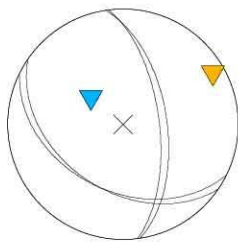
Pol Only



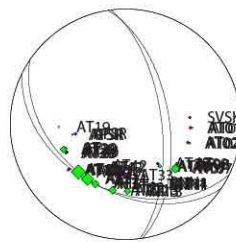
Pol + Ampl



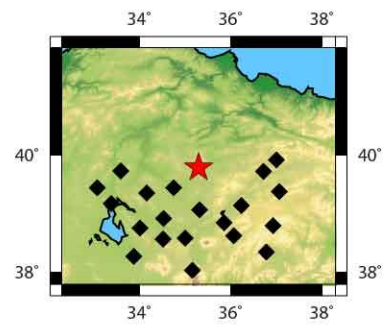
sta SH/P Pqual Squal	sta Pqual Squal
AFSR 4.46 g/E g/E	AFSR g/E g/
AT01 0.83 g/l g/E	AT01 g/l g/E
AT02 2.80 ok/E o/E	AT02 ok/E o/E
AT07 27.36 g/E g/E	AT07 g/E g/E
AT08 9.59 g/E o/E	AT08 g/E o/E
AT12 5.60 e/l e/E	AT12 e/l e/
AT13 23.32 g/E g/E	AT13 g/E g/E
AT15 12.74 g/E g/E	AT15 g/E g/E
AT20 3.97 g/E ok/E	AT20 g/E ok/E
AT21 40.05 g/E g/E	AT21 g/E g/E
AT22 26.16 g/E g/E	AT22 g/E g/E
AT29 20.75 g/E g/E	AT29 g/E g/E
AT30 47.64 g/E ok/E	AT30 g/E ok/E
AT31 23.91 ok/E g/E	AT31 ok/E g/E
AT42 2.61 ok/E g/E	AT42 ok/E g/E
BNN1 2.76 g/E ok/E	BNN1 g/E ok/E
	SVSK g/E



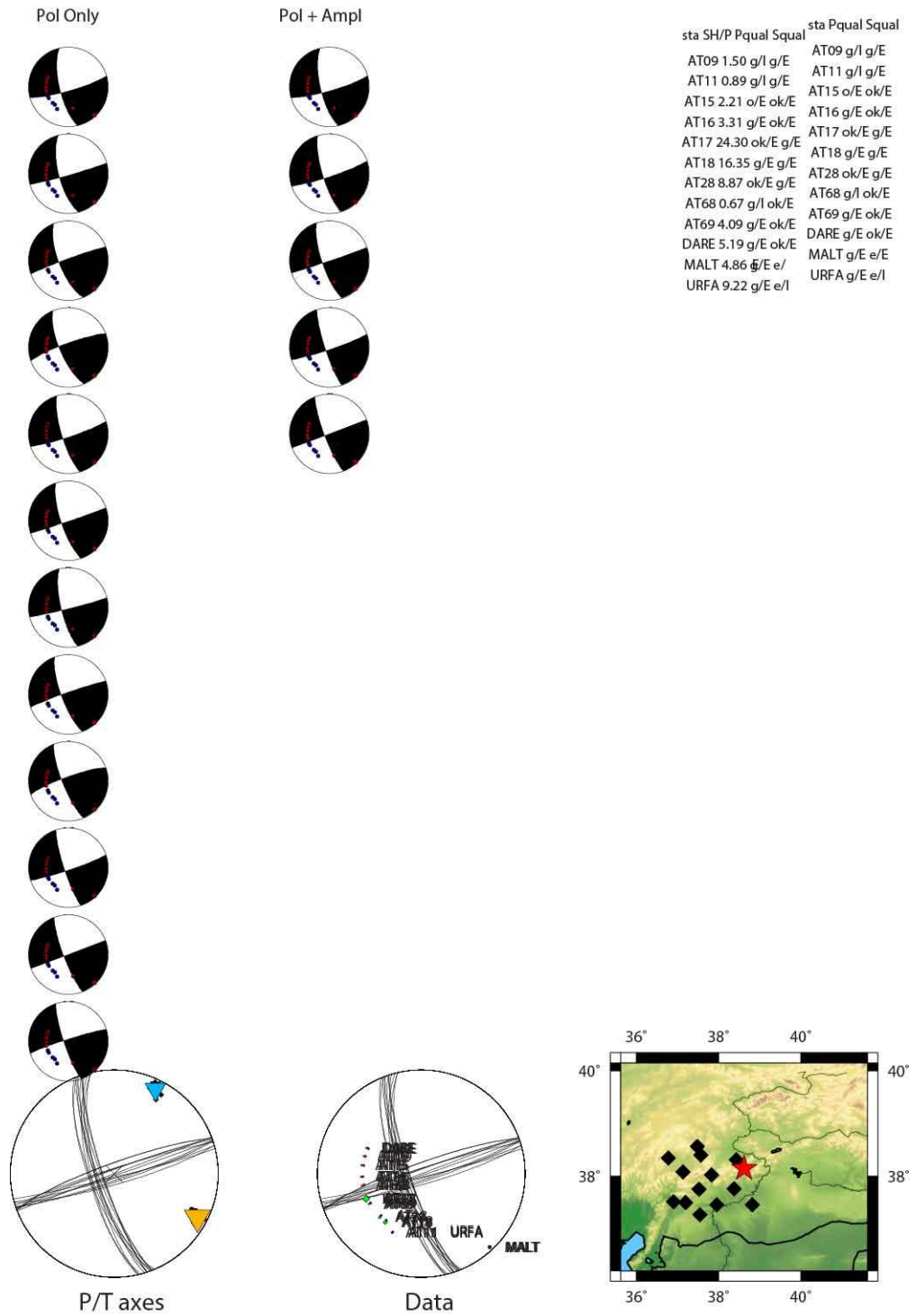
P/T axes



Data



P K: 292.8 95%: 14.6 T K: 732.6 95%: 9.2 Lon: 35.29 Lat: 39.79 Dep: 0.00 Mag: ML, 3.3
 cate00101 Data pts: 36 Solns: 2 Pol errs: 1 Nodal Wt: 0.1 Solns shown: 2 Search Inc: 5
 Ampl errs: 0 Ampl Data: 16 Solns: 2 Pol errs: 1 Nodal Wt: 0.1 Soln shown: 2 Search Inc: 5



P K: 216.0 95%: 3.0 TK: 218.7 95%: 2.9 Lon: 38.62 Lat: 38.15 Dep: 1.00 Mag: ML, 3.0
 cate00102 Data pts: 25 Solns: 12 Pol errs: 1 Nodal Wt: 0.8 Solns shown: 12 Search Inc: 5
 Ampl errs: 0 Ampl Data: 12 Solns: 5 Pol errs: 1 Nodal Wt: 0.8 Soln shown: 5 Search Inc: 5

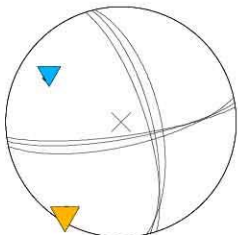
Pol Only



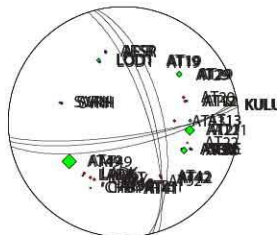
Pol + Ampl



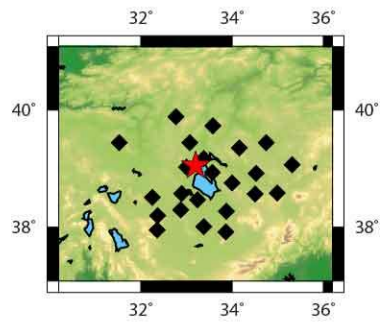
sta	SH/P	Pqual	Squal	sta	Pqual	Squal
AFSR	2.27	E/l	g/	AFSR	e/l	g/E
AT12	1.99	g/E	ok/E	AT12	g/E	ok/E
AT13	8.51	g/E	ok/E	AT13	g/E	ok/E
AT19	4.36	g/l	g/l	AT19	g/l	g/l
AT21	30.67	ok/E	ok/E	AT20	g/l	
AT29	17.91	g/E	g/E	AT21	ok/E	ok/E
AT30	23.39	g/E	g/E	AT29	g/E	g/E
AT41	3.68	g/E	g/E	AT30	g/E	g/E
AT42	2.38	ok/E	g/E	AT31	ok/E	
AT49	46.27	g/l	g/E	AT41	g/E	g/E
AT50	6.84	g/E	g/E	AT42	ok/E	g/E
CHBY	0.84	g/l	g/E	AT49	g/l	g/E
KULU	7.24	e/l	g/E	AT50	g/E	g/E
LADK	2.84	g/E	ok/	AT51	ok/E	
LOD1	12.35	ok/E	g/E	AT52	ok/E	
SERE	3.97	g/E	ok/	CHBY	g/l	g/E
SVRH	0.68	g/l	g/E	KONT	ok/E	
				KULU	e/l	g/
				LADK	g/E	ok/
				LOD1	ok/E	g/
				SERE	g/E	ok/E
				SVRH	g/l	g/E



P/T axes

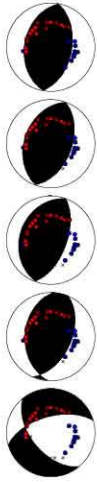


Data



P K: 406.5 95%: 6.1 TK: 171.4 95%: 9.4 Lon: 33.2 Lat: 39.06 Dep: 3.00 Mag: ML, 3.1
 cate00103 Data pts: 40 Solns: 3 Pol errs: 1 Nodal Wt: 0.8 Solns shown: 3 Search Inc: 5
 Ampl errs: 0 Ampl Data: 17 Solns: 3 Pol errs: 1 Nodal Wt: 0.8 Soln shown: 3 Search Inc: 5

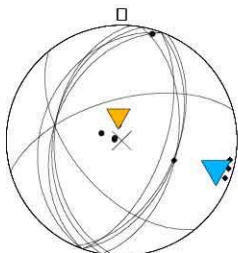
Pol Only



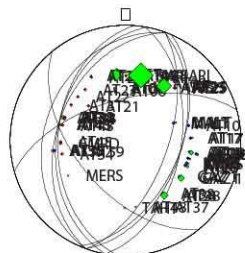
Pol + Ampl



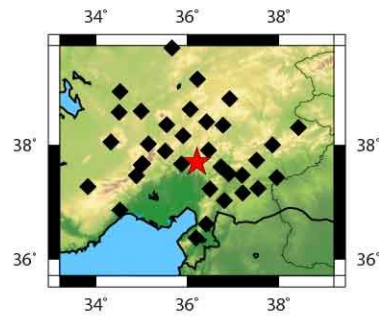
sta	SH/P	Pqual	Squal	sta	Pqual	Squal
AT06	4.97	ok/E	g/E	AT06	ok/E	g/E
AT14	40.99	ok/E	g/E	AT07	ok/E	
AT15	49.47	g/E	g/E	AT08	ok/E	
AT17	2.75	g/E	ok/E	AT10	ok/E	
AT18	17.00	g/E	g/	AT14	ok/E	g/E
AT24	4.25	g/l	g/E	AT15	g/E	g/E
AT25	0.96	g/E	ok/E	AT17	g/E	ok/E
AT26	6.47	ok/E	ok/E	AT18	g/E	g/R
AT27	5.65	g/E	g/E	AT21	g/E	
AT28	8.46	g/E	g/E	AT22	ok/E	
AT33	8.94	g/E	ok/E	AT23	g/E	
AT34	0.90	g/E	g/E	AT24	g/l	g/E
AT35	7.00	g/E	g/E	AT25	g/E	ok/E
AT38	25.27	g/E	g/E	AT26	ok/E	ok/E
AT43	5.98	g/E	g/E	AT27	g/E	g/E
GAZ1	22.78	ok/E	g/E	AT28	g/E	g/E
KMRS	0.76	g/E	ok/E	AT31	ok/E	
MALT	2.61	g/E	g/E	AT33	g/E	ok/E
SARI	82.43	g/E	g/	AT34	g/E	g/E
				AT35	g/E	g/E
				AT38	g/E	g/E
				AT43	g/E	g/E
				AT45	g/E	
				AT54	ok/E	
				CMRD	g/E	
				GAZ1	ok/E	g/
				KMRS	g/E	ok/E
				MALT	g/E	g/E
				SARI	g/E	g/E



P/T axes



Data



P K: 17.0 95%: 19.1 T K: 5.1 95%: 37.7 Lon: 36.21 Lat: 37.71 Dep: 1.00 Mag: ML, 3.6
 cate00104 Data pts: 53 Solns: 39 Pol errs: 2 Nodal Wt: 0.2 Solns shown: 5 Search Inc: 10
 Ampl errs: 0 Ampl Data: 19 Solns: 3 Pol errs: 2 Nodal Wt: 0.2 Soln shown: 3 Search Inc: 5

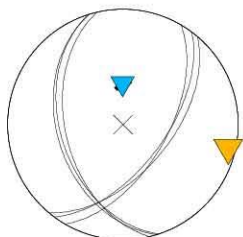
Pol Only



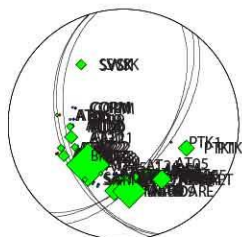
Pol + Ampl



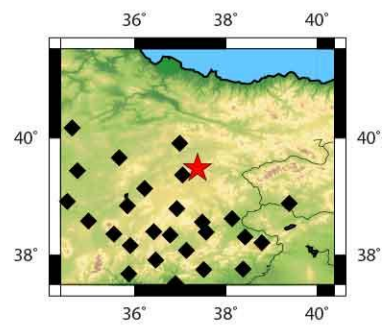
sta SH/P Pqual Squal	sta Pqual Squal
AT02 5.66 ok/E g/E	AT02 ok/E g/E
AT04 38.63 g/E ok/E	AT04 g/E ok/E
AT05 35.31 g/E g/E	AT05 g/E g/E
AT06 11.14 g/E g/E	AT06 g/E g/E
AT07 25.17 g/E o/E	AT07 g/E o/E
AT08 2.32 E/E o/	AT08 e/E o/E
AT09 48.84 o/E g/E	AT09 o/E g/E
AT11 25.46 ok/E g/E	AT11 ok/E g/E
AT12 4.86 g/E ok/E	AT12 g/E ok/E
AT15 6.51 E/E g/	AT15 e/E g/E
AT16 62.11 ok/E g/E	AT16 ok/E g/E
AT17 36.94 g/E g/E	AT17 g/E g/E
AT18 27.99 g/E g/E	AT18 g/E g/E
AT19 6.43 g/E g/E	AT19 g/E g/E
AT20 24.79 o/E ok/E	AT20 o/E ok/E
AT21 44.88 g/E o/E	AT21 g/E o/E
AT22 25.95 ok/E ok/E	AT22 ok/E ok/E
AT23 27.47 o/E ok/E	AT23 o/E ok/E
AT24 143.85 o/E ok/E	AT24 o/E ok/E
AT25 15.40 g/E g/E	AT25 g/E g/E
AT27 18.09 ok/E g/E	AT27 ok/E g/E
BNN1 38.64 g/E g/E	AT35 g/E
CORM 6.04 E/E ok/	AT38 g/E
DARE 111.65 o/E g/E	AT60 ok/E
KMRS 1.38 E/E g/	BNN1 g/E g/E
MALT 62.76 ok/E g/E	CORM o/E ok/E
PTK1 54.83 g/E g/E	DARE o/E g/E
SARI 18.08 g/E ok/	KMRS o/E g/E
SVSK 33.91 E/E g/	MALT ok/E g/E
URFA 7.54 E/E o/	PTK1 g/E g/E
	SARI g/E ok/E
	SVSK o/E g/E
	URFA g/E o/E



P/T axes

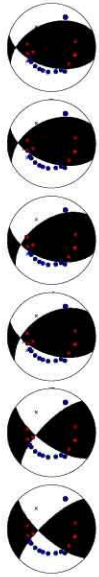


Data

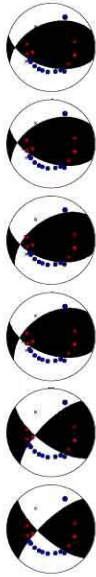


P K: 301.8 95%: 7.1 T K: 474.3 95%: 5.7 Lon: 37.38 Lat: 39.49 Dep: 1.00 Mag: ML, 4.4
 cate00105 Data pts: 64 Solns: 3 Pol errs: 1 Nodal Wt: 0.1 Solns shown: 3 Search Inc: 5
 Ampl errs: 0 Ampl Data: 30 Solns: 1 Pol errs: 1 Nodal Wt: 0.1 Soln shown: 1 Search Inc: 5

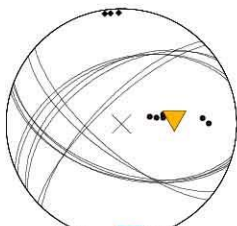
Pol Only



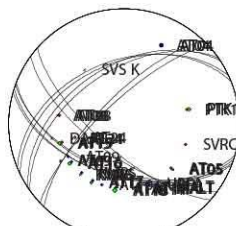
Pol + Ampl



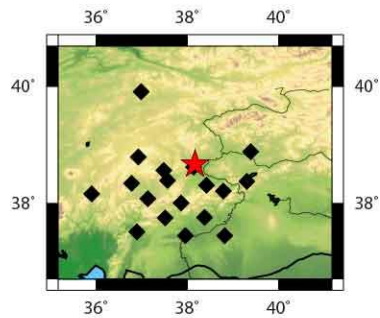
sta SH/P Pqual Squal	sta Pqual Squal
AT04 1.84 g/E g/E	AT04 g/E g/E
AT05 6.62 g/E g/E	AT05 g/E g/E
AT08 3.67 g/E ok/E	AT08 g/E ok/E
AT09 7.48 g/l g/E	AT09 g/l g/E
AT11 3.50 g/E g/E	AT10 g/E
AT15 13.05 g/E g/E	AT11 g/E g/E
AT16 13.68 g/E g/E	AT15 g/E g/E
AT17 8.11 g/E ok/E	AT16 g/E g/E
AT18 17.18 ok/E g/E	AT17 g/E ok/E
AT24 6.15 g/E g/E	AT18 ok/E g/E
KMRS 1.54 ok/E g/	AT24 g/E g/E
MALT 6.12 g/E e/	KMRS ok/E g/E
PTK1 11.72 g/E g/E	MALT g/E e/E
	PTK1 g/E g/E
	SVRC g/E
	URFA 0/0 ok/E



P/T axes

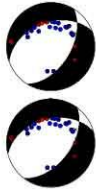


Data

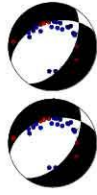


P K: 304.3 95%: 3.8 T K: 17.9 95%: 16. 3 Lon: 38.17 Lat: 38.68 Dep: 3.00 Mag: ML, 3.0
 cate00106 Data pts: 32 Solns: 6 Pol errs: 1 Nodal Wt: 0.5 Solns shown: 6 Search Inc: 5
 Ampl errs: 0 Ampl Data: 13 Solns: 6 Pol errs: 1 Nodal Wt: 0.5 Soln shown: 6 Search Inc: 5

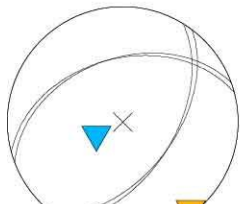
Pol Only



Pol + Ampl



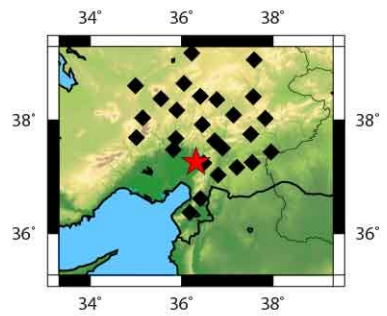
sta	SH/P	Pqual	Squal	sta	Pqual	Squal
AT09	2.01	g/E	g/E	AT02	ok/E	
AT14	8.90	ok/E	ok/E	AT03	ok/E	
AT15	15.51	g/E	ok/E	AT07	g/E	
AT16	14.52	g/E	g/E	AT09	g/E	g/E
AT17	29.94	g/E	g/E	AT14	ok/E	ok/E
AT23	1.13	ok/E	ok/E	AT15	g/E	ok/E
AT26	12.58	g/E	g/E	AT16	g/E	g/E
AT28	3.05	g/E	g/E	AT17	g/E	g/E
AT33	115.56	ok/E	g/E	AT22	g/E	
AT37	4.28	g/E	g/E	AT23	ok/E	ok/E
AT38	32.01	g/E	g/E	AT24	ok/E	
AT45	19.52	ok/E	ok/E	AT25	g/E	
AT48	7.43	g/E	g/E	AT26	e/E	g/E
AT68	18.33	ok/E	g/E	AT28	g/E	g/E
KMRS	10.69	g/E	g/E	AT33	ok/E	g/E
SARI	7.82	g/E	g/E	AT35	g/E	
TAHT	15.14	g/E	ok/E	AT37	g/E	g/E
				AT38	g/E	g/E
				AT45	ok/E	ok/E
				AT48	g/E	g/E
				AT68	ok/E	g/E
				KMRS	g/E	g/E
				KOZT	e/E	
				SARI	g/E	g/E
				TAHT	g/E	ok/E



P/T axes



Data



P K: 3795.8 95%: 4.1 T K: 470.7 95%: 11. 5 Lon: 36.32 Lat: 37.26 Dep: 3.00 Mag: ML, 3.2
 cate00107 Data pts: 44 Solns: 2 Pol errs: 1 Nodal Wt: 0.5 Solns shown: 2 Search Inc: 5
 Ampl errs: 0 Ampl Data: 17 Solns: 2 Pol errs: 1 Nodal Wt: 0.5 Soln shown: 2 Search Inc: 5

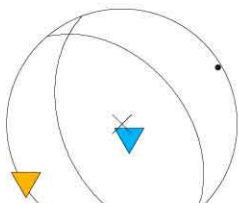
Pol Only



Pol + Ampl



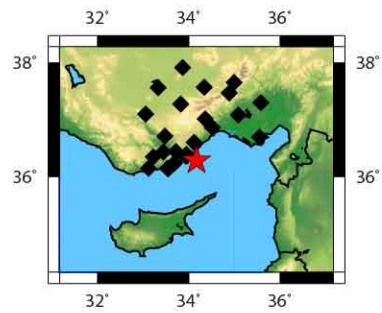
sta	SH/P	Pqual	Squal	sta	Pqual	Squal
AKK1	2.38	ok/E	g/	AKK1	ok/E	g/
AT46	2.87	g/E	ok/E	AKK2	ok/E	
AT53	4.88	g/E	g/E	AT46	g/E	ok/E
AT55	18.40	ok/E	ok/E	AT52	ok/E	
AT58	9.31	g/E	ok/E	AT53	g/E	g/E
AT62	1.94	g/E	g/E	AT55	ok/E	ok/E
AT63	4.16	g/E	g/E	AT56	g/E	
CMRD	4.75	ok/E	g/	AT58	g/E	ok/E
IKL1	2.65	g/E	g/	AT59	g/E	
KEBE	9.88	g/E	ok/E	AT60	g/E	
MERS	1.87	g/E	g/E	AT62	g/E	g/E
SILI	129.65	ok/E	e/	AT63	g/E	g/E
SLFK	6.22	ok/E	g/	AT64	g/E	
TEKE	3.68	g/E	g/E	BERE	g/E	
				CMRD	ok/E	g/E
				IKL1	g/E	g/E
				KEBE	g/E	ok/E
				MERS	g/E	g/E
				SILI	ok/E	e/
				SLFK	ok/E	g/E
				TEKE	g/E	g/E
				TEVE	ok/E	



P/T axes

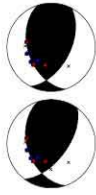


Data

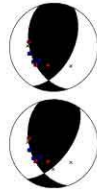


P K: NaN 95%: NaN T K: NaN 95%: NaN Lon: 34.17 Lat: 36.28 Dep: 2.00 Mag: ML, 3.2
 cate00108 Data pts: 37 Solns: 1 Pol errs: 1 Nodal Wt: 0.1 Solns shown: 1 Search Inc: 5
 Ampl errs: 0 Ampl Data: 14 Solns: 1 Pol errs: 1 Nodal Wt: 0.1 Soln shown: 1 Search Inc: 5

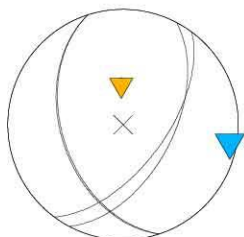
Pol Only



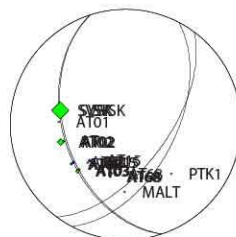
Pol + Ampl



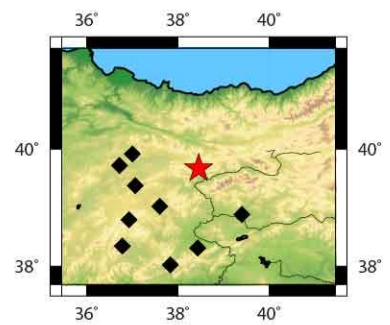
sta SH/P Pqual Squal	sta Pqual Squal
AT02 21.42 E/E g/	AT02 g/E g/
AT03 13.93 E/E g/	AT03 o/E g/
AT08 5.48 o/E g/	AT08 ok/E g/
AT15 1.79 o/E ok/	AT15 o/Eok/
AT68 4.96 o/E ok/	AT68 ok/Eok/
SVSK 58.09 o/E ok/	SVSK ok/Eok/



P/T axes

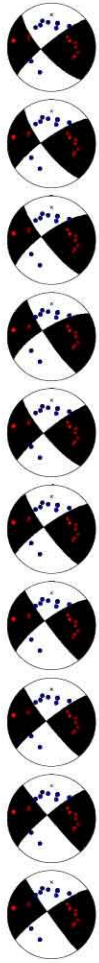


Data



P K: 239.8 95%: 16.2 T K: 359.4 95%: 13. 2 Lon: 38.45 Lat: 39.68 Dep: 4.00 Mag: ML, 3.0
 cate00109 Data pts: 15 Solns: 2 Pol errs: 1 Nodal Wt: 0.5 Solns shown: 2 Search Inc: 5
 Ampl errs: 0 Ampl Data: 6 Solns: 2 Pol errs: 1 Nodal Wt: 0.5 Solns shown: 2 Search Inc: 5

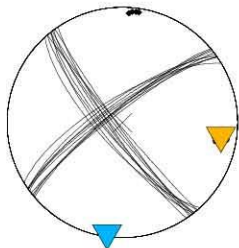
Pol Only



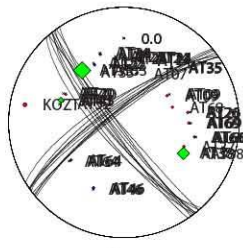
Pol + Ampl



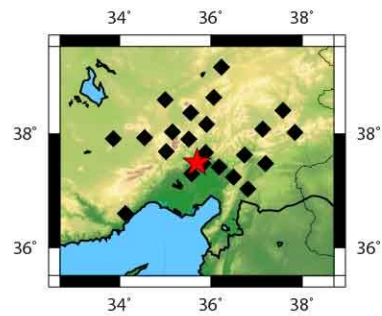
sta	SH/P	Pqual	Squal	sta	Pqual	Squal
AT09	3.03	g/E	E	AT07	g/E	
AT14	1.90	ok/E	g/E	AT09	g/E	g/E
AT22	1.12	ok/E	g/E	AT14	ok/E	g/E
AT23	0.32	e/l	ok/		0.0	
AT24	0.87	E/l	g/	AT22	ok/E	g/E
AT26	4.27	g/E	g/E	AT23	e/l	ok/E
AT33	58.14	g/E	g/E	AT24	e/l	g/
AT34	2.19	g/l	ok/E	AT26	g/E	g/E
AT35	7.21	g/E	g/E	AT33	g/E	g/E
AT38	40.95	ok/E	g/E	AT34	l	ok/E
AT45	18.79	g/E	g/E	AT35	g/E	g/E
AT46	3.18	g/E	g/E	AT37	ok/E	
AT64	2.77	ok/E	ok/E	AT38	ok/E	g/E
AT66	1.68	g/E	g/E	AT45	g/E	g/E
AT69	5.39	ok/E	g/E	AT46	g/E	g/E
AT70	1.14	ok/E	g/E	AT64	ok/E	ok/E
				AT66	g/E	g/E
				AT68	g/E	
				AT69	ok/E	g/E
				AT70	ok/E	g/E
				KOZT	g/E	



P/T axes



Data



P K: 264.6 95%: 3.0 T K: 268.7 95%: 3.0 Lon: 35.69 Lat: 37.5 Dep: 3.00 Mag: ML, 3.1
 cate00110 Data pts: 39 Solns: 10 Pol errs: 1 Nodal Wt: 0.5 Solns shown: 10 Search Inc: 5
 Ampl errs: 0 Ampl Data: 16 Solns: 10 Pol errs: 1 Nodal Wt: 0.5 Soln shown: 10 Search Inc: 5

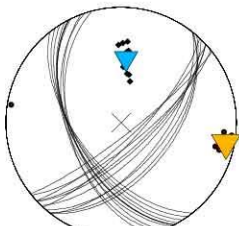
Pol Only



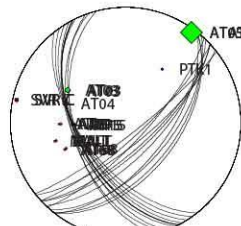
Pol + Ampl



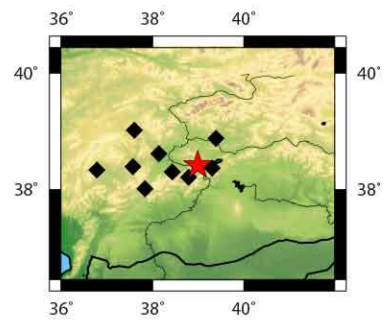
sta SH/P Pqual Squal	sta Pqual Squal
AT03 19.29 ok/E ok/E	AT03 ok/E ok/E
AT05 58.15 g/E o/E	AT04 g/l
AT09 1.87 g/E o/E	AT05 g/E o/E
AT15 1.32 o/E ok/E	AT09 g/E o/E
AT68 4.81 g/E g/E	AT15 o/E ok/E
MALT 1.22 E/l g/	AT68 g/E g/E
SVRC 0.76 E/l o/	MALT e/l g/E
	PTK1 g/E
	SVRC e/l o/E



P/T axes



Data



PK: 57.0 95%: 6.1 TK: 159.3 95%: 3. 6 Lon: 38.99 Lat: 38.43 Dep: 0.00 Mag: ML, 3.2
 cate00112 Data pts: 16 Solns: 11 Pol errs: 0 Nodal Wt: 0.9 Solns shown: 11 Search Inc: 5
 Ampl errs: 0 Ampl Data: 7 Solns: 11 Pol errs: 0 Nodal Wt: 0.9 Soln shown: 11 Search Inc: 5

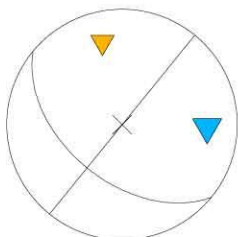
Pol Only



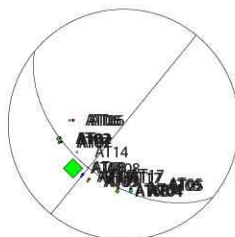
Pol + Ampl



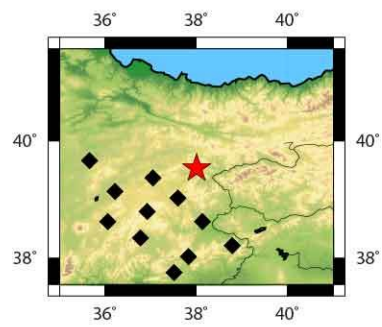
sta	SH/P	Pqual	Squal	sta	Pqual	Squal
AT02	14.09	g/E	g/E	AT02	g/E	g/E
AT03	4.29	g/E	g/E	AT03	g/E	g/E
AT04	13.29	ok/E	g/E	AT04	ok/E	g/E
AT05	3.63	g/E	ok/E	AT05	g/E	ok/E
AT06	2.32	g/E	g/E	AT06	g/E	g/E
AT07	10.30	ok/E	g/E	AT07	ok/E	g/E
AT08	62.01	g/E	g/E	AT08	g/E	g/E
AT15	2.68	g/E	g/E	AT15	g/E	g/E
AT17	2.97	ok/E	g/E	AT17	ok/E	g/E
AT68	12.77	g/E	g/E	AT68	g/E	g/E



P/T axes

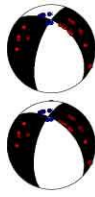


Data



P K: NaN 95%: NaN T K: NaN 95%: NaN Lon: 38.01 Lat: 39.54 Dep: 0.00 Mag: ML, 3.4
 cate00113 Data pts: 21 Solns: 1 Pol errs: 0 Nodal Wt: 0.9 Solns shown: 1 Search Inc: 5
 Ampl errs: 0 Ampl Data: 10 Solns: 1 Pol errs: 0 Nodal Wt: 0.9 Soln shown: 1 Search Inc: 5

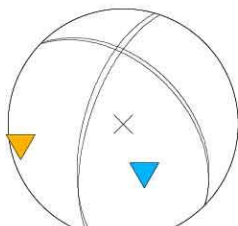
Pol Only



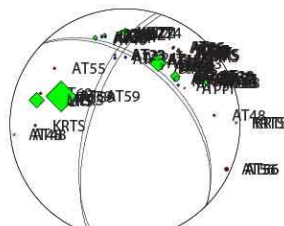
Pol + Ampl



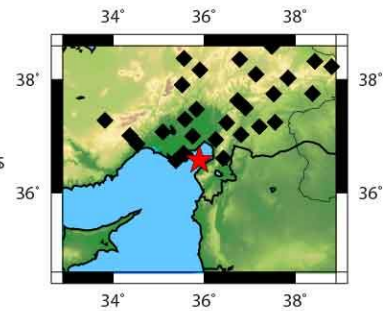
sta SH/P Pqual Squal	sta Pqual Squal
AT03 53.02 ok/E ok/E	AT03 ok/E ok/E
AT15 6.57 ok/E ok/E	AT05 ok/E
AT16 11.05 g/E g/E	AT15 ok/E ok/E
AT23 5.13 g/E ok/E	AT16 g/E g/E
AT24 27.00 ok/E ok/E	AT23 g/E ok/E
AT26 2.53 g/E ok/E	AT24 ok/E ok/E
AT28 17.81 ok/E ok/E	AT26 g/E ok/E
AT34 9.01 g/E g/E	AT28 ok/E ok/E
AT37 8.95 g/E g/E	AT34 g/E g/E
AT38 10.35 g/E ok/E	AT37 g/E g/E
AT46 16.12 g/E g/E	AT38 g/E ok/E
AT48 0.82 g/l g/E	AT46 g/E g/E
AT56 1.18 e/l e/E	AT48 g/l g/E
AT59 101.93 ok/E g/E	AT55 ok/E
AT67 3.23 g/E g/E	AT56 e/E e/E
AT68 31.83 g/E g/E	AT59 ok/E g/E
CEYT 3.40 g/l g/E	AT60 g/E
DARE 13.79 g/E g/E	AT67 g/E g/E
GAZ1 5.82 g/E g/E	AT68 g/E g/E
KMRS 5.47 g/E g/E	CEYT g/l g/E
KOZT 8.62 ok/E ok/E	DARE g/E g/E
KRTS 1.80 g/l g/E	GAZ1 g/E g/E
MALT 18.74 ok/E g/E	KMRS g/E g/E
MERS 51.07 g/E g/E	KOZT ok/E ok/E
	KRTS g/l g/E
	MALT ok/E g/E
	MERS g/E g/E



P/T axes



Data



P K: 3832.2 95%: 4.0 T K: 504.6 95%: 11. 1 Lon: 35.89 Lat: 36.58 Dep: 7.00 Mag: ML, 3.9
 cate00114 Data pts: 53 Solns: 2 Pol errs: 2 Nodal Wt: 0.1 Solns shown: 2 Search Inc: 5
 Ampl errs: 0 Ampl Data: 24 Solns: 1 Pol errs: 2 Nodal Wt: 0.1 Soln shown: 1 Search Inc: 5

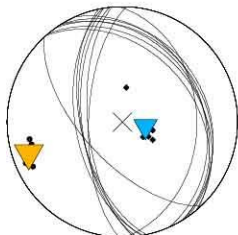
Pol Only



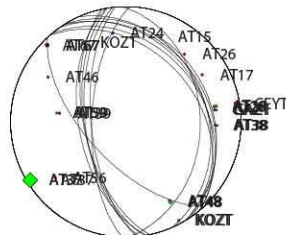
Pol + Ampl



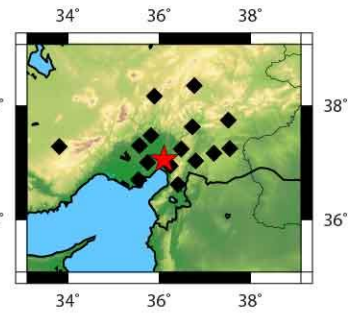
sta	SH/P	Pqual	Squal	sta	Pqual	Squal
AT28	8.43	ok/E	g/E	AT17	ok/E	
AT37	41.77	ok/E	g/E	AT24	g/E	
AT38	3.33	g/l	g/E	AT26	ok/E	
AT48	13.01	g/E	g/E	AT28	ok/E	g/E
AT59	5.59	g/E	ok/E	AT37	ok/E	g/E
AT67	1.36	E/l	g/	AT38	g/l	g/E
GAZ1	3.90	g/E	ok/E	AT46	g/E	
KOZT	5.12	g/E	ok/	AT48	g/E	g/E
				AT56	ok/E	
				AT59	g/E	ok/E
				AT67	eB	g/
				CEYT	ok/E	
				GAZ1	g/E	ok/
				KOZT	g/E	ok/



P/T axes



Data



P K: 33.4 95%: 10.6 T K: 168.4 95%: 4.7 Lon: 36.11 Lat: 37.06 Dep: 6.00 Mag: ML, 3.2
 cate00115 Data pts: 23 Solns: 7 Pol errs: 1 Nodal Wt: 0.5 Solns shown: 7 Search Inc: 5
 Ampl errs: 0 Ampl Data: 8 Solns: 1 Pol errs: 1 Nodal Wt: 0.5 Soln shown: 1 Search Inc: 5

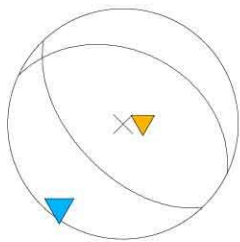
Pol Only



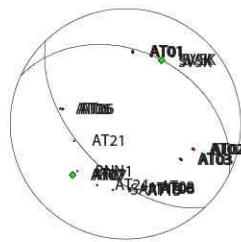
Pol + Ampl



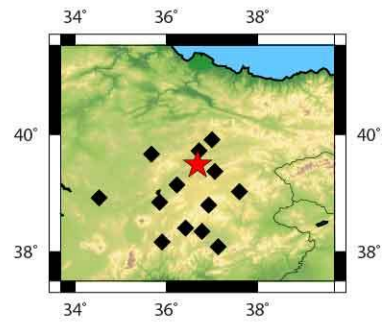
sta SH/P Pqual Squal	sta Pqual Squal
AT01 5.44 E/I g/	AT01 eE g/
AT02 0.55 g/E o/E	AT02 g/E o/E
AT03 3.43 g/E o/E	AT03 g/E o/E
AT06 1.71 g/I g/E	AT06 g/I g/E
AT07 20.65 ok/E g/E	AT07 ok/E g/E
AT08 8.41 g/E o/E	AT08 g/E o/E
AT15 9.38 ok/E ok/E	AT15 ok/E ok/E
SVSK 21.42 g/E g/	SVSK g/E g/E



P/T axes



Data



P K: NaN 95%: NaN T K: NaN 95%: NaN Lon: 36.68 Lat: 39.49 Dep: 3.00 Mag: ML, 3.0
 cate00116 Data pts: 21 Solns: 1 Pol errs: 1 Nodal Wt: 0.4 Solns shown: 1 Search Inc: 5
 Ampl errs: 0 Ampl Data: 8 Solns: 1 Pol errs: 1 Nodal Wt: 0.4 Soln shown: 1 Search Inc: 5

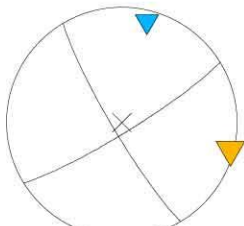
Pol Only



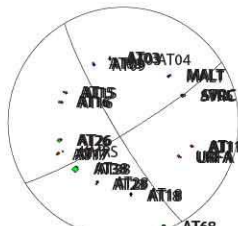
Pol + Ampl



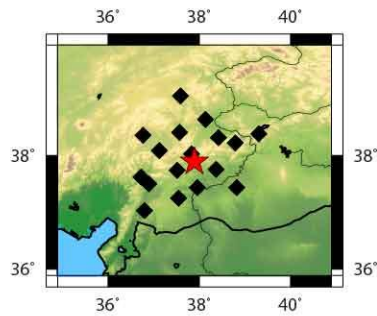
sta	SH/P	Pqual	Squal	sta	Pqual	Squal
AT03	6.01	o/E	g/E	AT03	o/E	g/E
AT09	3.11	g/E	g/E	AT04	g/l	
AT11	1.12	g/l	g/E	AT05	ok/E	
AT15	3.40	g/E	g/E	AT09	g/E	g/E
AT16	5.09	g/E	ok/E	AT11	g/l	g/E
AT17	2.31	g/E	g/E	AT15	g/E	g/E
AT18	2.54	e/l	g/	AT16	g/E	ok/E
AT26	12.78	g/E	g/E	AT17	g/E	g/E
AT28	3.61	g/E	ok/E	AT18	e/l	g/
AT38	23.49	ok/E	g/E	AT26	g/E	g/E
AT68	9.65	e/E	e/	AT28	g/E	ok/E
MALT	3.78	e/E	g/	AT38	ok/E	g/E
SVRC	8.55	ok/E	ok/E	AT68	e/E	e/l
URFA	1.69	e/l	ok/E	MALT	e/E	g/E
				SVRC	ok/E	ok/E
				URFA	e/l	ok/E



P/T axes



Data



P K: NaN 95%: NaN T K: NaN 95%: NaN Lon: 37.9 Lat: 37.89 Dep: 1.00 Mag: ML, 3.1
 cate00117 Data pts: 31 Solns: 1 Pol errs: 0 Nodal Wt: 0.9 Solns shown: 1 Search Inc: 5
 Ampl errs: 0 Ampl Data: 14 Solns: 1 Pol errs: 0 Nodal Wt: 0.9 Soln shown: 1 Search Inc: 5

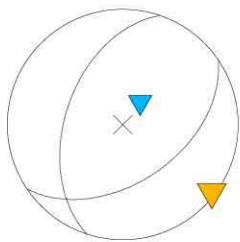
Pol Only



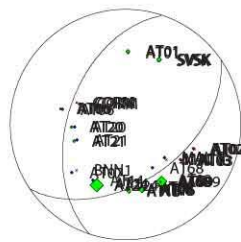
Pol + Ampl



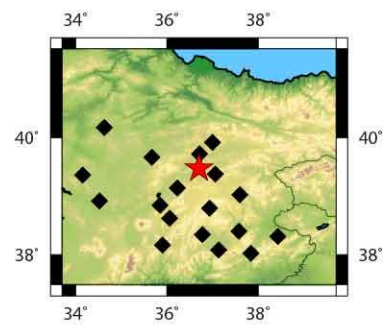
sta SH/P Pqual Squal	sta Pqual Squal
AT01 11.70 g/E e/	AT01 g/E e/E
AT02 1.15 g/l g/E	AT02 g/l g/E
AT03 3.43 g/l o/E	AT03 g/l o/E
AT06 5.38 g/l g/E	AT06 g/l g/E
AT08 7.11 g/E g/E	AT07 g/E
AT09 34.59 g/E g/E	AT08 g/E g/E
AT15 12.71 g/E g/E	AT09 g/E g/E
AT16 18.95 g/E g/E	AT14 ok/E
AT20 10.84 ok/E g/E	AT15 g/E g/E
AT21 10.33 g/E g/E	AT16 g/E g/E
AT24 44.81 ok/E g/E	AT20 ok/E g/E
AT68 5.72 ok/E g/E	AT21 g/E g/E
CORM 4.22 ok/E g/	AT24 ok/E g/E
MALT 1.26 g/E ok/E	AT68 ok/E g/E
SVSK 16.30 g/E g/	CORM ok/E g/E
	MALT g/E ok/E
	SVSK g/E g/E



P/T axes



Data



P K: 0.0 95%: NaN T K: NaN 95%: NaN Lon: 36.7 Lat: 39.48 Dep: 2.00 Mag: ML, 3.3
 cate00118 Data pts: 33 Solns: 1 Pol errs: 1 Nodal Wt: 0.1 Solns shown: 1 Search Inc: 5
 Ampl errs: 0 Ampl Data: 15 Solns: 1 Pol errs: 1 Nodal Wt: 0.1 Soln shown: 1 Search Inc: 5

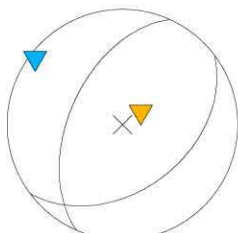
Pol Only



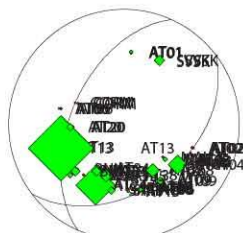
Pol + Ampl



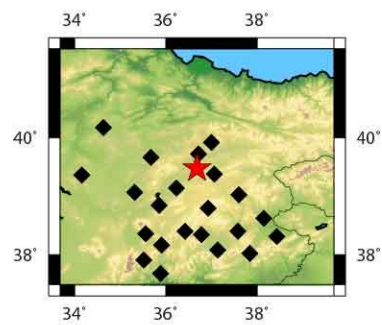
sta	SH/P	Pqual	Squal	sta	Pqual	Squal
AT01	12.25	g/l	g/E	AT01	g/l	g/E
AT02	1.52	g/E	g/E	AT02	g/E	g/E
AT03	4.05	g/E	g/E	AT03	g/E	g/E
AT04	62.15	ok/E	g/E	AT04	ok/E	g/E
AT06	5.14	g/E	ok/E	AT06	g/E	ok/E
AT07	19.43	g/E	g/E	AT07	g/E	g/E
AT08	9.35	g/E	g/E	AT08	g/E	g/E
AT09	26.26	g/E	ok/E	AT09	g/E	ok/E
AT13	215.47	ok/E	ok/E	AT13	ok/E	ok/E
AT15	10.76	g/E	g/E	AT15	g/E	g/E
AT16	17.42	g/E	g/E	AT16	g/E	g/E
AT20	24.17	g/E	g/E	AT20	g/E	g/E
AT24	131.32	ok/E	ok/E	AT23	ok/E	
AT34	30.42	ok/E	g/E	AT24	ok/E	ok/E
AT35	40.57	ok/E	g/E	AT34	ok/E	g/E
AT68	43.54	g/E	g/E	AT35	ok/E	g/E
BNN1	30.70	g/E	g/E	AT38	g/E	
CORM	1.72	g/E	g/E	AT68	g/E	g/E
MALT	17.34	ok/E	g/E	BNN1	g/E	g/E
SARI	24.90	g/E	g/E	CORM	g/E	g/E
SVSK	36.27	g/E	g/E	MALT	ok/E	g/E
				SARI	g/E	g/E
				SVSK	g/E	g/E



P/T axes



Data



P K: NaN 95%: NaN T K: NaN 95%: NaN Lon: 36.68 Lat: 39.48 Dep: 2.00 Mag: ML, 3.9
 cate00119 Data pts: 44 Solns: 1 Pol errs: 2 Nodal Wt: 0.2 Solns shown: 1 Search Inc: 5
 Ampl errs: 0 Ampl Data: 21 Solns: 2 Pol errs: 2 Nodal Wt: 0.1 Soln shown: 2 Search Inc: 5

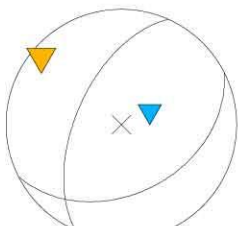
Pol Only



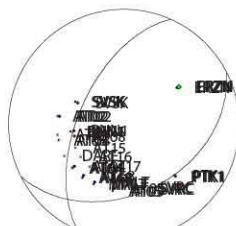
Pol + Ampl



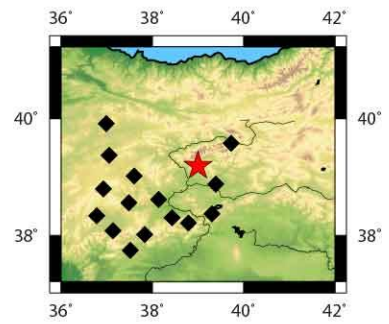
sta	SH/P	Pqual	Squal	sta	Pqual	Squal
AT02	1.34	g/E	g/E	AT02	g/E	g/E
AT04	5.79	g/E	g/E	AT04	g/E	g/E
AT05	2.90	g/E	g/E	AT05	g/E	g/E
AT08	1.81	g/E	g/E	AT08	g/E	g/E
AT68	6.02	ok/E	g/E	AT68	ok/E	g/E
BNN1	5.76	ok/E	ok/E	BNN1	ok/E	ok/E
ERZN	14.78	ok/E	g/E	ERZN	ok/E	g/E
MALT	1.67	g/E	g/E	MALT	g/E	g/E
PTK1	3.14	g/E	g/E	PTK1	g/E	g/E
SVRC	0.62	g/E	g/E	SVRC	g/E	g/E
SVSK	5.64	ok/E	g/E	SVSK	ok/E	g/E



P/T axes



Data



P K: NaN 95%: NaN T K: NaN 95%: NaN Lon: 39 Lat: 39.2 Dep: 3.00 Mag: ML, 3.2
 cate00120 Data pts: 27 Solns: 1 Pol errs: 1 Nodal Wt: 0.3 Solns shown: 1 Search Inc: 5
 Ampl errs: 0 Ampl Data: 11 Solns: 1 Pol errs: 1 Nodal Wt: 0.3 Solns shown: 1 Search Inc: 5

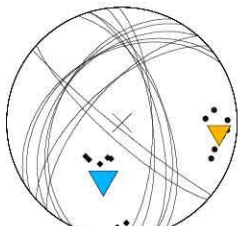
Pol Only



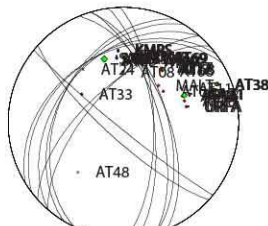
Pol + Ampl



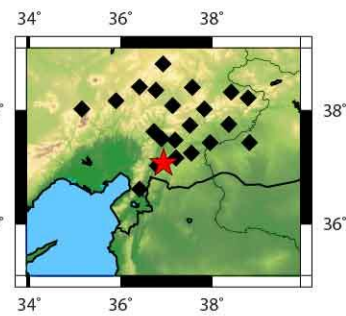
sta SH/P Pqual Squal	sta Pqual Squal
AT09 13.47 ok/E ok/E	AT05 ok/E
AT15 1.77 g/E g/E	AT08 ok/E
AT16 0.55 g/E g/E	AT09 ok/E ok/E
AT17 3.13 ok/E ok/E	AT15 g/E g/E
AT18 20.16 g/E ok/E	AT16 g/E g/E
AT26 23.80 g/E g/E	AT17 ok/E ok/E
AT38 8.80 E/l g/	AT18 g/E ok/E
AT68 8.83 ok/E ok/E	AT26 g/E g/E
AT69 4.31 g/E ok/E	AT28 g/l
GAZ1 4.50 g/E g/E	AT33 ok/E
KMRS 6.58 g/E ok/	AT38 eB g/
SARI 1.18 g/E g/	AT68 ok/E ok/E
URFA 4.07 g/E ok/	AT69 g/E ok/E
	GAZ1 g/E g/E
	KMRS g/E ok/E
	MALT ok/E
	SARI g/E g/E
	URFA g/E ok/E



P/T axes



Data



P K: 9.5 95%: 20.7 T K: 44.6 95%: 9.1 Lon: 36.94 Lat: 37.08 Dep: 3.00 Mag: ML 3.0
 cate00121 Data pts: 34 Solns: 7 Pol errs: 1 Nodal Wt: 0.5 Solns shown: 7 Search Inc: 5
 Ampl errs: 0 Ampl Data: 13 Solns: 3 Pol errs: 1 Nodal Wt: 0.5 Soln shown: 3 Search Inc: 5

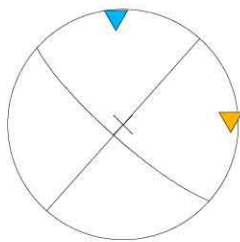
Pol Only



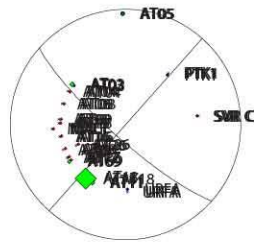
Pol + Ampl



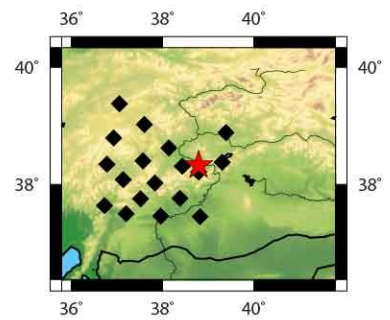
sta SH/P Pqual Squal	sta Pqual Squal
AT03 15.32 g/E g/E	AT03 g/E g/E
AT04 1.50 g/l ok/E	AT04 g/l ok/E
AT05 6.91 g/E g/E	AT05 g/E g/E
AT08 1.46 ok/E g/E	AT08 ok/E g/E
AT09 1.54 g/l g/E	AT09 g/l g/E
AT11 15.17 g/E g/E	AT11 g/E g/E
AT15 4.35 ok/E ok/E	AT15 ok/E ok/E
AT16 4.50 ok/E ok/E	AT16 ok/E ok/E
AT17 4.84 g/E g/E	AT17 g/E g/E
AT18 69.27 g/E g/E	AT18 g/E g/E
AT26 3.13 ok/E g/E	AT26 ok/E g/E
AT68 1.39 g/E g/E	AT68 g/E g/E
AT69 11.57 ok/E g/E	AT69 ok/E g/E
MALT 2.34 E/l g/	MALT e/l g/E
PTK1 3.22 g/l g/E	PTK1 g/l g/E
SVRC 0.48 g/l g/	SVRC g/l g/E
URFA 1.23 g/E g/	URFA g/E g/E



P/T axes



Data



P K: NaN 95%: NaN T K: 0.0 95%: NaN Lon: 38.79 Lat: 38.33 Dep: 1.00 Mag: ML, 3.1
 cate00122 Data pts: 35 Solns: 1 Pol errs: 0 Nodal Wt: 0.9 Solns shown: 1 Search Inc: 5
 Ampl errs: 1 Ampl Data: 17 Solns: 1 Pol errs: 0 Nodal Wt: 0.8 Solns shown: 1 Search Inc: 5

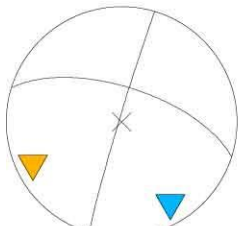
Pol Only



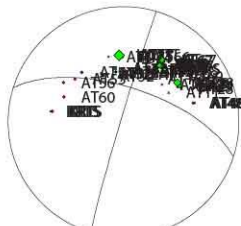
Pol + Ampl



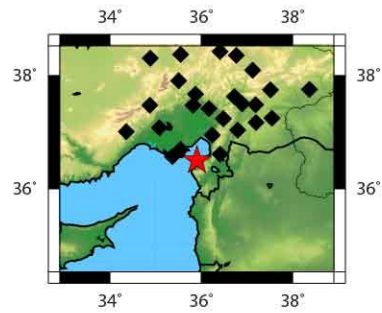
sta SH/P Pqual Squal	sta Pqual Squal
AT15 6.91 ok/E g/E	AT14 ok/E
AT23 8.65 ok/E ok/E	AT15 ok/E g/E
AT26 4.88 g/E g/E	AT16 g/E
AT32 4.93 ok/E g/E	AT22 ok/E
AT35 9.17 ok/E ok/E	AT23 ok/E ok/E
AT37 20.55 g/E ok/E	AT26 g/E g/E
AT38 25.89 g/E ok/E	AT32 ok/E g/E
AT48 0.51 g/l g/E	AT35 ok/E ok/E
AT67 21.73 ok/E g/E	AT37 g/E ok/E
GAZ1 14.20 g/E g/E	AT38 g/E ok/E
KMRS 11.75 g/E g/	AT48 g/l g/E
KOZT 33.88 g/E ok/	AT54 ok/E
KRTS 4.23 g/l g/	AT55 g/l
SARI 9.57 g/E g/	AT56 e/l
	AT60 g/E
	AT67 ok/E g/E
	GAZ1 g/E g/E
	KMRS g/E g/E
	KOZT g/E ok/
	KRTS g/l g/E
	SARI g/E g/E



P/T axes



Data



P K: NaN 95%: NaN T K: NaN 95%: NaN Lon: 35.91 Lat: 36.51 Dep: 2.00 Mag: ML, 3.5
 cate00123 Data pts: 41 Solns: 1 Pol errs: 1 Nodal Wt: 0.3 Solns shown: 1 Search Inc: 5
 Ampl errs: 0 Ampl Data: 14 Solns: 1 Pol errs: 1 Nodal Wt: 0.3 Soln shown: 1 Search Inc: 5

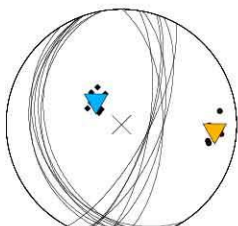
Pol Only



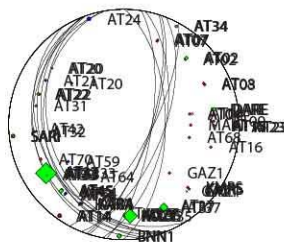
Pol + Ampl



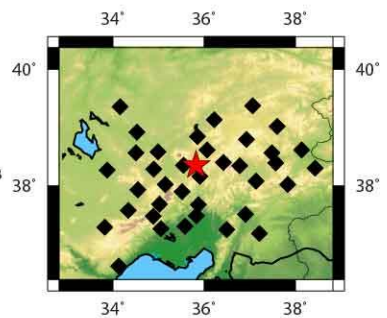
sta SH/P	Pqual	Squal	sta	Pqual	Squal
AT02	12.13	g/E g/E	AT02	g/E	g/E
AT04	1.30	g/E ok/E	AT03	g/E	
AT07	3.48	g/E g/E	AT04	g/E	ok/E
AT14	4.65	g/E g/E	AT07	g/E	g/E
AT15	4.59	g/E g/E	AT08	g/E	
AT20	3.89	g/E ok/E	AT09	g/E	
AT22	9.09	g/E g/E	AT14	g/E	g/E
AT23	2.96	g/E g/E	AT15	g/E	g/E
AT33	70.74	g/E g/E	AT16	g/E	
AT34	7.74	g/E ok/E	AT20	g/E	ok/E
AT35	46.38	g/E g/E	AT21	ok/E	
AT37	29.13	ok/E ok/E	AT22	g/E	g/E
AT45	14.91	g/E g/E	AT23	g/E	g/E
AT53	1.59	g/E g/E	AT24	g/E	
AT54	4.15	g/E g/E	AT31	g/E	
BNN1	12.06	g/E g/E	AT32	g/E	
DARE	12.60	ok/E g/E	AT33	g/E	g/E
GAZ1	1.08	g/E ok/E	AT34	g/E	ok/E
KARA	2.74	ok/E ok/E	AT35	g/E	g/E
KMRS	6.27	ok/E g/E	AT37	ok/E	ok/E
KOZT	5.59	g/E ok/E	AT45	g/E	g/E
SARI	7.32	g/E ok/E	AT46	g/E	
			AT53	g/E	g/E
			AT54	g/E	g/E
			AT59	ok/E	
			AT64	ok/E	
			AT68	g/E	
			AT70	g/E	
			BNN1	g/E	g/E
			DARE	ok/E	g/E
			GAZ1	g/E	ok/E
			KARA	ok/E	ok/E
			KMRS	ok/E	g/E
			KOZT	g/E	ok/E
			MALT	ok/E	
			SARI	g/E	ok/E



P/T axes



Data



P K: 96.3 95%: 6.2 TK: 99.7 95%: 6.1 Lon: 35.82 Lat: 38.36 Dep: 5.00 Mag: ML, 3.3
 cate00124 Data pts: 59 Solns: 58 Pol errs: 2 Nodal Wt: 0.1 Solns shown: 7 Search Inc: 10
 Ampl errs: 0 Ampl Data: 22 Solns: 58 Pol errs: 2 Nodal Wt: 0.1 Soln shown: 7 Search Inc: 10

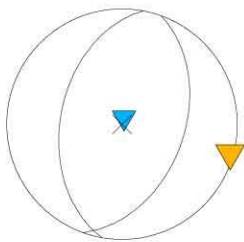
Pol Only



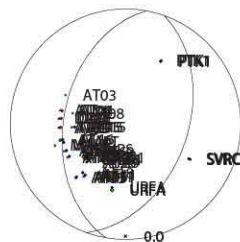
Pol + Ampl



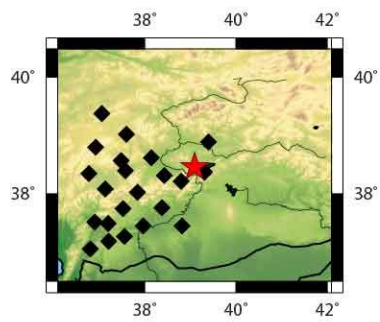
sta	SH/P	Pqual	Squal	sta	Pqual	Squal
			0.0			
AT04	0.87	g/l	ok/E	AT04	g/l	ok/E
AT05	2.43	g/E	g/E	AT05	g/E	g/E
AT09	3.37	ok/E	g/E	AT09	ok/E	g/E
AT11	4.59	g/E	ok/E	AT11	g/E	ok/E
AT15	1.15	g/E	ok/E	AT15	g/E	ok/E
AT16	8.08	ok/E	ok/E	AT16	ok/E	ok/E
AT17	1.41	g/E	g/E	AT17	g/E	g/E
AT28	1.13	g/E	ok/E	AT28	g/E	ok/E
AT38	8.09	ok/E	ok/E	AT38	ok/E	ok/E
AT68	1.17	g/E	g/E	AT68	g/E	g/E
DARE	2.91	g/E	ok/E	DARE	g/E	ok/E
GAZ1	6.43	ok/E	g/E	GAZ1	ok/E	g/E
MALT	3.44	g/E	e/	MALT	g/E	e/
PTK1	1.41	g/l	ok/E	PTK1	g/l	ok/E
SVRC	4.82	g/E	g/	SVRC	g/E	g/
URFA	11.71	g/E	g/	URFA	g/E	g/



P/T axes



Data



P K: NaN 95%: NaN T K: NaN 95%: NaN Lon: 39.09 Lat: 38.47 Dep: 3.00 Mag: ML, 3.5
 cate00125 Data pts: 39 Solns: 1 Pol errs: 1 Nodal Wt: 0.3 Solns shown: 1 Search Inc: 5
 Ampl errs: 0 Ampl Data: 16 Solns: 1 Pol errs: 1 Nodal Wt: 0.3 Solns shown: 1 Search Inc: 5

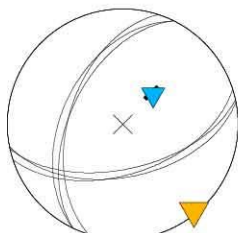
Pol Only



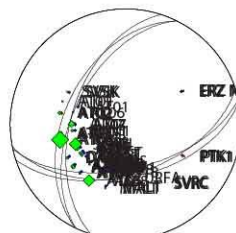
Pol + Ampl



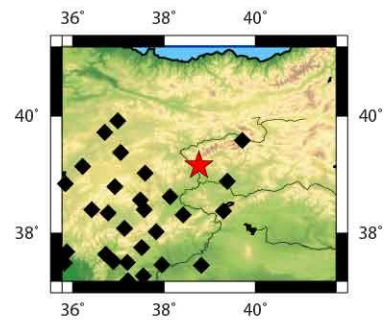
sta SH/P Pqual Squal	sta Pqual Squal
AT01 1.78 ok/E g/E	AT01 ok/E g/E
AT02 12.63 g/E g/E	AT02 g/E g/E
AT03 12.47 g/E g/E	AT03 g/E g/E
AT04 6.05 E/l g/	AT04 e/l g/
AT07 22.62 g/E ok/E	AT07 g/E ok/E
AT08 57.84 g/E g/E	AT08 g/E g/E
AT09 15.09 ok/E g/E	AT09 ok/E g/E
AT15 13.61 g/E g/E	AT13 ok/E
AT16 13.35 ok/E g/E	AT15 g/E g/E
AT17 2.48 g/E ok/E	AT16 ok/E g/E
AT35 9.64 g/E g/E	AT17 g/E ok/E
AT38 5.56 ok/E ok/E	AT18 e/E
AT68 37.43 g/E g/E	AT26 g/E
AT69 1.18 g/l g/E	AT28 g/l
BNN1 9.01 ok/E g/E	AT33 ok/E
DARE 10.83 g/E ok/E	AT35 g/E g/E
ERZN 4.27 ok/E g/E	AT38 ok/E ok/E
KMRS 5.25 E/l g/	AT68 g/E g/E
KOZT 8.78 ok/l g/	AT69 g/l g/E
MALT 1.36 E/l g/	BNN1 ok/E g/E
PTK1 0.51 e/l ok/E	DARE g/E ok/E
SARI 41.92 g/E e/l	ERZN ok/E g/E
SVRC 6.55 g/E g/E	GAZ1 g/l
SVSK 1.18 g/E g/	KMRS g/l g/E
	KOZT ok/l g/E
	MALT e/l g/E
	PTK1 e/l ok/E
	SARI g/E e/l
	SVRC g/E g/
	SVSK g/E g/E



P/T axes



Data



P K: 198.5 95%: 8.8 T K: 736.8 95%: 4.5 Lon: 38.77 Lat: 39.16 Dep: 4.00 Mag: ML, 4.4
 cate00126 Data pts: 56 Solns: 3 Pol errs: 1 Nodal Wt: 0.1 Solns shown: 3 Search Inc: 5
 Ampl errs: 1 Ampl Data: 24 Solns: 3 Pol errs: 1 Nodal Wt: 0.1 Soln shown: 3 Search Inc: 5

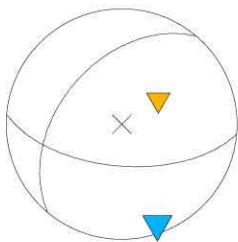
Pol Only



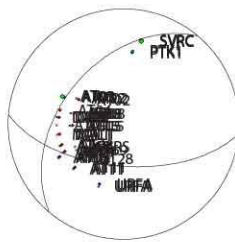
Pol + Ampl



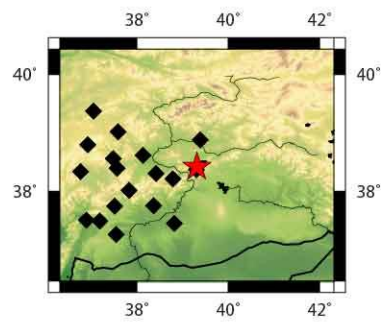
sta	SH/P	Pqual	Squal	sta	Pqual	Squal
AT02	1.89	ok/E	g/E	AT02	ok/E	g/E
AT03	14.90	ok/E	ok/E	AT03	ok/E	ok/E
AT05	2.50	g/E	g/E	AT04	g/E	
AT08	4.14	g/E	g/E	AT05	g/E	g/E
AT11	5.67	g/E	ok/E	AT08	g/E	g/E
AT15	3.50	ok/E	g/E	AT11	g/E	ok/E
AT17	4.16	g/E	g/E	AT15	ok/E	g/E
AT68	6.48	ok/E	ok/E	AT17	g/E	g/E
DARE	2.53	ok/E	ok/E	AT68	ok/E	ok/E
MALT	1.30	g/E	g/E	DARE	ok/E	ok/E
PTK1	8.50	g/E	g/E	MALT	g/E	g/E
SVRC	12.57	g/E	g/E	PTK1	g/E	g/E
URFA	3.02	g/E	g/	SVRC	g/E	g/
				URFA	g/E	g/E



P/T axes



Data

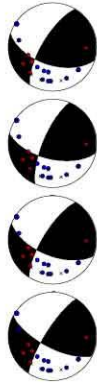


P K: NaN 95%: NaN T K: NaN 95%: NaN Lon: 39.32 Lat: 38.43 Dep: 3.00 Mag: ML, 3.5
 cate00127 Data pts: 31 Solns: 1 Pol errs: 1 Nodal Wt: 0.3 Solns shown: 1 Search Inc: 5
 Ampl errs: 0 Ampl Data: 13 Solns: 1 Pol errs: 1 Nodal Wt: 0.3 Soln shown: 1 Search Inc: 5

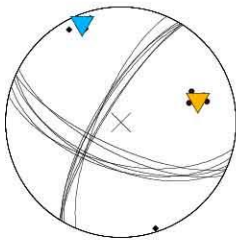
Pol Only



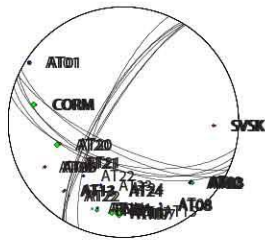
Pol + Ampl



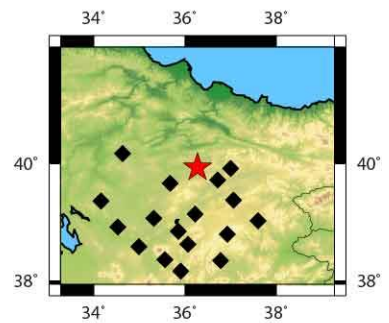
sta	SH/P	Pqual	Squal	sta	Pqual	Squal
AT01	4.03	g/l	g/E	AT01	g/l	g/E
AT02	1.18	g/l	g/E	AT02	g/l	g/E
AT03	12.43	ok/E	g/E	AT03	ok/E	g/E
AT06	0.66	E/l	g/	AT06	eE	g/
AT07	26.56	g/E	e/	AT07	g/E	e/E
AT08	4.78	g/E	ok/E	AT08	g/E	ok/E
AT13	6.49	g/E	g/E	AT13	g/E	g/E
AT14	14.56	ok/E	g/E	AT14	ok/E	g/E
AT20	19.60	g/E	g/E	AT20	g/E	g/E
AT21	4.23	ok/E	ok/E	AT21	ok/E	ok/E
AT22	2.33	g/E	g/E	AT22	g/E	g/E
AT23	1.82	g/E	ok/E	AT23	g/E	ok/E
AT24	5.85	g/E	ok/E	AT24	g/E	ok/E
BNN1	13.34	g/E	g/E	BNN1	g/E	g/E
CORM	19.10	g/E	ok/	CORM	g/E	ok/E
SVSK	2.29	g/l	g/	SVSK	g/l	g/E



P/T axes



Data



P K: 156.3 95%: 5.4 T K: 154.1 95%: 5.4 Lon: 36.27 Lat: 39.94 Dep: 5.00 Mag: ML, 3.0
 cate00128 Data pts: 33 Solns: 6 Pol errs: 1 Nodal Wt: 0.3 Solns shown: 6 Search Inc: 5
 Ampl errs: 0 Ampl Data: 16 Solns: 4 Pol errs: 1 Nodal Wt: 0.3 Soln shown: 4 Search Inc: 5

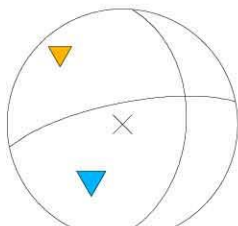
Pol Only



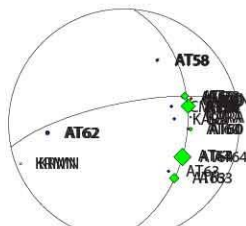
Pol + Ampl



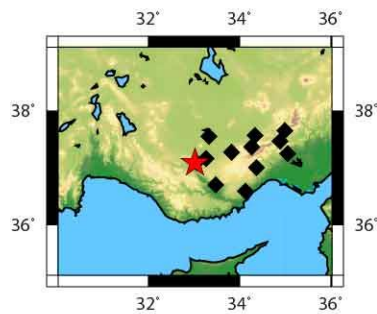
sta SH/P Pqual Squal	sta Pqual Squal
AT53 24.46 ok/E g/E	AT53 ok/E g/E
AT54 5.96 ok/E g/E	AT54 ok/E g/E
AT58 6.04 g/E g/E	AT58 g/E g/E
AT59 5.32 g/E g/E	AT59 g/E g/E
AT60 14.00 ok/E g/E	AT60 ok/E g/E
AT62 4.98 E/E g/	AT62 e/E g/E
AT63 32.88 ok/E g/E	AT63 ok/E g/E
AT64 55.78 ok/E g/E	AT64 ok/E g/E
AT71 49.11 g/E ok/E	AT71 g/E ok/E
CMRD 2.97 g/E g/	CMRD g/E g/E
KARA 2.03 ok/E g/E	KARA ok/E g/E
KRMN 0.86 g/E g/E	KRMN g/E g/E



P/T axes



Data



P K: NaN 95%: NaN T K: NaN 95%: NaN Lon: 33.02 Lat: 37.1 Dep: 2.00 Mag: ML, 3.2
 cate00129 Data pts: 24 Solns: 1 Pol errs: 1 Nodal Wt: 0.3 Solns shown: 1 Search Inc: 5
 Ampl errs: 0 Ampl Data: 12 Solns: 1 Pol errs: 1 Nodal Wt: 0.3 Soln shown: 1 Search Inc: 5

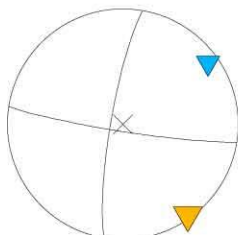
Pol Only



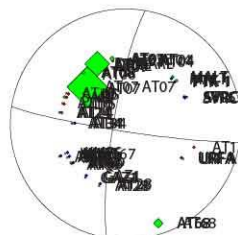
Pol + Ampl



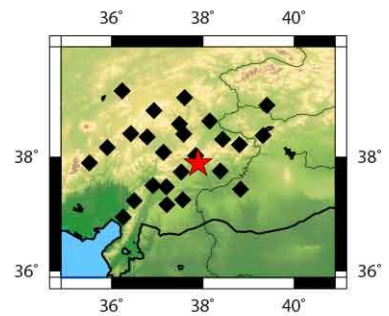
sta SH/P	Pqual	Squal	sta	Pqual	Squal
AT03	15.16	ok/E ok/E	AT03	ok/E	ok/E
AT04	1.00	g/l ok/E	AT04	g/l	ok/E
AT07	132.52	ok/E ok/E	AT07	g/E	
AT08	14.05	ok/E g/E	AT07	ok/E	ok/E
AT09	8.57	g/E g/E	AT08	ok/E	g/E
AT15	1.74	g/E g/E	AT09	g/E	g/E
AT16	1.48	g/E g/E	AT11	g/E	
AT17	0.92	g/E g/E	AT15	g/E	g/E
AT24	7.06	ok/E g/E	AT16	g/E	g/E
AT28	3.37	g/E g/E	AT17	g/E	g/E
AT34	4.04	g/E ok/E	AT24	ok/E	g/E
AT37	2.32	g/E g/E	AT28	g/E	g/E
AT67	7.90	ok/E g/E	AT34	g/E	ok/E
AT68	24.91	g/E g/l	AT37	g/E	g/E
AT69	1.21	g/E g/E	AT67	ok/E	g/E
DARE	83.92	g/E e/	AT68	g/E	g/l
GAZ1	3.35	ok/E g/E	AT69	g/E	g/E
KMRS	0.62	g/E ok/	DARE	g/E	e/E
MALT	10.39	g/E g/E	GAZ1	ok/E	g/
PTK1	10.05	ok/E g/E	KMRS	g/E	ok/E
SARI	8.81	g/E ok/	MALT	g/E	g/E
SVRC	5.97	ok/E g/E	PTK1	ok/E	g/E
URFA	1.18	g/E g/	SARI	g/E	ok/E
			SVRC	ok/E	g/
			URFA	g/E	g/E



P/T axes



Data



P K: 0.0 95%: NaN T K: NaN 95%: NaN Lon: 37.89 Lat: 37.89 Dep: 3.00 Mag: ML, 3.5
 cate00130 Data pts: 48 Solns: 1 Pol errs: 1 Nodal Wt: 0.3 Solns shown: 1 Search Inc: 5
 Ampl errs: 1 Ampl Data: 23 Solns: 1 Pol errs: 1 Nodal Wt: 0.3 Soln shown: 1 Search Inc: 5

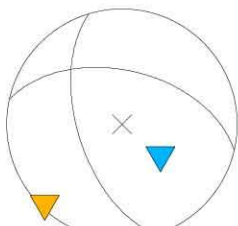
Pol Only



Pol + Ampl



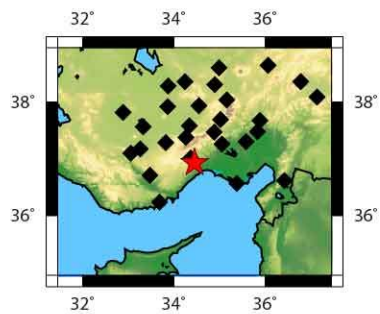
sta	SH/P	Pqual	Squal	sta	Pqual	Squal
AT13	ok/E			AT13	ok/E	
AT14	2.41	ok/E	ok/E	AT14	ok/E	ok/E
AT15	1.00	ok/E	g/E	AT15	ok/E	g/E
AT16	5.05	g/E	g/E	AT16	g/E	g/E
AT22	15.09	g/E	g/E	AT22	g/E	g/E
AT35	3.48	ok/E	ok/E	AT32	ok/E	
AT45	16.76	g/E	ok/E	AT33	ok/E	
AT46	7.87	g/E	ok/E	AT35	ok/E	ok/E
AT52	2.43	g/E	ok/E	AT42	g/E	
AT53	1.95	g/E	ok/E	AT45	g/E	ok/E
AT54	20.58	g/E	g/E	AT46	g/E	ok/E
AT58	9.78	g/E	g/E	AT48	ok/E	
AT59	8.59	g/E	ok/E	AT52	g/E	ok/E
AT60	2.03	g/E	ok/E	AT53	g/E	ok/E
AT63	39.79	g/E	e/l	AT54	g/E	g/E
AT71	2.24	g/E	ok/E	AT57	g/E	
IKL1	6.27	ok/E	g/	AT58	g/E	g/E
KARA	2.03	g/E	g/E	AT59	g/E	ok/E
KOZT	74.51	dk/E	g/	AT60	g/E	ok/E
KRTS	7.32	ok/E	g/	AT62	g/E	
				AT63	g/E	e/l
				AT70	g/E	
				AT71	g/E	ok/E
				GULA	g/E	
				IKL1	ok/E	g/E
				KARA	g/E	g/E
				KOZT	ok/E	g/
				KRMN	ok/E	
				KRTS	ok/E	g/E



P/T axes

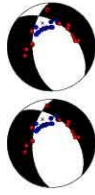


Data

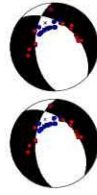


P K: NaN 95%: NaN T K: NaN 95%: NaN Lon: 34.45 Lat: 36.93 Dep: 1.00 Mag: ML, 4.0
 cate00131 Data pts: 48 Solns: 1 Pol errs: 1 Nodal Wt: 0.4 Solns shown: 1 Search Inc: 5
 Ampl errs: 0 Ampl Data: 19 Solns: 1 Pol errs: 1 Nodal Wt: 0.4 Soln shown: 1 Search Inc: 5

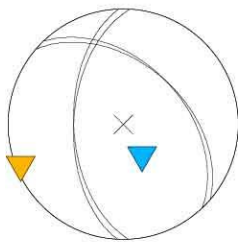
Pol Only



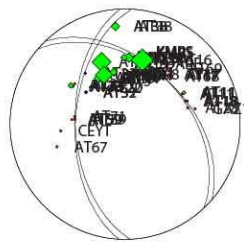
Pol + Ampl



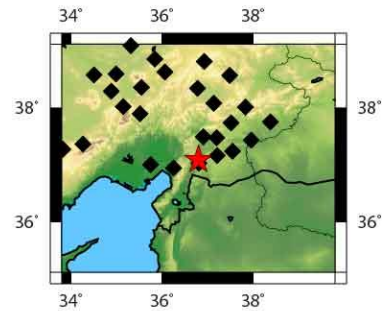
sta SH/P Pqual Squal	sta Pqual Squal
AT07 25.20 g/E g/E	AT01 g/E
AT08 33.15 g/E g/l	AT06 g/E
AT11 13.78 g/E g/E	AT07 g/E g/E
AT13 28.09 o/E g/E	AT08 g/E g/l
AT14 63.21 g/E g/l	AT11 g/E g/E
AT15 20.81 g/E g/E	AT13 o/E g/E
AT16 71.62 g/E g/E	AT14 g/E g/l
AT17 1.50 e/E g/	AT15 g/E g/E
AT18 5.29 e/l g/	AT16 g/E g/E
AT33 18.59 g/E g/E	AT17 e/E g/E
AT38 22.80 g/E g/E	AT18 e/l g/
AT59 5.32 g/E g/E	AT20 o/E
BNN1 58.71 o/E g/l	AT22 g/E
KMRS 7.85 e/l g/E	AT23 g/E
	AT28 e/l
	AT31 o/E
	AT32 g/E
	AT33 g/E g/E
	AT34 g/E
	AT38 g/E g/E
	AT59 g/E g/E
	AT67 e/l
	AT68 e/l
	AT69 e/l
	AT71 g/E
	BNN1 o/E g/l
	CEYT g/E
	DARE g/E
	GAZ1 e/l
	KMRS e/l g/E



P/T axes

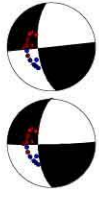


Data

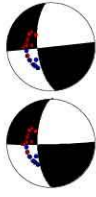


P K: 2316.7 95%: 5.2 T K: 430.6 95%: 12. 1 Lon: 36.8 Lat: 37.1 Dep: 2.00 Mag: ML, 4.7
 cate00132 Data pts: 44 Solns: 2 Pol errs: 2 Nodal Wt: 0.2 Solns shown: 2 Search Inc: 5
 Ampl errs: 0 Ampl Data: 14 Solns: 2 Pol errs: 2 Nodal Wt: 0.2 Soln shown: 2 Search Inc: 5

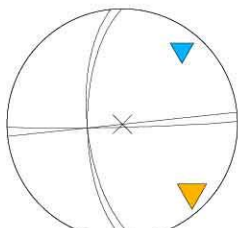
Pol Only



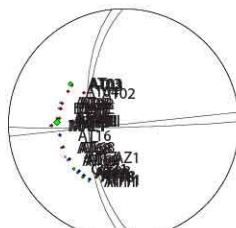
Pol + Ampl



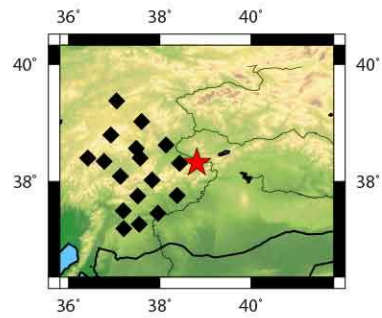
sta SH/P Pqual Squal	sta Pqual Squal
AT03 14.94 g/E g/E	AT02 g/E
AT08 1.36 g/E g/E	AT03 g/E g/E
AT09 5.68 g/l g/E	AT04 e/l
AT11 0.94 e/E ok/	AT08 g/E g/E
AT15 21.70 ok/E g/E	AT09 g/l g/E
AT18 9.59 g/E g/E	AT11 e/E ok/E
AT28 6.74 g/E g/E	AT15 ok/E g/E
AT68 3.28 g/E g/E	AT16 g/E
AT69 0.97 g/E g/E	AT18 g/E g/E
DARE 1.14 g/l g/E	AT28 g/E g/E
GAZ1 10.32 g/E g/E	AT68 g/E g/E
SARI 7.16 g/E g/	AT69 g/E g/E
	DARE g/l g/E
	GAZ1 g/E g/E
	MALT e/E e/
	SARI g/E g/E



P/T axes

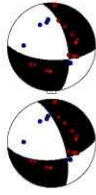


Data



P K: 525.2 95%: 10.9 T K: 523.8 95%: 10.9 Lon: 38.81 Lat: 38.32 Dep: 2.00 Mag: ML, 3.7
 cate00133 Data pts: 30 Solns: 2 Pol errs: 2 Nodal Wt: 0.3 Solns shown: 2 Search Inc: 5
 Ampl errs: 0 Ampl Data: 12 Solns: 2 Pol errs: 2 Nodal Wt: 0.3 Solns shown: 2 Search Inc: 5

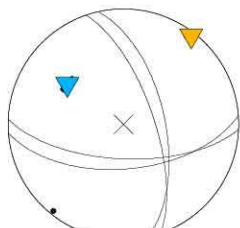
Pol Only



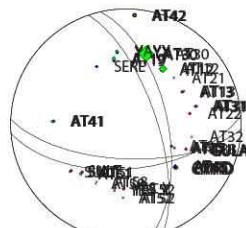
Pol + Ampl



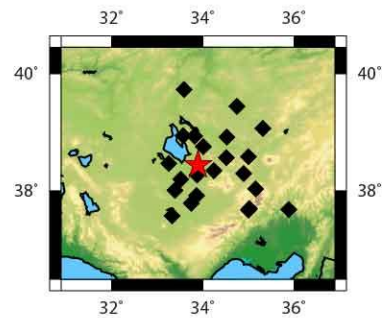
sta SH/P Pqual Squal	sta Pqual Squal
AT12 26.46 ok/E g/E	AT12 ok/E g/E
AT13 3.92 g/E g/E	AT13 g/E g/E
AT19 12.61 ok/E g/E	AT19 ok/E g/E
AT30 49.35 ok/E e/l	AT22 g/l
AT31 1.90 g/E g/E	AT30 ok/E e/
AT35 5.80 ok/E ok/E	AT31 g/E g/E
AT41 10.41 g/E e/l	AT33 g/E
AT42 6.90 E/l g/	AT35 ok/E ok/E
AT45 6.18 ok/E g/E	AT41 g/E e/l
AT51 9.70 g/E g/E	AT42 e/l g/
AT52 3.80 g/E g/l	AT45 ok/E g/E
AT58 2.91 g/E g/l	AT51 g/E g/E
CMRD 2.83 dk/E g/	AT52 g/E g/l
GULA 5.66 B/l g/	AT58 g/E
SULT 0.17 dl ok/	CMRD ok/E g/E
YAYX 10.30 fl ok/	GULA g/l g/E
YESY 3.02 g/E ok/E	SERE g/l
	SULT e/l ok/E
	YAYX g/l ok/E
	YESY g/E ok/E



P/T axes

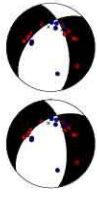


Data

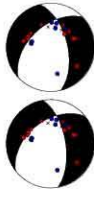


P K: 162.4 95%: 19.7 T K: 123.7 95%: 22. 6 Lon: 33.89 Lat: 38.45 Dep: 2.00 Mag: ML, 3.0
 cate00134 Data pts: 38 Solns: 2 Pol errs: 1 Nodal Wt: 0.5 Solns shown: 2 Search Inc: 5
 Ampl errs: 0 Ampl Data: 17 Solns: 2 Pol errs: 1 Nodal Wt: 0.5 Soln shown: 2 Search Inc: 5

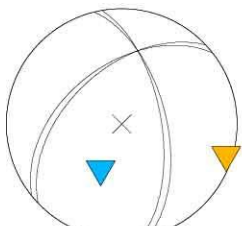
Pol Only



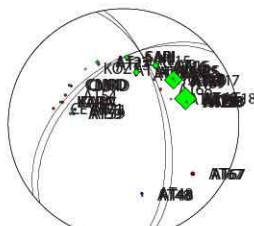
Pol + Ampl



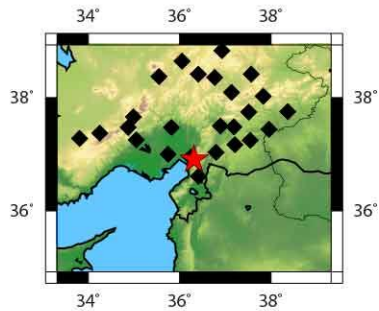
sta	SH/P	Pqual	Squal	sta	Pqual	Squal
AT08	21.40	ok/E	ok/E	AT08	ok/E	ok/E
AT16	21.12	g/E	ok/E	AT15	g/E	
AT17	59.14	ok/E	ok/E	AT16	g/E	ok/E
AT18	74.38	ok/E	g/E	AT17	ok/E	ok/E
AT23	11.66	ok/E	g/E	AT18	ok/E	g/E
AT28	7.81	g/E	g/E	AT23	ok/E	g/E
AT38	1.43	e/E	ok/	AT28	g/E	g/E
AT48	2.89	g/E	g/E	AT38	e/E	ok/E
AT59	10.88	ok/E	ok/E	AT48	g/E	g/E
AT67	3.46	e/l	g/	AT54	ok/E	
AT68	10.54	g/E	ok/E	AT59	ok/E	ok/E
AT69	3.25	g/E	ok/E	AT67	e/l	g/
AT71	10.57	g/E	ok/E	AT68	g/E	ok/E
CMRD	5.73	o/E	ok/	AT69	g/E	ok/E
KARA	7.67	ok/E	g/E	AT71	g/E	ok/E
KMRS	4.30	g/E	g/	CEYT	g/l	
SARI	14.60	o/E	ok/	CMRD	ok/E	ok/E
				GAZ1	g/E	
				KARA	ok/E	g/E
				KMRS	g/E	g/E
				SARI	ok/E	ok/E



P/T axes



Data



P K: 526.2 95%: 10.9 T K: 524.6 95%: 10.9 Lon: 36.32 Lat: 36.91 Dep: 4.00 Mag: ML, 3.5
 cate00135 Data pts: 42 Solns: 2 Pol errs: 1 Nodal Wt: 0.5 Solns shown: 2 Search Inc: 5
 Ampl errs: 0 Ampl Data: 17 Solns: 2 Pol errs: 1 Nodal Wt: 0.5 Soln shown: 2 Search Inc: 5

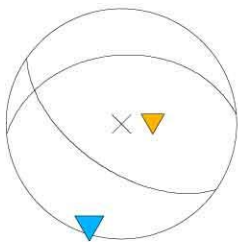
Pol Only



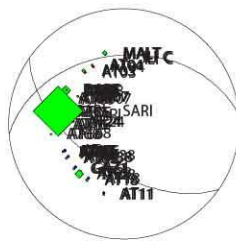
Pol + Ampl



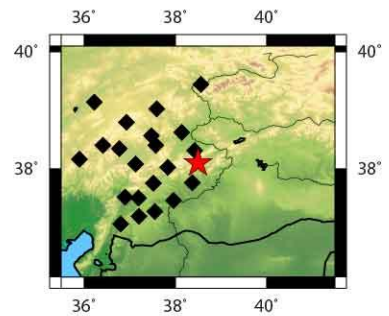
sta SH/P Pqual Squal	sta Pqual Squal
AT03 12.76 g/E g/E	AT03 g/E g/E
AT04 7.36 g/E g/E	AT04 g/E g/E
AT07 7.89 g/E g/E	AT07 g/E g/E
AT08 30.69 g/E ok/E	AT08 g/E ok/E
AT09 4.37 g/E g/E	AT09 g/E g/E
AT11 3.72 E/E g/	AT11 e/E g/E
AT15 3.85 ok/E ok/E	AT15 ok/E ok/E
AT16 3.72 g/E ok/E	AT16 g/E ok/E
AT17 3.05 g/E g/E	AT17 g/E g/E
AT18 9.31 g/E g/E	AT18 g/E g/E
AT24 7.90 ok/E g/E	AT24 ok/E g/E
AT28 28.05 g/E g/E	AT28 g/E g/E
AT38 8.41 ok/E ok/E	AT38 ok/E ok/E
AT68 2.77 g/E g/E	AT68 g/E g/E
AT69 7.51 g/E g/E	AT69 g/E g/E
DARE 5.83 g/E g/E	DARE g/E g/E
GAZ1 6.68 ok/E g/E	GAZ1 ok/E g/
ILIC 3.95 ok/E g/E	ILIC ok/E g/E
KMRS 4.55 g/E g/	KMRS g/E g/E
MALT 15.18 g/E e/	MALT g/E e/E
SARI 166.14 ok/E g/	SARI ok/E g/E



P/T axes



Data



P K: 0.0 95%: NaN T K: NaN 95%: NaN Lon: 38.5 Lat: 38.1 Dep: 2.00 Mag: ML, 3.6
 cate00136 Data pts: 42 Solns: 1 Pol errs: 1 Nodal Wt: 0.5 Solns shown: 1 Search Inc: 5
 Ampl errs: 0 Ampl Data: 21 Solns: 1 Pol errs: 1 Nodal Wt: 0.5 Soln shown: 1 Search Inc: 5

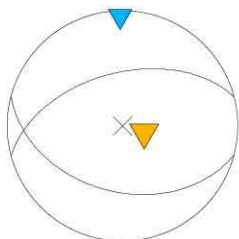
Pol Only



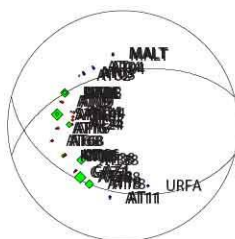
Pol + Ampl



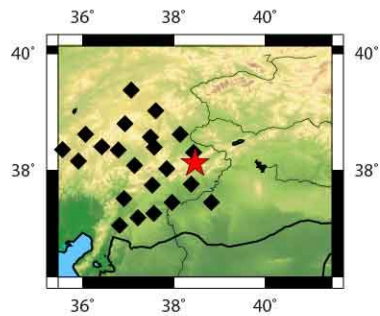
sta	SH/P	Pqual	Squal	sta	Pqual	Squal
AT03	6.90	g/E	g/E	AT03	g/E	g/E
AT04	0.42	g/l	g/E	AT04	g/l	g/E
AT08	29.24	ok/E	e/e	AT08	ok/E	e/E
AT09	4.70	g/l	e/	AT09	g/l	e/
AT11	2.21	E/E	e/	AT11	e/E	e/
AT14	4.38	ok/E	g/E	AT14	ok/E	g/E
AT15	38.67	ok/E	g/E	AT15	ok/E	g/E
AT16	4.60	g/E	ok/E	AT16	g/E	ok/E
AT17	9.93	g/E	ok/E	AT17	g/E	ok/E
AT18	27.45	g/E	g/E	AT18	g/E	g/E
AT24	20.54	g/E	ok/E	AT23	ok/E	
AT28	39.46	g/E	g/E	AT24	g/E	ok/E
AT38	29.50	ok/E	ok/E	AT28	g/E	g/E
AT68	0.64	g/E	g/E	AT38	ok/E	ok/E
DARE	15.58	g/E	g/E	AT68	g/E	g/E
GAZ1	3.18	ok/E	g/E	DARE	g/E	g/E
KMRS	8.55	g/E	g/	GAZ1	ok/E	g/
MALT	4.77	e/l	e/	KMRS	g/E	g/E
SARI	11.68	ok/E	ok/	MALT	e/l	e/l
				SARI	ok/E	ok/E
				URFA	g/l	



P/T axes

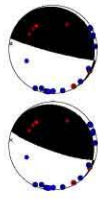


Data

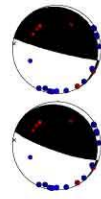


P K: NaN 95%: NaN T K: NaN 95%: NaN Lon: 38.46 Lat: 38.13 Dep: 3.00 Mag: ML, 3.8
 cate00137 Data pts: 41 Solns: 1 Pol errs: 1 Nodal Wt: 0.2 Solns shown: 1 Search Inc: 5
 Ampl errs: 0 Ampl Data: 19 Solns: 1 Pol errs: 1 Nodal Wt: 0.2 Soln shown: 1 Search Inc: 5

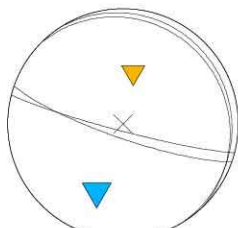
Pol Only



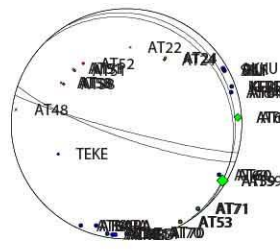
Pol + Ampl



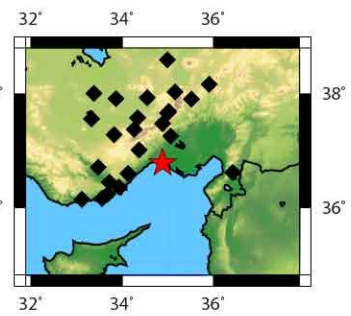
sta SH/P Pqual Squal	sta Pqual Squal
AT24 10.85 ok/E g/E	AKKU g/E
AT33 4.48 g/E g/E	AT24 ok/E g/E
AT34 2.83 g/E g/E	AT33 g/E g/E
AT45 1.19 g/l ok/E	AT34 g/E g/E
AT51 1.43 ok/E g/E	AT45 g/l ok/E
AT53 8.36 g/E g/E	AT51 ok/E g/E
AT58 4.34 g/E g/E	AT52 ok/E
AT59 29.30 g/E g/E	AT53 g/E g/E
AT60 2.20 g/E ok/E	AT54 g/l
AT63 21.51 g/E e/	AT58 g/E g/E
AT64 2.60 g/l g/E	AT59 g/E g/E
AT70 4.23 g/E g/E	AT60 g/E ok/E
AT71 7.15 g/E ok/E	AT63 g/E e/E
KARA 0.87 E/l g/	AT64 g/l g/E
KEBE 5.07 g/E g/E	AT70 g/E g/E
SILI 3.41 g/E g/E	AT71 g/E ok/E
	CMRD g/l
	IKL1 g/E
	KARA e/l g/E
	KEBE g/E g/E
	SILI g/E g/E
	TEKE g/E



P/T axes



Data

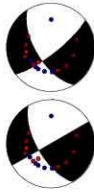


P K: 360.6 95%: 13.2 TK: 438.0 95%: 12. 0 Lon: 34.88 Lat: 36.79 Dep: 16.00 Mag: ML, 3.8
 cate00138 Data pts: 40 Solns: 2 Pol errs: 1 Nodal Wt: 0.5 Solns shown: 2 Search Inc: 5
 Ampl errs: 0 Ampl Data: 16 Solns: 2 Pol errs: 1 Nodal Wt: 0.5 Soln shown: 2 Search Inc: 5

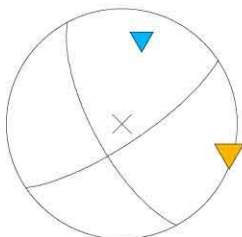
Pol Only



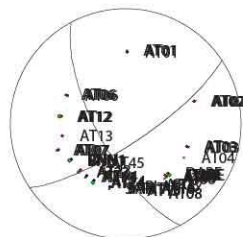
Pol + Ampl



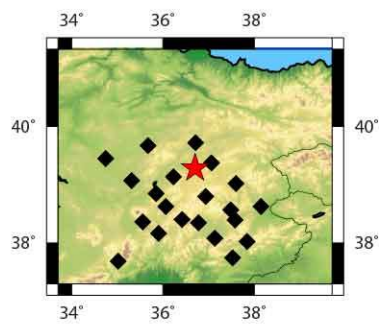
sta	SH/P	Pqual	Squal	sta	Pqual	Squal
AT01	4.55	g/E	g/E	AT01	g/E	g/E
AT02	0.97	g/E	g/E	AT02	g/E	g/E
AT03	1.87	g/E	g/E	AT03	g/E	g/E
AT06	3.11	g/l	g/E	AT06	g/l	g/E
AT07	4.59	g/E	g/E	AT07	g/E	g/E
AT08	10.79	g/E	g/E	AT08	g/E	g/E
AT09	6.02	g/E	ok/E	AT09	g/E	ok/E
AT12	14.24	ok/E	ok/E	AT12	ok/E	ok/E
AT14	3.68	g/E	ok/E	AT13	ok/E	
AT15	8.48	g/E	g/E	AT14	g/E	ok/E
AT16	6.65	ok/E	g/E	AT15	g/E	g/E
AT23	10.13	ok/E	g/E	AT16	ok/E	g/E
AT24	12.35	g/E	ok/E	AT23	ok/E	g/E
BNN1	13.34	g/E	ok/E	AT24	g/E	ok/E
DARE	13.98	g/E	g/E	AT45	ok/E	
SARI	2.72	g/E	g/E	BNN1	g/E	ok/E
				DARE	g/E	g/E
				SARI	g/E	g/E



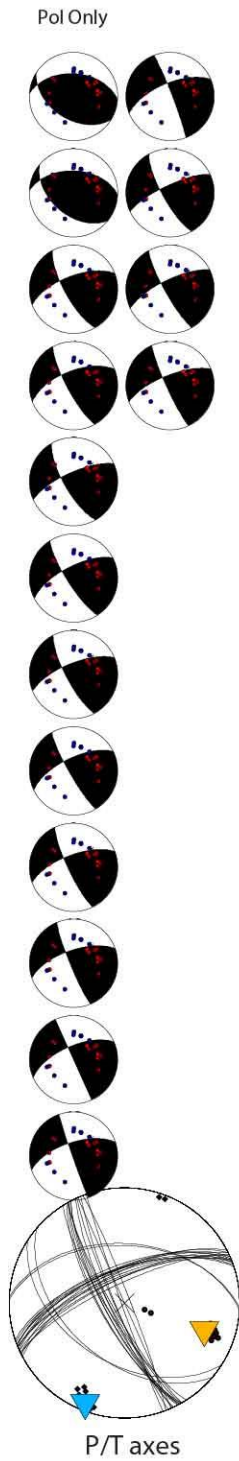
P/T axes



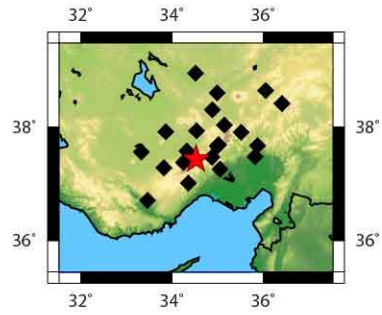
Data



P K: NaN 95%: NaN T K: NaN 95%: NaN Lon: 36.7 Lat: 39.29 Dep: 3.00 Mag: ML, 3.0
 cate00139 Data pts: 37 Solns: 1 Pol errs: 1 Nodal Wt: 0.5 Solns shown: 1 Search Inc: 5
 Ampl errs: 0 Ampl Data: 16 Solns: 2 Pol errs: 1 Nodal Wt: 0.3 Soln shown: 2 Search Inc: 5



sta SH/P Pqual Squal	sta Pqual Squal
AT14 4.11 g/E g/E	AT14 g/E g/E
AT21 1.71 ok/E ok/E	AT21 ok/E ok/E
AT22 4.92 g/E g/E	AT22 g/E g/E
AT32 3.32 ok/E g/E	AT32 ok/E g/E
AT33 17.66 g/E g/E	AT33 g/E g/E
AT34 48.08 ok/E g/E	AT34 ok/E g/E
AT45 2.41 g/E g/E	AT45 g/E
AT52 0.25 g/E g/E	AT45 g/E g/E
AT53 11.75 g/l g/E	AT52 g/E g/E
AT54 1.72 g/l g/E	AT53 g/l g/E
AT58 5.65 g/E o/E	AT54 g/l g/E
AT59 4.48 g/l g/E	AT58 g/E o/E
AT60 2.06 e/l ok/	AT59 g/l g/E
AT63 10.65 ok/E g/E	AT60 e/l ok/E
AT70 7.34 g/E g/E	AT63 ok/E g/E
AT71 46.34 e/l e/E	AT70 g/E g/E
CMRD 1.19 e/E g/E	AT71 e/l e/E
KARA 3.81 g/E g/E	CMRD e/E g/E
KOZT 1.61 g/E ok/	KARA g/E g/E
SARI 0.56 g/E ok/	KOZT g/E ok/
	SARI g/E ok/E



P K: 123.9 95%: 3.3 TK: 21.4 95%: 8. 2 Lon: 34.53 Lat: 37.44 Dep: 3.00 Mag: ML, 3.0
 cate00140 Data pts: 41 Solns: 16 Pol errs: 1 Nodal Wt: 0.5 Solns shown: 16 Search Inc: 5
 Ampl errs: 0 Ampl Data: 20 Solns: 4 Pol errs: 1 Nodal Wt: 0.5 Soln shown: 4 Search Inc: 5

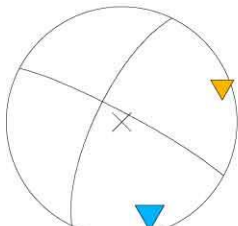
Pol Only



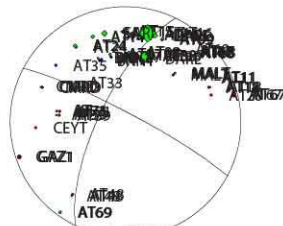
Pol + Ampl



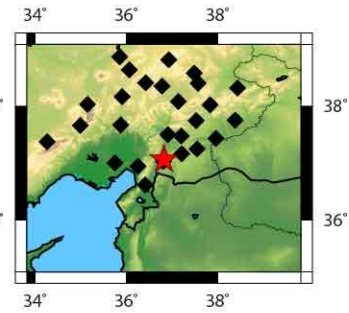
sta	SH/P	Pqual	Squal	sta	Pqual	Squal
AT07	9.79	g/E	ok/E	AT07	g/E	ok/E
AT08	9.22	ok/E	ok/E	AT08	ok/E	ok/E
AT09	10.85	ok/E	ok/E	AT09	ok/E	ok/E
AT11	9.77	g/E	ok/E	AT11	g/E	ok/E
AT14	13.33	g/E	g/E	AT14	g/E	g/E
AT15	3.82	g/E	g/E	AT15	g/E	g/E
AT16	56.86	g/E	g/E	AT16	g/E	g/E
AT17	3.26	g/E	o/E	AT17	g/E	o/E
AT18	2.85	g/E	g/E	AT18	g/E	g/E
AT24	11.38	g/E	g/E	AT24	g/E	g/E
AT38	22.86	g/E	e/l	AT28	g/l	
AT48	1.73	g/E	g/E	AT33	ok/E	
AT59	2.67	g/E	ok/E	AT35	g/E	
AT67	0.88	g/l	g/E	AT38	g/E	e/l
AT68	1.98	g/E	ok/E	AT48	g/E	g/E
AT69	7.43	g/E	g/E	AT59	g/E	ok/E
AT71	5.09	ok/E	g/E	AT67	g/l	g/E
BNN1	5.05	ok/E	ok/E	AT68	g/E	ok/E
CMRD	2.83	o/E	ok/	AT69	g/E	g/E
DARE	15.13	g/E	g/E	AT71	ok/E	g/E
GAZ1	4.14	g/E	ok/E	BNN1	ok/E	ok/E
KMRS	9.64	g/E	g/	CEYT	g/E	
MALT	5.71	g/E	g/E	CMRD	ok/E	ok/E
SARI	18.08	g/E	g/	DARE	g/E	g/E
				GAZ1	g/E	ok/
				KMRS	g/E	g/E
				MALT	g/E	g/E
				SARI	g/E	g/E



P/T axes



Data



P K: NaN 95%: NaN T K: NaN 95%: NaN Lon: 36.82 Lat: 37.07 Dep: 5.00 Mag: ML, 3.5
 cate00141 Data pts: 52 Solns: 1 Pol errs: 1 Nodal Wt: 0.2 Solns shown: 1 Search Inc: 5
 Ampl errs: 1 Ampl Data: 24 Solns: 1 Pol errs: 1 Nodal Wt: 0.2 Soln shown: 1 Search Inc: 5

G. Average Pressure (P) and Tension (T) axis azimuth (az.) and dip angles, maximum and minimum horizontal stress orientations (SHmax, SHmin) orientations and tectonic regimes obtained from all the focal mechanisms (FMS) for Central Anatolia (Chapter 4).

No	D.M.Yr	Hr:min	Long	Lat	Mag	P-az	P-dip	T-az	T-Dip	SHmax	SHmin	Regime
1	19.04.1938	10:59	33.70	39.50	6.8	348	18	250	23	164	74	SS
2	8.04.1951	21:38	36.10	36.60	6.0	343	5	251	26	162	72	SS
3	14.06.1964	12:15	38.48	38.08	5.5	222	51	92	27	14	104	UF
4	7.04.1967	17:07	36.13	37.37	4.8	224	21	131	8	42	132	SS
5	7.04.1967	18:33	36.18	37.37	4.9	17	7	109	21	18	108	SS
6	4.07.1967	18:33	36.20	37.40	5.1	348	47	115	29	12	102	UF
7	29.06.1971	09:08	36.86	37.13	5.0	312	11	65	62	136	46	TF
8	11.07.1971	20:12	36.83	37.16	5.0	217	4	307	7	37	127	SS
9	17.08.1971	04:29	36.79	37.11	4.9	133	32	331	56	123	33	TF
10	1.01.1975	00:30	36.48	36.78	5.2	317	55	103	30	180	90	NF
11	9.02.1978	21:10	36.80	37.08	4.5	12	18	234	67	7	97	TF
12	28.12.1979	03:09	35.85	37.49	5.4	186	1	96	1	6	96	SS
13	2.01.1980	12:52	36.33	36.57	4.7	1	30	147	55	14	104	TF
14	30.06.1981	07:59	35.89	36.17	4.7	201	21	306	34	28	118	UF
15	24.11.1983	00:14	36.13	37.05	4.7	184	21	91	8	2	92	SS
16	5.05.1986	03:35	37.78	38.00	6.0	218	19	116	30	33	123	SS
17	6.06.1986	10:39	37.91	38.01	5.8	205	1	115	1	25	115	SS
18	24.06.1989	03:09	35.94	36.75	5.1	299	73	115	17	25	115	NF
19	10.04.1991	01:08	36.12	37.30	5.3	327	58	104	24	4	94	NF
20	10.02.1994	06:15	35.89	36.93	4.9	156	31	51	23	148	58	UF
21	21.01.1995	03:48	36.25	37.37	4.5	137	81	267	6	176	86	NF
22	13.04.1995	20:23	36.20	37.42	4.9	260	85	80	5	170	80	NF
23	22.01.1997	17:57	35.96	36.21	5.7	219	41	104	26	24	114	UF
24	22.01.1997	18:22	36.03	36.26	4.3	177	27	283	27	5	95	UF
25	22.01.1997	18:24	36.06	36.13	5.2	206	55	94	14	10	100	NF
26	23.01.1997	14:53	36.05	36.26	4.2	354	31	99	23	2	92	UF
27	3.01.1998	21:15	35.77	37.20	4.1	175	17	77	25	171	81	SS
28	28.03.1998	00:30	38.75	38.20	4.5	206	39	98	21	15	105	UF
29	9.05.1998	15:38	38.95	38.25	5.1	207	10	117	0	27	117	SS
30	27.06.1998	13:55	35.33	36.53	6.2	184	4	275	11	4	94	SS
31	28.06.1998	03:59	35.49	36.92	4.9	181	21	89	5	180	90	SS
32	4.07.1998	02:15	35.44	36.90	5.1	193	14	287	14	15	105	SS
33	4.12.1998	04:59	35.58	37.01	4.0	197	7	289	21	18	108	SS
34	14.12.1998	13:06	35.79	38.92	4.7	205	9	300	28	27	117	SS
35	15.01.1999	02:04	35.85	37.04	4.2	352	18	261	3	172	82	SS
36	6.04.1999	00:08	38.23	39.37	5.4	185	24	291	31	12	102	UF
37	10.06.1999	23:25	35.96	37.38	4.5	184	4	275	11	4	94	SS
38	11.06.1999	05:25	36.80	39.53	4.9	49	54	303	11	37	127	NF
39	24.08.1999	17:33	32.68	39.41	4.9	349	27	246	24	162	72	UF
40	2.01.2000	20:28	38.96	38.30	3.7	208	36	112	8	24	114	SS
41	2.04.2000	11:41	37.08	37.61	4.2	170	18	272	33	175	85	SS
42	2.04.2000	17:26	37.32	37.54	4.0	178	11	270	10	179	89	SS
43	7.05.2000	09:08	38.83	38.26	4.2	186	6	278	17	7	97	SS
44	7.05.2000	23:10	38.91	38.27	4.4	6	7	275	11	5	95	SS
45	12.05.2000	03:01	36.06	36.99	4.7	196	79	291	1	21	111	NF
46	27.05.2000	07:49	35.28	36.23	4.2	34	36	285	24	23	113	UF
47	17.01.2001	12:09	36.21	37.07	4.4	21	31	288	5	19	109	SS

48	25.06.2001	13:28	36.27	37.22	4.6	165	74	64	3	155	65	NF
49	25.09.2001	11:53	32.33	35.97	4.5	189	16	281	6	10	100	SS
50	18.10.2001	15:50	35.22	36.86	4.5	7	39	129	33	24	114	UF
51	31.10.2001	12:33	36.25	37.26	4.9	125	80	305	10	35	125	NF
52	23.05.2002	01:08	36.35	37.41	4.4	197	48	107	1	17	107	NS
53	19.11.2002	01:25	38.39	38.02	4.7	201	13	294	9	22	112	SS
54	14.12.2002	01:02	36.19	37.47	4.8	55	81	292	5	23	113	NF
55	26.02.2003	03:08	36.27	35.86	4.4	250	6	160	3	70	160	SS
56	13.07.2003	01:48	38.95	38.28	5.5	207	0	297	1	27	117	SS
57	24.09.2003	08:13	38.23	39.55	4.7	230	6	138	16	49	139	SS
58	26.02.2004	04:13	38.25	37.91	4.8	202	18	311	46	29	119	TS
59	18.08.2004	05:57	34.40	36.80	4.3	123	60	300	30	28	118	NF
60	4.07.2005	21:33	36.08	39.16	4.5	30	68	128	3	37	127	NF
61	30.07.2005	21:45	33.11	39.39	5.2	169	4	79	1	169	79	SS
62	31.07.2005	00:45	33.13	39.43	4.3	322	11	226	29	139	49	SS
63	31.07.2005	15:18	33.08	39.42	4.6	338	26	68	1	158	68	SS
64	31.07.2005	23:41	33.10	39.44	4.8	161	11	69	13	160	70	SS
65	1.08.2005	00:45	33.07	39.44	4.7	164	0	74	11	164	74	SS
66	6.08.2005	09:09	33.10	39.39	4.7	336	5	68	18	157	67	SS
67	18.10.2005	07:17	39.00	38.78	4.3	229	10	136	16	48	138	SS
68	26.11.2005	15:56	38.86	38.21	5.1	206	39	104	15	18	108	SS
69	9.10.2006	05:01	35.56	35.88	4.1	276	69	64	18	150	60	NF
70	14.02.2007	11:59	34.14	39.76	3.9	345	61	229	14	144	54	NF
71	18.05.2007	23:27	33.26	37.32	4.6	154	46	44	18	141	51	NS
72	24.08.2007	02:53	37.45	38.15	4.4	184	37	295	26	16	106	UF
73	15.09.2007	05:26	37.00	37.81	4.4	233	3	340	79	54	144	TF
74	15.09.2007	23:28	36.92	37.79	4.3	221	40	77	44	16	106	UF
75	24.09.2007	23:21	35.47	39.77	3.5	206	29	97	31	16	106	UF
76	13.12.2007	18:06	33.07	38.83	4.9	184	23	83	25	178	88	UF
77	20.12.2007	09:48	33.16	39.41	5.7	167	1	76	24	167	77	SS
78	26.12.2007	23:47	33.11	39.42	5.6	187	12	93	20	5	95	SS
79	27.12.2007	13:48	33.14	39.44	4.7	2	50	92	0	2	92	NS
80	15.03.2008	10:15	33.05	39.50	4.8	360	20	265	13	178	88	SS
81	14.04.2008	15:16	35.91	39.95	3.4	161	8	57	58	158	68	TF
82	3.09.2008	02:22	38.50	37.51	5.0	175	15	85	1	175	85	SS
83	12.11.2008	14:03	35.52	38.84	5.1	186	23	93	5	5	95	SS
84	17.06.2009	04:29	36.02	36.05	4.6	322	70	101	15	7	97	NF
85	10.09.2009	18:29	32.52	37.94	4.8	55	82	292	4	22	112	NF
86	11.09.2009	01:58	32.44	37.94	4.9	52	80	286	7	17	107	NF
87	1.02.2010	04:01	38.12	39.56	4.5	40	21	133	10	42	132	SS
88	1.02.2010	04:01	37.99	39.56	4.5	40	21	133	10	42	132	SS
89	23.03.2010	19:33	38.65	39.89	3.7	15	45	281	4	12	102	NS
90	16.08.2010	06:41	38.92	39.72	3.6	200	13	109	8	19	109	SS
91	17.09.2010	10:17	38.95	38.14	4.9	185	21	275	1	5	95	SS
92	14.11.2010	23:08	36.08	36.48	4.9	274	82	117	8	27	117	NF
93	14.11.2010	23:08	36.01	36.59	4.9	332	78	129	12	38	128	NF
94	16.11.2010	10:50	36.32	37.33	4.7	37	57	242	31	163	73	NF
95	29.06.2011	19:48	35.87	37.41	4.4	14	6	249	80	13	103	TF
96	16.08.2011	07:53	35.90	39.08	4.1	24	28	293	1	24	114	SS
97	22.09.2011	03:22	38.60	39.68	5.6	195	13	104	6	14	104	SS
98	16.02.2012	11:01	37.46	38.65	4.6	157	74	305	15	33	123	NF
99	25.05.2012	11:22	38.72	38.16	4.4	25	11	116	4	25	115	SS
100	22.07.2012	09:26	36.23	37.34	4.8	353	77	120	7	28	118	NF
101	16.09.2012	07:54	35.77	37.44	4.6	210	10	117	16	29	119	SS
102	19.09.2012	09:17	37.12	37.28	5.0	178	35	71	22	169	79	UF
103	5.10.2012	10:25	33.80	39.35	4.6	161	42	71	0	161	71	NS
104	16.10.2012	01:16	37.11	37.30	4.5	169	32	262	4	170	80	SS
105	16.10.2012	10:25	37.16	37.27	4.5	194	19	98	19	11	101	SS
106	13.11.2012	23:55	37.12	37.20	4.9	167	19	71	19	164	74	SS
107	14.11.2012	00:02	37.14	37.28	4.4	169	24	278	35	177	87	UF

108	18.11.2012	19:18	37.13	37.33	3.9	263	27	121	57	72	162	TF
109	1.12.2012	03:51	38.35	37.47	4.1	199	14	88	56	14	104	TF
110	25.12.2012	15:35	34.10	39.85	3.9	352	1	258	75	172	82	TF
111	30.12.2012	09:11	35.72	37.48	4.1	7	23	119	41	16	106	UF
112	8.01.2013	06:05	37.96	37.93	4.3	6	1	276	2	6	96	SS
113	8.01.2013	06:15	37.96	37.92	4.4	195	6	105	6	15	105	SS
114	12.02.2013	20:20	36.95	37.11	3.7	177	30	84	6	175	85	SS
115	4.04.2013	06:34	37.12	37.32	3.7	0	32	90	0	0	90	SS
116	14.04.2013	18:25	36.21	37.31	3.5	13	15	270	39	8	98	SS
117	1.05.2013	06:47	37.10	37.31	3.7	339	10	245	23	157	67	SS
118	1.05.2013	06:50	37.11	37.30	3.9	351	68	248	5	160	70	NF
119	6.05.2013	18:33	37.13	37.30	3.8	331	20	62	3	152	62	SS
120	1.06.2013	19:41	39.03	38.33	3.0	20	24	113	6	22	112	SS
121	4.06.2013	04:12	37.41	38.62	4.1	180	69	313	15	39	129	NF
122	4.06.2013	23:55	37.36	38.61	3.3	215	13	308	15	37	127	SS
123	7.06.2013	00:33	32.03	37.33	3.3	300	90	210	0	120	30	NF
124	7.06.2013	19:56	31.98	37.35	3.2	37	73	236	16	148	58	NF
125	7.06.2013	19:57	32.05	37.35	3.2	16	72	230	15	143	53	NF
126	16.06.2013	20:31	37.08	38.11	4.6	35	3	304	24	34	124	SS
127	28.06.2013	19:30	32.75	39.18	3.0	307	65	46	4	135	45	NF
128	4.07.2013	19:01	32.15	39.37	3.5	346	28	227	42	154	64	UF
129	24.07.2013	03:41	35.86	37.78	3.0	315	70	135	20	45	135	NF
130	26.07.2013	00:22	35.87	36.06	4.0	248	57	79	33	176	86	NF
131	27.07.2013	20:13	35.61	37.00	3.6	190	19	291	29	15	105	SS
132	4.08.2013	19:59	36.12	37.58	3.5	189	69	86	5	177	87	NF
133	10.08.2013	11:56	33.40	38.40	3.0	181	21	279	21	5	95	UF
134	28.08.2013	06:26	38.95	38.36	4.1	20	5	290	2	20	110	SS
135	29.08.2013	23:20	38.93	38.36	3.1	197	15	294	25	20	110	SS
136	30.08.2013	07:54	36.98	39.36	3.1	184	34	90	6	2	92	SS
137	17.09.2013	10:37	35.65	36.85	3.4	30	30	210	60	30	120	TF
138	18.09.2013	21:10	36.20	37.35	3.9	203	65	113	0	23	113	NF
139	20.09.2013	02:02	36.99	37.37	3.0	182	22	81	26	176	86	UF
140	5.10.2013	21:31	33.14	37.03	3.3	172	36	274	15	179	89	SS
141	10.10.2013	09:48	33.40	36.87	3.1	269	54	152	18	69	159	NF
142	21.10.2013	04:09	34.16	39.77	3.4	17	60	279	4	11	101	NF
143	23.10.2013	12:24	34.38	36.29	4.7	192	63	83	9	176	86	NF
144	1.11.2013	01:27	35.19	38.10	3.6	347	2	78	25	167	77	SS
145	3.11.2013	22:42	36.19	37.14	3.0	214	60	116	4	28	118	NF
146	7.11.2013	06:39	36.20	37.35	4.1	182	59	279	4	8	98	NF
147	8.11.2013	05:55	36.77	38.51	3.6	35	5	125	2	35	125	SS
148	18.11.2013	06:18	36.03	37.90	3.4	198	70	106	1	16	106	NF
149	10.12.2013	09:30	36.05	37.84	3.0	355	1	263	70	175	85	TF
150	21.12.2013	10:17	36.42	37.42	3.3	170	75	80	0	170	80	NF
151	27.12.2013	05:44	37.14	37.31	3.4	157	63	265	9	172	82	NF
152	28.12.2013	17:05	36.35	38.48	3.0	177	9	268	5	177	87	SS
153	30.12.2013	00:02	38.36	37.85	3.7	39	30	131	5	40	130	SS
154	7.01.2014	21:17	38.35	37.86	3.1	187	3	278	10	7	97	SS
155	10.01.2014	13:20	36.23	37.27	4.2	185	65	284	4	13	103	NF
156	7.02.2014	04:48	36.23	37.30	3.8	177	70	85	1	175	85	NF
157	8.02.2014	17:48	37.35	38.61	3.3	16	4	108	24	17	107	SS
158	14.02.2014	00:33	35.99	36.73	4.7	194	59	291	4	20	110	NF
159	21.02.2014	00:54	37.43	37.68	3.2	17	13	108	8	18	108	SS
160	22.02.2014	15:42	36.42	37.42	4.5	179	44	83	7	175	85	NS
161	2.03.2014	04:25	35.21	36.75	4.3	236	75	102	10	14	104	NF
162	2.03.2014	04:29	35.18	36.76	3.5	211	27	102	33	22	112	UF
163	2.03.2014	05:33	35.17	36.77	3.0	196	10	105	3	16	106	SS
164	6.03.2014	13:40	35.86	37.78	3.0	187	10	53	76	5	95	TF
165	11.03.2014	10:23	31.90	38.48	3.7	211	39	315	17	40	130	SS
166	11.03.2014	13:56	38.08	37.24	3.1	156	4	250	40	157	67	UF
167	13.03.2014	14:28	38.09	37.21	3.2	5	6	95	8	5	95	SS

168	15.03.2014	09:39	36.28	37.13	3.3	175	16	286	50	1	91	TS
169	18.03.2014	17:01	37.14	37.32	3.2	355	2	85	5	175	85	SS
170	26.03.2014	14:00	38.62	38.11	4.3	59	24	327	4	58	148	SS
171	6.04.2014	22:06	34.56	36.87	3.2	166	70	74	1	164	74	NF
172	8.04.2014	03:54	35.86	37.02	3.0	347	32	108	39	1	91	UF
173	9.04.2014	00:37	38.40	38.13	3.0	185	24	68	45	175	85	UF
174	9.04.2014	12:27	36.77	38.49	3.0	214	8	305	13	35	125	SS
175	13.04.2014	08:00	33.67	36.69	3.4	168	9	262	23	170	80	SS
176	20.04.2014	12:28	36.21	37.71	3.6	109	45	15	4	106	16	NS
177	1.05.2014	07:36	37.38	39.49	4.4	8	59	105	4	14	104	NF
178	9.05.2014	13:14	35.59	37.02	3.1	31	15	289	36	26	116	SS
179	10.05.2014	22:45	38.17	38.68	3.0	359	2	90	25	179	89	SS
180	21.05.2014	23:26	36.32	37.26	3.2	242	69	139	5	50	140	NF
181	29.05.2014	21:22	34.17	36.28	3.2	149	79	59	0	149	59	NF
182	9.06.2014	03:38	36.03	36.71	4.9	138	41	241	14	146	56	NS
183	19.06.2014	05:21	35.69	37.50	3.1	189	1	99	15	9	99	SS
184	26.06.2014	07:29	37.08	37.30	3.0	321	10	116	79	142	52	TF
185	30.06.2014	14:40	38.99	38.43	3.2	4	30	105	17	10	100	SS
186	2.07.2014	14:22	35.80	37.05	3.0	221	35	101	36	26	116	UF
187	9.07.2014	07:27	38.01	39.54	3.4	91	26	346	28	84	174	UF
188	12.07.2014	21:58	35.89	36.58	3.9	157	54	258	8	165	75	NF
189	14.07.2014	14:08	36.11	37.06	3.2	120	65	260	19	164	74	NF
190	15.07.2014	11:45	36.68	39.49	3.0	217	10	83	76	35	125	TF
191	2.08.2014	07:38	32.46	37.50	3.0	295	72	149	15	62	152	NF
192	8.08.2014	15:01	37.90	37.89	3.1	14	10	284	0	14	104	SS
193	11.08.2014	04:10	36.70	39.48	3.3	39	70	307	1	37	127	NF
194	11.08.2014	04:22	36.68	39.48	3.9	115	5	358	79	114	24	TF
195	18.08.2014	22:54	39.00	39.20	3.2	64	68	311	9	44	134	NF
196	19.08.2014	04:19	36.94	37.08	3.0	182	10	87	28	180	90	SS
197	28.08.2014	10:22	36.91	37.08	4.0	206	31	102	22	18	108	UF
198	29.08.2014	00:19	34.37	36.57	3.2	164	44	273	19	176	86	NS
199	29.08.2014	23:03	38.79	38.33	3.1	357	7	87	7	177	87	SS
200	3.09.2014	03:15	35.91	36.51	3.5	150	19	245	16	153	63	SS
201	6.09.2014	22:25	35.82	38.36	3.3	298	72	82	15	169	79	NF
202	19.09.2014	19:17	39.09	38.47	3.5	15	90	285	0	15	105	NF
203	20.09.2014	02:52	38.77	39.16	4.4	44	55	139	4	48	138	NF
204	20.09.2014	03:09	39.32	38.43	3.5	161	8	57	58	158	68	TF
205	22.09.2014	21:33	36.27	39.94	3.0	340	8	75	34	162	72	SS
206	26.09.2014	21:24	37.47	38.13	3.4	39	1	130	10	39	129	SS
207	20.10.2014	15:45	38.68	38.17	3.9	202	27	298	12	25	115	SS
208	2.11.2014	04:58	39.25	38.47	3.7	19	8	123	59	22	112	TF
209	3.11.2014	21:39	36.28	38.29	3.2	141	0	231	80	141	51	TF
210	7.11.2014	17:20	34.64	36.96	3.5	214	26	117	14	30	120	SS
211	20.11.2014	20:12	34.73	39.70	3.0	353	24	260	6	172	82	SS
212	23.11.2014	08:54	36.28	38.29	3.4	332	5	229	69	150	60	TF
213	23.11.2014	12:07	39.17	38.31	3.0	80	54	339	8	72	162	NF
214	7.12.2014	08:49	34.54	36.75	3.6	319	10	51	11	140	50	SS
215	17.12.2014	14:24	37.35	37.28	3.0	43	29	137	8	45	135	SS
216	25.12.2014	06:52	35.77	37.69	3.2	190	21	280	2	10	100	SS
217	3.01.2015	23:24	37.89	37.89	3.5	54	10	145	3	54	144	SS
218	5.01.2015	06:46	38.82	38.32	3.9	65	70	333	1	63	153	NF
219	6.01.2015	22:16	34.45	36.93	4.0	129	55	224	4	133	43	NF
220	8.01.2015	18:44	36.80	37.10	4.7	146	65	245	4	154	64	NF
221	9.01.2015	21:54	36.19	37.41	3.5	131	68	282	19	8	98	NF
222	18.01.2015	16:01	38.81	38.32	3.7	36	17	132	17	39	129	SS
223	20.01.2015	13:27	33.89	38.45	3.0	312	39	219	3	130	40	SS
224	22.01.2015	19:27	36.30	37.40	3.9	258	65	100	23	15	105	NF
225	25.01.2015	22:21	36.32	36.91	3.5	201	55	106	4	17	107	NF
226	28.01.2015	14:25	38.50	38.10	3.6	197	9	84	68	14	104	TF
227	10.02.2015	04:01	36.02	35.80	4.3	187	33	279	3	8	98	SS

228	12.02.2015	18:52	38.46	38.13	3.8	358	5	107	74	179	89	TF
229	22.02.2015	10:06	36.70	39.29	3.0	13	24	104	4	14	104	SS
230	28.02.2015	22:03	34.53	37.44	3.0	206	21	110	14	23	113	SS
231	1.03.2015	02:16	36.82	37.07	3.5	163	18	71	8	162	72	SS
232	26.03.2015	02:14	35.60	38.88	3.7	30	4	300	3	30	120	SS
233	27.03.2015	12:19	38.37	39.36	3.0	1	17	101	30	6	96	SS
234	28.03.2015	05:04	35.60	38.89	3.9	14	30	106	3	15	105	SS
235	28.03.2015	10:08	36.42	37.47	4.2	201	55	106	4	17	107	NF
236	30.03.2015	03:16	37.73	38.11	3.2	208	6	117	13	27	117	SS
237	31.03.2015	04:16	36.87	37.01	3.4	265	68	114	19	28	118	NF
238	6.04.2015	00:27	36.82	37.10	3.0	157	65	256	4	165	75	NF
239	6.04.2015	04:35	34.57	37.09	3.0	220	5	310	2	40	130	SS
240	11.04.2015	15:23	33.65	38.70	3.0	260	65	138	14	52	142	NF
241	17.04.2015	11:49	38.81	37.53	3.7	350	11	90	41	174	84	TS
242	19.04.2015	02:17	39.00	38.45	3.1	150	46	44	15	139	49	NS
243	24.04.2015	22:18	35.29	39.79	3.3	313	63	61	9	148	58	NF
244	25.04.2015	21:57	38.62	38.15	3.0	29	18	122	7	30	120	SS
245	5.05.2015	19:37	33.20	39.06	3.1	300	24	210	0	120	30	SS
246	29.07.2015	00:56	34.95	36.58	4.9	352	62	85	2	175	85	NF
247	29.07.2015	22:01	34.94	36.58	4.9	127	64	272	22	176	86	NF
248	29.07.2015	22:01	34.87	36.44	5.0	132	68	275	18	1	91	NF
249	26.08.2015	23:01	36.93	37.33	4.0	161	82	270	3	180	90	NF
250	3.10.2015	21:08	38.93	38.18	3.8	12	0	282	27	12	102	SS
251	29.11.2015	00:28	37.75	38.82	5.1	32	26	302	0	32	122	SS
252	29.11.2015	00:28	37.87	38.90	5.0	204	4	296	14	24	114	SS
253	9.12.2015	09:03	37.92	38.88	4.5	22	18	290	6	21	111	SS
254	10.01.2016	17:40	34.33	39.72	5.0	323	12	232	4	143	53	SS
255	2.02.2016	14:21	37.84	38.84	4.1	50	11	318	8	49	139	SS
256	18.02.2016	07:56	35.84	39.01	3.9	0	49	107	14	12	102	NS
257	31.03.2016	21:33	35.85	36.97	4.2	6	16	96	3	6	96	SS
258	7.04.2016	11:11	35.09	37.92	3.8	357	69	99	5	8	98	NF
259	23.04.2016	19:51	36.62	36.91	3.7	162	36	278	31	176	86	UF
260	17.08.2016	01:07	38.15	38.70	4.2	198	7	83	73	16	106	TF
261	16.09.2016	05:12	36.90	37.21	3.6	185	42	86	11	179	89	NS
262	20.11.2016	22:52	38.59	39.95	3.8	344	53	110	24	10	100	NF
263	3.02.2017	06:33	38.09	38.69	3.7	27	12	292	23	25	115	SS
264	25.02.2017	21:06	36.10	37.01	4.5	347	82	253	1	163	73	NF
265	2.03.2017	11:07	38.45	37.53	5.6	181	24	274	6	2	92	SS
266	2.03.2017	17:03	38.50	37.58	3.7	176	15	272	21	179	89	SS
267	10.03.2017	22:23	38.51	37.58	3.7	345	24	83	18	169	79	SS
268	28.03.2017	21:53	37.18	38.29	4.0	22	24	120	18	26	116	SS
269	18.08.2017	04:30	37.54	37.57	4.0	196	29	95	19	10	100	SS
270	19.01.2018	13:53	38.82	38.29	4.1	185	4	95	8	5	95	SS
271	24.04.2018	00:34	38.50	37.58	5.1	338	4	68	0	158	68	SS
272	21.05.2018	01:09	38.60	37.46	4.0	142	8	232	6	142	52	SS
273	3.07.2018	13:16	37.40	37.69	4.1	199	4	109	1	19	109	SS
274	31.07.2018	14:36	36.08	37.02	4.1	196	52	314	20	36	126	UF
275	4.08.2018	07:09	36.31	37.46	4.3	355	23	264	3	174	84	SS
276	19.08.2018	15:22	36.39	37.38	4.8	203	36	96	22	13	103	UF
277	2.10.2018	15:29	37.40	37.69	4.4	201	8	292	1	21	111	SS
278	10.10.2018	09:08	35.85	37.43	4.1	24	22	283	26	18	108	UF
279	27.12.2018	14:36	38.63	39.56	4.1	49	44	265	40	20	110	UF
280	2.02.2019	12:20	35.82	37.27	4.3	9	3	278	21	8	98	SS

CURRICULUM VITAE

PERSONAL INFORMATION

Surname, Name : Shah, Syed Tanvir
Nationality : Pakistani (Pak)
Date and Place of Birth : 1 September 1987, Swabi
Phone : +90 5078249677
E-mail : e195093@metu.edu.tr

EDUCATION

Degree	Institution	Year of Graduation
MS	METU, Geological Engineering	2015
BS	Univ. of Peshawar, Geology	2010
High School	Islamia College Peshawar, Peshawar	2005

FOREIGN LANGUAGES

Advanced English, Basic Turkish

PUBLICATIONS

1. Gülerce, Z., Shah, S. T., Menekşe, A., Özacar, A. A., Kaymakci, N. and Çetin, K. O. 2017. Probabilistic Seismic-Hazard Assessment for East Anatolian Fault Zone Using Planar Fault Source Models, Bulletin of the Seismological Society of America, 107(5), 2353-2366.

HOBBIES

Cricket, Football, Movies